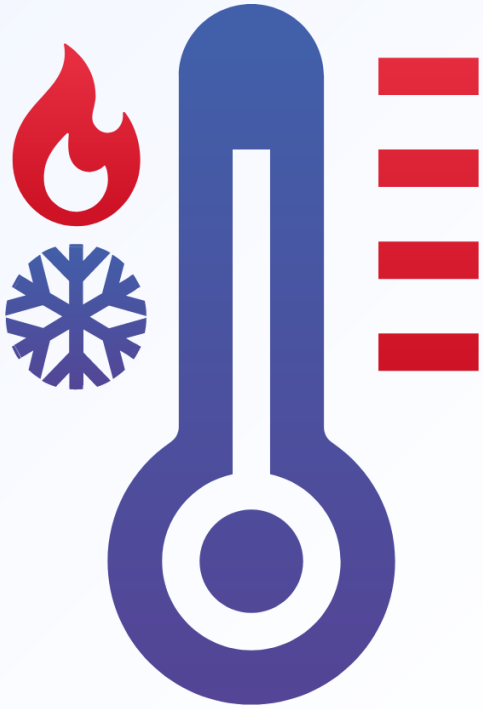
Vol. 47 No. 1 (2026)

ARCHIVES OF THERMODYNAMICS

ISSN: 1231-0956
ISSN: 2083-6023 (Online)



Co-published by

Institute of Fluid Flow Machinery
Polish Academy of Sciences

Committee on Thermodynamics and Combustion
Polish Academy of Sciences

WYDAWNICTWO IMP PAN

Aims and Scope

The aim of the quarterly journal Archives of Thermodynamics (AoT) is to disseminate knowledge between scientists and engineers worldwide and to provide a forum for original research conducted in the field of thermodynamics, heat transfer, fluid flow, combustion and energy conversion in various aspects of thermal sciences, mechanical and power engineering. Besides original research papers, review articles are also welcome.

The journal scope of interest encompasses in particular, but is not limited to:

- Classical and extended non-equilibrium thermodynamics
- Thermodynamic analysis including exergy
- Thermodynamics of heating and cooling
- Thermodynamics of nuclear power generation
- Thermodynamics in defence engineering
- Advances in thermodynamics
- Experimental, theoretical and numerical heat transfer
- Thermal and energy system analysis
- Renewable energy sources including solar energy
- Secondary fuels and fuel conversion
- Heat and momentum transfer in multiphase flows
- Nanofluids
- Energy transition
- Advanced energy carriers
- Energy storage and efficiency
- Energy in buildings
- Hydrogen energy
- Combustion and emissions
- Turbomachinery
- Thermal and energy system analysis
- Integrated energy systems
- Distributed energy generation
- Thermal incineration of wastes
- Waste heat recovery.

Supervisory Editors

- K. Badyda, Warsaw University of Technology, Poland
- M. Lackowski, Institute of Fluid Flow Machinery, Gdańsk, Poland

Honorary Editor

- J. Mikielewicz, Institute of Fluid Flow Machinery, Gdańsk, Poland

Editor-in-Chief

- P. Ocłoń, Cracow University of Technology, Cracow, Poland

Section Editors

- P. Lampart, Institute of Fluid Flow Machinery, Gdańsk, Poland
- S. Polesek-Karczewska, Institute of Fluid Flow Machinery, Gdańsk, Poland
- I. Szczygieł, Silesian University of Technology, Gliwice, Poland
- A. Szlęk, Silesian University of Technology, Gliwice, Poland

Technical Editors

- J. Frączak, Institute of Fluid Flow Machinery, Gdańsk, Poland
- S. Łopata, Institute of Fluid Flow Machinery, Gdańsk, Poland

Members of Programme Committee

- D. Kardaś, Inst. Fluid Flow Mach., Gdańsk, Poland (chairman)
- J. Badur, Inst. Fluid Flow Mach., Gdańsk, Poland
- T. Chmielniak, Silesian Univ. Tech., Gliwice, Poland
- P. Furmański, Warsaw Univ. Tech., Poland
- R. Kobyłecki, Częstochowa Univ. Tech., Poland
- S. Pietrowicz, Wrocław Univ. Sci. Tech., Poland
- J. Wajs, Gdańsk Univ. Tech., Poland

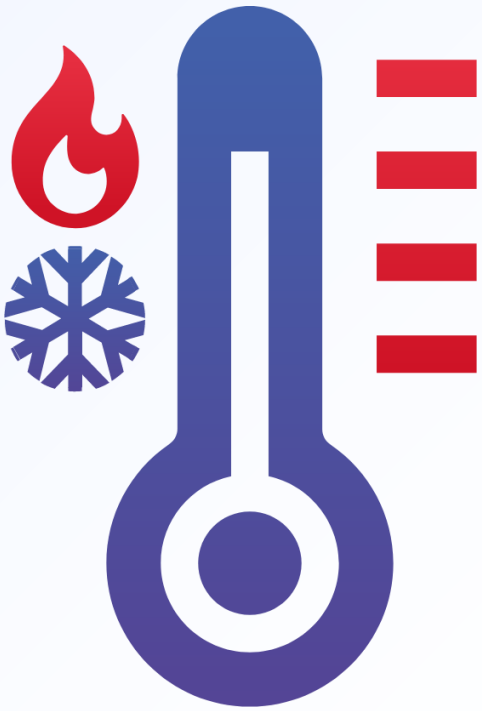
International Advisory Board

- J. Bataille, Ecole Centr. Lyon, France
- W. Błasiak, Royal Inst. Tech., Stockholm, Sweden
- A.C. Benim, Univ. Appl. Sci., Duesseldorf, Germany
- G.P. Celata, ENEA, Rome, Italy
- L.M. Cheng, Zhejiang Univ., Hangzhou, China
- M. Colaco, Federal Univ. Rio de Janeiro, Brazil
- J.M. Delhaye, CEA, Grenoble, France
- M. Giot, Univ. Catholique Louvain, Belgium
- K. Hooman, Univ. Queensland, Australia
- D. Jackson, Univ. Manchester, UK
- D.F. Li, Kunming Univ. Sci. Tech., China
- K. Kuwagi, Okayama Univ. Science, Japan
- J.P. Meyer, Univ. Pretoria, South Africa
- S. Michaelides, Texas Christian Univ., USA
- W. Muschik, Tech. Univ., Berlin, Germany
- I. Müller, Tech. Univ., Berlin, Germany
- H. Nakayama, JAEA, Japan
- S. Nizetic, Univ. Split, Croatia
- H. Orlande, Federal Univ. Rio de Janeiro, Brazil
- M. Podowski, Rensselaer Polyt. Inst., USA
- R.V. Rao, Sardar Vallabhbhai Nat. Inst. Techn., India
- A. Rusanov, Inst. Mech. Eng. Probl., Kharkiv, Ukraine
- A. Vallati, Sapienza Univ. Rome, Italy
- M.R. von Spakovsky, Virginia Polyt. Inst., USA
- H.R. Yang, Tsinghua Univ., Beijing, China

Vol. 47 No. 1 (2026)

ARCHIVES OF THERMODYNAMICS

ISSN: 1231-0956
ISSN: 2083-6023 (Online)



Co-published by

Institute of Fluid Flow Machinery
Polish Academy of Sciences

Committee on Thermodynamics and Combustion
Polish Academy of Sciences

WYDAWNICTWO IMP PAN

Editorial Office
IMP PAN Publishers
Institute of Fluid Flow Machinery, Fiszera 14, 80-231 Gdańsk, Poland,
Phone: (+48) 58-341-12-71 int. 230, e-mail: redakcja(at)imp.gda(.)pl
https://www.imp.gda.pl/archives-of-thermodynamics/
Journals PAS – Electronic Library Polish Academy of Sciences
https://journals.pan.pl/ather

Subscription outside Poland
From 2024, Archives of Thermodynamics appear only in electronic version as an open access journal. However, printed archive volumes or issues are still available. The price of a full volume outside Poland is **120 EUR**. The price of a single issue is **30 EUR**. Archived volumes or issues are available on request. Orders should be sent directly to IMP PAN Publishers:
Institute of Fluid-Flow Machinery,
Fiszera 14, 80-231 Gdansk, Poland,
e-mail: redakcja(at)imp.gda.pl or jfrk(at)imp.gda(.)pl or jrybka(at)imp.gda(.)pl.
Payments should be transferred to the bank account of IMP PAN:
IBAN 28 1130 1121 0006 5498 9520 0011 at Bank Gospodarstwa Krajowego; Code SWIFT: GOSKPLPW.

Prenumerata w Polsce
Od 2024, czasopismo ukazuje się tylko w formie elektronicznej otwartej. Osiągalne są jednak wydania papierowe archiwalne. Cena pojedynczego numeru wynosi **50 PLN**. Cena rocznika **200 PLN**. Zamówienia z określeniem numeru (rocznika), nazwiskiem i adresem odbiorcy należy kierować bezpośrednio do Wydawcy:
Instytut Maszyn Przepływowych PAN
ul. Fiszera 14, 80-231 Gdańsk,
e-mail: redakcja(at)imp.gda(.)pl lub jfrk(at)imp.gda(.)pl lub jrybka(at)imp.gda(.)pl.
Wpłaty prosimy kierować na konto Instytutu Maszyn Przepływowych PAN:
nr 28 1130 1121 0006 5498 9520 0011 w Banku Gospodarstwa Krajowego.

Articles in Archives of Thermodynamics are abstracted and indexed within:
Arianta • Baidu Scholar • BazTech • Cabell's Directory • Chemical Abstracts Service (CAS) – CAplus • CNKI Scholar (China National Knowledge Infrastucture) • CNPIEC • EBSCO • Elsevier – SCOPUS • Genamics JournalSeek • Google Scholar • Inspec • Index Copernicus • J-Gate • Journal Citation Reports (ESCI) • Journal TOCs • Naviga (Softweco) • POL-index • Polymer Library • Primo Central (ExLibris) • ProQuest • ReadCube • SCImago (SJR) • TDNet • TEMA Technik und Management • Ulrich's Periodicals Directory/Ulrichsweb • Web of Science (Core Collection) • WorldCat (OCLC)

ISSN 1231-0956
ISSN 2083-6023 (Online)
Copyright © 2026 by the Authors under license CC BY-NC-ND 4.0.
Publication funding of this journal is provided by resources of the Polish Academy of Sciences and the Institute of Fluid Flow Machinery

Contents

1) Balakrishnan Varun Kumar, Parthasarathy Rajesh Kanna, Chithirai Pon Selvan, Dawid Taler, Tomasz Sobota, Jan Taler
Machine Learning Approaches for Predicting and Optimising Thermal Performance of Solar Collectors 5–23

2) Jan Taler, Dawid Taler
An alternative formulation of the method of weighted residuals for the approximate solving of heat conduction problems 25–41

3) Farqad Rasheed Saeed, Hussein Fawzi Hussein, Natheer Basheer Mahmood
Finding a Correlation for Predicting the Effective Thermal Conductivity of CNT Nanofluid 43–53

4) Aleksandra Dzido, Piotr Krawczyk, Adrián Mota-Babiloni
Simulation-Based Design of a Two-Stage Heat Pump System Utilising Treated Wastewater for Urban Heating Applications 55–69

5) A. Manikandan, R. Thamizhvel, K. Kalaiselvan, S. Jassir Iqbal
Comparative Analysis of Performance and Emission Characteristics of a CI Engine Fueled with Biodiesel and Pyrolytic Oil Derived from Cottonseed 71–78

6) Maneesh Singh, Prashant Saini, Chandrakant Mishra, Saif Nawaz Ahmad
Implication of SiO_2 nanoparticles with novel water hyacinth biodiesel-diesel blends to improve the performance and emission parameters of a diesel engine 79–88

7) Rajammagari Hussain Vali, Vemuri Sai Srikanth, Mohammad Mujtaba Ahmed, A. Gouse Peera, P. Srikar
Optimising Injection Strategies and EGR in Modified Piston Diesel Engines Fuelled with Waste Plastic Oil 89–100

8) Ravi Pippal, Aditi Agrawal, Akshita, Tulip Biswas, Deepali, Pushpendra Kumar Shukla, Sumit Sinha-Ray
Heat transfer enhancement by drop impact onto a nanotextured superheated surface 101–111

9) Julian Piotr Jędrzejewski, Sebastian Lepszy, Sebastian Rulik
One-dimensional model of solid oxide fuel cell for advanced hybrid energy systems analysis 113–123

10) Tomasz Zygmunt Kaczmarczyk
Experimental investigation into the influence of heat source power on the performance of a scroll expander in an organic Rankine cycle system using HFE-7100 fluid 125–136

11) Hesham Hassanin ElKhatib, Asmaa Abo Elnoura, Ahmed Ramadan, Said Kotb, Magdy Zaky, Samy Dwidar
Safety enhancement of the Egyptian Second Research Reactor to reduce the effect of loss-off site power supply 137–144

12) Mohammed Wahody Eraiby, Abdulkhodor Kathum Nassir
Review of the Modified Kalina Cycle for Cogeneration Systems (MKCS) 145–160

13) Sachin Kaushik, Subash Chandra Ram, Chandra Kishor, Sunii Chamoli
Parametric Analysis of Heat Transfer and Flow Characteristics of the Cross-Flow Heat Exchanger with a Backwards Splitter Plate Using the Computational Fluid Dynamics (CFD) Model 161–176

14) Santhosh Kasula, M. N. Raja Shekar
Heat and Mass Transfer with Entropy Generation in Immiscible Fluid Flow through a Vertical Channel under Slip and Non-Uniform Thermal Conditions 177–194

15) Yining Shen
Energy consumption prediction and energy-saving retrofit design for office buildings in climate adaptation 195–204

16) Jarosław Mikielewicz, Dariusz Mikielewicz
Physical modelling in heat and fluid flow 205–212

17) M. S. Karthik, Mangalpady Aruna, P. Siva Kota Reddy
An Innovative Device for Measuring Thermal Conductivity of Solids Utilising Transient Measurement Methods 213–226

18) Jincheng Su, Jiliang Wang, Wei Zhou, Xiaozhuang Yang, Qinghua Miao, Bing Wang
Smart thermal management of bio-based aerogels: A paradigm shift from energy localisation to zero-energy anti-icing 227–235

19) Youcef Maalem, Hakim Madani
Novel design and energy analysis of hybrid system activated by low-grade thermal energy conversion 237–253

Co-published by
Institute of Fluid-Flow Machinery
Polish Academy of Sciences
Committee on Thermodynamics and Combustion
Polish Academy of Sciences

Copyright©2026 by the Authors under licence CC BY-NC-ND 4.0

http://www.imp.gda.pl/archives-of-thermodynamics/

Machine Learning Approaches for Predicting and Optimising Thermal Performance of Solar Collectors

Balakrishnan Varun Kumar[a], Parthasarathy Rajesh Kanna[b], Chithirai Pon Selvan[c], Dawid Taler[d], Tomasz Sobota[d], Jan Taler[e*]

[a]Thiagarajar College of Engineering, Madurai 625 015, Tamil Nadu, India
[b]CO_2 Research and Green Technologies Centre, Vellore Institute of Technology, Vellore 632014, Tamil Nadu, India
[c]School - Science and Engineering, Curtin University, Dubai, United Arab Emirates
[d]Cracow University of Technology, Faculty of Environmental Engineering and Energy, Department of Thermal Processes, Air Protection and Waste Utilization, Warszawska 24, 31-155 Cracow, Poland
[e]Cracow University of Technology, Faculty of Environmental Engineering and Energy, Department of Energy, Warszawska 24, 31-864 Cracow, Poland
*Corresponding author email: jan.taler@pk.edu.pl

Received: 08.08.2025; revised: 19.01.2026; accepted: 23.01.2026

Abstract

The application of machine learning techniques in the renewable energy sector has revolutionised the predictive modelling and optimisation of solar thermal systems. Solar air heaters with artificial roughness and phase change materials are widely used to enhance thermal performance, necessitating accurate thermo-hydraulic performance predictions for efficient design and operation. This study employs the XG-Boost machine learning model to predict thermo-hydraulic performance values based on experimental data obtained for polygonal and trapezoidal rib configurations at different relative roughness pitch ratios (p/e) and Reynolds numbers (Re = 2000 to 20000) in the absorber plate of a solar air heater. The experimental results reveal that a polygonal rib configuration with p/e = 7.5 exhibits the highest thermo-hydraulic performance value of 2.95 at Re = 4000, while the trapezoidal rib with p/e = 7.5 achieves a thermo-hydraulic performance of 2.93 at the same Reynolds number. The results were trained in the proposed machine learning model to validate the accuracy of predicted results. The coefficient of determination R^2, mean absolute percentage error, root mean squared error and mean absolute percentage error matrix were considered for the training and testing dataset. The model effectively captures the nonlinear thermal behaviour, achieving $R^2 = 0.976$, mean absolute error at 0.045, root mean squared error at 0.056 and mean absolute percentage error of 2.42%, demonstrating superior predictive capability. Further, this study provides the significance of plethora machine learning algorithms, data pre-processing strategies, feature selection and hybrid machine learning models for performance optimisation in solar air heaters. Additionally, few case studies highlight the practical implementation of machine learning in solar energy systems, demonstrating its potential for accurate prediction of thermal efficiency in real time assessment. Besides, it outlines future research directions, challenges, and emerging opportunities to advance machine learning applications in sustainable energy solutions. This „review-experimental" comparative article serves as a valuable resource for researchers and industry professionals, driving innovation in solar thermal energy systems through data-driven intelligence.

Keywords: Machine learning; Thermal performance; Solar collectors; Prediction models; Optimisation techniques; Renewable energy systems

Vol. 47(2026), No. 1, 5–23; doi: 10.24425/ather.2025.156852

Cite this manuscript as: Kumar, B.V., Kanna, P.R., Selvan, C.P., Taler, D., Sobota, T., & Taler, J. (2026). Machine Learning Approaches for Predicting and Optimising Thermal Performance of Solar Collectors. *Archives of Thermodynamics*, 47(1), 5−23.

1. Introduction

The abundant availability of solar radiation globally makes solar heating a highly viable and sustainable option for various applications in both domestic and industrial settings. With ongoing advancements and supportive policies, solar thermal energy is poised to play a significant role in meeting the world's heating needs while promoting environmental sustainability. Devices

Nomenclature

f – friction factor for the roughened configurations
f_o – friction factor for the smooth configurations
Nu – Nusselt number for the roughened configurations
Nu_o – Nusselt numbers for the smooth configurations
p/e – relative roughness parameter
R^2 – coefficient of determination
Re – Reynolds number
T_k – tree-based transformations learned by XG-boost

Greek symbols

α_k – model coefficients
β – bias term
η_{SC} – solar collector efficiency

Abbreviations and Acronyms

ALE – accumulated local effects
ANFIS – adaptive network-based fuzzy inference system
ANN – artificial neural networks
AT – ambient temperature
BNN – Bayesian neural networks
BPS – black pebble stone
BRT – boosted regression tree
CAPSC – corrugated absorber plate solar collector
CE – collector efficiency
CFD – computational fluid dynamics
CIT – collector inlet temperature
CNN – convolutional neural networks
COT – collector outlet temperature
CSP – concentrated solar power
DBN – deep belief networks
DCIT – drying chamber inlet temperature
DCOT – drying chamber outlet temperature
DT – decision trees
ELM – extreme learning machine
ENN – Elman neural network
ESE – energy storage element
FFS – forward feature selection
FPSC – flat plate solar collectors
GA – genetic algorithms
GBM – gradient boosting machines
GBRT – gradient boosting regression tree
GMDH – group method of data handling
GP – Gaussian processes
HE-ET – heat exchanger-evacuated tube
HGBR – hist gradient boosting regressor
HTF – heat transfer fluid
KNN – K-nearest neighbours
LR – linear regression
LSSVM – least squares support vector machines
LSTM – long short-term memory
MAE – mean absolute error
MAPE – mean absolute percentage error
MARS – multivariate adaptive regression splines
MC – moisture content
MWCNT – multi-wall carbon nanotube
MIM – metal insulator metal
ML – machine learning
MLR – multiple linear regression
MRMR – minimum redundancy – maximum relevance
MSE – mean squared error
NARX – nonlinear autoregressive exogenous
NF RV – nanofluid relative viscosity
NSE – Nash-Sutcliffe coefficient
OTA – optimal tilt angle
PCC – Pearson correlation coefficient
PCM – phase change materials
PDC – parabolic dish collector
PDP – partial dependence plot
PPO – proximal policy optimisation
PR – polynomial regression
PSO – particle swarm optimisation
PTC – parabolic trough solar collector
PVTC – photovoltaic thermal collector
PVT – photovoltaic thermal
RF – random forest
RMSE – root mean squared error
RNN – recurrent neural networks
SAH – solar air heater
SB – shot-basting nano-coating
SR – stacking regressor
STC – solar thermal collectors
SVR – support vector regression
SWCNT – single-wall carbon nanotube
SWH – solar water heater
TES – thermal energy storage
THP – thermo-hydraulic performance
TR – tweedie regressor
WI – Willmott's index
XG-boost – extreme gradient boosting

such as flat plate collectors (FPC), evacuated tube collectors (ETC) and concentrated solar power (CSP) were used in practice to generate heat energy for applications like drying agricultural products, providing hot water, cost-effective heating rooms during colder climates, generating high temperatures for industrial applications, etc. However, the performance of thermal efficacy in these collectors is very low owing to smooth surface absorber plates and limitation of the direct contact between the working fluid and the heating surface.

It needs design modification to augment the convective heat transfer between the working fluid and solid surface, like an absorber plate placed directly beneath of the solar radiation surface. Many researchers numerically and experimentally proved that implementing artificial rough surfaces in the absorber plates as an extension material acts to enhance the heat transfer rate. Rib or groove shapes such as broken arc rib [1], reverse L shape [2], S shape [3], W shape [4], discrete V-shaped rib [5], tri-angular rib and groove shaped rib [6], protruded shape [7], transverse square rib [8], discrete multi V rib in a staggered position [9], square duct with the internal surface [10] were positioned in the absorber plate with the varying pitch distance between ribs, varying height of rib, varying angle during positioning. Multiple shaped ribs arrangements in inline and staggered methods were investigated to ascertain the augmentation of thermal perfor-

mance. The research results reveal a significant improvement attained, such as thermo-hydraulic performance (THP) values having increased from 1.32 to a maximum of 1.89, specifically in the backwards trapezoidal-shaped rib in the solar collector.

Furthermore, to enhance heat transfer efficiency, nanofluids and hybrid nanofluid-based working fluids were introduced in solar collectors to maximise heat absorption during peak solar hours (11:00 AM to 3:00 PM), thereby optimising heat energy production for various heating applications. Hybrid nanofluids such as TiO_2-SiO_2 [11], Single-Wall Carbon Nano Tube (SWCNT), Multi-Wall Carbon Nano Tube (MWCNT) [12], MWCNT-Fe_3O_4/Water [13], Al_2O_3-CuO, TiO_2-Cu, Ag-MgO [14], MWCNT, Au-Cu/EO (EO – engine oil), and Cu-Al_2O_3 [15] were prepared in varying volume fractions (1%, 2%, 3%, and 4%) and utilised as working fluids in solar collectors integrated with artificial rough surfaces to enhance heat energy generation. Both numerical and experimental investigations revealed significant thermal performance improvements, ranging from 197% to 227%, depending on the nanofluid volume fraction used.

In continuation of the introduction of nanofluids, phase change materials are introduced to enhance heat transfer in solar applications. Both organic and inorganic phase change materials (PCMs), such as paraffin wax and high-latent-heat storage oils, were integrated into the solar collector. This integration enhances daytime heat generation while enabling the storage of thermal energy in high-latent-heat materials. The stored energy is then released during nighttime, facilitating prolonged heat distribution and ensuring consistent thermal performance over extended durations.

The study conducted by Kabeel et al. [16,17] investigated the performance of an FPC integrated with paraffin wax based phase change material (PCM) arranged in two different layers (2 cm and 4 cm) beneath the absorber plate in the heat storage chamber. PCM stored thermal energy during the daytime and released it at night. The results indicated that the 4 cm PCM layer maintained a temperature rise of 1.5°C to 7°C for 3.5 hours, while the 2 cm layer sustained a temperature increase of 1.5°C to 5.5°C for 2.5 hours after 6 pm. Additionally, the incorporation of fin-shaped ribs in the same setup further enhanced thermal performance, achieving a temperature rise of 8.6°C during nighttime.

Aymen et al. [18] investigated a rectangular cavity with PCM in a collector and reported that the maximum night-time temperature increased by 3–7°C, leading to a significant improvement in thermal efficiency. Sunil Raj and Eswarmoorthy [19] studied a V-shaped rib in a collector with paraffin wax-PCM blended with 10% of Al_2O_3. The research proved a 65% enhancement in thermal efficiency. Kalaiarasi et al. [20] investigated experimentally using a black copper tube with synthetic therminol-55 oil as the thermal energy storage (TES) system and reported achieving 67.7% thermal efficiency. It has been observed that enhancing the thermal performance of solar collectors involves employing various rib shapes with numerous modifications, such as varying pitch distances, rib heights and inclined rib positions. These design optimisations, when integrated with PCM, have been explored extensively in studies [21−23] to improve heat transfer efficiency and energy storage capabilities.

A comprehensive literature review reveals that although significant efforts have been devoted to enhancing solar collector performance through design modifications, hybrid nanofluids, and PCM integration, the novelty of the present work lies in emphasising machine learning–based frameworks as an integrated solution for accurate thermal performance prediction, adaptive control of operating parameters, predictive maintenance and sustainability assessment under dynamic climatic conditions. The primary objective of this study is to critically evaluate machine learning (ML) methodologies applied to solar collectors, identify dominant thermo-hydraulic and environmental parameters influencing performance, assess ML capabilities in fault detection, energy output forecasting, and techno-economic optimisation, and to highlight research gaps for the development of intelligent, reliable and high-efficiency solar thermal systems.

2. Machine learning algorithms in practice

To predict the thermal performance of solar collectors across diverse domestic and industrial applications, an ML algorithm plays a significant role in analysing the complexity of the experimental setup, including intricate patterns and practical key factors such as solar radiation, ambient temperature and thermal efficiency. ML models like gradient boosting machines (GBM) or neural networks (ANN) are widely used for predicting thermal efficiency and outlet temperature. Recurrent neural networks (RNN) and long short-term memory (LSTM) models are used for time-dependent variables at the hourly time scale. Bayesian models and Gaussian processes support the prediction of uncertainty in thermal performance.

Besides, ML algorithms are capable of analysing multiple parameters, such as solar intensity, water flow rate, the impact of solar collector tilt angle, ambient humidity, etc., using a randomised lasso algorithm based on real-time data recorded in a database to reduce experimental costs and save time and resources for further testing. By combining data-driven approaches with traditional thermodynamic principles, ML not only enhances the design and operation of solar thermal systems but also enables innovative solutions for achieving higher efficiency and reliability in renewable energy applications. The detailed machine learning models and algorithms that play a pivotal role in the prediction of thermal performance in solar energy-based applications are listed, and their significant applications are presented in Table 1 [24−26].

2.1. Regression techniques

They are supervised machine learning methods used to predict the relationship between dependent such as thermal performances, and independent variables, such as inlet temperature, solar intensity, mass flow rate, etc. It is classified into linear regression (LR) and polynomial regression (PR) and is suitable for analysing environmental impacts, optimising system design, forecasting time series, and reducing costs in solar thermal performance prediction.

2.2. Tree-based models

They are capable of complex interactions and non-linear relationships between input variables such as solar intensity, ambient temperature and humidity and can be categorised into:

a) decision trees (DT),
b) random forest (RF),
c) gradient boosting machines (GBM) and extreme gradient boosting (XG-boost),
d) gradient boosting regression tree (GBRT).

These models are mostly suitable for interpretable predictions, flexibility for mixing huge data in non-linear relationships, easy scalability, and the most accurate prediction performance. GBM and GBRT models are highly selected by researchers for effective and robust performance.

Table 1. Various machine learning algorithms and their significance [24–26].

No.	Model	Applications
1	Linear Regression (LR)	Evaluates simple relationships, such as the effect of solar intensity on outlet temperature.
2	Random Forest Regression	Handles complex data to predict energy output and efficiency in hybrid systems.
3	Gradient Boosting Machines (GBM)	Highly effective for thermal performance modelling, accounting for non-linear dependencies.
4	Support Vector Regression (SVR)	Models subtle interactions between variables like flow rates and collector performance
5	Random Forest (RF)	Predicts thermal efficiency and air temperature in hybrid solar collector systems.
6	Gradient Boosting Regression Tree (GBRT)	Provides highly accurate predictions of solar collector performance and energy output.
7	Decision Trees	Helps understand the influence of specific parameters (e.g., solar intensity, humidity) on performance.
8	XGBoost	Used for optimising solar thermal storage systems (PCM) and forecasting long-term energy outputs.
9	Recurrent Neural Networks (RNNs)	Forecast energy output based on time-series weather data.
10	Autoencoders	Detect faults or anomalies by identifying deviations from normal operating patterns.
11	K-Means	Group data on solar intensity and efficiency to identify regions with similar energy potential.
12	Density-Based Spatial Clustering of Applications with Noise (DBSCAN)	Identifies anomalies in operational data, such as sudden drops in efficiency.
13	Logistic Regression	Classifies collector output as efficient or inefficient.
14	Random Forest	Categorises faults in solar systems into overheating, shading, or flow issues.
15	Bayesian Neural Network (BNN)s	Integrates uncertainty estimation in solar energy predictions.
16	Gaussian Processes (GP)	Known for their ability to predict solar energy performance with uncertainty quantification.
17	Genetic Algorithms (GA)	Applied in optimising solar system configurations.
18	Particle Swarm Optimisation (PSO)	Used for parameter optimisation in solar energy systems.
19	Bagging Methods	Aggregate multiple models to improve prediction stability and accuracy.
20	Boosting Methods	Sequentially build models to minimise prediction errors.
21	Deep Belief Networks (DBN)	Advanced neural networks for hierarchical feature extraction.
22	Autoencoders	Used for anomaly detection and feature learning in solar systems.
23	Reinforcement Learning (RL)	Applied to optimise real-time solar energy operations, such as tracking maximum power points or adjusting solar collector angles.
24	Fuzzy Logic and ML Integration	Combines fuzzy logic principles with ML algorithms to handle uncertainty and improve solar energy predictions.

2.3. Support vector machines

It is an effective, better dimensional classification and regression supervision of ML tasks that works on a hyper plane decision boundary, which separates data in continuous regression output and minimises prediction error. Besides, it is most suitable for hybrid systems such as solar collectors integrated with PCM, predicting solar intensity, humidity, etc., and thermal performances for long-term forecasting.

2.4. Neural networks

They are structured and function like a human brain type ML called artificial neural networks (ANN) to predict real-time optimisation and autonomous operation in highly effective non-linear data for a long duration. They have further categories of convolutional neural networks (CNN) and recurrent neural networks (RNN), which support recording image-based solar energy systems like solar panel inspections or weather predictions, etc., and are suitable for time-series data, including solar intensity and weather-dependent parameters.

2.5. Clustering and classification

Clustering is an unsupervised learning technique where data, such as weather pattern analysis like humidity, solar radiation, etc., is grouped into clusters based on similarity by using algorithms like K-means, density-based Spatial clustering of applications with noise (DBSCAN) and hierarchical clustering. Classification is a supervised learning technique suitable for monitoring solar collectors for heating blockage, abnormal environmental conditions, etc., and helps classify days as sunny, cloudy, or low-thermal-energy days using a logistic regression classification tree.

2.6. Bayesian models

It is a probabilistic approach, particularly powerful for handling data on uncertainty and variability. The performance outcomes

based on prior probability and new likelihood data are calculated by using the formula:

$$P(A|B) = (P(B)\cdot P(B|A)\cdot P(A))/P(B), \quad (1)$$

where: P(A|B) = posterior probability (probability of A given B), P(B|A) = likelihood (probability of B given A), P(A) = prior probability (initial belief about A), P(B) = evidence (total probability of B).

In this mode, Bayesian neural networks (BNNs) and Gaussian processes (GPs) are used to quantify uncertainty in solar energy performance. They are also best to support the prediction of interdependency processes, such as solar collectors integrated with thermal storage systems or photovoltaic (PV) systems.

2.7. Evolutionary algorithms model

This model is preferred for selecting natural and biological evolution as a heuristic optimisation method to solve multi-objective and complex problems. Models such as genetic algorithms (GA) and particle swarm optimisation (PSO) were used to predict the complex design and material selection of solar collectors. And their thermal performance, based on their inclined position, was accurately predicted. Most suitable for predicting weather conditions and hybrid thermal storage efficiency, producing a Pareto-optimal set of solutions for decision-makers.

2.8. Ensemble learning techniques

These techniques leverage the strengths of individual models to improve the overall performance prediction, reduce overfitting, and enhance generalisation. They use a bagging-and-boosting model that operates autonomously to correct mistakes from earlier models.

2.9. Hybrid approaches

They are a combination of ML algorithms with optimisation techniques or physical models (thermodynamics metrology) for enhanced predictions. ANN integrated with PSO for optimising thermal performance parameters is the most suitable example.

2.10. Deep learning models

These models use multiple layers of interconnected nodes (neurons) to learn and represent complex patterns in data. Particularly effective in analysing large datasets with nonlinear relationships. They use deep belief networks (DBN) that act as advanced neural networks for hierarchical feature extraction, and auto encoders for dimensionality reduction and anomaly detection with feature learning in solar systems.

2.11. Reinforcement learning

In this, machine learning makes sequential decisions by interacting with an environment to exploit a cumulative reward. Unlike supervised learning, reinforcement learning **(**RL) does not rely on labelled data; instead, it learns through trial and error, receiving reactions in the form of rewards or consequences based on its actions. Algorithms such as Q-learning, deep Q-learning, and proximal policy optimisation (PPO) are notable in solar tracking applications.

2.12. Fuzzy logic and machine learning integration

It converts crisp input, such as solar intensity and ambient temperature, into fuzzy sets using linguistic terms like low, medium and high. An option like the if-then rule is used to relate the input to the output. If solar radiation is low and ambient temperature is high, then a reduced mass flow rate results in a lower control thermal efficiency. It supports enhanced prediction accuracy and adaptability, ensuring consistent thermal performance. It is necessary to describe in detail the procedures used in scientific research (experimental and computational procedures). It is also needed to explain why the above procedures are used and whether they are reliable (explain why the proposed procedure is correct for the class of problems).

In experimental work, it is necessary to specify the measurement accuracy.

3. Machine learning in drying applications

Machine learning (ML) has become a revolutionary technology across various agricultural applications, especially in optimising drying processes. This section begins with an exploration of how ML is integrated into agricultural drying systems, emphasising its role in improving efficiency, accuracy and overall performance. It then transitions to the application of ML in rough-surface solar collectors, particularly after PCM integration. Finally, the section delves into the numerical and experimental investigations of hybrid nanofluid performance in these systems.

3.1. Garlic clove

Kushwah et al. [27] presented a study on a dual-working-medium heat exchanger evacuated tube (HE-ET) solar drying system for garlic, emphasising the integration of thermodynamics and 5 different ML algorithms for performance optimisation in Python. Advanced ML algorithms, such as gradient boosting regression tree (GBRT), are highlighted for their predictive accuracy, with significant findings on the impact of ambient relative humidity and solar intensity. These results reveal that the mean absolute error (MAE) ranged between 0.31 and 0.59, root mean squared error (RMSE) between 0.54 and 0.72, and the coefficient of determination (R2) of 0.98 and 0.94 on training and testing values, providing valuable insights for enhancing the efficiency of solar drying systems. It underlines the potential of combining renewable energy technologies with data-driven approaches. The detailed integration of technology is illustrated in Fig. 1.

3.2. Sweet potato

Abdelkader et al. [28] developed an evaluation of an indirect solar dryer tailored for drying sweet potato cubes, integrating experimental, environmental and economic (3E) analyses alongside advanced ML techniques. Four algorithms, such as decision trees (DT), gradient boosting regression (GBR), multiple linear regression (MLR), and random forest (RF), were employed to predict critical performance metrics, including solar collector

(SC) energy and exergy efficiency, drying chamber mean temperature and exergy efficiency. The RF algorithm shows superior accuracy due to its adaptability. The dryer demonstrated solar collector efficiencies of 72.9% (energy) and 5.6% (exergy), storage unit efficiencies of 43.4% (thermal) and 18.4% (exergy) with a discharge time of 5.5 hours, and an average drying chamber thermal efficiency of 46.1%, ranging from 21.9% to 97.2% has been recorded.

The overall dryer efficiency was increased by 15% in consuming 4.509 kWh/kg of moisture removed. The Page model proved optimal for predicting drying kinetics. Environmental benefits included a CO_2 mitigation of 20.2 kg and carbon credit earnings of 56,771 RMB (RMB stands for Renminbi, the official currency of China), while economic analysis revealed a payback period of 29.24 months, annual revenue of 8,464 RMB, and a return on investment of 0.7 RMB. These results underscore the potential of integrating solar drying systems with machine learning to enhance system performance, optimise energy use, and deliver sustainable, economically viable solutions for agricultural drying applications.

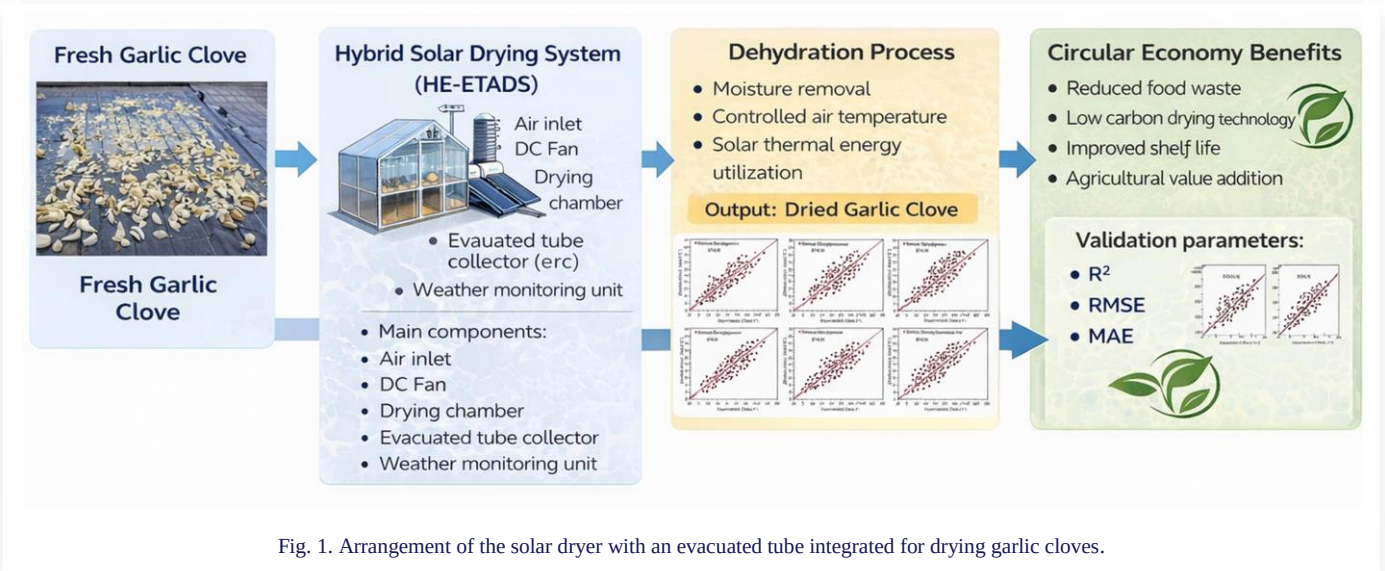


Fig. 1. Arrangement of the solar dryer with an evacuated tube integrated for drying garlic cloves.

3.3. Prediction of red chilli in a dryer

Arunkumar et al. [29] evaluated the drying performance of red chilli in an indirect solar dryer under varying energy storage element (ESE) cases like i) paraffin wax, ii) glass pieces blended with paraffin wax, and iii) crushed glass pieces mixed with paraffin wax in mass flow rates of 0.3 m/s, 0.4 m/s and 0.5 m/s. Key variables such as i) solar intensity, ii) mass flow rate, iii) ESE case, iv) ambient temperature (AT), v) collector inlet temperature (CIT), vi) collector outlet temperature (COT), vii) drying chamber inlet temperature (DCIT), and viii) drying chamber outlet temperature (DCOT) were analysed for their impact on moisture content (MC), and the collector efficiency (CE) was measured for research. Experimental results demonstrated that the dryer using case 3 ESE at a 0.5 m/s mass flow rate achieved the target MC within 25 hours.

GBRT emerged as the most accurate ML algorithm, with R^2 values of 0.999964 for MC prediction and 0.994064 for CE estimation, alongside minimal errors (MAE, RMSE, and mean squared error (MSE)). The solar collector outlet temperature was identified as the most influential factor for both MC and CE. This study highlights the importance of ESE, airflow rate and ML techniques in optimising agricultural drying processes as illustrated in Fig. 2.

3.4. Metal absorber comparison

Baz et al. [30] conducted a comparative study of solar absorber structures, specifically the single-layer metal-insulator-metal (MIM) structure, the gold-MgF_2-gold solar absorber (GMGSA), and the multilayer MIM structure, the gold-MgF_2-gold-MgF_2-gold solar absorber (GMGMGSA), highlighting advancements in solar thermal applications. Leveraging machine learning strategies used random forest regression analysis. The research achieved exceptional predictive accuracy, with an R^2 of 0.998836 and a mean square error of $2.8091 \cdot 10^5$. It enables the optimisation of absorber designs. The GMGMGSA structure demonstrates superior performance, including a broad absorption range (0.4−1.6 μm), high absorption efficiency under AM1.5 solar irradiation (93.10%), and excellent angular independence up to 70°. These findings underscore the potential of advanced absorber designs in applications such as concentrated solar power (CSP), solar water heater (SWH) and building-integrated photovoltaics (BIPV), emphasising the transformative role of machine learning in driving innovation in solar thermal technologies.

3.5. Machine learning and computational fluid dynamics simulation

Madhankumar et al. [31] focused on the computational analysis, empirical testing, and predictive modelling of a corrugated absorber plate solar collector (CAPSC) integrated with a fin-inserted TES system. Utilising computational fluid dynamics (CFD) simulation, governing equations of the CAPSC device were developed and analysed, complemented by experimental testing across varying mass flow rates (0.014–0.064 kg/s) during

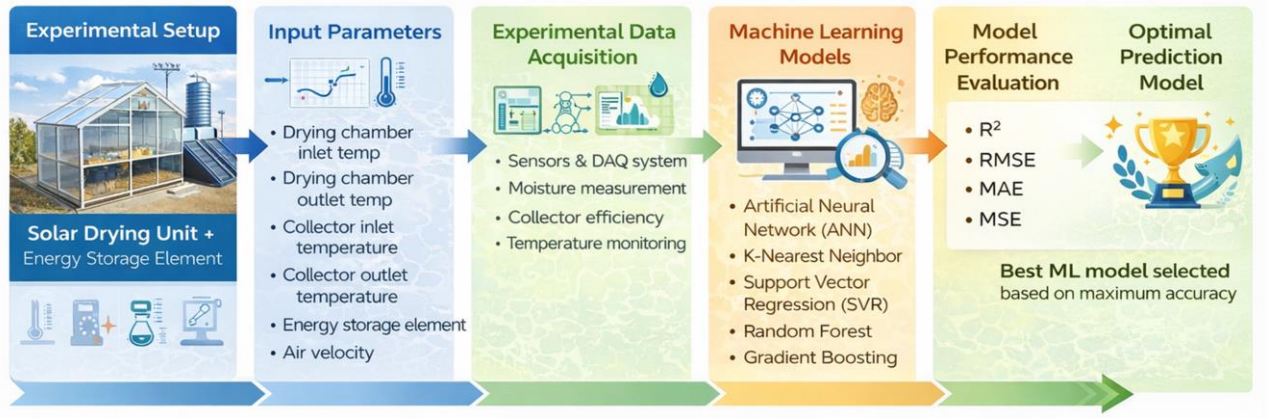


Fig. 2. Thermal performance of Red Chilli predicted by using an ML algorithm.

summer and winter seasons. The maximum deviation between computational and experimental outlet temperatures was 1.72°C at a mass flow rate of 0.044 kg/s, demonstrating close agreement. ML techniques, including MLR, RF, K-nearest neighbours (KNN), XG-boost and ANN, were employed to predict the thermal efficiency of the system, leveraging a dataset of 288 empirical samples. Among these, ANN and XG-boost emerged as the most accurate, with XG-boost excelling due to its robust handling of non-linear interactions. To further enhance prediction accuracy, computational CAPSC output temperatures were integrated as inputs into machine learning models, illustrating a synergistic improvement in thermal efficiency forecasts. This integration of CFD and machine learning provides a sophisticated framework for optimising solar collector designs and achieving precise thermal performance predictions, as detailed in Fig. 3.

3.6. Rough surface in a solar collector

3.6.1. Triangular-shaped rib

Nidhul et al. [32] provided an extensive review of artificial roughness designs for rectangular and triangular solar air heaters

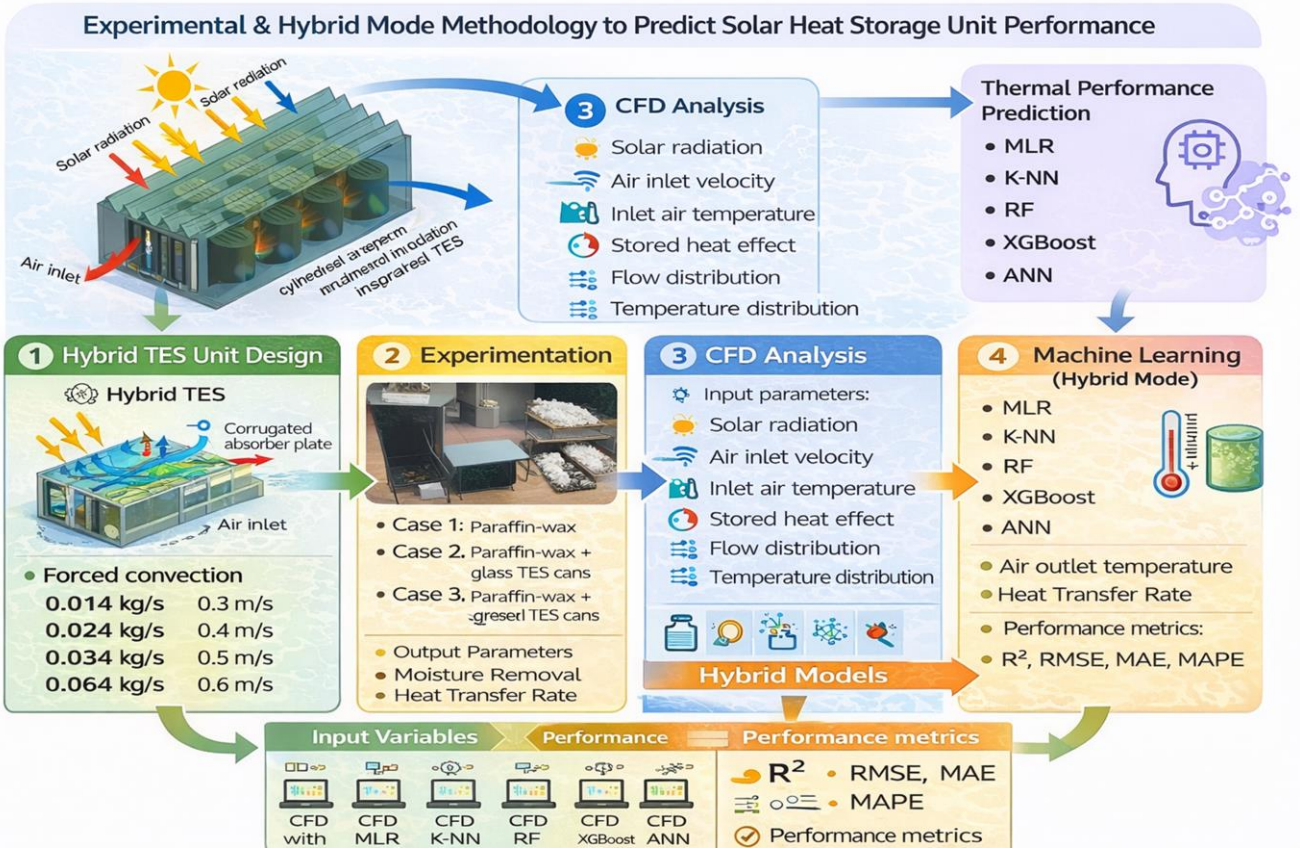


Fig. 3. Schematic layout of integration of experiment and CFD with ML.

(SAHs), helping researchers identify gaps in the field. An ANN-based ML model was developed using 454 datasets from 72 rib combinations to predict the performance of ribbed triangular SAHs. The model demonstrated high accuracy, with an average prediction deviation of less than 3%, and has the potential to improve accuracy by incorporating additional geometric and operational parameters. Second-law analysis revealed variations in collector efficiency and entropy generation with Reynolds numbers (Re) ranging from 4000 to 18000. The study identified optimal rib parameters, including height, pitch, chamfer angle and inclinations, enabling engineers to estimate the performance of ribbed triangular duct SAHs with various artificial roughness designs without the need for physical testing.

3.6.2. C-shaped fin

Saravanan et al [33] highlighted the use of ML techniques in predicting the thermal performance of SAH with advanced absorber designs, C-shaped finned panels. Experimental investigations coupled with ML models, including RF, LR, and KNN, demonstrate the capability of data-driven approaches to accurately model key performance parameters such as the Nusselt number (Nu), friction factor (*f*) and thermal efficiency (thermo-hydraulic performance (THP)). Among the models, RF exhibited superior predictive performance with a high R^2 value of 0.9783 and minimal errors, emphasising its potential as a robust tool for optimising SAH designs. This integration of ML with experimental studies offers a promising pathway for enhancing the design and operational efficiency of solar thermal systems.

3.6.3. Digital twin in solar flat plate collector

Zohdi et al. [34] introduced a digital twin model to optimise solar-thermal storage systems as a green energy solution during peak demand hours after sunset. The system comprises adaptable Fresnel mirrors, an optical receiver and a power distribution framework. A reduced-order Maxwell's equations model efficiently computes solar power flow, simulating mirror reflections, losses and energy delivery in microseconds. A genetic ML framework integrates sub-models for mirror tracking, thermal absorption and optimal temperature operation to balance radiative losses and heat storage. The approach optimises mirror-receiver configurations for long-term efficiency and demand fulfilment. Additionally, a deep-learning algorithm enhances simulation speed through an ANN representation, enabling rapid performance evaluations across an extended timeframe.

3.6.4. Grooved tube configuration in flat plate collector

Chilambarasan et al. [35] highlighted the enhanced performance of solar flat plate collectors (SFPC) using an internally grooved absorber tube combined with Al_2O_3-WEG-based nanofluids. Experimental investigations with varying nanoparticle concentrations (0.01%, 0.05%, 0.1%, 0.2%) and mass flow rates (0.024 kg/s, 0.036 kg/s, 0.048 kg/s) revealed significant efficiency improvements. At 0.2% nanoparticle concentration and 0.036 kg/s mass flow rate, model 2 achieved a maximum efficiency enhancement of 54.1% over model 1 with plain fluid. The ANN models developed for real-time prediction accurately mirrored experimental results, demonstrating their effectiveness in optimising SFPC performance. This synergistic approach addresses key challenges in enhancing the efficiency of solar thermal technology.

3.6.5. Solar panel tilt angle

Yadav et al. [36] research focuses on optimising the electricity output of photovoltaic (PV) systems in micro grids by accurately predicting the optimal tilt angle (OTA) of solar panels – a non-linear function of solar radiation parameters. Using feature selection-based ANN with numerous ML algorithms, the research recognises global solar radiation, diffuse solar radiation, clarity index and inclined surface radiation as critical predictors, while deeming extra-terrestrial radiation the least significant. By incorporating the appropriate input variables, prediction accuracy improved significantly from 38.59% to 90.72%. Among the ANNs evaluated, the Elman neural network (ENN) achieved the best performance, demonstrating its effectiveness in OTA prediction to maximise PV output.

3.6.6. V corrugation

Poongavanam et al. [37] enhanced SAH efficiency by modifying absorber plates with V-corrugation, shot-blasting (SB), nano-coating, and black pebble stone (BPS) integration. SB treats surfaces with high-speed abrasives, followed by coating with activated carbon (AC) based nano-materials in matt paint. The roughened and corrugated plate increases heat transfer to the air, and BPS acts as a thermal mass to maintain a consistent temperature. Machine learning (ML) models, including random forest regression (RFR), LR and support vector regression (SVR), are employed to predict SAH thermal efficiency using experimental data. The research reveals efficiency enhanced owing to surface modifications and BPS integration, significantly improving thermal transfer. The RFR model shows superior predictive accuracy, with a correlation coefficient of 0.999 for modified SAHs, and effectively estimates Nu values with minimal error. ML-based thermal efficiency models are validated using mean squared error and root mean squared error, confirming their predictive reliability.

Thakur et al. [38] investigated the thermal-hydraulic performance enhancement of dual passage solar thermal collectors (DP-STC) by employing single V-shaped staggered baffles (SVSSBs) on the absorber plate. Solar thermal collectors (STCs) are essential for converting solar energy into thermal energy, but the thermal performance of DP-STCs is typically suboptimal. The study focuses on the impact of various geometrical parameters, including relative staggered baffle position, relative staggered baffle size and relative roughness pitch, for Reynolds numbers ranging from 3000 to 19000. Fixed parameters, such as relative roughness height (0.40), relative gap position (0.67) and angle of attack (60°), are considered to isolate the effect of the varying geometrical factors.

The results indicate that SVSSBs outperform other types of turbulators reported in the literature, achieving a peak thermal-hydraulic performance of 3.67 under specific geometrical conditions (baffle size = 1.5, staggered baffle position = 0.65, roughness pitch = 3.5, at Re = 17000). Additionally, correlations for the Nusselt number (Nu) and the friction factor were develo-

ped using experimental data, providing valuable insights into the optimisation of thermal collectors for enhanced heat transfer and reduced friction losses.

3.7. Conical cavity in a solar-evacuated tube

Rajan and Reddy [39] integrated an optical-thermal model combining Monte-Carlo ray tracing and CFD to evaluate a 40 m² parabolic dish collector (PDC) under varying inclinations and wind conditions. Ray tracing in Solar Trace, coupled with ANSYS and MATLAB, was used to model solar heat transfer to Therminol 66 in a conical receiver. Validation against established studies confirmed the model's accuracy, with a ray count of 10^{-6} ensuring precise mapping of the heat flux distribution. The study found that 66%–80% of absorbed solar heat was transferred to the heat transfer fluid (HTF), with this transfer influenced by inclination, wind direction, and speed. Deep learning models were employed for thermal performance prediction, with optimal activation functions selected for accuracy. A comparative analysis demonstrated the superior performance of the developed model compared to existing approaches.

3.7.1. Twisted and way tape inserted in an evacuated tube

Bingbin et al. [40] investigated the impact of inlet flow velocity, structural enhancements, and ML models on the efficiency of a solar collector (SC). Higher inlet airflow velocities (2.1 m/s, 3.3 m/s and 4.5 m/s) improve collector efficiency by intensifying heat transfer and reducing temperature build-up. Structural enhancements, such as a spiral twisted tape and wave strip combination, significantly enhance heat transfer. This configuration, with an optimal wave plate length of 360 mm and a helical twist ratio of 5.14, achieved the highest efficiency and provided a promising direction for improving solar collector tube designs. Eight machine learning models, including XG-boost, were employed to predict collector performance, with XG-boost emerging as the most accurate (R^2 = 0.997, RMSE = 0.008 for training; R^2 = 0.988, RMSE = 0.008 for testing). Interpretable methods like partial dependence plot (PDP), accumulated local effects (ALE), and Shapley additive explanations (SHAP) analysis highlighted key performance drivers, such as inlet flow velocity, temperature difference and solar irradiance. These methods enable optimised design parameters and provide engineers with actionable insights to enhance collector performance, making interpretable machine learning a valuable tool in solar energy technology development.

Gupta et al [41] introduced a mixed-mode dryer with a semi-transparent photovoltaic thermal (PVT) collector, combining computational and experimental methods to assess drying and thermal performance. The research evaluates three inlet air velocities, such as i) 0.048 m/s, ii) 0.096 m/s, and iii) 0.144 m/s, to optimise airflow in the PVT dryer. Model 2 exhibited uniform temperature distribution, while Model 3 demonstrated the best performance, achieving enhanced thermal efficiencies of 33.20% (numerical) and 31.14% (experimental) compared to Model 1. Additionally, Model 3 improved Re and Nu by factors of 3.06 and 2.45, respectively. Experimental results closely aligned with simulations, showing deviations of only 2.24% to 4.90%. ML models, particularly ANN with different hidden layers, were utilised to predict and optimise drying performance parameters, ensuring optimal drying conditions. The detailed integration of the process is presented in Fig. 4.

3.8. Thermal performance prediction in nano-liquids

Alawi et al. [42] predictions of thermal performance (η) for flat plate solar collectors (FPSC) are critical for various engineering applications in thermal and energy sectors. This study explores the potential of ML models, including hist gradient boosting regressor (HGBR), multivariate adaptive regression splines (MARS), tweedie regressor (TR) and stacking regressor (SR), to predict η using Al_2O_3–H_2O nanofluids. A predictive matrix was

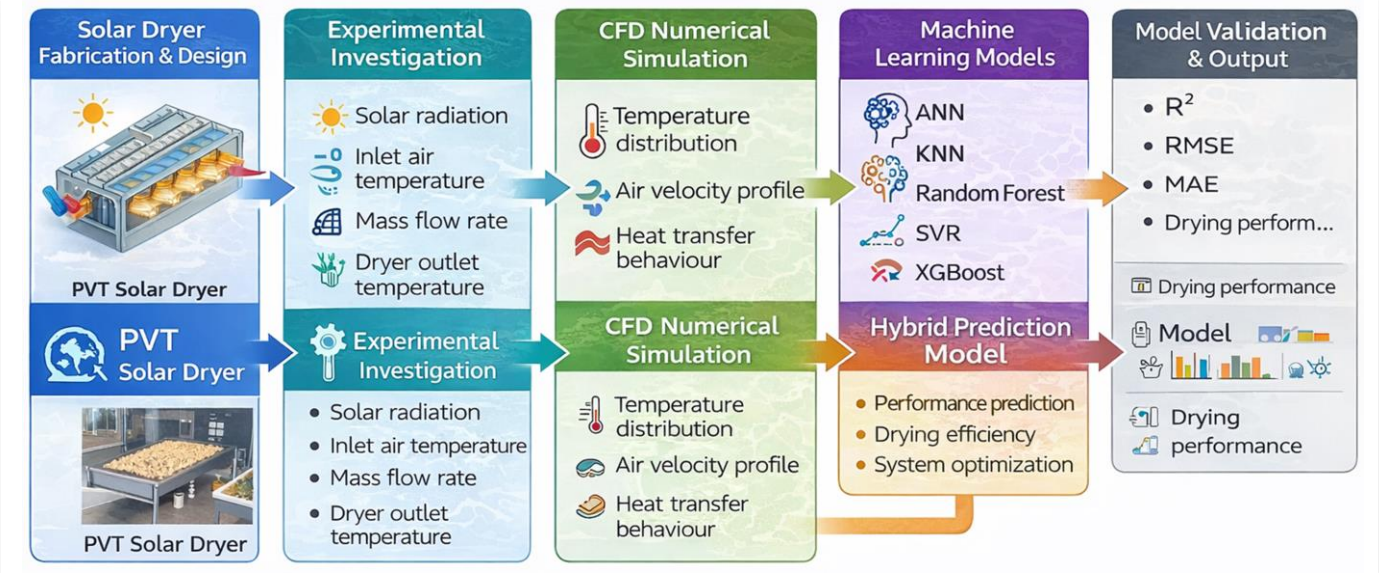


Fig. 4. Schematic layout of ML in semi-transparent photovoltaic thermal (PVT) collector.

developed incorporating five key predictors: nanoparticle size, collector slope, absorbed energy parameter, removed energy parameter and reduced temperature parameter. Forward feature selection (FFS) integrated with the RF algorithm was employed to construct different input combinations.

Among the models tested, Model 5 demonstrated superior performance across all metrics, achieving the lowest mean absolute percentage error (MAPE), root mean squared error (RMSE), U95 (95th percentile uncertainty), and residual error, alongside the highest coefficient of determination (R^2), Pearson correlation coefficient (PCC), Nash-Sutcliffe coefficient (NSE), and Willmott's index (WI). Model 4 showed strong results in R^2 and PCC, while Models 2 and 3 exhibited moderate performance. Model 1 lagged in most evaluation metrics. The stacking algorithm in Model 5 proved to be the most effective, with a prediction accuracy of 94.5%, surpassing HGBR (92.9%), MARS (92.7%) and TR (89.9%).

This research provides valuable insights into η prediction using thermal predictors, highlighting the efficiency of stacking algorithms and their applicability to improve the performance and design of FPSCs.

3.8.1. Specific heat prediction in nanofluid

Alade et al. [43,44] conducted research on nanofluids due to their superior thermal properties, which are critical for enhancing the solar thermal collector efficiency. Accurate modelling of their specific heat capacity is essential but underexplored, and existing analytical models exhibit significant predictive inconsistencies. A Bayesian support vector regression (BSVR) model was developed to address this, trained on 84 experimental datasets and validated on 17 test datasets. The model achieved remarkable accuracy, with a 99.95% Pearson correlation coefficient and an absolute average relative deviation (AARD) of 0.1888, outperforming existing models by a significant margin. This advancement ensures more reliable efficiency computations for solar collectors, optimising their design and performance.

Further, they extended to introduce a genetic algorithms/support vector regression (GA/SVR) model to accurately evaluate the specific heat capacity of Alumina (Al_2O_3)/water nanofluid at volume fractions of 3.7–9.3%. The GA/SVR model demonstrated exceptional accuracy, achieving a 99.998% correlation with experimental data and an RMSE of 0.0014. Comparative analysis revealed the GA/SVR model outperformed existing analytic models, providing an order-of-magnitude improvement over the thermal equilibrium model and a two-order-of-magnitude improvement over the simple mixing rule model. This advanced model offers rapid and precise predictions, optimising nanofluid performance in solar thermal applications.

3.8.2. Prediction of viscosity of nanofluids

Meybodi et al. [45] reported research on nanoparticles and a base fluid, which is extensively used in industrial processes such as engine cooling and enhanced oil recovery due to their unique properties, including viscosity, which is crucial for chemical and petroleum engineering applications. This study employs least squares support vector machines (LSSVM) to accurately predict the viscosity of water-based nanofluids containing Al_2O_3, TiO_2, SiO_2, and CuO nanoparticles. The LSSVM model demonstrates exceptional accuracy, achieving a coefficient of determination of 0.998 and outperforming existing models. The model accurately predicts viscosity trends across varying nanoparticle volume fractions and temperatures, aligning well with experimental data. Additionally, a leverage approach was used to identify outliers and validate the model's applicability domain. This robust, rapid and precise modelling approach significantly enhances viscosity prediction for nanofluids.

3.8.3. Relative viscosity of nanofluids

Baghban et al. [46] focused on nanofluid viscosity as a critical property in convective heat transfer, yet existing theoretical models have limited applicability. This study collected 1277 experimental data points of nanofluid relative viscosity (NF-RV) and developed a general predictive model using an adaptive network-based fuzzy inference system (ANFIS). The model incorporates variables such as temperature, nanoparticle diameter, nanofluid density, volumetric fraction and base fluid viscosity. Statistical analysis showed exceptional accuracy, with an R^2 value of 0.99997 and relative deviations of 0.42% (absolute) and 6.45% (maximum average). The ANFIS model outperformed existing theoretical models, demonstrating its ability to reliably predict NF-RV. This tool is invaluable for chemists and engineers, particularly in heat transfer applications using nanofluids.

Wu et al. [47] study presents a geometric analysis and optimisation of parabolic trough solar collectors (PTC) using a Python-based algorithm to calculate optical efficiency with a secondary hyperbolic mirror. Key features include the concentration ratio, intercept factor and optical efficiency, critical for PTC geometric optimisation. The algorithm integrates AutoCAD data for simulating varying incident angles and focal lengths, achieving a simulation-theory error margin of less than 3.13%. Using ML, optical efficiency was numerically fitted, yielding a high accuracy ($R^2 = 0.97874$). The study develops optical efficiency fitting formulas derived from secondary reflection hyperbolic data and validated using a ray-tracing model. This method enhances the design, energy analysis and optimisation of PTCs under diverse geometric and operational conditions.

3.9. ML in parabolic trough solar collector using hybrid nanofluids

Alhamayani [48] researched on the advancement of solar energy technologies, particularly for sustainable power generation, and emphasised the importance of optimising parabolic trough solar collectors (PTC) systems. This study explores the impact of hybrid nanofluids (1% Al_2O_3–2% multi-walled carbon nanotubes (MWCNT)/Syltherm-800, 1.5% Al_2O_3–1.5% MWCNT/Syltherm-800, and 2% Al_2O_3–1% MWCNT/Syltherm-800) on PTC performance. A mathematical model was developed to assess PTC efficiency across varying nanofluid concentrations. Additionally, ML models, DT, support vector machine (SVM) and ANN were trained to predict PTC outlet temperature efficiently. Results revealed that 2% Al_2O_3–1% MWCNT/Syltherm-800 achieved the highest thermal efficiency, averaging 70.54%. The

ANN model exhibited superior predictive accuracy, with an R^2 of 99.99%, MAPE of $4.8{\cdot}10^{-5}$, RMSE of 0.012 and MAE of 0.0057. This research highlights the potential of hybrid nanofluids and artificial intelligence (AI) to enhance the performance of PTC systems.

Said et al. [49] investigated the thermal performance of an FPSC using MWCNT + Fe_3O_4/Water hybrid nanofluids in an arid environment. Experiments revealed a 26.3% increase in the heat transfer coefficient, accompanied by an 18.9% increase in the friction factor (f). Experimental data were used to develop prediction models for heat transfer, Nu, f and thermal efficiency using boosted regression tree (BRT) and XG-boost ML techniques. The XG-boost models demonstrated superior performance, with R^2 values ranging from 0.9914 to 0.9997, lower mean squared errors (0.000081–9.11) and minimal mean absolute percentage errors (0.0025–0.3114). Statistical evaluations, complemented by Taylor's graphs, emphasised the effectiveness and accuracy of XG-boost over BRT for thermal performance predictions.

Al-Rashed et al. [50] numerically evaluated the performance of a novel PTC featuring a non-circular absorber tube and solid insulation, using a water-CMC/Al_2O_3 (carboxymethyl cellulose containing Al_2O_3) nanofluid as the working fluid. Performance metrics were analysed with respect to the Reynolds number (Re), nanoparticle volume concentration, particle size and insulation angle. Results reveal an ascending-descending pattern of efficiency variation with Re, achieving a peak efficiency of 61.7% for a dual-fluid collector with a 90° insulation angle, 1.5% nano-particle concentration and 100 nm particle diameter. Additionally, an ANN model with 8 neurons accurately predicted collector efficiency, with a maximum deviation of less than 0.2% and an R^2 of 0.9998, demonstrating its reliability for forecasting PTC performance.

Bouzgou and Gueymard [51] addressed the critical need for accurate solar irradiance forecasting to support the efficient utilisation of solar energy in a carbon-free economy. A novel forecasting approach combining minimum redundancy–maximum relevance (MRMR) and extreme learning machine (ELM) is proposed for irradiance time-series prediction. The method is tested across three forecasting horizons (15 minutes, 1 hour, and 24 hours) and evaluated against four scenarios: i) long window (latest 50 variables), ii) short window (latest 5 variables), iii) principal component analysis (PCA), and iv) a clear-sky model. Using irradiance data from 20 sites across diverse climates, the results demonstrate that selecting an optimal set of relevant variables through MRMR significantly enhances forecasting accuracy. The proposed approach outperformed the alternative scenarios, proving its efficacy in improving the prediction of global solar radiation and offering a robust solution for integrating solar energy into future energy systems.

Fuxi et al. [52] investigated the effect of spring turbulators on turbulent flow inside a pipe using TiO_2-Cu/water hybrid nanofluid and a single-phase model, focusing on heat transfer rate (HTR), pressure drop (ΔP) and solar collector efficiency (η_{SC}). The numerical analysis, based on the Reynolds number, the turbulator scale and the nanoparticle volume fraction (ϕ), reveals that increasing the turbulator scale improves fluid contact, increases turbulence and enhances nanofluid mixing, resulting in better heat transfer performance. The use of ANN for modelling predicts the system performance with high accuracy, offering predictions similar to those from fitting methods. The findings highlight the potential of spring turbulators in improving solar collector efficiency, with ANN providing a reliable tool for performance prediction.

3.10. Heat storage (with and without phase change materials)

Zayed et al. [53] evaluated the performance of wavy corrugated solar air collectors (WCSAC) with paraffin wax as thermal energy storage (TES). Experiments were conducted under airflow rates of 0.540 kg/min, 1.68 kg/min, and 3.72 kg/min with paraffin layer thicknesses of 2 cm and 4 cm. A 4 cm paraffin layer improved energy efficiency by 24.0%, 20.39% and 16.37% at the respective airflow rates compared to systems without PCM. The convective heat transfer coefficient was over 1.20 times higher in PCM-equipped systems.

Support vector machine (SVM) models, optimised with Karush-Kuhn-Tucker conditions, accurately predicted thermal performance metrics, achieving coefficients of determination of 0.990 (training) and 0.950 (testing). Sensitivity analysis identified the air inlet temperature, solar irradiance and PCM thickness as key parameters influencing performance. This study demonstrates the effectiveness of PCM and AI models in enhancing solar thermal systems.

Badji et al. [54] highlighted the effectiveness of integrating an SAH with an underground latent heat storage system (LTES) using $CaCl_2{+}6H_2O$ as a PCM to enhance greenhouse heating efficiency. Conducted in a semi-arid climate in Ghardaia, Algeria, the innovative system increased night-time air temperatures by 57% compared to conventional greenhouses. The LTES released 20 kJ of energy during the night, meeting 30% of the greenhouse's energy requirements. ML models, particularly the nonlinear autoregressive exogenous (NARX) model, achieved exceptional predictive accuracy, with an R^2 of 0.9986, surpassing the RNN model's R^2 of 0.9893. These findings demonstrate the potential of LTES systems and advanced ANN-based models in optimising greenhouse conditions, significantly contributing to sustainable agriculture and energy-efficient practices.

3.11. Parallel tube collector using hybrid nanofluid

Mausam et al. [55] investigated the thermal performance of a solar flat plate collector (FPC) using a hybrid nanofluid composed of Cu-MWCNTs-water. Experimental investigations varied flow rates, inclination angles and radiation intensities, with an ANN and a mathematical model developed to predict instantaneous efficiency. Inputs to the ANN included nanofluid concentration, flow rate, inclination angle and radiation intensity, while instantaneous efficiency was the output. The model identified optimal neurons based on the minimal MSE and a high coefficient of determination (R^2). Results revealed a 32.25% enhancement in instantaneous efficiency using the Cu-MWCNTs hybrid nanofluid, with R^2 values ranging from 0.8857 to 0.9989,

demonstrating strong predictive accuracy. This research highlights the effectiveness of hybrid nanofluids and ANN-based modelling for optimising FPC performance in heat transfer and thermal applications like fluid and space heating.

Mustafa et al. [56] investigated the thermal performance of a double-fluid parabolic trough solar collector (PTC) with a helical absorber tube, following the American Society of Heating, Refrigeration and Air Conditioning Engineers (ASHRAE) Standard 93 [57]. The study utilised non-Newtonian nanofluids as the working fluid, analysed using the finite volume method, the semi-implicit method for pressure linked equations (SIMPLE) algorithm and the k–ε turbulence model, with the importance of the turbulence model emphasised [58]. The results identified the optimal configuration as a double-fluid solar receiver featuring a helical absorber tube, a nanofluid volume fraction of 4% and a nanoparticle diameter of 50 nm. At a Re number of 5000, the single-flow PTC achieved a maximum efficiency (η_{max}) of 47.5% with nanofluids and 43.1% with water. In comparison, the double-flow PTC reached efficiencies of 56.5% at a 1% nanofluid concentration and 58.2% at 4%. Additionally, a deep learning-based ANN model was employed to predict efficiency, effectively correlating nanoparticle concentration, diameter and Re number with the system performance. This demonstrated the reliability of ANN models for predicting PTC efficiency.

3.12. ANN prediction in SAH

Ghritlahre et al. [59] focused on the application of ANN for predicting the thermal performance of SAH, comparing roughened surfaces like arc-shaped wire ribs and smooth duct designs. This research emphasises identifying and utilising relevant input parameters for performance prediction. Seven neural models were developed, varying the number of neurons, with ANN-II (8-14-1 architecture) identified as the optimal model based on metrics such as sum square error (SSE) (0.02138), mean relative error (MRE) (1.82%) and R^2 (0.99387). The ANN model outperformed the group method of data handling (GMDH) approach, demonstrating superior accuracy. Sensitivity analysis further revealed that the air mass flow rate is the most critical input parameter affecting SAH performance. This study underscores the efficacy of ANN in enhancing SAH performance predictions, setting a benchmark for data-driven modelling approaches in solar thermal research. Kumar et al. [60] demonstrated the effectiveness of ANN models trained with the Levenberg–Marquardt algorithm in accurately predicting the thermal efficiency of wire-screen porous bed solar air heaters under unidirectional and cross-flow configurations. High coefficients of determination (R^2 = 0.999 and 0.996) and low error metrics confirm that the ANN is a reliable and robust tool for predicting the thermal performance of porous bed SAHs.

Further research [61,62], particularly multi-layer perceptron (MLP) models, has shown them to be efficient and reliable tools for modelling and performance prediction of solar air heaters due to their capability to handle nonlinear and complex system behaviour. By critically analysing studies from 2009 to 2021, the paper identifies MLP as the most widely applied ANN architecture for SAH performance prediction and outlines research gaps to guide future optimisation and modelling efforts [63]. Emphasises artificial neural networks as efficient soft-computing tools for predicting and optimising solar air heater performance, offering faster and cost-effective alternatives to conventional experimental and analytical methods.

3.13. Field survey

Tschopp et al. [64] provided a comprehensive dataset from a large-scale solar thermal collector array at Fernheizwerk Graz, Austria, one of Central Europe's largest solar district heating installations, featuring a gross collector area of 516 m² (361 kW of nominal thermal power). High-precision operational data, collected throughout 2017 with a 1-minute sampling rate and rigorous quality assurance (8.2% missing data), include key parameters such as flow rates, inlet and outlet temperatures, various irradiance metrics and weather conditions. The dataset also provides calculated values, such as thermal power output and mass flow, along with detailed uncertainty information for most variables. Released under a Creative Commons Attribution-Share Alike (CC BY-SA) 4.0 license with metadata in machine-readable JavaScript Object Notation (JSON) format, this dataset is ideal for applications such as dynamic model validation, radiation algorithm development, performance optimisation and uncertainty analysis. Notably, it is the first publicly available dataset of its kind for large-scale solar thermal collector arrays.

3.14. Weather prediction

Falope et al. [65] introduced a 3-step forecasting architecture using low-level data fusion to syndicate weather parameters from physical on-site and nearby weather stations, significantly improving solar energy prediction accuracy. By applying the Pearson correlation coefficient, weather variables with strong correlations to solar radiation were identified, enhancing forecasting models. Pre-processing techniques like rescaling and list-wise deletion further improved accuracy, with utility-scale (1 MW) and residential rooftop PV systems (8 kW, 10.5 kW, and 15 kW) achieving low RMSE values, demonstrating versatility across different PV sizes.

The model improved prediction accuracy by 6% and 13% over single-source data and by 19% when combining multiple data sources without correlation-based feature selection. Solar radiation emerged as the most critical predictor, achieving an RMSE of 0.0859 with the boosted tree algorithm. While the architecture's reliance on solar radiation data and its United Kingdom (UK) centric scope are limitations, future research could extend the model globally, incorporate negatively correlated parameters and explore advanced validation and pre-processing methods. This approach could also support forecasting for other renewable energy (RE) sources, such as wind and tidal, broadening its applicability in renewable energy forecasting.

3.15. Failure prediction of PV plant

Pereira and Silva [66] emphasised the critical role of ML algorithms in the monitoring, classification and prediction of inverter failures in PV solar energy plants. By leveraging historical data, ML enables the anticipation and optimisation of inverter performance, thereby improving energy production and

efficiency. Recommendations include connecting standardised modules in series or parallel to enhance voltage, current and capacity in power-conversion systems, and incorporating clamp circuits to protect inverters from inrush and overcurrent. Seasonal variations in inverter failures inform tailored control strategies to enhance reliability, while continued and improved data collection is essential for robust evaluation of failure rates and recurrent patterns, aiding post-warranty maintenance. Techniques such as sinusoidal pulse-width modulation reduce harmonic distortion and control output voltage, contributing to enhanced power-conversion efficiency. Results demonstrate the effectiveness of ML in identifying failure modes and patterns, issuing alarms for parameter deviations and providing insights into root causes. The findings underline the importance of data-driven monitoring and predictive maintenance for improving reliability and operational performance in solar PV systems.

4. Performance of experimental analysis of solar air heater

In this study, the extreme gradient boosting (XG-boost) machine learning model is employed to predict the thermo-hydraulic performance score (THPS) of an SAH with polygonal ribs. Unlike conventional statistical approaches, XG-boost efficiently handles non-linear relationships between the geometric parameters and Re number by optimising decision trees through gradient boosting. The dataset comprises experimentally obtained THPS values for different rib geometries (polygonal and trapezoidal), pitch-to-height *p*/*e* ratios (*p*/*e* = 5, *p*/*e* = 7.5, and *p*/*e* = 10) and Reynolds numbers (Re = 2000 to Re = 20000). The input features include a) rib geometry type, b) *p*/*e* ratio, and c) Re, while the target variable is the corresponding THPS value. The model is trained using an 80:20 train-test split, and hyperparameters such as learning rate, tree depth and regularisation terms are optimised to enhance the prediction accuracy. The detailed schematic diagram is shown in Fig. 5, and the position of the thermocouples placed to record the temperature in the absorber plate as illustrated in Fig. 6.



Fig. 5. Experimental setup of SAH: a) side view, b) front view.

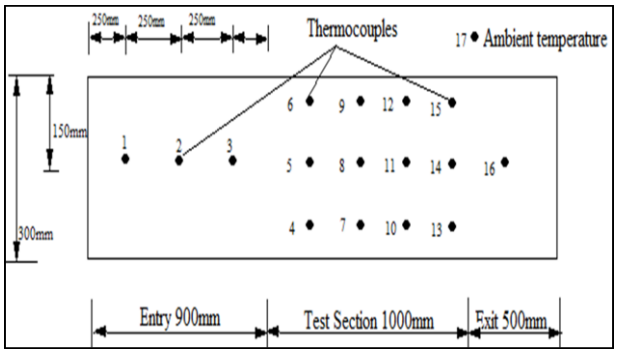


Fig. 6. Location of thermocouples for temperature measurement in flat plate SAH.

4.1. Experimental data

The experimental investigation was conducted on a rectangular duct under varying mass flow rates, different rib positions and a range of Reynolds numbers to analyse the thermo-hydraulic performance. The results, as presented in Table 2 [67], highlight the influence of rib positioning on the heat transfer characteristics and frictional losses.

Table 2. Experimental reading of various rib surfaces in the absorber plate.

Reynolds number	Rib shape and (*p*/*e*) ratio					
	Polygonal (*p*/*e* = 5)	Polygonal (*p*/*e* = 7.5)	Polygonal (*p*/*e* = 10)	Trapezoidal (*p*/*e* = 5)	Trapezoidal (*p*/*e* = 7.5)	Trapezoidal (*p*/*e* = 10)
2000	1.54	1.86	1.77	1.47	1.71	1.68
4000	2.43	2.95	2.86	2.34	2.93	2.86
6000	2.23	2.54	2.50	2.14	2.48	2.47
8000	2.26	2.48	2.49	2.17	2.46	2.43
10000	2.04	2.20	2.19	1.90	2.12	2.11
12000	1.97	2.08	2.09	1,92	2.09	2.08
14000	2.10	2.21	2.20	2.05	2.19	2.19
17000	1.88	2.01	2.01	1.82	1.96	1.99
20000	1.95	2.04	2.05	1.82	2.02	2.07

4.2. Prediction of XG-boost

The application of the extreme gradient boosting (XG-boost) machine learning model for predicting the thermo-hydraulic performance score (THPS) of an SAH integrated with polygonal and trapezoidal ribs has demonstrated high predictive accuracy [25]. The model's performance was evaluated using key statistical metrics, including R^2, mean absolute error (MAE), root mean squared error (RMSE), and mean absolute percentage error (MAPE), for both the training and test datasets.

To enhance the predictive accuracy of the THPS for an SAH integrated with polygonal ribs, the XG-boost machine learning model was employed. XG-boost is a powerful ensemble learning algorithm that constructs multiple decision trees sequentially, where each subsequent tree corrects the errors of the previous one, thereby improving overall prediction accuracy.

The dataset for training the XG-boost model was derived from experimental THPS values for different Reynolds numbers (Re = 2000 to Re = 20000) and (p/e) ratios (polygonal and trapezoidal ribs) with (p/e) = 5, p/e) = 7.5, and p/e) = 10. The input parameters included the Reynolds number, rib geometry and p/e ratio, while the target variable was THPS.

4.3. Mathematical modelling

The thermo-hydraulic performance (THP) of the system is evaluated using the following relationship [22]:

$$\mathrm{THP} = (\mathrm{Nu}/\mathrm{Nu_o}) / (f/f_o)\ 0.333, \quad (2)$$

where: Nu and $\mathrm{Nu_o}$ are the Nusselt numbers for the roughened and smooth configurations, respectively; f and f_o are the friction factors for the roughened and smooth configurations, respectively.

The exponent 0.333 accounts for the trade-off between heat transfer enhancement and pressure drop.

To predict the THP values under various operating conditions, the XG-boost algorithm is employed. XG-boost, a gradient-boosting decision tree-based model, is selected due to its efficiency in handling nonlinear relationships and complex datasets. The model is trained on the experimental dataset, with the Reynolds number, p/e ratio and geometric configuration as input features, and THP values as outputs. The relationship learned by XG-boost is expressed as:

$$\mathrm{THP_{pred}} = \sum_{k=1}^{n} \alpha_k \cdot T_k(\mathrm{Re}, p/e) + \beta, \quad (3)$$

where: α_k are the model coefficients, T_k represents the tree-based transformations learned by XG-boost, Re is the Reynolds number, p/e is the relative roughness parameter, β is the bias term.

4.4. Uncertainty analysis

The uncertainties and relative errors of key parameters, including temperature difference across the heater in the test section, air mass flow rate, solar radiation intensity, thermal efficiency, useful heat gained and the convective heat transfer coefficient of SAH were evaluated. The relative error results are presented in Table 3.

Table 3. Uncertainty analysis of experimental reading.

No.	Parameter	Attained values in SAH	Uncertainties	Relative error
1	Temperature differences [K]	16	±0.17	0.67
2	Mass-flow rate [kg s^{-1}]	0.062	±0.00103	1.67
3	Solar radiation [W m^{-2}]	900	±7	0.71
4	Thermal efficiency [%]	77.9	±0.02	0.027
5	Connective heat transfer [W m^{-2} K^{-1}]	47.9	±0.71	1.71
6	Useful heat gained by SAH [W]	872.8	±8.1	1.57

5. Results and discussion

The comparison between experimental and predicted values is conducted to validate the accuracy of the XG-boost model in forecasting the thermal performance of solar air heaters with different rib configurations. The detailed predicted values are presented in Table 4.

Table 4. Comparison of experimental and XG-boost-predicted THP values.

No.	Configuration (p/e)	Re = 2000	Re = 4000	Re = 6000	Re = 8000	Re = 10000	Re = 12000	Re = 14000	Re = 17000	Re = 20000	Mode
1	Polygonal (p/e = 5)	1.54	2.43	2.23	2.26	2.04	1.97	2.10	1.88	1.95	Experimental
		1.52	2.40	2.21	2.25	2.03	1.95	2.09	1.86	1.94	ML prediction
2	Polygonal (p/e = 7.5)	1.8	2.95	2.54	2.48	2.20	2.08	2.21	2.01	2.04	Experimental
		1.83	2.90	2.50	2.45	2.18	2.06	2.19	1.99	2.02	ML prediction
3	Polygonal (p/e = 10)	1.77	2.86	2.50	2.49	2.19	2.09	2.20	2.01	2.05	Experimental
		1.75	2.83	2.47	2.46	2.17	2.07	2.18	2.00	2.03	ML prediction
4	Trapezoidal (p/e = 5)	1.47	2.34	2.14	2.17	1.90	1.92	2.05	1.82	1.82	Experimental
		1.45	2.30	2.12	2.14	1.88	1.91	2.03	1.80	1.81	ML prediction
5	Trapezoidal (p/e = 7.5)	1.71	2.93	2.48	2.46	2.12	2.09	2.19	1.96	2.02	Experimental
		1.69	2.89	2.45	2.43	2.10	2.07	2.17	1.94	2.00	ML prediction
6	Trapezoidal (p/e = 10)	1.68	2.86	2.47	2.43	2.11	2.08	2.19	1.99	2.07	Experimental
		1.66	2.83	2.44	2.40	2.09	2.06	2.17	1.97	2.05	ML prediction

The comparison between the experimentally obtained values and machine learning (ML) predicted values using the XG-boost model provides significant insights into the reliability and efficiency of ML-based approaches in thermal performance prediction. The experimental results for the thermo-hydraulic performance (THP) under different rib configurations and Reynolds numbers were systematically evaluated and compared with the predicted values from the XG-boost model. The detailed comparison reveals that the ML predictions exhibit high accuracy, with deviations ranging between 2.24% and 4.90% from the experimental values, which falls within an acceptable error range for engineering applications.

The predictive capability of the XG-boost model highlights its effectiveness in capturing complex non-linear relationships

between the Re number, rib configurations and thermal performance metrics such as the Nu number, friction factor (*f*) and performance evaluation coefficient (PEC). The highest accuracy was achieved for mid-range Re numbers, where flow turbulence and heat transfer interactions were well represented in the training data.

From a technical standpoint, integrating ML models like XG-boost into thermal performance analysis presents several advantages for researchers and engineers. Traditional experimental methods require extensive resources, time, and high operational costs due to repeated physical setups, sensor calibrations and data acquisition processes. In contrast, once trained on experimental datasets, the XG-boost model can rapidly predict THP values under varied conditions without the need for additional physical testing, thereby reducing the overall time and cost by approximately 60−70% in iterative testing processes. This advantage is particularly beneficial for designing solar air heaters, heat exchangers and other thermal systems, where parametric studies involving multiple geometries and operating conditions can be computationally optimised before physical prototyping.

Figure 7 presents a heat map of the XG-boost model performance metrics for both training and testing datasets. The colour intensity highlights the magnitude of each metric, with lighter shades representing lower errors (MAE, RMSE and MAPE), and darker shades indicating higher values. The heat-map clearly shows that the model achieves high predictive accuracy ($R^2 \approx 0.98$) while maintaining low error values across both datasets, demonstrating its robustness and generalisation capability. This visual representation allows quick comparison of model performance metrics and effectively supports the reliability of the proposed ML approach.

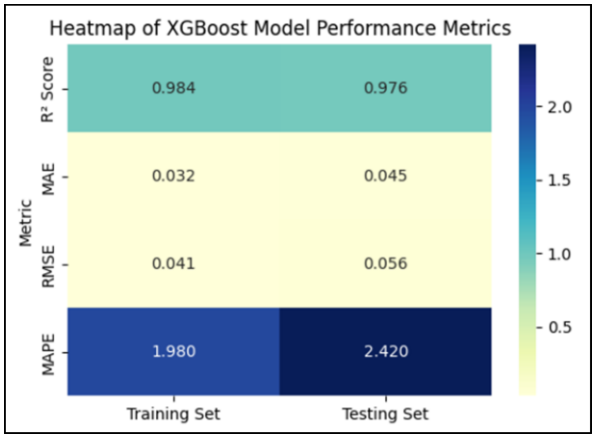


Fig. 7. Heat map of XG-boost model of THP prediction.

Additionally, ML-based predictions enable real-time analysis and optimisation, making them highly suitable for adaptive control systems in solar collectors. The model's ability to predict THP with high accuracy enables researchers to make data-driven decisions on material selection, rib design modifications and operational strategies, thereby enhancing the overall efficiency of thermal energy systems. The low MAE (0.032 for training and 0.045 for testing) and RMSE (0.041 for training and 0.056 for testing) demonstrate the model's robustness in minimising absolute and squared deviations between predicted and actual values. Moreover, the MAPE values (1.98% for training and 2.42% for testing) indicate that the XG-boost model maintains a low percentage error, ensuring reliable predictions even for unseen data points. The model's strong performance can be attributed to its ability to handle nonlinear dependencies, optimise feature importance and reduce over-fitting through gradient boosting and tree pruning techniques.

The implications of these findings are significant for the design and optimisation of energy-efficient solar air heaters. The ability to accurately predict THPS without extensive experimental iterations enables rapid prototyping of different rib configurations. This approach not only reduces computational costs but also accelerates the deployment of optimised solar air heater systems for sustainable energy applications. The performances are presented in Table 5.

These results strongly support the applicability of XG-boost for accurate THPS predictions and highlight its potential in enhancing thermo-hydraulic performance evaluations without the need for extensive experimental setups. Future studies can focus on integrating real-time sensor data with the XG-boost model to enable dynamic monitoring and adaptive control of solar air heater operations in varying climatic conditions.

Table 5. Performance metrics of XG-boost model for THPS prediction.

No.	Metric	Training Set	Testing Set
1	R^2 score	0.984	0.976
2	Mean absolute error (MAE)	0.032	0.045
3	Root mean squared error (RMSE)	0.041	0.056
4	Mean absolute percentage error (MAPE)	1.98%	2.42%

6. Challenges and future direction

6.1. Challenges

Despite notable progress in applying ML techniques to solar thermal energy systems, several critical challenges limit their large-scale implementation. One major issue is the limited availability of high-quality, real-time experimental data required for robust model training and validation. Additionally, developing generalised ML models that maintain prediction accuracy across diverse climatic zones, collector geometries and operating conditions remains challenging. The integration of ML algorithms with existing solar thermal infrastructure and control systems introduces practical complexities, including system compatibility and real-time deployment. Furthermore, high computational requirements, data pre-processing efforts and the need for models capable of handling highly nonlinear, transient and uncertain environmental conditions pose significant barriers to widespread adoption.

6.2. Future directions

Future research should prioritise the development of hybrid physics-informed machine learning models that couple energy

balance equations with data-driven algorithms to improve prediction accuracy, robustness, and physical interpretability. Emphasis should be placed on real-time implementation of ML models using edge computing and embedded systems for adaptive control, fault diagnosis and performance optimisation of solar thermal collectors. Advanced learning strategies such as deep neural networks, reinforcement learning for operational control, and transfer learning for climate-independent model generalisation are recommended to address data scarcity and site-specific limitations. Furthermore, tight integration of ML with Internet of Things (IoT) enabled sensor networks can enable high-resolution data acquisition for predictive maintenance and intelligent energy management. Finally, future studies should incorporate thermo-economic and sustainability metrics to support scalable, cost-effective and environmentally resilient solar thermal system design.

6.3. Research opportunities

Numerous research opportunities exist to advance ML applications in solar thermal energy. By optimising the integration of PCMs and hybrid nanofluids, ML can significantly enhance thermal storage and heat transfer efficiency, even under challenging weather conditions, while adhering to established guidelines [60]. ML can also be utilised for predictive maintenance, enabling proactive interventions that reduce downtime and operational costs. Developing localised solutions tailored to specific climatic and operational conditions can improve adoption rates, particularly in diverse regions. Furthermore, ML has the potential to optimise energy efficiency by minimising thermal and frictional losses and scaling applications for large solar thermal plants and decentralised systems, supporting the global transition to sustainable energy solutions.

7. Conclusions

The application of machine learning (ML) to solar collector systems marks a significant step forward in advancing solar thermal technologies by enabling highly accurate performance prediction, operational flexibility and improved system responsiveness. ML-based models provide reliable estimation of thermal and thermo-hydraulic behaviour, allowing real-time optimisation of heat transfer characteristics and reduction of operational expenses. In particular, tree-based learning approaches such as XG-boost have proven effective in representing complex nonlinear interactions in SAH, incorporating artificial roughness and PCM, with prediction errors consistently within acceptable limits when compared with experimental observations.

Beyond predictive modelling, ML enhances system reliability through continuous monitoring, early fault detection and intelligent control, thereby extending the operational lifespan of solar collectors. Data-driven insights further support the optimisation of hybrid nanofluids and PCM configurations, improving thermal storage and heat transfer performance across a wide range of climatic conditions. The capacity of ML algorithms to analyse large-scale datasets also enables the development of region-specific performance models, increasing the practical applicability of solar thermal systems in diverse environments.

Despite these advantages, challenges related to data quality, computational requirements, and system integration remain and require focused attention. Future advancements should emphasise physics-informed ML frameworks, hybrid learning strategies, and tighter coupling with CFD tools to enhance model generalisation and physical consistency. Overall, this study reinforces the role of ML as a powerful enabler for intelligent, efficient, and sustainable solar thermal energy systems, contributing meaningfully to next-generation renewable energy solutions.

Acknowledgements

The research was supported by the European Commission HORIZON 2020 project RESHeat in the field of research and innovation under grant agreement No. 956255.

References

[1] Gill, R.S., Hans, V.S., Saini, J.S., & Sukhmeet, S. (2016). Investigation on performance enhancement due to staggered piece in a broken arc rib roughened solar air heater duct. *Renewable Energy*, 104, 148–162. doi: 10.1016/j.renene.2016.12.002

[2] Vipin, B., Gawande, A.S., Dhoble, D.B., & Zodpe, S.C. (2016). Experimental and CFD investigation of convection heat transfer in solar air heater with reverse L-shaped ribs. *Solar Energy*, 131, 275–295. doi: 10.1016/j.solener.2016.02.040

[3] Kumar, K., Prajapati, D.R., & Samir, S. (2017). Heat Transfer and Friction Factor Correlations Development for Solar Air Heater Duct Artificially Roughened with 'S' Shape Ribs. *Experimental Thermal and Fluid Science*, 82, 249–261. doi: 10.1016/j.expthermflusci.2016.11.012

[4] Lanjewar, A., Bhagoria, J.L., & Sarviya, R.M. (2011). Heat transfer and friction in solar air heater duct with W-shaped rib roughness on absorber plate. *Energy*, 36, 531– 4541. doi: 10.1016/j.energy.2011.03.054

[5] Tanda, G. (2011). Performance of solar air heater ducts with different types of ribs on the absorber plate. *Energy*, 36, 6651–6660. doi: 10.1016/j.energy.2011.08.043

[6] Eiamsa-Ard, S., & Promvonge, P. (2009). Thermal characteristics of turbulent rib-grooved channel flows. *International Communications in Heat and Mass Transfer*, 36. 705–711. doi: 10.1016/j.icheatmasstransfer.2009.03.025

[7] Bhushan, B., & Singh, R. (2011). Nusselt number and friction factor correlations for solar air heater duct having artificially roughened absorber plate. *Solar Energy.* 85, 1109–1118. doi: 10.1016/j.solener.2011.03.007

[8] Yadav, A.S., & Bhagoria, J.L. (2014). A numerical investigation of square-sectioned transverse rib roughened solar air heater. *International Journal of Thermal Science*, 79. 111–131. doi: 10.1016/j.ijthermalsci.2014.01.008

[9] Anil, K., & Man-Hoe, K. (2015). Effect of roughness width ratios in discrete multi V-rib with staggered rib roughness on overall thermal performance of solar air channel. *Solar Energy*, 119, 399–414. doi: 10.1016/j.solener.2015.06.030

[10] Kamali, R., & Binesh, A.R. (2008). The importance of rib shape effects on the local heat transfer and flow friction characteristics of square ducts with ribbed internal surfaces. *International Communications in Heat and Mass Transfer*, 35, 1032–1040. doi: 10.1016/j.icheatmasstransfer.2008.04.012

[11] Ramadhan, A.I., Azmi., W.H., Mamat, R., & Hamid, K.A. (2020). Experimental and numerical study of heat transfer and friction factor of plain tube with hybrid nanofluids. *Case Studies*

in Thermal Engineering, 22(1), 100782. doi: 10.1016/j.csite.2020.100782

[12] Nadeem, S., Ali, S., Alzabut, J., Hamida, M.B.B., & Eldin, S.M. (2023). Numerical investigation of the influence of hybrid nanofluid on heat transfer in semi-annular channel. *Case Studies in Thermal Engineering*, 44, 102855. doi: 10.1016/j.csite.2023.102855

[13] Rahman, M.M., Chamkha, A.J., Elmasry, Y., Ullah, I., Pasha, A.A., Sadeghi, M.S., & Galal, A.M. (2022). The heat transfer behavior of MHD micro-polar MWCNT-Fe_3O_4/Water Hybrid Nano-fluid in an inclined ⊥ shaped cavity with semi-circular heat source inside. *Case Studies in Thermal Engineering*, 38, 102316. doi: 10.1016/j.csite.2022.102316

[14] Javidan, M., Gorji-Bandpy, M., & Al-Araji, A. (2023). Investigation and simulation of parabolic trough collector with the presence of hybrid nanofluid in the finned receiver tube. *Theoretical and Applied Mechanics Letters*, 13(6), 100465. doi: 10.1016/j.taml.2023.100465

[15] Rashid, F.L., Aljibori, H.S.., Mohammed, H.I., Ameen, A., Ahmad, S., Hamida, M.B.B., & Al-Rubaye, A.H. (2024). Recent advances and developments of the application of hybrid nanofluids in parabolic solar collector energy systems and guidelines for prospects. *Journal of Engineering Research*, 14(1), 246–265. doi: 10.1016/j.jer. 2024.04.023

[16] Kabeel, A.E., Khalil, A., Shalaby, S.M. & Zayed, M.E. (2016). Experimental Investigation of Thermal Performance of Flat and V-Corrugated Plate Solar Air Heaters with and without PCM as Thermal Energy Storage. *Energy Conversion and Management*, 113, 264−272. doi: 10.1016/j.enconman.2016.01.068

[17] Kabeel, A.E., Khalil, A., Shalaby, S.M., & Zayed, M.E. (2017). Improvement of Thermal Performance of the Finned Plate Solar Air Heater by Using Latent Heat Thermal Storage. *Applied Thermal Engineering*, 123, 546−553. doi: 10.1016/j.applthermaleng.2017.05.126

[18] Aymen, E.L., El Khadraoui, A., Bouadila, S., Kooli, S., Guizani, A., & Farhat, A. (2016). Solar Air Heater with Phase Change Material: An Energy Analysis and a Comparative Study. *Applied Thermal Engineering*, 107, 1057. doi: 10.1016/j.applthermaleng.2016.07.004

[19] SunilRaj, B.A., & Eswaramoorthy, M. (2020). Experimental Study on Hybrid Natural Circulation Type Solar Air Heater with Paraffin Wax Based Thermal Storage. *Materials Today: Proceedings*, 23(1). 49−52. doi: 10.1016/j.matpr.2019.06.381

[20] Kalaiarasi, G., Velraj, R., Vanjeswaran, M.N., & Pandian, N.G. (2020). Experimental Analysis and Comparison of Flat Plate Solar Air Heater with and without Integrated Sensible Heat Storage. *Renewable Energy*, 150, 255−265. doi: 10.1016/j.renene.2019.12.116

[21] Kumar, B.V., Manikandan, G., Kanna P.R., Taler, D., Taler, J., Nowak-Ocłoń, M., Mzyk, K., & Toh, H.T. (2018). A Performance Evaluation of Solar Air Heater Using Different Shape of Ribs Mounted in Absorber Plate – A Review. *Energies*, 11(11), 3104, 2−20. doi: 10.3390/en11113104

[22] Kumar, B.V., Manikandan, G., & Kanna, P.R. (2021). Enhancement of heat transfer in SAH with polygonal and trapezoidal shape of the rib using CFD. *Energy*, 234, 121154. doi: 10.1016/j.energy.2021.121154

[23] Kumar, B.V., Manikandan, G., Kanna, P.R., & Reddy V.P. (2022). Experimental Analysis of Solar Air Heater using Polygonal Ribs in Absorber Plate Integrated with Phase Change Material. *Thermal Science*, 26(4A), 3187−3199. doi: 10.2298/TSCI210518345V

[24] Elsheikh, A., Faqeha, H., Hammoodi, K.A., Bawahab, M., Fujii, M., Shanmugan, S., Essa, F.A., Abd-Elaziem, W., Ramesh, B., Sathyamurthy, R., & Egiza, M. (2025). Integrating predictive and hybrid Machine Learning approaches for optimizing solar still performance: A comprehensive review. *Solar Energy*, 295, 113536. doi: 10.1016/j.solener.2025.113536

[25] Shafian, N.B.A., Husen, M.N., Xie, L., & Kim, K. (2025). Predicting High-Performance Perovskite Solar Cells Using AI-based Machine Learning Models. *Materials Today Sustainability*, 31, 101176. doi: 10.1016/j.mtsust.2025.101176

[26] Khouili, O., Hanine, M., Louzazni, M., Flores, M.A.L., Villena, E.G., & Ashraf, I. (2025). Evaluating the impact of deep learning approaches on solar and photovoltaic power forecasting: A systematic review. *Energy Strategy Reviews*, 59, 101735. doi: 10.1016/j.esr.2025.101735

[27] Kushwah, A., Kumar, A., & Kumar, S. (2024). Predictive modelling with machine learning of garlic clove for novel designed solar drying system. *Solar Energy*, 284, 113070. doi: 10.1016/j.solener.2024.113070

[28] Abdelkader, T.K., Sayed, H.A.A., Refai, M., Ali, M.M., Zhang, Y., Wan, Q., Khalifa, I., Fan, Q., Wang, Y., & Abdelhamid, M.A. (2024). Machine learning, mathematical modeling and 4E (energy, exergy, environmental, and economic) analysis of an indirect solar dryer for drying sweet potato. *Renewable Energy*, 227, 120535. doi: 10.1016/j.renene.2024.120535

[29] Arunkumar, P.M., Balaji, N., Madhankumar, S., & Mohanraj, T. (2024). Prediction of red chilli drying performance in solar dryer with natural energy storage element using machine learning models. *Journal of Energy Storage*, 101, 113825. doi: 10.1016/j.est.2024.113825

[30] Baz, A., & Patel, S.K. (2024). Efficiency-aware machine-learning driven design of solar harvester for renewable energy application. *Results in Engineering*, 24, 103050. doi: 10.1016/j.rineng.2024.103050

[31] Madhankumar S., Ilangovan, D., & Viswanathan, K. (2024). Integrating computational models and machine learning for corrugated absorber plate solar collector thermal predictions. *Process Safety and Environmental Protection*, 188, 336–349. doi: 10.1016/j.psep.2024.05.069

[32] Nidhul, K., Thummar, D., Yadav, A.K., & Anish, S. (2023). Machine learning approach for optimization and performance prediction of triangular duct solar air heater: A comprehensive review. *Solar Energy*, 255, 396−415. doi: 10.1016/j.solener.2023.02.022

[33] Saravanan, A., Parida, S., Murugan, M.., Reddy, M.S., Elumalai, P.V., & Dash, S.K. (2023). Thermal performance prediction of a solar air heater with a C-shape finned absorber plate using RF, LR and KNN models of Machine learning. *Thermal Science and Engineering Progress*, 38, 101630. doi: 10.1016/j.tsep.2022.101630

[34] Zohdi, T.I. (2023). A machine-learning digital-twin for rapid large-scale solar-thermal energy system design. *Computer Methods in Applied Mechanics and Engineering*, 412, 115991. doi: 10.1016/j.cma.2023.115991

[35] Chilambarasan, L., Thangarasu, V., & Ramasamy, P. (2024). Solar flat plate collector's heat transfer enhancement using grooved tube configuration with alumina nanofluids: Prediction of outcomes through artificial neural network modelling. *Energy*, 289, 129953. doi: 10.1016/j.energy.2023.129953

[36] Yadav, A.K., Yadav, V., Kumar, A., Kumar, R., Lee, D., & Singh, T. (2024), Novel feature selection based ANN for optimal solar panels tilt angles prediction in microgrid. *Case Studies in Thermal Engineering.* 61. 104853. doi: 10.1016/j.csite.2024.104853

[37] Ganeshkumar, P., Sivalingam, V., Prasanth, B.M., Kumar, K.S., Kim, S.C., Vanaraj, R., Alodhayb, A.N., & Pandiaraj, S. (2024).

Predicting thermal performance in solar air heaters with V-corrugated, shot-blasted absorber plate, and black pebble-based sensible heat storage: A machine learning approach. *Journal of Energy Storage*, 100, 113450. doi: 10.1016/j.est.2024.113450

[38] Thakur, A., Kumar, R., Lee, D., Kumar, S., Kumar, P., Asif, M., & Ağbulut, Ü. (2024). Improved performance evaluation of a dual passage solar thermal collector using staggered turbulators. *Thermal Science and Engineering Progress*, 53, 102668. doi: 10.1016/j.tsep.2024.102668

[39] Rajan, A., & Reddy, K.S. (2024). Integrated optical-thermal model and deep learning technique to estimate the performance of a conical cavity receiver coupled solar parabolic dish collector. *Energy Conversion and Management*, 301, 118052. doi: 10.1016/j.enconman.2023.118052

[40] Bingbin, G., Dianwei Q., Zhou, J., Qian, N., & Zhang, L. (2024). Interpretable machine learning study of a collector based on combined twisted-tape and wavy-tape inserts. *Case Studies in Thermal Engineering*, 63, 105236. doi: 10.1016/j.csite.2024.105236

[41] Gupta, A., Das, B., Arslan, E., Das, M., Kosan, M., & Can, O.F. (2024). Artificial neural networks based computational and experimental evaluation of thermal and drying performance of partially covered PVT solar dryer. *Process Safety and Environmental Protection*, 183, 1170−1185. doi: 10.1016/j.psep.2024.01.068

[42] Alawi, O.A., Kamar, H.M., Salih, S,Q., Abba, S.I., Ahmed, W., Homod, R.Z., Jamei, M., Shafik, S.S., & Yaseen, Z.M. (2024). Development of optimized machine learning models for predicting flat plate solar collectors thermal efficiency associated with Al_2O_3-water nanofluids. *Engineering Applications of Artificial Intelligence*, 133, Part B, 108158. doi:10.1016/j.engappai.2024.108158.

[43] Alade, I.O., Rahman, M.A.A., & Saleh, T.A. (2019). Predicting the specific heat capacity of alumina/ethylene glycol nanofluids using support vector regression model optimized with Bayesian algorithm. *Solar Energy*, 183, 74−82. doi: 10.1016/j.solener.2019.02.060

[44] Alade, I.O., Rahman, M.A.A., & Saleh, T.A. (2019). Modeling and prediction of the specific heat capacity of Al_2O_3/water nanofluids using hybrid genetic algorithm/support vector regression model. *Nano-Structures and Nano-Objects*, 17, 103−111. doi:10.1016/j.nanoso.2018.12.001

[45] Meybodi, M.K., Naseri, S., Shokrollahi, A., & Daryasafar, A. (2015). Prediction of viscosity of water-based Al_2O_3, TiO_2, SiO_2, and CuO nanofluids using a reliable approach. *Chemometrics and Intelligent Laboratory Systems*, 149(5), 60−69. doi: 10.1016/j.chemolab.2015.10.001

[46] Baghban, A., Jalali, A., Shafiee, M., Ahmadi, M.H., & Chau, K. (2019). Developing an ANFIS-based swarm concept model for estimating the relative viscosity of nanofluids. *Engineering Applications of Computational Fluid Mechanic*s, 13(1), 26–39. doi: 10.1080/19942060.2018.1542345

[47] Wu, S., Wang, C., & Tang, R. (2022). Optical efficiency and performance optimization of a two-stage secondary reflection hyperbolic solar concentrator using machine learning. *Renewable Energy*, 188, 437−449. doi: 10.1016/j.renene.2022.01.117

[48] Alhamayani, A. (2024). Performance analysis and machine learning algorithms of parabolic trough solar collectors using Al2O3-MWCNT as a hybrid nanofluid. *Case Studies in Thermal Engineering*, 57, 104321. doi: 10.1016/j.csite.2024.104321

[49] Said, Z., Sharma, P., Sundar, L.S., Li, C., Tran, D.C., Pham, N.D.K., & Nguyen, X.P. (2022). Improving the thermal efficiency of a solar flat plate collector using MWCNT-Fe_3O_4/water hybrid nanofluids and ensemble machine learning. *Case Studies in Thermal Engineering*, 40, 102448. doi: 10.1016/j.csite.2022.102448

[50] Al-Rashed, A.A.A.A., Alnaqi, A.A., & Alsarraf, J. (2021). Numerical investigation and neural network modeling of the performance of a dual-fluid parabolic trough solar collector containing non-Newtonian water-CMC/Al2O3 nanofluid. *Sustainable Energy Technologies and Assessments*, 48, 101555. doi: 10.1016/j.seta.2021.101555

[51] Bouzgou, H., & Gueymard, C.A. (2017). Minimum redundancy – Maximum relevance with extreme learning machines for global solar radiation forecasting: Toward an optimized dimensionality reduction for solar time series. *Solar Energy*, 158, 595−609. doi: 10.1016/j.solener.2017.10.035

[52] Fuxi, S., Sina, N., Sajadi, S.M., Mahmoud, M.Z., Abdelrahman, A., & Aybar, H.Ş. (2022). Artificial neural network modeling to examine spring turbulators influence on parabolic solar collector effectiveness with hybrid nanofluids. *Engineering Analysis with Boundary Elements*, 143, 442−456. doi: 10.1016/j.enganabound.2022.06.026

[53] Zayed, M.E., Kabeel, A.E., Shboul, B., Ashraf, W.M., Ghazy, M., Irshad, K., Rehman, S., & Zayed, A.A.A. (2023). Performance augmentation and machine learning-based modeling of wavy corrugated solar air collector embedded with thermal energy storage: Support vector machine combined with Monte Carlo simulation. *Journal of Energy Storage*, 74, 109533. doi: 10.1016/j.est.2023.109533

[54] Badji, A., Benseddik, A., Boukhelifa, A., Bensaha, H., Erregani, R.M., Bendriss, A., Bouhoun, S., Nettari, C.H., Kaouane, M., & Lalmi, D. (2023). Solar air heater with underground latent heat storage system for greenhouse heating: Performance analysis and machine learning prediction. *Journal of Energy Storage*, 74, Part B, 109548. doi: 10.1016/j.est.2023.109548

[55] Mausam, K., Singh, S., Ghosh, S.K., & Singh, R.P. (2024). Thermal performance modelling of solar flat plate parallel tube collector using ANN. *Energy*, 303, 131940. doi: 10.1016/j.energy.2024.131940

[56] Mustafa, J., Alqaed, S., & Sharifpur, M. (2022). Numerical study on performance of double-fluid parabolic trough solar collector occupied with hybrid non-Newtonian nanofluids: Investigation of effects of helical absorber tube using deep learning. *Engineering Analysis with Boundary Elements*, 140, 562−580. doi: 10.1016/j.enganabound.2022.04.033

[57] ASHRAE Standard 93. *(*2003). *Method of testing to determine the thermal performance of solar collectors*. American Society of Heating, Refrigeration and Air Conditioning Engineers, 30329, Atlanta, USA.

[58] Taler, D., & Taler, J. (2017). Simple heat transfer correlations for turbulent tube flow. *E3S Web of Conferences*, 13, 02008. doi: 10.1051/e3sconf/20171302008

[59] Ghritlahre, H.K., Chandrakar, P., & Ahmad, A. **(**2020). Application of ANN model to predict the performance of solar air heater using relevant input parameters, *Sustainable Energy Technologies and Assessments*, 40, 100764. doi: 10.1016/j.seta.2020.100764

[60] Kumar, G.H., Purvi, C., & Ashfaque, A. (2020). Solar air heater performance prediction using artificial neural network technique with relevant input variables. *Archives of Thermodynamics*, 41(3), 255−282. doi: 10.24425/ather.2020.134579

[61] Ghritlahre, H.K., & Prasad, R.K. (2019). Modelling of back propagation neural network to predict the thermal performance of porous bed solar air heater. *Archives of Thermodynamics*, 40(4), 103−128. doi: 10.24425/ather.2019.131430

[62] Ghritlahre, H.K., & Verma, M. (2020). Solar air heaters performance prediction using multi-layer perceptron neural network–

A systematic review. *Energy Sources, Part A: Recovery, Utilization, and Environmental Effects*, 41(1), 7682−7699. doi: 10.1080/15567036.2021.1923869

[63] Ghritlahre, H.K., Chandrakar, P., & Ahmad, A. (2021). A Comprehensive Review on Performance Prediction of Solar Air Heaters Using Artificial Neural Network. *Annals of Data Science*, 8, 405−449. doi: 10.1007/s40745-019-00236-1

[64] Tschopp, D., Ohnewein, P., Stelzer, R., Feierl, L., Hamilton-Jones, M., Moser, M., & Holter, C. (2023). One year of high-precision operational data including measurement uncertainties from a large-scale solar thermal collector array with flat plate collectors, located in Graz, Austria. *Data in Brief*, 48, 109224. doi: 10.1016/j.dib.2023.109224

[65] Falope, T.O., Lao, L., & Hanak, D. (2024). A Three-Step Weather Data Approach in Solar Energy Prediction Using Machine Learning. *Renewable Energy Focus*, 50, 100615. doi: 10.1016/j.ref.2024.100615

[66] Pereira, F., & Silva, C. (2024). Machine learning for monitoring and classification in inverters from solar photovoltaic energy plants. *Solar Compass*, 9, 100066. doi: 10.1016/j.solcom.2023.100066

[67] Kumar, B.V., Kanna, P.R., Manikandan, G., Taler, D., Taler, J., Sobota, T., & Nowak-Ocłoń, M. (2023). Investigation of thermo-hydraulic performances of artificial ribs mounted in a rectangular duct. *Energies*, 16(11), 4404. doi: 10.3390/en16114404

[68] Holman, J.P. (2004). *Experimental methods for engineers* (7 th ed.). Tata McGraw-Hill Publishing Company Limited, New Delhi.

Co-published by
Institute of Fluid-Flow Machinery
Polish Academy of Sciences
Committee on Thermodynamics and Combustion
Polish Academy of Sciences

Copyright©2026 by the Authors under licence CC BY-NC-ND 4.0

http://www.imp.gda.pl/archives-of-thermodynamics/

An alternative formulation of the method of weighted residuals for the approximate solving of heat conduction problems

Jan Taler[a*], Dawid Taler[b]

[a]Cracow University of Technology, Faculty of Environmental Engineering and Energy, Department of Energy, 31-864 Cracow, Poland
[b]Cracow University of Technology, Faculty of Environmental Engineering and Energy, Department of Thermal Processes, Air Protection and Waste Utitilisation, 31-155 Cracow, Poland
*Corresponding author email: jan.taler@pk.edu.pl

Received: 27.01.2026; accepted: 19.02.2026

Abstract

An alternative formulation of the method of weighted residuals for Fourier's law of heat conduction is presented. In one-dimensional heat conduction, when the weighting factor equals unity and the heat-penetration-depth concept is used, the method reduces to the heat flux integral method. The paper also presents a comparison of the proposed heat flux integral method with the classic heat balance integral method developed by T.R. Goodman. In the heat balance integral method, the transient heat conduction equation is integrated with respect to the spatial coordinate, whereas in the heat flux integral method, Fourier's law is integrated over the spatial coordinate. The advantage of the heat flux integral method over the heat balance integral method is the greater accuracy, especially in bodies whose thermal conductivity depends on temperature or position. The greater accuracy of the proposed method is illustrated by the determination of the transient temperature distribution in a plate with temperature-dependent thermal conductivity. Additionally, for a straight fin with temperature-dependent thermal conductivity, the heat flux integral method provides greater accuracy in determining temperature and fin efficiency than the heat balance integral method. The temperature distribution in the plate and fin, as well as the fin efficiency, were also determined using the finite volume method to assess the accuracy of the heat flux integral method and heat balance integral method.

Keywords: Heat balance integral method; Heat flux integral method; Nonlinear heat conduction; Fin with variable thermal conductivity; Transient nonlinear heat conduction in a plate

Vol. 47(2026), No. 1, 25–41; doi: 10.24425/ather.2026.158663

Cite this manuscript as: Taler, J., & Taler, D. (2026). An alternative formulation of the method of weighted residuals for the approximate solving of heat conduction problems. *Archives of Thermodynamics*, 47(1), 25−41.

1. Introduction

A method of weighted residuals (MWR) is an approximate analytical method widely used to solve boundary and initial-boundary problems in thermal engineering. The popularity of the MWR stems from the simplicity and high accuracy of the analytical solutions obtained using this method, as well as the moderate effort required to calculate temperature values [1].

The MWR and its application to calculating temperature fields in boiler components are presented in [2]. Two-dimensional steady-state temperature and stress distributions in the tubes of the membrane walls of large steam boilers were determined. Using the MWR, transient temperature and stress distributions in pipelines, boiler drums and steam superheaters' headers were calculated [2]. In most cases, the solutions obtained not only illustrate the application of MWR but are also of great importance for industrial practice.

The MWR is an effective tool for solving nonlinear ordinary and partial differential equations, thanks to its simplicity and high accuracy. Hatami [3] demonstrated that MWRs, such as

Nomenclature

A – area, m^2
a, b, c – constants
$a_1, \ldots, a_n$ – unknown coefficients in the function approximating the temperature distribution
c – specific heat capacity, J/(kg·K)
C – constant
$C_1, \ldots, C_7$ – constants
$e_{\theta,i}$ – temperature difference $e_{\theta,i} = \theta_{i,num} - \theta_{i,app}$, $i = 1, \ldots, n$ between temperature values $\theta_{i,num}$ calculated by the numerical method and temperature $\theta_{i,app}$ calculated by HFIM or HBIM, K
$e_{\theta,\max}$ – maximum temperature difference between the temperature values $\theta_{i,num}$ calculated numerically by the method of lines, and the temperature $\theta_{i,app}$ calculated by the approximate analytical method HFIM or HBIM, K
$\bar{e}_\theta$ – mean-square temperature difference, K
Fo – Fourier number, Fo = $\alpha_0 \cdot t/L^2$
Fo$_1$ – Fourier number at the end of the first heat penetration phase, Fo$_1$ = $\alpha_0 \cdot t_1/L^2$
g, f, e – coefficients
H – heat transfer coefficient (HTC), W/(m^2·K)
k – thermal conductivity, W/(m·K)
K – dimensionless thermal conductivity,
L – plate thickness or fin height, m
m – power exponent in the heat conduction equation; $m = 1$ for cylindrical wall and $m = 2$ for spherical wall
n – number of nodes in the FVM grid
N – fin parameter, $N^2 = 2hL^2/[k(T_f)w]$
$\dot{q}$ – heat flux, W/m^2
$\dot{q}_{in}$ – heat flux at the inner surface, W/m^2
$\dot{q}_v$ – heat transfer rate per unit volume, W/m^3
$\dot{\mathbf{q}}$ – heat flux vector, W/m^2
$\tilde{q}$ – approximate solution for heat flux, W/m^2
r_{in} – inner radius, m
r_{out} – outer radius, m
R – radius, m
t – time, s
t_1 – the time after which the first phase of heat penetration ends, s
T – temperature, °C
T_b – fin base temperature, °C
T_f – fluid temperature, °C
T_s – slab surface temperature, °C
T_0 – initial temperature, °C
W – fin thickness, m
W_i – weighting factor
$\mathbf{W_i}$ – vector weighting factor
x, y, z – Cartesian coordinates, m
X – dimensionless x coordinate, $X = x/L$

Greek symbols

α – thermal diffusivity, m^2/s
$\alpha_C, \beta_C, \gamma_C, \alpha_c, \beta_c, \gamma_c$ – coefficients in a quadratic algebraic equation for determining the constant C
β, β_k – coefficients in functions determining the dependence of thermal conductivity on temperature
ΔX – dimensionless spatial step in FVM
∇ – gradient operator (nabla)
δ – heat penetration depth, m
δ^* – dimensionless heat penetration depth, $\delta^* = \delta/L$
Γ – boundary of the domain Ω
ε – constant in the function describing changes in the thermal conductivity as a function of temperature
η – fin efficiency
θ – dimensionless fin temperature, $\theta = (T - T_f)/(T_b - T_f)$
θ – dimensionless plate temperature, $\theta = (T - T_0)/(T_s - T_0)$
ρ – density, kg/m^3
Ω – domain with the boundary Γ

Subscripts and Superscripts

$\bar{}$ – mean
$\sim$ – approximate
$*$ – dimensionless
b – fin base
f – fluid temperature
i – node number or the weighting factor
in – inner surface
s – surface
out – outer surface
v – volume heat source
0 – at the initial state
I – the first phase of heat penetration
II – the second phase of heat penetration

Abbreviations and Acronyms

FVM – finite volume method
HBIM – heat balance integral method
HFIM – heat flux integral method
HTC – heat transfer coefficient
MWR – method of weighted residuals

collocation, Galerkin, Rayleigh–Ritz and least-squares methods, yield satisfactory results when solving numerous linear and nonlinear problems in heat transfer, nanotechnology and medicine. MRWs constitute a large group of methods, alongside other approximate analytical methods and analytical-numerical methods for solving ordinary and partial differential equations [4]. Ganji et al. [5] applied approximate analytical methods for direct nonlinear problems encountered in heat transfer. The homotopy perturbation, variational iteration and Adomian decomposition methods were used to solve nonlinear conduction-convection heat transfer problems, such as the cooling of a lumped system with a variable specific heat or heat transfer coefficient, and to determine the temperature distribution in a straight fin with a temperature-dependent conductivity. One of the most popular MWRs is the Galerkin method, which is now also used in the finite element method (FEM) [6]. Another widely used procedure is the method of moments, applied to approximate the distribution of substance concentration [7] or temperature in heat and mass transfer problems, as well as in electromagnetics [8]. A special case of MWR is the heat balance integral method (HBIM) proposed by Goodman [9]. An important and original feature of HBIM proposed by Goodman is the application of the boundary-layer thickness concept to transient heat conduction in solids. A counterpart of the thermal boundary layer thickness in convective heat transfer is the heat penetration depth in HBIM. The concept of boundary-layer thickness was originally pro-

posed by Pohlhausen [10] and von Kármán [11] to determine the distributions of velocity and temperature in a fluid near the channel surface. Due to the large velocity and temperature gradients normal to the channel surface, it is challenging to determine the correct distributions of fluid velocity and temperature near the channel wall, even with modern computational fluid dynamics (CFD) methods. A major advantage of HBIM, on the other hand, is the ability to determine the temperature of a solid near its surface for a very short heating or cooling time. Determining the temperature distribution in a solid at the beginning of a transient process using exact analytical methods can be subject to large errors due to the slow convergence of infinite series. Additionally, for numerical methods, it is necessary to integrate the heat conduction equation using very small time steps to achieve satisfactory accuracy in determining the temperature field near $t = 0$. The use of HBIM enables the determination of optimum fluid temperature changes at the beginning of heating pressurised structural elements over very small time intervals [12].

The HBIM method can also be used to solve problems of great practical importance, for example, to determine the optimal temperature changes in a fluid during the heating of a thick-walled pressure element with holes, accounting for the time-dependent pressure inside the component [13]. HBIM can also be used to approximate two-dimensional steady-state temperature distributions. The two-dimensional temperature distribution in tubes and flat bars (fins) connecting tubes in the tight waterwalls of the boiler combustion chamber was determined using HBIM in [14]. The temperature distribution in the boiler waterwall tube was also investigated in [15]. Examples of the application of HBIM to calculate transient temperature distributions in a half-space and a flat plate for various boundary conditions are presented in books [15,16]. HBIM is widely used for calculating temperature and thermal-stress fields in solids, as well as for thermal analysis of melting and solidification processes, and is continually being refined. Volkov and Li-Orlov [17] employed double integration of the heat conduction equation along the x-coordinate, as opposed to the single integration used in classical HBIM. Thanks to double integration, the accuracy of determining the transient temperature distribution in bodies with a temperature-dependent thermal conductivity has been increased. It should be emphasised that greater accuracy in the approximate solution for temperature-dependent thermal conductivity can also be achieved by using the Galerkin or moment method, with the concept of heat penetration depth used in HBIM. However, this requires slightly more mathematical transformations to determine the temperature distribution. The accuracy of HBIM, like all MWRs, depends on the accuracy of the solution obtained from the appropriate selection of the form of the function approximating the exact solution. Sitison and Edwards [18] applied the heat balance integral method to determine two-dimensional temperature distribution in cylindrical extruders. The problem was solved using a quasi-steady approximation in the crystal and HBIM in the melt.

Kumar and Rajeev [19] solved a time-fractional Stefan problem with a third-kind boundary condition and temperature-dependent thermal conductivity using HBIM. The conventional HBIM approach, utilising quadratic and exponential temperature profiles, was employed to determine an approximate temperature distribution.

A new approximation function for the temperature distribution using the Legendre wavelet was used by Chaurasiya et al. [20] in HBIM to solve a two-dimensional moving-boundary problem involving a moving phase-change material. They compared numerical results with the exact solution by transforming the analysed problem into a one-dimensional melting problem and found good agreement.

A review of the literature shows that the method of weighted residuals, in particular HBIM, is widely used in practice, both globally, where a single function approximates the temperature distribution across the entire analysed area, and in numerical methods such as FEM or hybrid FVM-FEM, in which MWR is applied locally, separately for each element. The abbreviation FVM stands for finite volume method, in which the energy conservation equation is satisfied for each finite volume with a node located inside it. In the case of heat conduction, MWR is formulated for the transient heat conduction equation, i.e. the energy conservation equation, which accounts for Fourier's law.

This paper presents a new formulation of MWR for solving heat conduction problems. MWR has been applied to Fourier's law, and not as in the classical MWR for the transient heat conduction equation, i.e. for the energy conservation equation.

The advantage of the new MWR formulation is its greater accuracy compared to the traditional MWR formulation, particularly when the weighting factor equals one. Both methods were compared using two examples: determining the transient temperature field in a plate with temperature-dependent thermal conductivity and determining the temperature and efficiency of a fin with temperature-dependent thermal conductivity. The new MWR formulation, with a weighting factor of 1, referred to as the heat flux integral method (HFIM), yields higher-accuracy solutions than the traditional MWR formulation (HBIM) in both cases.

The paper presents the following issues in sequence: characteristics of the classical MWR, a new formulation of MWR in heat conduction problems, determining the transient temperature of a flat wall with linearly dependent thermal conductivity using HBIM and HFIM, determining the temperature and efficiency of a fin with linearly dependent thermal conductivity using HBIM and HFIM, conclusions, future work, and, in the Appendix, two different approaches for determining one-dimensional steady-state temperature distributions.

The next section will provide a brief discussion of classical MWR, focusing on the integral heat balance method.

2. Classic MWRs in heat conduction problems

MWRs are widely used for approximate solutions to boundary and initial-boundary problems of heat conduction. The governing heat conduction equation is:

$$c(T)\rho(T)\frac{\partial T}{\partial t} = \nabla \cdot [k(T)\nabla T] + \dot{q}_v. \tag{1}$$

The boundary conditions and initial conditions are known. The initial condition is as follows:

$$T|_{t=0} = T_0(x,y,z). \quad (2)$$

The approximate solution $\tilde{T}$ of Eq. (1) satisfying the boundary conditions is sought in the form:

$$\tilde{T} = \tilde{T}[x,y,z,a_1(t),\ldots,a_n(t),t]. \quad (3)$$

The parameters $a_1(t)$, …, $a_n(t)$ are determined using the WRM method from the following system of equations:

$$\int_\Omega \left\{c(\tilde{T})\rho(\tilde{T})\frac{\partial \tilde{T}}{\partial t} - \nabla\cdot\left[k(\tilde{T})\nabla\tilde{T}\right] - \dot{q}_v\right\} W_i dV = 0, \quad i = 1,\ldots,n. \quad (4)$$

The initial values of parameters $a_1(0)$,…, $a_n(0)$ are determined from the solution of the following system of algebraic equations:

$$\int_\Omega \{\tilde{T}[x,y,z,a_1(0),\ldots,a_n(0)] - T_0(x,y,z)\}\ W_i dV = 0, \quad i = 1,\ldots,n. \quad (5)$$

A system of ordinary differential equations or algebraic equations from which the unknown coefficients a_i are determined consists of n equations. In practical applications, the unknown parameters a_1,…, a_n are independent of time.

Depending on the weighting factor W_i, several MWRs [1] can be distinguished, such as the heat balance method, when $W_1 = 1$ and $W_i = 0$ for $i = 2, \ldots, n$; the moment method, when for one-dimensional problems $W_i = x^i$, $i = 0, \ldots, n$; the Galerkin method when $W_i = \partial\tilde{T}/\partial a_i$, $i = 1, \ldots, n$; the least squares method, the collocation method, and the subdomain method. The weighting factors should be simple, and their number small, as the work involved in deriving the analytical form of the function for calculating the temperature field is usually considerable. The simplest MRW is the heat balance method, in which the equation of transient heat conduction is integrated over volume, as the weighting factor is equal to unity:

$$\int_\Omega \left[c(\tilde{T})\rho(\tilde{T})\frac{\partial \tilde{T}}{\partial t} = \nabla\cdot\left[k(\tilde{T})\nabla\tilde{T}\right] + \dot{q}_v\right] dV = 0. \quad (6)$$

Green's theorem [21,22] was used to transform Eq. (6):

$$\int_\Omega \nabla\cdot\left[k(\tilde{T})\nabla\tilde{T}\right] dV = \int_\Gamma k(\tilde{T})\frac{\partial \tilde{T}}{\partial n}\, dA, \quad (7)$$

where Γ denotes the boundary of the domain Ω, and $\partial\tilde{T}/\partial n$ is the derivative in the direction normal to the surface of the analysed domain.

Substituting Eq.(7) into Eq.(6) gives:

$$\int_\Omega c(\tilde{T})\,\rho(\tilde{T})\frac{\partial \tilde{T}}{\partial t} dV = \int_\Gamma k(\tilde{T})\frac{\partial \tilde{T}}{\partial n} dA + \int_\Omega \dot{q}_v\, dV. \quad (8)$$

Analysis of Eq. (8) shows that in the case of temperature-dependent thermal conductivity, the accuracy of determining the temperature field is low, as thermal conductivity is calculated only at the temperature of the boundary of the analysed area.

If the temperature field is determined in a small cell, such as in FEM or the hybrid FVM-FEM method [23], Eq. (8) provides good accuracy, as the temperature difference inside the element is small. The FVM-FEM method is used in commercial programmes STAR-CCM+CFD [24] and ANSYS-FLUENT [25] for modelling heat transfer processes. When determining the temperature field in bodies with temperature- or position-dependent thermal conductivity and large dimensions without discretisation, it is better to use the Galerkin or moment method. This can be demonstrated by transforming Eq. (4), in which the weight factor differs from one. The following equality was used to transform Eq. (4):

$$W_i\nabla\cdot\left[k(\tilde{T})\nabla\tilde{T}\right] = \nabla\cdot\left[W_i k(\tilde{T})\nabla\tilde{T}\right] - \nabla W_i\cdot\left[k(\tilde{T})\nabla\tilde{T}\right]. \quad (9)$$

Considering Eq. (9) in Eq. (4) results in:

$$\int_\Omega \left\{c(\tilde{T})\rho(\tilde{T})\frac{\partial \tilde{T}}{\partial t}W_i - \nabla\cdot\left[W_i k(\tilde{T})\nabla\tilde{T}\right] + \nabla W_i\cdot\left[k(\tilde{T})\nabla\tilde{T}\right] - \dot{q}_v W_i\right\} dV = 0, \quad i = 1,\ldots,n. \quad (10)$$

The second term in Eq. (10) was transformed using Green's theorem:

$$\int_\Omega \nabla\cdot\left[W_i k(\tilde{T})\nabla\tilde{T}\right] dV = \int_\Gamma W_i k(\tilde{T})\nabla\tilde{T}\cdot\boldsymbol{n}\, dA. \quad (11)$$

Considering that:

$$\nabla\tilde{T}\cdot\boldsymbol{n} = \frac{\partial \tilde{T}}{\partial n}, \quad (12)$$

Eq. (10) can be written as:

$$\int_\Omega \left\{c(\tilde{T})\rho(\tilde{T})\frac{\partial \tilde{T}}{\partial t}W_i + \nabla W_i\cdot\left[k(\tilde{T})\nabla\tilde{T}\right] - \dot{q}_v W_i\right\} dV = \int_\Gamma W_i k(\tilde{T})\frac{\partial \tilde{T}}{\partial n} dA, \quad i = 1,\ldots,n. \quad (13)$$

Comparing Eq. (13) with Eq. (8), it can be seen that Eq. (13) is derived with the weight factor $W_i = W_i(x,y,z)$. There is a term:

$$\int_\Omega \nabla W_i\cdot\left[k(\tilde{T})\nabla\tilde{T}\right] dV, \quad (14)$$

taking into account the temperature-dependent thermal conductivity throughout the analysed domain Ω, and not only at the edge Γ of the domain Ω. This can also be seen in the example of MRW used to determine the one-dimensional heat conduction equation while utilising the concept of heat penetration depth $\delta(t)$, for which Eq. (13) takes the following form:

$$\int_0^\delta \left[c(\tilde{T})\rho(\tilde{T})\frac{\partial \tilde{T}}{\partial t}W_i + k(\tilde{T})\frac{\partial W_i}{\partial x}\frac{\partial \tilde{T}}{\partial x} - \dot{q}_v W_i\right] dx = W_i\, k(\tilde{T})\frac{\partial \tilde{T}}{\partial x}\Big|_{x=\delta} - W_i\, k(\tilde{T})\frac{\partial \tilde{T}}{\partial x}\Big|_{x=0}, \quad i = 1,\ldots,n, \quad (15)$$

where $W_i = W_i(x)$.

It should be noted that in Eq. (15), the temperature distribution is approximated by the function $\tilde{T} = \tilde{T}[x, \delta(t), a_2, \ldots, a_n]$, since $a_1 = \delta(t)$. Analysis of Eq. (15) reveals that the second term in the integral accounts for changes in thermal conductivity throughout the entire analysed domain, rather than just at the boundary, as is the case in classical HBIM [9], where there is only one weighting coefficient $W_1 = 1$.

For this reason, the method of moments or Galerkin's method gives better results for temperature or space-dependent thermal conductivity than HBIM given by Eq. (8). However, the method of moments and Galerkin's method involve more work in determining the coefficients $a_1, \ldots, a_n$.

3. Alternative formulation of MWRs in heat conduction problems

It was shown in Appendix that the steady-state temperature distribution in a solid can be determined using the equation of energy conservation or Fourier's law. Following the same line of thought, an alternative formulation of MWR for solving heat conduction problems based on Fourier's law has been proposed:

$$\int_\Omega \left[\tilde{\mathbf{q}} + k(\tilde{T})\nabla\tilde{T}\right]\cdot \mathbf{W_i} dV = 0, \qquad i = 1, \ldots, n, \tag{16}$$

where: $\dot{\mathbf{q}} = (\dot{q}_x, \dot{q}_y, \dot{q}_z)$ – heat flux vector, $\nabla T = (\partial T/\partial x, \partial T/\partial y, \partial T/\partial z)$ – gradient of T, and $\mathbf{W}_i = (W_{x,i}, W_{y,i}, W_{z,i})$ – weighting factor.

The heat flux vector $\tilde{\mathbf{q}}$ is determined from the energy conservation equation:

$$c(\tilde{T})\rho(\tilde{T})\frac{\partial \tilde{T}}{\partial t} = -\nabla\cdot\tilde{\mathbf{q}} + \dot{q}_v. \tag{17}$$

Equations (16) and (17) take the following form in the Cartesian coordinate system:

$$\int_\Omega \left\{\left[\tilde{q}_x + k(\tilde{T})\frac{\partial \tilde{T}}{\partial x}\right]W_{x,i} + \left[\tilde{q}_y + k(\tilde{T})\frac{\partial \tilde{T}}{\partial y}\right]W_{y,i} + \left[\tilde{q}_z + k(\tilde{T})\frac{\partial \tilde{T}}{\partial z}\right]W_{z,i}\right\} dxdydz = 0, \tag{18}$$

$$i = 1, \ldots, n,$$

$$c(\tilde{T})\rho(\tilde{T})\frac{\partial \tilde{T}}{\partial t} = -\frac{\partial \tilde{q}_x}{\partial x} - \frac{\partial \tilde{q}_y}{\partial y} - \frac{\partial \tilde{q}_z}{\partial z} + \dot{q}_v. \tag{19}$$

The components $\tilde{q}_x$, $\tilde{q}_y$, $\tilde{q}_z$ of heat flux are determined respectively from the energy conservation equation written in the following forms:

$$c(\tilde{T})\rho(\tilde{T})\frac{\partial \tilde{T}}{\partial t} = -\frac{\partial \tilde{q}_x}{\partial x} + \frac{\partial}{\partial y}\left[k(\tilde{T})\frac{\partial \tilde{T}}{\partial y}\right] + \frac{\partial}{\partial z}\left[k(\tilde{T})\frac{\partial \tilde{T}}{\partial z}\right] + \dot{q}_v, \tag{20}$$

$$c(\tilde{T})\rho(\tilde{T})\frac{\partial \tilde{T}}{\partial t} = \frac{\partial}{\partial x}\left[k(\tilde{T})\frac{\partial \tilde{T}}{\partial x}\right] - \frac{\partial \tilde{q}_y}{\partial y} + \frac{\partial}{\partial z}\left[k(\tilde{T})\frac{\partial \tilde{T}}{\partial z}\right] + \dot{q}_v, \tag{21}$$

$$c(\tilde{T})\rho(\tilde{T})\frac{\partial \tilde{T}}{\partial t} = \frac{\partial}{\partial x}\left[k(\tilde{T})\frac{\partial \tilde{T}}{\partial x}\right] + \frac{\partial}{\partial y}\left[k(\tilde{T})\frac{\partial \tilde{T}}{\partial y}\right] - \frac{\partial \tilde{q}_z}{\partial z} + \dot{q}_v. \tag{22}$$

After determining the derivative $\partial\tilde{q}_x/\partial x$ from Eq. (20) and then integrating it with respect to x, the following expression for calculation $\tilde{q}_x$ is obtained:

$$\tilde{q}_x = \int\left\{-c(\tilde{T})\rho(\tilde{T})\frac{\partial \tilde{T}}{\partial t} + \frac{\partial}{\partial y}\left[k(\tilde{T})\frac{\partial \tilde{T}}{\partial y}\right] + \frac{\partial}{\partial z}\left[k(\tilde{T})\frac{\partial \tilde{T}}{\partial z}\right] + \dot{q}_v\right\}dx + C_x. \tag{23}$$

The components $\tilde{q}_y$ and $\tilde{q}_z$ were determined in a similar manner:

$$\tilde{q}_y = \int\left\{-c(\tilde{T})\rho(\tilde{T})\frac{\partial \tilde{T}}{\partial t} + \frac{\partial}{\partial x}\left[k(\tilde{T})\frac{\partial \tilde{T}}{\partial x}\right] + \frac{\partial}{\partial z}\left[k(\tilde{T})\frac{\partial \tilde{T}}{\partial z}\right] + \dot{q}_v\right\}dy + C_y, \tag{24}$$

$$\tilde{q}_z = \int\left\{-c(\tilde{T})\rho(\tilde{T})\frac{\partial \tilde{T}}{\partial t} + \frac{\partial}{\partial x}\left[k(\tilde{T})\frac{\partial \tilde{T}}{\partial x}\right] + \frac{\partial}{\partial y}\left[k(\tilde{T})\frac{\partial \tilde{T}}{\partial y}\right] + \dot{q}_v\right\}dz + C_z. \tag{25}$$

The constants C_x, C_y, and C_z in Eqs. (23)−(25) are determined from boundary conditions. After substituting the heat flux components $\tilde{q}_x$, $\tilde{q}_y$ and $\tilde{q}_z$, defined by Eqs. (23)−(25) into Eq. (18), a system of n first-order ordinary equations for transient problems, from which the desired parameters appearing in the approximate solution $\tilde{T}(x, y, z, t)$ are determined. If a steady-state problem is considered, Eq. (18) yields a system of n algebraic equations, from which the unknown parameters appearing in the approximate solution are determined.

When determining a one-dimensional transient temperature field in the 1D-region $[x_1, x_2]$, the system of Eq. (16) takes the following form:

$$\int_{x_1}^{x_2}\left[\tilde{q} + k(\tilde{T})\frac{\partial \tilde{T}}{\partial x}\right]W_i dx = 0, \quad i = 1, \ldots, n. \tag{26}$$

The heat flux $\tilde{q}$ in Eq.(26) is determined from Eq.(23), which in this case takes the following form:

$$\tilde{q} = \int\left[-c(\tilde{T})\rho(\tilde{T})\frac{\partial \tilde{T}}{\partial t} + \dot{q}_v\right]dx + C_x, \tag{27}$$

where $\tilde{q} = \tilde{q}_x$ is the x-component of the vector $\tilde{\mathbf{q}}$.

If the concept of heat penetration depth $a_1 = \delta(t)$ with $a_2 = 0, \ldots, a_n = 0$, and adopting $W_1 = 1$ and $W_i = 0$ for $I = 2, \ldots, n$ in order to approximate the temperature distribution in a half-space whose surface $x = 0$ is heated or cooled, then the system of Eq. (26) is reduced to a single equation:

$$\int_0^{\delta(t)}\left[\tilde{q} + k(\tilde{T})\frac{\partial \tilde{T}}{\partial x}\right]dx = 0. \tag{28}$$

Equation (28) is a counterpart to the classic HBIM method proposed by Goodman [9]. It should be expected that the approximate temperature profile determined using Eq. (28) will be more accurate for temperature-dependent conductivity than the temperature profile determined using the classical HBIM. In the classical HBIM, given by Eq. (8), in the heat balance equation for the analysed area, thermal conductivity is calculated only at the boundary temperature of the area, while in Eq. (28) the variability $k(T)$ is taken into account throughout the entire area. It should be noted that the classical HBIM method is obtained from Eq.(15) by assuming $W_1 = 1$, $W_2 = W_3 =, \ldots, = W_n = 0$.

The proposed method, as given by Eqs. (28) and (27), is referred to as the heat flux integral method (HFIM). The advantage of HFIM over HBIM is its greater accuracy in solving heat conduction problems, especially for bodies with position- or temperature-dependent thermal conductivity. HFIM applied to one-dimensional heat conduction problems is characterised by a high degree of transparency in the derivation of formulas for calcu-

lating transient temperature distributions and requires little more work than HBIM given by Eq. (8), which is formulated for the heat conduction equation.

Section 4 presents the application of the HFIM, HBIM and FVM methods to determine the transient temperature field in a plate and in a straight fin of constant thickness, taking into account the linear dependence of the thermal conductivity on temperature. The fin efficiency was also determined using the three methods mentioned above: HBIM, HFIM and FVM.

4. Examples of application of HFIM and HBIM for determining the temperature distributions in a plate and fin with temperature-dependent thermal conductivity

First, the transient temperature distribution in a plate with temperature-dependent thermal conductivity will be determined using three different methods, HBIM, HIFM and FEM.

4.1. Transient temperature distribution in a plate with temperature-dependent thermal conductivity

The thermal conductivity of the plate $k(T)$ is linearly dependent on temperature, and the density ρ and specific heat c are constant. The initial temperature of the plate is constant and equals T_0. The front surface of the plate with coordinate $x = 0$ for time $t > 0$ is constant and equals $T_s > T_0$, i.e., the change in the temperature of the plate surface is described by the Heaviside step function. The rear surface of the plate is thermally insulated. The transient temperature distribution in the plate is determined using the non-linear heat conduction equation:

$$\frac{\partial\theta}{\partial \mathrm{Fo}} = \frac{\partial}{\partial X}\left[K(\theta)\frac{\partial\theta}{\partial X}\right], \quad 0 < \mathrm{Fo}, \quad 0 \le X \le 1. \tag{29}$$

The dimensionless thermal conductivity is:

$$K(\theta) = 1 + \beta\theta. \tag{30}$$

Equation (29) is subject to the following boundary conditions:

$$\theta|_{X=0} = 1, \tag{31}$$

$$\left.\frac{\partial\theta}{\partial X}\right|_{X=1} = 0, \tag{32}$$

and the initial condition:

$$\theta|_{\mathrm{Fo}=0} = 0. \tag{33}$$

In Eqs. (29)–(33), the following symbols are used: $\theta = \frac{T-T_0}{T_s-T_0}$, $\mathrm{Fo} = \frac{\alpha_0 t}{L^2}$, $X = \frac{x}{L}$, $K = \frac{k}{k_0} = 1 + \beta\theta$, $k_0 = k(T_0)$, $\alpha_0 = \frac{k_0}{c\rho}$, and β is a constant.

The unsteady temperature distribution in the slab was determined using HFIM, HBIM and FVM in conjunction with the method of lines [26].

4.1.1. Determination of the unsteady temperature distribution in the plate using the HFIM method

If the concept of heat penetration depth is used, the plate heating process is divided into two phases (Fig. 1).

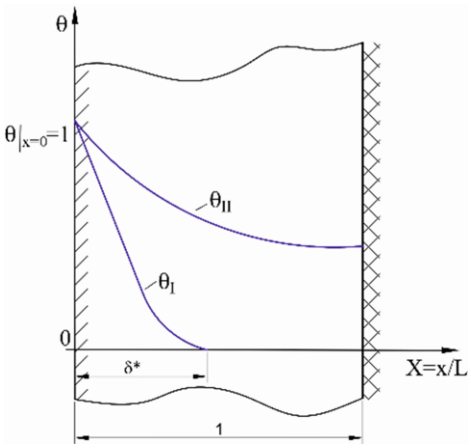


Fig. 1. Temperature distribution in the first and second phases of heat penetration.

The depth of heat penetration in the first phase is less than the thickness of the plate, and from the beginning of the second phase, the temperature of the rear surface of the plate increases (Fig. 1). In the first phase of heat penetration, when the depth of heat penetration $\delta(t)$ is less than or equal to the wall thickness L, the temperature distribution is approximated by a quadratic polynomial with respect to X:

$$\tilde{\theta}_I = aX^2 + bX + c, \qquad 0 \le X \le \delta^*, \tag{34}$$

where $\delta^* = \delta/L$.

The constants a, b and c are determined from the boundary condition (31) and from the conditions of zero temperature and heat flux at the point $X = \delta^*$:

$$\tilde{\theta}_I\big|_{X=\delta^*} = 0, \tag{35}$$

$$\left.\frac{\partial\tilde{\theta}_I}{\partial X}\right|_{X=\delta^*} = 0. \tag{36}$$

After determining the constants in Eq. (34) from boundary conditions (31), (35) and (36), and substituting them back into Eq. (34), the following temperature distribution is obtained:

$$\tilde{\theta}_I = \left(1 - \frac{X}{\delta^*}\right)^2, \qquad 0 \le X \le \delta^*, \tag{37}$$

$$\tilde{\theta}_I = 0, \qquad \delta^* \le X \le 1. \tag{38}$$

The dimensionless heat flux is determined using Eq. (27) written in dimensionless form with $\dot{q}_v = 0$:

$$\tilde{q}^*_I = -\int \frac{\partial\tilde{\theta}_I}{\partial \mathrm{Fo}} dX + C. \tag{39}$$

Considering that:

$$\frac{\partial\tilde{\theta}_I}{\partial \mathrm{Fo}} = 2\left(1 - \frac{X}{\delta^*}\right)\frac{X}{(\delta^*)^2}\frac{d\delta^*}{d\mathrm{Fo}}, \tag{40}$$

and determining a constant C in Eq. (39) from the condition:

$$\tilde{q}^*\big|_{X=\delta^*} = 0, \tag{41}$$

the following is obtained from Eq. (39):

$$\tilde{q}^*{}_I = \left[\left(1-\frac{X}{\delta^*}\right)^2 - \frac{2}{3}\left(1-\frac{X}{\delta^*}\right)^3\right]\frac{d\delta^*}{d\mathrm{Fo}} = \\ = \left[\frac{1}{3} - \left(\frac{X}{\delta^*}\right)^2 + \frac{2}{3}\left(\frac{X}{\delta^*}\right)^3\right]\frac{d\delta^*}{d\mathrm{Fo}}. \tag{42}$$

According to HFIM, the dimensionless heat penetration depth $\delta^* = \delta/L$ is determined from Eq. (28) written in dimensionless form, which in this case is:

$$\int_0^{\delta^*}\left[\tilde{q}^*{}_I + K(\tilde{\theta}_I)\frac{\partial\tilde{\theta}_I}{\partial X}\right]dX = 0. \tag{43}$$

After substituting Eqs. (37), (38), and Eq. (42) into Eq. (43) and taking into account that $K(\tilde{\theta}_I) = 1 + \beta\tilde{\theta}_I$, the following equation is obtained for determination of δ^*:

$$\frac{d\delta^*}{d\mathrm{Fo}} = \frac{3(2+\beta)}{\delta^*}. \tag{44}$$

The solution of Eq. (44) with initial condition:

$$\delta^*|_{\mathrm{Fo}=0} = 0 \tag{45}$$

has the following form:

$$\delta^* = \sqrt{6(2+\beta)\mathrm{Fo}}. \tag{46}$$

The first phase of heat penetration ends when $\delta^* = 1$. The value of the Fourier number Fo_1 at which the first phase of heat penetration ends and the second phase begins is determined from Eq. (46) after substitution $\delta^* = 1$:

$$\mathrm{Fo}_1 = \frac{1}{6(2+\beta)}. \tag{47}$$

Next, the temperature distribution in the plate during the second phase of heat penetration was determined.

During the second phase of heat penetration (Fig. 1), the temperature distribution $\tilde{\theta}_{II}(X, Fo)$ in the plate was approximated by a second-degree polynomial of X:

$$\tilde{\theta}_{II} = gX^2 + fX + e, \qquad 0 \le X \le 1, \qquad \mathrm{Fo}_1 \le \mathrm{Fo}, \tag{48}$$

where the symbols e, f, and g denote coefficients. After determining the coefficients f and e from boundary conditions, given by Eq. (35) and Eq. (36), and substituting them back into Eq. (48), one gets:

$$\tilde{\theta}_{II} = gX^2 - 2gX + 1, \qquad 0 \le X \le 1, \qquad \mathrm{Fo}_1 \le \mathrm{Fo}. \tag{49}$$

The constant g in Eq. (49) was determined using HFIM.

To determine the function $g(\mathrm{Fo})$ in the assumed temperature profile, HFIM is used, which in the second phase of heat penetration has the following form:

$$\int_0^1\left[\tilde{q}^*{}_{II} + K(\tilde{\theta}_{II})\frac{\partial\tilde{\theta}_{II}}{\partial X}\right]dX = 0. \tag{50}$$

The dimensionless heat flux is determined by using Eq. (27) written in dimensionless form with $\dot{q}_v = 0$:

$$\tilde{q}^*{}_{II} = -\int\frac{\partial\tilde{\theta}_{II}}{\partial\mathrm{Fo}}dX + C. \tag{51}$$

Considering that:

$$\frac{\partial\tilde{\theta}_{II}}{\partial\mathrm{Fo}} = (X^2 - 2X)\frac{dg}{d\mathrm{Fo}}, \tag{52}$$

and determining a constant C in Eq. (51) from the condition:

$$\tilde{q}^*\big|_{X=1} = 0 \tag{53}$$

the following is obtained from Eq. (51):

$$\tilde{q}^*{}_{II} = -\left(\frac{1}{3}X^3 - X^2 + \frac{2}{3}\right)\frac{dg}{d\mathrm{Fo}}. \tag{54}$$

Considering the temperature profile $\tilde{\theta}_{II}$ given by Eq. (49), the second term in Eq. (50) can be derived:

$$K(\tilde{\theta}_{II})\frac{\partial\tilde{\theta}_{II}}{\partial X} = 2g[1+\beta(gX^2 - 2gX + 1)](X-1) = \\ = 2g(X-1) + 2g\beta(X-1)(gX^2 - 2gX + 1). \tag{55}$$

Substituting Eq. (54) and Eq. (55) into Eq. (50) and performing integration gives the following differential equation:

$$\frac{5}{g[6\beta g - 12(1+\beta)]}\frac{dg}{d\mathrm{Fo}} = 1. \tag{56}$$

Equation (56) is subject to the following initial condition at the beginning of the second phase of heat penetration:

$$g(\mathrm{Fo})|_{\mathrm{Fo}=\mathrm{Fo}_1} = 1. \tag{57}$$

The solution to Eq. (56) with the initial condition (57) is:

$$ln\frac{(\beta+2)g}{-\beta g + 2\beta + 2} = -\mu^2(Fo - \mathrm{Fo}_1), \qquad \mathrm{Fo} \ge \mathrm{Fo}_1, \tag{58}$$

where

$$\mu^2 = \frac{12(1+\beta)}{5}. \tag{59}$$

Solving the algebraic Eq. (58) for g yields:

$$g(\mathrm{Fo}) = \frac{2(1+\beta)\,exp[-\mu^2(\mathrm{Fo}-\mathrm{Fo}_1)]}{2+\beta+\beta\,exp[-\mu^2(\mathrm{Fo}-\mathrm{Fo}_1)]}, \qquad \mathrm{Fo} \ge \mathrm{Fo}_1. \tag{60}$$

Analysis of Eq. (49) shows that the function $g(\mathrm{Fo})$ has a physical interpretation, since the temperature of the rear surface of the plate is:

$$\theta|_{X=1} = 1 - g, \qquad \mathrm{Fo} \ge \mathrm{Fo}_1. \tag{61}$$

4.1.2. Determination of the transient temperature distribution in the plate using the HBIM method

In HBIM, the heat conduction Eq. (29) is integrated. In the first phase of heat penetration, the depth of heat penetration $\delta^*(\mathrm{Fo})$ is determined from the equation:

$$\int_0^{\delta^*}\frac{\partial\tilde{\theta}_I}{\partial\mathrm{Fo}}dX = \int_0^{\delta^*}\frac{\partial}{\partial X}\left[K(\tilde{\theta}_I)\frac{\partial\tilde{\theta}_I}{\partial X}\right]dX, \qquad 0 \le X \le 1. \tag{62}$$

Using the Leibniz integral rule [22] for differentiation of a definite integral at the left side of Eq.(62) and integrating the right side of Eq. (62) gives:

$$\frac{d}{d\mathrm{Fo}}\int_0^{\delta^*}\tilde{\theta}_I dX = K(\tilde{\theta}_I)\frac{\partial\tilde{\theta}_I}{\partial X}|X=\delta^* - K(\tilde{\theta}_I)\frac{\partial\tilde{\theta}_I}{\partial X}|X=0. \quad (63)$$

Due to condition (36), the first term on the right-hand side of Eq. (63) is equal to zero, and Eq. (63) simplifies to the form:

$$\frac{d}{d\mathrm{Fo}}\int_0^{\delta^*}\tilde{\theta}_I dX = -K(\tilde{\theta}_I)\frac{\partial\tilde{\theta}_I}{\partial X}|X=0. \quad (64)$$

After considering Eqs. (37) and (38) in the heat balance equation (64), one obtains:

$$\frac{d}{d\mathrm{Fo}}\int_0^{\delta^*}\left(1-\frac{X}{\delta^*}\right)^2 dX = -(1+\beta)\left(\frac{-2}{\delta^*}\right). \quad (65)$$

After determining the integral in Eq. (65), a differential equation is obtained, which, after integration with the initial condition (45), gives the following result:

$$\delta^* = \sqrt{12(1+\beta)\mathrm{Fo}}. \quad (66)$$

The first phase of heat penetration ends when the depth of heat penetration δ equals the wall thickness L. The Fourier number Fo_1 at which the first phase of heat penetration ends and the second phase begins is obtained by assuming $\delta^* = 1$ in Eq. (66). Substituting $\delta^* = 1$ into Eq. (66) gives:

$$\mathrm{Fo}_1 = \frac{1}{12(1+\beta)}. \quad (67)$$

Next, the temperature distribution in the second phase of heat penetration was determined. The temperature distribution in the second phase is given by the function (49). The unknown parameter $g(t)$ was determined by HBIM using the following equation:

$$\int_0^1\left\{\frac{\partial\tilde{\theta}_{II}}{\partial\mathrm{Fo}} - \frac{\partial}{\partial X}\left[K(\tilde{\theta}_{II})\frac{\partial\tilde{\theta}_{II}}{\partial X}\right]\right\}dX = 0, \quad 0 \le X \le 1. \quad (68)$$

The following heat balance equation is obtained from the integral (68), taking into account Eq. (32):

$$\frac{d}{d\mathrm{Fo}}\int_0^1\tilde{\theta}_{II}dX = -K(\tilde{\theta}_{II})\frac{\partial\tilde{\theta}_{II}}{\partial X}|x=0, \quad 0 \le X \le 1. \quad (69)$$

After substituting Eq. (49) into Eq. (69) and performing the calculations, the following differential equation is obtained for $g(\mathrm{Fo})$:

$$\frac{dg}{dFo} = -3(1+\beta). \quad (70)$$

Integrating Eq. (70) with initial condition (57) gives:

$$g(\mathrm{Fo}) = exp[-\mu_1^2(\mathrm{Fo}-\mathrm{Fo}_1)], \quad \mathrm{Fo}_1 \le \mathrm{Fo}, \quad (71)$$

where:

$$\mu_1^2 = 3(1+\beta), \quad \mathrm{Fo}_1 = \frac{1}{12(1+\beta)}. \quad (72)$$

To assess the accuracy of temperature distributions determined using the HFIM and HBIM methods, the transient temperature distribution in the plate was calculated using the method of lines, where the partial heat conduction equation is replaced by a system of first-order ordinary differential equations.

4.1.3. Determination of the unsteady temperature distribution in the plate using FVM in conjunction with the method of lines

The method of lines [26] involves replacing a partial differential equation with a system of ordinary differential equations, which can then be solved using one of the many numerical methods available in the literature. The finite volume method (FVM) [15,23] was used to replace the transient heat conduction equation (29) with a system of ordinary differential equations. The division of the wall into (n–1) finite volumes is shown in Fig. 2. The symbol n denotes the number of nodes at which the wall temperatures are determined.

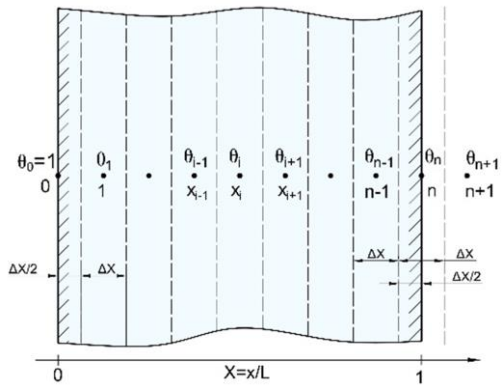


Fig. 2. Division of the wall into n finite volumes.

The coordinates of the nodes (Fig. 2) are defined as follows:

$$X_i = i\Delta X, \qquad i = 0, \ldots, n, \quad (73)$$

where the thickness of a single finite volume is:

$$\Delta X = \frac{1}{n-1}. \quad (74)$$

Integrating Eq. (29) over the thickness of one control volume within the range from (X_i – ΔX/2) to (X_i + ΔX/2) gives:

$$\Delta X\frac{d\theta_i}{d\mathrm{Fo}} = \frac{K(\theta_{i+1})+K(\theta_i)}{2}\frac{\theta_{i+1}-\theta_i}{\Delta X} + \frac{K(\theta_{i-1})+K(\theta_i)}{2}\frac{\theta_{i-1}-\theta_i}{\Delta X}, \quad (75)$$
$$i = 2, \ldots, n.$$

Considering that:

$$\frac{K(\theta_{i+1})+K(\theta_i)}{2} = 1+\beta\frac{\theta_i+\theta_{i+1}}{2}, \quad (76)$$

and

$$\frac{K(\theta_{i-1})+K(\theta_i)}{2} = 1+\beta\frac{\theta_i+\theta_{i-1}}{2}. \quad (77)$$

Equation (75) can be written as:

$$\frac{d\theta_i}{d\mathrm{Fo}} = \left(1+\beta\frac{\theta_i+\theta_{i+1}}{2}\right)\frac{\theta_{i+1}-\theta_i}{(\Delta X)^2} + \left(1+\beta\frac{\theta_i+\theta_{i-1}}{2}\right)\frac{\theta_{i-1}-\theta_i}{(\Delta X)^2}, \quad (78)$$
$$i = 2, \ldots, n.$$

The boundary condition (31) implies that at node $i = 0$, the temperature is known:

$$\theta_0 = 1. \tag{79}$$

For nodes $i = 2, \ldots, n-1$, the system of differential equations is defined by Eq. (78). The differential equation for node $i = n$ contains the temperature θ_{n+1} at the apparent node $i = n + 1$. It can be eliminated using the boundary condition (32). Approximating the derivative in Eq. (32) by the central difference quotient gives:

$$\frac{\theta_{n+1}-\theta_{n-1}}{2\Delta X} = 0. \tag{80}$$

Equation (80) yields:

$$\theta_{n+1} = \theta_{n-1}. \tag{81}$$

Equation (78) has the following form after taking into account Eq. (81) for $i = n$:

$$\frac{d\theta_n}{d\mathrm{Fo}} = 2\left(1 + \beta\frac{\theta_{n-1}+\theta_n}{2}\right)\frac{\theta_{n-1}-\theta_n}{(\Delta X)^2}. \tag{82}$$

The system of differential equations consisting of Eqs. (78) for $i = 1, \ldots, n-1$ and Eq. (82) with consideration of Eq. (79) was solved using the fourth-order Runge-Kutta method with the following initial condition:

$$\theta_i|_{t=0} = 0, \qquad i = 0, \ldots, n. \tag{83}$$

The calculations were performed using $n = 51$ and a dimensionless time step $\Delta\mathrm{Fo} = 0.00005$. The transient temperature distribution in the plate was determined in the dimensionless time interval $0 \le \mathrm{Fo} \le 1.0$.

Next, in Subsection 4.2, the temperature distribution and efficiency of a straight fin with a constant thickness and temperature-dependent thermal conductivity will be determined.

4.2. Temperature distribution and efficiency of a straight fin with a constant thickness and temperature-dependent thermal conductivity

The steady-state temperature distribution in the fin and its efficiency were determined using HFIM, HBIM and FVM, which allowed the accuracy of the solutions obtained using HFIM and HBIM to be assessed. The fin shown in Fig. 3, with a thermal conductivity that is linearly dependent on temperature, was analysed.

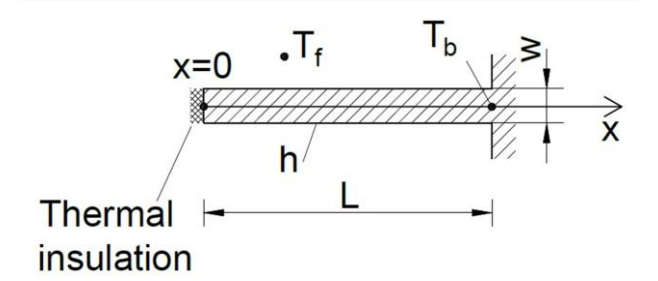


Fig. 3. Straight fin of constant thickness with insulated tip.

The symbols in Fig. 3 denote: h – HTC, L – fin height, T_b – fin base temperature, T_f – fluid temperature, w – fin thickness, x – Cartesian coordinate.

The governing heat conduction equation in a fin is:

$$\frac{d}{dx}\left[k(T)\frac{dT}{dx}\right] - \frac{2h}{w}(T - T_f) = 0. \tag{84}$$

The thermal conductivity of the fin material $k(T)$ is a linear function of the fin temperature and is given by the function:

$$k(T) = k(T_f)\left[1 + \beta_k(T - T_f)\right], \tag{85}$$

where the symbol β_k denotes a constant.

Equation (84) is subject to the following boundary conditions:

$$T|_{x=L} = T_b, \tag{86}$$

$$\left.\frac{\partial T}{\partial x}\right|_{x=0} = 0. \tag{87}$$

Introducing dimensionless variables:

$$\theta = \frac{T-T_f}{T_b-T_f}, \qquad X = \frac{x}{L}, \qquad N^2 = \frac{2hL^2}{k(T_f)w}$$

$$\varepsilon = \frac{k(T_b)-k(T_f)}{k(T_f)} = \beta_k(T_b - T_f), \tag{88}$$

Eqs. (84), (86) and (87) can be written in the following form:

$$\frac{d}{dX}\left[(1 + \varepsilon\theta)\frac{d\theta}{dX}\right] - N^2\theta = 0, \tag{89}$$

$$\theta|_{X=1} = 1, \tag{90}$$

$$\left.\frac{d\theta}{dX}\right|_{X=0} = 0. \tag{91}$$

4.2.1. Determination of temperature distribution in a fin using the HBIM method

The temperature distribution is approximated by the function [27]:

$$\tilde{\theta} = \frac{\cosh NX}{\cosh N} + C\left(\frac{\cosh 2NX}{\cosh\ 2N} - \frac{\cosh NX}{\cosh N}\right), \tag{92}$$

where C is a constant.

The constant C was determined using HFIM, i.e., from the following equation:

$$\int_0^1 \left[\tilde{q} + \left(1 + \varepsilon\tilde{\theta}\right)\frac{d\tilde{\theta}}{dX}\right] dX = 0. \tag{93}$$

To determine the heat flux, Eq. (89) was written in the form:

$$\frac{d\tilde{q}}{dX} + N^2\tilde{\theta} = 0. \tag{94}$$

Equation (94) is subject to the following boundary condition at the fin tip:

$$\tilde{q}|_{X=0} = 0. \tag{95}$$

After substituting the temperature distribution given by Eq. (92) into Eq. (94) and integrating this equation, considering

the boundary condition given by Eq.(95), an expression for the heat flux is obtained:

$$\tilde{q} = -N\left[\frac{sinh\,NX}{cosh\,N} + C\left(\frac{sinh2NX}{2cosh2N} - \frac{sinh\,NX}{cosh\,N}\right)\right]. \quad (96)$$

The second term under the integral in Eq. (93) is:

$$\left(1+\varepsilon\tilde{\theta}\right)\frac{d\tilde{\theta}}{dX} = \left(1+\varepsilon\frac{cosh\,NX}{cosh\,N} + C\varepsilon\frac{cosh\,2NX}{cosh\,2N} - C\varepsilon\frac{cosh\,NX}{cosh\,N}\right)\times$$
$$\times\left(\frac{N\,sinh\,NX}{cosh\,N} + C\frac{2Nsinh2NX}{cosh\,2N} - C\frac{N\,sinh\,NX}{cosh\,N}\right). \quad (97)$$

After substituting Eq. (96) and Eq. (97) into Eq. (93), the following second-degree algebraic equation is obtained to determine the constant C

$$\alpha_c C^2 + \beta_c C + \gamma_c = 0. \quad (98)$$

The constants α_c, β_c, and γ_c are given by the following expressions:

$$\alpha_c = \frac{\varepsilon\,sinh^2\,2N}{2\,cosh^2\,2N} - \frac{\varepsilon(cosh\,N-1)}{cosh\,N\,cosh\,2N} - \frac{2\varepsilon\,sinh^2\,N}{cosh\,2N} + \frac{\varepsilon\,sinh^2\,N}{2\,cosh^2\,N}, \quad (99)$$

$$\beta_c = \frac{3\,sinh^2\,N}{2\,cosh\,2N} + \frac{\varepsilon(cosh\,N-1)}{cosh\,N\,cosh\,2N} + \frac{2\varepsilon\,sinh^2\,N}{cosh\,2N} - \frac{\varepsilon\,sinh^2\,N}{cosh^2\,N}, \quad (100)$$

$$\gamma_c = \frac{\varepsilon\,sinh^2\,N}{2\,cosh^2\,N}. \quad (101)$$

A solution to Eq. (98) that makes physical sense is:

$$C = \frac{-\beta_c + \sqrt{\beta_c^2 - 4\alpha_c\gamma_c}}{2\alpha_c}. \quad (102)$$

The fin efficiency η, defined as the ratio of the heat flow rate dissipated by the actual fin to the maximum heat flow rate dissipated by an isothermal fin at temperature T_b, is calculated using the following formula:

$$\eta = \int_0^1 \tilde{\theta}(X)\,dX = \frac{tanh\,N}{N}\left(1 - C\frac{tanh^2\,N}{1+tanh^2\,N}\right). \quad (103)$$

Next, the temperature distribution in the fin and its efficiency will be determined using HBIM.

4.2.2. Determination of temperature distribution in a fin using the HBIM method

In the case of HBIM, the constant C in Eq. (103) is determined using the following equation:

$$\int_0^1 \left\{\frac{d}{dX}\left[\left(1+\varepsilon\tilde{\theta}\right)\frac{d\tilde{\theta}}{dX}\right] - N^2\tilde{\theta}\right\}dX = 0. \quad (104)$$

After substituting the function $\tilde{\theta}$, given by Eq. (92), approximating the temperature distribution in the fin, into Eq. (104), and performing the operations, the following formula for calculating the constant C is obtained:

$$C = \frac{\varepsilon\,tanh\,N}{\varepsilon\,tanh\,N - 2(1+\varepsilon)\,tanh\,2N + \frac{1}{2}tanh\,2N}. \quad (105)$$

4.2.3. Determination of temperature distribution in a fin using the FVM method

The FVM was used to determine the temperature distribution in the fin analysed. Examples of application of FVM for calculating the temperature field in straight and circular fins with constant thermal conductivity are presented in [28]. The division of the analysed fin into finite volumes is illustrated in Fig. 4.

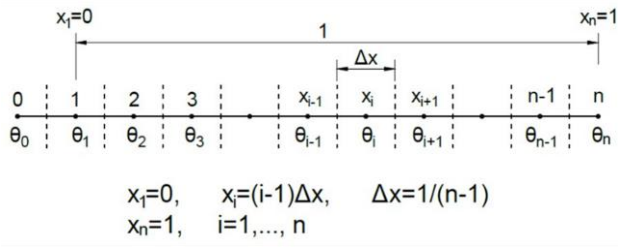


Fig. 4. Division of the fin into finite volumes.

The coordinates of the nodes are defined as follows:

$$X_i = (i-1)\Delta X, \quad \Delta X = 1/(n-1), \quad i = 1,\ldots,n. \quad (106)$$

According to the FVM method, Eq. (89) is integrated in the range from ($X_i - \Delta X/2$) to ($X_i + \Delta X/2$):

$$\int_{X_i-\Delta X/2}^{X_i+\Delta X/2}\left\{\frac{d}{dX}\left[\left(1+\varepsilon\theta\right)\frac{d\theta}{dX}\right] - N^2\theta\right\}dX = 0,$$
$$i = 1,\ldots,n-1. \quad (107)$$

Integrating Eq. (107) gives:

$$\left[\left(1+\varepsilon\theta\right)\frac{d\theta}{dX}\right]\Big|_{X_i+\Delta X/2} - \left[\left(1+\varepsilon\theta\right)\frac{d\theta}{dX}\right]\Big|_{X_i-\Delta X/2} - N^2\theta_i\Delta X = 0,$$
$$i = 1,\ldots,n-1. \quad (108)$$

Approximating the derivatives in Eq. (108) by forward difference quotients, one obtains after transformations:

$$\theta_i = \frac{1}{2+\varepsilon\frac{\theta_{i-1}+2\theta_i+\theta_{i+1}}{2}+N^2(\Delta X)}\cdot$$
$$\left[\left(1+\varepsilon\frac{\theta_{i-1}+\theta_i}{2}\right)\theta_{i-1} + \left(1+\varepsilon\frac{\theta_i+\theta_{i+1}}{2}\right)\theta_{i+1}\right], \quad (109)$$
$$i = 1,\ldots,n-1.$$

The equation for the first node is derived taking into account the boundary condition (91). Approximating the derivative in Eq. (91) with the central difference quotient gives:

$$\frac{\theta_2-\theta_0}{2\Delta X} = 0. \quad (110)$$

It follows from Eq. (110) that:

$$\theta_0 = \theta_2. \quad (111)$$

Considering Eq. (111) in Eq. (109) for i=1 gives:

$$\theta_1 = \frac{2\left(1+\varepsilon\frac{\theta_1+\theta_2}{2}\right)\theta_2}{2+\varepsilon(\theta_1+\theta_2)+N^2(\Delta X)^2}. \quad (112)$$

It follows from Eq. (90) that:

$$\theta_n = 1. \tag{113}$$

The system of equations consisting of Eq. (112), Eq. (109) for i = 2, …, n−1 and Eq. (113) was solved using the Gauss-Seidel iterative method [15,29]. The temperature in the fin was determined at n = 51 nodes, i.e., the fin was divided into (n−1) = 50 finite volumes. As a first approximation, it was assumed that the temperature of the fin at all nodes is equal to the temperature of the fin base, i.e., $\theta_i^{(0)} = 1.0$, i = 1, …, n. Then, after determining the temperature distribution, the efficiency η of the fin is determined

$$\eta = \int_0^1 \theta dX = \frac{\theta_1 \Delta X}{2} + \sum_{i=2}^{n-1} \theta_i \Delta X + \frac{\theta_n \Delta X}{2}. \tag{114}$$

The rectangle method was used to calculate the integral in Eq. (114).

In Section 5, HFIM and HBIM are compared using the examples of determining the transient temperature field in a plate and the steady-state temperature field in a straight fin of constant thickness made of a material with a temperature-dependent thermal conductivity. The temperature distributions and fin efficiency determined by HFIM and HBIM were also compared with numerical solutions.

5. Comparison of temperature distributions in the plate and fin obtained by HFIM, HBIM and FVM

5.1. Comparison of the unsteady temperature distribution in the plate obtained by HFIM, HBIM and numerical method of lines

The transient temperature distributions in the plate determined using HFIM and HBIM were compared with the numerical solution. The temperature distributions obtained from HFIM and HBIM during the first (Figs. 5−7) and second phase (Figs. 8, 9) of heat penetration were analysed. Temperature changes across the plate thickness are shown in Figs. 5a−7b for the first phase of heat penetration at Fourier number values of Fo = 0.004, 0.03, 0.05, and in Figs. 8, 9 for the second phase at Fo = 0.2 and 0.8.

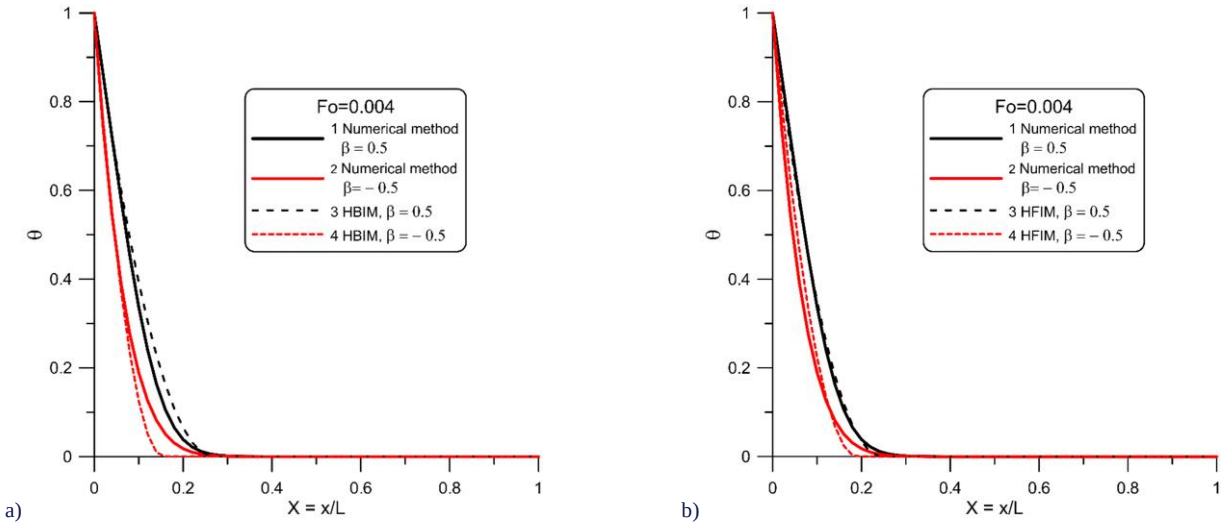


Fig. 5. Temperature distribution in the plate during the first phase of heat penetration for Fo = 0.004.

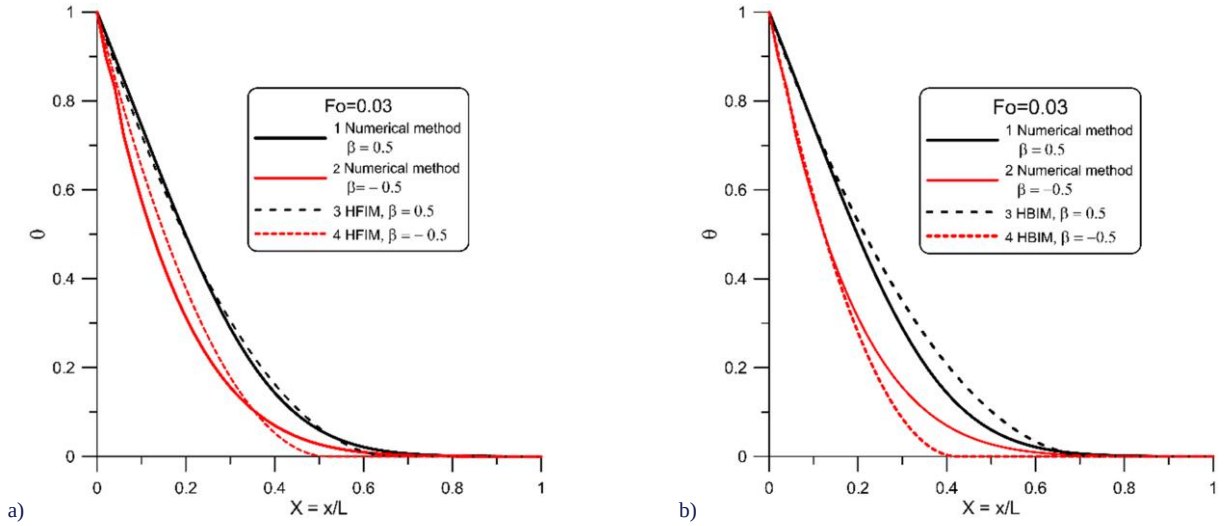


Fig. 6. Temperature distribution in the plate during the first phase of heat penetration for Fo = 0.03.

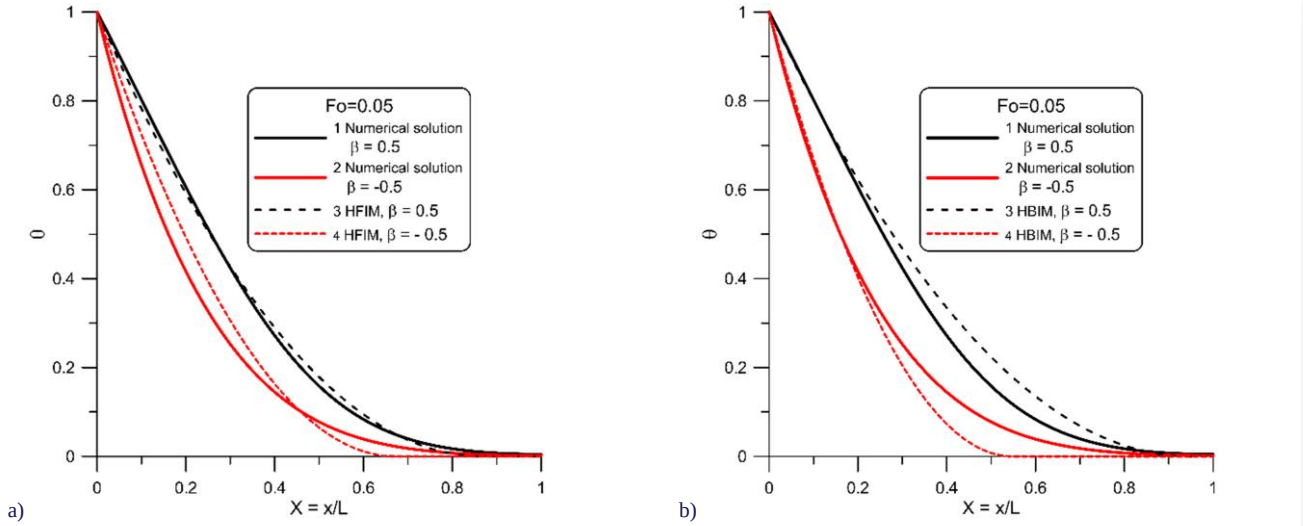


Fig. 7. Temperature distribution in the plate during the first phase of heat penetration for Fo = 0.05.

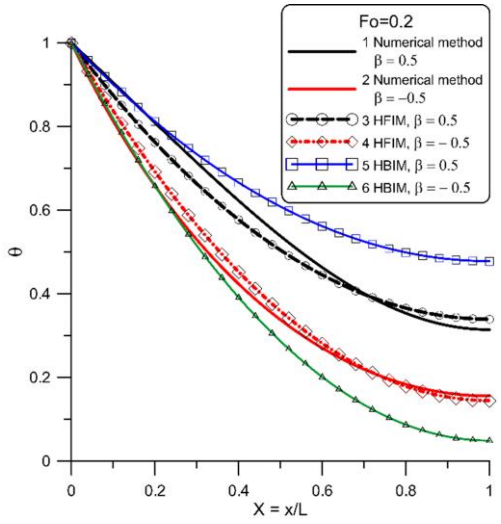


Fig. 8. Temperature distribution in the plate during the second phase of heat penetration for Fo = 0.2.

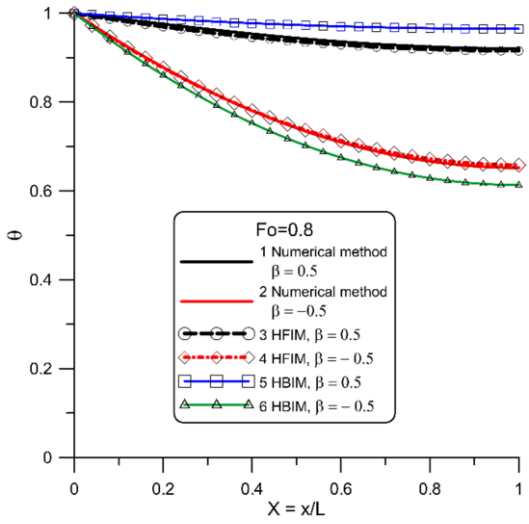


Fig. 9. Temperature distribution in the plate during the second phase of heat penetration for Fo = 0.8.

An analysis of results presented in Figs. 5–9 shows that HFIM provides more accurate results compared to HBIM. Both HFIM and HBIM are more accurate in determining the temperature distribution for $\beta = 0.5$ when the thermal conductivity increases with increasing temperature, compared to the case $\beta = -0.5$ when the thermal conductivity decreases with increasing temperature. The difference between the plate temperature calculated numerically $\theta_{i,num}$ and analytically $\theta_{i,app}$ using the HFIM or HBIM is given by:

$$e_{\theta,i} = \theta_{i,num} - \theta_{i,app}\,, \qquad i = 1,\ldots,n, \tag{115}$$

where the symbol n denotes the number of nodes in the thickness of the plate (Fig. 2) when determining the transient temperature in the plate using the finite volume method (FVM).

An inspection of the results presented in Figs. 10a–10e shows that HFIM proposed in the paper gives more accurate results than HBIM. The mean-square temperature difference $\bar{e}_\theta$ between the temperature values $\theta_{i,app}$ calculated by the approximate analytical method, HFIM or HBIM, and the numerical method $\theta_{i,num}$ was obtained using the formula:

$$\bar{e}_\theta = \sqrt{\frac{1}{n}\sum_{i=1}^{n} e_{\theta,i}^2}, \tag{116}$$

where (n+1) denotes the number of nodes in the thickness of the plate (Fig. 2).

In Table 1, the mean square errors $\bar{e}_\theta$ and the maximum errors $\varepsilon_{\theta,max}$ among all n errors calculated using Eqs. (116) and (115) are compared for HFIM and HBIM.

It can be seen from an inspection of Table 1 that both the mean square errors $\bar{e}_\theta$ and maximum errors $\varepsilon_{\theta,max}$ are significantly smaller for the plate temperature determined using HFIM than for those determined using HBIM. In the following example, the temperature distribution and efficiency of a straight fin with a constant thickness and a temperature-dependent thermal conductivity were determined using HFIM, HBIM and the method of lines.

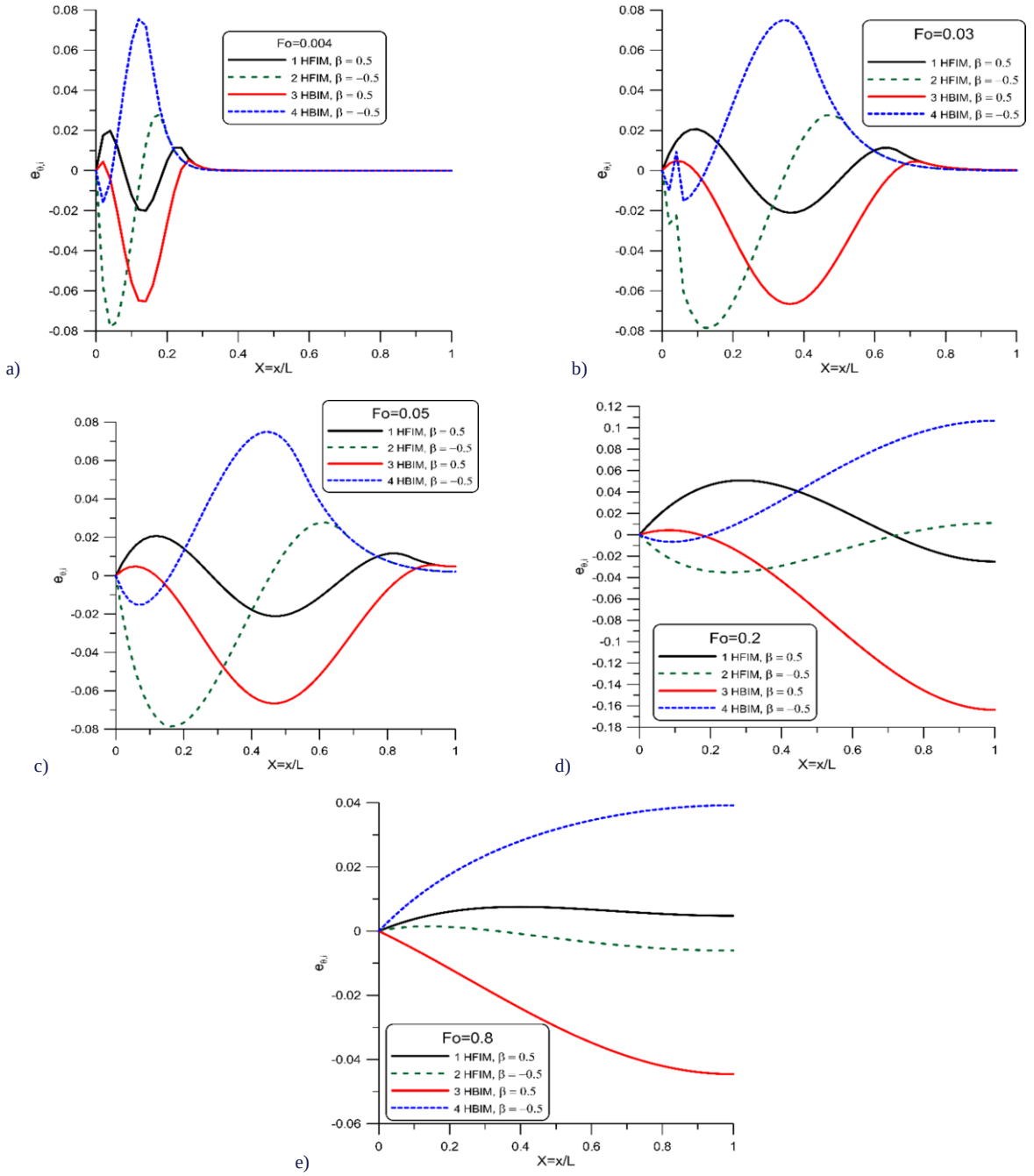


Fig. 10. The difference between the plate temperature calculated numerically $\theta_{i,num}$ and analytically using HFIM or HBIM; a) Fo = 0.004, b) Fo = 0.03, c) Fo = 0.05, d) Fo = 0.2, e) Fo = 0.8.

Table 1. The mean-square temperature difference $\bar{e}_\theta$ between the temperature values $\theta_{i,num}$ calculated numerically using the method of lines and temperatures $\theta_{i,app}$ obtained by approximate analytical methods, HFIM or HBIM.

Fo	Method	$\bar{e}_\theta$		$\lvert e_{\theta,max} \rvert$	
		$\beta = 0.5$	$\beta = -0.5$	$\beta = 0.5$	$\beta = -0.5$
0.004	HFIM	0.0068	0.0207	0.2005	0.0780
	HBIM	0.0196	0.0205	0.0652	0.0754
0.03	HIFM	0.0113	0.0336	0.0206	0.0278
	HBIM	0.0327	0.0333	0.0641	0.0750
0.05	HIFM	0.0129	0.0387	0.0207	0.0786
	HBIM	0.0372	0.0372	0.0664	0.0750
0.2	HIFM	0.0316	0.0212	0.0508	0.0353
	HBIM	0.0966	0.0648	0.1638	0.1067
0.8	HIFM	0.0060	0.0036	0.0076	0.0061
	HBIM	0.0306	0.0300	0.0446	0.0392

5.2. Comparison of the temperature distribution in the fin and the fin efficiency obtained by HFIM, HBIM and FVM

Figure 11a shows a comparison of the temperature distribution obtained using the analytical approximate HFIM presented in the article and using the numerical method FVM. Both methods yield nearly identical results, which demonstrates the high accuracy of HFIM. Inspection of the results presented in Fig. 11b shows that the accuracy of the classical HBIM method is significantly lower than that of the proposed HFIM method, as the differences in fin temperature calculated using FVM and HBIM are greater, especially for $\varepsilon = -0.6$ and $\varepsilon = 0.6$. The reason for the low accuracy of the HBIM method is that the thermal conductivity $K(\theta)$ in the heat balance equation is calculated only at the temperature θ_n of the fin base, i.e. a constant thermal conductivity $K(\theta_n)$ appears in HBIM.

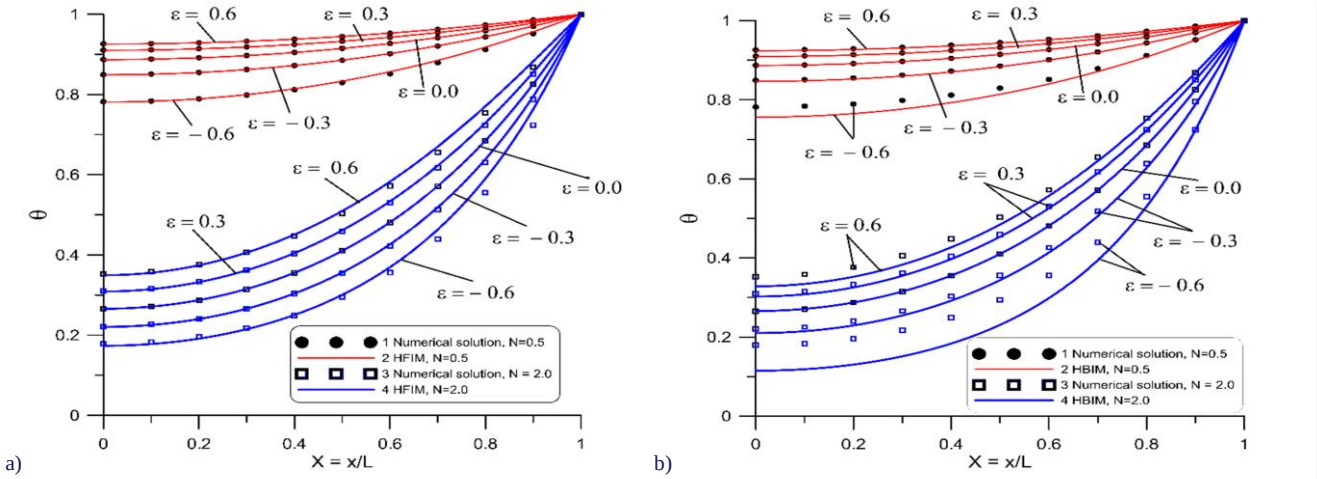


Fig. 11. Comparison of temperature distributions in the fin determined using approximate analytical methods HFIM and HBIM with the temperature distribution determined using the numerical method FVM: a) comparison of temperature distributions determined using HFIM and FVM, b) comparison of temperature distributions determined using HBIM and FVM.

The comparison of the fin efficiency η determined using HFIM and HBIM, with the efficiency determined numerically using FVM as a function of the coefficient ε for different values of the N parameter is presented in Fig. 12.

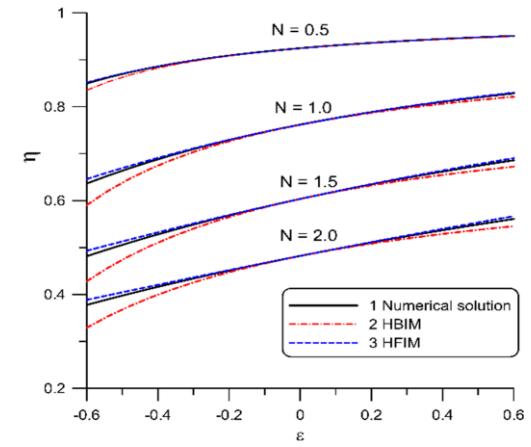


Fig.12. Comparison of the efficiency of the fin determined using HFIM and HBIM with the efficiency determined numerically using FVM as a function of the coefficient ε for different values of parameter N.

The comparison analysis presented in Fig. 12 shows that the efficiency values determined using HFIM are significantly more accurate than those obtained using the HBIM method. The differences between the values η obtained using HBIM and FEM are significant, especially for larger values of the coefficient ε.

To show the differences in fin efficiency η_{anal} determined using HFIM or HBIM and fin efficiency η_{num} determined using FVM, the relative difference e_η was calculated:

$$e_\eta = \frac{\eta_{anal} - \eta_{num}}{\eta_{num}} \cdot 100\%, \qquad (117)$$

where η_{anal} is the fin efficiency determined using the approximate analytical method HFIM or HBIM, and η_{num} denotes the fin efficiency determined numerically using the FVM.

The relative differences e_η for HFIM and HBIM are presented in Figs. 13 and 14, respectively. Figs. 13 and 14 confirm the higher accuracy of HFIM compared to HBIM.

The maximum difference value $|e_\eta|$ for HFIM is approximately 2.9% (Fig. 13), while for HBIM, it is approximately 13% (Fig. 14).

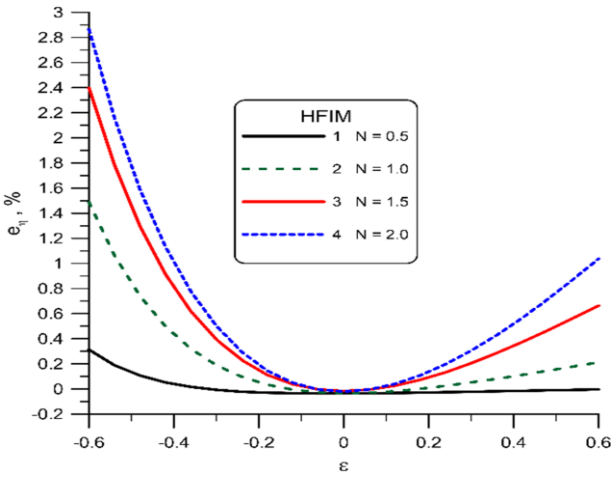


Fig. 13. The relative difference between η_{HFIM} and η_{num} calculated using Eq. (129).

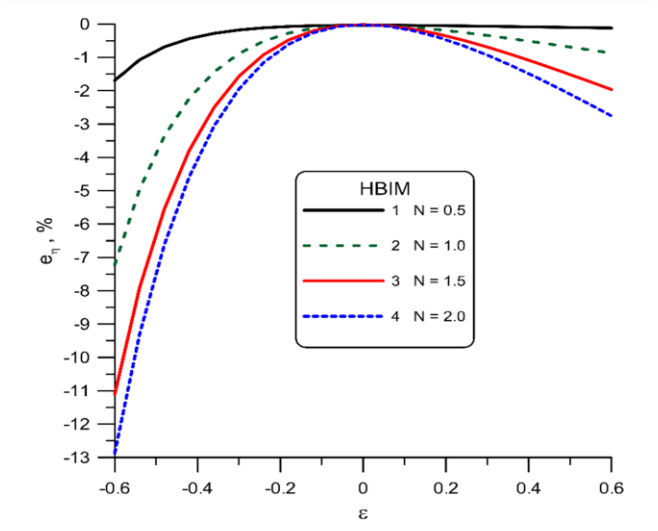


Fig. 14. The relative difference between η_{HBIM} and η_{num} calculated using Eq. (117).

6. Conclusions

This paper presents a new formulation of the method of weighted residuals for Fourier's law of heat conduction. In the case of one-dimensional heat conduction, when the weighting factor equals unity and the concept of a heat penetration depth is applied, the method simplifies to the heat flux integral method (HFIM) proposed. The paper also presents a comparison of the heat balance integral method (HBIM), developed by T.R. Goodman, with HFIM. In HBIM, the transient heat conduction equation is integrated with respect to the spatial coordinate, whereas in HFIM, Fourier's law is integrated over the spatial coordinate. The advantage of HFIM over HBIM is the greater accuracy of determining the temperature distribution, especially in bodies whose thermal conductivity depends on temperature or position. The greater accuracy of the proposed method is illustrated by the determination of the transient temperature distribution in a plate and the steady-state temperature distribution in the fin, both of which involve temperature-dependent thermal conductivity. The temperature distribution in the plate and fin, as well as the fin efficiency, were also determined using the FVM to assess the accuracy of the approximate analytical methods employed in the paper. The advantage of the proposed HFIM is the simplicity of the calculation formulas and the ability to determine the temperature distribution and, if necessary, thermal stresses for arbitrarily small times, i.e., at the beginning of the heating or cooling process of a body. Due to the short calculation time required for computer calculations, the HFIM method can be used to calculate the transient temperature field in thermal stress monitoring systems for pressure components of boilers and turbines.

7. Future work

The proposed weighted residual method for Fourier's law will be applied to approximate the transient temperature and thermal stress distribution in the pressure components of power engineering machinery and equipment. In addition, the application of the proposed method for the approximate determination of two-dimensional steady-state and transient temperature fields in flat, cylindrical and spherical components will be presented.

References

[1] Finlayson, B.A. (2013). *The method of weighted residuals and variational principles* (pp. 397–412). Society for Industrial and Applied Mathematics, 73. doi: 10.1137/1.9781611973242.bm

[2] Taler, J. (1980). *The method of weighted residuals and its application to the calculation of temperature fields in boiler components*, Monograph (14). Cracow University of Technology Press.

[3] Hatami, M. (Ed.). (2017). *Weighted residual methods* (1st ed.). Academic Press. doi: 10.1016/B978-0-12-813218-0.00002-9

[4] Chakraverty, S., Mahato, N.R., Karunakar, P., & Rao, T.D. (2019). *Advanced numerical and semi-analytical methods for differential equations*. John Wiley & Sons. doi: 10.1002/9781119423461

[5] Ganji, D.D., Sabzehmeidani, Y., & Sedighiamiri, A. (2018). *Nonlinear systems in heat transfer: Mathematical modelling and analytical methods* (1st ed.). Elsevier. doi: 10.1016/C2016-0-00401-1

[6] Thomée, V. (2006). *Galerkin finite element methods for parabolic problems* (2nd ed.). Springer. doi: 10.1007/3-540-33122-0

[7] Crank, J. (1980). *The mathematics of diffusion* (2nd ed.). Oxford University Press.

[8] Gibson, W.C. (2021). *The method of moments in electromagnetics* (3rd ed.). Chapman and Hall/CRC. doi: 10.1201/9780429355509

[9] Goodman, T.R. (1964). Application of integral methods to transient nonlinear heat transfer. *Advances in Heat Transfer*, 1, 51−122. doi: 10.1016/S0065-2717(08)70097-2

[10] Pohlhausen, K. (1921). Zur näherungsweisen Integration der Differentialgleichung der laminaren Grenzschicht. *Zeitschrift für Angewandte Mathematik und Mechanik*, 1, 252–268. doi: 10.1002/zamm.19210010401

[11] von Kármán, T. (1921). Über laminare und turbulente Reibung. *Zeitschrift für Angewandte Mathematik und Mechanik*, 1, 233−252. doi: 10.1002/zamm.19210010401

[12] Taler, D., Dzierwa, P., & Taler, J. (2020). New method for determining the optimum fluid temperature when heating pressure thick-walled components with openings. *Energy*, 200, 117527. doi: 10.1016/j.energy.2020.117527

[13] Taler, J., & Taler, D. (2024). Analysis of the possibility of reducing the heating time of thick-walled cylindrical components with holes. *Energy*, 303, 131982. doi: 10.1016/j.energy.2024.131982

[14] Taler, J. (1990). Messung der Wärmebelastung der gasdicht verschweißten Verdampfer-Rohrwände in Dampferzeugern. *VGB Kraftwerkstechnik*, 70, 644–650.

[15] Taler, J., & Duda, P. (2006). *Solving direct and inverse heat conduction problems* (1st ed.). Springer. doi: 10.1007/978-3-540-33471-2

[16] Yener, Y., & Kakaç, S. (2008). *Heat conduction* (4th ed.). Taylor & Francis. doi: 10.1201/9780203752166

[17] Volkov, V.N., & Li-Orlov, V.K. (1970). A refinement of the integral method in solving the heat conduction equation. *Heat Transfer: Soviet Research*, 2, 41–47.

[18] Sitison, J.W., & Edwards, D.A. (2020). The heat balance integral method for cylindrical extruders. *Journal of Engineering Mathematics*, 122, 1–16. doi: 10.1007/s10665-020-10041-y

[19] Kumar, A., & Rajeev. (2021). Heat balance integral method for a time-fractional Stefan problem with Robin boundary condition and temperature-dependent thermal conductivity. *Computational*

Thermal Sciences, 13(6), 71–84. doi: 10.1615/ComputThermalScien.2021038569
[20] Chaurasiya, V., Upadhyay, S., Rai, K.N., & Singh, J. (2022). A new look at the heat balance integral method for a two-dimensional Stefan problem with convection. *Numerical Heat Transfer, Part A: Applications*, 82, 1–14. doi: 10.1080/10407782.2022.2079829
[21] Greenberg, M.D. (1998). *Advanced engineering mathematics* (2nd ed.). Prentice Hall.
[22] Riley, K.F., Hobson, M.P., & Bence, S.J. (2000). *Mathematical methods for physics and engineering* (3rd ed., pp. 124–129). Cambridge University Press. doi: 10.2277/0521861535
[23] Taler, D. (2019). *Numerical modelling and experimental testing of heat exchangers* (1st ed.). Springer Nature. doi: 10.1007/978-3-319-91128-1
[24] Siemens Digital Industries Software. (2025). *Simcenter STAR-CCM+ CFD software*. Munich, Germany.
[25] Ansys, Inc. (2025). *Ansys Fluent: Fluid simulation software.*
[26] Schiesser, W.E. (1991). *The numerical method of lines: Integration of partial differential equations*. Academic Press.
[27] Muzzio, A. (1976). Approximate solution for convective fins with variable thermal conductivity. *Journal of Heat Transfer*, 98, 680–682.
[28] Taler, D. (2014). Fins of straight and circular geometry. In *Encyclopedia of thermal stresses* (pp. 1670–1683). Springer. doi: 10.1007/978-94-007-2739-7
[29] Chapra, S.C., & Canale, R.P. (2010). *Numerical methods for engineers* (6th ed.). McGraw-Hill.

Appendix. Methods for determining one-dimensional steady-state temperature distributions in solids

The purpose of this appendix is to show two different methods of determining temperature distributions in solids. In the first method, the temperature distribution is determined from the energy conservation equation, accounting for Fourier's law. In the second method, the temperature distribution is determined from Fourier's law, and the heat flux is obtained from the energy conservation equation.

In analogy to the second method of determining the temperature distribution, an MWR for Fourier's law has been formulated. The advantage of this approach is that it provides greater accuracy in approximating the temperature distribution than the classical MWR, while requiring a similar amount of work.

Two methods for determining steady-state temperature distributions are presented and illustrated by examples of a cylindrical wall (Fig. A.1) and a spherical wall (Fig. A.2).

In analogy with these methods for determining temperature distributions, two MWRs are formulated: the first based on the law of energy conservation and the second on Fourier's law.

The steady-state temperature distribution in a solid is defined by the equation of energy conservation:

$$\nabla \cdot \dot{\mathbf{q}} = \dot{q}_v. \tag{A.1}$$

The symbol $\dot{q}_v$ denotes the volumetric heat source density in W/m^3. The heat flux $\dot{\boldsymbol{q}}$ is defined by Fourier's law:

$$\dot{\mathbf{q}} = -k\nabla T, \tag{A.2}$$

where the symbol k denotes the thermal conductivity in W/(m·K).

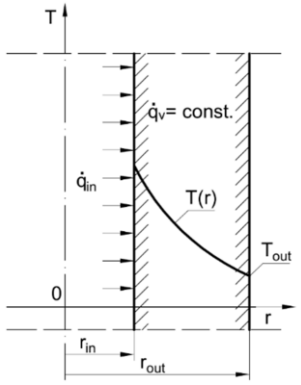


Fig. A.1. Long hollow cylinder subject to heat flux $\dot{q}_{in}$ at the inner surface and temperature T_{out} at the outer surface.

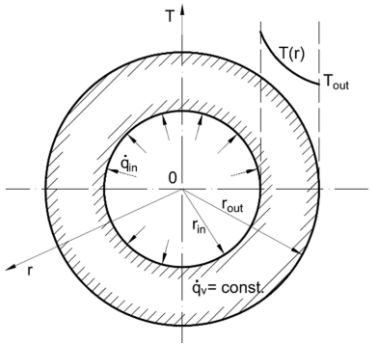


Fig. A.2. Hollow sphere with prescribed heat flux at the inner surface and temperature T_{out} at the outer surface.

To determine the temperature distribution, it is necessary to specify appropriate boundary conditions on the body's surface. In one-dimensional heat conduction, the energy conservation equation in cylindrical and spherical coordinate systems takes the following form:

$$\frac{1}{r^m}\frac{d}{dr}(r^m \dot{q}) = \dot{q}_v, \tag{A.3}$$

where m = 1 for a cylindrical wall and m = 2 for a spherical wall. The heat flux $\dot{q}$ is given by Fourier's law:

$$\dot{q} = -k\frac{\partial T}{\partial r}. \tag{A.4}$$

The temperature distribution is determined in a cylindrical and spherical wall under the following boundary conditions:

$$-k\frac{\partial T}{\partial r}|r = r_{in} = \dot{q}_{in}, \tag{A.5}$$

$$T|_{r=r_{out}} = T_{out}. \tag{A.6}$$

The heat flux $\dot{q}_{in}$ is specified at the inner surface of the cylindrical or spherical wall, and the temperature T_{out} is specified at the outer surface. The boundary problem (A.3)−(A.6) was solved for cylindrical and spherical walls using the above-mentioned approaches. In the first method, the temperature distribution was determined by applying the energy conservation equation (A.3), taking into account Fourier's law (A.4). In the second

method, the temperature distribution was determined by applying Fourier's law (A.4), taking into account the energy conservation equation (A.3).

A.1. Determination of the temperature distribution in a cylindrical and spherical wall using the first method

Substituting Fourier's law, given by Eq. (A.4), into Eq. (A.3) yields the following heat conduction equation:

$$\frac{1}{r^m}\frac{d}{dr}\left(r^m k\frac{\partial T}{\partial r}\right) = -\dot{q}_v. \tag{A.7}$$

Using Eq. (A.7), the temperature distributions in the cylindrical wall (m = 1) and spherical wall (m = 2) were determined separately:

- Cylindrical wall (m = 1):

  After multiplying Eq. (A.7) by r and dividing by k on both sides and integrating twice, the temperature distribution in the wall is obtained:

$$T = -\frac{1}{4}\frac{\dot{q}_v r^2}{k} + C\,ln\,r + C_1. \tag{A.8}$$

  Determining constants C and C_1 from boundary conditions (A.5) and (A.6), and then substituting them into the solution (A.8) gives:

$$T = T_{out} + \frac{1}{4}\frac{\dot{q}_v r_{out}^2}{k}\left(1 - \frac{r^2}{r_{out}^2}\right) + \\ + \left(\frac{\dot{q}_v r_{in}^2}{2k} - \frac{\dot{q}_{in} r_{in}}{k}\right) ln\frac{r}{r_{out}}. \tag{A.9}$$

- Spherical wall (m = 2):

  Multiplying Eq. (A.7) for m = 2 by r^2 and dividing by k and then integrating it twice gives:

$$T = -\frac{1}{6}\frac{\dot{q}_v r^2}{k} - \frac{C_3}{r} + C_4. \tag{A.10}$$

  After determining constants C_3 and C_4 from boundary conditions given by Eq. (A.5) and Eq. (A.6) and substituting them into Eq.(A.10), one gets:

$$T = T_{out} + \frac{1}{6}\frac{\dot{q}_v}{k}(r_{out}^2 - r^2) + \frac{1}{3}\frac{\dot{q}_v r_{in}^3}{k r_{out}}\left(\frac{1}{r_{out}} - \frac{1}{r}\right) + \\ + \frac{\dot{q}_{in} r_{in}^2}{k}\left(\frac{1}{r} - \frac{1}{r_{out}}\right). \tag{A.11}$$

Next, the temperature distributions in the cylindrical and spherical walls were determined using the second method.

A.2. Determination of the temperature distribution in a cylindrical and spherical wall using the second method

In the second method, the temperature distribution is determined using Fourier's law (A.4). First, the heat flux is determined from Eq. (A.3). After multiplying Eq. (A.3) by r^m and integrating it on both sides, one gets:

$$\dot{q} = \frac{\dot{q}_v}{m+1} r + \frac{C_5}{r^m}. \tag{A.12}$$

The boundary condition given by Eq. (A.6) can be written as:

$$\dot{q}|_{r=r_{in}} = \dot{q}_{in}. \tag{A.13}$$

Substituting Eq. (A.12) into Eq. (A.13) yields the constant C_5. Substituting the constant C_5 determined in this way into Eq. (A.12) gives:

$$\dot{q} = \frac{\dot{q}_v}{m+1} r + \left(\dot{q}_{in} r_{in}^m - \frac{\dot{q}_v}{m+1} r_{in}^{m+1}\right)\frac{1}{r^m}. \tag{A.14}$$

Substituting Eq. (A.14) into Eq. (A.4) representing Fourier's law, the following differential equation is obtained:

$$\frac{dT}{dr} = -\frac{\dot{q}_v}{(m+1)k} r - \left(\frac{\dot{q}_{in} r_{in}^m}{k} - \frac{\dot{q}_v}{(m+1)k} r_{in}^{m+1}\right)\frac{1}{r^m}. \tag{A.15}$$

Equation (A.15) will be used to determine the temperature distribution in the cylindrical and spherical walls:

- Cylindrical wall (m = 1):

  Integrating Eq. (A.15) for m = 1, results in:

$$T = -\frac{\dot{q}_v r^2}{4k} - \left(\frac{\dot{q}_{in} r_{in}}{k} - \frac{\dot{q}_v r_{in}^2}{2k}\right) ln\,r + C_6. \tag{A.16}$$

  By determining the constant C_6 from the boundary condition given by Eq. (A.6), Eq. (A.9) is obtained for calculating the temperature distribution in the cylindrical wall.

- Spherical wall (m = 2):

  Integrating Eq. (A.15) for m = 2, results in:

$$T = -\frac{\dot{q}_v r^2}{6k} + \left(\frac{\dot{q}_{in} r_{in}^2}{k} - \frac{\dot{q}_v r_{in}^3}{3k}\right)\frac{1}{r} + C_7. \tag{A.17}$$

  By determining the constant C_7 from the boundary condition given by Eq. (A.6), Eq. (A.11) is obtained for calculating the temperature distribution in the spherical wall.

Both methods then produce identical formulas for calculating the temperature distribution.

Co-published by
Institute of Fluid-Flow Machinery
Polish Academy of Sciences
Committee on Thermodynamics and Combustion
Polish Academy of Sciences

Copyright©2026 by the Authors under licence CC BY-NC-ND 4.0

http://www.imp.gda.pl/archives-of-thermodynamics/

Finding a Correlation for Predicting the Effective Thermal Conductivity of CNT Nanofluid

Farqad Rasheed Saeed[a*], Hussein Fawzi Hussein[a*], Natheer Basheer Mahmood[b]

[a]Scientific Research Commission, Baghdad, Iraq
[b]Ministry of Education, General Directorate of Baghdad Education Karkh2, Baghdad, Iraq
*Corresponding author email: hussein.f.hussein@src.edu.iq

Received: 16.06.2025; revised: 17.11.2025; accepted: 17.11.2025

Abstract

This study proposes a new correlation to predict the effective thermal conductivity of carbon-nanotube nanofluids by accounting for both carbon-nanotube characteristics (thermal conductivity, density, diameter and length) and base-fluid properties (thermal conductivity, density, specific heat, dynamic and kinematic viscosity, operating temperature and boiling point), in addition to the carbon-nanotube volume fraction. Using dimensional analysis, we constructed a set of π-groups and calibrated a regression-type model on 102 experimental data points gathered from the literature, and then assessed its accuracy against an independent set of 52 data points. Statistical indicators (mean absolute percentage error, signed mean error and standard deviation) demonstrate good agreement with measurements. Comparisons with widely used correlations further highlight the improved predictive capability of the present model, especially regarding the roles of carbon-nanotube length and diameter. Limitations: the current correlation does not explicitly incorporate nanofluid stability and aggregation metrics; thus, extrapolation beyond the calibration ranges should be made with caution. This correlation is suitable for engineering and numerical applications within the reported ranges.

Keywords: Carbon nanotubes; CNT nanofluids; Effective thermal conductivity; Dimensional analysis; Stability; Aggregation

Vol. 47(2026), No. 1, 43–53; doi: 10.24425/ather.2025.156854

Cite this manuscript as: Saeed, F.R., Hussein, H.F., & Mahmood, N.B. (2026). Finding a Correlation for Predicting the Effective Thermal Conductivity of CNT Nanofluid. *Archives of Thermodynamics*, 47(1), 43−53.

1. Introduction

Improving the thermal properties of working fluid used in different types of applications of heat transfer devices attracted the attention of researchers, which is associated with the growth of nanoparticle science [1]. The addition of nanoparticles to the base fluid to form what is known as a nanofluid enhances the thermal conductivity of the base fluid [2], and by its role improves the thermal performance of heat exchangers [3]. Nanofluids exhibit an interesting thermal behaviour that changes depending on the concentration, type, size and shape of the used nanoparticles [4]. The studies in the nanoparticles field divided into more than one competence such as, the stability of nanofluid [5,6], thermophysical properties of nanofluid [7,8], investigation of the heat transfer effects of nanofluid flow inside heat exchangers, studied both experimentally and numerically [9−12], and developing correlations to describe the effective thermophysical properties of nanofluid [13]. Most models were based on empirical data from experimental studies. Consequently, the resulting correlation is constrained by the specific experimental data and conditions used in its development and the conditions associated with the used procedure [14]. Maiga et al. [15], introduced models for predicting the effective thermal conductivity and effective viscosity of ultra-fine particles of

Nomenclature

ABS – absolute value
a – empirical constant
C – constant
d – CNT diameter, nm
k – thermal conductivity, W m^{-1} K^{-1}
l – CNT length, nm
n – shape factor
Pr – Prandtl number
T – temperature, K

Greek symbols

υ – kinematic viscosity, m^2 s^{-1}
π – dimensionless parameter
ρ – density, kg m^{-3}
Ø – volume fraction of nanoparticles, %
ψ – particle shape factor

Subscripts and Superscripts

br – Brownian motion
cal – calculated value
eff – effective property
exp – experimental value
f – base fluid
p – nanoparticle
r – reference value
ref – reference diameter

Abbreviations and Acronyms

CNT – carbon-nanotube
MAPE – mean absolute percentage error

Al_2O_3, TiO_2 and SiO_2 metal oxides based on experimental data. Simple models of Masuda et al. [16] have been used in many experimental and numerical studies. Koo and Kleinstreuer [17] used a model for predicting the effective thermal conductivity of nanofluids to study the laminar flow of nanofluids through a micro heat-sink. The model was obtained by considering experimental data of CuO nanoparticles. Das et al. [18] designed the model for thermal conductivity as a function of specific heat capacity, density of the base fluid, volume fraction of the nanoparticles, and finally, the temperature of the mixture. The range of the model validity is 0.01–0.04 volume fraction and 300–325 K in temperature. Chon et al. [19] applied the dimensional analysis to obtain a new correlation for predicting the effective thermal conductivity of Al_2O_3/water nanofluid. The correlation incorporated the following parameters: the thermal conductivity of the nanoparticles and base fluid, nanoparticle size and volume fraction, the molecular diameter of the base fluid, and the Prandtl and Reynolds numbers. The model applicability is limited for the nanoparticle size range of 11−150 nm, temperature range 294−344 K, and nanoparticles volume fraction 0.01−0.04. Prasher et al. [20] introduced a model for calculating the effective thermal conductivity of nanofluid by combining the Maxwell-Garnett conduction model with the effect of nanoparticle Brownian motion, which induces convection. The model is working with respect to the following parameters: nanoparticles volume fraction, nanoparticles size, temperature, interfacial resistance, thermal conductivity of the base fluid and thermal conductivity of the nanoparticles. The essential outcome of the model is that lighter nanoparticles improve the effective thermal conductivity of the nanofluid regardless the thermal conductivity of the nanoparticles. Sastry et al. [21] performed a theoretical model detecting the effective thermal conductivity of carbon-nanotubes (CNTs) nanofluid. The model is based on dimensionless parameters and considers the volume fraction of CNTs, shape of CNTs, their random orientation and the interaction among the CNTs. The results show an agreement of the models with experimental data. Vajjha and Das [22] investigated the effective thermal conductivity of three types of nanofluids. The used nanoparticles were Al_2O_3, CuO and ZnO. The base fluid was a mixture of ethylene glycol and water. Their experimental results had no agreement with the other models used to predict the effective thermal conductivity. They modified a model for predicting the effective thermal conductivity based on the classical model of Maxwell. The model incorporates the Brownian motion and works as a function of nanoparticles and base fluid thermal conductivity, volume fraction of the nanoparticles and temperature. The results exhibit an agreement between the model's outcomes and the experimental data.

Moghadassi et al. [23] used the dimensionless group to present a model for finding the effective thermal conductivity of Al_2O_3-water and Al_2O_3-ethylene glycol nanofluid. The model works as a function of volume fraction and particle size of alumina nanoparticles, thermal conductivity of Al_2O_3 nanoparticles, thermal conductivity of the base fluid and interfacial shell properties between the nanoparticles and base fluid. An agreement was found between the experimental data of Al_2O_3-water and Al_2O_3-ethylene glycol nanofluid and the predicted data from the model. The model also detected the effect of particle size, finding an inverse proportionality with thermal conductivity. Dimensionless groups applied by Hosseini et al. [24] were used to produce a model for predicting the effective thermal conductivity of CNTs nanofluid. The model was developed as a function of thermal conductivity of the nanoparticles, thermal conductivity of the base fluid and the effect of CNTs aspect ratio. The model shows a nonlinear behaviour with the rising volume fraction of CNTs. The comparison with the experimental data exhibits acceptable agreement. Emami et al. [25] suggested a model for estimating the effective thermal conductivity of nanofluids considering the mean distance between the particles, calculated through the Brownian motion approach. The validity of the model was achieved by comparison with the experimental data of the same work, which shows acceptable results. Patel et al. [26] performed a model to evaluate the effective thermal conductivity for metal and metal oxide nanoparticles. The model included the following parameters: nanoparticles volume fraction, nanoparticles thermal conductivity, nanoparticles diameters, temperature and base fluid thermal conductivity. The model works for the nanoparticles size ranging from 10 nm to 150 nm, nanoparticles thermal conductivity ranging from 20 W/(m·K) to 400 W/(m·K), the thermal conductivity of the base fluid ranging

from 0.1 W/(m·K) to 0.7 W/(m·K), nanoparticles volume fraction 0.001−0.03 and temperature range 293−323 K. Corcione [27] showed two empirical equations for predicting the effective thermal conductivity and effective dynamic viscosity of nanofluid. The correlation is a function of thermal conductivity of the nanoparticles and base fluid, nanoparticle volume fraction, and the Prandtl and Reynolds numbers. The model was based on collected experimental data from other studies of nanoparticles of metal and metal oxides like Cu, CuO, TiO_2 and Al_2O_3 [28−36]. The applicability of the model is in the range of nanoparticles size 10−150 nm, temperature 294−324 K and volume fraction 0.002−0.09. Azmi et al. [37] proposed a correlation for detecting the effective thermal conductivity of metal oxides nanoparticles and water-based fluid. The correlation is a function of thermal conductivity of the base fluid, thermal diffusivity of the nanoparticles, thermal diffusivity of the base fluid, temperature, nanoparticles size and nanoparticles volume fraction. The validity of the correlation is limited by the nanoparticle size 20−150 nm, temperature 293−343 K and volume fraction less than 0.04. Hosseini et al. [38] performed a nonlinear correlation for estimating the effective thermal conductivity of nanofluid. The model was generated considering the following parameters: the nanoparticle volume fraction and size, thermal conductivity of the nanoparticle and base fluid, interfacial shell properties and temperature. The model's validity was established through comparison with Al_2O_3/water experimental data, showing good agreement. All the aforementioned models are specific to particular nanoparticle types and are valid within the defined ranges of particle size, shape, temperature, volume fraction and thermal conductivity of both the nanoparticles and the base fluid.

Moreover, most models are based on and validated against experimental data from the same study or a limited number of datasets from other works. The aim of the present work is to present a model for predicting the effective thermal conductivity of CNTs using the π-terms, and based on a wide number of collected experimental data. In addition, the model covers all the parameters which may affect the effective thermal conductivity of the nanofluid. The model is also compared with experimental data from various works to detect the model's validity.

Beyond the classical thermal-conductivity models and CNT-specific correlations, several recent investigations have explored different routes for improving heat transfer in nanofluids and solar-thermal systems. Experimental and numerical analyses have demonstrated the impact of geometrical control, such as splitter-plate configurations and flow-field modifications, on the overall heat-transfer rate and stability of working fluids [65–67].

At the same time, local studies have addressed the thermal performance behaviour of solar and metallic systems under Iraqi climatic conditions, confirming the need for accurate correlations that account for temperature, viscosity and nanoparticle geometry effects [68–70]. In addition, investigations on carbon-based nanostructures such as graphene have highlighted transport similarities for CNTs, supporting the present work's emphasis on particle morphology and aggregation behaviour [71]. These recent findings collectively provide a broader context for the current correlation and validate its potential for engineering-scale thermal-modelling applications.

2. Methodology

2.1. Experimental data used to form the correlation

In order to present the correlation with acceptable accuracy, 102 data collected from different experimental investigations have been applied to derive the model. The data extracted from experimental studies have been used to characterise the thermophysical properties of CNTs/base fluid. The data contained various types of CNTs, such as multi-walled carbon nanotubes (MWCNTs) and single-walled carbon nanotubes (SWCNTs), with different lengths and diameters. Moreover, various types of base fluids were used in the mentioned experimental studies. Table 1 displays the used literature data to produce the present correlation for CNTs, and base fluids details.

Table 1. Literature data used to construct the correlation (CNT type, ranges of $\emptyset$, d, l, base fluid and T) [10].

References	Nanoparticles	$\emptyset$, %	d_p, nm	l_p, nm	Base fluid	T, K
[39]	SWCNTs	0.1	1	100−600	water	298−333
[39]	SWCNTs	0.2	1	100−600	water	298−333
[39]	SWCNTs	0.3	1	100−600	water	298−333
[40]	MWCNTs	0.04−1	25	50000	Polyalphaolefin	298
[41]	MWCNTs	0.25−1.5	50-80	10000−20000	Ethylene glycol	298
[42]	CS- SWCNTs	0.004−1.5	1−1.4	2400	Ethylene glycol	298
[42]	CNI-SWCNTs	0.004−1.1	1−1.4	1200	Polyalphaolefin	298
[43]	TCNTs	0.23−1	15	30000	Ethylene glycol	298
[43]	TCNTs	0.4−1	15	30000	Distilled water(DW)	298
[44]	MWCNTs	0.04−0.85	20−60	50000	water	293, 318
[45]	MWCNTs	0.25−1	10−30	10000−50000	water	300
[46]	CNTs	0.01−0.1	20	35000	water	298, 303
[47]	CNTs	0.1−1	10−20	10000−30000	water	293, 298, 303, 308, 313, 318

2.2. Effective thermal conductivity correlation

The effective thermal conductivity is a key parameter that governs the thermal performance of nanofluids and is influenced by other thermophysical properties, including the effective dynamic viscosity, specific heat and density. This study develops a correlation to predict the effective thermal conductivity of CNT nanofluids by incorporating all significant parameters related to both the nanoparticles and the base fluid. Using dimensional analysis [48,49], we derived the dimensionless groups (π-terms) for the correlation. Equation (1) expresses the effective thermal conductivity as a function of the following physical variables: CNT volume fraction, thermal conductivity of the base fluid and nanoparticles, Brownian velocity, specific heat capacity of the base fluid, CNT diameter and length, nanofluid temperature, boiling point of the base fluid, kinematic viscosity and a reference diameter.

Hassani et al. [50] proposed a correlation that includes most of these physical variables but omits the effect of nanoparticle length. Their model serves as a general tool for predicting the effective thermal conductivity of various nanofluids with different nanoparticles and base fluid types. However, CNTs possess a distinctive cylindrical geometry and exceptionally high intrinsic thermal conductivity, setting them apart from other nanomaterials. Therefore, the correlation presented in this work is specifically designed to predict the effective thermal conductivity of CNT-based nanofluids. The functional relationship is given by Eq. (1):

$$k_{eff} = f\left(\emptyset, k_f, k_p, v_{br}, C_{p.f}, d_p, l_p, T, d_{ref}, v_f, T_b\right). \quad (1)$$

Dimensional analysis resulted in 8 dimensionless groups, or the so-called π groups as shown in Table 2. The repetitive variables used in the derivation procedure are k_f, l_p, v_{br} and T.

Table 2. Dimensionless groups used in the correlation.

π-group	Physical variables
π_1	$\frac{k_{eff}}{k_f}$
π_2	$\emptyset$
π_3	$\frac{k_p}{k_f}$
π_4	$\frac{C_{p.f} \cdot T}{v_{br}^2}$
π_5	$\frac{d_{ref}}{l_p}$
π_6	$\frac{d_p}{l_p}$
π_7	$\frac{v_f}{l_p \cdot v_{br}}$
π_8	$\frac{T_b}{T}$
π_9	$\frac{\mu \cdot C_{p.f}}{k}$

Based on the dimensionless groups listed in Table 2 and the experimental data summarised in Table 1, the correlation was developed using a nonlinear regression analysis, resulting in Eq. (2):

$$\pi_1 = 1 + {\pi_2}^{1.02}{\pi_3}^{0.428} + 99.99{\pi_2}^{1.02}{\pi_9}^{-1.74} + -0.15{\pi_2}^{1.02}{\pi_3}^{0.428}{\pi_4}^{0.429}{\pi_5}^{0.92}{\pi_6}^{0.45}{\pi_7}^{0.56}{\pi_8}^{22.56}{\pi_9}^{-1.74}. \quad (2)$$

The Brownian motion is calculated according to Eq. (3), [51], as follows:

$$v_{br} = \sqrt{\frac{18\, k_b T}{\pi \rho_p d_p^3}}, \quad (3)$$

where d_{ref} is equal to 2.9 A° [52,53].

2.3. Correlation accuracy

The accuracy of the presented correlation Eq. (2), is measured by calculating the mean deviation, average deviation and standard deviation by using Eqs. (4), (5) and (6) [50], for the present correlation in comparison with 102 experimental data:

$$Mean\ deviation = \frac{1}{n}\sum_1^n ABS[100(\pi_{1,cal} - \pi_{1,exp})/\pi_{1,exp}], \quad (4)$$

$$Average\ deviation = \frac{1}{n}\sum_1^n [100(\pi_{1,cal} - \pi_{1,exp})/\pi_{1,exp}], \quad (5)$$

$$Standard\ deviation = \sqrt{\left(\frac{1}{n}\sum_1^n [100(\pi_{1,cal} - \pi_{1,exp})/\pi_{1,exp}]^2 - Average\ deviation^2\right)}. \quad (6)$$

2.4. Correlation validity

In order to ensure the validity of the present correlation, 52 data of external experimental studies have been used to test Eq. (2). These experimental data were not included in the database used to form Eq. (2). Table 3 shows the experimental studies used to achieve the validity of the present correlation. The results exhibit acceptable outcomes between the predicted data and the experimental data.

Table 3. Literature data used for external validation.

References	Nanoparticles	Ø, %	d_p, nm	l_p, nm	Base fluid	T, K
[54]	SWCNTs	0.03–0.2	1	150-500	Ethylene glycol	298
[55]	MWCNTs	0.006–0.3	9.2	1500	water	293
[55]	MWCNTs	0.006–0.3	9.2	1500	water	303
[55]	MWCNTs	0.006–0.3	9.2	1500	water	313
[56]	MWCNTs	0.2	11	10000	water	303–363
[56]	MWCNTs	0.5	11	10000	water	303–363
[56]	MWCNTs	0.75	11	10000	water	303–363
[56]	MWCNTs	1	11	10000	water	303–363
[57]	MWCNTs	0.3	20–30	10000–30000	water	293–318

2.5. Comparison with other models

The present correlation has been compared with previous models used to specify the effective thermal conductivity of CNTs/base fluid. The models are applied to the 154 data mentioned in Tables 1 and 3, and compared to the present correlation. One of the most used models to predict the effective thermal conductivity of nanofluid, considering the shape of nanoparticles is the Hamilton–Crosser model, Eq. (7) [58]. The model works as a function of thermal conductivity of the base fluid, nanoparticles thermal conductivity, nanoparticles volume fraction and nanoparticles shape

$$\frac{k_{eff}}{k_f} = \frac{k_p+(n-1)k_f+(n-1)(k_p-k_f)\emptyset}{k_p+(n-1)k_f-(k_p-k_f)\emptyset}, \quad (7)$$

where:

$$n = \frac{3}{\psi}, \quad (8)$$

$$\psi = \frac{surface\ area\ of\ the\ sphere}{surface\ area\ of\ the\ real\ particle\ with\ an\ equal\ volume}. \quad (9)$$

The second model used for comparison was presented by Patel et al. [59], Eq. (10), and considered a general equation for predicting the effective thermal conductivity of CNTs. The model works as a function of thermal conductivity of the base fluid, thermal conductivity of the CNTs, volume fraction of CNTs, diameter of CNTs and liquid particle size

$$\frac{k_{eff}}{k_f} = 1 + \frac{k_p \emptyset\, d_f}{k_f(1-\emptyset)d_p}. \quad (10)$$

The value of d_f was determined by Patel et al. [59] for water, so the only data for water from Tables 1 and 3 are included in the comparison.

Dimensionless groups were used by Hosseini et al. [24] in their model as given by Eq. (11):

$$\frac{k_{eff}}{k_f} = 1 + 51.84\left(\frac{1}{d}\right)^{0.441}(a_r)^{0.14}(\emptyset)^{0.749}, \quad (11)$$

where a_r is the aspect ratio, which is l_p/d_p. The model has been compared with the present correlation for 154 data items.

The last correlation used for comparison is introduced by Hassani et al. [50], Eq. (12), the correlation based on dimensionless groups and used to predict the effective thermal conductivity for all types of nanoparticles, including CNTs, as a function of all parameters which may affect the nanofluid properties, excluding the nanoparticles length

$$\frac{k_{eff}}{k_f} = 1.04 + \emptyset^{1.11}\left(\frac{k_p}{k_f}\right)^{0.33}\mathrm{Pr}^{-1.7} \times \quad (12)$$

$$\times\left[\frac{1}{\mathrm{Pr}^{-1.7}} - \frac{262}{\left(\frac{k_p}{k_f}\right)^{0.33}} + 135\left(\frac{d_{ref}}{d_p}\right)^{0.23}\left(\frac{v_f}{d_p v_{br}}\right)^{0.82}\left(\frac{C_p}{T^{-1}v_{br}^2}\right)^{-0.1}\left(\frac{T_b}{T}\right)^{-7}\right].$$

Another comparison has been made with the models of Wen and Ding [44], and Jiang et al. [56]. Experimental data were used to predict the effective thermal conductivity of the nanofluid using the present model (Eq. (2)) and four previously published models (Eqs. (7), (10), (11) and (12)).

3. Results and discussion

The present correlation, Eq. (2), was generated by applying a nonlinear regression analysis for the data mentioned in Table 1, which includes 102 data collected from different experimental studies. The correlation was verified through statistical calculations using Eqs. (4–6) to determine the mean, average and standard deviations; the results are shown in Table 4. The standard deviation was equal to 8.46%, 18.04% and 21.84% for water, polyalphaolefin and ethylene glycol, respectively. The lowest values for the mean, average and standard deviation were found for the water data, which can be interpreted by the fact that a large number of data points (78) for water were used to produce the correlation. The comparison between the experimental data from Table 1, and the predicted data by the present correlation is shown in Fig. 1.

Table 4. The comparison of the predicted data found from the present correlation with the experimental data from Table 1.

	Base fluid	Mean deviation (%)	Average deviation (%)	Standard deviation (%)	Number of data
Based on Table 1	Water	5.96	−3.08	8.46	78
	Polyalphaolefin	12.62	−10.01	18.04	11
	Ethylene glycol	19.61	19.61	21.84	13
	All data	8.42	−0.94	12.47	102

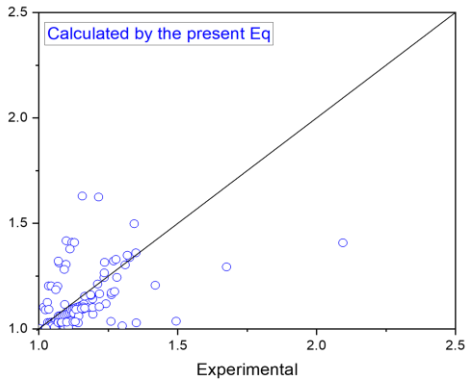


Fig. 1. The calculated data found from Eq. (2) in comparison with the experimental data from Table 1.

The validity of the correlation has been checked by testing Eq. (2) on 52 new experimental data, which were not included in the base data used to generate the correlation. The data used to validate the correlation are shown in Table 3. The validity results are shown in Table 5.

Table 5. The comparison of the predicted data found from the present correlation with the experimental data from Table 3.

	Base fluid	Mean deviation (%)	Average deviation (%)	Standard deviation (%)	Number of data
Based on Table 3	Water	12.89	4.80	15.48	46
	Ethylene glycol	2.65	−2.63	3.25	6
	All data	11.71	3.94	14.61	52

However, data for polyalphaolefin are limited; therefore, the validation was performed using only water and ethylene glycol data. The standard deviations for water and ethylene glycol were recorded at 15.48% and 3.25%, respectively, and the total standard deviation for the 52 data is 14.61%. The high value of standard deviation for water may be explained by the wide range of data used to validate the present correlation, which includes 46 data from three different references at various experiment conditions.

Four models to predict the effective thermal conductivity of CNTs are compared with the present model by using the data from Tables 1 and 3. The models are shown in Eqs. (7), (10), (11) and (12), and the results of statistical calculations applied to the four models in comparison with the present correlation are shown in Table 6. The statistical calculations were achieved for water, polyalphaolefin and ethylene glycol separately, and for the all data together. However, the model by Patel et al. [59], represented by Eq. (10), was applied only to the water-based fluid data because the model requires the liquid particle size as an input. To ensure accuracy, the comparison for this model was restricted to water data, using the water particle size specified by Patel et al. [59] as shown in Table 6.

Table 5. The comparison of the predicted data found from the present correlation with the other models using the experimental data from Table 1 and 3.

Based on Table 1 and Table 3	Base fluid	Mean deviation (%)	Average deviation (%)	Standard deviation (%)	Number of data
By using Eq. (7)	Water	7.40	−4.76	9.14	124
	Polyalphaolefin	16.57	−16.57	22.52	11
	Ethylene glycol	6.40	3.21	7.96	19
	All data	7.93	−4.62	10.64	154
By using Eq. (10)	Water	31.04	23.53	52.11	124
By using Eq. (11)	Water	52.45	50.54	66.34	124
	Polyalphaolefin	62.88	59.23	111.35	11
	Ethylene glycol	104.60	104.60	159.95	19
	All data	59.63	57.83	87.60	154
By using Eq. (12)	Water	13.92	7.63	27.72	124
	Polyalphaolefin	18.07	−17.30	24.62	11
	Ethylene glycol	4.05	2.39	4.50	19
	All data	13.00	5.20	25.82	154
By using the present correlation, Eq. (2)	Water	8.53	−0.16	11.58	124
	Polyalphaolefin	12.62	−10.01	18.04	11
	Ethylene glycol	14.26	12.59	18.49	19
	All data	9.53	0.70	13.23	154

The results of standard deviation shown in Table 6, exhibit the minimum standard deviation for 154 data recorded for Eq. (7), and increased standard deviation for Eqs. (2), (12) and (11). However, a closer examination of the results shows that Eq. (7) works as a function for the nanoparticles volume fraction, so the only parameter that may affect the variation of the results is the volume fraction of nanoparticles. Accordingly, Eq. (7) produced similar results with temperature variation at a fixed CNT volume fraction. However, temperature has a significant effect on the effective thermal conductivity of the nanofluid, and similar results lead to a negligible reduction in the standard deviation. To further evaluate the four models, including Eq. (10), a detailed examination of the standard deviation for the water data was performed. The minimum standard deviation was obtained for the 124 water data points, which exhibited behaviour similar to that of the overall dataset and led to the same interpretation.

Equation (12) was generated based on experimental data for various nanoparticle types. Consequently, the model is not specific to CNTs. However, some data used to form the model were from experimental studies for CNTs, with the number of CNTs data lower than used in the present correlation. In addition, the present model considers the effect of CNTs length, which is an important parameter to be taken into account in the present correlation. According to the previous explanations, Eq. (12) can give accurate results with some limitations in comparison to the present correlation. Eq. (10) has limitations in the high temperatures of nanofluids, and Eq. (11), which was developed based on specific experimental data. Thus, these models show excellent results when applied to data within their specific calibration ranges. However, when evaluated against the wider range of data used in our study, they exhibit a higher standard deviation.

Another comparison was performed between the four models and the present correlation using specific experimental data in order to evaluate the mean, average and standard deviation for selected studies. The comparison presented in Fig. 2(a) is based on the experimental data of Wen and Ding [44]. As shown in Fig. 2(a), the minimum values of the mean, average and standard deviation were obtained using the present correlation. However, the applied data were part of the basic dataset used to develop the correlation. Figure 2(b) presents another comparison using the data of Jiang et al. [56], where the minimum values of the mean, average and standard deviation were obtained using Eq. (7), followed by the present correlation. It is important to note that the data used in Fig. 2(b) were obtained at a constant nanoparticle volume fraction and different temperatures.

The present correlation was applied to predict some properties of the CNTs/base fluid using CNTs with a thermal conductivity of 2000 W/(m·K) and density of 1900 kg/m³. The effective thermal conductivity versus temperature in the range of 293 K to 342 K and volume fraction in the range of 0.001 to 0.009 is shown in Fig. 3(a). The curve exhibits that effective thermal conductivity improved with the increasing CNTs volume fraction and temperature. The variation in the effective thermal conductivity with dynamic viscosity at CNTs volume fraction ranging from 0.001 to 0.009 and temperature ranging from 293 K to 342 K is shown in Fig. 3(b). The curve illustrates the decrease in the effective thermal conductivity with the increase in the dynamic viscosity, and enhancement in the effective thermal conductivity with the rising CNTs volume fraction. The dynamic viscosity affects the effective thermal conductivity of the nanofluid, and this relation is more pronounced at low dynamic viscosities. This behaviour agrees with the findings of Hassani et al. [50]. From the above explanation, it can be concluded that temperature affects the dynamic viscosity and consequently influences the effective thermal conductivity.

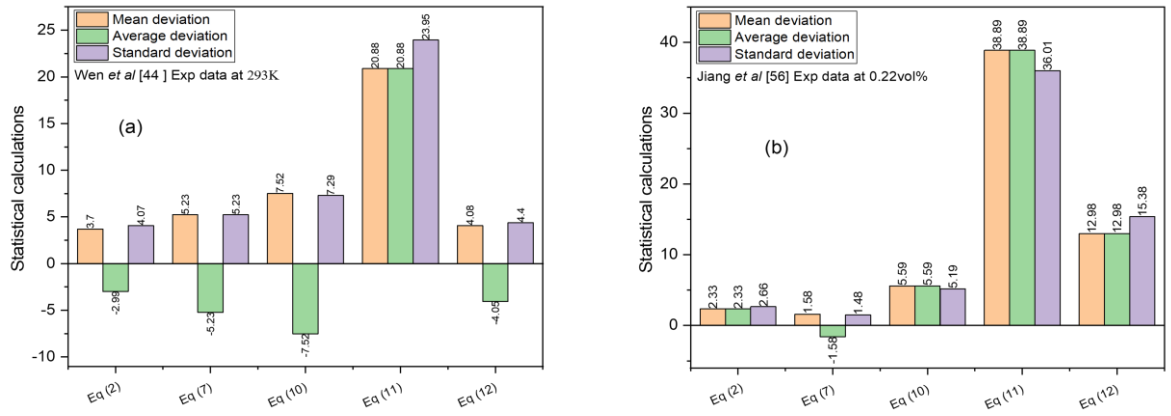


Fig. 2. Validation of the present correlation by comparison with other models for predicting the effective thermal conductivity using the experimental data of (a) Wen and Ding [44], (b) Jiang et al. [56].

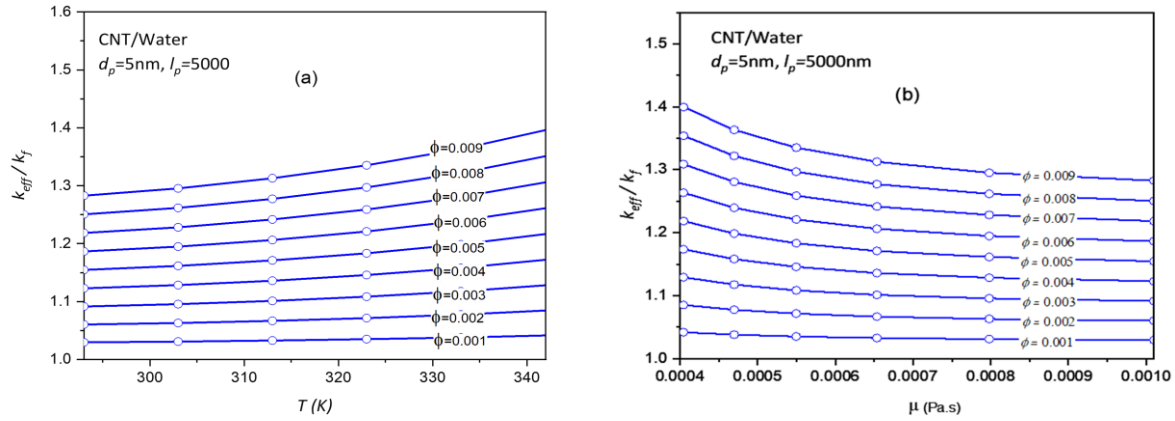


Fig. 3. Normalised thermal conductivity for CNTs/water found from the present correlation versus (a) temperature, (b) dynamic viscosity.

The effect of CNTs diameters on the effective thermal conductivity of the nanofluid is shown in Fig. 4(a), which exhibits an increase in the effective thermal conductivity of the nanofluid with the reduction in the CNTs diameter ranging from 1 nm to 100 nm, for CNTs volume fraction ranging from 0.3 to 1 % vol. at 298 K. Figure 4(b) shows the effect of CNTs length on the effective thermal conductivity of nanofluid, which increases with the increasing CNTs length ranging from 150 nm to 1000 nm, for CNTs volume fraction ranging from 0.3 to 1 % vol. at 298 K.

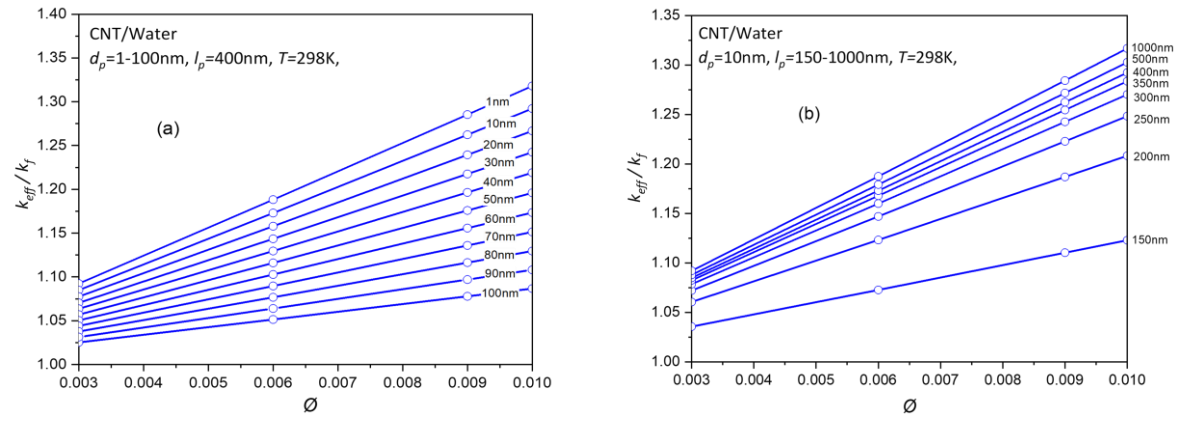


Fig. 4. Normalised thermal conductivity for CNTs/water found from the present correlation versus CNTs volume fraction at different (a) CNTs diameters, (b) CNTs lengths.

The effect of CNTs diameter on the effective thermal conductivity of CNTs/ethylene glycol is presented in Fig. 5(a). The effective thermal conductivity improved with the decreasing diameters of CNTs. The range of the used CNTs diameters is 1−40 nm, for CNTs volume fraction ranging from 0.3−1 % vol. at 298 K. Figure 5(b) indicates the effect of CNTs length on the effective thermal conductivity of CNTs/ethylene glycol. The curves exhibit an increase in the effective thermal conductivity

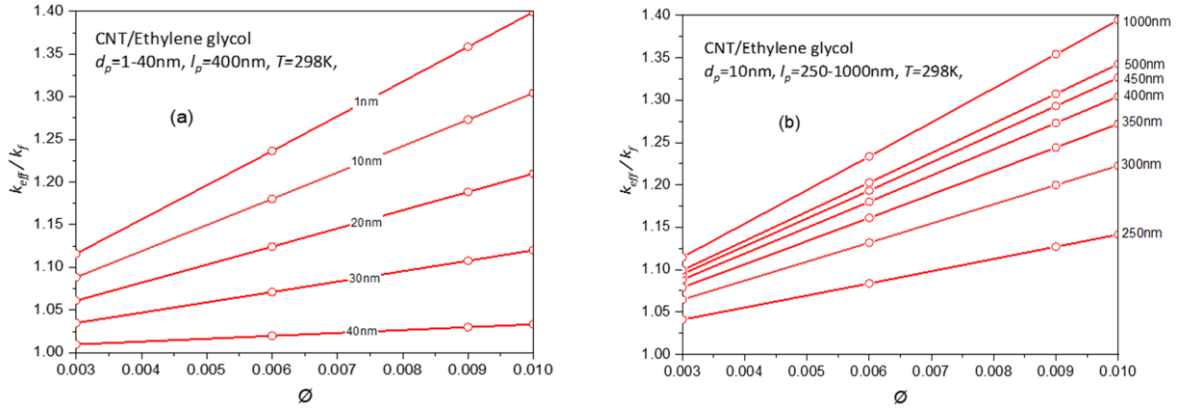


Fig. 5. Normalised thermal conductivity for CNTs/ethylene glycol found from the present correlation versus CNTs volume fraction at different (a) CNTs diameters, (b) CNTs lengths.

of the nanofluid with the increasing CNTs length ranging from 250 nm to 1000 nm, and CNTs volume fraction ranging between 0.3−1 % vol. at 298 K.

From Fig. 5(b) and Fig. 4(b), it can be noticed that the effective thermal conductivity is enhanced with the increasing CNTs length, and the amount of increase is reduced gradually with the increasing CNTs length over a specific value. In other words, the maximum improvement in the effective thermal conductivity was recorded at CNTs length from 250 nm to 300 nm, and decreased with the further increasing CNTs length, the minimum value found for 500 nm to 1000 nm. This behaviour can be interpreted by ballistic and ballistic-diffusive transport. The ballistic thermal transport takes place in CNTs of small length. The ballistic thermal transport produces a thermal resistance because of scattering of the phonon at the boundary, which improves the thermal conductivity. The ballistic-diffusive transport enhances with the increasing CNTs length, which occurs together with ballistic thermal transport and results in phonon scattering with both other phonons and the boundaries. Accordingly, the thermal resistance is generated because of the phonon-phonon scattering and phonon-boundary scattering, and whenever the CNTs length is increased, the phonon-boundary scattering is decreased. This interpretation agrees with the results of Cao and Qu [60], who determined that the length of zigzag single walled (SW) CNTs dominated by phonon-boundary scattering is ≤ 200 nm, and for armchair SW CNTs is ≤ 300 nm. Another interpretation related to the thermal boundary resistance, which controls the heat transfer at the interface between the base fluid and CNTs. Therefore, heat transfer improves when the thermal boundary resistance is small, and is reduced when it is high. Furthermore, since the effective thermal conductivity is a function of the CNT aspect ratio, as explained by Duong et al. [61], it improves with the increasing CNT length up to a point. The improvement of the effective thermal conductivity gets almost constant with the increasing CNTs length over a specific range due to the increase in the thermal boundary resistance that blocks the heat transfer. Duong et al. [61] determined the improvement in the effective thermal conductivity of SW CNTs/base fluid with an aspect ratio of SW CNTs reaching 80, and recorded almost a constant behaviour for the effective thermal conductivity for the SW CNTs aspect ratio greater than 80.

The comparison between the effective thermal conductivity of water and ethylene glycol at various volume fractions of CNTs, and at a fixed diameter and length, at 298 K, is shown in Fig. 6(a). The results indicate a higher effective thermal conductivity for CNTs/ethylene glycol than for CNTs/ water. This behaviour has been recorded in the experimental work presented by Harish et al [39], and compared with this work using the present correlation as shown in Fig. 6(b). A good agreement between the experimental and calculated data is found, which supports the validity of the present correlation.

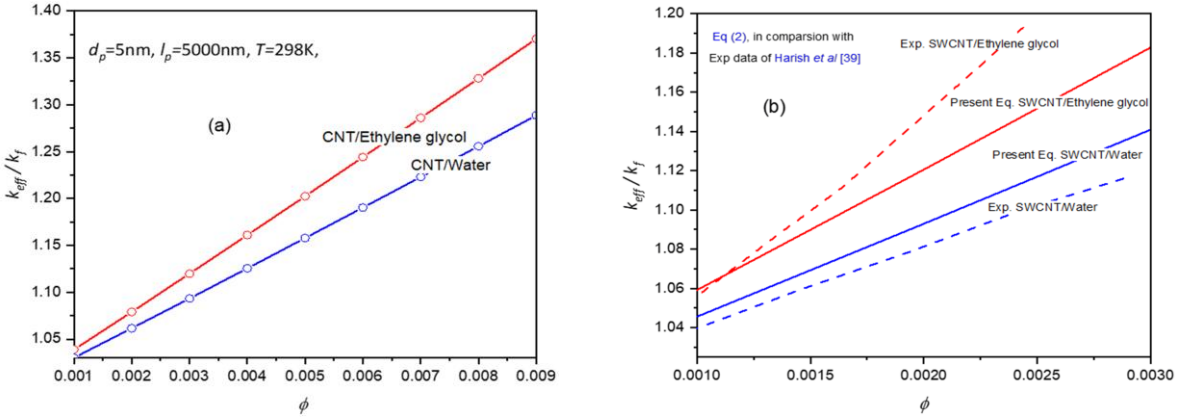


Fig. 6. Effective thermal conductivity versus CNTs volume fraction: (a) comparison between CNTs/ethylene glycol and CNTs/water (b) comparison between CNTs/ethylene glycol and CNTs/water with experimental work of Harish et al [39].

Research in this field remains active, with numerous recent studies providing experimental and theoretical insights into the effect of CNTs on the effective thermal conductivity of nanofluids. The models have been presented in these studies based on their specific empirical data, which reflect the conditions of their experiment.

To develop robust correlations for predicting the effective thermo-physical properties of nanofluids, periodic updates based on accumulating datasets are essential [62−64].

4. Limitations and future work

Although the present correlation was validated using a wide dataset of CNT nanofluids, it does not explicitly include the effects of particle aggregation and fluid stability, which can influence thermal conductivity through interfacial resistance and micro convection. Future work will incorporate these parameters and expand the database toward hybrid nanofluids and higher temperature ranges

5. Conclusions

A comprehensive correlation was developed to predict the effective thermal conductivity of CNT-based nanofluids by incorporating the combined effects of nanoparticle geometry (length and diameter), thermophysical properties of both the base fluid and CNTs, and operating temperature. The model was constructed through dimensional analysis and calibrated using 102 experimental data points from multiple literature sources, then validated on 52 independent datasets.

The correlation exhibited excellent agreement with experimental results, with low mean absolute percentage error and standard deviation, confirming its robustness and applicability for engineering analysis.

Comparative evaluation against several established models revealed that conventional correlations primarily depend on nanoparticle volume fraction and base-fluid conductivity while neglecting geometric characteristics. In contrast, the present model explicitly accounts for CNT length and diameter, demonstrating superior predictive accuracy and closer alignment with experimental data across a broad range of temperatures and concentrations.

The sensitivity analysis emphasised that the CNT aspect ratio (l/d), concentration and base-fluid viscosity are dominant factors influencing the effective thermal conductivity. These insights advance the understanding of nanoscale heat transport mechanisms and provide practical guidelines for the design and optimisation of thermal systems employing CNT nanofluids.

Although the proposed correlation performs effectively within its calibration range, future extensions should include nanoparticle aggregation and stability effects to enhance its applicability to hybrid nanofluids and high-temperature operations.

Overall, the developed correlation offers a reliable and physically consistent framework for predicting CNT nanofluid conductivity and represents a meaningful contribution toward accurate modelling of advanced nanofluid-based energy systems.

References

[1] Okonkwo, E.C., Wole-Osho, I., Almanassra, I.W., Abdullatif, Y.M., & Al-Ansari, T. (2021). An updated review of nanofluids in various heat transfer devices. *Journal of Thermal Analysis and Calorimetry*, 145(6), 2817–2872. doi: 10.1007/s10973-020-09760-2

[2] Choi, S.U.S., & Eastman, J.A. (1995). Enhancing thermal conductivity of fluids with nanoparticles *ASME International Engineering Congress & Exposition*, November 12−17, San Francisco, USA. Paper No. ANL/MSD/CP-84938; CONF-951135-29). https://www.osti.gov/biblio/196525 [accessed 17 Sept. 2025].

[3] Pordanjani, A.H., Aghakhani, S., Afrand, M., Mahmoudi, B., Mahian, O., & Wongwises, S. (2019). An updated review on application of nanofluids in heat exchangers for saving energy. *Energy Conversion and Management*, 198, 111886. doi: 10.1016/j.enconman.2019.111886

[4] Gupta, M., Singh, V., Kumar, R., & Said, Z. (2017). A review on thermophysical properties of nanofluids and heat transfer applications. *Renewable and Sustainable Energy Reviews*, 74, 638–670. doi: 10.1016/j.rser.2017.02.073

[5] Rashmi, W., Ismail, A.F., Sopyan, I., Jameel, A.T., Yusof, F., Khalid, M., & Mubarak, N.M. (2011). Stability and thermal conductivity enhancement of carbon nanotube nanofluid using gum arabic. *Journal of Experimental Nanoscience*, 6(6), 567–579.

[6] Zafarani-Moattar, M.T., & Majdan-Cegincara, R. (2013). Investigation on stability and rheological properties of nanofluid of ZnO nanoparticles dispersed in poly(ethylene glycol). *Fluid Phase Equilibria*, 354, 102–108. doi: 10.1016/j.fluid.2013.06.030

[7] Sabiha, M.A., Mostafizur, R.M., Saidur, R., & Mekhilef, S. (2016). Experimental investigation on thermo physical properties of single walled carbon nanotube nanofluids. *International Journal of Heat and Mass Transfer*, 93, 862–871. doi: 10.1016/j.ijheatmasstransfer.2015.10.071

[8] Sadri, R., Ahmadi, G., Togun, H., Dahari, M., Kazi, S.N., Sadeghinezhad, E., & Zubir, N. (2014). An experimental study on thermal conductivity and viscosity of nanofluids containing carbon nanotubes. *Nanoscale Research Letters*, 9(1), 151. doi: 10.1186/1556-276X-9-151

[9] Wen, D., & Ding, Y. (2004). Experimental investigation into convective heat transfer of nanofluids at the entrance region under laminar flow conditions. *International Journal of Heat and Mass Transfer*, 47(24), 5181–5188. doi: 10.1016/j.ijheatmasstransfer.2004.07.012

[10] Meisam, A., Ahmad, A., & Hamed, M. (2019). Experimental investigation of metal oxide nanofluids in a plate heat exchanger. *Journal of Thermophysics and Heat Transfer*, 33(4), 994–1005. doi: 10.2514/1.T5581

[11] Bianco, V., Chiacchio, F., Manca, O., & Nardini, S. (2009). Numerical investigation of nanofluids forced convection in circular tubes. *Applied Thermal Engineering*, 29(17–18), 3632–3642. doi: 10.1016/j.applthermaleng.2009.06.019

[12] Saeed, F.R., & Al-Dulaimi, M.A. (2021). Numerical investigation for convective heat transfer of nanofluid laminar flow inside a circular pipe by applying various models. *Archives of Thermodynamics*, 42(2), 71–95. doi: 10.24425/ather.2021.136948

[13] Phuoc, T.X., Massoudi, M., & Chen, R.H. (2011). Viscosity and thermal conductivity of nanofluids containing multi-walled carbon nanotubes stabilized by chitosan. *International Journal of Thermal Sciences*, 50(1), 12–18. doi: 10.1016/j.ijthermalsci.2010.09.008

[14] Vanaki, S.M., Ganesan, P., & Mohammed, H.A. (2016). Numerical study of convective heat transfer of nanofluids: A review. *Renewable and Sustainable Energy Reviews*, 54, 1212–1239. doi: 10.1016/j.rser.2015.10.042

[15] Maïga, S.E.B., Palm, S.J., Nguyen, C.T., Roy, G., & Galanis, N. (2005). Heat transfer enhancement by using nanofluids in forced convection flows. *International Journal of Heat and Fluid Flow*, 26(4), 530–546. doi: 10.1016/j.ijheatfluidflow.2005.02.004

[16] Masuda, H., Ebata, A., Teramae, K., & Hishinuma, N. (1993). Alteration of thermal conductivity and viscosity of liquid by dispersing ultra-fine particles (dispersion of γ-Al_2O_3, SiO_2 and TiO_2 ultra-fine particles). *Netsu Bussei*, 7(4), 227–233.

[17] Koo, J., & Kleinstreuer, C. (2005). Laminar nanofluid flow in microheat-sinks. *International Journal of Heat and Mass Transfer*, 48(13), 2652–2661. doi: 10.1016/j.ijheatmasstransfer.2005.01.029

[18] Das, S.K., Putra, N., Thiesen, P., & Roetzel, W. (2003). Temperature dependence of thermal conductivity enhancement for nanofluids. *Journal of Heat Transfer*, 125(4), 567–574. doi: 10.1115/1.1571080

[19] Chon, C.H., Kihm, K.D., Lee, S.P., & Choi, S.U.S. (2005). Empirical correlation finding the role of temperature and particle size for nanofluid (Al_2O_3) thermal conductivity enhancement. *Applied Physics Letters*, 87(15), 153107. doi: 10.1063/1.2093936

[20] Prasher, R., Bhattacharya, P., & Phelan, P.E. (2006). Brownian-motion-based convective-conductive model for the effective thermal conductivity of nanofluids. *Journal of Heat Transfer*, 128(6), 588–595. doi: 10.1115/1.2188509

[21] Sastry, N.N.V., Bhunia, A., Sundararajan, T., & Das, S.K. (2008). Predicting the effective thermal conductivity of carbon nanotube based nanofluids. *Nanotechnology*, 19(5), 055704. doi: 10.1088/0957-4484/19/05/055704

[22] Vajjha, R.S., & Das, D.K. (2009). Experimental determination of thermal conductivity of three nanofluids and development of new correlations. *International Journal of Heat and Mass Transfer*, 52(21–22), 4675–4682. doi: 10.1016/j.ijheatmasstransfer.2009.06.027

[23] Moghadassi, A., Hosseini, S.M., Henneke, D., & Elkamel, A. (2009). A model of nanofluids effective thermal conductivity based on dimensionless groups. *Journal of Thermal Analysis and Calorimetry*, 96(1), 81–84. doi: 10.1007/s10973-008-9843-z

[24] Hosseini, S.M., Moghadassi, A., & Henneke, D. (2011). Modelling of the effective thermal conductivity of carbon nanotube nanofluids based on dimensionless groups. *The Canadian Journal of Chemical Engineering*, 89(1), 183–186. doi: 10.1002/cjce.20389

[25] Emami-Meibodi, M., Vafaie-Sefti, M., Rashidi, A.M., Amrollahi, A., Tabasi, M., & Sid-Kalal, H. (2010). A model for thermal conductivity of nanofluids. *Materials Chemistry and Physics*, 123(2–3), 639–643. doi: 10.1016/j.matchemphys.2010.05.031

[26] Patel, H.E., Sundararajan, T., & Das, S.K. (2010). An experimental investigation into the thermal conductivity enhancement in oxide and metallic nanofluids. *Journal of Nanoparticle Research*, 12(3), 1015–1031. doi: 10.1007/s11051-009-9658-2

[27] Corcione, M. (2011). Empirical correlating equations for predicting the effective thermal conductivity and dynamic viscosity of nanofluids. *Energy Conversion and Management*, 52(1), 789–793. doi: 10.1016/j.enconman.2010.06.072

[28] Pak, B.C., & Cho, Y.I. (1998). Hydrodynamic and heat transfer study of dispersed fluids with submicron metallic oxide particles. *Experimental Heat Transfer*, 11(2), 151–170. doi: 10.1080/08916159808946559

[29] Lee, S., Choi, S.U.S., Li, S., & Eastman, J.A. (1999). Measuring thermal conductivity of fluids containing oxide nanoparticles. *Journal of Heat Transfer*, 121(2), 280–289. doi: 10.1115/1.2825978

[30] Eastman, J.A., Choi, S.U.S., Li, S., Yu, W., & Thompson, L.J. (2001). Anomalously increased effective thermal conductivities of ethylene glycol-based nanofluids containing copper nanoparticles. *Applied Physics Letters*, 78(6), 718–720. doi: 10.1063/1.1341218

[31] Yu, W., & Choi, S.U.S. (2003). The role of interfacial layers in the enhanced thermal conductivity of nanofluids. *Journal of Nanoparticle Research*, 5(1–2), 167–171. doi: 10.1023/A:1024438603801

[32] Chon, C.H., Kihm, K.D., Lee, S.P., & Choi, S.U.S. (2005). Empirical correlation finding the role of temperature and particle size for nanofluid (Al_2O_3) thermal conductivity enhancement. *Applied Physics Letters*, 87(15), 153107. doi: 10.1063/1.2093936

[33] Chon, C.H., & Kihm, K.D. (2005). Thermal conductivity enhancement of nanofluids by Brownian motion. *Journal of Heat Transfer*, 127(8), 810. doi: 10.1115/1.2033316

[34] Murshed, S.M.S., Leong, K.C., & Yang, C. (2008). Investigations of thermal conductivity and viscosity of nanofluids. *International Journal of Thermal Sciences*, 47(5), 560–568. doi: 10.1016/j.ijthermalsci.2007.05.004

[35] Mintsa, H.A., Roy, G., Nguyen, C.T., & Doucet, D. (2009). New temperature dependent thermal conductivity data for water-based nanofluids. *International Journal of Thermal Sciences*, 48(2), 363–371. doi: 10.1016/j.ijthermalsci.2008.03.009

[36] Duangthongsuk, W., & Wongwises, S. (2009). Measurement of temperature-dependent thermal conductivity and viscosity of TiO_2-water nanofluids. *Experimental Thermal and Fluid Science*, 33(4), 706–714. doi: 10.1016/j.expthermflusci.2009.01.005

[37] Azmi, W.H., Sharma, K.V., Mamat, R., Alias, A.B.S., & Misnon, I.I. (2012). Correlations for thermal conductivity and viscosity of water based nanofluids. *IOP Conference Series: Materials Science and Engineering*, 36(1), 012029. 5–7 December 2011, Kuantan, Pahang, Malaysia. doi: 10.1088/1757-899X/36/1/012029

[38] Hosseini, S.M., Safaei, M.R., Goodarzi, M., Alrashed, A.A.A.A., & Nguyen, T.K. (2017). New temperature, interfacial shell dependent dimensionless model for thermal conductivity of nanofluids. *International Journal of Heat and Mass Transfer*, 114, 207–210. doi: 10.1016/j.ijheatmasstransfer.2017.06.061

[39] Harish, S., Ishikawa, K., Einarsson, E., Aikawa, S., Inoue, T., Zhao, P., Watanabe, M., Chiashi, S., Shiomi, J., & Maruyama, S. (2012). Temperature dependent thermal conductivity increase of aqueous nanofluid with single walled carbon nanotube inclusion. *Materials Express*, 2(3), 213–223. doi: 10.1166/mex.2012.1074

[40] Choi, S.U.S., Zhang, Z.G., Yu, W., Lockwood, F.E., & Grulke, E.A. (2001). Anomalous thermal conductivity enhancement in nanotube suspensions. *Applied Physics Letters*, 7(14), 2252–2254. doi: 10.1063/1.1408272

[41] Lamas, B.C., Fonseca, A., Gonçalves, F.A.M M., Ferreira, A.G.M., Fonseca, I.M.A., Kanagaraj, S., Martins, N., & Oliveira, M.S.A. (2011). EG/CNTs nanofluids engineering and thermo-rheological characterization. *Journal of Nano Research*, 13, 69−74. doi: 10.4028/www.scientific.net/JNanoR.13.69

[42] Nanda, J., Maranville, C., Bollin, S.C., Sawall, D., Ohtani, H., Remillard, J.T., & Ginder, J.M. (2008). Thermal conductivity of single-wall carbon nanotube dispersions: Role of interfacial effects. *The Journal of Physical Chemistry C*, 112(3), 654–658. doi: 10.1021/jp711164h

[43] Xie, H., Lee, H., Youn, W., & Choi, M. (2003). Nanofluids containing multiwalled carbon nanotubes and their enhanced thermal conductivities. *Journal of Applied Physics*, 94(8), 4967–4971. doi: 10.1063/1.1613374

[44] Wen, D., & Ding, Y. (2004). Effective thermal conductivity of aqueous suspensions of carbon nanotubes (carbon nanotube nanofluids). *Journal of Thermophysics and Heat Transfer*, 18(4), 481–485. doi: 10.2514/1.9934

[45] Hwang, Y.J., Ahn, Y.C., Shin, H.S., Lee, C.G., Kim, G.T., Park, H.S., & Lee, J.K. (2006). Investigation on characteristics of thermal conductivity enhancement of nanofluids. C*urrent Applied Physics*, 6(6), 1068–1071. doi: 10.1016/j.cap.2005.07.021

[46] Walvekar, R., Faris, I.A., & Khalid, M. (2012). Thermal conductivity of carbon nanotube nanofluid—experimental and theoretical study. *Heat Transfer—Asian Research*, 41(2), 145–163. doi: 10.1002/htj.20405

[47] Almanassra, I.W., Manasrah, A.D., Al-Mubaiyedh, U.A., Al-Ansari, T., Malaibari, Z.O., & Atieh, M.A. (2020). An experimental study on stability and thermal conductivity of water/CNTs nanofluids using different surfactants: A comparison study. *Journal of Molecular Liquids*, 304, 111025. doi: 10.1016/j.molliq.2019.111025

[48] Vaschy, A. (1892). On the laws of similarity in physics. *Annales Télégraphiques*, 19, 25–28.

[49] Buckingham, E. (1914). On physically similar systems; illustrations of the use of dimensional equations. *Physical Review*, 4(4), 345–376.

[50] Hassani, S., Saidur, R., Mekhilef, S., & Hepbasli, A. (2015). A new correlation for predicting the thermal conductivity of nanofluids; using dimensional analysis. *International Journal of Heat and Mass Transfer*, 90, 121–130. doi: 10.1016/j.ijheatmasstransfer.2015.06.040

[51] Koo, J., & Kleinstreuer, C. (2004). A new thermal conductivity model for nanofluids. *Journal of Nanoparticle Research*, 6(6), 577–588. doi: 10.1007/s11051-004-3170-5

[52] Kumar, K.V., Preuss, K., Titirici, M.M., & Rodríguez-Reinoso, F. (2011). Molecular simulation of hydrogen physisorption and chemisorption in nanoporous carbon structures. *Adsorption Science and Technology*, 29(8), 799–817. doi: 10.1260/0263-6174.29.8.799

[53] Xu, X., Yang, W., Song, C., Liu, J., & Lin, L. (2003). Hydrogen separation by zeolite membranes. *ACS Division of Fuel Chemistry*, 48(1), 284–285.

[54] Harish, S., Ishikawa, K., Einarsson, E., Aikawa, S., Chiashi, S., Shiomi, J., & Maruyama, S. (2012). Enhanced thermal conductivity of ethylene glycol with single-walled carbon nanotube inclusions. *International Journal of Heat and Mass Transfer*, 55(13–14), 3885–3890. doi: 10.1016/j.ijheatmasstransfer.2012.03.001

[55] Halelfadl, S., Maré, T., & Estellé, P. (2014). Efficiency of carbon nanotubes water based nanofluids as coolants. *Experimental Thermal and Fluid Science*, 53, 104–110. doi: 10.1016/j.expthermflusci.2013.11.010

[56] Jiang, H., Zhang, Q., & Shi, L. (2015). Effective thermal conductivity of carbon nanotube-based nanofluid. *Journal of the Taiwan Institute of Chemical Engineers*, 55, 76–81. doi: 10.1016/j.jtice.2015.03.037

[57] Sadri, R., Ahmadi, G., Togun, H., Dahari, M., Kazi, S.N., Sadeghinezhad, E., & Zubir, N. (2014). An experimental study on thermal conductivity and viscosity of nanofluids containing carbon nanotubes. *Nanoscale Research Letters*, 9(1), 151. doi: 10.1186/1556-276X-9-151

[58] Hamilton, R.L., & Crosser, O.K. (1962). Thermal conductivity of heterogeneous two-component systems. *Industrial & Engineering Chemistry Fundamentals*, 1(3), 187–191. doi: 10.1021/i160003a005

[59] Patel, H.E., Anoop, K.B., Sundararajan, T., & Das, S.K. (2008). Model for thermal conductivity of CNT-nanofluids. *Bulletin of Materials Science*, 31(3), 387–390. doi: 10.1007/s12034-008-0060-y

[60] Cao, A., & Qu, J. (2012). Size dependent thermal conductivity of single-walled carbon nanotubes. *Journal of Applied Physics*, 112(1), 013503. doi: 10.1063/1.4730908

[61] Duong, H.M., Papavassiliou, D.V., Mullen, K.J., Wardle, B.L., & Maruyama, S. (2008). Calculated thermal properties of single-walled carbon nanotube suspensions. *The Journal of Physical Chemistry C*, 112(50), 19860–19865. doi: 10.1021/jp710021n

[62] Qin, J., Tao, Y., Liu, Q., Li, Z., Zhu, Z., & He, N. (2023). Experimental and theoretical studies of different parameters on the thermal conductivity of nanofluids. *Micromachines*, 14(5), 964. doi: 10.3390/mi14050964

[63] Mahdi, E.J., Hussein, H.F., Hassoon, I.A., & Jasim, A.A.-A. (2025). Analysis of solar panel surface thermal distribution using thermal imaging. *Journal of Renewable Energy and Environment*, 12(4), 74–80. doi: 10.30501/jree.2025.495645.2207

[64] Sarkar, S., Pal, P., & Ghosh, N.K. (2024). Enhancing the thermal conductivity and viscosity of ethylene glycol-based single-walled carbon nanotube (SWCNT) nanofluid: An investigation utilizing equilibrium molecular dynamics simulation. *Chemical Thermodynamics and Thermal Analysis*, 16, 100142. doi: 10.1016/j.ctta.2024.100142

[65] Hussein, H.F., Druga, L., Cojocaru, M., Dumitru, C., & Ghinea, A. (2018). Predicting and monitoring eutectic carbides proportion in cast austenitic Cr–Ni stainless steels. *U.P.B. Scientific Bulletin, Series B: Chemistry and Materials Science*, 80(4), 169–180.

[66] Hussein, H.F., Druga, L., Cojocaru, M., Dumitru, C., & Ghinea, A. (2020). The structural evolution of refractory steel spare parts during the successive carburizing. *U.P.B. Scientific Bulletin, Series B: Chemistry and Materials Science*, 82(1), 247–257.

[67] Batros, S.S., Saeed, F.R., & Hussein, H.F. (2025). Antibacterial activity and microstructure properties of copper oxide particles doped with cadmium prepared by chemical precipitation method. *Iranian Journal of Materials Science and Engineering*, 22(1), 107–117. doi: 10.22068/ijmse.3864

[68] Obaid, A.H., Mahdi, E.J., Hassoon, I.A., Hussein, F.H., Jasime, A.A.A-S., Jafar, A.N., & Abdulghani, A.S. (2024). Evaluation of degradation factor effect on solar panels performance after eight years of life operation. *Archives of Thermodynamics*, 45(3), 221–226. doi: 10.24425/ather.2024.151223

[69] Mahdi, E.J., Hussein, H.F., & Saeed, F.R. (2025). Thermal performance comparison of aluminum and iron alloys in heat exchangers for solar water-heating systems: Experimental study under Iraqi climate conditions. *Next Materials*, 8, 100935. doi: 10.1016/j.nxmate.2025.100935

[70] Hasoon, I.A., Inad, K.I., Mahdi, E.J., Salih, S.M. & Hussein, H.F. (2025). Design and performance evaluation of an off-grid photovoltaic system for metallurgical laboratories. *JOM (Journal of The Minerals, Metals & Materials Society)*, 77, 10158−10164. doi: 10.1007/s11837-025-07867-1

[71] Ahmed, S.B., Al-Naemi, A.N.A., Kamar, F.H., Hussein, H.F., & Nawar, M.S. (2024). Adsorption of phenol from aqueous solution using graphene nano-particles. *The 4th International Conference on Sustainable Engineering Techniques*, 5−6 October, Baghdad, Iraq. *AIP Conference Proceedings*, 3105(1), 070003. doi: 10.1063/5.0212296

Co-published by
Institute of Fluid-Flow Machinery
Polish Academy of Sciences
Committee on Thermodynamics and Combustion
Polish Academy of Sciences

Copyright©2026 by the Authors under licence CC BY-NC-ND 4.0

http://www.imp.gda.pl/archives-of-thermodynamics/

Simulation-Based Design of a Two-Stage Heat Pump System Utilising Treated Wastewater for Urban Heating Applications

Aleksandra Dzido[a*], Piotr Krawczyk[a], Adrián Mota-Babiloni[b]

[a]Warsaw University of Technology, Institute of Heat Engineering, Nowowiejska 21/25, 00-665 Warsaw, Poland
[b]ISTENER Research Group, Department of Mechanical Engineering and Construction, Universidad Jaume I, Castellon de la Plana, E-12071, Spain
*Corresponding author email: aleksandra.dzido@pw.edu.pl

Received: 10.07.2025; revised: 13.01.2026; accepted: 23.01.2026

Abstract

In light of current energy policies, integrating renewable energy and waste heat recovery into district heating systems has become increasingly crucial. There is a particular need to identify locally available, low-temperature heat sources that can be effectively upgraded to meet the high supply temperatures required by existing networks. This study examines the technical and economic viability of high-temperature heat pumps utilising treated sewage as a renewable heat source in district heating systems. A comprehensive mathematical model of a high-capacity, two-stage centrifugal heat pump was developed and implemented in Aspen HYSYS to simulate its performance under varying operational conditions typical of Central-Eastern Europe. The model accounts for seasonal variations in sewage flow and temperature, as well as regulatory constraints of district heating networks and technical requirements such as temperature lift (ΔT_{lift}) and part-load operation. Two operating scenarios are evaluated: a conventional coal-based system and a hybrid system incorporating a 3 MW sewage heat pump. Results indicate that the heat pump can meet domestic hot water demand in the summer and reduce annual CO_2 equivalent emissions by approximately 9500 tonnes, assuming the use of renewable electricity. Despite minor degradation in the coefficient of performance at part-load and low-flow conditions, the system demonstrated stable, efficient performance. An economic assessment using the levelised cost of heat method confirmed cost competitiveness in the Polish market context. The findings underscore the strategic role of sewage-source heat pumps in decarbonising urban heating.

Keywords: High-temperature heat pumps; Waste heat recovery; District heating; Off-design conditions; Mathematical modelling

Vol. 47(2026), No. 1, 55–69; doi: 10.24425/ather.2025.156855

Cite this manuscript as: Dzido, A., Krawczyk, P., & Mota-Babiloni, A. (2026). Simulation-Based Design of a Two-Stage Heat Pump System Utilising Treated Wastewater for Urban Heating Applications. *Archives of Thermodynamics*, 47(1), 55−69.

1. Introduction

Currently, energy policy and global trends are promoting increased shares of renewables and the use of waste heat. The green energy transformation is driving changes not only in electricity generation but also in district heating [1]. The European Union (EU) has introduced an ambitious climate and energy package to reduce greenhouse gas emissions, promote renewable energy sources, and enhance energy efficiency. Initially outlined in the 2020 framework and later extended to 2030, these measures aim to transition the EU economy to climate neutrality by 2050. To achieve this transformation, the European Commission introduced the „Fit for 55” initiative, a comprehensive legislative package designed to update existing regulations and create new policies. This effort aligns EU actions with the climate goals set by the European Parliament and the Council.

In the realm of district heating (DH), significant legislative updates affect directives such as the Emission Trading System (ETS) and the Energy Efficiency Directive (EED). A key change under the EED redefines what constitutes an efficient heating

Nomenclature

a, b – constants
CF – correction factor
COP_i – value of COP at time range i
C_V – coefficient
h – enthalpy of the flow, kJ/kg
h_i, h_j – specific enthalpies, kJ/kg
k – adiabatic exponent
$LMDT$– logarithmic mean temperature difference, K
$\dot{m}$ – mass flow rate, kg/s
M – number of outlet streams
n – volume exponent
$\dot{n}$ – molar flow rate, kmol/s
N – number of inlet streams
p – pressure, Pa
Δp – pressure drop, Pa
P – power, kW
q – heat provided to the shell side, kW
q_{loss} – heat losses, kW
Q – heat exchanger power, MW
r – compression ratio
R – individual gas constant, J/(mol·K)
t – time, s
T – temperature, K
ΔT_{lift} – temperature lift, K
UA – overall heat exchanger heat load, W/K
υ – specific volume, m^3/kg
V – volume, m^3
$\dot{V}$ – volumetric flow,

Greek symbols

ρ – density, kg/m^3

Subscripts and Superscripts

design– design point parameters
i, j – streams
in – inlet
lift – lift
loss – losses
new – new value
out – outlet
shell – shell side of heat exchanger
tot – total
tube – tube side of heat exchanger

Abbreviations and Acronyms

CAPEX– capital expenditures
CFD – computational fluid dynamics
COP – coefficient of performance
DH – district heating
DHC – district heating and cooling
DHCN – district heating and cooling networks
DHN – district heating networks
DHS – district heating system
EED – Energy Efficiency Directive
ETS – Emission Trading System
EU – European Union
GDH – generation district heating
GDHC – generation district heating and cooling
GEA – GEA Group, Germany
GWP – global warming potential
HFO – hydrofluoroolefin
HP – heat pump
HTHP – high-temperature heat pump
IEG – Research Institution for Energy Infrastructures and Geothermal Systems IEG
IGV – inlet guide vanes
LCOH – levelised cost of heat
ODP – ozone depletion potential
OPEX – operating expenditures
PCM – phase change material
sCOP – seasonal COP
VHC – volumetric heating capacity

system. Starting in 2028, only systems that incorporate heat generated from renewable sources or waste heat will qualify as efficient. The required share of such heat will gradually increase to 100% by 2050 [2]. These new requirements pose considerable challenges for heat suppliers and producers, compelling them to adapt their operations to meet the updated efficiency standards. It is worth noting that in 2021, in Poland, 69.5% of heat used for heating was generated from coal, while slightly more than 20% was generated from renewables [3]. When assessing potential heat sources for centralised heating systems, compliance with these evolving regulations is critical.

Currently, only a few technologies possess the technical potential to serve as significant heat sources for centralised heating systems in medium- and large-sized cities. These include solid biomass boilers, particularly those with cogeneration capabilities, and large-scale heat pumps [4]. Additionally, using treated wastewater as a low-temperature heat source for heat pumps offers numerous benefits, including predictable, stable flow, high medium temperatures and high energy density.

In many countries, such as those in Scandinavia, high-temperature sewage heat pumps are commonly used for DH. For instance, studies on the potential of heat pumps in Denmark can be found in Johansen et al. [5] and Østergaard et al. [6], while case studies on Stockholm (Sweden) are presented by Levihn [4].

High-temperature heat pumps have been studied in conjunction with district heating networks (DHN), yielding promising results. Alarnaot et al. [7] carried out a multi-perspective assessment of an experimental moderately-high-temperature heat pump (HTHP) for district heating and cooling networks (DHCN), obtaining a 1.96-year payback period when connected to 4G DHCN. Sadeghi et al. [8] used heat from a DHN at 85°C to produce steam at 160°C using HTHP and considered several configurations, including combinations of vapour compression and steam cycles. Passamonti et al. [9] presented a HTHP pilot plant at the Fraunhofer Research Institution for Energy Infrastructures and Geothermal Systems IEG (IEG) location in Bochum for 120°C heating production, which can save up to 4800 tonnes of CO_2 equivalent emissions annually. In [10], De-

gelin et al. presented a techno-economic analysis of a centralised heat pump dedicated to district heating, including the influence of supply temperature (10−75°C) on seasonal coefficient of performance (sCOP), which varies from 3.43 to 4.6. The levelised cost of heat (LCOH) for analysed cases remained in the range of 213−297 EUR/MWh$_{th}$. Zhu et al. [11] experimentally investigated the cooperation of booster heat pumps with ultra-low-temperature DHN, achieving a coefficient of performance (COP) of 4.95. Barco-Burgos et al. [12] presented a review of high-temperature heat pumps in DHCN. They have identified factors influencing the feasibility of heat pumps (HP) in DH, including electricity and fuel prices, supply temperature, availability of external waste heat and other local conditions. The 5th generation of DHCN was analysed by Calise et al. [13]. The integration of renewable energy sources, a ground-source heat pump, and a low-temperature network resulted in 64% primary energy savings and a 76% reduction in CO_2-equivalent emissions. The same authors in [14] analysed seawater HP cooperation with district heating and cooling (DHC). The simple payback period of the system was relatively long – 14.7 years. However, coupling the system with renewable energy plants allows for achieving zero primary energy consumption and CO_2 emissions. Another work related to seawater HP implementation in DH was presented by Ali et al. [15]. Authors report 88% electricity savings, 65% reduction in CO_2 emissions and a 76% decrease in LCOH in the Norwegian case, with slightly worse coefficients in Tallinn due to sea water freezing in winter. In the northern part of Central-Eastern Europe, the heating season extends from October to April, spanning more than half the year. Additionally, heating systems provide domestic hot water year-round, including during the summer months. Given the extended operational period, implementing environmentally friendly innovations in this sector is crucial.

Heat pumps can be operated with various refrigerants, including hydrofluoroolefines (HFO) and other increasingly popular natural refrigerants. The selection of a refrigerant should be based on thermodynamic properties, safety considerations and environmental impact. A comparison of the main parameters for HP operation with typical refrigerants is presented in Table 1.

Table 1. Comparison of the main parameters for HP operation with typical refrigerants.

Refrigerant	R1234ze(E)	NH_3 (R717)	CO_2 (R744)
Chemical formula	$C_3H_2F_4$	NH_3	CO_2
Type	HFO (Synthetic)	Natural	Natural
GWP / ODP	<1 / 0 [63]	0 / 0 [38]	1 / 0 [64]
Safety class	A2L [65]	B2L (toxic) [65]	A1 (non-toxic) [65]
Operating pressure	Standard (~25−30 bar) [38]	Medium (10−35 bar) [66]	Very high (30−90 bar) [67]
COP range	2.5−6.2 [16]	3.0−5.9 [16,21]	1.8−4.2 [20,24]
Typical max. outlet temperature	80−95°C [37]	95−120°C [25,26]	90−120°C [38]

R1234ze(E) has emerged as a promising hydrofluoroolefin refrigerant for heat pump applications due to its favourable environmental characteristics and thermodynamic properties. Experimental studies have demonstrated that R1234ze(E) exhibits superior performance compared to other HFO refrigerants in specific applications, achieving a COP of up to 6.2 [16]. Among the disadvantages of this refrigerant, carcinogenic effects and a high medium cost could be enumerated.

Ammonia (R717) demonstrates superior thermodynamic performance in large-scale district heating applications. Industrial installations by GEA (GEA Group, Germany) show ammonia heat pumps achieving COPs above 3.5, with systems delivering 40 MW of heating capacity for district networks [17]. However, ammonia's primary limitation is its toxicity and associated safety risks. Ammonia is classified as toxic and requires stringent safety measures, extensive leak detection systems, and specialised operator training. Modern low-charge ammonia systems have reduced refrigerant inventory, but even these installations require comprehensive safety protocols due to leakage risks. In applications near populated areas, ammonia presents significant safety management challenges that can complicate implementation and increase liability concerns.

Carbon dioxide (R744) transcritical heat pumps offer unique advantages for ultra-high-temperature applications, with systems capable of producing heated water up to 120°C. Performance data show COPs ranging from 1.8 to 4.2, depending on operating conditions, which is lower than for other considered refrigerants. The critical limitation of CO_2 systems is their extremely high operating pressure. CO_2 transcritical cycles operate at pressures significantly higher than those of conventional refrigerant systems, with maximum design pressures exceeding 90 bar. These elevated pressures require specialised compressors, robust heat exchangers and heavy-duty piping components, substantially increasing capital costs. Additionally, CO_2 systems show higher sensitivity to operating condition variations than alternative refrigerants, resulting in reduced performance flexibility [18].

Urban areas often harbour significant sources of waste heat that remain underutilised or inefficiently exploited. Optimising the use of these resources represents a promising avenue for improving heating systems. One notable example of such waste heat is treated sewage, which holds substantial potential as an energy source [4]. However, the low temperatures of treated sewage make it unsuitable for direct use in heating applications.

To address this limitation, treated sewage can serve as a low-temperature heat source for HP, which raises the medium's temperature to a usable level [19]. This method aligns with decarbonisation strategies [20], which project that heat pumps will meet nearly 25% of heating needs by 2050. Consequently, heat pumps are widely regarded as a promising and forward-thinking solution for future heating systems.

Sewage water has been considered as a potential heat recovery source that can be upgraded with heat pumps. Wang et al. [18] addressed the challenges of unequal sewage water flows, scale formation, corrosion, and a rapid decline in heat transfer capacity over time by considering a non-metallic immersed heat exchanger as an evaporator in HP. Supply temper-

atures varied from 40.4°C to 60.6°C, with a sCOP of 5.65 achieved. Ma et al. [21] considered sewage HP integrated with phase change material (PCM) heat storage. Although integrating a phase change heat storage unit substantially improves both economic viability and energy efficiency, the simple payback period remains long – over 15 years. A techno-economic analysis of sewage HP for domestic hot water purposes was shown by Xu et al. [22]. Authors emphasise that individual requirements and conditions affect installation performance, although in the analysed case, a 64.8% reduction in CO_2-equivalent emissions was achieved. A small sewage HP dedicated to trigeneration was analysed by Gao et al. [23]. The study shows a strong dependence of COP on ambient temperature, with values of 8.97 in the summer and 2.44 in the winter. In [24], Xu et al. developed a CO_2-equivalent emission-reduction model for sewage HP implementation in an example city in northern China. Typical reductions are approximately 60%, depending on the building type. Brands and Fung [25] analysed large-scale wastewater HP performance in cold climates, achieving significant reductions in CO_2-equivalent emissions (45−60% in fossil-fuel-dependent regions and up to 95% in areas with renewable electricity production). Ozcan et al. [26] studied the energy, exergy, economic, environmental and sustainability impacts of a wastewater-source heat pump system for DH applications.

A heat pump in such an application is constrained by the existing network and its parameters, as well as by the sewage system, safety requirements and legal conditions, including power connection requirements and heat output specifications. Furthermore, it must adapt to the current demand for heat. These complex technical and operational conditions make the integration and optimisation of the heat pump unit within the existing heating system highly challenging. Heat pumps often operate under off-design conditions, making their analysis essential.

Assessing the operating conditions of large heat pumps can significantly benefit from the use of mathematical models. However, there is limited literature dedicated to this topic. Typically, heat pump-related models are implemented in Modelica, MATLAB, TRNSYS and IDEA ICE [27]. Additionally, some scientists employed analytical or semi-analytical methods to calculate HP components, as well as computational fluid dynamics (CFD) tools such as Open FOAM [28]. Tan et al. [29] analysed a low-temperature waste recovery heat pump. The system was modelled in Aspen Plus without off-design analysis. Considered cases covered waste temperatures in the range 100−120°C, which is significantly higher than the temperature levels considered in this study.

In this research, the authors developed a mathematical model of the main processes occurring in large, high-temperature HPs and implemented it within the Aspen HYSYS numerical environment. This software is typically used in the chemical industry [30], for petrochemical engineering calculations [31], in hydrogen-related installations [32], for carbon capture and storage [33], in modelling compressed air energy storage systems [34], for liquid air energy storage [35], and in other applications.

Aspen HYSYS is not widely used for HP modelling, despite being equipped with all the required functionalities. This software was chosen for its ability to perform calculations in off-design mode, a feature not widely described in the available literature. The developed model was subsequently used to analyse the HP performance.

The objective of this work was to provide a comprehensive mathematical description of the operating conditions and phenomena within the heat pump unit, facilitating its optimal utilisation, even under off-design conditions commonly encountered in urban heating systems. Poland has been considered a representative case for this work in Central-Eastern Europe. Additionally, the developed tool can assist in selecting appropriate HP units and accurately predicting their performance. The developed model was then used to predict the performance of the heating system under the green energy transformation. Another goal of this study was to evaluate the technical, environmental and economic impacts of integrating a sewage-source heat pump into an existing coal-based DH system. Two operational scenarios were analysed: the current configuration with two coal-fired boilers and a proposed hybrid system that includes a sewage heat pump. The analysis compared heat generation, fuel consumption and equivalent CO_2 emissions for both cases, demonstrating that introducing a heat pump could reduce annual coal use and lower equivalent CO_2 emissions. Furthermore, an economic assessment based on the levelised cost of heat (LCOH) was conducted to determine the cost-effectiveness and competitiveness of the proposed solution within the Polish DH sector.

2. Materials and methods

2.1. System considered

2.1.1. Sewage scenario

Heat pumps that use treated sewage as a heat source are dependent on both demand and supply factors. The supply side consists of waste heat from sewage, with varying temperature and mass flow over time. Typically, temperature fluctuations are seasonal [36] (weather-dependent) and generally range between 10–22°C [37]. Data on sewage and outside temperatures collected over 4 years in a specific city in Poland enabled the creation of a correlation between these variables (Fig. 1), which was used in this study.

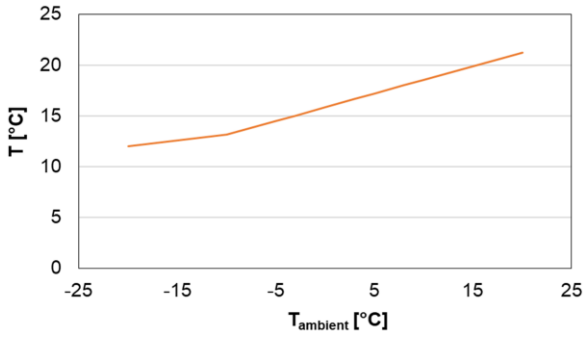


Fig. 1. Treated sewage temperature as a function of ambient temperature.

The amount of available sewage depends on the size of the agglomeration. However, it can be assumed that the daily sewage production per adult in Central-Eastern Europe is approximately 150 litres. Despite this, sewage mass flow is not constant

and fluctuates throughout the day. Example relative data from one Polish city are shown in Fig. 2.

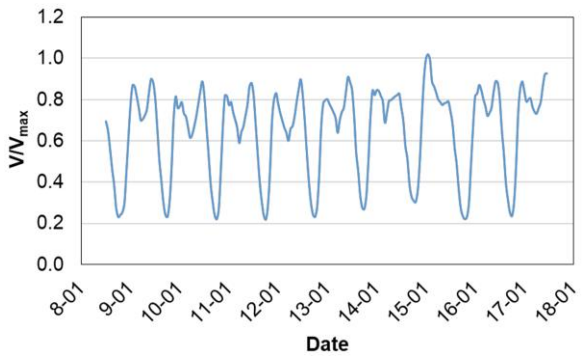


Fig. 2. Relative sewage flow fluctuations during a representative week.

On the other hand, there is the demand side. When considering heat pumps for integration with an existing DHN, they must meet network requirements. Therefore, high-temperature units should be considered [38]. Typically, the supply and return temperatures of DH water are determined by a regulatory table (Table 2). In Poland, high-temperature networks are typical; however, the transition to green energy may necessitate lowering the supply temperature, as in Scandinavian countries. Despite this, the heat pump must be capable of operating under these fixed conditions, taking into account both the available sewage parameters and the district heating system requirements.

Table 2. Selected values of the regulatory table for the district heating network in a Central-Eastern European city.

Operational point	1	2	3	4	5	6	7	8	9	10
Ambient temperature [°C]	20	10	8	5	3	0	−3	−5	−10	−20
DHN return [°C]	43.0	43.5	44.0	46.0	47.5	50.0	50.5	52.0	55.0	60.0
DHN feed [°C]	73	74	74	80	85	92	95	99	105	122

2.1.2. Heat pump

There are various configurations of the HP systems, starting from simple, relatively cheap constructions to more complex sets characterised by, i.e., higher COP. The simple system is typically a subcritical cycle with single-stage compression. The compressor can be a piston, scroll or centrifugal type, depending mainly on the unit's power [39]. This is currently the most widely used cycle in heat pumps. Although it achieves a high COP with a relatively low temperature difference, the maximum temperature rise is limited by the single-stage compressor's compression limit. Another characteristic feature is that as the temperature difference increases, expansion losses also increase, and their value depends primarily on the thermo-physical properties of the working medium, particularly its viscosity. To overcome these drawbacks, various HP configurations were developed [40]. A review of possible solutions can be found in [41]. The system, commonly found in industrial applications, is the HP cycle with two-step compression. In such a system, two compressors allow for a higher temperature lift. Furthermore, the gaseous fraction after the first reduction valve is combined with the gas from the first compressor, thereby reducing energy consumption during compression.

As the considered application requires a high-temperature output, a two-stage centrifugal compressor system was selected, similar to the one described in [42]. Such a system ensures a compromise between efficiency, the desired ΔT_{lift}, and system complexity, which is strictly related to investment costs [43]. The system used in this study is illustrated in Fig. 3.

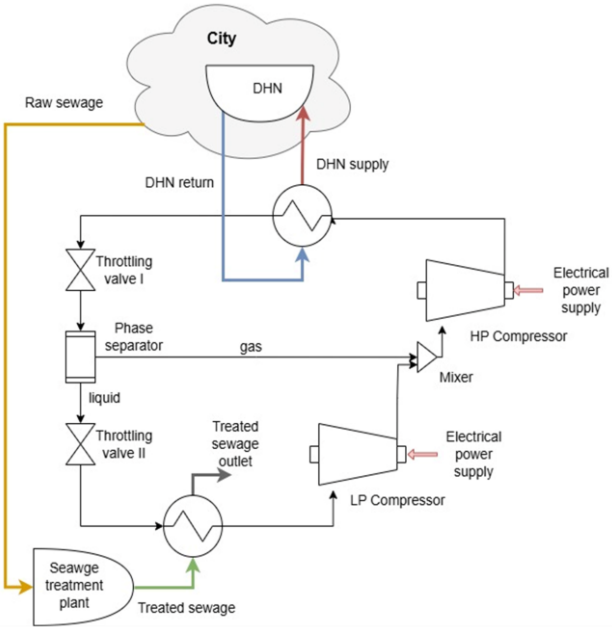


Fig. 3. Heat pump unit scheme.

2.1.3. Working fluid

For effective and safe HP operation, the proper selection of the working fluid (refrigerant) is essential. There are several factors determining its choice, which can be divided into categories [38]: thermo-physical: high critical temperature, low critical pressure; environmental: global warming potential (GWP) below 10, ozone depletion potential (ODP) = 0, future-proof regarding regulations; safety: non-toxic, non or low flammable, non-reactive with steel, copper, and aluminium; efficiency: high COP, even with high ΔT_{lift}, high volumetric heating capacity (VHC); and availability: low price, accessible in the market.

One of the popular refrigerants in European applications is R1234ze(E) [44]. This medium has a relatively low negative global warming potential [14] and simultaneously allows the desired phase-change temperatures to be achieved at a reasonable pressure. It has been classified as A2L [42] and is considered relatively safe. Its physical properties allow it to operate within the assumed temperature range. Several studies have highlighted the high energy efficiency of vapour-compression systems using this fluid, even at high condensation temperatures [7,51,52]. Taking the above into account, R1234ze(E) was selected for this research, as in [47].

2.1.4. Boundary conditions and connection with district heating networks

As boundary conditions, the sewage temperature and DHN water temperature at the return (HP inlet) were assumed to be functions of the outside temperature (Table 3). The selected values were based on experimental data and a regulatory table for a specific city in Poland. Ten operational points of the system were selected. The HP water-side outlet temperature should generally match the DHN feedwater temperature; however, due to HP constructional conditions during the winter season, several discrepancies occur. It will be discussed in the further part of this study.

Table 3. Boundary conditions for selected operational points of HP.

Operational point	1	2	3	4	5	6	7	8	9	10
Atmospheric temperature [°C]	20.0	10.0	8.0	5.0	3.0	0.0	−3.0	−5.0	−10.0	−20.0
Treated sewage temperature [°C]	21.2	18.5	18.0	17.2	16.6	15.9	15.0	14.5	13.2	12.0
DHN return [°C]	43.0	43.5	44.0	46.0	47.5	50.0	50.5	52.0	55.0	60.0
DHN feed [°C]	73.0	74.0	74.5	80.0	85.0	92.0	95.0	99.0	105.0	122.0

2.2. Equations

Numerical analysis encompassed the development of mathematical models, their implementation in numerical software, and the selection of initial and boundary conditions.

First, the energy balance equation and mass balance equation need to be fulfilled:

$$\sum_{i=1}^{i=N} \dot{m}_i h_i = \sum_{j=1}^{j=M} \dot{m}_j h_j, \quad (1)$$

$$\sum_{i=1}^{i=N} \dot{m}_i = \sum_{j=1}^{j=M} \dot{m}_j, \quad (2)$$

where N is the number of inlet streams, M is the number of outlet streams, $\dot{m}_i$ represents the mass flow rate at the inlet side [kg/s], $\dot{m}_j$ means the mass flow rate at the outlet side [kg/s], h_i and h_j are the specific enthalpies of each stream [kJ/kg].

In the system, two fluids are used: water (treated sewage and heating water) and refrigerant (R1234ze(E)) in the heat pump circuit. Due to the various properties of the fluids in the proposed case, two mathematical models of the media were selected. Water circuits were described using the ASME steam model [54], while the refrigerant cycle was modelled using the Peng-Robinson model of real gas in the form (3) [48]:

$$p = \frac{RT}{v-b} = \frac{a(T)}{v(v+b)+b(v-b)}, \quad (3)$$

where p is the pressure [Pa], R represents the individual gas constant [J/(mol·K)], T is temperature [K], v means specific volume [m^3/kg], and a and b are constants.

The energy balance equation for the shell side is expressed in Eq. (4):

$$\dot{m}_{shell} \cdot (h_{in} - h_{out})_{shell} - q_{loss} + q = \rho \frac{d(V \cdot h_{out})_{shell}}{dt}, \quad (4)$$

where $\dot{m}_{shell}$ is the mass flow rate at the shell side [kg/s], h_{in} and h_{out} are the inlet and outlet enthalpy of the flow [kJ/kg], q_{loss} represents heat losses [kW], q means heat provided to the shell side [kW], ρ is the density [kg/m^3], t represents time [s] and V is volume [m^3].

The energy balance equation for the tube side is given by (5):

$$\dot{m}_{tube} \cdot (h_{in} - h_{out})_{tube} - q_{loss} + q = \rho \frac{d(V \cdot h_{out})_{tube}}{dt}, \quad (5)$$

where $\dot{m}_{tube}$ is the mass flow rate at the tube side [kg/s], h_{in}, h_{out} are inlet and outlet enthalpies of the flow [kJ/kg], q_{loss} represents heat losses [kW], q is heat provided to the tube side [kW], ρ means density [kg/m^3], t is time [s], V means volume [m^3].

Heat exchanger power was described by Eq. (6):

$$Q = |m_{in} h_{in} - m_{out} h_{out}|, \quad (6)$$

where: Q means heat exchanged, m_{in} and m_{out} are inlet and outlet mass flow rates [kg/s], h_{in} and h_{out} are specific enthalpies of inlet and outlet streams, respectively.

The overall heat exchanger heat load (UA, W/K) can be expressed as [36]:

$$UA = \frac{Q}{LMTD}, \quad (7)$$

where Q represents the heat exchanger power [MW], $LMTD$ is the logarithmic mean temperature difference [K], which can be expressed as:

$$LMTD = \frac{\Delta T_{side\,1} - \Delta T_{side\,2}}{\ln\left(\frac{\Delta T_{side\,1}}{\Delta T_{side\,2}}\right)}. \quad (8)$$

In off-design mode, changes in the medium's volume flow rate affect the exchangers' heat load – Eq.(9), where $\dot{V}$ is the volumetric flow of the media entering the heat exchanger and subscripts denote design point conditions.

$$\frac{UA}{UA_{design}} = \left(\frac{\dot{V}}{\dot{V}_{design}}\right)^{0.8}. \quad (9)$$

The flow through the valves was calculated based on [49]:

$$\dot{m} = k\sqrt{\Delta p}, \quad (10)$$

where $\dot{m}$ is the mass flow rate [kg/s], k is the coefficient representing the inverse of flow resistance (conductivity) [$\sqrt{\text{kg} \cdot \text{m}}$], Δp is the pressure drop [Pa].

The mass flow rate was calculated as a function of inlet (p_{in}) and outlet pressure (p_{out}) and the coefficient C_v, which corresponds to the inverse of flow resistance (11):

$$\dot{m} = f(p_{in}, p_{out}, C_V). \quad (11)$$

The compressor assumed in this study is a centrifugal one [50]. Its electrical consumption power was calculated as shown in Eq. (12):

$$P = \dot{n}_{in} \cdot M \cdot \left(\frac{n}{n-1}\right) \cdot CF \cdot \left(\frac{p_{in}}{\rho_{in}}\right) \cdot \left[\left(\frac{p_{out}}{p_{in}}\right)^{\left(\frac{n-1}{n}\right)} - 1\right], \quad (12)$$

where P is the device's electrical consumption power [kW], $\dot{n}$ means the molar flow rate [kmol/s], M represents the molar mass of the working medium [kg/kmol], n is the volume exponent, p_{in} and p_{out} are the inlet and outlet pressures and ρ_{in} is the inlet density [kg/m^3].

The correction factor (CF) was Eq. (13):

$$CF = \frac{h'_{out} - h_{in}}{\left(\frac{n-1}{n}\right)\left(\frac{p_{out}}{\rho'_{out}} - \frac{p_{in}}{\rho_{in}}\right)}. \quad (13)$$

The power imparted to the working medium during the compression process is described in Eq. (14):

$$P = \dot{n}_{in} \cdot M \cdot (h_{out} - h_{in}). \quad (14)$$

In off-design mode, the maximum compressor pressure depends on the design pressure and the medium inlet temperature, as shown in Eq. (15), where r is the compression ratio, T is the temperature [K], and k is the adiabatic exponent:

$$r_{new} = \left[\frac{T_{inlet,design}}{T_{inlet,new}}\left(r_{design}{}^{\frac{k-1}{k}} - 1\right) + 1\right]^{\frac{k}{k-1}}. \quad (15)$$

The compressor was assumed to be a constant-speed machine, as is typical for high-power units. In some operating states, the heat pump is controlled by throttling. This is achieved in practice by changing the angle of the inlet guide vanes (IGV). Assumed characteristics of the efficiency change depending on the blade closure angle, based on data presented in [50], are shown in Fig. 4.

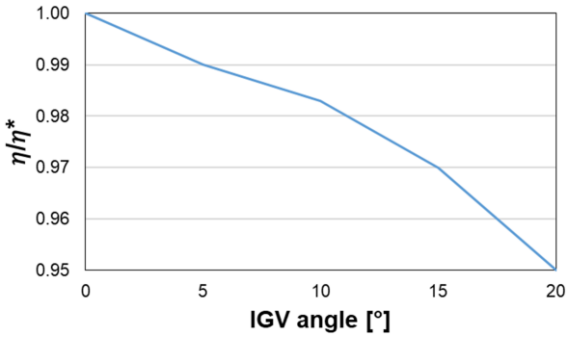


Fig. 4. Relative efficiency as a function of the compressor IGV angle (own work based on [50]).

As the medium's parameters change, its specific volume changes. Compressors, as displacement machines, operate at a constant volume flow. Reducing it requires choking. An example compressor throttling characteristic, used in this study, is shown in the chart (Fig. 5). The mathematical model presented above was implemented in the Aspen HYSYS numerical environment, which is designed explicitly for heat-flow calculations, including complex systems.

An economic assessment of the investment in water heat pumps was conducted based on the levelised cost of heat (LCOH) parameter [51].

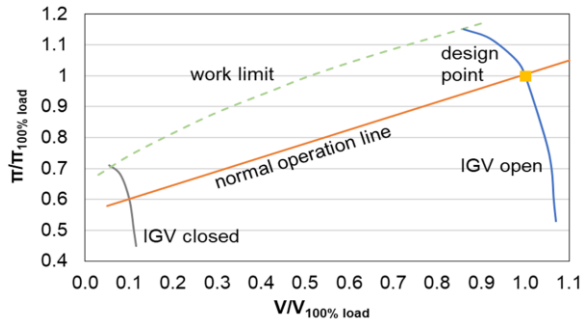


Fig. 5. Pressure ratio as a function of volumetric flow at the compressor inlet.

LCOH provides a comprehensive measure of the unit cost of heat production throughout the installation's lifecycle. This parameter accounts for investment expenses, operational costs, and system efficiency, enabling objective, consistent comparisons of technologies. Consequently, it serves as a key tool for the economic optimisation of heat source portfolios and informed investment decision-making, which is why it was selected as an assessment parameter in this study. LCOH was calculated using Eq. (16):

$$LCOH = \frac{\sum_{i=0}^{N}\left(\frac{I_i + M_i}{(1+r)^i}\right)}{\sum_{i=0}^{N}\frac{Q_i}{(1+r)^i}}, \quad (16)$$

where I_i represents investment expenditures in year i [EUR/a] (CAPEX and OPEX), M_i are operating expenditures and operational costs [EUR/a], Q_i is heat production in year i [EUR/a], r means discount rate, and takes a value of 5% in this study as in [52], and N represents the lifetime of the installation (economic operational period), 20 years.

2.3. System balance model

Small heating plants in Poland are still predominantly based on water-coal boilers, such as WR-10. This study analysed the integration of systems utilising such sources with a heat pump, where the lower heat source is treated wastewater. Based on the typical heating load of a system for a medium-sized city under Polish weather conditions (Fig. 6), a balance model with an hourly resolution was developed.

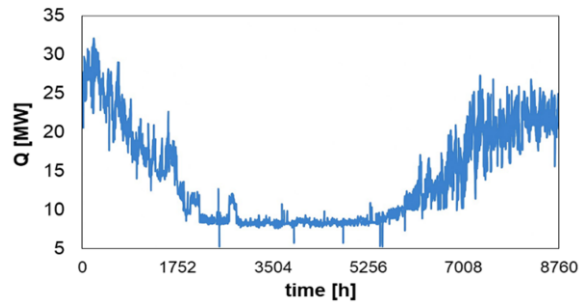


Fig. 6. Heat demand in the system over the year.

The system scheme is shown in Fig. 7. In each hour of system operation, the amount of heat produced by each source was

determined. Priority was given to the heat pump installation as a renewable source, provided treated wastewater was available as the lower heat source, and its temperature allowed achieving the desired supply water parameters in the network. Two WR-10 boilers operated as supplementary sources, with constraints such as the power range (3−15 MW). The size of the heat pump installation was selected based on the potential for utilising sludge waste heat (3 MW).

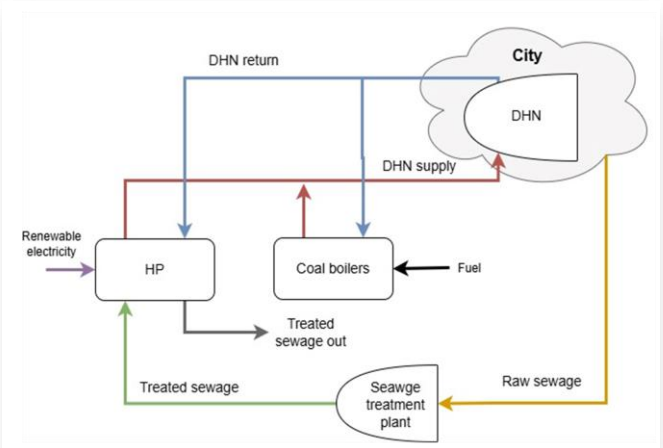


Fig. 7. Scheme of the analysed system.

3. Results and discussion

Determining the HP design point is a critical yet complex task. It is influenced by various factors, including the maximum temperature lift, mass flows of sewage and district heating water, and their variations, as well as the anticipated temperature ranges of the operating mediums. The selection of design-point parameters has a significant impact on the HP unit's operating conditions, as these parameters are interdependent. This section analyses how the variability of selected parameters affects the operation of the HP unit under the given conditions, using a developed mathematical model. The data obtained from the HP modelling were then used in the system balance model to predict the annual heat production by source and the environmental impact of the implemented changes (equivalent CO_2 emission reduction).

3.1. Designed temperature lift

First design condition, which should be determined, is temperature lift, defined as the maximum temperature difference between the heating water outlet and treated sewage inlet temperatures:

$$\Delta T_{lift} = T_{H,out} - T_{L,in}. \quad (17)$$

The maximum values of ΔT_{lift} occur during the winter season, when sewage temperatures are at their lowest. The required heating water temperatures are at their highest (Fig. 8). Conversely, considering the thermodynamic cycle in heat pumps, the highest value of ΔT_{lift} is achieved with the most significant difference between evaporator and condenser pressures, which corresponds to the highest compression rate. Based on this outcome, the system should be designed to operate in winter conditions. During the summer season, the pressure ratio can be reduced, for instance, by throttling; however, if the system is designed with a pressure ratio that is too low, there will be no way to increase it when needed. In this analysis, the design point was assumed to correspond to winter conditions.

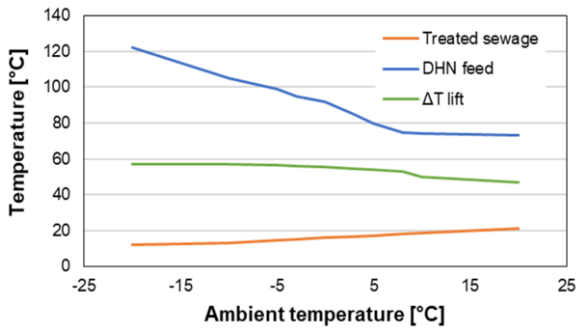


Fig. 8. Treated sewage, DHN feed and ΔT_{lift} temperatures as a function of ambient temperature.

3.2. Outflow temperature

The second key parameter of the design point is the outflow temperature (district heating supply water at the outlet of the HP module), which significantly influences the system's operating parameters, such as the coefficient of performance (COP). It should also be adjusted to reflect the evolution of district heating systems, which have progressed from the first generation based on steam to today's fifth-generation low-temperature networks, illustrating a consistent trajectory toward higher energy efficiency, reduced distribution losses, and greater integration of renewable and waste heat sources. While the first and second generations relied on high-temperature steam and pressurised hot water systems fuelled by fossil energy [52,53], subsequent generations progressively lowered operating temperatures (to around 70–100°C in the third generation) [54]. They introduced technological innovations such as pre-insulated pipes and automatic control systems [53]. The fourth generation district heating (4 GDH) marked the shift to low-temperature networks (30−70°C) based on renewable energy and smart control technologies [12], whereas the fifth generation (5 GDHC) expanded this concept to include both heating and cooling within decentralised, bidirectional networks operating near ambient temperatures (10–40°C), where buildings can act as prosumers of heat [54]. In the light of increasing demands for energy efficiency, decarbonisation and system flexibility, existing district heating networks now face the urgent need to transform toward 4 GDH and 5 GDHC solutions. This transformation requires integrating heat pumps, thermal storage, waste and low-temperature heat sources, along with smart management systems that enable dynamic balancing of supply and demand while minimising the use of solid fuels, which are key steps toward achieving a sustainable future for urban heating.

Given the dynamic development of district heating networks and current local network requirements (3 GHD), two operating scenarios for the heat pump module were selected and analysed under specific weather conditions. The analysis was divided into two scenarios (see also Table 4):

- **Scenario 1**: A higher upper heat source temperature (maximum 95°C), adjusted for high-temperature networks (2 GDH).
- **Scenario 2**: A lower upper heat source temperature (maximum 75°C), suitable for low-temperature district heating networks (3−5 GDH).

Table 4. Design parameter points for the analysed scenarios.

Parameter	Scenario 1	Scenario 2
DHN supply temperature [°C]	95.0	75.0
Sewage inlet temperature [°C]	12.0	
ΔT_{lift} max	89.0	69.0
Total pressure ratio	10.7	7.6
LP compressor pressure ratio	3.3	2.8
HP compressor pressure ratio	3.3	2.8
Evaporator pinch point temperature [°C]	3.3	
Condenser pinch point temperature [°C]	5.0	
Adiabatic efficiency of the compressors [%]	75	

Figure 9 compares the district heating water temperatures provided by the HP unit with the requirements in the regulatory table. The heat pump system is primarily designed as a low-temperature source due to its specifications. Heating the network water to meet regulatory requirements for temperatures below −3°C would significantly decrease efficiency. This is partly due to the need to design the system for conditions that occur for only a few hours annually. Therefore, the maximum source temperature at the network water outlet was set to 95°C in scenario 1. While this configuration accommodates most conditions, particularly during very low outside temperatures, achieving higher desired system supply temperatures may still require additional measures.

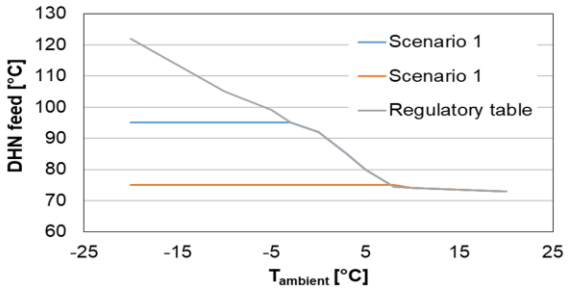


Fig. 9. District heating water supply temperature as a function of ambient temperature.

In scenario 2, the maximum network water temperature at the HP outlet is limited to 75°C. This configuration is sufficient to meet high-temperature network requirements for over half the year and serves as an example of a system suitable for low-temperature networks. Such networks are expected to become increasingly common in Poland in the future and are already successfully implemented in several European countries, including those in Scandinavia.

During periods when higher temperatures are needed, district heating water at the supply side is heated using an auxiliary heat source, such as an electric boiler or other supplementary systems, to cover the heat load. To compare these scenarios, the systems' operations in both configurations were simulated.

Figure 10 illustrates COP for each analysed scenario as a function of the outside temperature. While scenario 2 achieves a higher COP, it requires additional heating over a more extended period throughout the year or necessitates investments in network transformation, including demand-side adaptations. The results clearly indicate that lowering the design temperature enhances the overall system efficiency, reducing electricity consumption and improving the economic performance of the heat pump installation. Similar trends have been reported in the literature, where a decrease in the required supply temperature of district heating networks led to a noticeable improvement in heat pump efficiency. For instance, Degelin et al. [10] showed that reducing the supply temperature from 55°C to 45°C can increase COP by approximately 33%. Likewise, Pospíšil et al. [55] observed a correlation between the temperature difference between the water temperature at the condenser outlet and the air temperature at the evaporator inlet. When the measured temperature difference remains below 30°C, COPs above 4 were obtained.

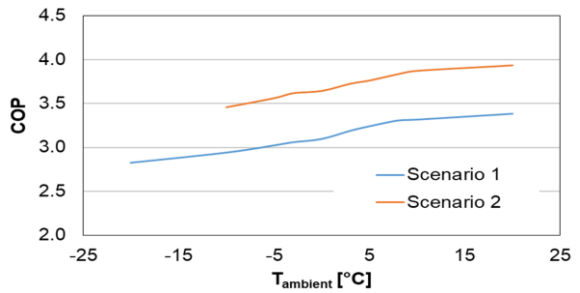


Fig. 10. COP as a function of ambient temperature.

A seasonal COP (sCOP) was used as a comparative parameter, calculated as the average annual COP, weighted by the number of hours at the selected system operating point (Eq. 18). For each scenario, the year was divided into ten periods (Table 5).

$$\mathrm{sCOP} = \frac{\sum \mathrm{COP}_i \cdot t_i}{t_{tot}}, \tag{18}$$

where COP_i is the value of COP at time range i, t_i is the amount of hours installation is being operated with COP_i [h], and t_{tot} is the total amount of hours when the installation is operated [h].

Table 5. Data for sCOP calculations.

Operational point	1	2	3	4	5	6	7	8	9	10
Ambient temperature [°C]	20.0	10.0	8.0	5.0	3.0	0.0	−3.0	−5.0	−10.0	−20.0
Amount of hours [h]	2560	1712	789	763	865	1031	452	284	278	26
COP_i scenario 1	3.47	3.41	3.36	3.30	3.21	3.14	3.07	3.06	2.99	2.91
COP_i scenario 2	3.87	3.85	3.74	3.65	3.66	3.50	3.52	3.46	3.38	3.25

In the analysed case, sCOP equals 3.32 in scenario 1, which complies with the literature. For scenario 2, sCOP was 3.72, which is significantly higher; however, this HP could be operated for a limited time over the year. Considering the Polish technical and weather conditions, scenario 1 was taken as the base model for further calculations. In the literature, sCOP for treated sewage HP equals 3.29 [36] and 3.3−3.5 [4]. It means that even the sCOP value obtained for scenario 1 remains at a similar level.

3.3. Treated sewage mass flow

Using the previously described mathematical model, various scenarios of the HP unit's operation were analysed, ranging from minimum to maximum sewage flow under winter conditions, which were selected as less favourable. The operational data presented in Fig. 2 indicated a relatively high daily variability of sewage flow. The variability characteristics were relatively constant throughout the year, in repeatable daily fluctuations. The minimum flow occurs for approximately 5−6 hours a day.

Designing the heat pump module for minimum flow requires throttling the compressors in operating conditions with higher output, which occurs most of the time. Throttling reduces compressor efficiency and COP, so it should be avoided whenever possible. Designing the system for maximum flow would entail the risk of failing to meet the network water parameters at lower flows (low pressure, making it impossible to achieve the desired temperature on the network water side at the HP module outlet).

To examine the impact of changes in the mass flow of treated sewage on the HP module's operation, three simulations were performed at 100% (max. mass flow), 70% and 30% (min. mass flow). The simulation results are shown in the form of graphs of the dependence of COP and thermal power on ΔT_{lift} (Fig. 11a and Fig. 11b, respectively).

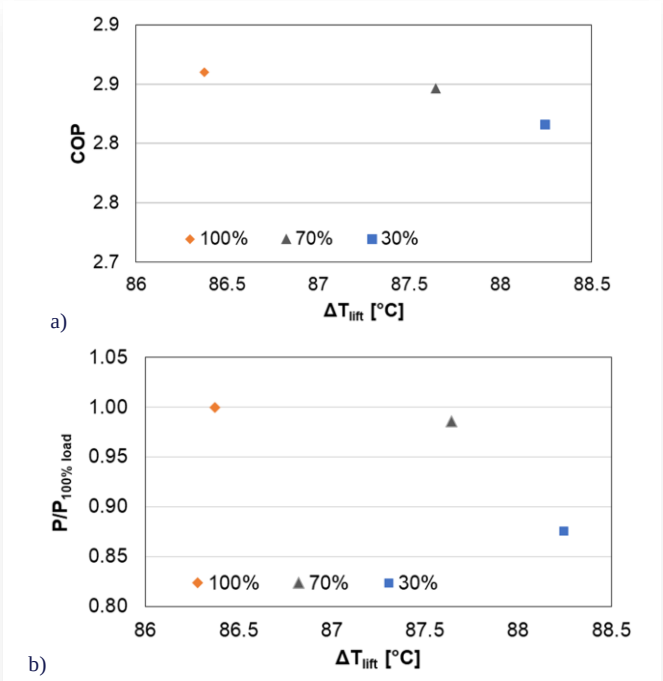


Fig. 11. COP (a) and heating power (b) as a function of ΔT_{lift}; treated sewage mass flow: 100%, 70%, 30%.

For the average and maximum flows, the assumed network water-side parameters (60/95°C) were met. In the case of minimum flow, due to the specific operation of heat pump units and the need to maintain a minimum temperature difference (pinch point) on the exchangers, the temperature of the network water at the outlet was 90°C. The decrease in flow was associated with a slight decrease in COP. In contrast, in the minimum flow case, the unit power drops noticeably (lower treated sewage flow is associated with lower manageable waste heat, as wastewater cannot be cooled below 6°C for design and operational reasons).

The power drop is expected only in winter conditions with low sewage flow (night conditions). Analysis of actual data on sewage flow and temperature indicates that this situation occurs for approximately 300 hours a year, mainly during winter months and at night (when temperatures are low and sewage flow is minimal). In other operating conditions (higher external temperature and/or higher sewage flow), the assumed unit power will be maintained. Such conditions occur for at least 8 000 hours per year.

3.4. Partial load states

The operation of the HP unit depends not only on the availability of treated sewage but also on the heating network's requirements. Due to demand-side constraints, the unit will have to operate at partial load (the system will not be able to absorb heat at the rate the HP could produce under the given conditions) or cooperate with the heat store [56]. In the first case (no store), the HP unit can be operated at partial load by throttling (closing the IGV guide vanes). The analysis aimed to determine the impact of HP unit operation at partial load on COP. Three simulations were performed for load levels of 100%, 75% and 50% under selected operating conditions: an external temperature of 8°C and average flow. As shown in the graph (Fig. 12), varying the HP module load from 50% to 100% has little effect on COP.

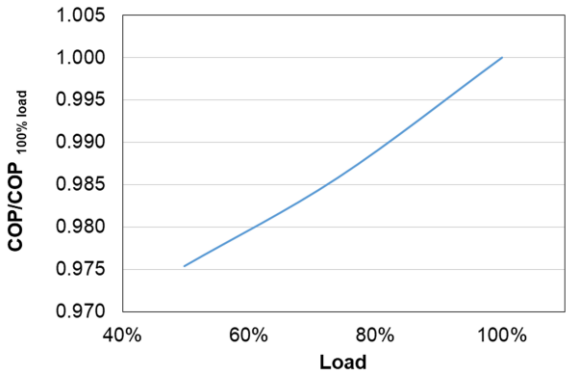


Fig. 12. Relative COP as a function of relative load for the selected operating condition and average flow, at external temperature of 8°C.

This is a consequence of the overlap of several competing characteristics. A change in the flow of the working medium in the system necessitates throttling the compressors, thereby decreasing compressor efficiency. Within the analysed range, efficiency also decreases with increasing pressure. As a result, the impact of compressor behaviour at reduced load should reduce COP. However, in the evaporator, less heat can be received from

the same treated sewage stream, so the temperature of the treated sewage leaving the evaporator increases as the load decreases. As a result, ΔT_{lift} decreases while maintaining the upper source parameters at a constant level (Fig. 13). These are phenomena that increase COP. Due to the comparable impact on the system, COP remains almost constant (in the example considered, decreasing by 0.08 when the load is changed from 100% to 50%).

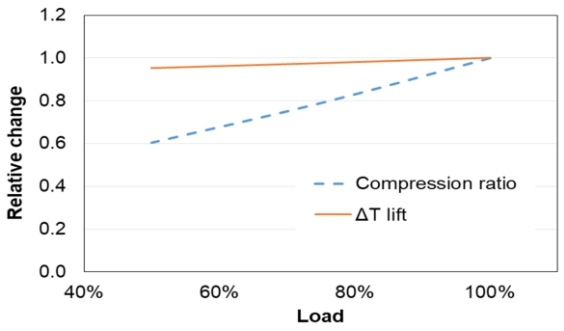


Fig. 13. Relative compression ratio and ΔT_{lift} as a function of relative load for the selected operating condition and average flow, at external temperature of 8°C.

3.5. District heating system analysis

Two district heating system (DHS) scenarios of heat supply in the analysed system were evaluated:

- **DHS Scenario 1:** Two existing coal-fired water boilers with a capacity of 15 MW, without a heat pump (current state),
- **DSH Scenario 2:** Two existing coal-fired water boilers with a capacity of 15 MW and a sewage heat pump with a capacity of 3 MW (proposed).

The heat generation by sources for each scenario is illustrated in Fig. 14. As shown, using waste heat from sewage in a small city, combined with a heat pump, can typically meet domestic hot water demand during the summer season (Fig. 13). However, when heat demand exceeds 3 MW, the heat pump must be switched off. This is because the difference between heat demand and the heat pump's capacity is insufficient to maintain the technical minimum for coal boiler operation.

To improve heat pump utilisation, a different energy source mix, such as incorporating an electric boiler, could be considered. However, this approach poses challenges, including the need for additional power supply agreements. Given the occasional use of an electric boiler, such arrangements could lead to high costs and reduce the system's economic viability. While a heat storage system could be introduced, it would result in frequent on-and-off cycling of the coal-fired boiler, which is technically discouraged.

During peak heat-demand periods (typically winter), the heat pump is not used due to its inability to achieve the required output temperatures and its relatively low COP. This period can instead be utilised for scheduled maintenance work.

The heat generated by each source is summarised in Table 6. The environmental benefits of implementing Scenario 2, measured by equivalent CO_2 emission reduction, were calculated using the CO_2 emission indicator from source [57].

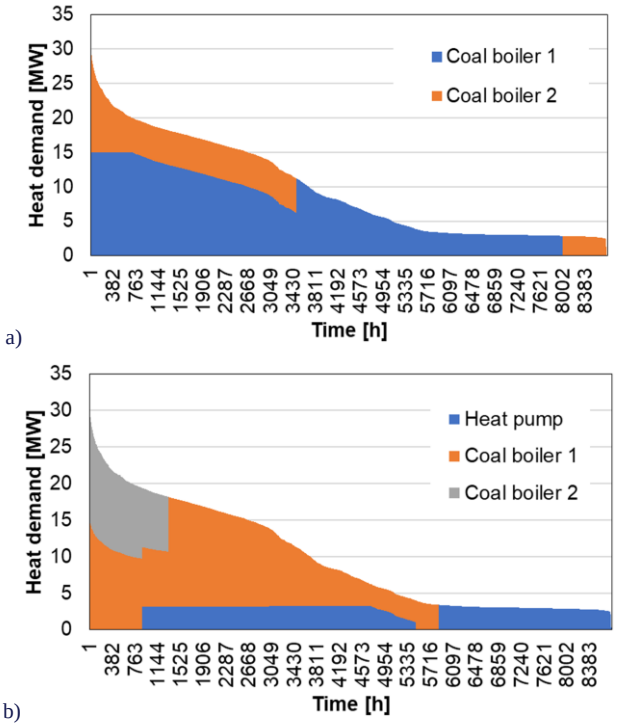


Fig. 14. Heat supplied by the source, ordered chart: a) scenario 1, b) scenario 2.

Table 6. Annual heat generation by source.

Source	DHS Scenario 1	DHS Scenario 2
Coal boiler 1	229.4 TJ	178.3 TJ
Coal boiler 2	77.2 TJ	47.5 TJ
Heat pump	0	80.7 TJ (electricity consumed 6.22 GWh)

The proposed system transformation results in a significant reduction in CO_2-equivalent emissions, estimated at approximately 9500 tonnes annually compared to the baseline scenario (Table 7). This value assumes that the electricity used to power the HP is 100% green. This reduction primarily results from decreased coal consumption and from substituting fossil-based heat generation with renewable electricity powering the heat pumps. Such a shift not only lowers the district heating system's carbon intensity but also aligns with broader decarbonisation and energy transition goals.

Table 7. Fuel consumption and CO_2-equivalent emission reduction.

	DHS Scenario 1	DHS Scenario 2
Coal boiler 1 [TJ/year]	270.0	205.6
Coal boiler 2 [TJ/year]	90.3	54.8
Total coal consumption [TJ/year]	360.2	260.4
Difference [TJ/year]	99.8	
Emission indicator [kg/GJ]	95.05	
Equivalent CO_2 emission reduction [t/year]	9486.44	

3.5. Economic analysis

The investment expenditures were estimated based on data from the literature for similar investments. They are presented in Table 8. The estimation was made using unit economic expenditures (Fig. 15). In this study, CAPEX (capital expenditures) was assumed to be 4.8 million EUR. The OPEX (operating expenditures) was 3.5% of the CAPEX yearly. The electricity cost was 155 EUR/MWh, while the sewage heat price was 2.5 EUR/MWh. The levelised cost of heat for a heat pump is 19.35 EUR/GJ. This value can be compared with other prices available in the literature for the analysed region. In [58], the 25-year horizon is considered, and the average heat process varies from approximately 7 EUR/GJ to nearly 19 EUR/GJ. The presented systems are primarily based on fossil fuels, cement plants and municipal waste. In [59], LCOH for two heating scenarios is presented: in the centralised one (heat pump and biomass boiler, with auxiliary operation of an existing coal boiler), LCOH was 20.7 EUR/GJ. In the distributed system (modules consisting of PV panels, heat pumps, an electric boiler and a heat store), LCOH was higher at 85.6 EUR/GJ. It can be concluded that the obtained result falls within the standard price range for district heating in Poland. The obtained result can also be compared with prices in other countries. For example, in Helsinki, Finland, heat prices vary from 11.3 EUR/GJ (in summer) to 33.9 EUR/GJ (in winter) [60].

Table 8. CAPEX for water heat pumps.

Location	Year	Nominal power [MW]	CAPEX [MLN EUR]	Source
Helsinki, Finland	2025	90	100	[69]
Wroclaw, Poland	2024	12.5	19.3	[70]
Vienna, Austria	2023	110	70	[71]
Hamburg, Germany	2023	20	15	[72]
Viborg, Denmark	2021	90	41	[73]

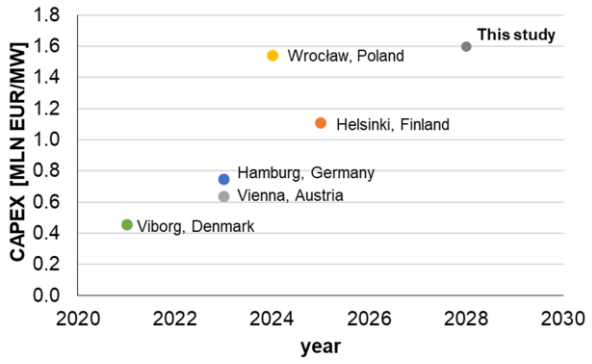


Fig. 15. Unit CAPEX for water heat pumps.

To show the impact of CAPEX and the electricity prices on LCOH, the sensitivity analysis was conducted. Changes of both within ±25% were considered. Results are presented in Table 9. The electricity price has a greater influence on the final LCOH value, although both factors have comparable impacts on the final results.

Table 9. Sensitivity analysis of LCOH.

LCOH [EUR/GJ]		Electricity price		
		−25%	base	25%
CAPEX	−25%	14.65	17.63	20.62
	base	16.36	19.35	22.33
	25%	18.08	21.06	24.04

4. Conclusions

The green energy transition necessitates changes not only in electricity generation but also in the sources of heat production. One potential solution for cities with existing district heating systems is the use of heat pumps powered by treated sewage. Due to the unique operating conditions of heat pumps in urban systems, each case must be analysed individually. In this paper, a mathematical model of the processes occurring in an HP with centrifugal compressors is presented. This model serves as a valuable tool for analysing HP units.

Based on a literature review, the heat pump configuration and working medium were selected. Since the unit uses treated sewage as a heat source and operates within a district heating system, a high-temperature lift is required, along with a significant power output (on the order of several megawatts). This demand exceeds the capabilities of a single-compressor, simple unit due to insufficient pressure ratios. Therefore, a two-stage configuration was chosen, as it enables higher temperature lifts and improved performance under high-demand conditions. This configuration strikes a balance between efficiency, investment costs and technical complexity. Centrifugal compressors were selected for the desired power range. The working medium R1234ze(E) was chosen for its suitable temperature ranges, reasonable pressure levels and relatively low environmental impact.

The implemented model was used to assess HP unit performance under various operating conditions typical of a city in a Central-Eastern European climate. Winter conditions were assumed as the design parameters, with an external temperature of −20°C, network water parameters within the HP module at 60°C and 95°C, and a sewage temperature of 12°C. Design point parameters for winter conditions correspond to the highest ΔT_{lift} required, resulting in the highest compression ratio in the HP circuit.

Modelling part-load states for large sewage heat pumps is critical, as these systems operate under highly dynamic conditions in which variable sludge availability significantly affects heat extraction, leading to transient performance changes that steady-state, full-load models cannot accurately capture [27]. Fluctuations in heat demand necessitate models that account for rapid shifts in operational loads and corresponding changes in the system's coefficient of performance [61]. Furthermore, network requirements impose additional constraints that demand flexible, modulating operation to support demand response and stability in power networks. Detailed part-load state modelling

thus enables an accurate representation of operational parameters under varying load conditions, ensuring that system control strategies remain robust in real-world applications. This comprehensive modelling approach is essential for optimising energy management, enhancing operational flexibility, and ensuring system resilience in response to rapidly changing environmental and demand scenarios. Part-load state modelling in off-design mode is essential for large sewage heat pumps to address fluctuations in sludge supply, occupancy-driven heat demand, and network integration challenges. This approach ensures that dynamic operating conditions are represented more accurately than in simple balance models. Heat pump systems operating at partial loads exhibit minimal COP degradation. This suggests that HPs can operate efficiently without heat storage systems, although storage may enhance system flexibility and performance.

The seasonal coefficient of performance (sCOP) values demonstrate that heat pumps can achieve higher efficiency in low-temperature district heating networks. There is a relatively small difference in the sCOP between a system operating with a network water heating outlet temperature of 95°C (scenario 1) and a system operating with a reduced outlet temperature (75°C, scenario 2). Under current district heating conditions, it is recommended to design the system according to scenario 1 to maintain operational flexibility. However, when planning future modernisations or designing new networks, low-temperature networks should be considered. These networks are more effective, with reduced heat losses, higher COP values, and better compatibility with renewable heat sources, such as HPs. Modernising district heating systems to accommodate lower feed temperatures could significantly improve overall efficiency and compatibility with renewable sources.

The system should be designed to operate with treated sewage mass flow rates close to the average. Low flow rates, which occur only during a short period of the year, can be offset by higher flow rates and power output during summer. Operating the HP unit under partial loads, as determined by demand-side conditions, does not significantly worsen COP. This indicates that HP can operate effectively even in systems without heat storage, although incorporating heat storage could still enhance system performance.

An environmental analysis of heat pump operation in a typical district heating system for a small city in Poland, representative of Eastern European cities, was conducted. The amount of waste heat in sewage is suitable for a domestic hot water supply in the summer season. There are periods when the technical minimum load of other existing sources limits HP's operation. Despite that, HP implementation may help reduce CO_2-equivalent emissions by nearly 9,500 tonnes annually.

The obtained LCOH value of 19.35 EUR/GJ indicates that the proposed system remains economically competitive within the typical price range for district heating in the region. The sensitivity analysis confirmed that the electricity price has a greater impact on LCOH than investment costs, although both parameters have a comparable influence on the overall result. These findings demonstrate that integrating sewage-source heat pumps can provide cost-effective, sustainable heat generation, particularly under stable electricity prices and favourable investment frameworks [62].

References

[1] Buffa, S., Fouladfar, M.H., Franchini, G., Gabarre, I.L., & Chicote, M.A. (2021). Advanced control and fault detection strategies for district heating and cooling systems - A review. *Applied Sciences*, 11(1), 455. doi: 10.3390/app11010455

[2] Lund, H., Østergaard, P.A., Nielsen, T.B., Werner, S., Thorsen, J.E., Gudmundsson, O., Arabkoohsar, A., & Mathiesen, B.V. (2021). Perspectives on fourth and fifth generation district heating. *Energy*, 227, 120520. doi: 10.1016/j.energy.2021.120520

[3] Understanding Renewable Energy Targets. *Forum Energii. Analyses and Dialogue*. https://www.forum-energii.eu/zrozumiec-cele-oze (in Polish) [accessed 25 Sept. 2025].

[4] Levihn, F. (2017).CHP and heat pumps to balance renewable power production: Lessons from the district heating network in Stockholm. *Energy*, 137, 670–678. doi: 10.1016/j.energy.2017.01.118

[5] Johansen, K., & Werner, S. (2022). Something is sustainable in the state of Denmark: A review of the Danish district heating sector. *Renewable and Sustainable Energy Reviews*, 158, 112117. doi: 10.1016/j.rser.2022.112117

[6] Østergaard, D.S., Smith, K.M., Tunzi, M., & Svendsen, S. (2022). Low-temperature operation of heating systems to enable 4th generation district heating: A review. *Energy*, 248, 123529. doi: 10.1016/j.energy.2022.123529

[7] Alarnaout, G.A., Navarro-Esbrí, J., & Mota-Babiloni, A. (2024). Operational, economic, and carbon footprint feasibility of a moderately-high-temperature heat pump as an alternative to conventional boilers in various scenarios. *Energy Conversion and Management*, 309, 118424. doi: 10.1016/j.enconman.2024.118424

[8] Sadeghi, M., Petersen, T., Yang, Z., Zühlsdorf, B., & Madsen, K.S. (2024). Thermal and economic performance assessment of different high temperature heat pump layouts for upgrading district heating to process heating of steam production at 160°C. *Energy*, 313, 133832. doi: 10.1016/j.energy.2024.133832

[9] Passamonti, A., Sachse, F., Bombarda, P., & Bracke, R. (2024). Design, construction, and commissioning of a 500 kW high-temperature heat pump plant for the district heating network of Bochum, Germany. *Energy Reports*, 13, 548–561. doi: 10.1016/j.egyr.2024.11.080

[10] Degelin, A., Tassenoy, R., Vieren, E., Demeester, T., T'Jollyn, I., & De Paepe, M. (2024). Influence of supply temperature and booster technology on the energetic performance and levelized cost of heat of a district heating network with central heat pump. *Energy*, 312, 133589. doi: 10.1016/j.energy.2024.133589

[11] Zhu, T., Du, Y., Liang, J., Rohlfs, W., Thorsen, J.E., & Elmegaard, B. (2023). Integration of booster heat pumps in ultra-low temperature district heating network: Prototype demonstration and refrigerant charge investigation. *Energy and Buildings*, 298, 113516. doi: 10.1016/j.enbuild.2023.113516

[12] Barco-Burgos, J., Bruno, J.C., Eicker, U., Saldaña-Robles, A.L., & Alcántar-Camarena, V. (2022). Review on the integration of high-temperature heat pumps in district heating and cooling networks. *Energy*, 239, part E, 122378. doi: 10.1016/j.energy.2021.122378

[13] Calise, F., Cappiello, F.L., Dentice d'Accadia, M., Petrakopoulou, F., & Vicidomini, M. (2022). A solar-driven 5th generation district heating and cooling network with ground-source heat

pumps: a thermo-economic analysis. *Sustainable Cities and Society*, 76, 103438. doi: 10.1016/j.scs.2021.103438

[14] Calise, F., Liberato Cappiello, F., Cimmino, L., Dentice d'Accadia, M., & Vicidomini, M. (2022). Optimal design of a 5th generation district heating and cooling network based on seawater heat pumps. *Energy Conversion Management*, 267, 115912. doi: 10.1016/j.enconman.2022.115912

[15] Ali, H., Hlebnikov, A., Pakere, I., & Volkova, A. (2024). An evaluation and innovative coupling of seawater heat pumps in district heating networks. *Energy*, 312, 133461. doi: 10.1016/j.energy.2024.133461

[16] Adamson, K.M., Walmsley, T.G., Carson, J.K., Chen, Q., Schlosser, F., Kong, L., & Cleland, D.J. (2022). High-temperature and transcritical heat pump cycles and advancements: A review. *Renewable and Sustainable Energy Reviews*; 167:112798. doi: 10.1016/j.rser.2022.112798

[17] *GEA*. https://www.gea.com/en/products/heat-pumps/redastrum-ammonia-heatpump/ [accessed 25 Nov. 2025].

[18] Navarro-Peris, E., Masip, X., Barcelo, F., & Corberan, J.M. (2021). Comparison of Transcritical and Subcritical Heat Pump Systems for Domestic Hot Water Production in Energy Recovery Applications. *18th International Refrigeration and Air Conditioning Conference at Purdue 2021*, 24−28 May, West Lafayette, USA.

[19] Hepbasli, A., Biyik, E., Ekren, O., Gunerhan, H., & Araz, M. (2014). A key review of wastewater source heat pump (WWSHP) systems. *Energy Conversion Management*, 88, 700–722. doi: 10.1016/j.enconman.2014.08.065

[20] Tatarewicz, I., Lewarski, M., & Skwierz, S. (2019). *Scenarios of low-emission Energy sector for Poland and the EU until 2050*. Institute of Environmental Protection − National Research Institute (KOBiZE), Warsaw 2019.

[21] Ma, J., Zhang, X., Yu, J., & Wei, P. (2024). Thermo-economic assessments on building heating by a sewage source heat pump coupled with heat storage system. *Thermal Science and Engineering Progress*, 53, 102756. doi: 10.1016/j.tsep.2024.102756

[22] Xu, T., Wang, X., Wang, Y., Li, Y., Xie, H., Yang, H., Wei, X., Gao, W., Lin, Y., & Shi, C. (2023). Integration of sewage source heat pump and micro-cogeneration system based on domestic hot water demand characteristics: A feasibility study and economic analysis. *Process Safety and Environmental Protection*, 179, 796–811. doi: 10.1016/j.psep.2023.09.053

[23 Gao, C., Hao, Y., & Liu, Q. (2021). Design and analysis of a small sewage source heat pump triple supply system. *Energy Engineering: Journal of the Association of Energy Engineers*, 118, 667–78. doi: 10.32604/EE.2021.014703

[24] Xu, T., Fan, Y., Wang, P., Zhou, Y., Li, Y., Xie, J.,Wang, X., Hu, J., Lin Y., Wei, X., Gao, W., & Shi, C. (2024). Carbon emission reduction model for sewage heat recovery and utilization in a northern Chinese city. *Sustainable Cities and Society*, 115, 105825. doi: 10.1016/j.scs.2024.105825

[25] Brands, M., & Fung, A.S. (2025). Viability of large-scale wastewater- and ground-source distributed heat pump systems for cold-climate urban decarbonization: case study of a proposed campus building. *Journal of Building Engineering*, 108, 112776. doi: 10.1016/j.jobe.2025.112776

[26] Ozcan, H.G., Hepbasli, A., Abusoglu, A., & Anvari-Moghaddam, A. (2023). Energy, exergy, economic, environmental and sustainability (4ES) analyses of a wastewater source heat pump system for district heating applications based on real operational data. *Sustainable Energy Technologies Assessments*, 56, 103077. doi: 10.1016/j.seta.2023.103077

[27] Clauß, J., & Georges, L. (2029). Model complexity of heat pump systems to investigate the building energy flexibility and guidelines for model implementation. *Applied Energy*, 255, 113847. doi: 10.1016/j.apenergy.2019.113847

[28] Salhein, K., Salheen, S.A., Annekaa, A.M., Hawsawi, M., Alhawsawi, E.Y., Kobus, C.J., & Zohdy, M. (2025). A Comprehensive Review of Geothermal Heat Pump Systems. *Processes*, 13(7), 2142. doi: 10.3390/pr13072142

[29] Tan, Z., Feng, X., & Wang, Y. (2021). Performance comparison of different heat pumps in low-temperature waste heat recovery. *Renewable and Sustainable Energy Reviews*, 152, 111634. doi: 10.1016/j.rser.2021.111634

[30] Yandrapu, V.P., & Kanidarapu, N.R. (2022). Energy, economic, environment assessment and process safety of methylchloride plant using Aspen HYSYS simulation model. *Digital Chemical Engineering*, 3, 100019. doi: 10.1016/j.dche.2022.100019

[31] Rafeek, M., Elwardany, M., Nassib, A.M., Ahmed, M.S., Mohamed, H.A., & Abdelaal, M.R. (2025). Enhancing energy and exergy efficiency in a petroleum refining unit: a case study. *Journal of Thermal Analysis and Calorimetry*, 150(21), 1−21. doi: 10.1007/s10973-025-14700-z

[32] Budhraja, N., Pal, A., & Mishra, R.S. (2023). Optimizing Methanol Reforming Parameters for Enhanced Hydrogen Selectivity in an Aspen Hysys Simulator using Response Surface Methodology. *Energy Technology*, 11, 1–10. doi: 10.1002/ente.202300203

[33] Shirdel, S., Valand, S., Fazli, F., Winther-Sørensen, B., Aromada, S.A., Karunarathne, S., & Øi, L.E. (2022). Sensitivity Analysis and Cost Estimation of a CO_2 Capture Plant in Aspen HYSYS. *Chemical Engineering*, 6(2), 28. doi: 10.3390/chemengineering6020028

[34] Krawczyk, P., Szabłowski, Ł, Karellas, S., & Kakaras, E. (2018). Comparative thermodynamic analysis of compressed air and liquid air energy storage systems. *Energy*, 142, 46–54. doi: 10.1016/j.energy.2017.07.078

[35] Dzido, A., Krawczyk, P., Wołowicz, M., & Badyda, K. (2022). Comparison of advanced air liquefaction systems in Liquid Air Energy Storage applications. *Renewable Energy*, 184, 727–739. doi: 10.1016/j.renene.2021.11.095

[36] Pieper, H., Krupenski, I., Brix Markussen, W., Ommen, T., Sirde, A., & Volkova, A. (2021). Method of linear approximation of COP for heat pumps and chillers based on thermodynamic modelling and off-design operation. *Energy*, 230, 120743. doi: 10.1016/j.energy.2021.120743

[37] Schlosser, F., Jesper, M., Vogelsang, J., Walmsley, T.G., Arpagaus, C., & Hesselbach, J. (2020). Large-scale heat pumps: Applications, performance, economic feasibility and industrial integration. *Renewable and Sustainable Energy Reviews*, 133, 110219. doi: 10.1016/j.rser.2020.110219

[38] Arpagaus, C., Bless, F., Uhlmann, M., Schiffmann, J., & Bertsch, S.S. (2018). High temperature heat pumps: Market overview, state of the art, research status, refrigerants, and application potentials. *Energy*. 152, 985–1010. doi: 10.1016/j.energy.2018.03.166

[39] Jiang, J., Hu, B., Wang, R.Z., Deng, N., Cao, F., & Wang, C.C. (2022). A review and perspective on industry high-temperature heat pumps. *Renewable and Sustainable Energy Reviews*, 161, 112106. doi: 10.1016/j.rser.2022.112106

[40] Chua, K.J., Chou, S.K., & Yang, W.M. (2010). Advances in heat pump systems: A review. *Applied Energy*, 87, 3611–3624. doi: 10.1016/j.apenergy.2010.06.014

[41] Mateu-Royo, C., Arpagaus, C., Mota-Babiloni, A., Navarro-Esbrí, J., & Bertsch, S.S. (2021). Advanced high temperature heat pump configurations using low GWP refrigerants for industrial waste heat recovery: A comprehensive study. *Energy Conversion and Management*, 229, 113752. doi: 10.1016/j.enconman.2020.

113752

[42] Friedel, P. (2019). *Technology Collaboration Programme on Heat Pumping Technologies (HPT TCP)*, Annex 45, Hybrid Heat Pumps.

[43] De Pasquale, A.M., Giostri, A., Romano, M.C., Chiesa, P., Demeco, T., & Tani, S. (2017). District heating by drinking water heat pump: Modelling and energy analysis of a case study in the city of Milan. *Energy*, 118, :246–263. doi: 10.1016/j.energy.2016.12.014

[44] Li, H., Cao, F., Bu, X., Wang, L., & Wang, X. (2014). Performance characteristics of R1234yf ejector-expansion refrigeration cycle. *Applied Energy*, 121, 96–103. doi: 10.1016/j.apenergy.2014.01.079

[45] Colombo, L.P.M., Lucchini, A., & Molinaroli, L. (2020). Experimental analysis of the use of R1234yf and R1234ze(E) as drop-in alternatives of R134a in a water-to-water heat pump. *International Journal of Refrigeration*, 115, 18–27. doi: 10.1016/j.ijrefrig.2020.03.004

[46] Pérez-García, V., Méndez-Méndez, D., & Belman-Flores, J.M., (2025). Experimental energy comparison of R516A and R1234ze(E) using ejector and internal heat exchanger in hot climates. *Applied Thermal Engineering*, 278, 127486. doi: 10.1016/j.applthermaleng.2025.127486

[47] Uusitalo, A., Turunen-Saaresti, T., Honkatukia, J., Tiainen, J., & Jaatinen-Värri, A. (2020). Numerical analysis of working fluids for large scale centrifugal compressor driven cascade heat pumps upgrading waste heat. *Applied Energy*, 269, 115056. doi: 10.1016/j.apenergy.2020.115056

[48] Peng, D.Y., & Robinson, D.B. (1976). A New Two-Constant Equation of State. *Industrial & Engineering Chemistry Fundamentals*, 15, 59–64. doi: 10.1021/i160057a011

[49] *Aspen HYSYS – Operations Guide*. (2018).

[50] Vanyashov, A.D., & Karabanova, V.V., Vasenko, E.M. (2016). Influence Analysis of Flow Entry Conditions on the Centrifugal Compressor Impeller Blades to Integral Gasodynamic Characteristics in a Combine Regulation Method. *Procedia Engineering*, 152, 389–394. doi: 10.1016/j.proeng.2016.07.719

[51] Yang, T., Liu, W., Kramer, G.J., & Sun, Q. (2021). Seasonal thermal energy storage: A techno-economic literature review. *Renewable and Sustainable Energy Reviews*, 139, 110732. doi: 10.1016/j.rser.2021.110732

[52] Ahmed, M.M., Das, B.K., Das, P., Hossain, M.S., & Kibria, M.G. (2024). Energy management and sizing of a stand-alone hybrid renewable energy system for community electricity, fresh water, and cooking gas demands of a remote island. *Energy Conversion and Management*, 299. doi: 10.1016/j.enconman.2023.117865

[53] von Rhein, J., Henze, G.P., Long, N., & Fu, Y. (2019). Development of a topology analysis tool for fifth-generation district heating and cooling networks. *Energy Conversion and Management*, 196, 705–716. doi: 10.1016/j.enconman.2019.05.066

[54] Wirtz, M., Kivilip, L., Remmen, P., & Müller, D. (2020). 5th Generation District Heating: A novel design approach based on mathematical optimization. *Applied Energy*, 260, 114158. doi: 10.1016/j.apenergy.2019.114158

[55] Pospíšil, J., Špiláček, M., & Charvát, P. (2019). Seasonal Cop of an air-to-water heat pump when using predictive control preferring power production from renewable sources in the Czech Republic. *Energies*, 12(17), 3236. doi: 10.3390/en12173236

[56] Diller, T., Soppelsa, A., Nagpal, H., Fedrizzi, R., & Henze, G. (2023). A dynamic programming based method for optimal control of a cascaded heat pump system with thermal energy storage. *Optimization and Engineering*, 25, 229–251. doi: 10.1007/s11081-023-09853-5

[57] National Centre for Emissions Balancing and Management. (2017). *Calorific Values (CV) and CO_2 Emission Factors (EF) for 2015 for Reporting under the Emissions Trading System for the Year 2018*. KOBiZE, Warsaw 2017 (in Polish).

[58] Kalina, J., Tańczuk, M., & Jendryasek, Ł. (2025). Planning energy transition and decarbonisation of district heating systems in Poland. *Energy*, 328. doi: 10.1016/j.energy.2025.136578

[59] Krawczyk, P., Badyda, K., & Dzido, A. (2025). Techno-Economic Analysis of Increasing the Share of Renewable Energy Sources in Heat Generation Using the Example of a Medium-Sized City in Poland. *Energies*, 18(4), 884, 1–13. doi: 10.3390/en18040884

[60] *Helen Ltd official webpage*. https://www. helen.fi/en/heating/district-heat-prices 2024 [accessed 25 Sept. 2025].

[61] Kul, O., & Uğural, M.N. (2022). Comparative Economic and Experimental Assessment of Air Source Heat Pump and Gas-fired boiler: A Case Study from Turkey. *Sustainability*, 14(21), 14298. doi: 10.3390/su142114298

[62] Park, H.Y., Faulkner, M., Turrell, M.D., Stopford, P.J., & Kang, D.S. (2010). Coupled fluid dynamics and whole plant simulation of coal combustion in a tangentially-fired boiler. *Fuel*, 89(8), 2001−2010. doi: 10.1016/j.fuel.2010.01.036

[63] Zanchi, V., Boban, L., & Soldo, V. (2019). Refrigerant Options in the Near Future. *Journal of Sustainable Development of Energy Water and Environment Systems*, 7(2), 293–304. doi: 10.13044/j.sdewes.d6.0250

[64] Bruno F., Belusko, M., & Halawa, E. (2019). CO_2 Refrigeration and Heat Pump Systems—A Comprehensive Review. *Energies*, 12(15), 2959. doi: 10.3390/en12152959

[65] Jiang, J., Hu, B., Wang R.Z., Deng, N., Cao, F., & Wang C.C. (2022). A review and perspective on industry high-temperature heat pumps. *Renewable and Sustainable Energy Reviews*, 161, 112106. doi: 10.1016/j.rser.2022.112106

[66] Kumar, S., Raibhole, V.N., Majumder, H. (2024). Performance of Heat Pump Air Conditioning with R1234ze (HFO) as a Refrigerant. *Journal of Optimization*, 2024; 1−16. doi: 10.1155/2024/9101945

[67] Zhao, W., Zhang, Y., Sun, C., Li, L., Li, B., & Xu. J. (2025). Thermodynamic analysis of a transcritical CO_2 heat pump for heating applications. *Energy*, 318(C), 134896. doi: 10.1016/j.energy.2025.134896

[68] Sun, J., Wang, Y., Qin, Y., Wang, G., Liu, R., & Yang, Y.A. (2023). Review of Super-High-Temperature Heat Pumps over 100°C. *Energies*, 16(12), 4591. doi: 10.3390/en16124591

[69] *Helen is building a new heat pump plant in Helsinki – An innovative solution to enable carbon-neutral energy production*. (2022). https://observatorial.com/ [accessed 25 Sept. 2025].

[70] *Wrompa – Thermal Energy from Wastewater Will Heat Wrocław*. (2023). https://wodnesprawy.pl/ [accessed 25 Sept. 2025].

[71] Authorities in Vienna. (2022). *Vienna's district heating will be powered by waste water*. www.themayor.eu/ [accessed 25 Sept. 2025].

[72] *Climate positivity, here we come!* www.bayernlb.com [accessed 25 Sept. 2025].

[73] *Viborg Power Station*. https://en.wikipedia.org/wiki/Viborg_Power_Station [accessed 25 Sept. 2025].

Co-published by
Institute of Fluid-Flow Machinery
Polish Academy of Sciences
Committee on Thermodynamics and Combustion
Polish Academy of Sciences

Copyright©2026 by the Authors under licence CC BY-NC-ND 4.0

http://www.imp.gda.pl/archives-of-thermodynamics/

Comparative Analysis of Performance and Emission Characteristics of a CI Engine Fueled with Biodiesel and Pyrolytic Oil Derived from Cottonseed

A. Manikandan, R. Thamizhvel*, K. Kalaiselvan, S. Jassir Iqbal

IFET College of Engineering, Villupuram 605108, Tamil Nadu, India
*Corresponding author email: rthamizhvel@gmail.com

Received: 14.05.202; revised: 23.11.2025; accepted: 25.11.2025

Abstract

The increasing accumulation of biowaste in the environment, hence the need to investigate alternate energy sources has arisen due to the depletion of fossil fuel stocks. Eco-friendly, non-toxic, stable and biodegradable fuels with a high flash point and suitability for combustion are gaining attention. In this study, cottonseed biodiesel and pyrolytic oil were investigated as alternative fuels for compression ignition engines. Transesterification of cottonseed oil with sodium hydroxide as a catalyst and methyl alcohol as a reactant made biodiesel. Pyrolysis, a controlled thermal degradation process that is done in a safe environment, was used to make pyrolytic oil. A compression ignition engine was used to test the extracted biodiesel and pyrolytic oil after they were mixed with diesel in an 8:2 ratio. The performance and emission characteristics of ordinary diesel were compared with those of carbon monoxide, nitrogen oxides, hydrocarbons, smoke emissions, brake specific fuel consumption, brake thermal efficiency and other factors. The B20 blend showed 28.5% brake thermal efficiency, 0.32 kg/kWh brake specific fuel consumption, 22% lower CO, 19% lower HC, and 24% reduced smoke emissions than diesel, highlighting improved combustion and reduced emissions despite higher fuel consumption. According to the findings, cottonseed biodiesel is a suitable substitute fuel for compression ignition engines since it emits less CO and NO_x.

Keywords: Cotton seed; Bio diesel; Pyrolytic oil; Engine performance; Emission

Vol. 47(2026), No. 1, 71–78; doi: 10.24425/ather.2025.156853

Cite this manuscript as: Manikandan, A., Thamizhvel, R., Kalaiselvan, K., &, Iqbal, S.J. (2026). Comparative Analysis of Performance and Emission Characteristics of a CI Engine Fueled with Biodiesel and Pyrolytic Oil Derived from Cottonseed. *Archives of Thermodynamics*, 47(1), 71−78.

1. Introduction

Energy is a vital component for the progress and stability of modern societies. It powers industries, transportation, communication systems and domestic applications, thus serving as a foundation for economic growth and technological advancement. Broadly, energy resources are classified as renewable and non-renewable. Renewable sources such as solar, wind, tidal, and hydro power are sustainable and naturally replenished, while non-renewable sources, including coal, petroleum and natural gas, are finite and depleting with continued exploitation [1]. Historically, biomass, primarily in the form of wood, supplied nearly 70% of the world's energy demand. However, in recent decades, fossil fuels have replaced wood as the dominant energy source due to their high energy density, well-established extraction infrastructure and relatively low cost [1].

Despite these advantages, fossil fuels have serious drawbacks. Large amounts of greenhouse gases, including carbon dioxide (CO_2), nitrogen oxides (NO_x), and sulphur oxides (SO_x),

Nomenclature

Abbreviations and Acronyms

ASTM – American Society for Testing and Materials
B20 – biodiesel 20% and diesel 80%
BP – break power
BSFC – brake specific fuel consumption
BTE – brake thermal efficiency
CI – compression ignition
CO – carbon monoxide
D100 – diesel 100%
FAME – fatty acid methyl esters
FFA – free fatty acid
HC – hydrocarbons
IC – internal combustion
KOH – potassium hydroxide
NO_x – oxides of nitrogen
PID – proportional-integral-derivative (control system)
PY20 – pyrolytic oil 20% and diesel 80%
SO_x – oxides of sulphur
TGA – thermogravimetric analysis
VCR – variable compression ratio

which cause acid rain and contribute to global warming, are released as they burn. Additionally, carbon monoxide (CO) and particulate emissions degrade air quality and pose significant health risks [2].

The search for sustainable energy alternatives has accelerated due to the dual problems of climate change and depleting fossil fuel supplies. Among these, biofuels have gained considerable attention because they can be produced locally from renewable biomass, are biodegradable, and generally result in lower pollutant emissions compared to petroleum-based fuels. Edible and non-edible oils, used cooking oil, agricultural leftovers and animal fats are some of the sources from which biofuels can be made. Two major routes for liquid biofuel production are biodiesel generation via transesterification and bio-oil generation via pyrolysis. Fatty acid methyl esters (FAME) and glycerol are the products of the transesterification process, which produces biodiesel by combining triglycerides with an alcohol (often methanol) in the presence of a catalyst. Animal fats, vegetable oils and leftover cooking oil are just a few of the feedstocks that can be used in this process [3]. Because of their physical and chemical characteristics comparable to petroleum diesel, biodiesel made this way may be utilised in internal combustion (IC) engines without requiring any hardware changes [4]. Additionally, compared to fossil fuel, using biodiesel improves environmental performance by reducing emissions of CO, SO_x and unburned hydrocarbons.

Pyrolysis, in contrast, is a thermochemical conversion process where organic material is heated in the absence of oxygen, leading to the breakdown of macromolecules into smaller, energy-rich products. These products typically include pyrolytic oil (bio-oil), syngas and char. The process is highly versatile, capable of utilising a broad range of feedstocks such as agricultural residues, forestry waste, seeds and even certain plastics [5]. Pyrolytic oil is a liquid fuel that can be directly used in IC engines after suitable upgrading or blending, offering a renewable alternative to fossil fuels. Among the numerous biomass feedstocks available, cottonseed holds significant promise for both biodiesel and pyrolytic oil production.

Cotton is one of the most widely cultivated crops in India, and its seeds are generated in large quantities as a by-product of fibre extraction. Cottonseed oil is non-edible, has a relatively high oil content, and is available in abundance at low cost [6,7]. This makes it an attractive feedstock from both economic and sustainability perspectives. Importantly, utilising non-edible feedstocks like cottonseed avoids the "food versus fuel" conflict associated with biodiesel derived from edible oils. While biodiesel production from cottonseed oil is well documented in the literature, research on pyrolytic oil derived from cottonseed is comparatively limited. This presents an opportunity for further exploration. Pyrolytic oil production offers several advantages over biodiesel in certain contexts. For instance, when the feedstock has a high free fatty acid (FFA) content, biodiesel production requires a pre-treatment esterification step to avoid soap formation (saponification) and improve glycerol separation efficiency [15,16]. Pyrolysis, however, is not hindered by high FFA levels, which can simplify processing and reduce costs. Additionally, pyrolytic oil contains a broader spectrum of combustible compounds, potentially enhancing combustion efficiency under specific engine conditions. Therefore, developing pyrolytic oil from cottonseed could diversify renewable fuel production pathways and reduce the limitations associated with biodiesel. Before selecting and optimising a conversion process, a detailed characterisation of the feedstock is necessary. This is typically achieved through ultimate analysis and proximate analysis. Ultimate analysis quantifies the elemental composition, carbon, hydrogen, nitrogen, sulphur and ash content of the biomass, usually following the ASTM D3176-09 standard [8] (see Table 1). These values influence the fuel's calorific value and combustion behaviour. Proximate analysis, often carried out according to ASTM D5142, determines moisture content, volatile matter, fixed carbon, and ash content. These parameters are critical for designing an efficient pyrolysis process and predicting product yield and quality.

Table 1. Ultimate and proximate analysis values.

Parameters	Ultimate (%)	ASTM standard	Parameters	Proximate (%)	ASTM standard
Oxygen	31.59	D3176	Moisture	4.51	D3173
Carbon	54.81	D3176	Volatile	79.37	D3175
Nitrogen	4.38	D3176	Ash	3.29	D3174
Hydrogen	8.42	D3176	Fixedcarbon	11.97	D3172

Thermogravimetric analysis (TGA) is another important tool in biomass characterisation, Fig. 1. TGA provides information on thermal stability and breakdown kinetics by measuring changes in sample mass as a function of temperature or time in a controlled environment [9]. It can identify the temperature ranges at which major decomposition phases occur, aiding in the

selection of optimal pyrolysis operating conditions. In this study, TGA was conducted on a 10 mg sample of cottonseed using an SDT Q600 instrument in an inert atmosphere. The heating rate was set at 10°C/min, from ambient temperature up to 600°C. The results showed that the primary decomposition occurred between 320°C and 550°C, with a weight loss of approximately 71%, and a stable plateau was reached near 600°C. The maximum decomposition rate was observed around 400°C [10,11]. These findings suggest that the most suitable pyrolysis temperature range for cottonseed lies between 300°C and 550°C, balancing high oil yield with controlled energy input.

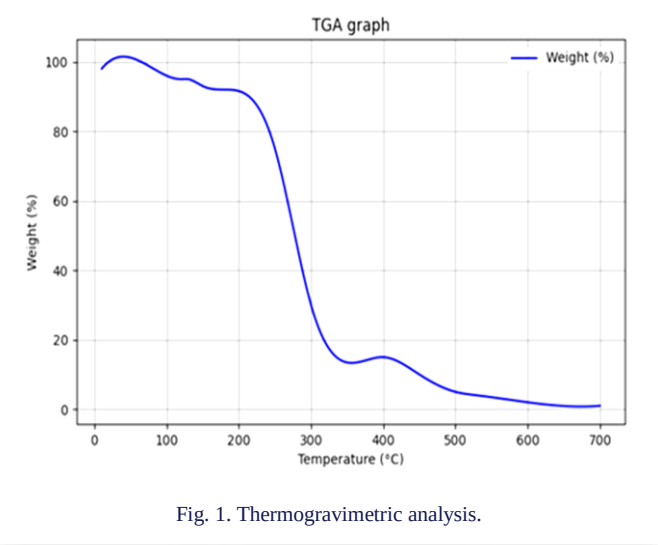


Fig. 1. Thermogravimetric analysis.

For the pyrolysis experiments, cotton seeds were procured from a local market in Villupuram, Tamil Nadu, India [12,13]. Prior to processing, the seeds were dried in an oven at 105°C to remove residual humidity. They were then crushed using a chopper, and oil was extracted using 0.8 L of n-hexane in a water bath for six hours. A rotating evaporator operating under vacuum at 45°C was used to extract the solvent [14]. The FFA content of the extracted oil plays a decisive role in determining its conversion pathway. Oils with FFA content below 2% can be processed directly through transesterification, while those with FFA levels above this threshold require pre-treatment via esterification to reduce FFA and prevent saponification [15,16]. This requirement underscores one of the key benefits of pyrolysis, its ability to handle high-FFA feedstocks without additional processing steps. From a broader perspective, producing pyrolytic oil from cottonseed aligns with multiple sustainability goals. It enables the valorisation of agricultural byproducts, reduces reliance on finite fossil fuels, and supports decentralised energy production, particularly in rural areas where cotton cultivation is widespread. Additionally, pyrolytic oil can be co-fired with petroleum diesel or blended with upgraded bio-oils to meet specific performance and emissions targets, offering flexibility in fuel applications.

The current study is on employing a semi-batch reactor to produce pyrolytic oil from cottonseed, guided by detailed feedstock characterisation through ultimate, proximate, and thermogravimetric analyses. By investigating optimal pyrolysis operating conditions and evaluating the resulting fuel's properties. This work adds to the expanding literature of research on non-food, alternative fuels made from biomass for internal combustion engines. The insights gained are expected to facilitate the development of scalable, cost-effective and environmentally sustainable fuel production processes that can be adapted to regions with abundant cotton cultivation and limited access to petroleum-based fuels.

2. Materials and methods

Cotton is one of the most important agricultural crops in India, serving as the largest source of natural fibre for the textile industry. The optimal temperature range for cotton cultivation in India lies between 25°C and 35°C. A cotton boll typically consists of 35–40% fibre and approximately 60% seed. While the primary economic value of cotton lies in its fibre, the seed is also an important raw material in the edible oil and biofuel industries. Cottonseed oil has been utilised in biodiesel production due to its calorific value and suitability for transesterification processes [17].

However, the relatively low oil content of cottonseed, generally between 17% and 24%, limits the quantity of oil available for commercial use. India, as the world's largest cotton producer, yields an average of about 5800 thousand metric tonnes of cotton annually. Globally, cottonseed production reaches approximately 40 million tonnes, with India contributing a major share, followed by China, the United States, Brazil, Pakistan, and Uzbekistan [18]. Cottonseed is a traditional oilseed crop in India, with around 85% of the harvested seeds processed for oil extraction, while roughly 20% are used as animal feed [19]. The oil extracted from cottonseed can be converted into bio-oil and biodiesel through processes such as pyrolysis and transesterification. Because it is sustainable and has a similar energy content to fossil fuels, bio-oil in particular presents a possible substitute. Cottonseed oil and methanol combine chemically to produce biodiesel when a potent base catalyst, such as potassium hydroxide, is present. This transesterification reaction converts the triglycerides in the oil into methyl esters, the main components of biodiesel, and glycerol as a by-product.

2.1. Preparation of biodiesel

The transesterification was dispensed employing with 1 litre flat bottomed beaker, thermometer, mechanical stirrer, heater and conical shaped beaker. Initially, 500 ml of cottonseed oil is heated on a heating plate to the desired temperature of 60°C, whereas methoxide solutions of 150 ml of methanol and potassium hydroxide KOH were appended to the oil as a catalyst, and the catalyst added solution was stirred constantly with a stirrer at 600 rpm. The experiment was conducted again with raw oil for the whole conversion of the oil into FAMEs. Once the reaction was completed, the solution was moved into a conical formed beaker to simmer down for 10−15 h. The resulting bio-oil is formed at the upper layer, while the bottom is made up of glycerin mixed with other components. The product is washed with a prepared solution to remove water, alcohol and residual catalyst present in the mixture [20]. The flow of cottonseed preparation is shown in Fig. 2.



Fig. 2. Flow of cottonseed preparation.

2.2. Preparation of pyrolytic oil

The experimental setup consists of a pyrolysis reactor, ceramic band heater, proportional-integral-derivative (PID) controller, thermocouple, monitor, condenser and oil collector. The PID controller is used to maintain the temperature of the reactor. The cottonseed is directly fed to the reactor [21]. According to data from thermogravimetric analysis, the pyrolysis temperature is selected between 300−450°C. A semi batch type reactor is used to do this experiment, and the ceramic band heater is vertically inserted in it. The PID controller is used to maintain the constant temperature of the reactor [22]. 250 g of cotton seed has been feed inside the reactor. While heating the reactor, the vapour has been generated inside the reactor and condensed in the water cooled condenser. After passing through the condenser, the pyrolytic oil has been collected. The photographic view of the pyrolytic setup is shown in Fig. 3, and Fig. 4 shows a sample of pyrolytic oil.



Fig. 3. Pyrolytic experimental setup.



Fig. 4. Cotton seed pyrolytic oil.

The fuel properties of cottonseed biodiesel blend of B20 and cottonseed pyrolytic oil blend of PY20 are shown in Table 2. The measured fuel properties show that B20 biodiesel and PY20 pyrolytic oil have slightly higher viscosity and density than diesel. While their heating values are marginally lower, both exhibit higher cetane indices and significantly elevated flash and fire points, indicating improved ignition quality and enhanced safety in handling and storage.

Table 2. Properties of diesel, biodiesel and cotton seed pyrolytic oil.

Property	Diesel	Biodiesel (B20)	Pyrolytic oil (PY20)	ASTM Standard
Viscosity (cSt) at 40°C	3.1	3.6	3.6	D445
Density at 15°C	830	890	920	D4052
Heating value (kJ/kg)	42 000	40 000	39 278	D240
Cetane index	46	50.4	52	D976
Flash point (°C)	58	120	150	D93 (Pensky–Martens)
Fire point (°C)	62	135	175	D92 (Cleveland Open Cup)

3. Experimentation

Using a variable compression ratio (VCR) direct injection (DI) diesel engine and fuels such as diesel, biodiesel and pyrolytic oil, the current study is conducted, and the experimental setup is shown in Fig. 5. The engine's working state is set by the fuel and air flow, exhaust gas temperature, and the required loads and measurement equipment.

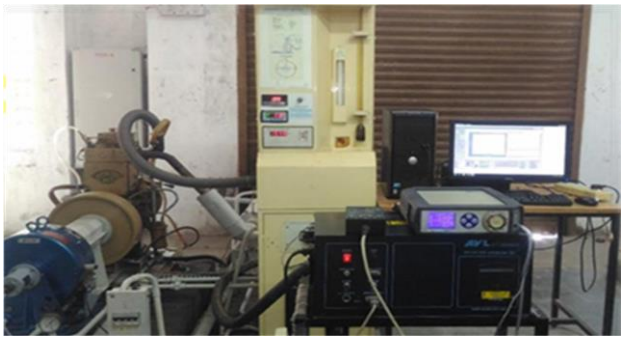


Fig. 5. Compression ignition (CI) engine experimental setup.

The experiment is carried out using different loads, including 0%, 20%, 40%, 60%, 80% and the maximum load. This investigative procedure uses an eddy current dynamometer to alter the load. Thermocouples are used to measure exhaust gas temperature, while emissions such as hydrocarbons (HC), carbon monoxide (CO), smoke and nitrogen oxides (NO_x) are measured using AVL smoke meters and five-gas analysers [23,27]. We quantify diesel engine CO, HC, CO_2, NO_x emissions, as well as brake-specific fuel consumption and thermal efficiency [24,28].

4. Results and discussion

The performance and emission characteristics of the B20 cotton seed biodiesel oil and PY20 cotton seed pyrolytic oil, which are initially utilised independently as fuel in CI engines, are covered here. Efficiency-based load performance graphs, BSFC, and CO, NO_x and HC load emission graphs are displayed.

4.1. Effect on brake specific fuel consumption

The differences in BSFC with BP for diesel D100, B20 and PYRO oil (PY20) blends are shown in Fig. 6. The bio-oil shows higher BSFC compared to diesel. The key factor behind the rise of BSFC is the reduced calorific value of bio-oil, which requires a higher volume of fuel to produce the same power.

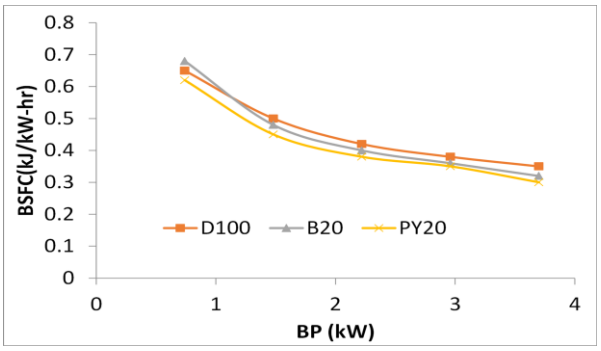


Fig. 6. BP versus BSFC of B20, PY20 and diesel.

4.2. Effect on brake thermal efficiency

Figure 7 shows the differences in brake thermal efficiency (BTE) with brake power (BP) for D100, B20 and PY20 fuels. As the load increases, BTE decreases, which can be attributed to the occurrence of water in the fuel. The results indicate that the B20 blend exhibits better performance compared to the other fuels.

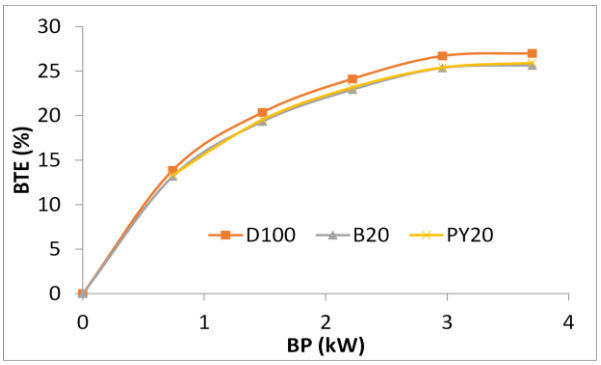


Fig. 7. BP versus BTE of B20, PY20 and diesel.

The higher BTE of B20 and lower BSFC of pyrolytic oil blends are attributed to differences in calorific value and combustion efficiency. Additionally, the lower viscosity of bio-oils compared to diesel facilitates better atomization, further contributing to the improved BTE [25].

4.3. Effect on carbon monoxide

A rich air-fuel combination or inadequate oxygen availability are the main causes of carbon monoxide (CO) emission, a byproduct of incomplete combustion.

The relationship between CO emissions and braking power (BP) for B20, pyrolytic oil (PY20) and diesel is shown in Fig. 8. Because the temperature of the cylinder gas rises with increased load, the data show that CO emissions drop as the braking power increases. The B20 blend had the lowest CO emissions of all the evaluated fuels. An increased oxygen concentration, which encourages the oxidation of carbon atoms and improves combustion efficiency, is the cause of this decrease.

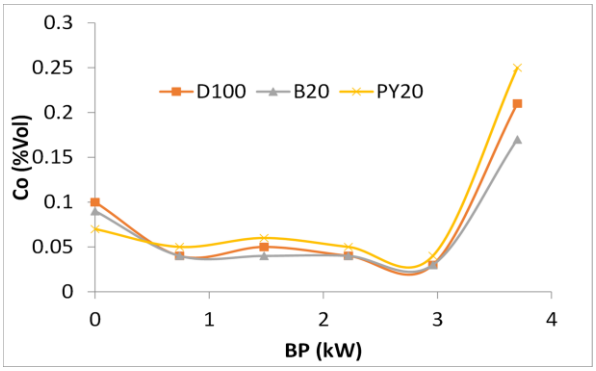


Fig. 8. Variation of CO with brake power.

4.4. Exhalation of oxides of nitrogen

Figure 9 illustrates the difference in NO_x emissions with mechanical power for B20, pyrolytic oil (PY20) and diesel. The results show fluctuations in NO_x emissions across different fuels as brake power (BP) increases. With the increase in cylinder gas temperature, NO_x emissions tend to decrease with increasing load. Among the tested fuels, the B20 biodiesel blend exhibits lower NO_x emissions with respect to diesel. This decrease can be attributed to the presence of moisture in bio-oil, which helps lower the in-cylinder temperature, thereby reducing NO_x formation [26].

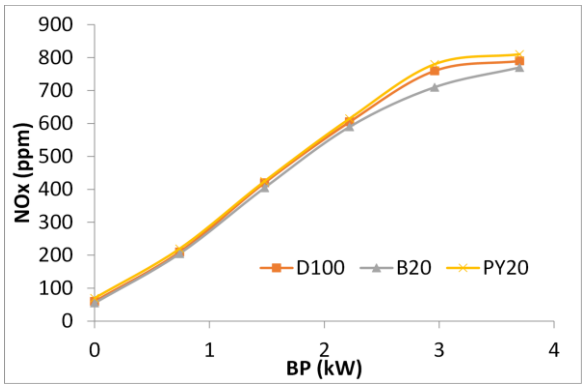


Fig. 9. Variation of NO_x with brake power.

4.5. Effect on hydrocarbon

Figure 10 presents the difference in hydrocarbon (HC) emissions with brake power (BP) for B20, pyrolytic oil (PY20) and diesel. The results indicate that HC emissions reduce as the brake power increases. Among the tested fuels, the B20 biodiesel blend exhibits the lowest HC emissions [27]. This decrease can be attributed to the enhanced combustion efficiency of the B20 blend compared to the other fuels, resulting in more complete fuel oxidation and lower unburned hydrocarbon emissions.

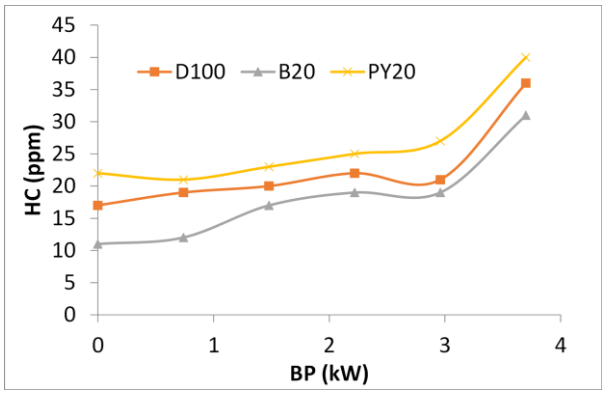


Fig. 10. Fluctuation of HC with brake power.

4.6. Exhaust smoke characteristics

Figure 11 illustrates the difference in smoke emissions with brake power (BP) for diesel, B20 and pyrolytic oil (PY20). The results show that smoke emissions decrease as the brake power increases. Among the tested fuels, the B20 biodiesel blend exhibits the lowest smoke emissions. This reduction is attributed to the quenching result of water in the biofuel, which enhances combustion efficiency, leading to reduced particulate formation compared to the other tested fuels.

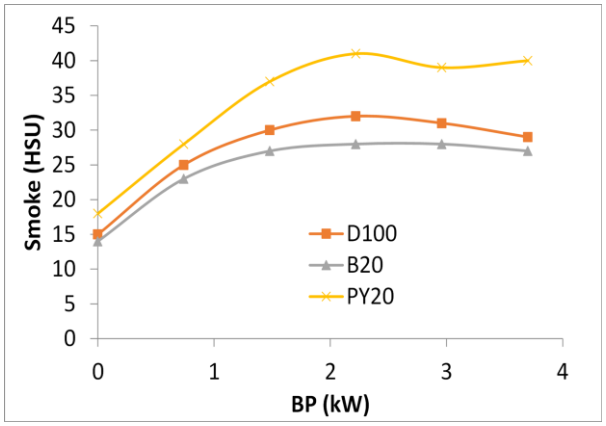


Fig. 11. Variation of smoke with brake power

4.7. Cylinder pressure

Figure 12 illustrates cylinder pressure changes with crank angle for diesel (D100), biodiesel blend (B20), and pyrolytic oil blend (PY20). All fuels display nearly the same pressure profile, with the highest pressure occurring close to the top dead centre. PY20 records a marginally higher peak pressure, followed by B20, while D100 shows the lowest. This outcome suggests that both biofuels provide effective combustion performance comparable to conventional diesel.

4.8. Heat release rate

Figure 13 presents the heat release rate (HRR) versus crank angle for D100, B20 and PY20 fuels. D100 exhibits a sharp peak around top dead centre, reflecting a higher combustion intensity.

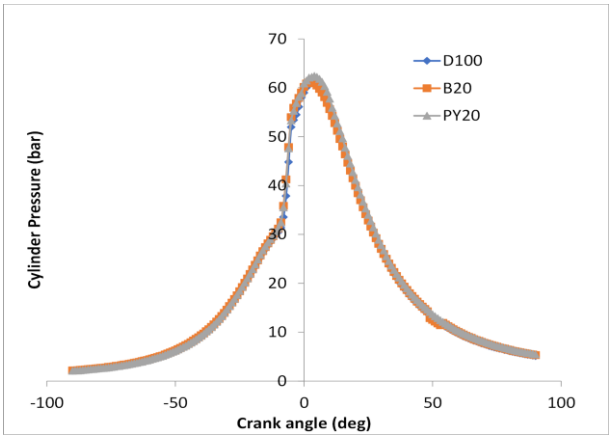


Fig. 12. Cylinder pressure vs. crank angle.

B20 also shows a notable peak, but slightly lower than for D100. PY20 demonstrates a smaller and broader profile, indicating slower combustion and reduced HRR. Overall, the comparison highlights the stronger performance of diesel and biodiesel blends compared to pyrolysed fuel.

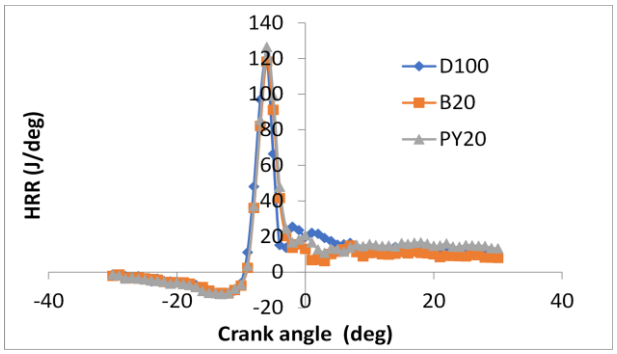


Fig. 13. HRR vs. crank angle.

The similarity in emission trends is attributed to the oxygenated nature of both biodiesel and pyrolytic oil, which promotes more complete combustion. Additionally, higher in-cylinder temperatures influenced by the fuels calorific values have led to simultaneous changes in NO_x along with CO, HC and smoke.

5. Conclusions

In this study, cottonseed oil was successfully converted into biodiesel and pyrolytic oil using transesterification and pyrolysis, respectively. Performance and emission characteristics of a CI engine were analysed using diesel (D100), biodiesel (B20) and pyrolytic oil (PY20) blends under varying loads and compression ratios:

1. Brake thermal efficiency (BTE): BTE of the B20 blend was lower than that of diesel at all loads, primarily due to the presence of moisture and the inherent properties of cottonseed oil. At full load, BTE for B20 was 28.5%, while for diesel, it was 30.2%.
2. Brake specific fuel consumption (BSFC): BSFC of B20 was higher than that of diesel, attributed to its lower heating

value. At full load, BSFC for B20 was 0.32 kg/kWh, compared to 0.29 kg/kWh for diesel, indicating that the same amount of power is produced, and more fuel is needed.

3. Carbon monoxide (CO): B20 exhibited a 22% reduction in CO emissions compared to diesel because biodiesel has a greater oxygen concentration, which improves combustion efficiency.
4. Hydrocarbons (HC): B20 showed a 19% lower HC emission than that of diesel, further demonstrating improved combustion characteristics.
5. Smoke emissions: In B20, there is a 24% reduction in smoke emissions, attributed to the quenching effect of water in biodiesel.
6. Cylinder pressure: The in-cylinder pressure traces of B20 followed a similar pattern to that of diesel, with the peak pressure occurring near the top dead centre. However, B20 exhibited a slightly higher peak pressure, suggesting better premixed combustion due to the oxygenated nature of biodiesel.
7. Heat release rate (HRR): HRR for B20 was lower than that of diesel in the premixed combustion phase, but showed a smoother diffusion phase. This indicates a slower energy release, attributed to the higher viscosity and lower volatility of biodiesel.

Overall, the study demonstrates that B20 biodiesel blend is a viable alternative fuel with reduced emissions and acceptable engine performance, making it a promising option for sustainable energy applications. However, further optimisation in terms of heating value and moisture content can improve its efficiency.

References

[1] Agarwal, A.K., Park, S., Dhar, A., Lee, C.S., Park, S., Gupta, T., & Gupta, N.K. (2018). Review of experimental and computational studies on spray, combustion, performance, and emission characteristics of biodiesel fueled engines. *Journal of Energy Resources Technology*, 140(12), 120801. doi: 10.1115/1.4040584

[2] Ahmed, M.M., Pali, H.S., & Khan, M.M. (2024). Allometry of nanoparticles in diesel-biodiesel blends for CI engine performance, combustion and emissions. *Archives of Thermodynamics*, 45(1), 99–108. doi: 10.24425/ather.2024.150442

[3] Singh, A.K., Pali, H.S., & Khan, M.M. (2024). Experimental investigations of CI engine performance using ternary blends of n-butanol/biodiesel/diesel and n-octanol/biodiesel/diesel. *Archives of Thermodynamics*, 45(1), 109–118. doi: 10.24425/ather.2024.150443

[4] Dubba, S.K., Pisini, R., Kelli, D., Bammidi, R., Vanam, J.P., & Turali, N. (2025). Experimental Investigation of the Performance and Emission Characteristics of Cotton Seed Biodiesel/Diesel Blends with Titanium Dioxide Nanoparticles. *Archives of Thermodynamics*, 46(3) 151−161. doi: 10.24425/ather.2025.156587

[5] Haq, M., Jafry, A., Ahmad, S., Cheema, T., Ansari, M., & Abbas, N. (2022). Recent advances in fuel additives and their spray characteristics for Diesel-Based blends. *Energies*, 15(19), 7281. doi: 10.3390/en15197281

[6] Krishna, M.M., Rao, N.D.P., Prasad, B.A., & Murthy, P. (2014). Comparative Performance with Different Versions of Low Heat Rejection Combustion Chambers with Crude Rice Bran Oil. *Archive of Mechanical Engineering*, 61(4), 627–651. doi: 10.2478/meceng-2014-0036

[7] Ramalingam, S., Rajkumar, T., Subramanian, S., & Palani, S. (2024). Investigation of combustion, emission, and performance parameters of a natural antioxidant additives using hydrogen and biodiesel as dual fuel in CI engine operation. *International Journal of Hydrogen Energy*, 110, 44–54. doi: 10.1016/j.ijhydene.2025.01.425

[8] Thamizhvel, R., Sethuraman, N., Sakthivel, M., & Prabhakaran, R. (2020). Experimental investigation of diesel engine by using paper cup waste as the producer gas with help of down-draft gasifier. *International Conference on Recent Developments in Material Science and Applications*, 25–26 September, Chennai, India. *IOP Conference Series: Materials Science and Engineering*, 988, 012015. doi: 10.1088/1757-899X/988/1/012015

[9] Senthil, R., Thamizhvel, R., & Sudagar, S. (2024). A comparative analysis of pyrolytic oil from medical waste and its suitability as fuel in a Compression Ignition engine. *Energy Sources, Part A: Recovery, Utilization, and Environmental Effects*, 46(1), 2040–2058. doi: 10.1080/15567036.2024.2302369

[10] Thamizhvel, R., Vinodraj, S., & Sethuraman, N. (2020). Performance on biomass gasification of groundnutshell in down draft fixed bed reacter. *International Journal of Mechanical and Production Engineering Research and Development*, 10(3), 4963–4970, doi: 10.24247/IJMPERDJUN2020470

[11] Thamizhvel, R., Naveen Raj, S, & Krishna Raj, S. (2025). Production Of Oil From Plastic Waste Through Thermal Degradation Process. *Turkish Journal of Engineering*, 9(3), 409−416. doi: 10.31127/tuje.1535115

[12] Thamizhvel, R., Manikandan, A., Praveen Kumar, S., & Sivasankaran, S. (2023). Potential Use of Cathode Ray Tube as an Abrasive Particle in Abrasive Jet Machine. *2023 International Conference on Energy, Materials and Communication Engineering*, 14−15 December, Madurai, India. doi: 10.1109/ICEMCE57940.2023.10434107

[13] Thamizhvel, R., Suryavarman, K., Velmurugan, V., & Sethuraman, N. (2021). Comparative study of gasification and pyrolysis derived from coconut shell on the performance and emission of CI engine. *Materials today: Proceedings*, 47(4), 978–983. doi: 10.1016/j.matpr.2021.05.350

[14] Sethuraman, N., Surya Varman, K., Venkatakrishnan, R., & Thamizhvel, R. (2021). An experimental investigation of crude glycerol into useful products by using IC engine in dual fuel mode. *Materials today: Proceedings*, 44, 3914–3918. doi: 10.1016/j.matpr.2021.02.160

[15] Kadupu, R., Subramanian, P., Kaliyamoorthy, A., Thamizhvel, R., Subramanian, S., & Rajendran, S. (2024). Assessing the thermal insulation properties of thermoplastic bricks for energy-efficient building solutions. *Matéria (Rio de Janeiro)*, 29(4). doi: 10.1590/1517-7076-rmat-2024-0583

[16] Ramalingam, S., Thamizhvel, R., Sudagar, S., & Silambarasan, R. (2023). Production of third generation bio-fuel through thermal cracking process by utilizing Covid-19 plastic wastes, *Materials Today: Proceedings*, 72(3), 1618-1623. doi: 10.1016/j.matpr.2022.09.430

[17] Sethuraman, N., Karthikeyan, D., Vinodraj, S., Thamizhvel, R., & Kumarasamy, G. (2023). Performance and Emission Characteristics on CI Engine by Using Waste Cooking Oil and Waste Transformer Oil as Substitute Fuel with Coconut Shell as a Catalyst. *Materials Today: Proceedings*, 72(4), 2469–2475. doi: 10.1016/j.matpr.2022.09.457

[18] Thamizhvel, R., Molly Irine, G.S., Vaithianathan, N., & Ganesh, M. (2023). Evaluating the performance and emission characteristics of jackfruit seed as bio-oil in CI engine. *Materials Today: Proceedings*. doi: 10.1016/j.matpr.2023.08.100

[19] Mikulski, M., Ambrosewicz-Walacik, M., Hunicz, J., & Nitkiewicz, S. (2021). Combustion engine applications of waste tyre pyrolytic oil. *Progress in Energy and Combustion Science*, 85, 100915. doi: 10.1016/j.pecs.2021.100915

[20] Patel, H., Rajai, V., Das, P., Charola, S., Mudgal, A., & Maiti, S. (2018). Study of Jatropha curcas shell bio-oil-diesel blend in VCR CI engine using RSM. *Renewable Energy*, 122, 310–322. doi: 10.1016/j.renene.2018.01.071

[21] Prabhahar, R.S.S., Nagaraj, P., & Jeyasubramanian, K. (2020). Promotion of bio oil, H2 gas from the pyrolysis of rice husk assisted with nano silver catalyst and utilization of bio oil blend in CI engine. *International Journal of Hydrogen Energy*, 45(33), 16355–16371. doi: 10.1016/j.ijhydene.2020.04.123

[22] Sudagar, S. (2022). Analysis of Different Production Methods of Biodiesel from Pyrolytic Oil and its Influence on CI Engine. Available at *SSRN*. doi: 10.2139/ssrn.4054241

[23] Syu, J., Chang, Y., Tseng, C., Yan, Y., Chang, Y., Chen, C., & Lin, W. (2014). Effects of water-emulsified fuel on a diesel engine generator's thermal efficiency and exhaust. *Journal of the Air and Waste Management Association*, 64(8), 970–978. doi: 10.1080/10962247.2014.905508

[24] Thanigaivelan, V., Singh, S.K., Rajhans, S.S., & Jagtap, A.S. (2021). Influence of nano additives with cashew nut shell bio-oil in CI diesel engine. *International Conference on Advances in Thermal Engineering and Applications*, 19-20 March, Tamil Nadu, India. *Journal of Physics Conference Series*, 2054(1), 012018. doi: 10.1088/1742-6596/2054/1/012018

[25] Narayanan, S., Subramanian, V., Rajkumar, T., & Nadarajan, V. (2025). Machine Learning Optimisation of CI Engine Characteristics with WSA Algorithm and Prosopis Juliflora Biofuel. *Archives of Thermodynamics*, 46(4), 117–125. doi: 10.24425/ather.2025.156842

[26] Venu, H., & Madhavan, V. (2016). Influence of diethyl ether (DEE) addition in ethanol-biodiesel-diesel (EBD) and methanol-biodiesel-diesel (MBD) blends in a diesel engine. *Fuel*, 189, 377–390. doi: 10.1016/j.fuel.2016.10.101

[27] Senthil, R., Thamizhvel, R., Sudagar, S., & Bahuruteen, A.A.H. (2025). Production of high grade fuels from biomass and waste plastics and its influence in a CI engine. *Polymer Bulletin*, 82, 6095−6114. doi: 10.1007/s00289-025-05740-4

[28] Ramalingam, S., Rajkumar, T., Subramanian, S., & Palani, S. (2024). Investigation of combustion, emission, and performance parameters of a natural antioxidant additives using hydrogen and biodiesel as dual fuel in CI engine operation. *International Journal of Hydrogen Energy*, 110, 44–54. doi: 10.1016/j.ijhydene.2025.01.425

Co-published by
Institute of Fluid-Flow Machinery
Polish Academy of Sciences
Committee on Thermodynamics and Combustion
Polish Academy of Sciences

Copyright©2026 by the Authors under licence CC BY-NC-ND 4.0

http://www.imp.gda.pl/archives-of-thermodynamics/

Implication of SiO_2 nanoparticles with novel water hyacinth biodiesel-diesel blends to improve the performance and emission parameters of a diesel engine

Maneesh Singh, Prashant Saini*, Chandrakant Mishra, Saif Nawaz Ahmad

Department of Mechanical Engineering, Madan Mohan Malaviya University of Technology, Gorakhpur 273010, Uttar Pradesh, India
*Corresponding author email: psme@mmmut.ac.in

Received: 22.01.2025; revised: 26.11.2025; accepted: 03.12.2025

Abstract

The current research explores experimentally the crude oil production from water hyacinth weed (potential renewable biomass), its biodiesel preparation and implication of SiO_2 nanoparticles (25 ppm, 50 ppm, 75 ppm, 100 ppm) with biodiesel (fixed 20%) and diesel (fixed 80%) blends on the performance and emission parameters of a 4-S single cylinder diesel engine. Crude water hyacinth oil is produced through the chemical Soxhlet extraction technique, and its biodiesel is prepared by transesterification. Metal oxide oxygenated SiO_2 nanoparticles are dispersed through ultrasonication in water hyacinth biodiesel blends to improve their combustion quality and make them more efficient. Prepared fuel blends' properties are examined as per the standards of the American Society for Testing and Materials. The experiment reveals that crude water hyacinth oil has 85.6% biodiesel yield. Dispersion of SiO_2 nanoparticles in WHB20 fuel decreases the brake specific fuel consumption by 12.61% and improves the brake thermal efficiency by 12.55% at a maximum load. HC and CO emissions are found to be decreased by 25.85% and 22.64%, respectively, whereas NO_x and CO_2 emissions are found to be increased by 45.85% and 10.87%, respectively, for WHB20$SiO_2$100ppm compared to fossil diesel at a maximum load. Overall, research concludes that WHB20$SiO_2$100ppm fuel is the best performer and suitable alternative for diesels without change in engine design.

Keywords: Transesterification; Water hyacinth biodiesel; Ultrasonication; Silicon dioxide nanoparticles; Performance and emission

Vol. 47(2026), No. 1, 79–88; doi: 10.24425/ather.2025.156856

Cite this manuscript as: Singh, M., Saini, P., Mishra, Ch., & Ahmad, S.N. (2026). Implication of SiO_2 nanoparticles with novel water hyacinth biodiesel-diesel blends to improve the performance and emission parameters of a diesel engine. *Archives of Thermodynamics*, 47(1), 79−88.

1. Introduction

Power generation in different sectors, increase in population, transportation, urbanisation, industrial developments and globalisation have enhanced the demand for fossil fuels (depleting rapidly) worldwide. Over the last two decades, energy has played an increasingly important role on both the social and economic fronts in emerging and industrialised nations. The world's energy requirements have been met mostly through fossil fuels, including gas, coal and mineral oils. Countries have emphasised utilising local and regional biomass feedstocks to meet the energy requirements and minimise the dependency on conventional fuels worldwide [1]. When the demand for fossil fuels begins to outstrip supply, prices will rise. Considering all that, the researchers' quest for a viable alternative feedstock for current unmodified diesel engines has been exacerbated by the rapid fossil fuel depletion and rising exhaust pollution.

India is currently 85% reliant on imports to satisfy its oil needs, which is extremely expensive. According to the Ministry of Petroleum & Natural Gas, Government of India, a mixture of

Nomenclature

Abbreviations and Acronyms

ASTM – American Society for Testing and Materials
BD – biodiesel
BSFC – brake specific fuel consumption
BTE – brake thermal efficiency
CO – carbon monoxide
CO_2 – carbon dioxide
EGT – exhaust gas temperature
HC – hydrocarbon
NO_x – nitrogen oxides
RPM – revolution per minutes
SiO_2 – silicon dioxide
WHB – water hyacinth biodiesel
WHB20– water hyacinth biodiesel 20%, diesel 80%
WHB20$SiO_2$25ppm – WHB20%, diesel 80%, SiO_2 25 ppm
WHB20$SiO_2$50ppm – WHB20%, diesel 80%, SiO_2 50 ppm
WHB20$SiO_2$75ppm – WHB20%, diesel 80%, SiO_2 75 ppm
WHB20$SiO_2$100ppm – WHB20%, diesel 80%, SiO_2 100 ppm
WHO – water hyacinth oil

5% biodiesel with the current diesel fuel is acceptable now to save thousands of crores per year. Usmani [2] discussed the potential use of agroforestry residues and biomass for biofuel and energy production. Rasid et al. [3] discussed recent pretreatment methods and their future utilisation for enhancing the biofuel production. The utilisation of highly potential metal oxides nano-catalysts for biofuel production strategies was presented by Manikandan et al. [4] and Hosseinzadeh-Bandbafha et al. [5].

Biodiesel is gaining popularity across the world; hence, many countries are producing biodiesel from different feedstocks to meet their energy demands. Nowadays, millions of litres of biodiesel are consumed in a number of countries globally (United States, European countries, Asian countries). In this regard, different biodiesels derived from different sources of biomass are presented subsequently.

The first-generation (corn, sugarcane and vegetable oil), second-generation (municipal waste and agricultural residues) and third-generation algal biomass renewable feedstocks for biofuel production were reviewed by Ho et al. [6]. The production of biodiesel from different feedstocks was reviewed by Zhang et al. [7], and revealed that microalgae, jatropha curcas, vegetable oil and waste cooking oil are the most widely utilised biodiesels.

Diesel engine performance parameters utilising corn oil biodiesel were examined by Saini et al. [8]. Extraction of microalgae oil, biodiesel production and its various blends with diesel were tested in a diesel engine [9]. The numerical model for lipid extraction from avocado seeds has been presented by Sathish et al. [10]. Oil extraction from mango seed and its utilisation with diesel-butanol blends were examined in Ahmad and Saini [11]. The production of biodiesel from soybean oil with higher conversion efficiency as an alternative fuel for diesel engines was discussed by Wang et al. [12]. The potential utilisation of synthesised lemongrass biodiesel with diesel blends for an unmodified diesel engine was discussed by Kumar et al. [13].

Bioethanol production from water hyacinth and its blends with diesel were utilised to investigate diesel engine characteristics by Choudhary et al. [14]. Different blends of water hyacinth biodiesel (WHB) with diesel were tested on a diesel engine by Venu et al. [15] and Alagu et al. [16]. Both studies reported that mixing of twenty percent water hyacinth biodiesel with eighty percent diesel was the best performer in terms of improved engine performance and reduced emissions parameters. In Indonesia, an experimental study recommended that the blending of up to 40% biodiesel in diesel without engine modifications is acceptable, Sukmono et al. [17]. Moreover, research is not limited to exploration of new renewable biomass sources for biodiesel generation. Worldwide, explorations of different metal oxide nanoparticles with biodiesel blends to improve performance and reduce emissions of unmodified diesels are an emerging research need.

The effect of nanoparticles as an additive in diesel and biodiesel blends on stability, engine performance and emission characteristics was reviewed by Soudagar et al. [18] and Alli and Kotha [19]. The studies suggested that metal oxide nanoparticles with biodiesel blends further improve the engine characteristics. Diesel engine running on biodiesels combined with nano-additives emits less carbon monoxide and unburned hydrocarbon with enhanced engine performance as reviewed by Damanik et al. [20], Manigandan et al. [21], and Tomar and Kumar [22]. Moreover, some studies of metal oxides nanoparticles as an oxygenated additive with various kinds of biodiesel to improve performance and reduce emissions of compression ignition (CI) engines have been reported in recent literature, such as: silver oxide nano-additive with neem oil biodiesel, Devarajan et al. [23]; aluminium oxide nanoparticles with palm oil biodiesel, Sundar et al. [24]; titanium dioxide nano-additive with mustered oil biodiesel, Yuvarajan et al. [25]; titanium dioxide nano-additive with azolla algae biodiesel, Narayanasamy and Jeyakumar [26]; silicon dioxide nano-additive with corn biodiesel, Saravankumar et al. [27]; cerium dioxide nano-additive with waste cooking oil biodiesel, Dinesha at al. [28]; titanium dioxide nano-additive with water emulsified soybean oil biodiesel, Vellaiyan et al. [29]; silicon dioxide nano-additive with mahua biodiesel, Nutakki et al. [30]; titanium dioxide nano-additive with polanga oil biodiesel, Praveen et al. [31]; silicon dioxide nano-additive with mahua biodiesel blends, Ramachander et al. [32]; titanium dioxide nano-additive with lemongrass biodiesel blends, Kumar et al. [33]; titanium dioxide nano-additive with eichhornia crassipes biodiesel, Jain et al. [34].

Although the above reviewed literature reported the biodiesel production from different renewable biomass, dispersion of nanoparticles with them and their utilisation in unmodified diesels, scarce research opportunity on water hyacinth biomass (abundantly available renewable feedstock worldwide) has attracted authors to explore for crude oil production from this biomass, biodiesel preparation, dispersion of silicon dioxide oxygenated nanoparticles with biodiesel blends and their applicability in diesels as sustainable alternate fuel.

In this paper, performance and emission parameters of a 4-S single cylinder diesel engine fuelled by binary blends of diesel (fixed 80%) and water hyacinth biodiesel (fixed 20%) with dif-

ferent SiO_2 nano-additive concentrations (25 ppm, 50 ppm, 75 ppm and 100 ppm) at various engine loads are investigated experimentally. These four concentrations are chosen based on standard incremental ranges reported in recent nanoparticle fuel studies, taking into account practical stability limits for stable dispersion, and economic feasibility for blending. Novelties of the current research may be considered twofold:

(i) Soxhlet chemical extraction of crude oil from potential renewable water hyacinth biomass and its biodiesel preparation through transesterification;

(ii) Dispersion of SiO_2 nanoparticles (oxygenated additives improve combustion quality) with WHB and diesel blends through the ultrasonication technique.

The prepared tested fuels are named as WHB20, WHB20$SiO_2$25ppm, WHB20$SiO_2$50ppm, WHB20$SiO_2$75ppm, and WHB20$SiO_2$100ppm, respectively. Important fuel properties of blends are determined as per the American Society for Testing and Materials (ASTM) standards. Eventually, experimental investigations are made to obtain performance characteristics: brake specific fuel consumption (BSFC), brake thermal efficiency (BTE), exhaust gas temperature (EGT), and emission characteristics: hydrocarbon (HC), carbon monoxide (CO), carbon dioxide (CO_2), nitrogen oxides (NO_x). The characteristics of the prepared blends are obtained at different engine loads, and the results are compared with WHB20 and fossil diesel fuels.

2. Materials and methods

This section deals with the materials and methods used to extract crude water hyacinth oil, and prepare biodiesel and its different blending samples with SiO_2 oxygenated nanoparticles as an additive. In addition, the important property values of prepared samples are examined for utilisation in a 4-S single cylinder vertical diesel engine.

2.1. Water hyacinth plant collection and drying

Water hyacinth is an aquatic weed, which is available abundantly in the eastern region of India and is now prevalent across the country except in the dry western region. The plants may grow up to 1 m tall, with the average recorded height of 40 cm. Six to ten blooms, each about 4 to 7 cm in diameter, can be seen on the flowers. The stems and leaves feature air-filled tissue that allows it to float effortlessly, with a high growth rate of 60−100 tonnes per hectare per year.

In this research, water hyacinth plants were collected from the Ramgarh lake (covering an area of 723 hectares) located at Gorakhpur, Uttar Pradesh, India. Further, drying of green water hyacinth is done in sunlight, preceded by oven drying at 70°C. The ambient temperature varies between 21−26°C in the months of December and January. It is found that 3.6 kg of green water hyacinth plants is converted into 1 kg after drying. After drying, the dried plants are chopped into small pieces and crushed into powder using a grinder. Figure 1 depicts the appearance and colour of water hyacinth (WH) from day one to day twenty eight.

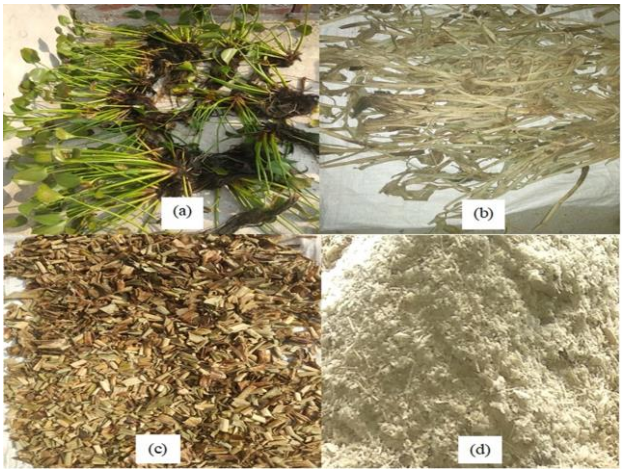


Fig. 1. Collection and drying of water hyacinth plant in sunlight: (a) day 1, (b) day 14, (c) day 21, (d) day 28 – powder form.

2.2. Soxhlet oil extraction and biodiesel preparation

All the chemicals which are used in this research are of analytical grade and are purchased from a government authorised local distributor (Lucknow, India), like NaOH, methanol and n-hexane. Figure 2 shows the crude water hyacinth oil extraction from waste biomass. The Soxhlet apparatus (effective technique for oil extraction) basically consists of four main parts: a condenser, Soxhlet flask and heating mantle, as shown in Fig. 2(a). To extract oil from water hyacinth, take 50 gm of dried powder form the water hyacinth sample in a thimble and keep it in the Soxhlet apparatus. A conical flask is filled three-fourth part with n-hexane and kept on the heating mantle. The condenser is connected with the top of the extractor, the outlet and inlet pipes of the condenser are joined with a pipe where cold water enters, and hot water exits, respectively. After these arrangements, the Soxhlet apparatus heating mantle is switched on and set to the temperature 69°C (which is the boiling point of n-hexane). A few moments later, n-hexane starts boiling and is converted into vapour, which goes into the condenser via a vapour tube where it condenses into a liquid form. The liquid form is then passed through a thimble, after a fixed level it returns along with extracted water hyacinth oil into a conical flask via a syphon tube. Due to the high boiling point temperature of the extracted water hyacinth oil, it is not vaporised with n-hexane. The same procedure as discussed above is repeated 4–5 times for complete extraction of oil from water hyacinth biomass, and it takes approximately 2 hours for each thimble. The same process is done for all 20 thimbles (50 gm each) of samples. This results in a mixture of water hyacinth oil and n-hexane in a conical flask. After that, the separation of crude water hyacinth oil is done from the above extracted mixture by a horizontal condenser distillation setup as shown in Fig. 2(b). The flask mixture (water hyacinth oil and n-hexane) heating is done at a temperature of 69 °C (boiling point of n-hexane) and the flask is connected with the horizontal condenser, which has an inlet and outlet for cold water supply and hot water exit. This way, n-hexane starts boiling and is evaporated from the mixture, which condenses in the condenser, and is collected in another flask. Finally, crude water hyacinth oil remains in the heated flask as shown in Fig. 2(c). Each 50 gm of water hyacinth powder sample produces an average of 10.5 ml crude WHO.

After that, water hyacinth biodiesel was prepared from extracted crude WHO through the well-known transesterification

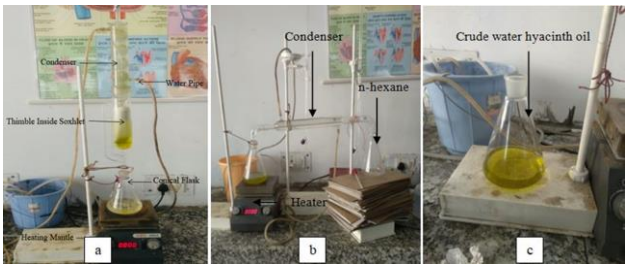


Fig. 2. Water hyacinth oil extraction: (a) Soxhlet apparatus, (b) distillation, (c) crude WHO.

technique. For the purpose of biodiesel preparation, NaOH of 1.4 gm is mixed with 25 ml of methanol by a magnetic stirrer until NaOH dissolves completely, and meanwhile, 100 ml of crude WHO is heated in a flask at 60°C by a heating mantle to reduce its viscosity and remove moisture from oil. During the process, the temperature should not be higher than 60°C (less than the boiling point of methanol), otherwise it may evaporate. After that, the prepared mixture of NaOH and methanol is mixed with heated WHO, and finally, the solution is stirred at 600 rpm for approximately120 minutes. During the process, heat may release: hence, a condenser is placed vertically over the flask and closed from the top as shown in Fig. 3(a). After that, the stirred solution is kept in a separating funnel for one day as shown in Fig. 3(b). In this way, glycerine and WHB were separated. The biodiesel yield can be calculated as the ratio of the total weight of water hyacinth methylesters and the total weight of oil in the sample. In this way, water hyacinth oil transesterification results in 85.6% yield of biodiesel.



Fig. 3. Biodiesel preparation: (a) magnetic stirring, (b) biodiesel and glycerine separation.

2.3. Tested fuel preparation

In this research, the SiO_2 nanoparticles of an average size of 25 nm with 99.9% purity are purchased from a government registered company in India. The SiO_2 nanoparticles (25 ppm, 50 ppm, 75 ppm and 100 ppm) are mixed individually with water hyacinth biodiesel and diesel through the well-known ultrasonication technique. Firstly, the mixing of nanoparticles (25 ppm, 50 ppm, 75 ppm and 100 ppm) is done by dispersing them in water hyacinth biodiesel (20 ml each) separately with the help of an ultrasonicator at a power and frequency of 120 W and 50 kHz, respectively, for half an hour shown in Fig. 4(a). SiO_2 nanoparticles are smaller than the size of the fuel injector nozzle diameter, hence not obstructing the fuel flow. Secondly, prepared blends of SiO_2 with water hyacinth biodiesel (25 ppm, 50 ppm, 75 ppm and 100 ppm) are mixed with diesel in a volume proportion 20% of biodiesel and 80% of diesel with the help of a magnetic stirrer for a time period of 30 minutes at 600 rpm, as shown in Fig. 4(b).

Finally, the prepared tested fuels were named as WHB20$SiO_2$25ppm (water hyacinth biodiesel 20%, diesel 80%, SiO_2 25 ppm), WHB20$SiO_2$50ppm (water hyacinth biodiesel 20%, diesel 80%, SiO_2 50 ppm), WHB20$SiO_2$75ppm (water hyacinth biodiesel 20%, diesel 80%, SiO_2 75 ppm) and WHB20$SiO_2$100ppm (water hyacinth biodiesel 20%, diesel 80%, SiO_2 100 ppm) respectively. These prepared fuels are shown in Fig. 5. The important examined fuel properties measured by various apparatuses are given in Table 1.



Fig. 4. Sample preparation: (a) ultrasonicator, (b) mixing of diesel and biodiesel.

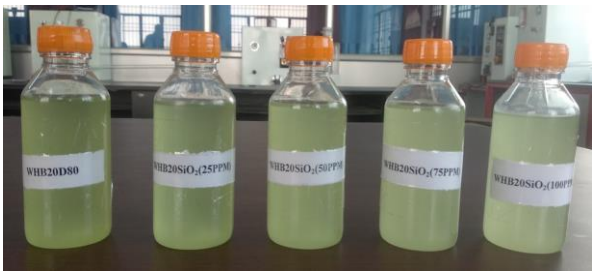


Fig. 5. Tested fuel samples.

Table 1. Important fuel properties.

Properties	Apparatus used	Diesel	WHB20	WHB20$SiO_2$25ppm	WHB20$SiO_2$50 ppm	WHB20$SiO_2$75 ppm	WHB20$SiO_2$100 ppm
Density, kg/m³	Hydrometer	830	847	851	853	854	855
Flash point, ℃	Pensky-Martens apparatus	61	97	91	89	88	87
Kinematic viscosity, mm²/sec	Viscometer	2.76	2.87	2.85	2.84	2.83	2.81
Calorific value, kJ/kg	Bomb calorimeter	42830	41910	42124	42262	42458	42620

3. Experimental procedure

To evaluate the performance, prepared samples are investigated on a 4-stroke, 1-cylinder water cooled vertical diesel engine. Table 2 shows the detailed specifications of the test engine setup. The engine loading is done through a rope brake, which is connected to the engine through a coupling. A multichannel digital temperature indicator measures the temperature of exhaust gasses and at various locations. The load on the test engine is gradually increased between 1−5 kW brake power, and the time it takes at each load to consume 10 ml of the prepared sample is recorded. Experiments on each fuel sample were carried out through the same way as stated above. All the tests were run three times, and the average value obtained is used to make calculations of performance parameters. Figure 6 shows the flow chart for the whole episode.

Table 2. Detailed engine specifications.

Particular	Description or value	Unit
Engine type	4-S single cylinder, water cooled, vertical CI engine	–
Cylinders number	1	–
Diameter of bore	120	mm
Length of stoke	139.7	mm
Cubic capacity	1580	cm^3
Compression ratio	17.5:1	–
Rated power	7.5	kW
Rated speed	1500	rpm
Number of nozzle holes	3	–
Injection pressure	202	bar
Fuel injection	Direct injection	–
Revolution of flywheel	Clockwise	–
Maximum HP	10	Horsepower

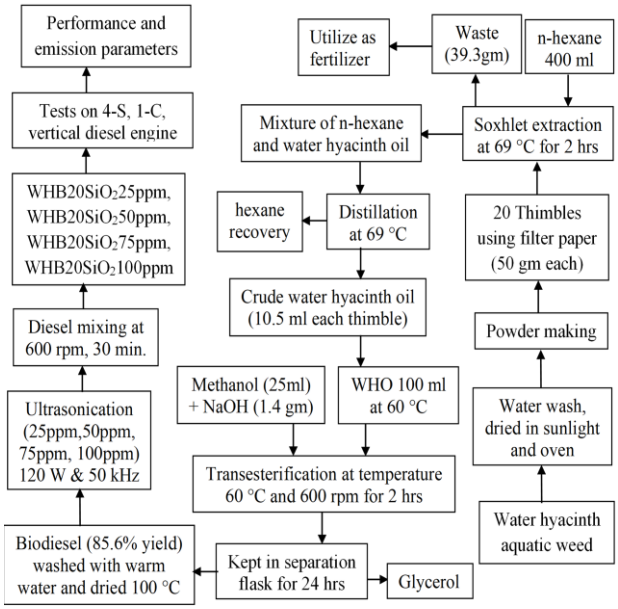


Fig. 6. Flow chart for the whole episode.

Blending samples performances are analysed in the diesel engine in terms of BSFC, BTE and EGT. BSFC (kg/kWh) and BTE (%) are determined, respectively, as:

$$BSFC = \frac{FCR}{BHP}, \quad (1)$$

$$BTE\ (\%) = \frac{BHP \times 3600}{FCR * CV} \cdot 100, \quad (2)$$

where BHP (kW) is the brake horsepower and CV (kJ/kg) is the calorific value of fuel.

3.1. Uncertainty percentage error

The instruments like tachometer, fuel meter, temperature indicator, bomb calorimeter, load indicator, Pensky-Marten's apparatus and exhaust gas analyser are used to record the speed, liquid column height, temperature, heating value, load, flash point and exhaust emissions, respectively.

Table 3 shows the instrumental uncertainty to identify the experimental percentage error.

Table 3. Instruments uncertainty.

Instruments	Parameter	Uncertainty (±)
Tachometer	Speed (rpm)	0.90%
Fuel meter	Heights of liquid column	0.5%
Temperature indicator	Temperature (°C)	0.30%
Bomb calorimeter	Heating value	1.4%
Load indicator	Load	0.3%
Pensky-Marten's apparatus	Flash point (°C)	0.45%
Exhaust gas analyser (ATS-206A):	HC	0.25%
	CO	0.75%
	NO_x	0.5%
	CO_2	0.5%

The instrumental uncertainty error (x) of this experimental research is identified as:

$$x = square\ root\ of\ uncertainity\ of\ [\text{temperature}^2 + \text{speed}^2 + \text{load}^2 + \text{fuel measuring}^2 + \text{heat value}^2 + \text{flash point}^2 + HC^2 + CO^2 + NO_x^2 + CO_2^2],$$

$$x = \sqrt{\begin{matrix}0.3^2 + .90^2 + 0.3^2 + 0.5^2 + 1.4^2 + 0.45^2 \\ +0.25^2 + 0.75^2 + 0.5^2 + 0.5^2\end{matrix}}.$$

In this way, the total uncertainty of experiments is identified as $x = \pm 2.127\%$.

4. Results and discussion

In this section, prepared tested blends performance and emission results with varying engine load are presented and compared with those of WHB20 fuel and fossil diesel. All experiments are performed thrice to ensure the accuracy and repeatability of results, and their average values are considered to make final calculations of performance parameters (BSFC, BTE and EGT). Further, important emission parameters (HC, CO, CO_2 and NO_x) of prepared test blends are recorded by an ATS-206A exhaust

gas analyser model. In addition, these recorded emission parameters are compared with the WHB20 fuel and fossil diesel. Finally, the present study is compared with other available studies in the same field for validation purposes.

4.1. Brake specific fuel consumption

Figure 7 shows the implication of SiO_2 nanoparticles with WHB and diesel blends on BSFC for gradually increasing engine load.

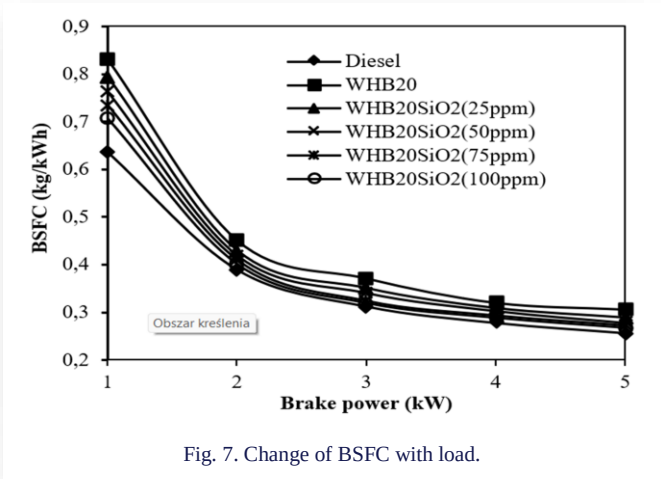


Fig. 7. Change of BSFC with load.

BSFC refers to the quantity of fuel required to produce unit power and should be lower for an efficient fuel. It depends on density, heating value and cetane number of individual fuels. Experimental results reveal that BSFC decreases with the increasing engine load for all tested blends. Additionally, increasing SiO_2 nanoparticles concentration in the blend increases their calorific values, resulting in a decrease in BSFC at all individual loads. BSFC (kg/kWh) for diesel, WHB20, WHB20$SiO_2$25ppm, WHB20$SiO_2$50ppm, WHB20$SiO_2$75ppm and WHB20SiO_2-100ppm was calculated as 0.2569, 0.3061, 0.2884, 0.2781, 0.273 and 0.2675 at the maximum load, respectively. It was observed to increase by 19.15%, 12.26%, 8.25%, 6.27% and 4.13% for WHB20, WHB20$SiO_2$25ppm, WHB20$SiO_2$50ppm, WHB20$SiO_2$75ppm and WHB20$SiO_2$100ppm, respectively, in comparison to fossil diesel. Whereas it was observed to decrease by 5.78%, 9.15%, 10.81% and 12.61% for WHB20$SiO_2$25ppm, WHB20$SiO_2$50ppm, WHB20$SiO_2$75ppm and WHB20SiO_2-100ppm, respectively, in comparison to WHB20 fuel. Overall, increasing SiO_2 nanoparticles concentration in WHB20 fuel may further reduce BSFC, approaching that of the fossil diesel fuel.

4.2. Brake thermal efficiency

Figure 8 shows the implication of SiO_2 nanoparticles with WHB and diesel blends on BTE for the gradually increasing engine load. BTE refers to the combustion of fuel within the combustion chamber and transformation of it into useful work. BTE depends on the calorific value and available oxygen content (proper burning) of the individual fuel. Experimental results reveal that BTE increases with the increasing engine load for all tested blends. Additionally, increasing SiO_2 nanoparticles concentration in the blend decreases BSFC, resulting in an increase in BTE at all individual loads. BTE (%) for diesel, WHB20, WHB20$SiO_2$25ppm, WHB20$SiO_2$50ppm, WHB20$SiO_2$75ppm and WHB20$SiO_2$100ppm was identified as 32.71%, 28.05%, 29.63%, 30.62%, 31.05% and 31.57% at the maximum load, respectively. It was observed to decrease by 14.26%, 9.42%, 6.39%, 5.07% and 3.49% for WHB20, WHB20$SiO_2$25ppm, WHB20$SiO_2$50ppm, WHB20$SiO_2$75ppm and WHB20SiO_2-100ppm, respectively, in comparison to fossil diesel. Whereas it was observed to increase by 5.63%, 9.16%, 10.70% and 12.55% for WHB20$SiO_2$25ppm, WHB20$SiO_2$50ppm, WHB20SiO_2-75ppm and WHB20$SiO_2$100ppm, respectively, in comparison to WHB20 fuel. Overall, increasing SiO_2 nanoparticles concentration in WHB20 fuel may further enhance the fuel quality, approaching that of the fossil diesel fuel.

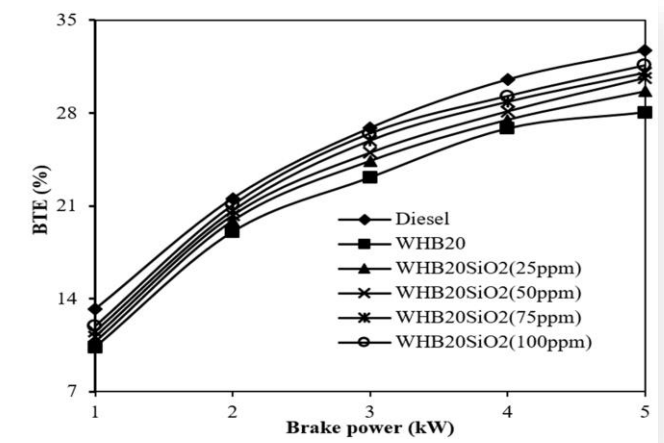


Fig. 8. Change of BTE with load.

4.3. Exhaust gas temperature

Figure 9 shows the variation in EGT for all tested samples with the gradually increasing engine load. EGT describes the quantity of heat discharge during combustion.

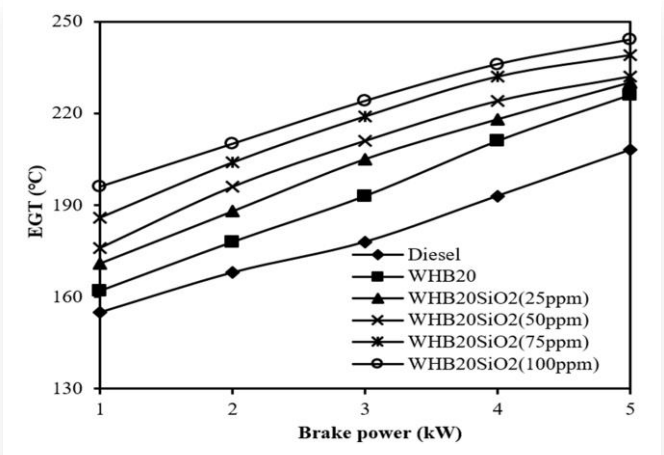


Fig. 9. Change of EGT with load.

The increase of EGT exhibits the presence of oxygen content in the fuel blends. Measurements reveal that EGT increases with the increasing engine load for all tested blends. As biodiesel has a higher content of oxygen than diesel, and further mixing of SiO_2 oxygenated nano-additive in biodiesel blends leads to pro-

per combustion, due to which the inside cylinder temperature increases, resulting in an increased EGT. EGT was recorded for fossil diesel, WHB20, WHB20$SiO_2$25ppm, WHB20$SiO_2$50ppm, WHB20$SiO_2$75ppm and WHBD20$SiO_2$100ppm as 208°C, 226°C, 230°C, 232°C, 239°C and 244°C, respectively, at the maximum load.

4.4. HC emission

Figure 10 shows the implication of SiO_2 nanoparticles with WHB and diesel blends on hydrocarbon emission for the gradually increasing engine load. HC emission shows the incomplete fuel/air combustion in the engine cylinder.

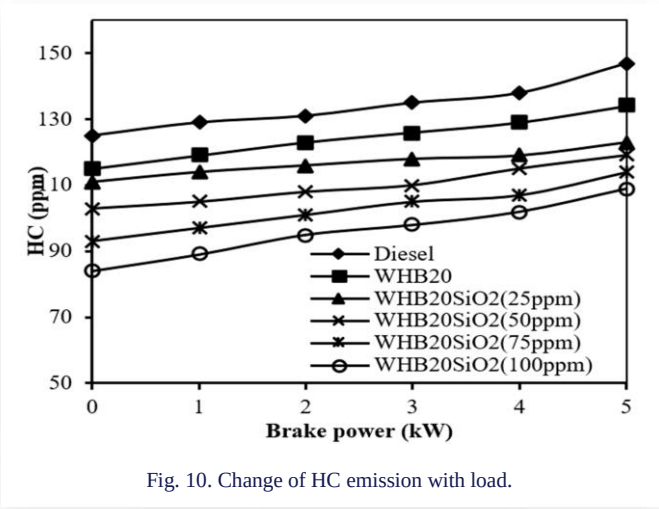


Fig. 10. Change of HC emission with load.

Recorded data reveal that the HC emission decreases with increasing SiO_2 nanoparticles concentration in the blends at a particular engine load. Additionally, it is always maximum for diesel fuel and minimum for WHBD20$SiO_2$100ppm fuel at all loads. The addition of metal oxide nanoparticles in the biodiesel blend accelerates fuel combustion further because they function as a catalyst (oxidising nature), which improves flame spread, thus lowers the carbon initiation temperature, resulting in reduced HC emissions. Hydrocarbon (ppm) emissions for diesel, WHB20, WHB20$SiO_2$25ppm, WHB20$SiO_2$50ppm, WHB20$SiO_2$75ppm and WHBD20$SiO_2$100ppm are recorded as 147, 134, 123, 119, 114 and 109 at the maximum load, respectively. It was observed to decrease by 8.84%, 16.33%, 19.05%, 22.45% and 25.85% for WHB20, WHB20$SiO_2$25ppm, WHB20$SiO_2$50ppm, WHB20$SiO_2$75ppm and WHB20$SiO_2$100ppm, respectively, in comparison to fossil diesel. Overall, dispersion of SiO_2 nanoparticles as additives in the WHB blends may reduce HC emission by 25%.

4.5. CO emission

Figure 11 shows the implication of SiO_2 nanoparticles with WHB and diesel blends on carbon monoxide emission for the gradually increasing engine load. Silicon dioxide (oxygenated nano-additive) dispersion in the WHB blends supports better quality of fuel, and enhances conversion of CO into CO_2, resulting in reduced CO emissions. Recorded data reveal that it is always maximum for diesel fuel and minimum for WHBD20$SiO_2$100ppm fuel at all individual loads. CO emissions (% vol.) for diesel, WHB20, WHB20$SiO_2$25ppm, WHB20$SiO_2$50ppm, WHB20$SiO_2$75ppm and WHBD20$SiO_2$100ppm are recorded as 0.53, 0.50, 0.48, 0.46, 0.43 and 0.41, respectively, at the maximum load. It was observed to decrease by 5.66%, 9.43%, 13.21%, 18.87% and 22.64% for WHB20, WHB20$SiO_2$25ppm, WHB20$SiO_2$50ppm, WHB20$SiO_2$75ppm and WHB20$SiO_2$100ppm, respectively, in comparison to fossil diesel. Although an increased load increases the CO emission, the increasing concentration of SiO_2 nanoparticles in the blends reduces the CO emission.

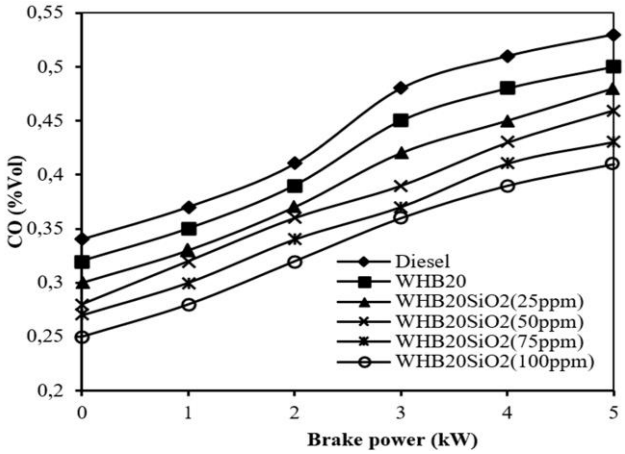


Fig. 11. Change of CO emission with load.

4.6. NO_x emission

Figure 12 shows the variation in NOx emissions for all tested samples with the gradually increasing engine load. Various factors may be responsible for the formation of NO_x, such as important fuel properties, operating conditions, reaction time, combustion temperature and engine design.

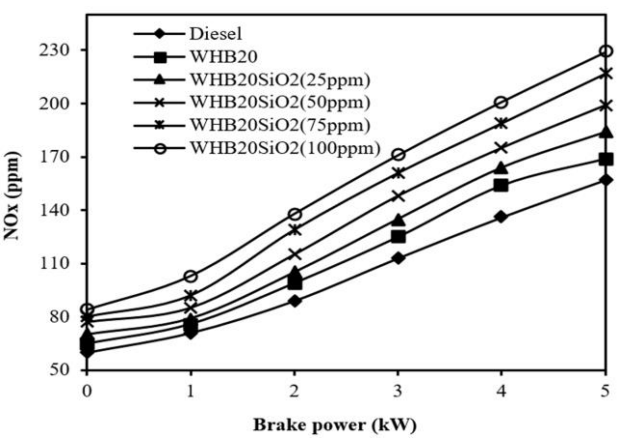


Fig. 12. Change of NO_x emission with load.

The increased oxygenated SiO_2 nanoparticles concentration (increases oxygen content in blends) leads to complete combustion, which in turn increases the cylinder temperature, resulting in higher NO_x emissions with the increasing engine load. NO_x emissions (ppm) for diesel, WHB20, WHB20$SiO_2$25ppm, WHB20$SiO_2$50ppm, WHB20$SiO_2$75ppm and WHBD20SiO_2-

100ppm are recorded as 157, 169, 184, 199, 217 and 229, respectively, at the maximum load. It was observed to increase by 7.64%, 17.19%, 26.75%, 38.21% and 45.85% for WHB20, WHB20$SiO_2$25ppm, WHB20$SiO_2$50ppm, WHB20$SiO_2$75ppm and WHB20$SiO_2$100ppm, respectively, in comparison to fossil diesel. Overall, NO_x emissions were found to be increased with the increasing load, but they can be controlled by the well-known exhaust gas recirculation technique and adjustments in combustion timing.

4.7. CO_2 emission

Figure 13 shows the variation in CO_2 emissions for all tested samples with the gradually increasing engine load. Increasing SiO_2 nanoparticles concentration increases CO_2 emissions at all individual engine loads due to enhanced quality of combustion. CO_2 emissions (% vol.) for diesel, WHB20, WHB20SiO_2-25ppm, WHB20$SiO_2$50ppm, WHB20$SiO_2$75ppm and WHB-20$SiO_2$100ppm are recorded as 2.30, 2.34, 2.40, 2.44, 2.50 and 2.55, respectively, at the maximum load. It was observed to increase by 1.74%, 4.35%, 6.09%, 8.70% and 10.87% for WHB20, WHB20$SiO_2$25ppm, WHB20$SiO_2$50ppm, WHB-20$SiO_2$75ppm and WHB20$SiO_2$100ppm, respectively, in comparison to fossil diesel. Overall, dispersion of SiO_2 nanoparticles in blends increases CO_2 emissions with the increasing engine load.

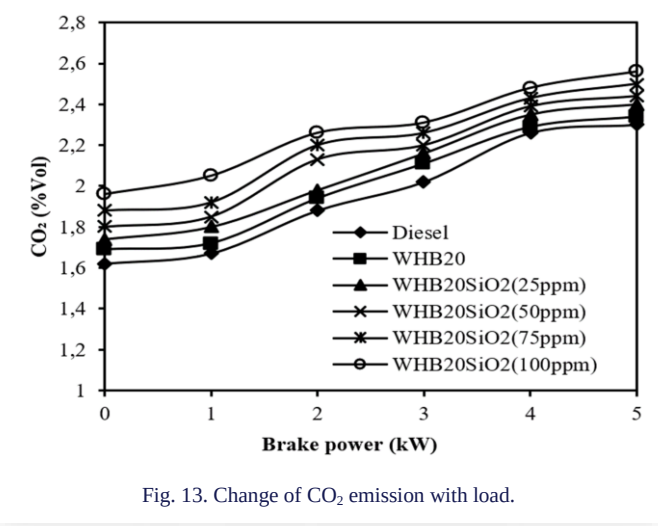


Fig. 13. Change of CO_2 emission with load.

4.8. Research validation

The present research is validated in terms of biodiesel yield, performance and emission characteristics with available recent literature data. In studies of Venu et al. [15] and Alagu et al. [16], WHB and fossil diesel blends in different volume proportions were tested on a single cylinder 4-stroke diesel engine, and revealed the WHB20D80 (water hyacinth biodiesel 20% + diesel 80%) fuel as the best performer compared to engine performance and emissions with neat diesel. A study of Rahman and Aziz [35] reported water hyacinth biodiesel yields of 87%, reduced HC and CO emissions by 48% and 21.9%, respectively, and increased NO_x emissions by 47.3% with induction of hydroxy compared to neat diesel, CO_2 not reported. Whereas the current research reported:

(i) Water hyacinth biodiesel yield of 85.6%;
(ii) Dispersion of SiO_2 nanoparticles in WHB20D80 fuel decreases BSFC by 12.61% and improves BTE by 12.55% at the maximum load;
(iii) Dispersion of SiO_2 nanoparticles reduced HC and CO emissions by 25.85% and 22.64%, respectively, and increased NO_x and CO_2 emissions by 45.85% and 10.87%, respectively, compared to neat diesel at the maximum load.

Additionally, aluminium oxide nanoparticles with biodiesel are frequently reported to improve atomisation/evaporation and increase BTE while reducing HC/CO, whereas NO_x effects vary but often increase due to improved combustion [24]. Cerium dioxide nano-additive with biodiesel is significant for oxygen storage/catalytic soot oxidation, reducing CO/HC/particulate matter, and may reduce or moderate NO_x emission in some formulations (because of catalytic soot oxidation and alternative reaction pathways), though results depend on the concentration and engine conditions [28]. Titanium dioxide nano-additive with biodiesel acts as an oxygen-bearing catalyst; many studies report smoke and CO/HC reductions and BTE improvement; CO_2 and NO_x may increase depending on the temperature rise, but smoke and particulate reductions are often more substantial. Moreover, the present study shows a reduced BSFC and improved BTE, and substantial HC/CO reductions, but a notable increase in nitrogen oxides. This pattern (better combustion, lower HC/CO, higher NO_x) is consistent with many oxide nanoparticle studies. The differences in magnitude depend on particle chemistry, oxygen content, catalytic surface and dispersion stability. Finally, WHB20$SiO_2$100ppm is recommended for future alternate fuel due to the favourable oil yield, enhanced performance and comparable emissions for the unmodified diesel engine.

5. Conclusions

This research dealt with crude oil extraction from water hyacinth waste biomass and its conversion into transesterified biodiesel as an alternate fuel for energy generation purposes. SiO_2 nanoparticles (25 ppm, 50 ppm, 75 ppm and 100 ppm) were dispersed through ultrasonication in WHB-diesel blends to make them more efficient. The prepared fuel blends' properties were examined as per ASTM standards. The prepared blends were tested on a 4-S single-cylinder, water cooled, vertical diesel engine to examine their performance and emissions characteristics, and compare them with those of WHB20 and diesel. The main research outcomes of this experimental work can be written as follows:

- One kilogram of water hyacinth powder (after drying 3.5 kg green WH plant) produces an average of 210 ml of crude oil, which has 85.6% transesterification biodiesel yield.
- Dispersion of SiO_2 nanoparticles in WHB20 fuel decreased BSFC by 12.61%, hence improved BTE, which approaches that of fossil diesel at the maximum load.
- HC emission decreased by 8.84%, 16.33%, 19.05%, 22.45% and 25.85% for WHB20, WHB20$SiO_2$25ppm, WHB20$SiO_2$50ppm, WHB20$SiO_2$75ppm and WHB-20$SiO_2$100ppm, respectively, compared to fossil diesel.

- CO emission decreased by 5.66%, 9.43%, 13.21%, 18.87% and 22.64% for WHB20, WHB20$SiO_2$25ppm, WHB-20$SiO_2$50ppm, WHB20$SiO_2$75ppm and WHB20SiO_2-100ppm, respectively, compared to fossil diesel.
- Both NO_x and CO_2 emissions increased by 45.85% and 10.87%, respectively, for WHB20$SiO_2$100ppm fuel compared to fossil diesel at the maximum load. Higher NO_x emissions can be controlled by the well-known exhaust gas recirculation technique and adjustments in combustion timing.
- Overall, it can be concluded that the WHB20$SiO_2$100ppm fuel is the best performer and a suitable alternative for diesel without any change in engine design because its quality and performance are similar to those of fossil diesel, with comparable emissions.

The current study focused on the investigation of engine performance and emission parameters. Whereas an optimisation study across a wider range of nanoparticles (> 100 ppm), a cost-benefit assessment considering large-scale production, lifecycle aspects, and long-term durability study (injector wear, filter fouling and lubricant contamination) with periodic injector inspection, filter analysis and lubricant ferrous particle monitoring may be proposed as a future scope of work.

References

[1] Firouzi, S., Allahyari, M.S., Isazadeh, M., Nikkhah, A., & Haute, S.V. (2021). Hybrid multi-criteria decision-making approach to select appropriate biomass resources for biofuel production. *Science of the Total Environment*, 770, 144449. doi: 10.1016/j.scitotenv.2020.144449

[2] Usmani, R.A. (2020). Potential for energy and biofuel from biomass in India. *Renewable Energy*, 155, 921−930. doi: 10.1016/j.renene.2020.03.146

[3] Rasid, N.S.A., Shamjuddin, A., Rahman, A.Z.A., & Amin, N.A.S. (2021). Recent advances in green pre-treatment methods of lignocellulosic biomass for enhanced biofuel production. *Journal of Cleaner Production*, 321, 129038. doi: 10.1016/j.jclepro.2021.129038

[4] Manikandan, S., Subbaiya, R., Biruntha, M., Krishnan, R.Y., Muthusamy, G., & Karmegam, N. (2022). Recent development patterns, utilization and prospective of biofuel production: Emerging nanotechnological intervention for environmental sustainability - A review. *Fuel*, 314, 122757. doi: 10.1016/j.fuel.2021.122757

[5] Hosseinzadeh-Bandbafha, H., Panahi, H.K.S., Dehhaghi, M., Orooji, Y., Shahbeik, H., Mahian, O., Karimi-Maleh, H., Sulaiman, A., Mei, C., Kiehbadroudinezhad, M., & Nizami, A.S. (2023). Nanomaterials and their role in advancing biodiesel feedstock production: A comprehensive review. *Biofuel Research Journal*, 10(3), 1901−1932. doi: 10.18331/BRJ2023.10.3.4

[6] Ho, D.P., Ngo, H.H., & Guo, W. (2014). A mini review on renewable sources for biofuels. *Bioresource Technology*, 169, 742−749. doi: 10.1016/j.biortech.2014.07.022

[7] Zhang, M., Gao, Z., Zheng, T., Ma, Y., Wang, Q., Gao, M., & Sun, X. (2018). A bibliometric analysis of biodiesel research during 1991–2015. *Journal of Material Cycles and Waste Management*, 20(1), doi:10-18. 10. 1007/s10163-016-0575-z

[8] Saini, P., Gupta, C., & Shankar, R. (2019). Characterization of corn oil biodiesel and its application in diesel engine. *Energy Sources, Part A: Recovery, Utilization, and Environmental Effects*, 45(3), 9498−9512. doi: 10.1080/15567036.2019.1679913

[9] Mishra, C., Saini, P., Singh, R.K., Azharuddin., & Rai, N. (2023). Oil Extraction from Microalgae, its Performance and Emission Analyses in Diesel Engine using Different Blending Mixtures with Fossil Diesel. In Emerging Trends in Mechanical and Industrial Engineering. *Lecture Notes in Mechanical Engineering* (pp. 205−221). Springer, Singapore. doi: 10.1007/978-981-19-6945-4_15

[10] Sathish, S., Narendrakumar, G., Vaithyasubramanian, S., & Sinduri, E. (2021). Mechanistic model for the batch extraction of oil from avocado seeds available for biofuel production. *International Journal of Green Energy*, 18(15), 1645−1657. doi: 10.1080/15435075.2021.1930001

[11] Ahmad, K., & Saini, P. (2022). Effect of butanol additive with mango seed biodiesel and diesel ternary blends on performance and emission characteristics of diesel engine. *Energy Sources, Part A: Recovery, Utilization, and Environmental Effects*, 44(4), 9988−10005. doi: 10.1080/15567036.2022.2143954

[12] Wang, J., Xia, A., Deng, Z., Huang, Y., Zhu, X., Zhu, X. & Liao, Q. (2022). Intensifying biofuel production using a novel bionic flow-induced peristaltic reactor: biodiesel production as a case study. *Biofuel Research Journal*, 9(4), 1721−1735. doi: 10.18331/BRJ2022.9.4.3

[13] Kumar, P., Kumar, D., Shankar, R., Kumar, S., Saini, P., & Kumar, N. (2023). Effect of synthesized lemongrass biodiesel on the performance and emission characteristics of a CI engine. *Sustainable Energy Technologies and Assessments*, 57, 103221. doi: 10.1016/j.seta.2023.103221

[14] Choudhary, A.K., Chelladurai, H., & Kannan, C. (2016). Performance analysis of bioethanol (Water Hyacinth) on diesel engine. *International Journal of Green Energy*, 13(13), 1369−1379. doi: 10.1080/15435075.2016.1185724

[15] Venu, H., Venkataraman, D., Purushothaman, P., & Vallapudi, D.R. (2019). Eichhornia crassipes biodiesel as a renewable green fuel for diesel engine applications: performance, combustion, and emission characteristics. *Environmental Science and Pollution Research*, 26(18),18084−18097. doi: 10.1007/s11356-019-04939-z

[16] Alagu, K., Venu, H., Jayaraman., J., Raju, V.D., Subramani, L., Appavu, P., & Dhanasekharn, S. (2019). Novel water hyacinth biodiesel as a potential alternative fuel for existing unmodified diesel engine: performance, combustion and emission characteristics. *Energy*, 179, 295−305. doi: 10.1016/j.energy.2019.04.207

[17] Mokhtar, M., Sukmono A., Setiapraja, H., Ma'ruf, M., Yubaidah, S., Haryono, I., Rochmanto, B., Soewono, R.T., Adhi Sukra, K.F., Thahar, A., Manurung, E., Wibowo, C.S., Widodo, S., Supriyadi, F., Abriyant, R.Y., Suntoro, D., Faridha., & Reksowardojo, I.K. (2023). Towards nationwide implementation of 40% biodiesel blend fuel in Indonesia: a comprehensive road test and laboratory evaluation. *Biofuel Research Journal*, 10(3), 1876−1889. doi: 10.18331/BRJ2023.10.3.2

[18] Soudagar, M.E.M., Nik-Ghazali, N.N., Kalam, M.A., Badruddin, I.A., Banapurmath, N.R., & Akram, N. (2018). The effect of nano-additives in diesel-biodiesel fuel blends: A comprehensive review on stability, engine performance and emission characteristics. *Energy Conversion and Management*, 178, 146−177. doi: 10.1016/j.enconman.2018.10.019

[19] Alli, A.K., & Kotha, M.M. (2023). Significance of fuel additives on the performance and emission characteristics of diesel engine with biodiesel fuel: a review. *International Journal of Ambient Energy*, 44(1), 1990−2004. doi: 10.1080/01430750.2023.2204891

[20] Damanik, N., Ong, H.C., Tong, C.W., Mahlia, T.M.I., & Silitonga, A.S. (2018) A review on the engine performance and ex-

haust emission characteristics of diesel engines fueled with biodiesel blends. *Environmental Science and Pollution Research*, 25(16), 15307−15325. doi: 10.1007/s11356-018-2098-8

[21] Manigandan, S., Gunasekar, P., Nithya, S., & Devipriya, J. (2020). Effects of nanoadditives on emission characteristics of engine fuelled with biodiesel. *Energy Sources, Part A: Recovery, Utilization, and Environmental Effects*, 42(1), 1−9. doi: 10.1080/15567036.2019.1587048

[22] Tomar, M., & Kumar, N. (2020). Influence of nanoadditives on the performance and emission characteristics of a CI engine fuelled with diesel, biodiesel, and blends – a review. *Energy Sources, Part A: Recovery, Utilization, and Environmental Effects*, 42(23), 2944−2961. doi: 10.1080/15567036.2019.1623347

[23] Devarajan, Y., Munuswamy, D.B., & Mahalingam, A. (2018). Influence of nano-additive on performance and emission characteristics of a diesel engine running on neat neem oil biodiesel. *Environmental Science and Pollution Research*, 25, 26167–26172. doi: 10.1007/s11356-018-2618-6

[24] Sundar, S.P., Vijayabalan, P., Kaliappan, V.K., Sathyamurthy, R., Kabeel, A.E., & Kamalakkannan, K. (2022). Emission reduction and performance enhancement of diesel engine fuelled using palm oil biodiesel and nanoparticle as additive. *Environment, Development and Sustainability*, 27, 22691−22710. doi: 10.1007/s10668-022-02467-4

[25] Yuvarajan, D., Babu, M.D., Kumar, N.B., & Kishore, P.A. (2018). Experimental investigation on the influence of titanium dioxide nanofluid on emission pattern of biodiesel in a diesel engine. *Atmospheric Pollution Research*, 9(1), 47−52. doi: 10.1016/j.apr.2017.06.003.

[26] Narayanasamy, B., & Jeyakumar, N. (2019). Performance and emission analysis of methyl ester of Azolla algae with TiO_2 Nano additive for diesel engine. *Energy Sources, Part A: Recovery, Utilization, and Environmental Effects*, 41(12), 1434−1445. doi: 10.1080/15567036.2018.1548519

[27] Saravankumar, P.T., Suresh, V., Vijayan, V., & Antony, A.G. (2019). Ecological effect of corn oil biofuel with SiO_2 nano-additives. *Energy Sources, Part A: Recovery, Utilization, and Environmental Effects*, 41(23), 2845−2852. doi: 10.1080/15567036.2019.1576079

[28] Dinesha, P., Kumar, S., & Rosen, M.A. (2021). Effects of particle size of cerium oxide nanoparticles on the combustion behavior and exhaust emissions of a diesel engine powered by biodiesel/diesel blend. *Biofuel Research Journal*, 8(2), 1374−1383. doi: 10.18331/BRJ2021.8.2.3

[29] Vellaiyan, S., Subbiah, A., & Chockalingam, P. (2021). Effect of Titanium dioxide nanoparticle as an additive on the working characteristics of biodiesel-water emulsion fuel blends. *Energy Sources, Part A: Recovery, Utilization, and Environmental Effects*, 43(9), 1087−1099. doi: 10.1080/15567036.2019.1634776

[30] Nutakki, P.K., Gugulothu, S.K., & Ramachander, J. (2021). Effect of metal-based SiO_2 nanoparticles blended concentration on performance, combustion and emission characteristics of CRDI diesel engine running on mahua methyl ester biodiesel. *Silicon*, 13(12), 4773−4787. doi: 10.1007/s12633-021-01001-x

[31] Praveen, A., Krupakaran, R.L., Rao, G.L.N., & Balakrishna, B. (2022). An assessment of the TiO_2 nanoparticle concentration in the C. inophyllum biodiesel blend on the engine characteristics of a DI diesel engine. *International Journal of Ambient Energy*, 43(1), 5464−5477. doi: 10.1080/01430750.2021.1953584

[32] Ramachander, J., Gugulothu, S.K., & Sastry, G.R.K. (2022). Performance and emission reduction characteristics of metal based SiO_2 nanoparticle additives blended with ternary Fuel (Diesel-MME-Pentanol) on CRDI diesel engine. *Silicon*, 14(5), 2249−2263. doi: 10.1007/s12633-021-01024-4

[33] Kumar, P., Saini, P., Kumar, D., Shankar, R., Yadav. G., & Singh, J. (2023). Experimental analysis on performance and emission characteristics of diesel engine using lemongrass biodiesel and TiO_2 nano additives blends. *NanoWorld Journal*, 9(S1), S419−S424. doi: 10.17756/nwj.2023-s1-081

[34] Jain, A., Bora, B.J., Kumar, R., Sharma, P., Medhi, B.J., Farooque, A.A., Tirth, V., Senthilkumar, N., & Peyyala. P.K. (2023). Impact of titanium dioxide (TiO_2) nanoparticles addition in Eichhornia Crassipes biodiesel used to fuel compression ignition engine at variable injection pressure. *Case Studies in Thermal Engineering*, 49, 103295. doi: 10.1016/j.csite.2023.103295

[35] Rahman, M.A., & Aziz, M.A. (2021). Biodiesel from water hyacinth biomass and its influence on CI engine performance, emission, combustion and heat loss characteristics with the induction of hydroxy. *Energy*, 224, 120151. doi: 10.1016/j.energy.2021.120151

Co-published by
Institute of Fluid-Flow Machinery
Polish Academy of Sciences
Committee on Thermodynamics and Combustion
Polish Academy of Sciences

Copyright©2026 by the Authors under licence CC BY-NC-ND 4.0

http://www.imp.gda.pl/archives-of-thermodynamics/

Optimising Injection Strategies and EGR in Modified Piston Diesel Engines Fuelled with Waste Plastic Oil

Rajammagari Hussain Vali[a]*, Vemuri Sai Srikanth[b], Mohammad Mujtaba Ahmed[c], A. Gouse Peera[a], P. Srikar[d]

[a]Department of Mechanical Engineering, Rajeev Gandhi Memorial College of Engineering and Technology, Nandyal 518501, Andhra Pradesh, India.
[b]Department of Mechanical Engineering, MRCET, Hyderabad 500100, Telangana, India.
[c]Department of Mechanical Engineering, MRECW, Hyderabad 500100, Telangana, India.
[d]Deputy Registrar, Department of Mechanical Engineering,OP Jindal University, Punjipathra, Raigarh 496109, Chhattisgarh, India.
*Corresponding author email: hussainvali.rajammagari@gmail.com

Received: 03.07.2025; revised: 10.01.2026; accepted: 30.01.2026

Abstract

Growing concerns over plastic pollution and fossil fuel depletion have driven research toward alternative fuels and engine optimisation strategies. The transition from fossil-based fuels to alternative fuels is imperative for reducing greenhouse gas emissions and addressing plastic waste. This study investigates the synergistic effects of injection pressure, ignition timing and exhaust gas recirculation on a single-cylinder diesel engine with modified piston bowl geometry using waste plastic oil-diesel blends. Waste plastic oil, derived via pyrolysis of municipal plastic waste, was blended with diesel in varying proportions (25–100%). Tests on engines were performed with varying injection pressures (200–500 bar), ignition timing (17°–23° before top dead centre) and exhaust gas recirculation rates (0–9%). Results reveal that the D25WP75 blend at 500 bar and 23° before top dead centre offers a peak brake thermal efficiency, minimum brake specific fuel consumption, and reduced emissions of CO, HC, NO_x and smoke opacity. Optimal exhaust gas recirculation at 6% further reduced NO_x. The maximum cylinder pressure and heat release rate are obtained at 73.02 bar and 52.66 J/deg. The improvement percentage in brake thermal efficiency at 500 bar for the D25WP75 blend compared with D100 is 10.8%, with a reduction in brake specific fuel consumption of 11.76%. It is also observed that NO_x reduces by 5.46%, CO by 44%, HC by 8.82% and smoke by 35.38%. The combined impact of piston geometry modification and injection strategies improved combustion uniformity and emission control. The findings suggest that integrating fuel modification with combustion optimisation offers a viable pathway to cleaner diesel engine operation.

Keywords: Injection pressure; Injection timing; Piston bowl geometry modification; Exhaust gas recirculation, Emissions; Waste plastic oil

Vol. 47(2026), No. 1, 89–100; doi: 10.24425/ather.2025.156857

Cite this manuscript as: Vali, R.H., Srikanth, V.S., Ahmed, M.M., Peera, A.G., & Srikar, P. (2026). Optimising Injection Strategies and EGR in Modified Piston Diesel Engines Fuelled with Waste Plastic Oil. *Archives of Thermodynamics*, 47(1), 89–100.

1. Introduction

Diesel engines are playing a significant role in the industrial, power, automotive and agricultural sectors because of their heavy-duty application and high thermal efficiency. However, with the increase in population, global energy demand and strict emission regulations, it is mandatory to improve fuel economy and reduce the emission concentrations evolving from diesel engines. Also, the challenge of plastic waste accumulation has become a global concern. One promising solution lies in the conversion of municipal plastic waste into usable liquid fuel via pyrolysis. Transforming waste plastic into fuel through pyrolysis provides a dual advantage, such as waste reduction and the production of energy-dense alternative fuels [1]. Recently, many

Nomenclature

Abbreviations and Acronyms

BSFC– brake specific fuel consumption
BTE – brake thermal efficiency
bTDC– before top dead centre
CA – crank angle
CO – carbon monoxide
CP – cylinder pressure
CR – compression ratio
D25WP75 – 25% diesel + 75% waste plastic oil
D50WP50 – 50% diesel + 50% waste plastic oil
D75WP25 – 75% diesel + 25% waste plastic oil
D100 – 100% diesel
EGR – exhaust gas recirculation
HC – hydrocarbon
HRR – heat release rate
IP – injection pressure
IT – ignition timing
NO_x – oxides of nitrogen
PPO – plastic pyrolysis oil
VCR – variable compression ratio
WPO – waste plastic oil
WP100 – 100% waste plastic oil

researchers have concentrated on the conversion of waste plastic into biodiesel because of increased utilisation of plastic and its waste across the globe [2]. Also, waste plastic causes pollution, which affects the environment by contaminating land and oceans mainly. It is estimated that 396 million tonnes of plastic waste were produced globally in the year 2018, which is expected to double in the next 20 years. The method known as pyrolysis is employed to convert waste plastic into plastic oil [3]. Waste plastic oil (WPO) is derived through pyrolysis, a thermochemical process in which plastic waste is decomposed at elevated temperatures in an inert atmosphere, typically in the absence of oxygen. This method breaks down long-chain polymer structures into shorter hydrocarbon molecules, yielding liquid fuel, gases and a minor amount of solid residue. The overall efficiency and product yield of the pyrolysis process can be significantly improved by introducing suitable catalysts, which promote cracking reactions and influence the composition of the resulting oil [4,5].

A comprehensive review by Pradeep et al. [6] examined the application of WPO as a fuel in diesel engines, focusing on its impact on engine performance, combustion efficiency and emissions. Their study compared thermal pyrolysis with catalytic pyrolysis and emphasised how different plastic feedstocks and catalyst types affect the quality and suitability of the oil for engine use. The review highlighted the potential of WPO as a viable alternative to conventional diesel, especially when produced and utilised under optimised conditions. Mangesh et al. [7] examined diesel engine performance using pyrolysis oil-diesel blends (5%, 10%, 15%). It was observed that the increased heat release rate (HRR) and ignition delay are attributed to alkenes in the oil. However, the blends showed a lower brake thermal efficiency (BTE) due to higher viscosity and reduced calorific value. NO_x emissions were found to be lower. In contrast, Janarthanan et al. [8] reported higher NO_x emissions with WPO, due to elevated adiabatic flame temperatures.

Pal et al. [9] tested blends from 25% to 100% plastic oil, noting a higher in-cylinder pressure (CP) and HRR, which led to increased NO_x emissions. However, BTE dropped by up to 6.8%, while CO and smoke emissions decreased by 21.8% and 4.47%, with 100% plastic oil at full load. Yaqoob et al. [10] evaluated diesel engines using 5–15% plastic pyrolysis oil (PPO) blends. The 5% blend achieved the highest thermal efficiency at 51.6%, outperforming pure diesel (47.44%), and showed reduced CO emissions. Similarly, Sudalaimani et al. [11] explored the use of WPO blends in a variable compression ratio (VCR) diesel engine. They observed that increasing the compression ratio by 12–20% improved BTE across all blends. The blends showed a slightly higher HRR and elevated combustion temperatures, leading to increased NO_x emissions. The study suggests using higher compression ratios in compression ignition (CI) engines running on plastic oil blends to optimise both BTE and brake specific fuel consumption (BSFC). Previous studies have shown mixed results for engines using WPO blends. Lower blend ratios often exhibit comparable performance to diesel, but higher WPO ratios may reduce brake thermal efficiency and increase NO_x emissions. To address these limitations, researchers have explored strategies such as adjusting injection pressure (IP), ignition timing (IT), and using exhaust gas recirculation (EGR).

Youssef et al. [12] researched the impact of varying compression ratio (CR) and IT, affecting emissions of NO_x in engines powered by diesel, biodiesel and butanol blends. They observed that advancing IT from 15° to 5° before the top dead centre (bTDC) significantly lowered NO_x emissions, a trend also noted by Munivenkaeshappa et al. [13]. Similarly, Khoa et al. [14] achieved NO_x reduction through increased EGR. Ashok et al. [15] studied diesel engines running on pure calophyllum inophyllum biodiesel under various ITs and EGR levels. While retarding injection timing reduced NO_x by 11%, it compromised engine performance. Advancing timing led to a 21% rise in NO_x. EGR was more effective, with NO_x emissions dropping by 51%, 54% and 57% at increasing EGR rates under full load. Table 1 shows a brief description of the effects of EGR and WPO biodiesel blends on diesel engines.

Barik et al. [24] also reported improved performance and lower hydrocarbon (HC) emissions when IT was advanced from 23° to 24.5° bTDC, compared to standard timing and diesel. Agarwal et al. [25] evaluated the cumulative impact of IT and IP on spray behaviour, combustion and emissions using a B20 blend derived from karanja oil. It has been noticed that there is a reduction in NO_x emissions. Hirkude et al. [26] examined the influence of IT, IP and CR on diesel engine performance using a blend of WPO and diesel. The study revealed an increase in BTE and a reduction in brake specific fuel consumption (BSFC). However, raising the compression ratio from 18 to 19 slightly reduced BTE and increased BSFC – an expected engine behaviour. An optimal performance was achieved at 27° bTDC IT, 250 bar IP, and a CR of 18. EGT rose with increases in IP, IT

and CR, while smoke opacity declined. Shrivastava et al. [27] conducted an experimental evaluation of roselle biodiesel blends under varying IP and engine load conditions. Their findings indicated that at an IP of 220 bar, the RB20 blend exhibited a marginal increase in CO emissions by approximately 1.6%, relative to conventional diesel. However, this was accompanied by a reduction in smoke and NO_x emissions by 2.2% and 3.18%, respectively, suggesting that optimised injection parameters can enhance the combustion characteristics of biodiesel while mitigating key exhaust pollutants. Teoh et al. [28] used the grey-Taguchi method to optimise diesel-coconut oil blends based on parameters such as blend ratio, engine speed and load. The method identified the best blend for minimising emissions and maximising performance at 3850 rpm and 25% load.

Table 1. The effect of EGR and WPO biodiesel blends on diesel engines.

Paper	Focus	Key findings
Chaitanya et al. [16]	1-hexanol/WPO blends, EGR	Higher EGR rates reduce NO_x but decrease brake thermal efficiency; higher alcohol blends can mitigate some emission issues.
Kumar et al. [17]	WCO+WPO blends, EGR, optimisation	Optimal blend and EGR settings improve efficiency and emissions; RSM is used for optimisation.
Saha et al. [18]	EGR, nano-additives, WPO-diesel-water emulsion	5% EGR offers the best trade-off: lower NO_x, minimal penalty on CO, HC, smoke, and fuel consumption.
Kaewbuddee et al. [19]	n-butanol/WPO blends	Alcohol addition reduces efficiency, increases HC/CO; optimisation needed for best trade-off.
Rajendran et al. [20]	Plasto-oil/diesel blends, PCCI, EGR	EGR reduces NO_x, but can increase carbon-based emissions; blends outperform diesel alone.
Saravanan et al. [21]	WPO, EGR, nano-coated chamber	EGR reduces NO_x, but increases CO/HC; nano-coating improves combustion performance.
Jayanth et al. [22]	WHDPE oil/diesel blends, EGR, injection strategy	10% EGR with optimized injection improves BTE, reduces NO_x and smoke.
Balaji et al. [23]	WPO/diesel blends, EGR	EGR (up to 15%) reduces NO_x, increases smoke; blends operate without engine modification.

Kumar et al. [29] explored the effects of EGR and IT on the performance and emission behaviour of CI engine fuelled with biofuels-diesel blends. At the optimisation point, NO_x was reduced to 12.4% and BSFC was increased to 2.9% when compared to that of neat diesel. Hirkude et al. [30] examined the combined effects of CR, IT and IP on the performance and emission behaviour of a CI engine operating on a blend of waste fried oil biodiesel blends. Their experimental analysis identified optimal operating parameters at a CR of 18, IT of 27° bTDC and an IP of 250 bar. Adjustments to both IT and CR were found to significantly enhance overall engine efficiency while concurrently reducing harmful exhaust emissions, thereby confirming the importance of integrated tuning for biodiesel applications.

The earlier research has shown that the modification of injection parameters with biodiesel blends has shown a significant effect on diesel engine working characteristics. However, studies often examine these variables in isolation, without considering the synergistic effects of modifying the combustion chamber geometry, specifically the piston bowl shape. In view of this, further studies are needed to study the impact of different injection strategies on a modified piston diesel engine with waste plastic oil.

Therefore, the current work made an attempt to change the piston geometry, and in addition to this, the injection pressure and injection timing of the engine were varied to study the effect on the modified piston geometry engine with varied proportions of WPO. The study is novel in its integrated approach, specifically the use of waste plastic oil biodiesel with a modified piston bowl and adjusted injection parameters. Further, the cooled EGR has been mixed with the intake air. The waste plastic oil biodiesel blends were used as a fuel for a single cylinder common rail direct injection (CRDI) VCR diesel engine. To the best of the author's knowledge, no study has been conducted on the modification of piston bowl geometry with different injection strategies and waste plastic oil as a fuel. The gap has been filled with the present study.

The current research work is split into three stages. In the first stage, the biodiesel was produced from waste plastic by the pyrolysis process. In the second stage, piston geometry modification was carried out to find out the influence on the engine working characteristics. In the third stage, the effects of injection pressure, injection timing and EGR on the modified piston diesel engine have been investigated. The present investigation has been carried out at a constant speed of 1500 rpm.

2. Materials and methods

2.1. Waste plastic oil production

In this investigation, WPO has been chosen as a biodiesel source for blending with conventional diesel fuel. The production of WPO was carried out using the pyrolysis technique, a thermochemical method that decomposes plastic waste into usable liquid fuel in an oxygen-free environment. The conversion process was conducted using a dedicated pyrolysis unit, which is illustrated in Fig. 1.

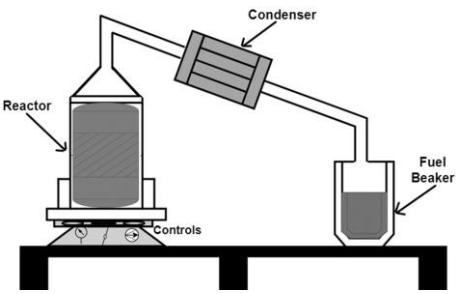


Fig. 1. Plastic oil production from waste plastic (pyrolysis).

This setup enabled the recovery of liquid hydrocarbons suitable for engine testing after appropriate condensation and collection. For the purpose of this experimental investigation, waste plastics were obtained from the municipal solid waste management department in Kurnool, Andhra Pradesh, India, and then pulverised into small pieces with sizes ranging from 0.50 to 1.5 cm^2 in area. To remove dust, dirt and unwanted particles from the plastic, it was washed with water, and a filter was used. It was washed over and over again to get rid of dirt, and then it was dried out in an electric oven set to 150°C to get rid of water. As shown in Fig. 1, the pyrolytic reactor was fed with 6 kg of waste plastic, 0.60 kg of coal (10% by weight of plastic waste), and 0.8 kg of aeolite as a catalyst in a single batch. The pyrolytic reactor consists of a heating chamber, an exhaust chute and a control unit. The sliced plastic was fed to the reactor in a sequential manner based on the batch size. The reactor operates in the range up to 900°C. A thermocouple was used to measure the temperature, and it is digitally controlled. The process followed to produce the waste plastic oil is that the crushed waste plastic is heated in a heating chamber within the temperature range of 600°C to 800°C for thermal cracking of waste plastic. The temperature was maintained for 3 hours. The produced gases due to thermal cracking of waste plastic occupied the chamber's uppermost layer before being moved to the cooling area (condenser) through the exhaust chute so that they could be condensed. For the condensation process, the cooling chamber was filled with water, which condenses the gases and forms the pyrolytic oil. The produced pyrolytic oil is collected in a beaker as illustrated in Fig.1. As shown in Fig. 2, the produced WPO was mixed with diesel fuel in various ratios. Table 2 lists the results of the test samples' properties in compliance with the American Society for Testing and Materials (ASTM) standard procedure.

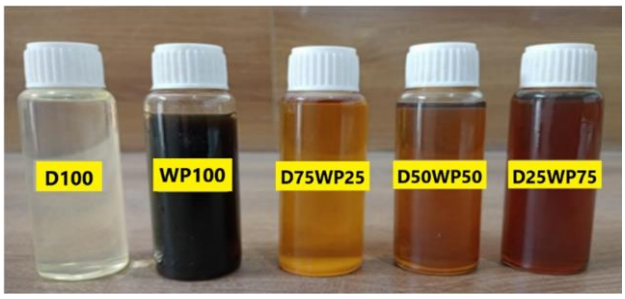


Fig. 2. Physical appearance of diesel, plastic oil and their blends.

Table 2. Fuel properties of different blends.

No.	Characteristics	WP100	WP75–D25	WP50–D50	WP25–D75
1	Kinematic viscosity at 40°C, cSt	1.45	1.55	1.57	1.47
2	Flash point, °C	Nil	27	28	35
3	Fire point, °C	32	30	34	40
4	Gross calorific value, kJ/kg	42 763	42 697	42 631	42 565
5	Density, kg/m^3	813	822	826	837

2.2. Experimental setup

To conduct the experimental analysis, a single-cylinder, water-cooled diesel engine equipped with a common rail direct injection (CRDI) system was employed. A schematic diagram of the experimental setup is presented in Fig. 3, while detailed engine specifications are listed in Table 3.

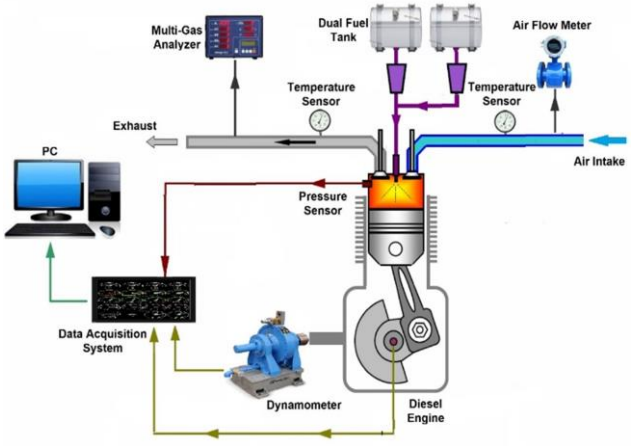


Fig. 3. Schematic experimental setup for the present study.

Table 3. Description of diesel engine.

Description	Specifications
Make	Kirloskar
Type	4 stroke single cylinder CRDI diesel engine
Compression ratio	12–18
Bore × stroke	87.5 mm × 110 mm
Swept volume	661cc
Rated power	3.5 kW
Length of connecting rod	234 mm
Rated speed	1500 rpm

Engine loading was managed using an eddy current dynamometer, which enabled precise application and control of load conditions. A proximity sensor has been employed to record engine speed, and calibrated flow transmitters were employed to determine the air and fuel flow rates. All test data, including combustion and performance parameters, were acquired and processed using a computerised engine analysis system. Exhaust emissions, specifically NO_x, HC and CO, were continuously monitored using a multi-gas analyser. The CRDI system featured electronically controlled fuel injection, allowing for independent adjustment of IP irrespective of engine speed. An external EGR loop was integrated into the intake system to reduce NO_x emissions. The recirculated exhaust gases were passed through a water-cooled heat exchanger to lower their temperature before mixing with the intake air.

2.3. Engine piston bowl geometry modification

For this experimental work, instead of the traditional hemispherical cavity combustion chamber (HCP), the piston bowl shape

was modified to create a toroidal cavity combustion chamber (TCP). Surface grinding was used to remove material until the desired form was obtained. The bowl capacity was maintained constant for both combustion chamber arrangements, such that the compression ratio matched that of the typical engine. Figure 4 depicts the cross-sectional and photographic views of the two pistons used in this study.

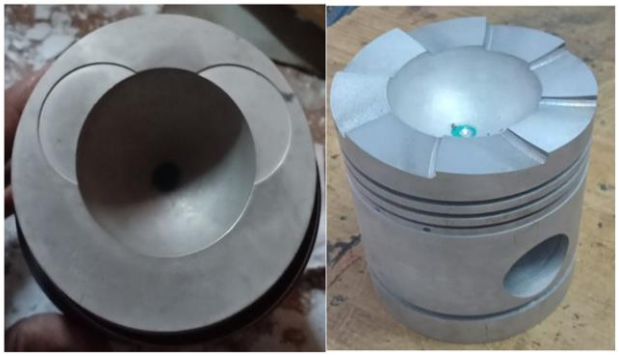


Fig. 4. Real view of unmodified and modified piston geometry.

Diesel engine combustion is influenced by the combustion chamber's form and the fluid dynamics present inside. The geometry of the combustion chamber must be thoroughly studied since the combustion chamber shape can act as a guide for the turbulence. The parameters used to choose the design of the combustion chamber will produce a strong squish and air movement, comparable to that of the well-known smoke ring. In the combustion chambers, the coupling between the swirl, squish, bowl shape, and turbulence is even more prominent. The quality of air fuel mixing and squish action is determined by the cavity created by the modified piston.

2.4. Injection pressure variation

The variation in injector opening pressure was achieved by manually adjusting the spring preload within the injector assembly. This was done by tightening or loosening the adjustment screw located at the top of the injector housing, thereby altering the force required to lift the nozzle valve. Experimental trials were subsequently conducted at four distinct injection pressures, such as 200 bar, 300 bar, 400 bar and 500 bar, using the engine equipped with the modified piston bowl geometry. These settings were selected to evaluate the impact of IP on fuel atomisation, combustion behaviour and emission characteristics under controlled test conditions.

2.5. Exhaust gas recirculation setup

This experiment uses the cold EGR approach since it lowers cylinder temperature and raises charge density. The inlet manifold was designed to receive the exhaust gases. Based on optimisation work done by the authors [31], the rate of recirculation was varied. The exhaust fumes were surrounded by a tube that circulates tap water, lowering the temperature of the gases to 350°C. A cold EGR with an orifice diameter of 4 mm was used in the setup.

$$\% \text{ of EGR} = (CO_2 \text{ at (inlet)})/(CO_2 \text{ at (outlet)}) \times 100.$$

The above equation shows the regulation of the exhaust gas flow by the control valve.

2.6. Modification in injection timing

The spill technique was applied in order to modify the test engines' initial IT. Finding the spill's position was made easier with the use of a specially designed adaptor with a hypodermic needle tip. By adjusting the quantity of shims inside the pump, static or original IT might be changed. The number of shims inside the fuel injection pump can be changed in order to alter the timing of the fuel injection.

Three shims were previously fitted in the injection pump when the engine was initially manufactured. A 0.3 mm thick shim was added to acquire the delayed IT, then the shim was removed to obtain the advanced IT. Depending on how many shims are in the pump, each shim has the capacity to deliver either advanced or retarded flow.

The time of injection was manually changed by employing the spill timing method by altering the number of shims within the fuel pump assembly. Each addition or removal of shims effectively advanced or retarded the injection timing, allowing for precise calibration of fuel delivery relative to the crank angle. The engine was significantly affected by the changes to the fuel injection timing brought about by [32].

3. Results and discussion

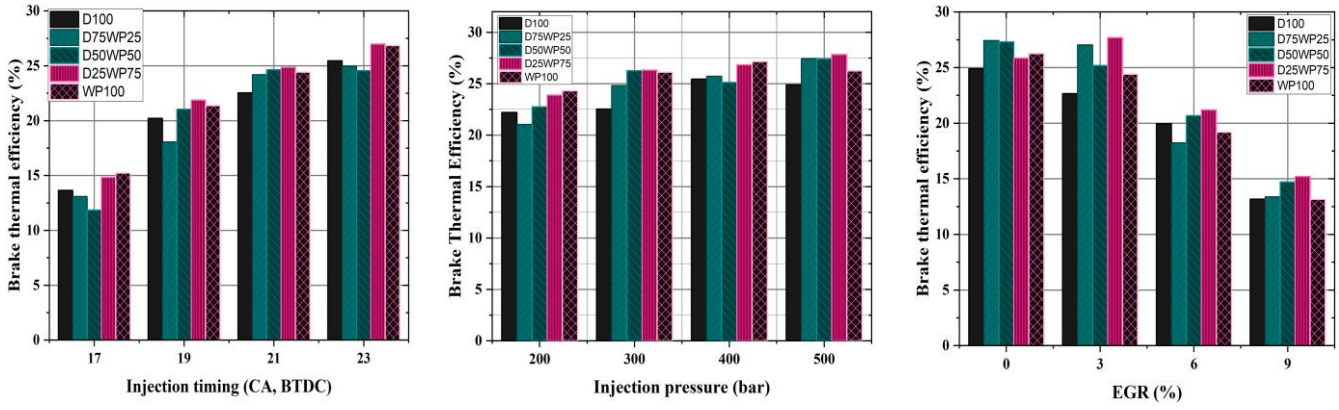
The performance, combustion and emissions characteristics of the engine with a modified geometry piston at different injection strategies (IT and IP) and variable EGR in percentage were determined and compared with pure diesel.

3.1. Brake thermal efficiency

Brake thermal efficiency (BTE) represents the effectiveness of converting chemical energy from the fuel into useful mechanical energy. This parameter also helps in finding the combustion behaviour of the engine [33]. In this study, a consistent increase in BTE was observed with increasing IP and advanced IT, whereas a reduction in BTE was noted with the increased EGR ratio. Figure 5(a, b and c) shows the variations in BTE of the modified piston geometry engine with neat diesel, plastic oil and their blends at different injection strategies (IT and IP) and various EGR percentages.

The highest BTE of 27.69% was achieved for the D25WP75 blend at 500 bar and 23° bTDC. This improvement can be attributed to several synergistic factors such as enhanced atomisation, intense swirl, turbulence and a higher calorific value of WPO. Moreover, the fuel blends D25WP75 and WP100 show a maximum BTE compared with the other fuel blends at all IPs and IT.

Notably, at lower IPs (200–300 bar), BTE values were significantly lower due to poor atomisation, especially for higher WPO blends, confirming that the injection pressure plays a dominant role in fuel-air preparation for viscous fuels.

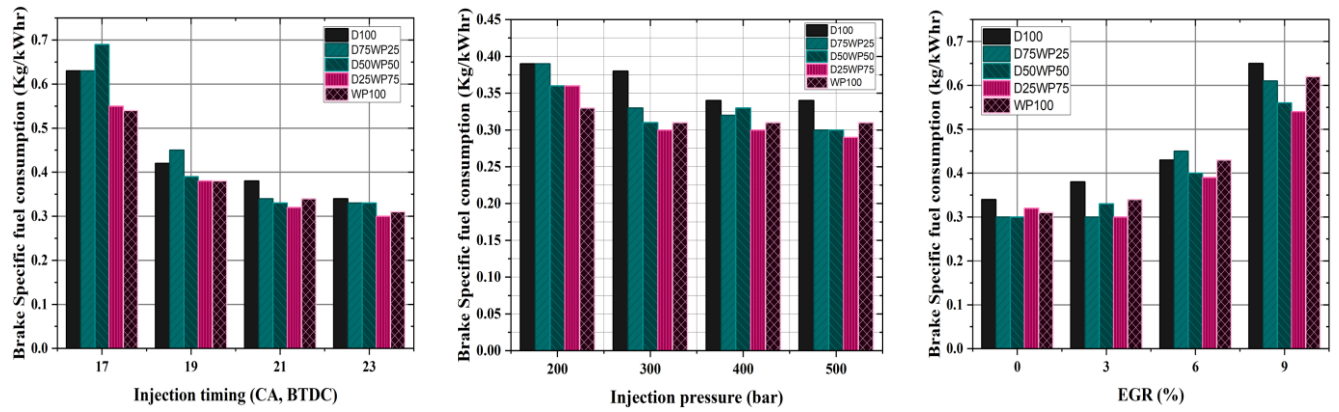


a) b) c)

Fig. 5. Change in BTE in relation to: a) IT, b) IP, c) EGR.

3.2. Brake specific fuel consumption

Brake specific fuel consumption **(**BSFC) is inversely related to engine efficiency, representing the amount of fuel consumed per unit of power output. Figure 6(a, b and c) depicts the variation in BSFC of the engine with modified piston head geometry, fuelled with neat diesel and its plastic oil blends, with respect to different injection strategies and EGR. A consistent decline in BSFC has been noted with increasing IPs and IT across all WPO blends. The lowest BSFC, 0.31 kg/kWh, was recorded for the D25WP75 blend at 500 bar and 23° bTDC. This was primarily due to efficient combustion facilitated by enhanced atomisation and optimal combustion phasing [34]. Figure 6a shows the plot of BSFC with respect to IT (CA, BTDC), and Fig. 6b illustrates the variation in BSFC with respect to IP, which shows that advanced IT and higher IPs also reduce BSFC for modified piston geometry because of better atomisation and vaporisation. It was also noted that BSFC increases with the increase in EGR percentage, and a minimum was found at 3% EGR for the blend D25WP75, as the carbon present in the exhaust gases leads to improper combustion of fuel.



a) b) c)

Fig. 6. Change in BSFC in relation to: a) IT, b) IP, c) EGR.

3.3. Hydrocarbon emissions

Hydrocarbon (HC) emissions typically originate from flame quenching and crevice volume fuel deposition. The influence of IT, IP and EGR rate on HC emissions is illustrated in Fig. 7(a, b, c).

From Fig. 7a, it is observed that for conventional diesel, HC levels are relatively higher at an IT of 18° bTDC and decrease progressively as the timing is advanced to 23° bTDC. Notably, at 21° and 23° bTDC, higher concentration WPO-based blends emit lower hydrocarbons than diesel, likely due to more favourable combustion phasing and enhanced volatility of the blend. Figure 7b shows that IP exerts a notable effect on HC formation. For neat diesel, HC emissions tend to increase with pressure, peaking at 500 bar. However, under the same condition, WPO blends – particularly at higher concentrations – demonstrate reduced HC emissions. This contrast suggests that high-pressure injection enhances fuel atomisation more effectively in WPO blends, improving vaporisation and reducing incomplete combustion zones. As shown in Figure 7c, increasing the EGR rate up to 9% contributes to a further decline in HC emissions for all tested blends. This improvement is attributed to optimised in-cylinder thermal conditions that facilitate oxidation, alongside the dilution effect of recirculated gases, which moderates local flame quenching [35,36]. Additionally, the modified piston

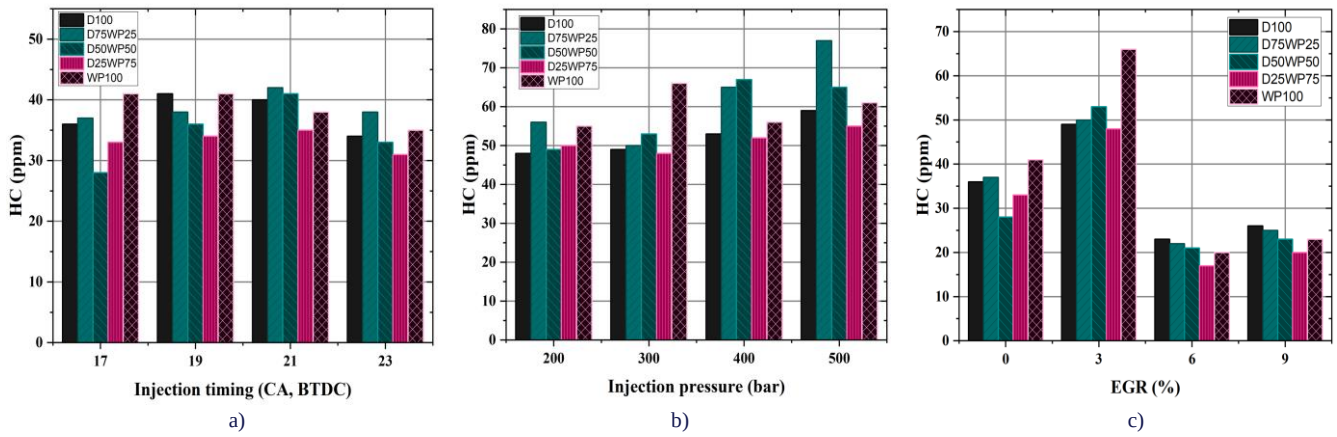


Fig. 7. Change in HC in relation to: a) IT, b) IP, c) EGR.

bowl geometry contributes to this reduction by promoting efficient air-fuel mixing and limiting quench layer formation.

3.4. Carbon monoxide emissions

Carbon monoxide (CO) emissions arise from incomplete combustion, particularly in rich zones or under low oxygen availability [37]. Other factors that may affect CO emissions include delay duration, short residence time, insufficient or excessive equivalence ratios, and insufficiently high flame temperature [38]. The effects of IT, IP and EGR percentage on CO emissions for diesel, WPO and their respective blends are illustrated in Fig. 8(a, b, c).

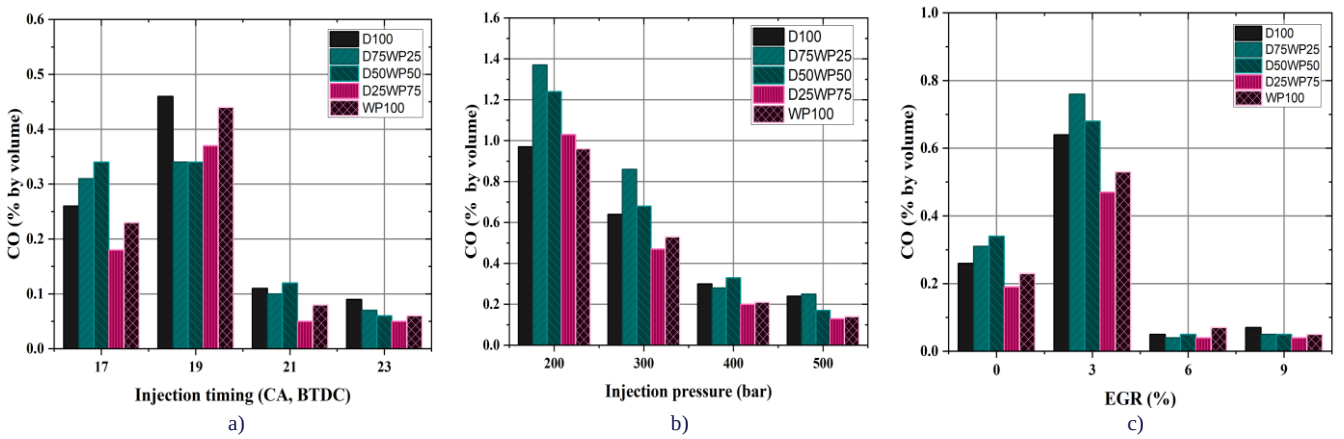


Fig. 8. Change in CO emission in relation to: a) IT, b) IP, c) EGR.

As shown in Fig. 8a, the pure WPO blend (WP100) consistently produced lower CO emissions than conventional diesel across all injection timings. Advancing IT from 19° to 23° crank angle (bTDC) led to noticeable reductions in CO emissions across the fuel samples – by approximately 8%, 16.5% and 10.3%, respectively. These reductions can be attributed to improved combustion phasing, which ensures that a higher fraction of the fuel undergoes oxidation within the optimal crank angle window. A similar trend is evident in Fig. 8b, where increasing the injection pressure resulted in a marked decline in CO emissions for all tested fuels. This behaviour can be linked to the finer fuel spray and enhanced atomisation achieved at higher pressures, which promote thorough mixing with air and more complete combustion.

Figure 8c presents the relationship between CO emissions and EGR percentage. It is evident that CO emissions decreased progressively with increasing EGR rates up to 9% across all fuel types. This trend can be explained by the dilution effect of EGR, which lowers combustion temperatures and facilitates more uniform in-cylinder combustion, thus minimising localised rich zones where CO typically forms. The piston bowl modification, which enhances in-cylinder swirl and promotes superior fuel vaporisation, likely contributed to this reduction as well. Additionally, the higher heat release rate (HRR) observed under optimal injection settings supports faster flame propagation and more complete fuel oxidation, further suppressing CO formation [39].

3.5. Oxides of nitrogen emissions

The formation of oxides of nitrogen (NO_x) during combustion is primarily governed by three interrelated factors: oxygen concentration within the combustion chamber, peak flame temperature, and the residence time of the high-temperature gas. Figure 9(a, b, c) illustrates the variation in NO_x emissions for diesel and WPO-based blends under different injection strategies and EGR rates.

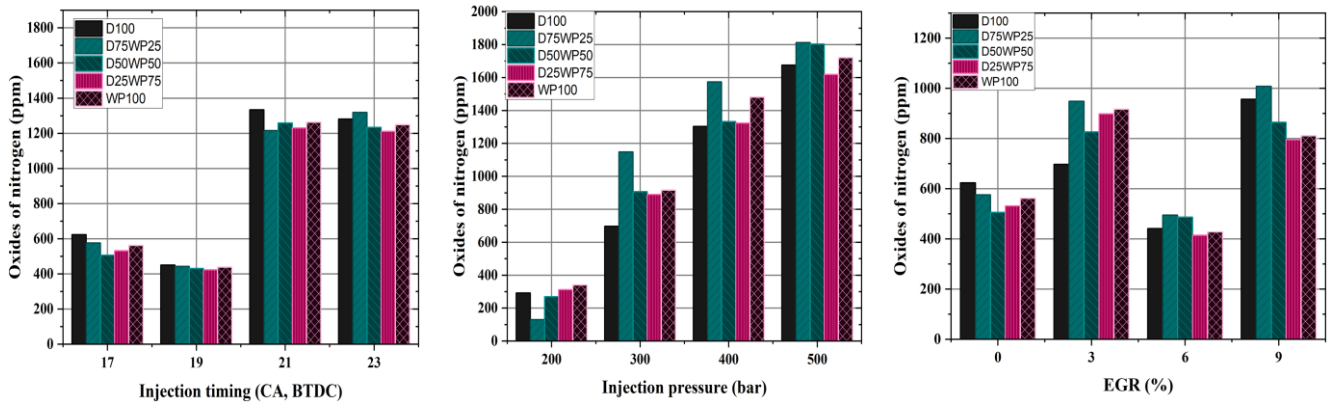


Fig. 9. Change in NO_x emission in relation to: a) IT, b) IP, c) EGR.

Figure 9a displays the effect of IT on NO_x generation across various fuel blends, including diesel, D75WP25, D50WP50, D25WP75 and WP100. The results indicate that NO_x emissions tend to increase when injection timing is advanced (i.e., closer to the top dead centre), due to the higher in-cylinder pressures and elevated flame temperatures resulting from increased premixed combustion. Conversely, retarding the injection timing to 19° bTDC significantly lowered NO_x formation across all fuel samples. This reduction is linked to delayed combustion phasing, which reduces peak temperature and shortens the duration available for thermal NO_x formation [40,41].

Figure 9b explores the influence of varying IP from 200 bar to 500 bar, on NO_x emissions. A clear trend emerges: as IP rises, NO_x emissions increase notably. This behaviour can be attributed to improved fuel atomisation and air–fuel mixing at higher pressures, which enhances combustion efficiency but also raises combustion temperature – a key driver of NO_x synthesis [42].

The effect of EGR percentage on NO_x mitigation is shown in Fig. 9c. Among the tested EGR rates, 6% emerged as the most effective in reducing NO_x emissions. Introducing EGR into the intake stream displaces a portion of the intake air with inert gases, which in turn lowers oxygen concentration and peak combustion temperature, both essential for limiting NO_x formation. Notably, beyond 6%, additional EGR did not yield significant further reductions and occasionally resulted in compromised combustion stability and elevated hydrocarbon emissions. These observations are consistent with findings by Leung et al. [43], who noted that advancing the injection timing increases peak pressure and temperature, thereby promoting NO_x formation.

3.6. Smoke opacity

The influence of IT, IP and EGR rate on smoke opacity for all tested fuel blends, using a modified piston bowl geometry, is presented in Fig. 10(a, b, c).

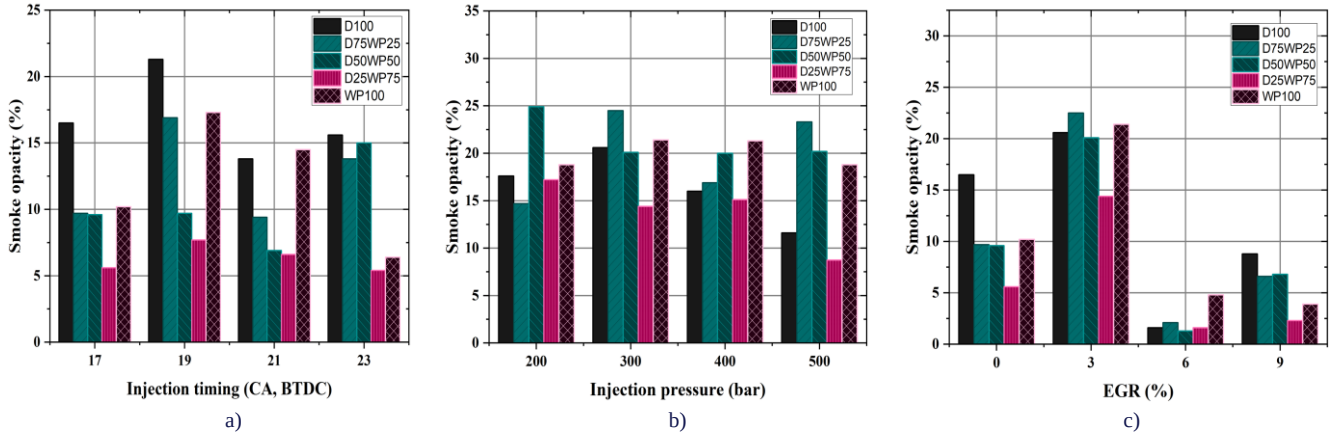


Fig. 10. Change in Smoke Opacity emission in relation to: a) IT, b) IP, c) EGR.

Across all conditions, the D25WP75 blend consistently exhibited lower smoke in contrast to other blends and baseline diesel, demonstrating the effectiveness of the toroidal piston design in improving combustion efficiency. The reduction in smoke emissions is largely attributed to enhanced air motion within the cylinder, which promoted more effective air-fuel mixing and reduced the presence of fuel-rich zones that typically lead to soot formation.

Figure 10a shows the variation of smoke opacity with IT. At a timing of 23° bTDC, D25WP75 achieved the lowest smoke

value of 5.3%, a marked improvement over other injection timings and all other fuel combinations tested. Damodharan et al. [44] also noted a similar kind of increment in their studies. This decrease is a result of more complete combustion achieved by better premixing and combustion phasing at this timing. Figure 10b displays smoke emissions as a function of injection pressure. At 500 bar, the D25WP75 blend recorded a smoke opacity of just 8.2%, which is significantly lower than that of diesel and other blends at the same pressure. In their studies, Saba et al. [45] also found that the rise in injection pressure lowers the smoke opacity. Figure 10c illustrates the impact of EGR on smoke emissions. At an EGR rate of 6%, the D25WP75 blend yielded the lowest smoke opacity of 1.1%, benefiting from moderated combustion temperatures and extended ignition delay, which allowed more time for fuel-air mixing. Collectively, these results show that the application of a modified piston bowl geometry, combined with optimised injection and EGR strategies, dramatically reduces smoke emissions. Specifically, in comparison to neat diesel, smoke opacity for the D25WP75 blend was reduced by approximately 62% at 23° bTDC injection timing, 44% at 500 bar injection pressure, and 32% at 6% EGR. These reductions confirm the synergy between in-cylinder flow enhancements and precise fuel delivery control in achieving cleaner combustion with a waste plastic oil blend.

3.7. Cylinder pressure

Figure 11 depicts the fluctuation in in-cylinder pressure versus crank angle under optimal conditions for various fuel blends. Several factors influence cylinder pressure development during combustion, including the energy density and volatility of the fuel, ignition delay and the extent of premixed combustion [46,47].

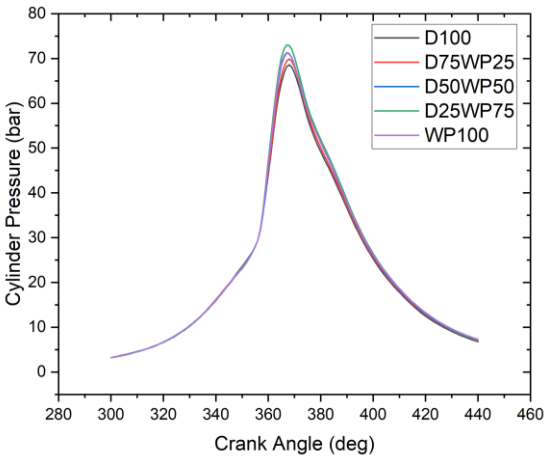


Fig. 11. CP variation in relation to crank angle.

The incorporation of WPO into diesel resulted in a noticeable rise in peak CP for blended fuels compared to neat diesel. Mangesh et al. [48] also noticed that the addition of WPO raises the cylinder pressure in their studies. Among the blends, the D25WP75 blend exhibited the highest CP peak. Quantitatively, the peak cylinder pressures for diesel, D75WP25, D50WP50, D25WP75 and WP100 were observed at 68.57 bar at 368° crank angle (CA), 69.47 bar at 367° CA, 71.21 bar at 367° CA, 73.02 bar at 366° CA and 71.33 bar at 368° CA, respectively. Compared to diesel, the percentage increases in peak pressure were 2.05% for D75WP25, 3.85% for D50WP50 and 4.02% for D25WP75. These results confirm that blending WPO with diesel enhances in-cylinder combustion characteristics, particularly when combined with geometrical and injection optimisations. The elevated peak pressures reflect a more rapid and complete combustion process, which is advantageous for thermal efficiency.

3.8. Heat release rate

Figure 12 shows how the heat release rate (HRR) varies with crank angle for different fuel mixes under optimal operating conditions. HRR is a vital combustion parameter that provides insight into the energy liberation characteristics of the fuel-air mixture within the cylinder. During the ignition delay phase, HRR registers negative values due to the latent heat absorbed during fuel vaporisation and thermal losses to the cylinder walls. Once auto-ignition occurs, HRR becomes positive and exhibits a steep rise, marking the commencement of premixed combustion [49].

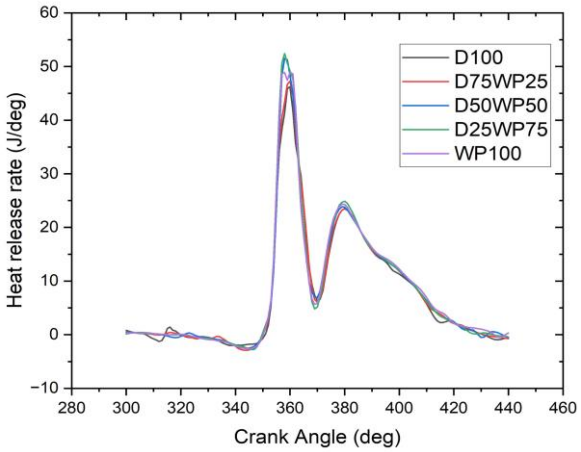


Fig. 12. HRR variation in relation to crank angle.

The experimental outcomes showed that increasing the concentration of WPO in the diesel blend enhances HRR, particularly during the premixed combustion phase. This enhancement is attributed to more favourable combustion conditions enabled by improved volatility and better in-cylinder mixing facilitated by the modified piston bowl geometry. Blends containing higher proportions of WPO exhibited a noticeable advancement in the CA position of peak HRR compared to neat diesel, reflecting a reduction in ignition delay and earlier combustion onset.

Zhang et al. [50] also noticed the same pattern in HRR by adding WPO to diesel blends. Among the tested fuels, the D25WP75 blend delivered the highest HRR peak of 52.66 J/deg at 357° CA, indicating the superior combustion intensity. In comparison, the peak HRR values for diesel, D75WP25, D50WP50 and WP100 were 46.25 J/deg at 360° CA, 47.27 J/deg at 359° CA, 52.48 J/deg at 358° CA and 48.94 J/deg at 360° CA, respectively. These results correspond to an in-

crease of 2.2%, 13.5%, 13.85% and 5.81% in HRR for D75WP25, D50WP50, D25WP75 and WP100 blends relative to diesel. The shift in peak position to earlier crank angles with increasing WPO concentration underscores the role of pre-mixed combustion enhancement in accelerating the heat release process.

4. Conclusions

This experimental investigation explored the combined effects of WPO blending, injection strategies and EGR on the performance, combustion and emission behaviour of a diesel engine equipped with a modified piston bowl geometry. The findings provide compelling evidence that strategic integration of fuel composition and engine parameter optimisation can significantly enhance combustion efficiency and reduce pollutant formation.

Among the tested configurations, the D25WP75 blend (25% diesel and 75% WPO) demonstrated superior performance across all operating metrics. The following conclusions are drawn from the study:

- All WPO-diesel blends showed improved BTE relative to neat diesel, especially under higher IP and advanced IT with no EGR. The highest efficiency gain was observed for the D25WP75 blend.
- The incorporation of WPO led to a measurable reduction in BSFC compared to pure diesel. Specifically, at 23° CA injection timing, the D25WP75 blend exhibited a BSFC decrease of 8.81% relative to diesel.
- Emissions of CO and HC declined with increasing IP and IT for all blends. The D25WP75 blend consistently reported the lowest CO and HC levels across test conditions.
- A rise in NO_x emissions has been noticed with increased IP and advanced IT, due to elevated combustion temperatures. However, this effect was mitigated by introducing cooled EGR. A 6% EGR rate proved optimal in reducing NO_x without adversely affecting performance.
- WPO blends exhibited a pronounced reduction in smoke emissions across all injection settings. Notably, the D25WP75 blend at 23° CA reduced smoke opacity by approximately 64.1% compared to diesel, attributable to improved air-fuel mixing and in-cylinder turbulence.

The optimal engine configuration – D25WP75 blend, 500 bar injection pressure, 23° CA injection timing and 6% cooled EGR – achieved a balanced improvement in efficiency and emissions.

References

[1] Awogbemi, O., & Von Kallon, D.V. (2023). Achieving affordable and clean energy through conversion of waste plastic to liquid fuel. *Journal of the Energy Institute*, 106, 101154. doi: 10.1016/j.joei.2022.101154

[2] Miandad, R., Rehan, M., Barakat, M.A., Aburiazaiza, A.S., Khan, H., Ismail, I.M., Dhavamani, J. Gardy, J. Hassanpour A, & Nizami, A.S. (2019). Catalytic pyrolysis of plastic waste: moving toward pyrolysis based biorefineries. *Frontiers in Energy Research, Sec. Bioenergy and Biofuels*, 7, 437000. doi: 10.3389/fenrg.2019.00027

[3] Hussam, W.K., Nabi, M.N., Chowdhury, M.W., Hoque, M.E., Rashid, A.B., & Islam, M.T. (2021). Fuel property improvement and exhaust emission reduction, including noise emissions, using an oxygenated additive to waste plastic oil in a diesel engine. *Biofuels, Bioproducts and Biorefining*, 15(6), 1650−1674. doi: 10.1002/bbb.2262

[4] Damodharan, D., Rajesh Kumar, B., Gopal, K., De Poures, M. V., & Sethuramasamyraja, B. (2019). Utilization of waste plastic oil in diesel engines: a review. *Reviews in Environmental Science and Bio/Technology*, 18(4), 681−697. doi: 10.1007/s11157-019-09516-x

[5] Raguraman, D., Kumar, A., Prasanna Raj Yadav, S., Patil, P.Y., Samson Isaac, J., Sowmya Dhanalakshmi, C., Madhu, P., & Isaac Joshua Ramesh Lalvani, J. (2021). Performance and emission characteristics of pyrolysis oil obtained from neem de Oiled cake and waste polystyrene in a compression ignition engine. *Advances in Materials Science and Engineering*, 2021(1), 3728852. doi: 10.1155/2021/3728852

[6] Pakiya Pradeep, A., & Gowthaman, S. (2022). Combustion and emission characteristics of diesel engine fuelled with waste plastic oil–a review. *International Journal of Ambient Energy*, 43(1), 1269−1287. doi: 10.1080/01430750.2019.1684994

[7] Mangesh, V.L., Padmanabhan, S., Tamizhdurai, P., & Ramesh, A. (2020). Experimental investigation to identify the type of waste plastic pyrolysis oil suitable for conversion to diesel engine fuel. *Journal of Cleaner Production*, 246, 119066. doi: 10.1016/j.jclepro.2019.119066

[8] Janarthanan, K., & Sivanandi, P. (2022). Extraction and characterization of waste plastic pyrolysis oil for diesel engines. *Journal of Cleaner Production*, 366, 132924. doi: 10.1016/j.jclepro.2022.132924

[9] Pal, S., Kumar, A., Ali, M.A., Gupta, N.K., Pandey, S., Ghodkhe, P.K., Bhurat, S., Alam, T., Eldin, S.M. & Dobrota, D. (2023). Experimental evaluation of diesel blends mixed with municipal plastic waste pyrolysis oil on performance and emission characteristics of CI engine. *Case Studies in Thermal Engineering*, 47(8), 103074. doi: 10.1016/j.csite.2023.103074

[10] Yaqoob, H., Ali, H.M., Sajjad, U., & Hamid, K. (2024). Investigating the potential of plastic pyrolysis oil-diesel blends in diesel engine: Performance, emissions, thermodynamics and sustainability analysis. *Results in Engineering*, 24, 103336. doi: 10.1016/j.rineng.2024.103336

[11] Sudalaimani, A., Rajendran, B., Jothi, T., & Mariappan, M. (2024). Combustion, emission, and performance characteristics of hybrid biofuel at different compression ratios: Original scientific paper. *Chemical Industry & Chemical Engineering Quarterly*, 30(3), 207−221. doi: 10.2298/CICEQ230203024A

[12] Youssef, A., & Ibrahim, A. (2024). A numerical investigation into the effect of altering compression ratio, injection timing, and injection duration on the performance of a diesel engine fuelled with diesel–biodiesel–butanol blend. *Clean Energy*, 8(5), 73−96. doi: 10.1093/ce/zkae055

[13] Munivenkaeshappa, M.D., Mannar, U.R., Banapurmath, N.R., Reddy, C.P., Halewadimath, S.S., Sajjan, A.M., Harari, P.A., Vadlamudi, C., & Krishnappa, S. (2024). Effect of Injection Timing on the Dual Fuel Engine Performance Operated with Hydrogen and Nano-Biodiesel Blends. *Journal of Advanced Research in Fluid Mechanics and Thermal Sciences*, 114(1), 13−29. doi: 10.37934/arfmts.114.1.1329

[14] Khoa, N.X., Nghia, N.T., Quan, V.H., & Ngoc, N.A. (2024). The effects of EGR and oxygen content on the GCI engine performance under two-injection modes and fueled biodiesel blends. *Arabian Journal for Science and Engineering*, 49(8), 10859−10866. doi: 10.1007/s13369-023-08477-2

[15] Ashok, B., Nanthagopal, K., Mohan, A., Johny, A., & Tamilarasu, A. (2017). Comparative analysis on the effect of zinc oxide and ethanox as additives with biodiesel in CI engine. *Energy*, 140, 352−364. doi: 10.1016/j.energy.2017.09.021

[16] Chaitanya, A.V.K., & Mohanty, D.K. (2024). Influence of 1-Hexanol/Waste Plastic Oil Blends on Combustion, Performance, and Emission Characteristics of a Common Rail Direct Injection Diesel Engine. *ACS Omega*, 10(1), 456−472. doi: 10.1021/acsomega.4c06693

[17] Kumar, M., Gautam, R., & Ansari, N.A. (2024). Optimisation of an experimental and feasibility research on a CRDI diesel engine based on a blend of waste cooking oil and waste plastic oil using RSM: A value addition for disposed waste oil. *Journal of the Energy Institute*, 117, 101564. doi: 10.1016/j.joei.2024.101564

[18] Saha, D., Roy, B., Pattanayak, S., Mishra, L., & Kundu, P.P. (2024). Performance, emission, combustion, exergy, exergoeconomic and sustainability analyses of EGR incorporated CI engine fuelled with areca nut husk nano-additive dosed plastic oil-water-diesel emulsion blend. *Thermal Science and Engineering Progress*, 47, 102317. doi: 10.1016/j.tsep.2023.102317

[19] Kaewbuddee, C., Maithomklang, S., Aengchuan, P., Wiangkham, A., Klinkaew, N., Ariyarit, A., & Sukjit, E. (2023). Effects of Alcohol-Blended Waste Plastic Oil on Engine Performance Characteristics and Emissions of a Diesel Engine. *Energies*, 16(3), 1281. doi: 10.3390/en16031281

[20] Rajendran, K.M., Kumar, D., Lamba, B.Y., Ghodke, P.K., Sharma, A.K., Matsakas, L., & Patel, A. (2023). Effect of Plasto-Oil Blended with Diesel Fuel on the Performance and Emission Characteristics of Partly Premixed Charge Compression Ignition Engines with and without Exhaust Gas Recirculation (EGR). *Energies*, 16(9), 3750. doi: 10.3390/en16093750

[21] Saravanan, P., Ettappan, M., Kumar, N., & Elangkeeran, N. (2022). Exhaust Gas Recirculation on a Nano-Coated Combustion Chamber of a Diesel Engine Fueled with Waste Plastic Oil. *Sustainability*, 14(3), 1148. doi: 10.3390/su14031148

[22] Jayanth, B., Depoures, M., Kaliyaperumal, G., Dillikannan, D., Jawahar, D., Palani, K., & Shivappa, G. (2021). A comprehensive study on the effects of multiple injection strategies and exhaust gas recirculation on diesel engine characteristics that utilize waste high density polyethylene oil. *Energy Sources, Part A: Recovery, Utilization, and Environmental Effects*, 47, 7749−7766. doi: 10.1080/15567036.2021.1924313

[23] Balaji, G., Saheel, A., Hariharan, M., & Palaniappan, P. (2021). Effect of EGR on a diesel engine fueled with waste plastic oil blend. *IOP Conference Series: Materials Science and Engineering*, 1130, 012012. doi: 10.1088/1757-899x/1130/1/012012

[24] Barik, D., & Murugan, S. (2016). Experimental investigation on the behavior of a DI diesel engine fueled with raw biogas–diesel dual fuel at different injection timing. *Journal of the Energy Institute*, 89(3), 373−388. doi: 10.1016/j.joei.2015.03.002

[25] Agarwal, A.K., Gupta, J.G., Maurya, R.K., Kim, W.I., Lee, S., Lee, C.S., & Park, S. (2016). Spray evolution, engine performance, emissions and combustion characterization of Karanja biodiesel fuelled common rail turbocharged direct injection transportation engine. *International Journal of Engine Research*, 17(10), 1092−1107. doi: 10.1177/1468087416641802

[26] Hirkude, J., Belokar, V., & Randhir, J. (2018). Effect of compression ratio, injection pressure and injection timing on performance and smoke emissions of CI engine fuelled with waste fried oil methyl esters-diesel blend. *Materials Today: Proceedings*, 5(1), 1563−1570. doi: 10.1016/j.matpr.2017.11.247

[27] Shrivastava, P., & Verma, T.N. (2020). Effect of fuel injection pressure on the characteristics of a CI engine fuelled with biodiesel from Roselle oil. *Fuel*, 265, 117005. doi: 10.1016/j.fuel.2019.117005

[28] Teoh, Y.H., How, H.G., Lee, S.W., Loo, D.L., Le, T.D., Nguyen, H.T., & Sher, F. (2022). Optimization of engine-out responses with different biodiesel fuel blends for energy transition. *Fuel*, 318, 123706. doi: 10.1016/j.fuel.2022.123706

[29] Kumar, B.R., Saravanan, S., Rana, D., & Nagendran, A. (2016). Combined effect of injection timing and exhaust gas recirculation (EGR) on performance and emissions of a DI diesel engine fuelled with next-generation advanced biofuel–diesel blends using response surface methodology. *Energy Conversion and Management*, 123, 470−486. doi: 10.1016/j.enconman.2016.06.064

[30] Hirkude, J.B., & Padalkar, A.S. (2014). Performance optimization of CI engine fuelled with waste fried oil methyl ester-diesel blend using response surface methodology. *Fuel*, 119, 266−273. doi: 10.1016/j.fuel.2013.11.039

[31] Praveena, V., Martin, M.L.J., & Geo, V.E. (2020). Effect of EGR on emissions of a modified DI compression ignition engine energized with nanoemulsive blends of grapeseed biodiesel. *Fuel*, 267, 117317. doi: 10.1016/j.fuel.2020.117317

[32] Kumar, A., Pali, H.S., & Kumar, M. (2023). Effect of injection timing of waste plastic oil and its blends on CRDI diesel engine. *International Journal of Engine Research*, 24(11), 4490−4499. doi: 10.1177/14680874221119131

[33] Tomar, M., Dewal, H., Kumar, L., Kumar, N., & Bharadvaja, N. (2021). Biodiesel additives: status and perspectives. In *Biodiesel Fuels. Science, Technology, Health, and Environment* (pp. 283−298). Boca Raton, CRC Press. doi: 10.1201/9780367456238

[34] Mangesh, V.L., Padmanabhan, S., Tamizhdurai, P., & Ramesh, A. (2020). Experimental investigation to identify the type of waste plastic pyrolysis oil suitable for conversion to diesel engine fuel. *Journal of Cleaner Production*, 246, 119066. doi: 10.1016/j.jclepro.2019.119066

[35] Shirneshan, A., & Nedayali, A. (2016). Investigation of the effects of biodiesel-diesel fuel blends on the performance and emission characteristics of a diesel engine. *Jurnal Teknologi (Sciences and Engineering)*, 78(6), 169–177. doi: 10.11113/jt.v78.4443

[36] Mani, M., & Nagarajan, G. (2009). Influence of injection timing on performance, emission and combustion characteristics of a DI diesel engine running on waste plastic oil. *Energy*, 34(10), 1617−1623. doi: 10.1016/j.energy.2009.07.010

[37] Devaraj, J., Robinson, Y., & Ganapathi, P. (2015). Experimental investigation of performance, emission and combustion characteristics of waste plastic pyrolysis oil blended with diethyl ether used as fuel for diesel engine. *Energy*, 85, 304−309. doi: 10.1016/j.energy.2015.03.075

[38] Senthilkumar, P., & Sankaranarayanan, G. (2016). Effect of Jatropha methyl ester on waste plastic oil fueled DI diesel engine. *Journal of the Energy Institute*, 89(4), 504−512. doi: 10.1016/j.joei.2015.07.006

[39] Czajczyńska, D., Nannou, T., Anguilano, L., Krzyżyńska, R., Ghazal, H., Spencer, N., & Jouhara, H. (2017). Potentials of pyrolysis processes in the waste management sector. *Energy Procedia*, 123, 387−394. doi: 10.1016/j.egypro.2017.07.275

[40] Bharathy, S., Gnanasikamani, B., & Radhakrishnan Lawrence, K. (2019). Investigation on the use of plastic pyrolysis oil as alternate fuel in a direct injection diesel engine with titanium oxide nanoadditive. *Environmental Science and Pollution Research*, 26(10), 10319−10332. doi: 10.1007/s11356-019-04293-0

[41] Chaudhary, A., Panchal, S.H., Surana, A., Sreekanth, M., Ismail, S., & Feroskhan, M. (2022). Performance, emission and combustion characteristics of various biodiesel blends. *Journal of Thermal Analysis and Calorimetry*, 147(3), 2455−2479. doi: 10.1007/s10973-021-10642-4

[42] Das, A.K., Hansdah, D., Mohapatra, A.K., & Panda, A.K. (2020). Energy, exergy and emission analysis on a DI single cylinder diesel engine using pyrolytic waste plastic oil diesel blend. *Journal of the Energy Institute*, 93(4), 1624−1633. doi: 10.1016/j.joei.2020.01.024

[43] Leung, D.Y., Luo, Y., & Chan, T.L. (2006). Optimization of exhaust emissions of a diesel engine fuelled with biodiesel. *Energy & Fuels*, 20(3), 1015−1023. doi: 10.1021/ef050383s

[44] Damodharan, D., Sathiyagnanam, A.P., Rana, D., Kumar, B.R., & Saravanan, S. (2018). Combined influence of injection timing and EGR on combustion, performance and emissions of DI diesel engine fueled with neat waste plastic oil. *Energy Conversion and Management*, 161, 294−305. doi: 10.1016/j.enconman.2018.01.045

[45] Saba, G., Paramasivam, P., Kandasamy, T., Swaghatha, A., Majdi, H., Alfaisal, F., Alam, S., & Ayanie, A. (2025). Comprehensive Investigations on Split Injection System Using Diesel/Biodiesel Blends Powered Common Rail Direct Injection Engine: Multi-Objective Optimization. *Energy Science & Engineering*, 13, 1662–1678. doi: 10.1002/ese3.2087

[46] Dubba, S.K., Pisini, R., Kelli, D., Bammidi, R., Vanam, J.P., & Turali, N. (2025). Experimental Investigation of the Performance and Emission Characteristics of Cotton Seed Biodiesel / Diesel Blends with Titanium Dioxide Nanoparticles. *Archives of Thermodynamics*, 46(3), 151–161. doi: 10.24425/ather.2025.156587

[47] Banoth, K., Banoth, M., & Mukuloth, S. (2025). Investigating the Impact of TiO_2 Nanoparticles on Waste Plastic Pyrolysis Oil and DEE Diesel Blends for Diesel Engine Performance and Emission Optimisation. *Archives of Thermodynamics*, 46(3), 237–245. doi: 10.24425/ather.2025.156594

[48] Mangesh, V., Padmanabhan, S., Tamizhdurai, P., & Ramesh, A. (2020). Experimental investigation to identify the type of waste plastic pyrolysis oil suitable for conversion to diesel engine fuel. *Journal of Cleaner Production*, 246, 119066. doi: 10.1016/j.jclepro.2019.119066

[49] Kumar, A., Kumar, S., Verma, V.K., Singh, S., Shukla, R., Jain, A., Bist, A.S., Pradeep Vishnoi, P., Kumar, V., & Bhandari, P. (2025). Experimental analysis of ethanol-diesel blends stabilised with jatropha methyl ester: Engine performance and emission characteristics. *Archives of Thermodynamics*, 46(3), 229–236. doi: 10.24425/ather.2025.156593

[50] Zhang, Z., Tian, J., Li, J., Lv, J., Wang, S., Zhong, Y., Dong, R., Gao, S., Cao, C., & Tan, D. (2022). Investigation on combustion, performance and emission characteristics of a diesel engine fueled with diesel/alcohol/n-butanol blended fuels. *Fuel*, 320, 123975. doi: 10.1016/j.fuel.2022.123975

Co-published by
Institute of Fluid-Flow Machinery
Polish Academy of Sciences
Committee on Thermodynamics and Combustion
Polish Academy of Sciences

Copyright©2026 by the Authors under licence CC BY-NC-ND 4.0

http://www.imp.gda.pl/archives-of-thermodynamics/

Heat transfer enhancement by drop impact onto a nanotextured superheated surface

Ravi Pippal[a], Aditi Agrawal[a], Akshita[a], Tulip Biswas[a], Deepali[a], Pushpendra Kumar Shukla[a], Sumit Sinha-Ray[a,b*]

[a]Department of Textile and Fibre Engineering, Indian Institute of Technology - Delhi, Hauz Khas, New Delhi 110016, India
[b]Department of Mechanical and Industrial Engineering, University of Illinois at Chicago, Chicago, IL 60607-7022, USA
*Corresponding author email: ssinharay@textile.iitd.ac.in

Received: 22.05.2025; revised: 30.01.2026; accepted: 11.02.2026

Abstract

Thermal management of microelectronics has become a major concern for the semiconductor industry, especially for high-power applications, due to the requirements of large computations in a smaller packing. Here in this work, spray/drop impact cooling of microelectronics (hot spot cooling) is studied, using a heat sink with novel nanotexture on the surface. The adherent nanotexture with highly porous architecture was fabricated with polymeric nanofibres obtained from supersonic solution blowing. The impacting drops on the superheated bare surface visibly bounced and escaped, exhibiting a Leidenfrost phenomenon, whereas, for the coated surface, complete suppression of the Leidenfrost effect was observed. For a nanotextured surface, the impacting droplet was focused hydrodynamically to penetrate the porous layer and wick through the network, thereby getting pinned, despite the fibrous architecture being hydrophobic. The overall heat transfer rate was measured to be in excess of 1000 kW/m^2 from the coated surface, as calculated from the wetting area. Later, it was also found that a drop interval time of 2.5 s yielded the optimised cooling for both short- and long-time applications. The long-time heating and cooling cycles exhibited a repeatable cooling pattern between the upper critical (130^{o}C) and lower safe (80^{o}C) range, demonstrating the excellent robustness of the nanofibrous texture and a possible route of preservation of coolant.

Keywords: Drop impact cooling; Nanofibre; Nanotextured surface; Thermal management; Leidenfrost phenomenon.

Vol. 47(2026), No. 1, 101–111; doi: 10.24425/ather.2025.156858

Cite this manuscript as: Pippal, R., Agarwal, A., Akshita, Biswas, T., Deepali, Shukla, P.K., & Sinha-Ray, S. (2026). Heat transfer enhancement by drop impact onto a nanotextured superheated surface. *Archives of Thermodynamics*, 47(1), 101−111.

1. Introduction

The advent of electronic computers in the 1940s initiated a significant industrial transformation, focusing on the creation of faster and more efficient calculations [1]. With the progress of mankind, yielding the need for large data computation, a notable shift in integrated circuit designs resulted in significant enhancements in processing speed within a strict geometric confinement. Consequently, the thermal loads on these devices have increased considerably. Modern electronic devices now generate a substantial heat flux (~200 W), while most such microelectronic devices fail beyond their operating temperatures of 75−80^{o}C [2]. According to a report by Industrial Credit and Investment Corporation of India (ICICI) Direct, India's electronic manufacturing sector is expected to experience significant growth, expanding from USD 12 billion to USD 250 billion within the next five years [3], out of which thermal management of electronic packages will constitute a major part.

The current requirement of heat removal from microelectronic chips can be as high as 1 MW/m^2. Efficient cooling systems are required to manage this heat, with heat transfer coefficients (HTC) ranging from 10 to 30 kW/(m^2·K) to maintain safe operating temperatures [4]. This cannot be achieved via air cooling, since HTC of forced air can only be as high as

Nomenclature

C – specific heat, J/(kg·K)
g – gravitational acceleration, m^2/s
h – convective heat transfer coefficient, W/(m^2·K)
k – thermal conductivity, W/(m·K)
p – pressure, kPa
Pr – Prandtl number
Re – Reynolds number, Re = $Dv\rho\ /\mu$
t – time, s
T – temperature, K
U – hydrodynamic focusing velocity, m/s
V – impregnation velocity, m/s

Greek symbols

α – thermal diffusivity, m^2/s
μ – dynamic viscosity, Pa·s
ρ – density, kg/m^3
σ – surface tension, N/m

Subscripts and Superscripts

∞ – atmospheric
eff – effective
pore – pore of textured surface

Abbreviations and Acronyms

CPU – central processing unit
DMF – dimethylformamide
HTC – heat transfer coefficient
PAN – polyacrylonitrile
PCL – polycaprolactone
PTFE– polytetrafluoroethylene
PVDF– poly-vinylidene fluoride

5−20 W/(m^2·K). Hence, air cooling is not a viable solution for future computing techniques, which also poses a significant environmental hazard in terms of total carbon emissions.

To mitigate these issues, microelectronics cooling techniques are intensified with direct cooling techniques. Direct cooling methods include approaches such as spray and jet impingement cooling, boiling, immersion cooling, drop impact and droplet electrowetting [5–9], etc. Although methods like boiling, immersion, etc. are highly efficient and can potentially remove the desired quantity of heat (~1 MW/m^2), the rationale for choosing liquid drop impact (a type of flash evaporative technique) is to minimise the size of cooling components and concentrate cooling efforts where they are most needed. By focusing on the primary heat source, the central processing unit (CPU), the cooling system's size and complexity can be reduced [10]. Other components, such as the random access memory (RAM), hard drives, fans and the motherboard, typically generate less heat. Thus, effective cooling of CPU can significantly reduce the overall thermal load. The significant cooling potential of drop impact is linked to the evaporation of liquid at the hot surface. The efficiency of this process is greatly influenced by the hydrodynamics and heat transfer associated with drop impact on hot surfaces. However, the usual receding motion of the spread-out liquid lamellae on superheated metal surfaces often results in complete drop bouncing, interrupting the cooling process. Additionally, the insulating vapour layer that forms between the drop and the surface significantly reduces the heat flux, generating a Leidenfrost-like effect.

Surfaces, modified to become wettable [11] or rendered porous/textured [12], can often lead to minimisation of the Leidenfrost phenomenon and can improve heat transfer. In various cases, such surface modification techniques are not cost-effective and scalable. A novel method of surface modification involves coating of superheated surfaces with non-woven polymer nanofibre mats [13,14], which are highly porous, and can enhance wettability effects or reduce surface energy [15]. The advantages of using nanofibre mats in flash evaporative cooling, like drop impact cooling, primarily stem from their impact on the hydrodynamic behaviour of the impacting drops and the increased heat transfer area. Previous studies have identified two key features of drop impact on nanofibre mats [14]. Firstly, receding, splashing and bouncing during the impact on polymer nanofibre mats are almost eliminated. The drop spreads similarly to an impermeable surface, but the contact line gets pinned at the maximum spread diameter, which prohibits receding. Secondly, drop spreading is accompanied by the impregnation of pores, which takes place almost instantaneously. This enables the liquid to wick inside the nanofibre mat over a substantially wider area than that enclosed by the fixed contact line. Both features enhance heat transfer by enlarging the contact area between water and the underlying hot surface [5].

This research delves into the outcome of drop spreading on and within nanofibre mats. The primary focus is to investigate the effects of liquid drop impact on a nanofibrous textured surface and the associated temperature distribution, along with the fate of the impacting drop and superheated substrate. This is examined under various conditions – different frequencies of drop impact and cycles of test conditions.

2. Literature review and objectives

Drop impact on superheated substrate is a well-researched topic. This domain of study is often considered under spray cooling techniques. Voluminous research data are available to address the hydrodynamic behaviour of an impacting drop, which is often governed by the impact parameters like impact velocity, impacting drop diameter/mass, liquid's thermophysical properties, surface texture and wettability [16].

Along with experimentation studies of impacting drop-surface interaction with variable surface or process parameters [17,18], several computational approaches have also been utilised, like molecular dynamic simulation [19], Lattice-Boltzmann method [20], volume of fluid method [21], or a more recent approach of phase-field modelling [22]. Out of these computational approaches, the phase-field method has gained immense popularity due to its robustness in droplet impact/interaction-based studies on a solid medium [23,24].

Despite the recent advances, one of the concerning aspects of drop impact on surfaces is the non-isothermal case, where the surface superheat is to be considered along with several other phase-change heat transfer regimes like nucleate boiling, transition boiling, atomisation and film boiling (Leidenfrost phe-

nomenon), and natural convection affecting sensible heat. Several studies have focused on microstructural surfaces like micropillar [25,26], mesh [27], sputtered network [28], and many more, to understand the phase change at the pinning sites of impacting liquid droplets and their behaviour during film boiling conditions. Especially, such studies have focused intensively on variable wettability and varying roughness.

For the sake of brevity, this literature review specifically focuses on nanotextured surfaces having a 'furry coat' like architecture, derived from a polymeric fibrous network and surface-impacting drop interaction at atomisation and film boiling conditions. One of the earliest studies of drop impact on fibrous structure was conducted by Srikar et al. [13], which demonstrated the phenomenon of hydrodynamic focusing of droplets onto electrospun nanofibrous textured surfaces, aiding liquid penetration into the net-like structures and enhancing wicking, while preventing liquid receding and bouncing. Further, it was shown that such a nanofibrous structure, due to the spontaneous wicking at a specific impacting velocity, could potentially reverse the Leidenfrost effect [29]. These nanofibrous membranes after copper plating revealed a 'thorny-devil' like architecture having nanoscale roughness on individual fibres. This process enhanced hydrophilicity and increased heat transfer from superheated surfaces. Potentially such a surface could remove heat at the rate of ~10MW/m^2 [30]. In all these cases, it was observed that the liquid penetration velocity within the pores can be significantly higher than the Washburn velocity (wettability), or the Tanner velocity (spreading), since a large amount of kinetic energy of an impacting drop can be channelised through the interconnected pores of the nanotextured surfaces. This focusing velocity is by 2−3 orders of magnitude higher than the impacting liquid drop velocity [14]. This makes the hydrodynamic focusing possible even on superhydrophobic porous surfaces. Sahu et al. [8] studied the impact of polar (water) and non-polar liquid (Fluorinert FC7500, hexane) drops onto electrospun nanofibre membranes made of varying degrees of wettability, with polymers like: PAN (polyacrylonitrile), nylon, PCL (polycaprolactone) and teflon. It was observed that liquid penetration occurred at velocities of 1.5−3 m/s, regardless of surface hydrophobicity, with less wettable membranes requiring higher threshold velocities. Liquids with lower surface tension penetrated more easily, mimicking a millipede-like jet system, whereas high surface tension liquids, like water, pass through a thin electrospun membrane like a jet. Even superhydrophobic teflon membranes could not prevent water penetration at high-impact velocities, especially at thinner dimensions (<100 μm).

Although the study emphasised an important breakthrough in terms of dynamic penetration of liquids, long-term degradation of nanofibre coatings remained a potential concern, especially under mechanical stress and repeated impacts. The same was discussed by Sahu et al. [31], who examined the penetration of aqueous nanofluid drops into non-wettable porous membranes through hydrodynamic focusing. This phenomenon enabled liquid penetration into materials like PTFE (polytetrafluoroethylene), which typically repel water. The study compared a wettable porous surface (glass fibre) and a non-wettable membrane (PTFE), highlighting the dominance of drop impact dynamics over wettability.

Sinha-Ray and Yarin [32] investigated the heat transfer enhancement of nanotextured surfaces during droplet cooling using water and Fluorinert FC-7300. Smaller droplets of water at higher frequencies, especially at 4 Hz, resulted in maximum heat flux removal of 0.9 MW/m^2, balancing coolant supply and evaporation. The study emphasised the previously discussed conditions and showed the importance of dynamic focusing of liquid droplets and wicking into the nanotextured porous surface. A similar behaviour was seen even in zero-g conditions as well [33]. However, both studies were limited to short-term effects and lacked insights into long-term surface degradation, if any. A very recent study conducted by Park et al. [5] demonstrated a significant improvement in thermal management of microelectronics components using electrospun/supersonically sprayed/electrodeposited thorny-devil-like nanofibrous/nanowire architecture and reported a maximum 56% enhancement in effective heat transfer coefficient [5]. They also reported heat flux removal as high as 1.1−2 MW/m^2 from the metal nanowire textured surface. Although all these studies elucidated the numerous benefits of nanofibrous architecture, it is needless to mention that the above-mentioned articles utilised metal-plated surfaces, which are cost-ineffective, requiring significant sophistication and lacking in scalability and generalisability. At the same time, electrospun polymeric fibrous layers are highly fluffy in nature, and they can only be deposited on limited geometries, while facing significant threats of delamination during any vigorous heat transfer studies.

A greater need is therefore required to understand the effect of pure polymeric nanofibrous coating on heat removal from microelectronics cooling and/or a significant reduction of surface superheat. It has been previously discussed in Refs. [34–37] that a pure polymeric nanofibrous network deposited by supersonic solution blowing exhibited a robust behaviour under vigorous boiling regime, whereas in the work of Jun et al. [6], a possible delamination of metal-plated fluffy electrospun layers was discussed. The supersonically blown nanofibres were reported to be instrumental in boiling heat transfer, as they could potentially withstand several hours of rigorous heat transfer processes [38], and reduce significant surface superheat. This begs an important question – can such an ultrafine polymeric surface withstand a flash evaporation of an impacting liquid drop when the surface is under superheated conditions? All the previous articles concerning drop impact and associated heat transfer studies on polymeric/polymeric-metal coated surfaces have been related to wettable/semi-wettable surfaces, with fluffy architecture, where a coating thickness of ~50−100 μm was considered [5,13,29]. However, none of these articles resorted to a long-time or cyclic test pattern. Hence, in this article, the authors reported an investigative study on drop impact heat transfer of water on a hydrophobic and thin (~ 10 μm) polymeric architecture, which was deposited on a superheated copper substrate. The substrate mimicked an electronic surface exposed to extreme conditions (>120°C) for compact integrated circuits. To the best of the authors' knowledge, such a study is rarely available, which elaborately discusses the drop impact heat transfer on a thin hydrophobic polymeric fibrous coated superheated surface and tests

its robustness in a long-term study. Our hypothesis is that the impacting velocity of the droplet would surpass the wettability effects due to hydrodynamic focusing and would still allow the droplet to spread and evaporate without allowing the Leidenfrost effect, even in such thin coating. Eventually, the said layer is expected to be robust and effective in evaporative cooling.

3. Materials and methods

3.1. Materials

Poly-vinylidene fluoride (PVDF) was acquired from Thermo Fisher Scientific (Alfa Aesar). Dimethylformamide (DMF) was acquired from Alfa Aesar. Acetone was purchased from Thermo Fisher Scientific. Copper and teflon were sourced from the local suppliers in Delhi. Thermal paste (MX-4 thermal compound) was also purchased locally. A thermometer (USB TC08) and K-type thermocouples were obtained from Omega. Cartridge heaters (50 W each) were sourced from Watlow.

3.2. Coating of nanofibres on copper block via supersonic solution blowing

The schematic of the experimental set-up is shown in Fig. 1.

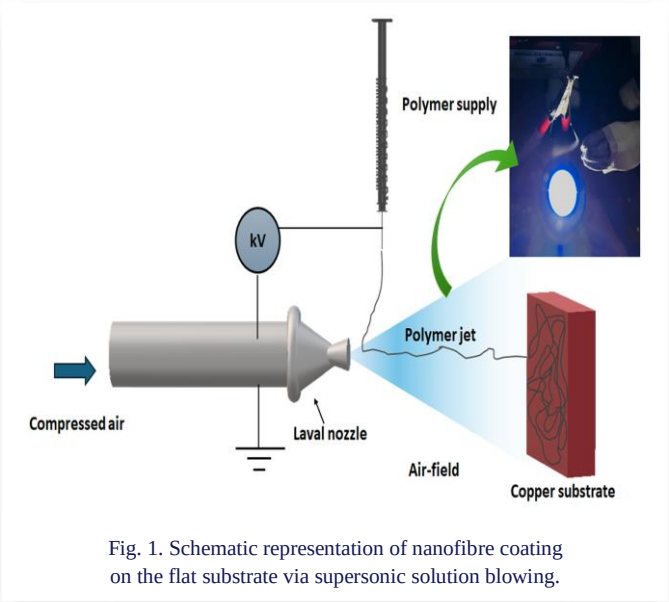


Fig. 1. Schematic representation of nanofibre coating on the flat substrate via supersonic solution blowing.

For supersonic solution blowing, an 8 % wt. PVDF solution was prepared in dimethylformamide (DMF) and acetone in a 1:1 ratio. The polymer solution was kept on a hot plate magnetic stirrer at 60°C and 600 rpm overnight to ensure homogeneous mixing and dissolution. The prepared polymer solution was loaded into a 5 ml syringe and pumped through a 22G needle at a flow rate of 0.7 ml/hr with the use of a syringe pump (New Era Pump System Inc.). A compressor, operating at 150 psi (≈10,34 bar), was linked to a supersonic de Laval nozzle (Silvent 209 L). The needle tip, dispensing the polymer solution, and the gas nozzle exit were positioned 1.5 cm and 1cm apart in horizontal and vertical directions, respectively. The nozzle was grounded, while a 6.5 kV electric potential was supplied to the needle tip. The nanofibres were collected on a copper block positioned 25 cm from the nozzle exit. The nanofibres were deposited on a copper substrate for a duration of 3 minutes to have a milky appearance on the copper block of dimensions 25 mm (length) × 12.5 mm (width) × 5 mm (thickness).

3.3. Characterisation

Following the coating process, the fibrous architecture was analysed using scanning electron microscopy (SEM) (ZEISS EVO 50), and the contact angles of bare and nanotextured surfaces were measured using a goniometer (Data Physics OCA 15LJ). The SEM images exhibited a highly porous architecture with a mean fibre diameter of 244 nm with a standard deviation of 63 nm. Contact angle measurements revealed that the bare copper surface was wetted by water droplets, having a contact angle of 77°, Fig. 2C(a), indicating hydrophilic behaviour. This is likely attributed to the presence of oxide layers on the copper substrate. In contrast, the nanofibrous nanotextured surface substrate exhibited a contact angle of approx. 137°, Fig. 2C(b), demonstrating a hydrophobic modification of the surface.

3.4. Experimental setup

The schematic of the drop impact setup is shown in Fig. 2 (both schematic and the actual image). The components of the experimental setup are as follows:

- Primary components: (a) copper substrate, (b) teflon block, (c) auto-transformer connected to (d) two cartridge heaters, placed into the copper block to supply uniform heat, (e) 24G bent needle connected to (f) syringe pump to supply the liquid to the heated surface, (g) thermometer, and (h) two thermocouples,
- Secondary components: (i) high-speed camera, (j) light source, (k) computer.

The copper substrate was placed onto the heated copper block of similar dimensions, where the heated block acted as the heat source, powered by two cartridge heaters (3 mm in diameter and 25 mm in length), operating at a certain voltage, and the copper substrate was the sink, which was subjected to drop impact. A thin layer of thermal paste was applied between these two copper blocks to eliminate any air gap. The whole assembly was affixed within a groove of teflon to resist heat loss from the sides, and only the top surface of the heat sink was exposed to the environment. Two holes having a diameter of 1.5 mm were drilled up to the centre of the upper copper substrate, 2 mm from the top surface. This was done to understand the surface temperature. The distance between the thermocouples was 1 cm, and every time the liquid was dropped between these two thermocouples to read an average temperature of the surface. These thermocouples were read as T_1 and T_2. Since copper has a very high thermal diffusivity (~10^{-4} m^2/s), the thermal transient time between the upper surface and the thermocouple locations would be (L^2/α) < 40 ms, and hence, a steady thermal gradient would prevail. Consequently, for a measured temperature of 125°C and room temperature of 25°C with the heat transfer coefficient of still air as 5 W/(m^2·K), the heat loss from the surface could be estimated as $Q_{loss} = h \cdot A \cdot \Delta T$, yielding a value of 0.15 W. This value was much smaller compared to the overall heat supply mentioned in the latter section, and hence, the thermocouples allowed an accurate estimate of the surface temperature.

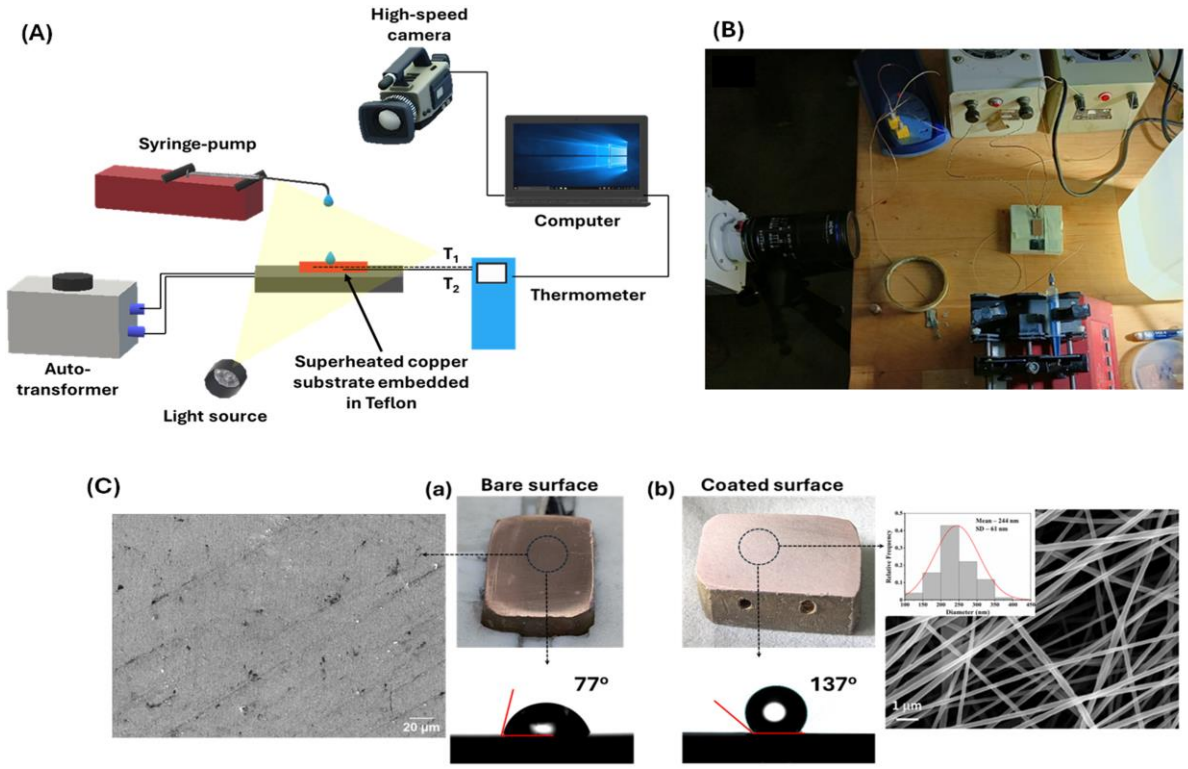


Fig. 2. (A) Graphical representation of the test scheme; (B) an actual photograph of the experimental setup; (C) the real image of the copper substrate, and its SEM image and contact angle measurement, followed by a fibre coated surface having a milky white appearance along with the SEM image of the fibrous network and fibre size distribution.

A high-speed camera, connected to a computer, was employed to capture the dynamics of water droplets impacting both the bare and nanotextured superheated surfaces.

3.5. Drop impact experiment

First, the copper substrate was smoothened using 1000, 1200 and 2500 grit sandpaper, in s sequential manner to obtain a mirror finish. Once the setup was assembled, two K-type thermocouples (T_1 and T_2, accuracy of ±1°C) were inserted into the copper substrate and connected (by USB TC08) to a thermometer (refer to Fig. 2 for locations of T_1 and T_2). The thermometer was then connected to a PC to record temperature readings. Two separate variable autotransformers provided electric power to the cartridge heater assembly. Throughout the trials, the supply voltage was maintained at a specific value, resulting in an overall supply of power 40 W ($P = V{\cdot}I$, V – voltage, I – current) or heat flux of 128 kW/m^2. When the temperatures (T_1 and T_2) reached 125°C, water droplets were introduced onto the superheated surface. The voltage supply to the heaters was cut off when the temperatures (T_1 and T_2) reached 140°C or above, and the experiments were stopped. This is later called a dry-out situation in later sections. In a separate scenario, the drop impact was halted again, when the temperatures (T_1 and T_2) came close to 105−110°C, when a liquid puddle started to form. This is indicated as a flooding regime in later sections. Experiments were conducted at various drop impact rates of water to ascertain the critical and optimised droplet frequency. The optimisation ensured a steady surface temperature, while preserving the coolant. Here, a steady temperature can be visualised as constant working of high-power microelectronics, without overheating. Temperature readings were recorded and analysed using logging software to gain insights into heat transfer dynamics under these optimised conditions. A high-speed camera was employed to capture droplet dynamics such as receding, splashing, bouncing and spreading. Separately, the experiments were conducted to obtain the optimum flow rate to distinguish between bare and nanotextured surfaces. Surface robustness was also evaluated at the optimised flow rates to ensure sufficient heat removal, while not allowing the surface to go beyond a specific upper limit. During such tests, the heat supply was not cut off, mimicking a consistent microelectronics performance throughout.

3.6. Drop size evolution during impact

To capture the dynamic behaviour of the water droplet during impact and atomisation, a high-speed imaging system (Phantom VEO 1310L) was employed. The camera view was set at a resolution of 640×360 pixels, with a sampling rate of 10000 fps, and an exposure of 50 µs to ensure precise spatial resolution. The initial radius of the droplet was used as the calibration, precisely measured from its mass and thereafter converted to volume, using the density of 1000 kg/m^3 (at room temperature). The oncoming droplet can be observed in the first frame in Fig. 3. The droplet radius was measured to be 0.142 cm (for a droplet mass of 11.9 mg), corresponding to an estimated volume of 0.012 cm^3. All the successive image analyses were done using the above-mentioned calibration and ImageJ software. A total of 700 individual frames from an entire video were analysed for a single droplet impact-bouncing-atomisation event. The gap

between the two analysing frames was 150, capturing the entire droplet life cycle till it left the heater surface. The frame gap of 150 was rationally chosen to avoid in calculations any satellite droplets generated during atomisation. This helped to reduce the overestimation of satellite droplet counting. The visualisation area (in pixels) was converted to physical units (cm or cm^3), approximating a spherical contour.

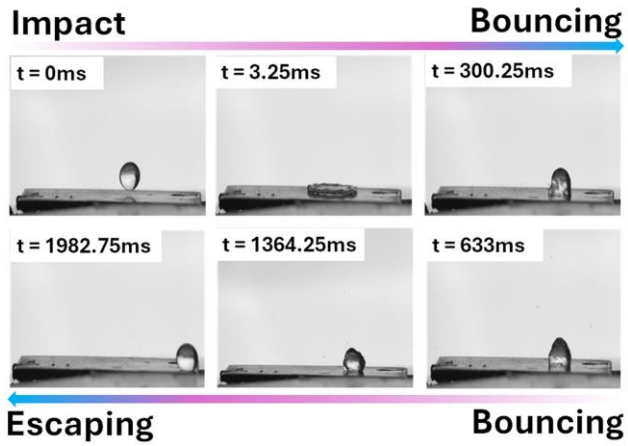


Fig. 3. Snapshots from high-speed imaging of a water droplet impacting on the superheated bare substrate, which reflect a complete impact-spread-bounce-escape pattern.

3.7. Uncertainty of measurements

The maximum estimated uncertainty of heat flux was measured to be [39]:

$$\frac{\Delta(Q/A)}{(Q/A)} = \sqrt{\left(\frac{\Delta I}{I}\right)^2 + \left(\frac{\Delta V}{V}\right)^2}.$$

As per the manufacturer, the voltage uncertainty was ±2%, and the uncertainty in current was ±10 mA. This led to an overall error of 2.24% in heat flux measurements, i.e. an error of ±5.12 kW/m^2.

4. Results and discussion

The experiments were initially focused on understanding the water droplet behaviour on the superheated surface, after it made an impact. A high-speed camera was configured to capture the complete impact, receding, bouncing, spreading and atomisation behaviour, at 4000 fps. During the tests, it was observed that on a bare surface, the liquid drop exhibited a bouncing and escaping pattern, a phenomenon akin to the Leidenfrost effect. The liquid droplet of mass 11.9 mg (radius 0.142 cm) was released from a height of 30 cm, indicating an impact velocity of nearly 2.42 m/s. At this velocity, the Weber number ($We = \rho u^2 d/\sigma$, with ρ as the liquid density, u as the impacting velocity, d as the drop diameter and σ as the surface tension) could be calculated as 124.45, which signifies an inertia driven phenomenon surpassing the surface tension. This would invariably lead to an imminent liquid rebound with complete splashing below 5 ms. Figure 3 shows the impacting drop behaviour on the superheated bare surface with the surface temperature of 125°C.

The images in Fig. 3 show the life cycle of the droplet and its interaction with the superheated surface, where a small change in the droplet's actual size is self-explanatory. It clearly shows that the impacting drop stayed on the surface for nearly 2 s before escaping the surface completely. This happened due to the rapid evaporation at the contact line, almost like film boiling, helping to create a vapour cushion, which levitated the drop from the superheated surface. A more detailed visualisation, with an illumination corrected image, is shown in Fig. 4.

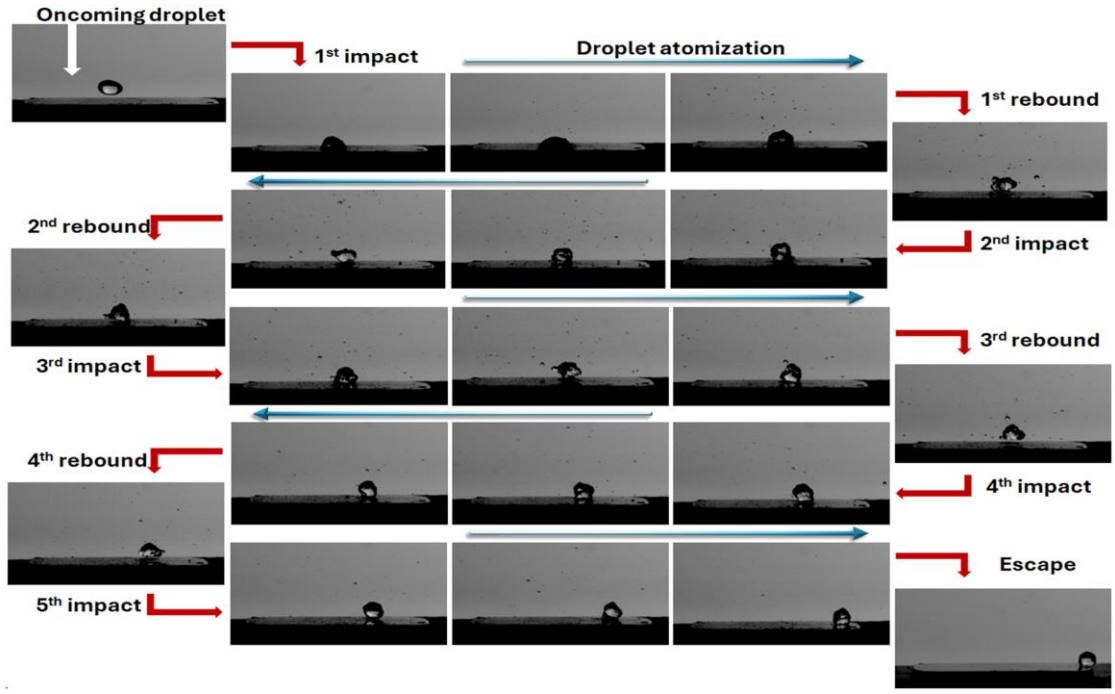


Fig. 4. Snapshots from high-speed imaging of a water droplet impacting on the superheated bare substrate, which shows different stages of impact, atomisation, rebounding and escape patterns.

A close-up view of the same impacting droplet, recorded at a higher speed (10000 fps) helped observe the entire impact, rebound and escape route, along with atomisation. This is commonly observed in film boiling like situations, which were enhanced due to inertial effects during impact. Five stages of impact-bouncing-escaping and atomisation are shown in the figures, and one can easily find the small droplets escaping from a parent droplet and the viewing window. The departing droplet was calculated to have a radius of 0.13 cm, as measured from image analysis, with a calculated volume of 0.0092 cm^3 or mass of 9.2 mg. This suggested a 61.35% of mass escaping due to the Leidenfrost effect. A careful calculation from image analysis, using the routine mentioned in Section 3.6, shows that about 30% of mass was lost due to fragmentation or atomisation. The remaining mass loss could be accounted for (a) insignificant evaporation during impact stages, leading to almost no temperature change of the surface, (b) minor error in calculations in droplet sizes arising during pixel to physical unit conversion, or (c) inaccuracy of droplet count due to ultra-small size in the narrow depth of the field. The error could also come from conversion of arbitrary shape droplets into equivalent spheres. The lattermost error affected the calculation by an order of 'r', as droplet information was acquired from 2D images and the pixel area of any droplet was converted into an equivalent sphere area and thereafter a sphere volume. However, qualitative calculation did indicate that insignificant evaporation happened at the bare superheated surface. The temporal and spatial evolution of the impacting droplet and its atomisation behaviour is vivid in Fig. 4.

For the nanotextured surface, a complete opposite phenomenon was observed, where complete spreading followed by liquid contact line pinning and complete evaporation could be observed (see Fig. 5). To better observe this behaviour, a top-view approach was considered to understand the heat removal. This phenomenon was similar to situations observed for Sinha-Ray and Yarin [32]. A stark dissimilarity between the work of Sinha-Ray and Yarin [32] and the current work was the surface wettability. Wherein the metal-plated surfaces offered excellent wettability to facilitate enhanced spreading followed by wicking, the PVDF coating in the current work was hydrophobic in nature. Albeit they performed similarly in terms of enhanced hydrodynamic focusing on high impact speed. As the liquid drop was focused through the porous network and spread within the architecture, the quick attainment of high temperature also led to a reduction of surface tension of water. Both phenomena led to complete wetting of the surface, which echoes the concept coined by Sahu et al. [8]. As per Lembach et al. [14], wettability driven impregnation velocity (V) is given as:

$$V = \left|\sigma d_{pore} cos\theta_a / 8\mu H\right|,$$

where θ_a is the advancing contact angle, μ is the dynamic viscosity, and H is the layer thickness or the pore length [40].

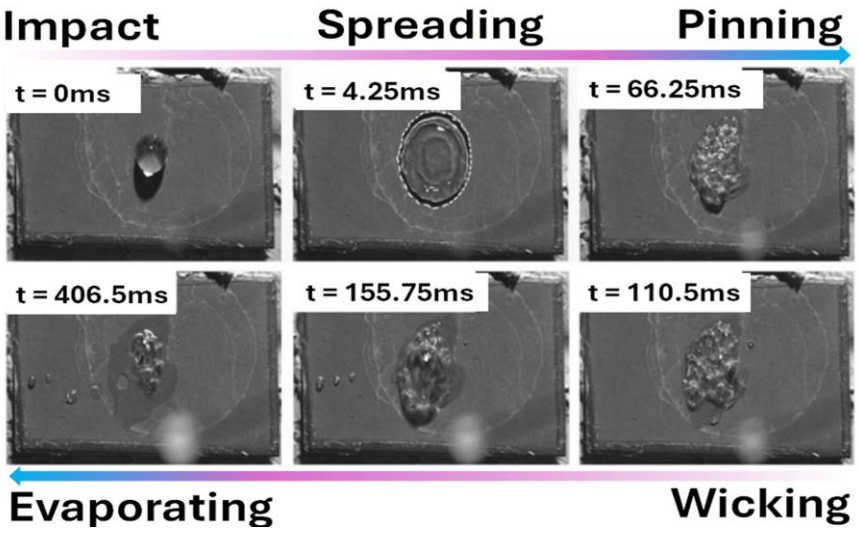


Fig. 5. Snapshots from high-speed imaging of a water droplet impacting on the superheated coated substrate; the coated surface shows impact-spread-pin-wick-evaporation behaviour.

However, this ideology works well for static cases. For the advancing contact angle greater than 90°, the above-mentioned equality does not hold. Several articles have reported penetration of liquid in hydrophobic nanofibrous membranes, like Srikar et al. [13], Sahu et al. [8], etc. For a completely non-wettable case, where $|cos\theta| \sim 1$, the above equation predicts a velocity of ~1 m/s, for the fibrous layer having H ~10 μm and d_{pore} ~1 μm.

During the hydrodynamic impact at one open channel, aka one pore, the focusing velocity can be approximated as, $U \approx \left(d/d_{pore}\right)V$. Considering the drop diameter ~2.8 mm, the focusing velocity (U) could be $>10^3$ m/s [8]. Although the liquid drop impacted several pores, and thus, dissipation of kinetic energy took place, this analysis could be safely extended to fibrous layers ~100 μm, which was a critical thickness to stop complete penetration of the impacting liquid. In our case, the kinetic energy driven hydrodynamic focusing on the thin layer ensured imbibition in the porous network and spreading of the same. This total kinetic energy dissipation and pinning of the liquid film within the nanofibres affected complete evaporation on the superheated surface.

As mentioned above, the bare surface did not affect the droplet evaporation. And hence, the bare surface did not demon-

strate any drop in surface temperature, unless complete flooding was considered. However, for an optimised condition, flooding should not be the contention in the current scope of research, as it might seem akin to jet impingement-like cooling. For the nanotextured surface, significant temperature drops were noted, and they are discussed in later sub-sections.

Using Fig. 5, we could use a simple image analysis, as described by Sinha-Ray and Yarin [32], to estimate the overall heat removal. The overall heat supply rate was 40 W, as mentioned before, whereas the loss due to convection was estimated to be 0.15 W. The wetted area on the PVDF nanofibrous coated copper substrate was obtained from top view images by first calibrating the spatial scale using the initial droplet size, which was measured gravimetrically (mass ~11.9 mg) and converted to volume (0.012 cm^3) using the density of water at room temperature. This radius provided the pixel-to-length conversion in ImageJ, after which the projected footprint of the spreading droplet on the coated surface was segmented frame-by-frame, and the maximum pinned wetting contour (see Fig. 5) was traced to determine the instantaneous wetted area. The maximum wetting area on the PVDF nanofibre coating was thus calculated as $A_{wetting}$ = 0.368 cm^2 by converting the enclosed pixel count to physical area, and an effective wetting radius r_{eff} = 0.34 cm was inferred, assuming an equivalent circular footprint. With no change in initial drop volume, the heat transfer could be calculated as:

$$Q_{experiment} = (Q_{supplied} - Q_{loss})/A_{wetting},$$

suggesting a value of 108 W/cm^2 or 1080 kW/m^2.

It is to be noted that in this case, no influence of the previous droplet was present, as the drop impact happened only after complete evaporation of a previous droplet. However, since the droplet hit the surface at 125°C and eventually boiled and evaporated, another approach could be considered for measurement of the heat flux. Since the water drop, upon spreading, reached a thickness of about 0.25 mm, the thermal transient time could be estimated as $t \sim (thickness^2/\alpha_{water})$, with thermal diffusivity of water being ~1.46 ×10^{-7} m^2/s, the evaporation time suggested a value of ~430 ms, which is similar to that in Fig. 5. Hence, the liquid layer could potentially be completely evaporated at 100°C. In this case, the total heat removal can be considered as:

$$Q_{calculation} = \frac{m[C_p(T_{saturation} - T_{impact}) + L]}{(A_{wetting} \times t_{evaporation})}.$$

With appropriate values, we can obtain $Q_{calculation}$ to be 264 W/cm^2 or 2640 kW/m^2, much higher than the visual observation and power supply. At the same time, following Ref. [32], we can find the axial heat transfer as:

$$Q_{axis} = \kappa \left[\frac{(T_\infty - T_o)}{d_{eff}}\right],$$

where κ is the thermal conductivity of copper (~400 W/(m·K)), T_∞ is the boiling temperature, T_o is the wetted area temperature, and d_{eff} is the effective wetting radius, which is 0.34 cm. This calculation yields a value of 294 W/cm^2 or 2940 kW/m^2. The calculation discrepancy shows that both Q_{axis} and $Q_{calculation}$ consider a highly simplified version of total heat removal, whereas $Q_{experiment}$ tends to show a real value pertaining to the amount of heat flow and loss. It is to be noted that the average temperature was monitored using two thermocouples placed equidistant from the edges, and gave a near accurate value of the overall surface, as the droplet was accurately placed between two thermocouples. Neither of the theoretical calculations considered the amount of mass loss which happened during atomisation of impacting drops at film boiling conditions. It is to be noted that nearly 30% atomisation of impacting drops was observed by Park et al. [5], when the authors released a drop from a 16 cm height, nearly half the height considered here. The droplet splashing became prominent since the Ohnesorge (Oh) number was much less than 1 [$Oh = \sqrt{We}/Re$], as the viscous forces became weak, and the surface tension forces became dominant. Figure 5, bottom panels, suggested that several satellite drops could be observed on the nanotextured substrate, resulting from film boiling of the impacted drop. Such satellite drops may affect the overall calculation of heat transfer rates, since only the primary wetted area was considered here. Nevertheless, complete evaporation of the droplet occurred within a shorter time frame, and a smaller wetting area rendered the nanotextured substrate more efficient than the bare surface.

The effect of drop impact frequency was studied next to understand the steady heat transfer behaviour, especially to hasten the cooling process, yet conserving the coolant. Considering this, four such flow rates were considered: 2.85, 2.63, 2.5 and 2 s/drop (in Fig. 6, the same is indicated by s), indicating 18.9, 20.52, 21.6 and 27 ml/h. The data for bare and nanotextured surfaces are shown in Fig. 6.

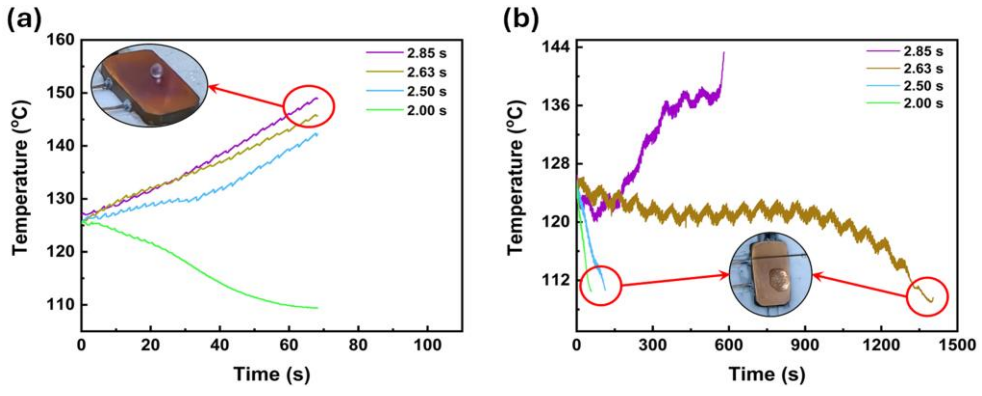


Fig. 6. Comparison of surface temperatures of (a) bare and (b) coated sample for various drop intervals, where the legends indicate the interval between two successive drops. The inset image in (a) shows the Leidenfrost effect, and in (b) shows puddle formation, respectively, for a drop interval of 2.63 s.

In the case of a bare surface, the temperature vs time behaviour was monotonous. In all cases, the upper critical temperature was kept as 140−150ºC, and upon reaching the same, the heat supply was manually stopped. During the tests, a minimum of 20 drops was allowed, and the temperature data were recorded for accurate comparison between the surfaces. For high drop intervals, the surface temperature increased nearly linearly with an upward slope (heating) of 0.33ºC and 0.28ºC per second, for 2.85 and 2.63 drops/s, respectively. This was obtained by fitting a linear relation, having an adj-R^2 value >0.99. For 2.5 drops/s, the slope is visibly less steep, and it showed much sluggish temperatures at the initial level. The resultant thermal increase was 0.23ºC/s (adj-R^2 0.93). The higher flow rate situation, i.e., 2 drops/s, yielded a flooding condition (droplet merging with pre-existing liquid film), and eventually the surface temperature was reduced to ~110ºC, where boiling conditions did not prevail under a non-isothermal condition. From Figs. 3−4, one can notice that the impact droplet remained on the surface for nearly 2 s, which could help in liquid merging with an oncoming liquid drop, and eventually could flood the system.

The nanofibre nanotextured surface offered a favourable situation. It can be clearly seen that for the nanofibre nanotextured surface, except for a drop interval of 2.85 s, all surface coatings eventually led to surface temperature reduction to 110ºC, i.e. flooding. The drop interval time of 2.63 s led to sluggish reduction in surface temperature, eventually leading to rapid cooling and flooding after 1000 s. However, for a drop interval of 2.5 s, unlike a bare surface, the nanotextured surface showed a gradual decline of surface temperature at a rate of 0.13ºC/s. The final condition of drop interval of 2 s demonstrated the steepest cooling rate to reach 110ºC (0.24ºC/s). As per Fig. 5, the droplet evaporated within 0.4−0.5 s of drop impact, and hence, almost no interaction between previous droplets could be observed. This led to a rapid decline of the surface superheat to a significantly low value, where flooding eventually took place, in the absence of rapid evaporation.

After several trials, it was observed that for a critical drop interval of 2.7 s, relating to a flow rate of 20 ml/h, the surface temperature remained nearly constant between 122−125ºC for a 10 minute of experimentation window, when the initial test condition was 125ºC (see Fig. 7).

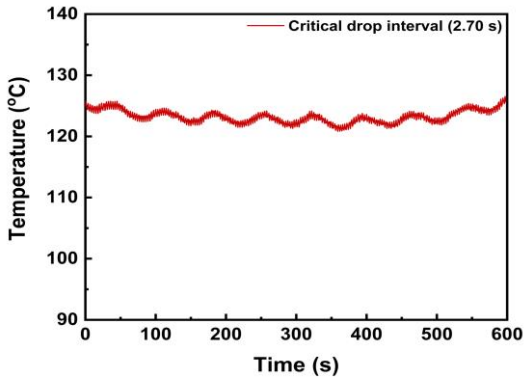


Fig. 7. Experimentally observed critical drop interval of 2.7 s, when the surface temperature varied between 122−125ºC, for an initial superheated surface temperature of 125ºC.

The repetition of the experiment yielded similar results. The term ‘critical’ here refers to a sufficient flow rate that helps remain a consistent surface temperature, neither causing a dry-out, nor resulting in any flooding on the surface. It is to be kept in mind that during the droplet frequency optimisation, two consecutive droplets never interacted. This information helps us understand the critical flow rate that allows a maximum conservation of the coolant to enhance the overall system efficiency, yet a microelectronic component performing at similar conditions. It is to be noted that this cyclic test surpassed the duration of most of the reported literature experiments, where robustness could pose a concern. One of the longest test durations of drop impact heat transfer on a polymeric fibre mediated surface at a constant elevated temperature was 180 s, as per Ref. [33]. Figure 7 showed that for 600 s, the architecture remained the same as the heating-cooling cycles were identical.

To evaluate the long-term durability of the nanotextured sample, cyclic testing was conducted over an extended period. Representative cyclic testing data are shown in Fig. 8. In this case, the upper limit of 130ºC was considered as the baseline of the high-power IC degradation temperature, and can be called an upper critical limit, whereas 110ºC was considered its operating temperature. It was already observed that for a drop interval of 2.5 s, the superheated surface temperature reduction followed a steady optimised decline. Hence, in this case, the same drop interval was chosen. However, in this case, puddle formation was allowed, and temperature drop was followed. The temperature drop was allowed till 80ºC, where puddle formation was seen at 110ºC. Once the temperature reached 80ºC, the coolant supply was stopped till the temperature reached 125ºC again. During the whole process, the heat supply was maintained. This was analogous to the continuous operation of an integrated circuit (IC) at the same power.

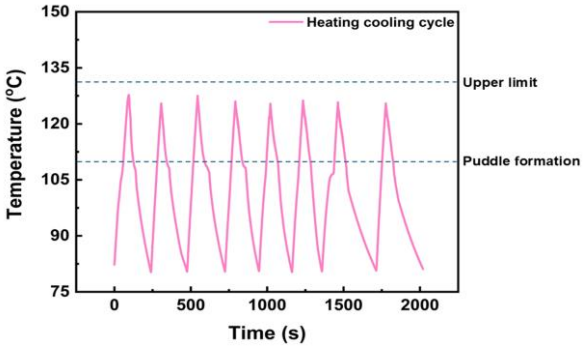


Fig. 8. Cyclic heating-cooling of a coated copper sample at a drop interval of 2.5 s – a representative data set of the entire cyclic heating-cooling.

In industry practices, high-power ICs are often tested against 125ºC and in such consideration, the test method mentioned here may provide a positive exposure to the robustness of the coating. The heating-cooling cycles for the entire time duration were identical. This truly demonstrates the excellent adherence of the nanofibrous coating and displays the robustness of the porous architecture despite the demanding applications. At the same time, this test demonstrated that for a 2.5 s interval per drop,

a significant amount of coolant can be preserved. A single cycle of 80ºC−125ºC−80ºC required 240 s, out of which about 95 s was required for the substrate to reach 125ºC from 80ºC. This also meant that during the experiment, 0.57 ml of water was preserved during the heating operation, whereas 0.87 ml of water was utilised during the entire cooling process. This signifies that during the entire process of heating and cooling, a 39.6% coolant volume was preserved, in comparison to continuous cooling.

5. Conclusions

The present study aims to investigate the effect of polymer nanofibrous nanotexture on superheated surface exposed to drop-impact cooling, especially related to microelectronics thermal management. A novel coating technique was employed, called supersonic solution blowing, to deposit nanofibres of diameter <250 nm on a copper substrate mimicking a heat sink for high-power microelectronics. The deposited layer exhibited a thin adherent milky appearance. The nanofibrous architecture retained its structure after water drop impact with a high Weber number. Unlike the bare copper surface, where impacting liquid drop bouncing and a Leidenfrost like escape could be observed, here, a complete pinning of liquid drops, along with wetting and wicking through porous architecture was evident. Despite the layer being hydrophobic, strong hydrodynamic focusing allowed liquid imbibition upon impact. The nanotexture surface could potentially remove as high as a ~1080 kW/m^2 heat flux. This high value opens a great scope to explore spray cooling like applications on soft polymeric materials.

Further studies focusing on interval/drop rate optimisation established a drop interval of 2.5 s to be the most effective one in controlling the heating of microelectronics. A long cyclic testing of heating and cooling demonstrated the robustness of such nanotexturing without any sign of delamination. Such a test also showed that instead of continuous cooling, a periodic supply of coolant can be equally effective in preserving the coolant.

Acknowledgements

The authors would like to thank the Indian Institute of Technology Delhi (IIT Delhi) for its research support, including assistance from the Central Research Facility and the Central Workshop of IIT Delhi. RP appreciates the financial support provided by the Ministry of Education, Government of India. PKS and SS-R acknowledge the financial assistance from National Technical Textile Mission (NTTM), under the Ministry of Textiles, Government of India (project code RP04675). This work was presented at ICRAME 2025.

References

[1] Kumar, H., & Sehga, S.S. (2013). Study of fluid flow and heat transfer through mini-channel heat sink. *Asian Journal of Engineering and Applied Technology*, 2(2), 25–28. doi: 10.51983/ajeat-2013.2.2.686

[2] Slattery, O.F., Kelly, G., & Greer, J. (2000). Thermal and mechanical problems in microelectronics. In *Benefiting from Thermal and Mechanical Simulation in Micro-Electronics* (pp. 17–26). Springer, Boston. doi: 10.1007/978-1-4757-3159-0_2

[3] BW Online Bureau. (2024). *India's Electronics Manufacturing Likely To Double In Next 5 Yrs: Report* - BW BusinessWorld. https://www.businessworld.in/article/indias-electronics-manufacturing-likely-to-double-in-next-5-yrs-report-529982 [accessed 30 Dec. 2025].

[4] Alahmad, M., & Abd El-Aleem, F. (2003). Heat transfer challenges in semiconductors processing and the applications of heat pipes for efficient heat removal. *Journal of King Saud University-Engineering Sciences*, 15(1), 141–154. doi: 10.1016/S1018-3639(18)30767-0

[5] Park, C., Seol, J., Aldalbahi, A., Rahaman, M., Yarin, A.L., & Yoon, S.S. (2023). Drop impact phenomena and spray cooling on hot nanotextured surfaces of various architectures and dynamic wettability. *Physics of Fluids*, 35(2), 027126. doi: 10.1063/5.0139960

[6] Jun, S., Sinha-Ray, S., & Yarin, A.L. (2013). Pool boiling on nano-textured surfaces. *International Journal of Heat and Mass Transfer*, 62(1), 99–111. doi: 10.1016/j.ijheatmasstransfer.2013.02.046.

[7] Kareem, R., Panicker, M.R.R., & Namboothiri, V.N.N. (2023). A review on immersion cooling of electronic systems. *AIP Conference Proceedings*, 2863, 020007. doi: 10.1063/5.0155307

[8] Sahu, R.P., Sinha-Ray, S., Yarin, A.L., & Pourdeyhimi, B. (2012). Drop impacts on electrospun nanofiber membranes. *Soft Matter*, 8(14), 3957–3970. doi: 10.1039/C2SM06744G

[9] Yan, Z., Jin, M., Li, Z., Zhou, G., & Shui, L. (2019). Droplet-based microfluidic thermal management methods for high performance electronic devices. *Micromachines*, 10(2), 89. doi: 10.3390/mi10020089

[10] Don Houk (2020). *What You Should Know About Computers and Heat.* Next7 IT. https://www.next7it.com/insights/know-about-computers-heat/ [accessed 30 Dec. 2025].

[11] Kim, S., Wang, T., Zhang, L., & Jiang, Y. (2020). Droplet impacting dynamics on wettable, rough and slippery oil-infuse surfaces. *Journal of Mechanical Science and Technology*, 34, 219−228. doi: 10.1007/s12206-019-1223-z

[12] Vaikuntanathan, V., & Sivakumar, D. (2012). Directional motion of impacting drops on dual-textured surfaces. *Physical Review E—Statistical, Nonlinear, and Soft Matter Physics*, 86(3), 36315. doi: 10.1103/PhysRevE.86.036315

[13] Srikar, R., Gambaryan-Roisman, T., Steffes, C., Stephan, P., Tropea, C., & Yarin, A.L. (2009). Nanofiber coating of surfaces for intensification of drop or spray impact cooling. *International Journal of Heat and Mass Transfer*, 52(25–26), 5814–5826. doi: 10.1016/ j.ijheatmasstransfer.2009.07.021

[14] Lembach, A.N., Tan, H.B., Roisman, I.V., Gambaryan-Roisman, T., Zhang, Y., Tropea, C., & Yarin, A.L. (2010). Drop impact, spreading, splashing, and penetration into electrospun nanofiber mats. *Langmuir*, 26(12), 9516–9523. doi:10.1021/la100031d.

[15] Reneker, D.H., & Yarin, A.L. (2008). Electrospinning jets and polymer nanofibers. *Polymers with Aligned Carbon Nanotubes: Active Composite Materials*, 49(10), 2387–2425. doi: 10.1016/j.polymer.2008.02.002.

[16] Marengo, M., Antonini, C., Roisman, I.V, & Tropea, C. (2011). Drop collisions with simple and complex surfaces. *Current Opinion in Colloid & Interface Science*, 16(4), 292–302. doi: 10.1016/j.cocis.2011.06.009

[17] Lee, M., Chang, Y.S., & Kim, H.-Y. (2010). Drop impact on microwetting patterned surfaces. *Physics of Fluids*, 22(7), 072101. doi: 10.1063/1.3460353

[18] Li, H., Fang, W., Zhao, Z., Li, A., Li, Z., Li, M., Li, Q., Feng, X., & Song, Y. (2020). Droplet precise self-splitting on patterned adhesive surfaces for simultaneous multidetection. *Angewandte*

Chemie International Edition, 59(26), 10535–10539. doi: 10.1002/anie.202003839

[19] Zhao, Y.-P., & Yuan, Q. (2015). Statics and dynamics of electrowetting on pillar-arrayed surfaces at the nanoscale. *Nanoscale*, 7(6), 2561–2567. doi: 10.1039/C4NR06759B

[20] Xiong, Y., Huang, H., & Lu, X.-Y. (2020). Numerical study of droplet impact on a flexible substrate. *Physical Review E*, 101(5), 53107. doi: 10.1103/PhysRevE.101.053107

[21] Liu, X., Zhang, X., & Min, J. (2019). Maximum spreading of droplets impacting spherical surfaces. *Physics of Fluids*, 31(9), 092102. doi: 10.1063/1.5117278

[22] Teja, T.C., Reddy, N.V.D., & Santra, S. (2025). Spreading and breakup dynamics of successive droplets impacting a curved surface. *Colloids and Surfaces A: Physicochemical and Engineering Aspects*, 717, 136794. doi: 10.1016/j.colsurfa.2025.136794

[23] Santra, S., Mandal, S., & Chakraborty, S. (2021). Phase-field modeling of multicomponent and multiphase flows in microfluidic systems: A review. *International Journal of Numerical Methods for Heat and Fluid Flow*, 31(10), 3089–3131. doi: 10.1108/HFF-01-2020-0001

[24] Fu, Z., Jin, H., Yao, G., & Wen, D. (2024). Droplet impact simulation with Cahn–Hilliard phase field method coupling Navier-slip boundary and dynamic contact angle model. *Physics of Fluids*, 36(4), 042115. doi: 10.1063/5.0202604

[25] Kim, H., Truong, B., Buongiorno, J., & Hu, L.-W. (2011). On the effect of surface roughness height, wettability, and nanoporosity on Leidenfrost phenomena. *Applied Physics Letters*, 98(8), 083121. doi: 10.1063/1.3560060

[26] Kwon, H., Bird, J.C., & Varanasi, K.K. (2013). Increasing Leidenfrost point using micro-nano hierarchical surface structures. *Applied Physics Letters*, 103(20), 201601. doi: 10.1063/1.4828673

[27] Geraldi, N.R., McHale, G., Xu, B.B., Wells, G.G., Dodd, L.E., Wood, D., & Newton, M.I. (2016). Leidenfrost transition temperature for stainless steel meshes. *Materials Letters*, 176, 205–208. doi: 10.1016/j.matlet.2016.04.124

[28] Takata, Y., Hidaka, S., Cao, J.M., Nakamura, T., Yamamoto, H., Masuda, M., & Ito, T. (2005). Effect of surface wettability on boiling and evaporation. *Energy*, 30(2–4), 209–220. doi: 10.1016/j.energy.2004.05.004

[29] Weickgenannt, C.M., Zhang, Y., Lembach, A.N., Roisman, I.V., Gambaryan-Roisman, T., Yarin, A.L., & Tropea, C. (2011). Non-isothermal drop impact and evaporation on polymer nanofiber mats. *Physical Review E - Statistical, Nonlinear, and Soft Matter Physics*, 83(3), 1–13. doi: 10.1103/PhysRevE.83.036305

[30] Sinha-Ray, S., Zhang, Y., & Yarin, A.L. (2011). Thorny devil nanotextured fibers: The way to cooling rates on the order of 1 kW/cm^2. *Langmuir*, 27(1), 215–226. doi: 10.1021/la104024t

[31] Sahu, R.P., Sett, S., Yarin, A.L., & Pourdeyhimi, B. (2015). Impact of aqueous suspension drops onto non-wettable porous membranes: Hydrodynamic focusing and penetration of nanoparticles. *Colloids and Surfaces A: Physicochemical and Engineering Aspects*, 467, 31–45. doi: 10.1016/j.colsurfa.2014.11.023

[32] Sinha-Ray, S., & Yarin, A.L. (2014). Drop impact cooling enhancement on nano-textured surfaces. Part I: Theory and results of the ground (1 g) experiments. *International Journal of Heat and Mass Transfer*, 70, 1095–1106. doi: 10.1016/j.ijheatmasstransfer.2013.11.007

[33] Sinha-Ray, S., Sinha-Ray, S., Yarin, A.L., Weickgenannt, C.M., Emmert, J., & Tropea, C. (2014). Drop impact cooling enhancement on nano-textured surfaces. Part II: Results of the parabolic flight experiments [zero gravity (0g) and supergravity (1.8g)]. *International Journal of Heat and Mass Transfer*, 70, 1107–1114. doi: 10.1016/j.ijheatmasstransfer.2013.11.008

[34] Thakur, S.S., Chandel, S.S., Kakoria, A., & Sinha-Ray, S. (2022). Enhancement in pool boiling heat transfer of ethanol and nanofluid on novel supersonic nanoblown nanofiber textured surface. *Experimental Heat Transfer*, 35(4), 516–532. doi: 10.1080/08916152.2021.1919243

[35] Pippal, R., Shukla, P.K., & Sinha-Ray, S. (2025). Enhancing boiling heat transfer on an ultrafine nanofibrous coated superheated surface using ethanol/SWCNT Nanofluid. *Thermal Science and Engineering Progress*, 65, 103876. doi: 10.1016/j.tsep.2025.103876

[36] Sahu, R.P., Sinha-Ray, S., Sinha-Ray, S., & Yarin, A.L. (2016). Pool boiling of Novec 7300 and self-rewetting fluids on electrically-assisted supersonically solution-blown, copper-plated nanofibers. *International Journal of Heat and Mass Transfer*, 95, 83–93. doi: 10.1016/j.ijheatmasstransfer.2015.11.094

[37] Sinha-Ray, S., Zhang, W., Stoltz, B., Sahu, R.P., Sinha-Ray, S., & Yarin, A.L. (2017). Swing-like pool boiling on nano-textured surfaces for microgravity applications related to cooling of high-power microelectronics. *npj Microgravity*, 3, 9. doi: 10.1038/s41526-017-0014-z

[38] Sinha-Ray, S., Zhang, W., Sahu, R.P., Sinha-Ray, S., & Yarin, A.L. (2017). Pool boiling of Novec 7300 and DI water on nano-textured heater covered with supersonically-blown or electrospun polymer nanofibers. *International Journal of Heat and Mass Transfer*, 106, 482–490. doi: 10.1016/j.ijheatmasstransfer.2016.08.101

[39] Khooshehchin, M., Mohammadidoust, A., & Ghotbinasab, S. (2020). An optimization study on heat transfer of pool boiling exposed ultrasonic waves and particles addition. *International Communications in Heat and Mass Transfer*, 114, 104558. doi: 10.1016/j.icheatmasstransfer.2020.104558

[40] Washburn, E.W. (1921). Note on a method of determining the distribution of pore sizes in a porous material. *Proceedings of the National Academy of Sciences*, 7(4), 115–116. doi: 10.1073/pnas.7.4.115

Co-published by
Institute of Fluid-Flow Machinery
Polish Academy of Sciences
Committee on Thermodynamics and Combustion
Polish Academy of Sciences

Copyright©2026 by the Authors under licence CC BY-NC-ND 4.0

http://www.imp.gda.pl/archives-of-thermodynamics/

One-dimensional model of solid oxide fuel cell for advanced hybrid energy systems analysis

Julian Piotr Jędrzejewski[a,b*], Sebastian Lepszy[a], Sebastian Rulik[a]

[a]Silesian University of Technology, Faculty of Energy and Environmental Engineering, Konarskiego 18, 44-100 Gliwice, Poland
[b]Antea Polska S.A., Dulęby 5, 40-833 Katowice, Poland
*Corresponding author email: sebastian.lepszy@polsl.pl

Received: 02.11.2024; revised: 23.12.2025; accepted: 23.01.2026

Abstract

Growing demand for electricity and the intensification of the use of renewable energy sources create the need for the development of energy technologies, including hydrogen-based solutions. In the context of generating energy from hydrogen, fuel cells are characterised by particularly favourable operating parameters. The literature identifies several types of fuel cells, among which high-temperature solid oxide fuel cells (SOFCs) show significant application potential. This is related, among other factors, to the possibility of integrating these cells into hybrid energy systems (fuel cell − gas cycle − steam cycle) with various configurations and high energy efficiency. To determine the optimal structures of hybrid systems, detailed system analyses are essential, requiring accurate modelling of fuel cell characteristics. Depending on the objective of the analyses, the cell models may vary in complexity. This paper presents an advanced one-dimensional fuel cell model, enabling more realistic preliminary thermodynamic and economic analyses of hybrid systems. This model facilitates the assessment of efficiency, dimensions and exhaust media parameters. Furthermore, it allows for the verification of whether the cell parameters used in the analyses align with their practical implementation capabilities.

Keywords: Hybrid energy systems; SOFC; One-dimensional modelling; High-temperature fuel cell

Vol. 47(2026), No. 113–123; doi: 10.24425/ather.2025.156859

Cite this manuscript as: Jędrzejewski, J.P., Lepszy, S., & Rulik, S. (2026). One-dimensional model of solid oxide fuel cell for advanced hybrid energy systems analysis. *Archives of Thermodynamics*, 47(1), 113–123.

1. Introduction

The increase in installed capacity in renewable energy sources, driven by the fight against global warming and the growing demand for electricity, is driving the development of energy storage technologies. One promising energy carrier which offers the possibility of long-term storage and zero-emission generation of electricity and heat is hydrogen. In the context of generating energy from hydrogen, fuel cells exhibit particularly favourable operating parameters. Fuel cells are electrochemical systems that convert the chemical energy from a fuel oxidation reaction directly into electricity and heat [1]. The literature identifies several types of fuel cells, including polymer electrolyte membrane fuel cells (PEM), alkaline fuel cells (AFC), phosphoric acid fuel cells (PAFC) and solid oxide fuel cells (SOFC) [2−4]. Among these, SOFCs show significant application potential, as evidenced by various review works, such as [5−7], just to name the most recent. Fuel cells of this type operate at very high temperatures – up to 1000°C – eliminating the need for precious-metal catalyst [2]. High-temperature SOFCs are also noted by their high electrical efficiency [1,8] reaching up to 49% [9]. In addition, SOFCs can be integrated into hybrid systems, achieving electrical efficiencies of up to 60% [10]. Numerous studies have explored cogeneration systems based on high-temperature SOFC. In [11], the authors analyse the economic feasibility of SOFC-based cogeneration systems for non-residential buildings, particularly supermarkets.

Nomenclature

A – channel area, m^2
c_p – specific heat at constant pressure, J/(kg K)
d – diameter or characteristic linear dimension, m
f – friction coefficient
FUF– fuel utilisation factor
$\dot{H}$ – physical enthalpy flow, W
I – current intensity, A
L – length, m
LHV– lower heating value, J/kg
$\dot{m}$ – mass flow rate, kg/s
N – power, W
Nu – Nusselt number
O – fluid-wetted perimeter of the channel, m
p – pressure, Pa
Pr – Prandtl number
$\dot{Q}$ – thermal energy flow, W
r – unit resistance, Ω/cm^2
R – resistance, Ω
Re – Reynolds number
t – temperature, °C
U – voltage, V
w – velocity, m/s

Greek symbols

α – heat transfer coefficient, W/(m^2 K)
Δ – change (drop or increase)
η – efficiency
λ – thermal conductivity coefficient, W/(m·K)
μ – dynamic viscosity coefficient, Pa·s
ν – kinematic viscosity coefficient, m^2/s
ρ – density, kg/m^3

Subscripts and Superscripts

a – air
el – electric
f – fuel
FC – fuel cell
H2 – hydrogen
i – inlet
l – laminar
lim – limit
o – outlet
s – series
t – turbulent
0 – no load

Abbreviations and Acronyms

CHP – combined heat and power
LSM – $La_{0.8}Sr_{0.2}MnO_{3-\delta}$ (perovskite-type oxide)
PEM – polymer electrolyte membrane fuel cell
SOEC – solid oxide electrolyser cell
SOFC – solid oxide fuel cell
YSZ – yttria stabilised zirconia
0D – zero-dimensional
1D – one-dimensional
2D – two-dimensional
3D – three-dimensional

While [12] presents designing and optimising a hybrid cogeneration system for off-grid applications, based on an SOFC as the primary energy source, integrated with hydrogen storage, a PEM fuel cell, and a battery, to enhance system flexibility, reduce investment costs, and extend SOFC lifetime by enabling steady-load operation. The authors of [13] aim to design and analyse a novel, carbon-free tri-generation system that utilises a combined SOFC and solid oxide electrolyser cell (SOEC) to produce hydrogen, electricity, and heat from natural gas, while enabling efficient CO_2 capture and decentralised energy supply. In [14], the authors provide a comprehensive review of fuel cell-based micro-combined-heat-and-power (micro-CHP) systems, focusing on their configurations, fuel processing methods, thermal management, and integration with other technologies like energy storage and renewable sources.

To determine the optimal structure of hybrid systems, detailed system analyses are necessary, requiring accurate modelling of fuel cell characteristics.

According to [15,16], there are three core types of approaches of SOFC modelling based on how much physical knowledge is embedded in the model:

- physical (white-box) models, which are based purely on physics and chemistry laws;
- black-box models, which are based on empirical data and machine learning;
- grey-box (hybrid) models, which are the combination of physical modelling and data-driven components.

Physical models are used for design, simulation and diagnostics, while black-box models are used for control and fault detection. The grey-box models are used for real-time modelling and diagnostics [15]. In this paper, the authors focused on physical models.

Physical models are fully physics-based models, derived from electrochemistry, thermodynamics, heat and mass transfer, as well as electrical conduction laws [16]. These models are characterised by high interpretability and accuracy, and are typically represented by partial differential equations (PDEs) or ordinary differential equations (ODEs). These models require detailed material and geometry data.

Physical models are divided into:

- multi-dimensional models, which are used for modelling from full spatial detail to system-level specifications [15,16];
- electrochemical impedance spectroscopy (EIS) based equivalent circuit models, which use impedance spectroscopy for parameter estimation and fault diagnosis [15].

Dimensional models can be divided into:

- Three-dimensional (3D) models are the most detailed and accurate, capturing full spatial variations in all directions. They are used to analyse local behaviours, such as temperature gradients, current density distribution and fuel utilisation. These models are computationally intensive and best suited for design optimisation and high-fidelity simulations [15,16].

- Two-dimensional (2D) models simplify geometry by neglecting one spatial dimension. They are commonly applied to symmetric or repetitive designs (e.g. planar or tubular cells). These models are useful for analysing cross-sectional behaviour and allow a good trade-off between accuracy and computational efficiency [15].
- One-dimensional (1D) models assume variation along a single direction – typically the gas flow direction. Effects like concentration and ohmic losses in neglected dimensions are often handled using empirical corrections or averaged parameters. These models are suitable for evaluating overall cell performance, dynamic response, and simplified control or hybrid system studies [15].
- Zero-dimensional (0D) models treat the entire SOFC or system as a lumped unit with spatially averaged parameters. These models are used in system-level simulations, such as SOFC–gas turbine hybrids or CHP systems. While they cannot capture internal cell phenomena, they are ideal for rapid performance estimation, control and parametric/system-level optimisation [15].

In [17], the authors present a 1D dynamic model of SOFC developed to enhance real-time predictions of temperature and pressure variations along the cell, outperforming existing 0D models. The model demonstrates that activation overpotentials are significant and that optimising gas channel configurations can reduce the required pumping power.

In [18], the authors present two computational models for predicting the electrical performance of a tubular SOFC designed by Siemens Westinghouse Corporation. The first model employs simplifying assumptions for activation and concentration polarisations to obtain an analytical solution, while the second model allows these polarisations to vary with current density and solves the equations numerically. Both models show good agreement with experimental results, making the simpler analytical model useful for predicting cell performance based on dimensions and aiding in cost-performance analysis.

The paper [19] compares 0D and 1D modelling techniques for predicting the performance of tubular SOFCs. It finds that, while 0D models tend to overestimate voltage, power and temperature, 1D models offer more accurate local current density predictions along the cell. The study underscores the importance of discretisation in enhancing model accuracy and demonstrates that temperature distribution is critical for optimising SOFC design and performance.

The work [20] specifically examines mathematical modelling of SOFCs, focusing on both tubular and planar configurations. It discusses various factors, including mass, energy and momentum transfer, diffusion through porous media, electrochemical reactions and polarisation losses, while also comparing the effects of different fuels on SOFC performance. Additionally, the review highlights novel modelling approaches, including data-driven techniques like artificial neural networks, and suggests areas for further research to enhance SOFC models and improve predictions of fuel cell behaviour.

Paper [21] presents a detailed 1D, axial-symmetric model of a tubular SOFC, incorporating advanced descriptions of electrochemical reactions, internal reforming kinetics, and thermodynamic balances to predict temperature, pressure and composition profiles along the cell. A comprehensive case study and sensitivity analysis demonstrate how key design and operational parameters impact performance, challenging common simplifications in existing SOFC models.

The study presented in [22] develops a fast, high-fidelity 1D thermodynamic model for SOFC stacks that uses experimental data to identify optimal operating conditions and efficiency-performance trade-offs without requiring costly simulations or experiments.

The literature also contains numerous papers addressing 2D models [23,24] as well as 3D models [25,26]. The study presented in [27] introduces a computationally efficient 3D multiphysics model using backpropagation neural networks to optimise the structural design of large-scale SOFC stacks and towers, improving flow uniformity, temperature distribution, and overall performance.

Paper [28] presents a detailed 3D numerical simulation of a 1 kW hydrogen-fuelled planar SOFC stack to investigate internal thermal conditions and heat transfer mechanisms under realistic operating conditions and actual geometry. The study reveals that air flow and heat capacity dominate the temperature distribution and gradients, with air advection and interconnect conduction being the key heat transfer pathways, highlighting the importance of thermal management strategies for reducing thermal stress and enhancing stack reliability.

Unlike the study presented in [28], this work focuses on simpler system models that require less computational memory and time. System models simulate the overall behaviour of the cell within a complete power generation system, rather than resolving all the internal physical and chemical processes in fine detail. These models are preferably used when multiple variants of a case (numbering in hundreds) have to be analysed [17].

The primary objective of this study is to develop an analytical model that utilises available current-voltage (*I-V*) characteristics to estimate both the geometric sizing of a solid oxide fuel cell and the thermodynamic properties of the electrochemical reaction products. Rather than aiming to replicate the detailed internal electrochemical and transport phenomena typically captured in high-resolution one-dimensional models, this work focuses on constructing a phenomenological framework that balances physical realism with numerical simplicity. The model is designed specifically for integration into broader hybrid energy systems − such as configurations combining SOFCs with air turbines − where system-level optimisation and computational efficiency are critical.

The proposed approach prioritises scalability and computational speed over high-fidelity resolution, enabling its application in iterative design processes, parametric analyses and techno-economic evaluations. By introducing justified simplifications that preserve core predictive capabilities, the model facilitates significant reductions in computational demand, making it practical for early-stage design and decision-making workflows.

Key outputs of the model include the specific power density of the fuel cell, the active electrochemical surface area, internal energy losses and the thermodynamic characteristics of exhaust

gases. These parameters provide a foundation for subsequent cost estimation algorithms and system-level performance evaluations. Ultimately, the model supports the optimisation of hybrid configurations with respect to both energy efficiency and economic performance, offering a valuable tool for the development of advanced, high-efficiency energy systems.

2. Fuel cell model

The analyses employed a 1D model of tubular SOFC fuel cells. The presented model utilises current-voltage characteristics based on experimental data or physical models developed by other researchers, in such a way that it enables the determination of the size of the modelled fuel cell and the output parameters of the products of electrochemical reactions occurring within the cell. The model's calculation algorithm divides the fuel cell into elementary ring-shaped sections, for which the outlet parameters are computed based on the input parameters. Additionally, the algorithm assumes that there is no voltage drop during current flow along the electrodes. The omission of voltage drops along the electrodes − resulting from electronic and ionic resistances within the electrode materials − can lead to an overestimation of both the efficiency and power output predicted by the model. While these internal losses may be negligible in small-scale fuel cells or under moderate current densities, they become increasingly significant in larger systems or during high-current operation. Under such conditions, the associated non-uniformities in potential and temperature distributions can impact local reaction rates and overall system performance. Nonetheless, the level of accuracy retained is considered sufficient for the intended application of the model, which prioritises computational efficiency and system-level analysis over detailed intra-cell resolution.

To determine the operating parameters of the fuel cell, the characteristic proposed by Milewski [29] was utilised. The cell for which the characteristics are given has the main layers as follows:

- first anode layer made of Ni + YSZ (yttria stabilised zirconia),
- second anode layer made of Ni + YSZ,
- electrolyte layer made of YSZ,
- second cathode layer made of LSM ($La_{0.8}Sr_{0.2}MnO_{3-\delta}$) + YSZ,
- first cathode layer made of LSM.

The current-voltage characteristic has been compared with actual experimental data [29]. The literature includes publications presenting current-voltage characteristics of SOFCs based on the same electrode and electrolyte materials [30−33]. The characteristic used in this study is consistent with the results reported in the aforementioned works.

To simplify the calculations, linearised current-voltage characteristics (Fig. 1) for three operating temperatures were used as a data source for the substitute fuel cell model.

The linearisation of the current-voltage characteristic constitutes a fundamental simplification of the inherently nonlinear electrochemical behaviour of solid oxide fuel cells (SOFCs). In practice, the cell voltage is governed by a combination of activation, ohmic and concentration overpotentials, all of which exhibit increasingly nonlinear behaviour as current density rises. By

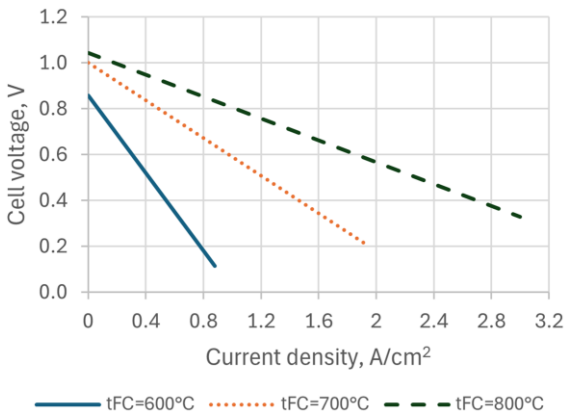


Fig. 1. Simplified current-voltage characteristic of the fuel cell for three cell operating temperatures.

adopting a linear approximation of the current-voltage relationship, the model may inadequately represent these phenomena, potentially resulting in either underestimation or overestimation of cell voltage, depending on the specific operating conditions. This limitation becomes particularly pronounced under extreme operational scenarios − such as high load demand − where nonlinear effects dominate the electrochemical response. Nevertheless, the proposed linear approximation demonstrates satisfactory agreement with experimental data, providing an acceptable level of accuracy for the model's intended applications, which prioritise computational efficiency and system-level integration.

Linearisation of the fuel cell characteristics enables the use of an electrical model of an elementary fuel cell represented as a voltage source in series with a resistance (Fig. 2).

Based on the fuel cell model and the linearised characteristics, the relationship between the unit series resistance and no-load voltage as a function of temperature was established. This relationship is expressed by the following formulas:

$$r_s = 36.374 \exp(-0.006t), \tag{1}$$

$$U_0 = 0.00093t + 0.3, \tag{2}$$

where: r_s – unit series resistance, U_0 – no-load cell voltage, t – fuel cell temperature.

The 1D model uses the principle of conservation of momentum to determine the pressure drop during the flow of agents. In these calculations, it is assumed that the velocity and density of the agent remain constant within the elementary section and are equal to the outlet values from the previous element. Consequently, the pressure losses during the flow of agents are calculated using the Darcy-Weisbach equation:

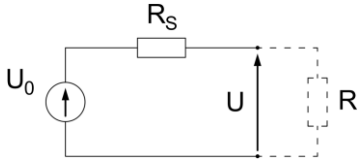


Fig. 2. Simplified model of a fuel cell.

$$\Delta p = f\frac{\rho w^2}{2}\frac{O}{4A}\Delta L, \tag{3}$$

where: Δp – pressure loss, f – friction coefficient, ρ – density of an agent, w – velocity of an agent, O – agent-wetted perimeter of the channel, A – channel area, ΔL – section length.

The friction coefficient was determined using the equation proposed by Churchill [34], which is applicable for laminar, turbulent and transitional flow for smooth pipes:

$$f = 2\left[\left(\frac{8}{\mathrm{Re}}\right)^{12} + \frac{1}{(A+B)^{\frac{3}{2}}}\right]^{\frac{1}{12}}, \tag{4}$$

$$A = \left[2.457\ln\left(\frac{1}{\frac{7}{\mathrm{Re}}+0.27\frac{O}{d}}\right)\right]^{16}, \tag{5}$$

$$B = \left(\frac{37.53}{\mathrm{Re}}\right)^{16}, \tag{6}$$

where: Re – Reynolds number, d – diameter or characteristic linear dimension.

Dynamic viscosity was determined using the CoolProp library [35]. Kinematic viscosity was determined according to the formula

$$\nu = \frac{\mu}{\rho}, \tag{7}$$

where μ is the dynamic viscosity coefficient.

The Reynolds number was calculated using the formula

$$\mathrm{Re} = \frac{w\cdot d}{\nu}. \tag{8}$$

The Prandtl number was calculated using the formula

$$\mathrm{Pr} = \frac{\mu c_p}{\lambda}, \tag{9}$$

where: c_p – specific heat at constant pressure, λ – thermal conductivity coefficient.

The thermal conductivity coefficient and specific heat were also determined using the CoolProp library.

Dynamic viscosity and thermal conductivity were determined as functions of temperature and partial pressure.

For the elementary section of the fuel cell, the energy balance was formulated using equations in the following form:

$$\dot{H}_{ai} + \dot{H}_{fi} + \dot{Q}_{\mathrm{FC}} = \dot{H}_{ao} + \dot{H}_{fo} + N_{\mathrm{elFC}}, \tag{10}$$

$$\dot{Q}_{\mathrm{FC}} = (1-\eta_{\mathrm{elFC}})\Delta\dot{m}_{\mathrm{H2}}\mathrm{LHV}_{\mathrm{H2}}, \tag{11}$$

$$N_{\mathrm{elFC}} = \eta_{\mathrm{elFC}}\Delta\dot{m}_{\mathrm{H2}}\mathrm{LHV}_{\mathrm{H2}}, \tag{12}$$

where: $\dot{H}_{ai}$ – physical enthalpy flow of air at the inlet, $\dot{H}_{fi}$ – physical enthalpy flow of fuel at the inlet, $\dot{Q}_{\mathrm{FC}}$ – thermal energy flow from the chemical reaction of hydrogen and oxygen, $\dot{H}_{ao}$ – physical enthalpy flow of air at the outlet, $\dot{H}_{fo}$ – physical enthalpy flow of fuel at the outlet, N_{elFC} – electrical energy from the reaction of hydrogen and oxygen, η_{elFC} – electrical efficiency of the fuel cell, $\Delta\dot{m}_{\mathrm{H2}}$ – mass flow of hydrogen reacting with oxygen, and $\mathrm{LHV}_{\mathrm{H2}}$ – lower heating value of hydrogen.

Physical enthalpy is also determined using the CoolProp library. The input data required to calculate the physical enthalpy of a gas mixture are the mass composition of the gas, its temperature and pressure, and the reference temperature.

It was assumed that the primary mechanism influencing heat transfer in the elementary element is heat convection. This assumption simplifies the calculations while ensuring a balanced temperature in the modelled fuel cell element.

The key parameter for determining the amount of heat flowing from the fuel cell to the surrounding medium is the heat transfer coefficient. Its value was calculated based on the friction coefficient. The Nusselt number developed by Gnieliński (after [36]) was used to determine the heat transfer coefficient:

$$\mathrm{Nu}_t = \frac{\frac{f}{8}\mathrm{Pr}(\mathrm{Re}-1000)}{1+12.7\sqrt{\frac{f}{8}}\left(\mathrm{Pr}^{\frac{2}{3}}-1\right)}, \tag{13}$$

$$\mathrm{Nu}_l = \left\{3.66^3 + 0.7^3 + \left[1.615\left(\mathrm{RePr}\frac{d}{L}\right)^{\frac{1}{3}} - 0.7\right]^3 + \left(\frac{2}{1+22\mathrm{Pr}}\right)^{\frac{1}{6}}\left(\mathrm{RePr}\frac{d}{L}\right)^{\frac{1}{2}}\right\}, \tag{14}$$

$$\mathrm{Nu} = \mathrm{Nu}_{l,2300} + \frac{(\mathrm{Nu}_{t,4000}-\mathrm{Nu}_{l,2300})(\mathrm{Re}-2300)}{4000-2300}, \tag{15}$$

where: Nu_t – Nusselt number for turbulent flow, Nu_l – Nusselt number for laminar flow, $\mathrm{Nu}_{l,2300}$ – Nusselt number for laminar flow at Re = 2300, $\mathrm{Nu}_{t,4000}$ – Nusselt number for turbulent flow at Re = 4000, d – channel diameter, L – channel length.

The heat transfer coefficient was determined based on the calculated Nusselt number:

$$\alpha = \frac{\mathrm{Nu}\lambda}{d}, \tag{16}$$

where: α – heat transfer coefficient, d – characteristic linear dimension.

The presented model has been implemented in the SciLab environment. The model's results were obtained by solving the energy balance equations using an iterative method.

The main element determining the parameters of the fuel cell in the proposed model is its current-voltage characteristics. This approach ensures an accurate representation of the behaviour of real fuel cells across different scales. Modelling other types of cells with different designs (e.g. planar cells) requires significant changes in heat flow modelling, and obtaining reliable results in such cases necessitates three-dimensional analyses, which are more demanding in terms of model detail and computation time.

Modelling other flow directions is possible, but of limited relevance from the standpoint of the resulting exhaust gas temperatures and their potential for generating additional electrical energy in gas-based systems. Modelling cells made of other materials essentially reduces to changing the current-voltage characteristics of the cells used in the model.

3. Input parameters for analysis

In the modelling process, it was assumed that the fuel for the cell is hydrogen, comprising 95% by volume. Additionally, the fuel contains 4% nitrogen and 1% water vapour by volume. The fuel temperature is set at 20°C, and its pressure is equal to 1 bar(a). These values are based on the assumption that the model will be used for the analysis of a combined system with a gas turbine, where the fuel cell operates at a pressure close to the ambient pressure.

For the fuel cell, the air was assumed to have the following molar composition: nitrogen 78.1%, argon 0.9% and oxygen 21.0%. The analysis considered a high initial air temperature to enable the cell to start operating. The air pressure was maintained at 1 bar(a), with an air flow rate of 1 kg/s. The fuel flow rate was determined based on the assumed excess air coefficient λ. This assumption was made to decouple the model from the system scale.

One of the primary operating parameters of a stack, or multiple fuel cell elements connected in parallel, is the operating voltage of individual cells and the entire assembly. Theoretically, this voltage can range from 0 to U_{MAX}, depending on the operating temperature and the concentration of components, specifically hydrogen and oxygen. Due to simplifications in the form of linearisation of fuel cell characteristics, the range of operating voltage has been limited to between 0.2 V and 0.8 V.

Parametric calculations were performed assuming five variables for calculations:

- air velocity at the inlet to the cell, w_a (5–15 m/s);
- cell operating voltage, U (0.2–0.8 V);
- fuel utilisation limit factor, FUF_{lim} (0.6–0.8);
- excess air coefficient, λ (2.0–3.0);
- air temperature at the inlet to the cell, t_a (500–600°C).

The developed algorithm also provides error codes that indicate the following events:

- too many iterations of a given case (for the number of iterations exceeding 3000),
- fuel cell temperature exceeded 1000°C,
- the value of hydrogen used for at least one of the iterations is negative,
- the cross-sectional diameter of the cell channel is smaller than 5 mm,
- the fuel pressure drop exceeded 200 hPa,
- the air pressure drop exceeded 200 hPa.

The operational limitations embedded in the model's error-handling routine serve a dual purpose: they ensure numerical stability during simulations and help maintain the physical plausibility of results. If any of the predefined error conditions are encountered − such as violations of thermodynamic or electrochemical constraints − the algorithm automatically excludes the corresponding input set by returning an error code and terminating that specific computation. As a result, the range of output results presented is narrower than the full set of initially simulated conditions. While this approach enhances the reliability of the simulation by filtering out infeasible operating points, it also restricts the model's capacity to explore the full spectrum of scenarios encountered in practical SOFC-based hybrid systems, particularly near operational boundaries. Despite these constraints, the adopted simplifications are justified within the context of the model's intended application: early-stage design exploration, performance assessment and parametric analysis, where computational efficiency and simulation stability take precedence.

4. Results and discussion

The authors do not aim to model the fuel cell itself in detail, but rather to develop an analytical model of the cell that can subsequently be integrated into a hybrid system model – such as one in which the fuel cell operates in conjunction with an air turbine – to maximise electricity production within the analysed system. The outputs of the developed model include parameters such as specific power, properties of exhaust products and fuel cell active surface area. These parameters will, in the future, serve as a foundation for extending the model with an algorithm for calculating the cost of the fuel cell and the entire hybrid system, as well as for optimising the system in terms of both energy efficiency and economic performance. Results associated with error codes have been excluded from the analysis.

4.1. Unit power of the fuel cell as a function of the fuel cell operating voltage

Figure 3 shows the unit power of the fuel cell as a function of the cell operating voltage for various values of temperature and air velocity at the inlet to the fuel cell.

Parametric calculations were performed for voltages ranging from 0.2 V to 0.8 V, but the possible operating range of the cell is much narrower. For low voltages, the cell reached a temperature above 1000°C, which could result in its melting. This results from the low electrical efficiency of the cell for low voltages. The lower the electrical efficiency of the cell, the higher the amount of heat generated during the electrochemical reaction occurring in the cell, which results from Eq. (11). It should be noted that the higher the air temperature at the inlet to the cell, the higher the cell temperature for a larger range of low voltages. This can be explained directly from the energy balance of the cell (Eq. (10)), because the higher the enthalpy of the substrates, the faster the cell heats up to a given temperature. On the other hand, however, with an increase in the air temperature at the inlet to the fuel cell, the unit power obtained in the fuel cell increases, which results from Fig. 1 and Eq. (2).

Figure 3 clearly shows three groups of curves presenting the results for three given air temperatures at the inlet to the cell, i.e. 500°C, 550°C and 600°C – the higher the temperature, the higher the unit power obtained by the cell. This is related to an increase in the unit current intensity with an increase in the cell temperature (Fig. 1). In addition, the graph presented in Fig. 3

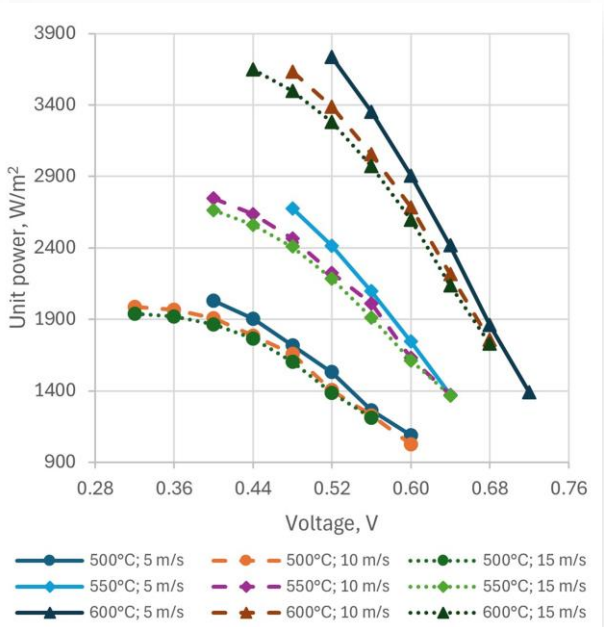


Fig. 3. Unit power of the fuel cell as a function of the cell operating voltage for different values of temperature and velocity of air at the fuel cell inlet (FUF_{lim} = 0.6, λ = 2.5).

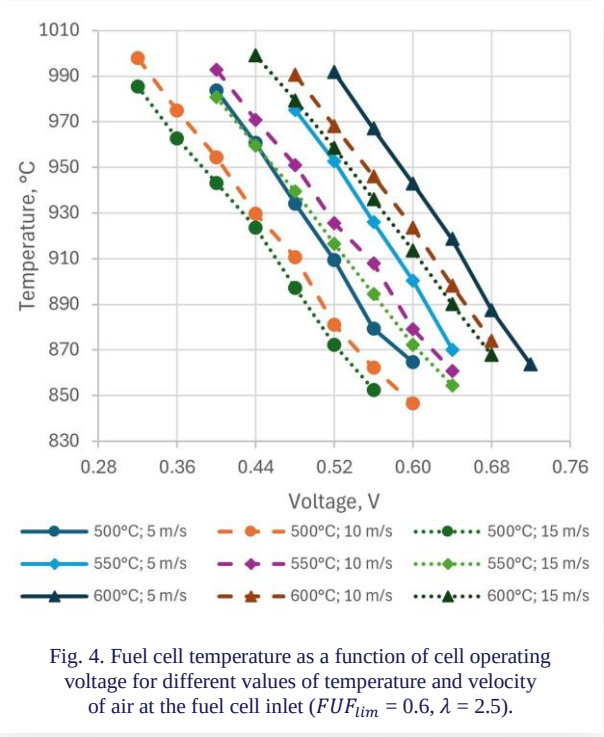


Fig. 4. Fuel cell temperature as a function of cell operating voltage for different values of temperature and velocity of air at the fuel cell inlet (FUF_{lim} = 0.6, λ = 2.5).

shows that the unit power of the fuel cell decreases with an increase in voltage, because the higher the voltage, the amount of fuel used per unit of the cell surface area decreases.

Another issue is the effect of the air velocity at the inlet to the cell on the unit power obtained in the cell. It is clearly visible that for each of the three temperature groups discussed above, the highest unit power values are obtained at the lowest values of inlet air velocity, i.e. 5 m/s. With the increase in this velocity, the results obtained for the individual voltages decrease slightly, and the possible range of the cell's operation shifts to higher voltages. Here comes the issue of the results obtained for the upper voltage range, for which the fuel pressure drop exceeded 200 hPa. The obtained fuel pressure drop results from the model assumptions and the efficiency of the fuel cells. One of the model input data is the value of the FUF. The model performs calculations until the set limit value FUF_{lim} is obtained. As mentioned earlier, the higher the voltage, the lower the fuel utilisation per unit of cell surface area, so to obtain the required FUF_{lim}, the cell surface area increases (the cell lengthens), which directly affects the increase in the fuel pressure drop at flow that results from Eq. (3).

4.2. Fuel cell temperature as a function of the fuel cell operating voltage

Figure 4 shows a graph of the fuel cell temperature as a function of the cell operating voltage for different values of temperature and velocity of air at the inlet to the cell. The graph clearly shows that the fuel cell temperature decreases with an increase in voltage. This results from the fact that the amount of fuel used per unit area decreases with an increase in the cell operating voltage (the unit fuel utilisation factor decreases). Also, the electrical efficiency of the fuel cell increases with an increase in the cell operating voltage, which means that less heat is released from the electrochemical reaction taking place in the cell (Eq. (11)). The graph also shows that as the air temperature at the inlet to the fuel cell increases, the cell operating range shifts to higher voltages. This results from the increase in electrical efficiency of the cell and the decrease in the amount of hydrogen reacted per unit area of the cell.

4.3. Fuel temperature at the outlet of the fuel cell as a function of the fuel cell operating voltage

Figure 5 shows a graph of the fuel temperature at the outlet of the fuel cell as a function of the fuel cell operating voltage for different values of temperature and velocity of air at the inlet to the fuel cell. The graph clearly shows that the fuel temperature at the outlet of the fuel cell decreases as the cell operating voltage increases. In addition, the graph shows three groups of curves characterised by the same air velocity at the inlet to the cell. For the lowest analysed air velocity at the inlet to the cell equal to 5 m/s, the lowest values of fuel temperature at the outlet of the fuel cell were obtained for the given values of air temperature at the inlet to the fuel cell and cell operating voltage. These values increased with the increase of air velocity at the inlet to the fuel cell and reached maximum values for the highest analysed velocity equal to 15 m/s. For each group discussed, one can observe the dependence of the increase in the fuel temperature at the outlet of the fuel cell on the increase in the air temperature at the inlet to the fuel cell, which, as mentioned above, results directly from the fuel cell balance equation (Eq. (10)). In addition, the graph (Fig. 5) shows that, among others, for the lowest air velocity at the inlet to the cell (5 m/s) and the air temperature at the inlet to the cell equal to 500°C and 600°C, a local minimum occurs, after which the fuel temperature rises as the cell operating voltage increases. With an increase in the cell operating voltage, the amount of heat delivered to the fuel and air

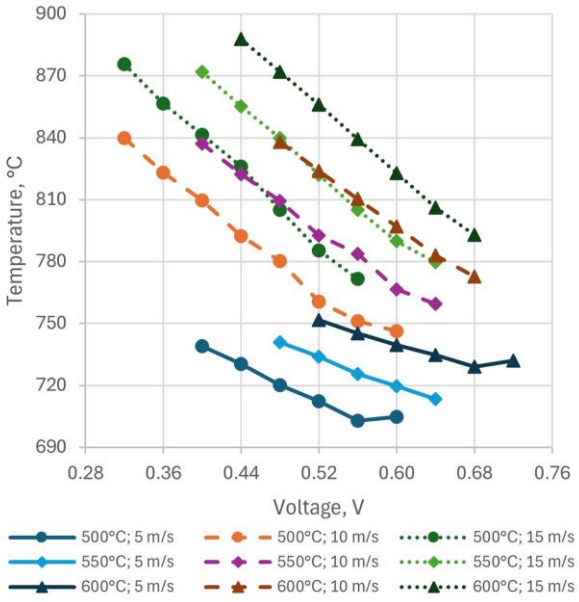


Fig. 5. Fuel temperature at the outlet of the fuel cell as a function of the cell operating voltage for different values of temperature and velocity of air at the inlet to the cell (FUF_{lim} = 0.6, λ = 2.5).

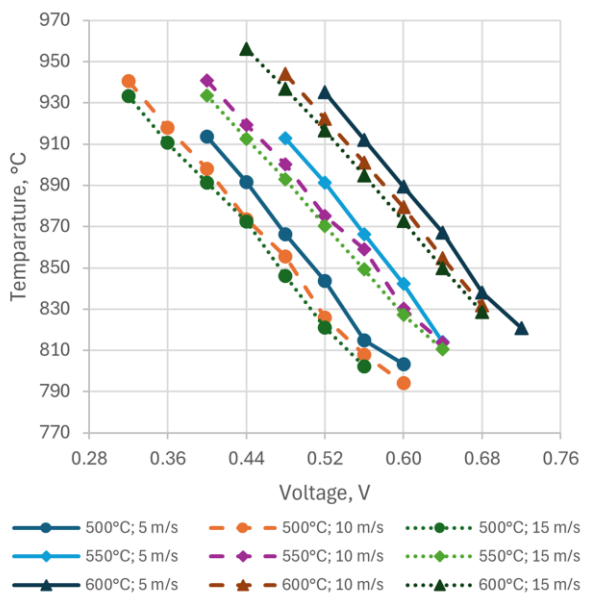


Fig. 6. Air temperature at the outlet of the fuel cell as a function of the fuel cell operating voltage for different values of temperature and velocity of air at the inlet to the cell (FUF_{lim} = 0.6, λ = 2.5).

decreases, but the decrease in this heat slows down from a certain limiting moment. At the same time, the temperature difference between the air and the fuel decreases because as the voltage increases, the cell lengthens. As a result, for low voltages, the decrease in the amount of heat with the increase in voltage prevails, while for higher voltages, the decrease in the temperature difference between the air and the fuel begins to be important. For a temperature of 500°C, the trend changes at a voltage of around 0.56 V, while for a temperature of 600°C, the trend changes at a voltage of approximately 0.68 V.

4.4. Air temperature at the outlet of the fuel cell as a function of the fuel cell operating voltage

Similar dependencies can be seen in the graph showing air temperature at the outlet of the fuel cell as a function of the cell operating voltage for different values of air temperature and velocity at the inlet to the cell (Fig. 6), i.e. as the cell operating voltage increases, the air temperature at the outlet of the fuel cell decreases. However, in this graph, the curves are grouped depending on the air temperature at the inlet to the fuel cell. Thus, the lowest values of the air temperature at the outlet of the fuel cell for the set values of air velocity at the inlet to the fuel cell and fuel cell operating voltage were obtained for the lowest set value of air temperature at the inlet to the fuel cell, i.e. 500°C. The air temperature at the outlet of the fuel cell increased with the increase of air temperature at the inlet to the fuel cell and obtained maximum values for the temperature of 600°C. As aforementioned, this follows directly from the cell balance equation (Eq. (10)). In addition, for individual groups, a relationship can be found between the drop in air temperature at the outlet of the fuel cell and the increase in air velocity at the inlet to the cell. This is due to the shorter contact time of the air with the hot fuel cell for higher air velocities.

4.5. Fuel pressure drop as a function of the fuel cell operating voltage

Figure 7 presents a graph illustrating the relationship between fuel pressure drop and fuel cell operating voltage for different air temperatures and velocities at the inlet to the fuel cell. The graph clearly shows that the fuel pressure drop increases with increasing voltage. As mentioned earlier, the described phenomenon results primarily from the model assumptions and specific properties of fuel cells. One of the key input parameters of the

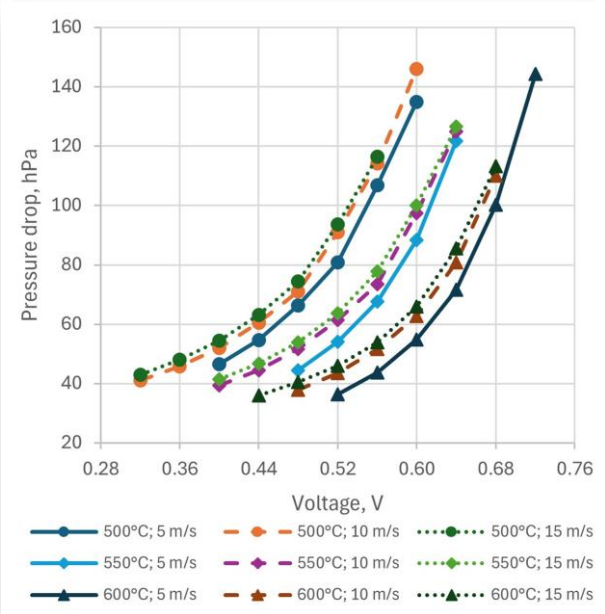


Fig. 7. Fuel pressure drop during flow through the fuel cell as a function of the fuel cell operating voltage for different values of temperature and velocity of air at the inlet to the fuel cell (FUF_{lim} = 0.6, λ = 2.5).

model is the FUF_{lim}. Calculations in the model are continued until the set limit value of the FUF_{lim} is reached. Higher voltage results in reduced fuel utilisation per unit of cell surface area. In order to achieve the required value FUF_{lim}, it is necessary to increase the cell surface area (by extending it), which directly affects an increase in the fuel pressure drop as it flows through the fuel cell (Eq. (3)).

The pressure drop value is also related to the temperature of the flowing gas, i.e. the higher the temperature, for a given voltage, the higher the unit current intensity in the fuel cell, according to Fig. 1. In turn, the higher the unit current intensity, the smaller the required fuel cell surface area to obtain the assumed FUF_{lim}; the cell is shorter, so the pressure drop associated with linear losses during flow through the channel is lower. The above relationship is evident from the graph, i.e. the decrease in fuel pressure losses during flow through the fuel cell with the increase in air temperature at the inlet to the fuel cell for a constant voltage.

4.6. Pressure drop of air flowing through the fuel cell as a function of the fuel cell operating voltage

Figure 8 shows a graph of the air pressure drop during flow through the fuel cell as a function of the fuel cell operating voltage for different values of temperature and velocity of air at the inlet to the fuel cell. Similarly to the case of the fuel, the air pressure drop during flow through the fuel cell increases with the increase of the cell operating voltage, which results, as previously described, from the decrease in the amount of reacted hydrogen per unit of the fuel cell surface and the model assumptions. Furthermore, three groups of curves for the assumed air velocities at the inlet to the fuel cell are clearly visible. The lowest values of the air pressure drop were obtained for the lowest air velocities at the inlet to the cell, and these values increase as the velocity increases. This results directly from Eq. (3), according to which the pressure drop during flow is proportional to the square of the flowing medium velocity. Moreover, for these three groups, a correlation can be observed between the increase in the air pressure drop as it flows through the fuel cell and the decrease in the air temperature at the inlet to the fuel cell. This dependence results from the decrease in the unit current intensity in the fuel cell with the decrease in the fuel cell temperature. The lower the unit current intensity, the lower the hydrogen utilisation. This affects the cell elongation, which in turn contributes to an increase in linear pressure losses. The relationship was described in detail in the previous paragraph.

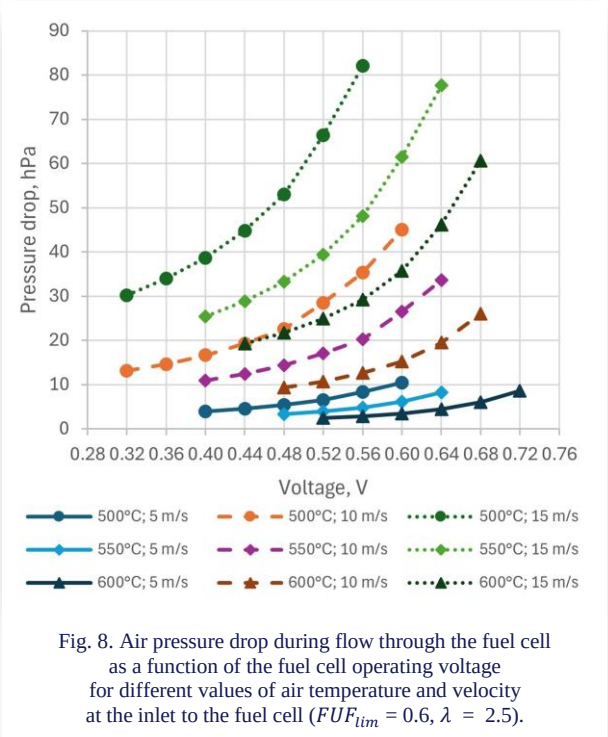


Fig. 8. Air pressure drop during flow through the fuel cell as a function of the fuel cell operating voltage for different values of air temperature and velocity at the inlet to the fuel cell (FUF_{lim} = 0.6, λ = 2.5).

4.7. Fuel cell electrical efficiency as a function of the excess air coefficient

Figure 9 shows a graph of the electrical efficiency of the fuel cell as a function of the excess air factor for different values of the cell operating voltage. The graph clearly shows that the excess air coefficient λ has no effect on the value of the electrical efficiency of the fuel cell, which in turn is strongly dependent on the value of the fuel cell operating voltage. It can be seen that with the increase in the cell operating voltage, the electrical efficiency of the fuel cell increases. The minimum value of over 13.5% is achieved for a voltage of 0.28 V, while the maximum value of about 31% is achieved for a voltage of 0.64 V.

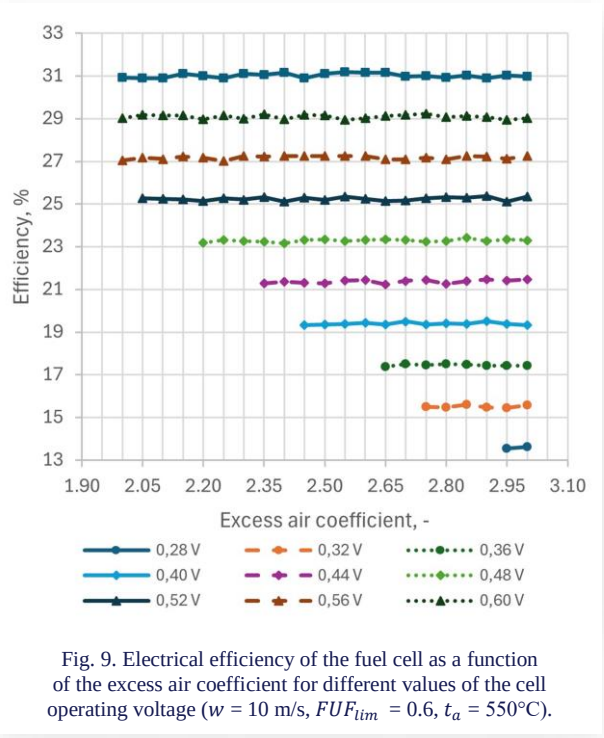


Fig. 9. Electrical efficiency of the fuel cell as a function of the excess air coefficient for different values of the cell operating voltage (w = 10 m/s, FUF_{lim} = 0.6, t_a = 550°C).

4.8. Electric power generated by the fuel cell as a function of the excess air coefficient

Figure 10 shows a plot of the electric power generated by the fuel cell as a function of the excess air coefficient for different values of the fuel cell operating voltage. Based on the graph, it can be concluded that the power of the fuel cell decreases as the

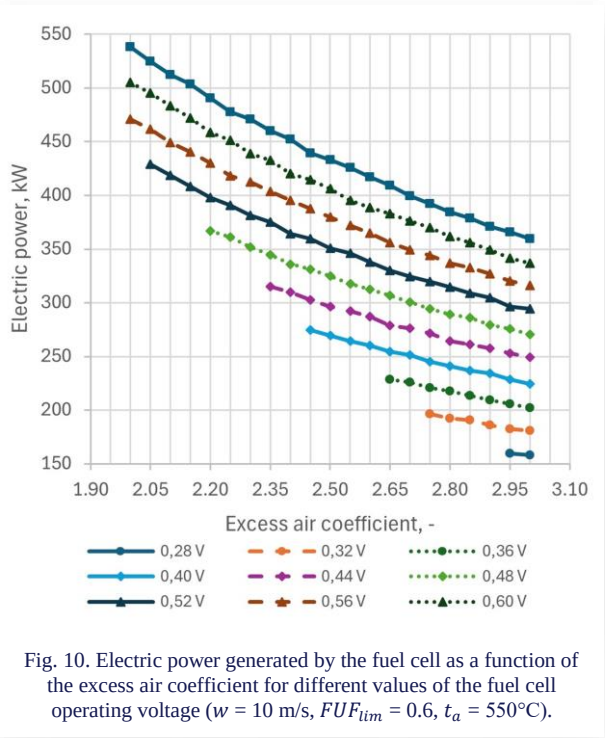


Fig. 10. Electric power generated by the fuel cell as a function of the excess air coefficient for different values of the fuel cell operating voltage (w = 10 m/s, FUF_{lim} = 0.6, t_a = 550°C).

excess air coefficient increases, which directly results from the calculation assumptions. The value of the air flow at the inlet to the fuel cell is a constant value, and for each case is 1 kg/s. In turn, the fuel flow is determined based on the excess air coefficient. With the increase of the excess air coefficient, the fuel flow supplied to the cell decreases, which directly results in a drop in the cell power output. Another relationship evident from the graph is that the cell power increases as its operating voltage increases. This results from the cell efficiency dependency on the cell operating voltage, which was discussed in the description of Fig. 9.

5. Conclusions

This paper presents a proposal for a 1D model of a solid oxide fuel cell. This model enables the determination of the fuel cell's operating range and key parameters, such as the power generated, surface area, length and operating temperature. It also calculates output parameters, including the temperature and pressure of the fuel and air at the cell's outlet. Additionally, the model assesses the variability of these values along the length of the cell.

Based on the conducted parametric analyses of the model, it was demonstrated that the proposed model accurately reflects the electro-physical properties of high-temperature fuel cells. Specifically, it was found that as the cell's operating voltage increases, its efficiency also increases; however, the unit fuel utilisation factor decreases. This decrease contributes to an increase in the fuel cell's surface area (cell elongation), which in turn affects the pressure drop of both air and fuel with the rise in voltage. Additionally, as voltage increases, the temperatures of the cell, air and fuel decrease. This phenomenon occurs because the amount of heat released by the cell diminishes due to the increase in electrical efficiency and the reduction in the unit fuel utilisation factor at higher voltages. Furthermore, as the temperature rises, the unit power of the fuel cell increases, which is directly related to the cell's current-voltage characteristics.

To ensure numerical robustness and physical validity, the model incorporates an error-handling routine that automatically discards input sets violating thermodynamic or electrochemical constraints. While this increases simulation reliability by eliminating unfeasible scenarios, it also narrows the output range and limits the model's ability to represent edge-case or transient operating conditions typical for advanced hybrid systems.

Despite its limitations, the model offers a computationally efficient and practical tool for early-stage solid oxide fuel cell design, including preliminary sizing, performance estimation and system-level techno-economic evaluation. Its implementation has already shown potential for use in conceptual design workflows, particularly in estimating operating conditions and supporting feasibility studies.

The primary limitation of the proposed model lies in its reliance on a specific current-voltage characteristic obtained from a fuel cell equipped with electrodes composed of a particular material. Consequently, to simulate a different type of fuel cell, the appropriate characteristic must be incorporated into the model. Future work will focus on extending the model by incorporating experimentally derived current-voltage characteristics for fuel cells utilising alternative electrode materials and operating under varied pressure conditions. This effort aims to build a database of diverse fuel cell configurations, thereby enhancing the model's versatility and broadening its applicability in system-level analyses.

Acknowledgements

The research was conducted as part of the implementation doctorate project, edition V, contract number RJO/SDW/005-14.

References

[1] Wang, J., Xu, Y., She, C., Xu, P., & Bagal, H.A. (2022). Optimal parameter identification of SOFC model using modified gray wolf optimization algorithm. *Energy*, 240, 122800. doi: 10.1016/j.energy.2021.122800

[2] www.energy.gov [accessed 12 Jan. 2024].

[3] Carrette, L., Friedrich, K.A., & Stimming, U. (2000). Fuel cells: principles, types, fuels, and applications. *ChemPhysChem*, 1(4), 162−193. doi: 10.1002/1439-7641(20001215)1:4<162::AID-CPHC162>3.0.CO;2-Z

[4] Faghri, A., & Guo, Z. (2005). Challenges and opportunities of thermal management issues related to fuel cell technology and modelling. *International Journal of Heat and Mass Transfer*, 48(19–20), 3891−3920. doi: 10.1016/j.ijheatmasstransfer.2005.04.014

[5] He, V., Gaffuri, M., Herle, J.V., & Schiffmann, J. (2023). Readiness evaluation of SOFC-MGT hybrid systems with carbon capture for distributed combined heat and power. *Energy Conversion and Management*, 278, 116728. doi: 10.1016/j.enconman.2023.116728

[6] Feng, Y., Qu, J., Zhu, Y., Wu, B., Wu, Y., Xiao, Z., & Liu, J. (2023). Progress and prospect of the novel integrated SOFC-ICE hybrid power system: System design, mass and heat integration, system optimization and techno-economic analysis. *Energy Con-*

version and Management: X, 18, 100350. doi: 10.1016/ j.ecmx. 2023.100350

[7] Alaedini, A.H., Tourani, H.K., & Saidi, M. (2023). A review of waste-to-hydrogen conversion technologies for solid oxide fuel cell (SOFC) applications: Aspect of gasification process and catalyst development. *Journal of Environmental Management*, 329, 117077. doi: 10.1016/j.jenvman.2022.117077

[8] Song, S., Xiong, X., Wu, X., & Xue, Z. (2021). Modeling the SOFC by BP neural network algorithm. *International Journal of Hydrogen Energy*, 46(38), 20065−20077, doi: 10.1016/ j.ijhydene.2021.03.132

[9] Barelli, L., Bidini, G., Cinti, G., & Ottaviano, P.A. (2022). Solid oxide fuel cell systems in hydrogen-based energy storage applications: Performance assessment in case of anode recirculation. *Journal of Energy Storage*, 54, 105257. doi: 10.1016/ j.est.2022. 105257

[10] Peters, R., Deja, R., Engelbracht, M., Frank, M., Nguyen, V.N., Blum, L., & Stolten, D. (2016). Efficiency analysis of a hydrogen-fueled solid oxide fuel cell system with anode off-gas recirculation. *Journal of Power Sources*, 328, 105−113. doi: 10.1016/ j.jpowsour.2016.08.002

[11] Marocco, P., Gandiglio, M., & Santarelli, M. (2022). When SOFC-based cogeneration systems become convenient? A cost-optimal analysis. *Energy Reports*, 8, 8709−8721. doi: 10.1016/ j.egyr.2022.06.015

[12] Baldi, F., Wang, L., Pérez-Fortes, M., & Maréchal, F. (2019). A cogeneration system based on solid oxide and proton exchange membrane fuel cells with hybrid storage for off-grid applications. *Frontiers in Energy Research*, 6, 139. doi: 10.3389/fenrg.2018. 00139

[13] Perdikaris, N., Panopoulos, K.D., Hofmann, Ph., Spyrakis, S., &, Kakaras, E. (2010). Design and exergetic analysis of a novel carbon free tri-generation system for hydrogen, power and heat production from natural gas, based on combined solid oxide fuel and electrolyser cells. *International Journal of Hydrogen Energy*, 35(6), 2446−2456. doi: 10.1016/j.ijhydene.2009.07.084

[14] Arsalis, A. (2019). A comprehensive review of fuel cell-based micro-combined-heat-and-power systems. *Renewable and Sustainable Energy Reviews*, 105, 391−414. doi: 10.1016/ j.rser.2019.02.013

[15] Wang, K., Hissel, D., Péra, M.C., Steiner, N., Marra, D., Sorrentino, M., Pianese, C., Monteverde, M., Cardone, P., & Saarinen, J. (2011). A Review on solid oxide fuel cell models. *International Journal of Hydrogen Energy*, 36(12), 7212−7228. doi: 10.1016/ j.ijhydene.2011.03.051

[16] Bove, R., & Ubertini, S. (2006). Modeling solid oxide fuel cell operation: Approaches, techniques and results. *Journal of Power Sources*, 159(1), 543−559. doi: 10.1016/j.jpowsour.2005.11.045

[17] Cheddie, D.F., & Munroe, N.D.H. (2007). A dynamic 1D model of a solid oxide fuel cell for real time simulation. *Journal of Power Sources*, 171(2), 634−643. doi: 10.1016/j.jpowsour.2007. 06.170

[18] Bharadwaj, A., Archer, D., & Rubin, E. (2005). Modeling the performance of a tubular solid oxide fuel cell. *Journal of Fuel Cell Science and Technology*, 2(1), 38−44. doi: 10.1115/1.1842781

[19] Karcz, M. (2009). From 0D to 1D modeling of tubular solid oxide fuel cell. *Energy Conversion and Management*, 50(9), 2307−2315. doi: 10.1016/j.enconman.2009.05.007

[20] Hajimolana, S.A., Hussain, M.A., Daud, W.M.A.W., Soroush, M., & Shamiri, A. (2011). Mathematical modeling of solid oxide fuel cells: A review. *Renewable and Sustainable Energy Reviews*, 15(4), 1893−1917. doi: 10.1016/j.rser.2010.12.011

[21] Calise, F., Dentice d'Accadia, M., Palombo, A., & Vanoli, L. (2008). One-dimensional model of a tubular solid oxide fuel cell. *Journal of Fuel Cell Science and Technology*, 5(2), 021014. doi: 10.1115/1.2784296

[22] Min, G., Park, Y.J., & Hong, J. (2020). 1D thermodynamic modeling for a solid oxide fuel cell stack and parametric study for its optimal operating conditions. *Energy Conversion and Management*, 209, 112614. doi: 10.1016/j.enconman.2020.112614

[23] Luo, X.J., & Fong, K.F. (2016). Development of 2D dynamic model for hydrogen-fed and methane-fed solid oxide fuel cells. *Journal of Power Sources*, 328, 91−104. doi: 10.1016/j.jpowsour. 2016.08.005

[24] Conti, B., Bosio, B., McPhail, S.J., Santoni, F., Pumiglia, D., & Arato, E. (2019). A 2-D model for intermediate temperature solid oxide fuel cells preliminarily validated on local values. *Catalysts*, 9(1), 36. doi: 10.3390/catal9010036

[25] Ferguson, J.R., Fiard, J.M., & Herbin, R. (1996). Three-dimensional numerical simulation for various geometries of solid oxide fuel cells. *Journal of Power Sources*, 58(2), 109−122. doi: 10.1016/0378-7753(95)02269-4

[26] Al-Masri, A., Peksen, M., Blum, L., & Stolten, D. (2014). A 3D CFD model for predicting the temperature distribution in a full scale APU SOFC short stack under transient operating conditions. *Applied Energy*, 135, 539−547. doi: 10.1016/j.apenergy. 2014.08.052

[27] Xiong,. X., Liang, K., Ma, G., & Ba, L. (2023). Three-dimensional multi-physics modeling and structural optimization of SOFC large-scale stack and stack tower. *International Journal of Hydrogen Energy*, 48(7), 2742−2761. doi: 10.1016/ j.ijhydene. 2022.10.146

[28] Kim, D.H., Bae, Y., Lee, S., Son, J.-W., Shim, J.H., & Hong, J. (2020). Thermal analysis of a 1-kW hydrogen-fueled solid oxide fuel cell stack by three-dimensional numerical simulation. *Energy Conversion and Management*, 222, 113213. doi: 10.1016/ j.enconman.2020.113213

[29] Milewski, J. (2012). A *Mathematical Model* of SOFC: A proposal. *Fuel cells*, 12(5), 709−721. doi: 10.1002/fuce.201100150

[30] dos Santos-Gómez, L., Zamudio-García, J., Porras-Vázquez, J.M., Losilla, E.R., & Marrero-López, D. (2018). Highly efficient $La_{0.8}Sr_{0.2}MnO_{3-\delta}$ - $Ce_{0.9Gd0.1}O_{1.95}$ nanocomposite cathodes for solid oxide fuel cells. *Ceramics International*, 44(5), 4961−4966. doi: 10.1016/j.ceramint.2017.12.089

[31] Esposito, V., Gadea, Ch., Hjelm, J., Marani, D., Hu, O., Agersted, K., Ramousse, S., & Jensen, S.H. (2015). Fabrication of thin yttria-stabilized-zirconia dense electrolyte layers by inkjet printing for high performing solid oxide fuel cells. *Journal of Power Sources*, 273, 89−95. doi: 10.1016/j.jpowsour.2014.09.085

[32] Shimada, H., Yamaguchi, T., Sumi, H., Nomura, K., Yamaguchi, Y., & Fujishiro, Y. (2017). Extremely fine structured cathode for solid oxide fuel cells using Sr-doped $LaMnO_3$ and Y_2O_3-stabilized ZrO_2 nano-composite powder synthesized by spray pyrolysis. *Journal of Power Sources*, 341, 280−284. doi: 10.1016/ j.jpowsour.2016.12.002

[33] Shimada, H., Sumi, H., Yamaguchi, Y., Nomura, K., Mizutani, Y., Fujishiro, Y., & Shin, W. (2023). Boosting power density of solid oxide fuel cells by synergistic effect of nanocomposite cathode and anode. *Journal of Power Sources*, 563, 232781. doi: 10.1016/j.jpowsour.2023.232781

[34] Churchill, S.W. (1973). Empirical expressions for the shear stress in turbulent flow in commercial pipe. *American Institute of Chemical Engineers Journal*, 19(2), 375−376. doi: 10.1002/aic. 690190228

[35] http://www.coolprop.org/ [accessed 12 Jan. 2024].

[36] Klemes, J.J., Arsenyeva, O., Kapustenko, P., & Tovazhnyanskyy, L. (2017). *Compact heat exchangers for energy transfer intensification − low grade heat and fouling mitigation*. CRC Press.

Co-published by
Institute of Fluid-Flow Machinery
Polish Academy of Sciences
Committee on Thermodynamics and Combustion
Polish Academy of Sciences

Copyright©2026 by the Authors under licence CC BY-NC-ND 4.0

http://www.imp.gda.pl/archives-of-thermodynamics/

Experimental investigation into the influence of heat source power on the performance of a scroll expander in an organic Rankine cycle system using HFE-7100 fluid

Tomasz Zygmunt Kaczmarczyk

Institute of Fluid Flow Machinery, Polish Academy of Sciences, Fiszera 14, 80-231 Gdańsk, Poland
Author email: tkaczmarczyk@imp.gda.pl

Received: 17.07.2025; revised: 04.12.2025; accepted: 23.01.2026

Abstract

This work presents the results of an experimental study on a 1 kW scroll expander in an organic Rankine cycle (ORC) system. The low-boiling, non-flammable hydrofluoroether HFE-7100, was used as the working fluid. The research was conducted at heat source power levels ranging from 10 kW_t to 18 kW_t. The flow rate of the working medium was in the range of 30 g/s to 60 g/s. The generator of the expansion unit, on the other hand, was loaded with electrical receivers, with a load ranging from 200 W_e to 2000 W_e. The study shows that, for the same working fluid flow rate and expander rotational speed, an increase in the thermal power of the heat source resulted in higher voltage at the generator terminals and increased electrical output power of the ORC system. It was found that, regardless of the HFE-7100 flow rate, the inclination angles of the electrical power and voltage curves with respect to the expander's rotational speed axis increased as the thermal power of the heat source increased. Thus, for each level of a thermal power, there is an optimum generator load at which the electrical output power of the system is maximised. The research conducted shows that the maximum electrical output of 635 W_e was obtained for a heat source power of 16 kW_t and a fluid flow rate of 60 g/s. In addition, it was found that for the tested ranges of heat source power and HFE-7100 flow rate, the optimum load for the expander generator was between 3.5 Ω and 4.8 Ω.

Keywords: Scroll expander; Heat source; ORC system, HFE-7100; Experimental research

Vol. 47(2026), No. 1, 125–136; doi: 10.24425/ather.2026.158664

Cite this manuscript as: Kaczmarczyk, T.Z. (2026). Experimental investigation into the influence of heat source power on the performance of a scroll expander in an organic Rankine cycle system using HFE-7100 fluid. *Archives of Thermodynamics*, 47(1), 125–136.

1. Introduction

The need to move away from the exploitation of fossil fuels [1] necessitates the use of low-carbon fuel cells [2,3], the development of new environmentally friendly energy technologies [4], the decentralisation of power generation [5] and the utilisation of biofuels and unconventional fuels [6]. Therefore, technologies that enable integration with renewable energy sources (RES) are of considerable interest [7]. One such technology that meets the above requirements is the organic Rankine cycle (ORC) system [8]. ORC systems can be powered not only by RES (e.g. biomass [9] or solar energy [10]). These systems can be supplied with low- [11], medium- [12] and high-temperature [13] waste heat [14]. The utilisation of waste heat to generate electricity [15] increases the operational efficiency of these systems [16]. The literature indicates that ORC systems are associated with energy storage [17], air storage [18] and thermal energy storage (TES) systems [19], nuclear power systems [20], refrigeration systems [21,22], trilateral flash cycle (TFC) systems [23], partial evaporator–organic Rankine cycle (PE-ORC) systems [24], organic Rankine cycle–vapour compression cycle (ORC-VCC) systems [25]; as well as engines, including gas engines (GEs) [26], internal combustion engines (ICEs) [27], thermal engines [28] and direct-fired hot water boilers [29].

Nomenclature

I – current, A
m – mass flow rate, kg/s
n – rotational speed, rpm
N – power, W
p – pressure, kPa
PR – pressure ratio
R – resistance, Ω
T – temperature, °C
U – voltage, V
x – vapour quality

Subscripts and Superscripts
e – electrical
t – thermal

Abbreviations and Acronyms
AC – alternating current
DC – direct current
ORC – organic Rankine cycle
RES – renewable energy sources
TES – thermal energy storage
WHR– waste heat recovery

Hence, theoretical analyses [30] and experimental studies of complete ORC systems or their components [31−33] are conducted to improve their operating efficiency [34]. Volumetric expanders [35,36] and flow expanders [37] are used in ORC systems. Flow expanders include Tesla turbines [38], radial inflow turbines [39], axial turbines [40], radial outflow turbines [41], radial-axial turbines [42], or combinations thereof [43]. Turbines are built as either single-stage [44] or multi-stage [45] units, which can be manufactured as partial admission turbines [46]. The literature indicates that research [47] and optimisation work are being carried out on turbines, such as blade [48,49] and nozzle [50,51] shape optimisation, with a focus on thermodynamic cycle efficiency [52] and mechanical aspects, such as rotor vibrations [53].

In contrast, the most commonly used volumetric expansion units include Wankel expanders [54], scroll expanders [55], Stirling engines [56], vane expanders [36], screw expanders [57] and reciprocating engines [58]. Volumetric expansion units are often analysed and studied in parallel [59] or in series [60] operation within ORC systems. Pumps [61] used in the working medium cycle are also the subject of investigation, owing to their significant influence on the back work ratio [62]. New working fluids (fourth-generation refrigerants) [63] are also being analysed and studied [64] in terms of thermal stability [65] and ORC system efficiency [66]. Expanders are tested mechanically [67] or electrically [68] to determine, among other factors, their efficiency.

For example, a study by Murthy et al. [69] found that the efficiency of a four-intersecting-vane expander prototype, operating in an ORC system with R134a as the working fluid, was approximately 35%. The electrical output power and the rotational speed of the expander were approximately 33 W and 500 rpm, respectively. A similar efficiency of approximately 36% was achieved by an axial turbine operating in an ORC system with R1233zde as the working fluid [70]. In contrast, the microturbine's rotational speed and electrical power were 8000 rpm and 812 W, respectively. The recorded thermal efficiency of the ORC system was 2.15%. As the electrical power of the expander increases, the thermal efficiency of the ORC system also increases. Research on the scroll expander using HFE-7100 fluid showed that, at an electrical power output of approximately 980 W, the efficiency of the expander and the thermal efficiency of the ORC system were 49.3% and approximately 3%, respectively. In contrast, research conducted on a scroll expander by Sun et al. [71] indicates that the maximum thermal efficiency of the ORC system and the shaft power were approximately 6.4% and 1.8 kW, respectively.

This paper presents the results of an experimental study of a scroll expander with a rated power of 1 kW_e, using the low-boiling fluid HFE-7100. The study was conducted parametrically, based on the heat source power, working fluid flow rate and electrical load of the scroll expander generator. The parametric current-voltage characteristic curves of the expansion unit address a clear gap in the existing research and literature. The novelty of this work lies in the interpolation of the test results based on the inclination angles of the lines representing electrical power and voltage with respect to the expander's rotational speed axis. Based on the study conducted, a methodology is presented for estimating the optimum load of the expander generator, depending on the heat source power and the flow rate of the low-boiling fluid. The generalised conclusions will allow the research findings to be used by a wide range of readers for both practical and theoretical purposes.

2. Experimental test stand

Research on a scroll expander with a rated power of 1 kW_e was carried out in an ORC system using the low-boiling fluid HFE-7100. The tested expansion unit, comprising a generator and a scroll expander connected by a clutch, is a commercial product manufactured by Air Squared. The technical data for the scroll expander and the generator are provided in Table 1.

Table 1. Technical parameters of the expansion unit components [60].

Parameter	Unit	Value
Scroll expander		
Model	–	E15H22N4.25
Nominal power	kW	1.0
Maximum pressure	kPa	1380
Displacement	cm^3/rev.	12
Maximum speed	rpm	3600
Maximum inlet temperature	°C	175
Expansion ratio	–	3.5
Generator		
Model	–	AB30L
Rated power	kW	2.4
Maximum rotational speed	rpm	3000
Rated voltage	V	240
Maximum current	A	10

Hydrofluoroether HFE-7100 was used as the working fluid in the ORC system. The fluid was selected based on thermodynamic and energy considerations, taking into account the environmental and safety factors. HFE-7100 is a dry fluid (as shown by the saturated liquid-vapour curve in Fig. 1), which helps prevent erosion of the flow components of the expansion unit. Its boiling point is approximately 61°C at atmospheric pressure. HFE-7100 is a non-flammable, non-explosive, non-mutagenic and non-toxic fluid. It has an ozone depletion potential (ODP) of zero. Selected thermodynamic properties of the HFE-7100 fluid are provided in Table 2.

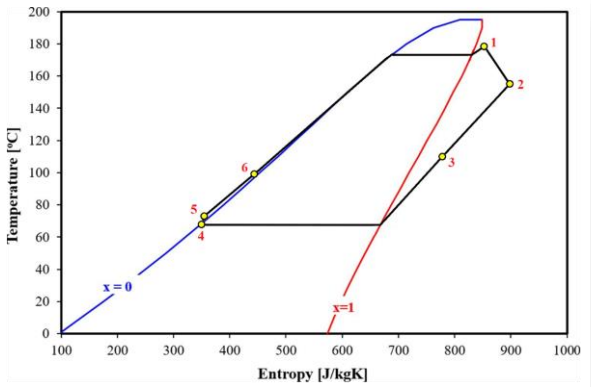


Fig. 1. Temperature-entropy (*T-s*) diagram of the test cycle with the scroll expander unit; *x* – vapour quality.

Table 2. Properties of HFE-7100 fluid at 25℃ [72].

Property	Value	Unit
Molecular weight	250	g/mol
Boiling point	61	°C
Critical temperature	195	°C
Critical pressure	2.23	MPa
Liquid density	1510	kg/m^3
Surface tension	13.6	mN/m
Dynamic viscosity	0.61	mPa s
Heat of vaporisation	112	kJ/kg
Vapour pressure	27.0	kPa
Coefficient of expansion	0.0018	1/K
Kinematic viscosity	0.38	cSt
Absolute viscosity	0.58	cP
Specific heat	1183	J/(kg K)
Thermal conductivity	0.069	W/(m K)



Fig. 2. Test stand used for testing a 1 kW scroll expander: 1 – scroll expander, 2 – generator, 3 – clutch, 4 – system for measuring pressure and temperature at the expander inlet, 5 – system for measuring pressure and temperature at the expander outlet, 6 – converter system, 7 – resistive load system, 8 – heat exchanger unit.

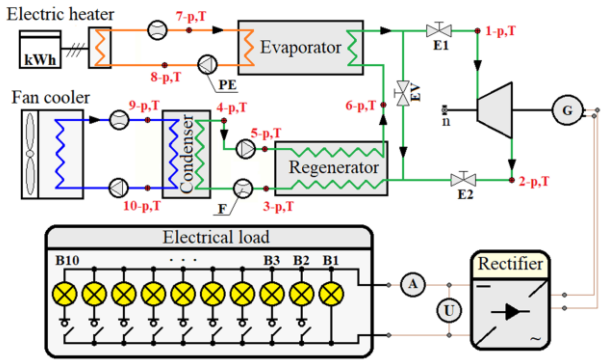


Fig. 3. Measurement diagram of the ORC system with a 1 kW scroll expander: PE – pumping engine, F – flowmeter, n – rotational speed measurement system, EV – expansion valve, E1 and E2 – valves at the expander's inlet and outlet, B(1–10) – electrical bulb, A – ammeter, U – voltmeter, G – generator, T – temperature measurement, p – pressure measurement, 1–10 – state points.

A photograph of the ORC system is shown in Fig. 2, and a measurement diagram is provided in Fig. 3. The working medium was heated using thermal oil.

The thermal oil was heated using a two-module electrical system. Only one module was used in the study. The heating device is a prototype unit made to special order, with a maximum power of 24 kW$_e$ per module. According to the manufacturer (Table 3), the measurement limit error for the electrical power of a single 24 kW$_e$ module is ±0.12 kW$_e$. The heating power could be adjusted in increments of 0.1 kW$_e$. The heat source was equipped with a PID controller (proportional–integral–derivative controller), which enabled the oil heating temperature to be set up to 400°C in increments of 0.1°C. The flow rates of the working fluids (thermal oil, HFE-7100 and a 40% ethylene glycol solution) were controlled using inverters mounted on the drives of the circulating pumps.

During the heating stage, the working medium was directed from the evaporator via a bypass (Fig. 3) directly to the regenerator, and then to the condenser. From the condenser, the medium

Table 3. List of measurement apparatus.

Instrument	Type/ Model	Range	Accuracy
Coriolis mass flowmeter (Siemens)	Sitrans FC Mas-sflo Mass 2100	0–5600 kg/h	±0.1%
Thermocouple (tolerance class 1, CZAKI Thermo-Product)	K-type	-40–600 ºC	±1.5ºC[A]
Pressure transducer (Trafag)	NAH 8253	0–1600 kPa(a)	±0.15%[B]
Pressure transducer (Trafag)	NAH 8253	0–400 kPa(a)	±0.15%[B]
Rotational speed measurement system – a prototype design (based on electromagnetic induction) that was ordered and subsequently manufactured	M1 TG-3	0–300 Hz	±1 rpm
Electrical power measurement system – a prototype design that was ordered and subsequently manufactured	M2 TG-3	0–16 A_{DC} 0–300 V_{DC} 0–2×24 kW	±0.5%[B] ±0.5%[B] ±0.5% (of the power)

[A] – the maximum measurement error of the thermocouple, according to the PN-EN 60584 standard.
[B] – full scale (of the measuring range).

is directed to a tank that supplies the circulating pump. The working medium pump supplies the regenerator, where the HFE-7100 fluid is preheated before being directed to the evaporator. Heat from the condenser was dissipated to the outside by means of a 50 kW_t fan cooler. In the second stage, once the working medium had reached the required pressure at the set flow rate, the HFE-7100 fluid was directed to the scroll expander inlet. The scroll expander was connected to the generator using a clutch, forming an expansion unit. The generator was loaded using a resistive load system, which consisted of 10 DC bulbs, each with a rated power of 200 W_e, connected in parallel. The load of a generator was varied by disconnecting or connecting the bulbs using switches fitted to each one. Hence, the generator was loaded using electrical receivers (light bulbs) ranging from 200 W_e to 2000 W_e. A list of control and measurement instruments, as well as sensors mounted on the test rig, is presented in Table 3.

The uncertainty of the electrical power output of the ORC system (after the AC/DC frequency converter, which converts an alternating current input voltage to a direct current output voltage) was calculated using the square error propagation rule from the following relationship:

$$\delta N_e = \sqrt{\left(\left|\frac{\delta N_e}{\delta u}\right| \delta u\right)^2 + \left(\left|\frac{\delta N_e}{\delta i}\right| \delta i\right)^2}, \quad (1)$$

where u is voltage and i represents current. The output power of the ORC system was calculated using the following relationship:

$$N_e = UI, \quad (2)$$

where U is the DC voltage and I is the current measured after the AC/DC converter.

Based on Table 3, the limit (maximum) errors of DC voltage and current measurements were estimated to be ±1.5 V and ±0.08 A, respectively. For a nominal power of the scroll expander of 1 kW (Table 1) and a maximum voltage at the generator terminals of 240 V (Table 1), the load current is 4.17 A, and the uncertainty of the electrical output power of the ORC system, determined from Eq. (1), is 1000 ± 20.2 W_e. In contrast, at the maximum power of the scroll expander of 1 kW and the maximum load current of the generator of 10 A (Table 3), the voltage is 100 V, and the uncertainty in determining the output power of the ORC system is 1000 ± 17.0 W_e.

3. Research procedures and methodology

In the first stage of the tests, the preset thermal power and the flow rate of the HFE-7100 working fluid were adjusted (e.g. 10 kW_t and 30 g/s). Next, the working fluid was directed through the bypass (with the EV valve open and the E1 and E2 valves closed), as shown in Fig. 3. It circulated within the cycle without an expander until the ORC system reached stable operating parameters (i.e. temperature and pressure). The tests were conducted at five heat source power levels (i.e. from 10 kW_t to 18 kW_t) and for HFE-7100 flow rates ranging from 30 g/s to 60 g/s (Fig. 4).

Once stable operating parameters were reached, the second stage of operation began: the EV valve was closed and the E1 and E2 valves were opened. The working fluid was then directed

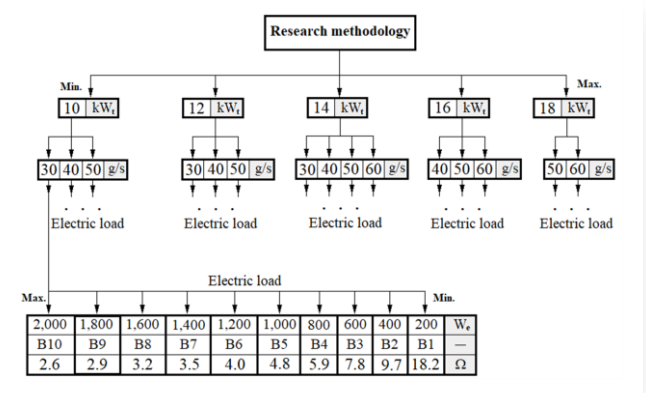


Fig. 4. Research procedure used for the scroll expander.

to the scroll expander inlet. During the start-up of the expansion unit, the generator was always loaded with energy receivers with a maximum power of 2000 W_e (i.e. ten light bulbs). The preset parameters (settings) for heat source power, generator load and working fluid flow rate were maintained at a constant level throughout the entire measurement series. Then, at a constant/preset heat source power level and HFE-7100 flow rate, the generator load was gradually reduced in steps of 200 W. This procedure was repeated until the minimum load of the expander unit's generator, 200 W, was reached. Then, with the heat source power kept constant, the flow rate was increased according to Fig. 2 (e.g. 10 kW_t and 40 g/s), and the procedure was continued until the maximum HFE-7100 flow rate was reached at the preset power level. This research procedure was applied for each thermal power level of the heat source until the maximum settings were reached, i.e. a thermal power of 18 kW_t and an HFE-7100 flow rate of 60 g/s.

4. Results and discussion

The performance characteristics of the expansion unit, illustrating the influence of the scroll expander's rotational speed on the operation of the ORC system, are presented in Sec. 4.1. The current-voltage characteristics, on the other hand, are demonstrated in Section 4.2.

4.1. Effect of the scroll expander's rotational speed

It can be seen from Fig. 5 that, at a constant thermal power of 10 kW_t for each preset and constant HFE-7100 flow rate, there is an optimum rotational speed of the scroll expander at which the electrical output power is maximised.

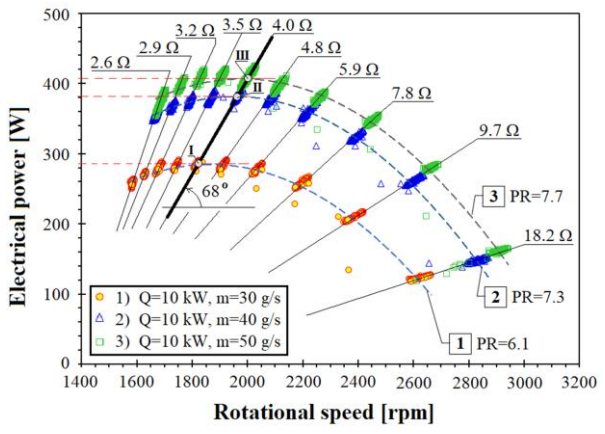


Fig. 5. Effect of the scroll expander's rotational speed on electrical power for a heat source power of 10 kW_t.

For a thermal power of 10 kW_t, the optimum rotational speed values for flow rates of 30 g/s, 40 g/s and 50 g/s were 1820 rpm, 1960 rpm and 2000 rpm, respectively. In contrast, the maximum electrical output powers of the ORC system were 282 W_e (marked as I), 390 W_e (marked as II), and 406 W_e (marked as III), respectively. By connecting points I, II and III, the optimal load line (in terms of maximum electrical power) was obtained, inclined at approximately 68° to the rotational speed axis.

The same methodology for determining the optimal load line was applied to the cases analysed below. The study found that an increase in the flow rate of the low-boiling fluid from 30 g/s to 40 g/s, i.e. by 33.3%, resulted in increases in PR and electrical output power of 19.7% and 38.3%, respectively. In contrast, the increase in HFE-7100 flow rate from 30 g/s to 50 g/s, i.e. by 66.7%, resulted in increases in PR and electrical power of 26.2% and 44%, respectively.

On the other hand, it can be seen that, irrespective of the working fluid flow rate, the voltage at the generator terminals increased linearly with the rising rotational speed of the scroll expander (Fig. 6). It was found that the inclination angle of the voltage line at the generator terminals was approximately 20°.

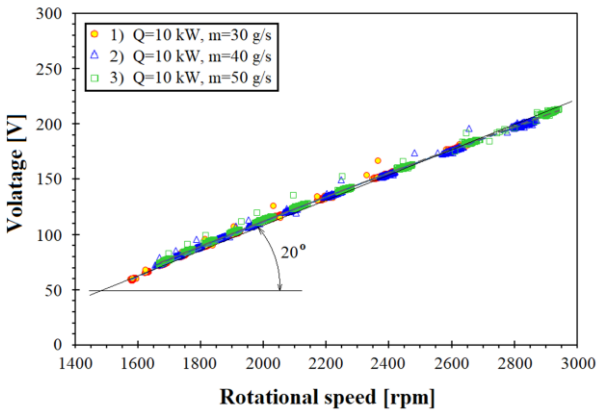


Fig. 6. Effect of the scroll expander's rotational speed on voltage at the generator terminals for a heat source power of 10 kW_t.

When the power of a heat source was 12 kW_t (Fig. 7), electrical power maxima of 282 W_e, 420 W_e and 480 W_e were obtained for HFE-7100 flow rates of 30 g/s, 40 g/s and 50 g/s, respectively. In contrast, power maxima were recorded at the expander rotational speeds of 1920 rpm, 2020 rpm and 2070 rpm, respectively. This means that as the HFE-7100 flow rate increased, both the electrical output power and the expander's rotational speed increased. The electrical power maxima lie on the load line, which has an inclination angle of approximately 75°

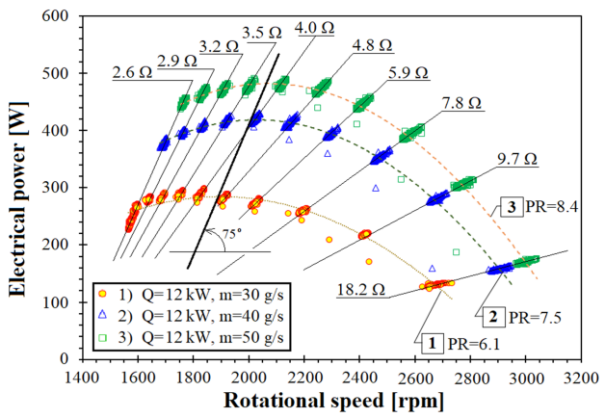


Fig. 7. Effect of the scroll expander's rotational speed on electrical power at the generator terminals for a heat source power of 12 kW_t.

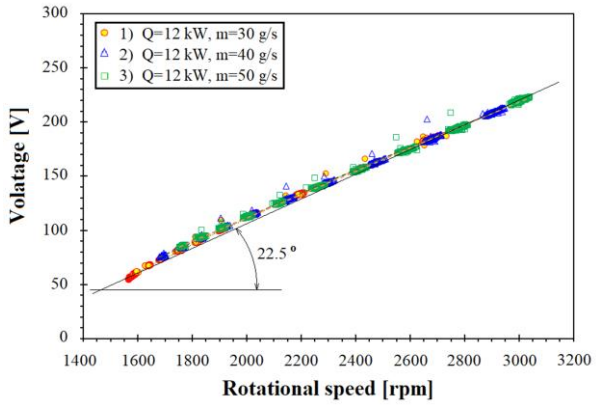


Fig. 8. Effect of the scroll expander's rotational speed on voltage at the generator terminals for a heat source power of 12 kW_t.

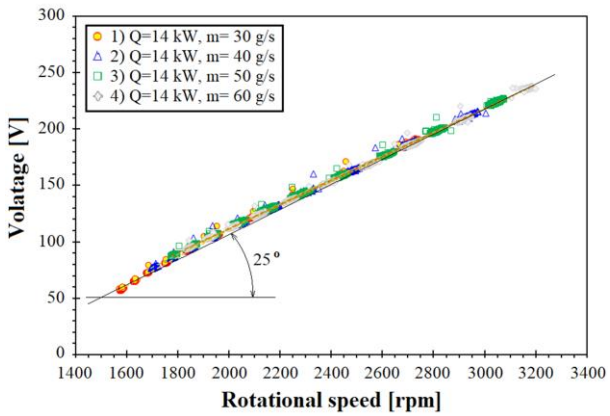


Fig. 10. Effect of the scroll expander's rotational speed on voltage at the generator terminals for a heat source power of 14 kW_t.

relative to the expander's rotational speed axis. This signifies that the inclination angle of the line representing the voltage dependence on rotational speed for a heat source power of 12 kW_t has increased compared to that for 10 kW_t by approximately 10.3%. Additionally, it was observed that the line representing the voltage dependence on rotational speed has an inclination angle of 22.5° (Fig. 8). Thus, the inclination angle of the line representing the voltage dependence on rotational speed for a heat source power of 12 kW_t, relative to that of the line obtained for a heat source power of 10 kW_t, has increased by approximately 12.5%. Meanwhile, the increase in thermal power from 10 kW_t to 12 kW_t was 20%. In contrast, the increases in electrical power at the same working fluid flow rates — i.e. 30 g/s, 40 g/s and 50 g/s — were 0%, 7.8% and 18%, respectively. This means that, as the thermal power and HFE-7100 flow rate increase, the energy losses in the ORC system decrease. Thus, for a given thermal power of the heat source, there is an optimum value of the working medium flow rate and the generator load of the scroll expander at which the electrical output power of the ORC system is maximised.

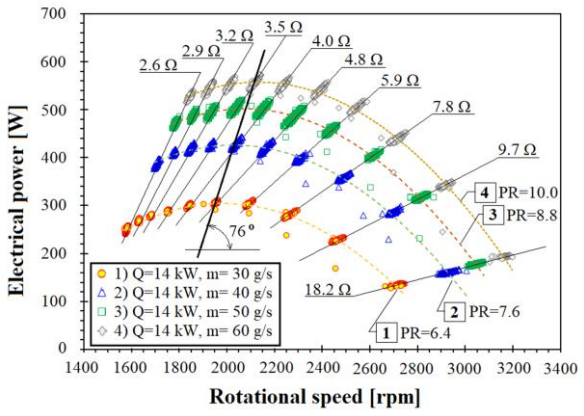


Fig. 9. Effect of the scroll expander's rotational speed on electrical power for a heat source power of 14 kW_t.

For a thermal power of 14 kW_t, an increase in the flow rate of the working medium resulted in an increase in PR and the electrical output power of the ORC system (Fig. 9). The maximum electrical powers for HFE-7100 flow rates of 30 g/s, 40 g/s, 50 g/s and 60 g/s were 304 W_e, 426 W_e, 502 W_e and 560 W_e, respectively. The electrical power maxima lie on the load line, which forms an inclination angle of approximately 76° with the expander's rotational speed axis. Consequently, the inclination angle of the load line with respect to the expander speed axis increased by approximately 11.8% compared to that at a heat source power of 10 kW_t, with a 40% increase in working medium flow rate. In contrast, the inclination angle of the voltage line with respect to the rotational speed axis increased by 25%, from 20° to 25° (Fig. 10). Hence, for the same working medium flow rate, as the thermal power of the heat source increases, higher voltages can be obtained at the generator terminals for the same rotational speed of the scroll expander.

When the power of the heat source was 16 kW_t, compared to the base power source (i.e. 10 kW_t), there was an increase in the inclination angle of the load line (Fig. 11) and in the inclination angle of the line representing the voltage at the generator terminals (Fig. 12) with respect to the expander's rotational speed axis, of approximately 13.2% and 30%, respectively. As a result, for the same HFE-7100 flow rates, an increase in the rotational

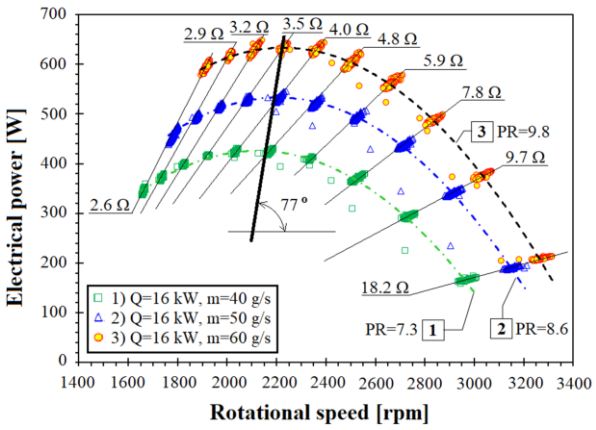


Fig. 11. Effect of the scroll expander's rotational speed on electrical power for a heat source power of 16 kW_t.

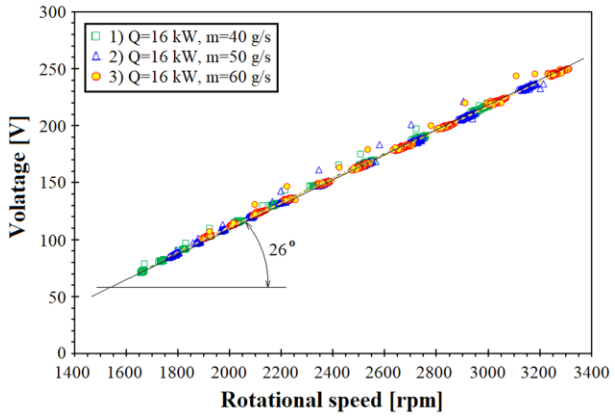


Fig. 12. Effect of the scroll expander's rotational speed on voltage at the generator terminals for a heat source power of 16 kW_t.

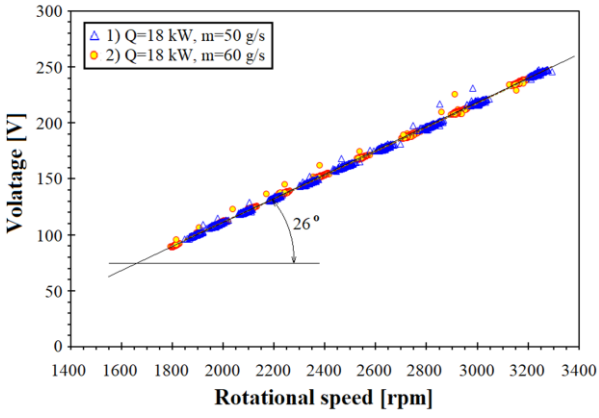


Fig. 14. Effect of the scroll expander's rotational speed on voltage at the generator terminals for a heat source power of 18 kW_t.

speed of the expander was noted, along with an increase in the electrical output power of the ORC system, as the power of the heat source increased. For example, at a flow rate of 50 g/s, the increase in the rotational speed of the expander was approximately 9.5%, and the increase in electrical power was about 32%. It is worth noting that at an HFE-7100 flow rate of 40 g/s, the increase in rotational speed with respect to the base heat source for maximum electrical power was approximately 9.2%, with speeds being 2140 rpm and 2190 rpm, respectively. In contrast, the increase in electrical power was approximately 8.7%. Since the rotational speeds of the expander were similar at flow rates of 40 g/s and 50 g/s, it can be assumed that they had little effect on the electrical output power of the system. Thus, an increase in electrical power was a direct result of the generator load current. At a heat source power of 18 kW_t, it was noted that for a low-boiling fluid flow rate of 60 g/s, the maximum electrical output power was approximately 620 W_e (Fig. 13), while at a heat source power of 16 kW_t, it was approximately 635 W_e, i.e. 2.4% higher (Fig. 11).

It was observed that the inclination angle of the line representing the voltage at the generator terminals with respect to the rotational speed was the same for heat source powers of 16 kW_t and 18 kW_t, i.e. approximately 26° (Fig. 14). Similarly, the rotational speeds of the expander were nearly identical — approximately 2190 rpm in both cases. It is noteworthy, however, that the inclination angle of the line representing the electrical power with respect to the expander's rotational speed axis was 85°, which was approximately 10.4% greater than in the case where the heat source power was 16 kW_t. Therefore, it follows from the above that for any given value of the working fluid flow rate, there is an optimum heat source power at which the electrical output power of the ORC system is maximised.

In summary, it should be noted that, irrespective of the working fluid flow rate, the inclination angles of lines representing electrical power and voltage with respect to the expander's rotational speed axis increased as the thermal power of the heat source increased.

4.2. Effect of the generator electrical load

It can be seen from Figs. 15 and 16 that the maximum electrical output powers of the system for HFE-7100 flow rates of 30 g/s, 40 g/s and 50 g/s were obtained at electric currents of approximately 3.2 A, 3.6 A and 3.7 A, respectively. For a heat source power of 10 kW_t, the inclination angle of the line representing

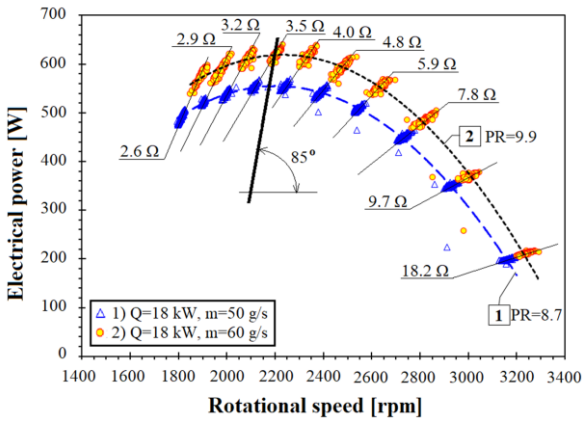


Fig. 13. Effect of the scroll expander's rotational speed on electrical power for a heat source power of 18 kW_t.

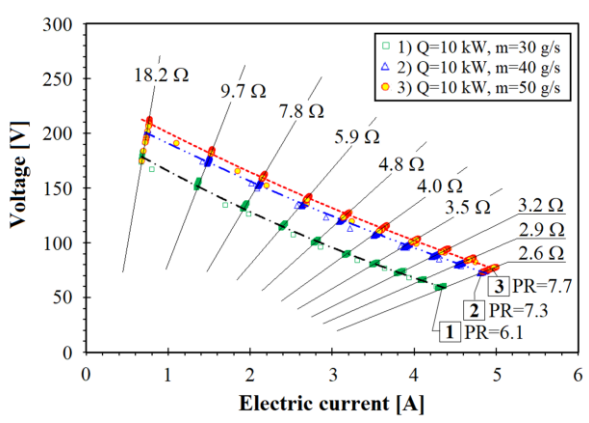


Fig. 15. Effect of electric current on the voltage at the generator terminals for a heat source power of 10 kW_t.

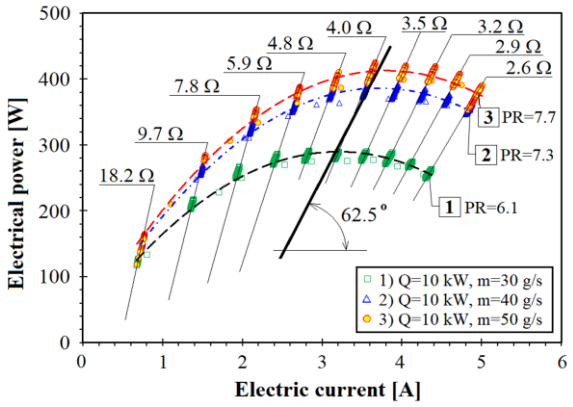


Fig. 16. Effect of electric current on the electrical output power of the ORC system for a heat source power of 10 kW_t.

electrical power versus generator load current was approximately 62.5° (Fig. 16). On the other hand, the voltage-current characteristic curve (Fig. 15) shows that, for a thermal power of 10 kW_t, the optimum generator load at which the electrical power was maximised ranged from 3.8 Ω to 4.0 Ω.

For a power of 12 kW_t, the inclination angle of the line representing the maximum electrical power with respect to the generator load current was approximately 60° (Fig. 17), which was about 4% smaller than the angle obtained for the case with a heat source power of 10 kW_t. It was observed that, for a working fluid flow rate of 30 g/s, when the thermal power was increased from 10 kW_t to 12 kW_t, the electric currents at maximum electrical power remained the same. In contrast, for 40 g/s and 50 g/s, the electric currents obtained at 12 kW_t were higher than those for a heat source power of 10 kW_t by 2.8% and 8.1%, respectively (Fig. 18). The research indicates that the optimum generator load for maximum electrical power was in the range of 3.8 Ω to 4.0 Ω.

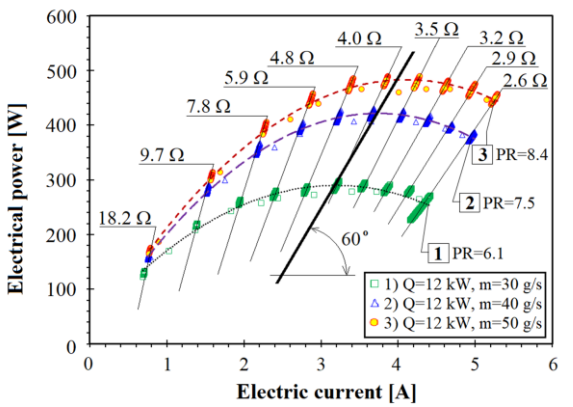


Fig. 17. Effect of electric current on the electrical output power of the ORC system for a heat source power of 12 kW_t.

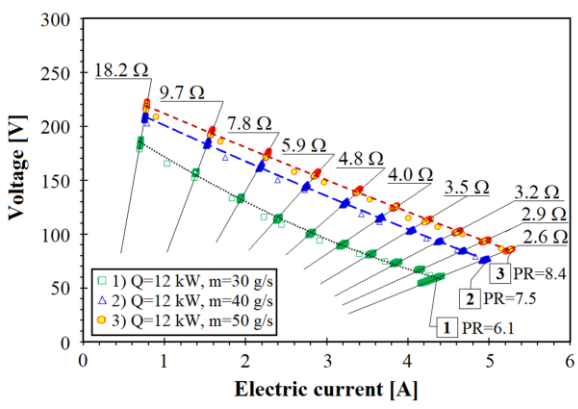


Fig. 18. Effect of electric current on the voltage at the generator terminals for a heat source power of 12 kW_t.

When the power of the heat source was 14 kW_t, the inclination angle of the line representing the maximum electrical power with respect to the generator load current was approximately 45° (Fig. 19), which was about 28% smaller than the angle obtained for a heat source power of 10 kW_t.

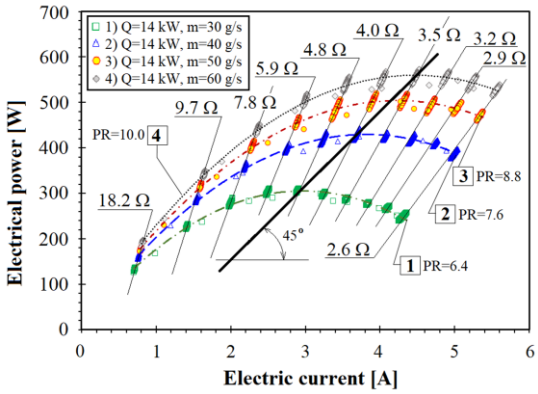


Fig. 19. Effect of electric current on the electrical output power of the ORC system for a heat source power of 14 kW_t.

In contrast, the generator load currents for HFE-7100 flow rates of 40 g/s and 50 g/s were 2.8% and 10.8% higher, respectively, than those obtained at a power of 10 kW_t (Fig. 20). At a flow rate of 30 g/s, the electric current was approximately 9.4% lower. The research showed that, with a heat source power of 14 kW_t, the optimum generator load value was in the range of 3.5 Ω to 4.7 Ω.

The research indicates that an increase in the power of the heat source from 10 kW_t to 16 kW_t resulted in a 32% decrease

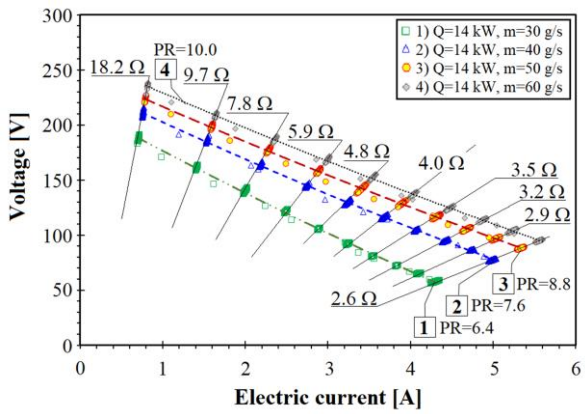


Fig. 20. Effect of electric current on the voltage at the generator terminals for a heat source power of 14 kW_t.

in the inclination angle of the line representing electrical power with respect to the electric current axis, compared to the angle obtained with a heat source power of 10 kW_t (Fig. 21).

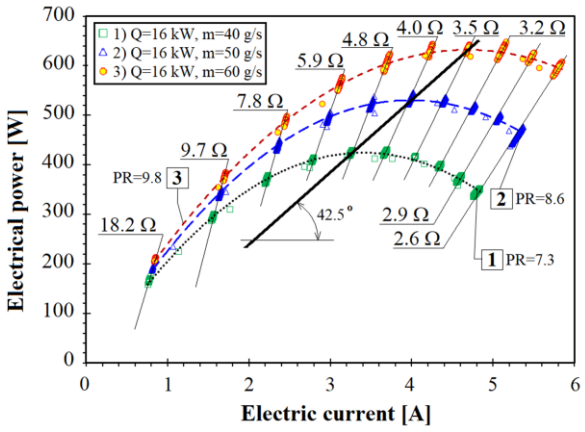


Fig. 21. Effect of electric current on the electrical output power of the ORC system for a heat source power of 16 kW_t.

At a flow rate of 40 g/s, a decrease of approximately 8.3% in the electric current was noted compared to the heat source power of 10 kW_t. Whereas, for an HFE-7100 flow rate of 50 g/s, the increase in the electric current was approximately 8.1%. It was found that the optimum load values for maximum electrical power were in the range of 3.5 Ω to 4.8 Ω (Fig. 22).

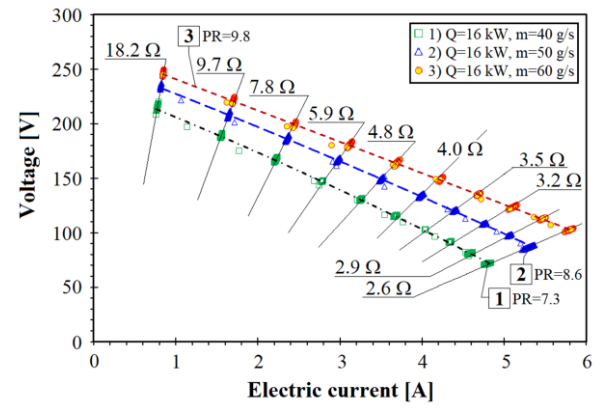


Fig. 22. Effect of electric current on the voltage at the generator terminals for a heat source power of 16 kW_t.

For a flow rate of 50 g/s and a heat source power of 18 kW_t (Fig. 23), an increase in the load current was the same, i.e. by 8.1%, as for a heat source power of 16 kW_t, compared to the base power (10 kW_t). In contrast, the inclination angle of the line representing electrical power with respect to the electric current axis was 56% smaller compared to the angle recorded for a heat source power of 10 kW_t. The research indicates that the load current of the expander generator was in the range of 3.6 Ω to 4.0 Ω (Fig. 24).

Summarising the above, it can be concluded that for the heat source powers and HFE-7100 flow rates in the ranges of 10 kW_t to 18 kWt and 30 g/s to 60 g/s, respectively, the scroll expander's generator load should be in the range of 3.5 Ω to 4.8 Ω (Table 4).

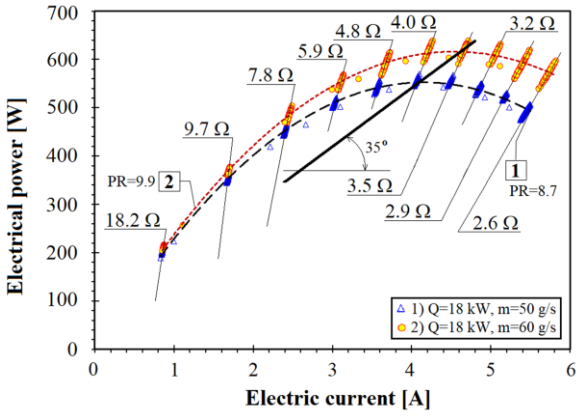


Fig. 23. Effect of electric current on the electrical output power of the ORC system for a heat source power of 18 kW_t.

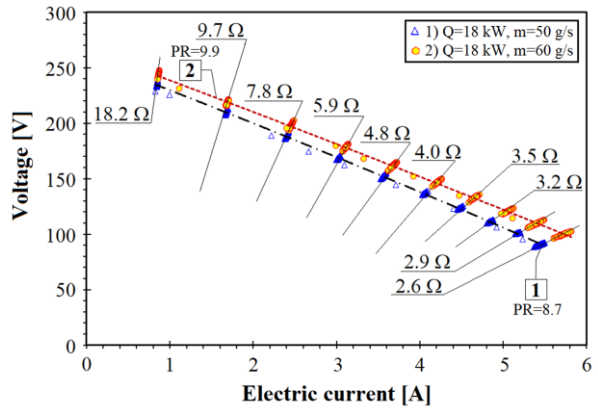


Fig. 24. Effect of electric current on the electrical output power of the ORC system for a heat source power of 18 kW_t.

Table 4. Summary of the test results for the system's maximum electrical output.

N_t (kW_t)	m (g/s)	N_e (kW_e)	PR_{av} (–)	n (rpm)	U (V)	I (A)	R_{opt} (Ω)
10	30	282	6.1	1820	90	3.2	3.8–4.0
	40	390	7.3	1960	106	3.6	
	50	406	7.7	2000	110	3.7	
12	30	282	6.1	1920	90	3.2	3.8–4.0
	40	420	7.5	2020	113	3.7	
	50	480	8.4	2070	122	4.0	
14	30	304	6.4	1990	103	2.9	3.5–4.7
	40	426	7.6	2050	113	3.7	
	50	502	8.8	2090	120	4.1	
	60	560	10.0	2120	125	4.5	
16	40	424	7.3	2140	130	3.3	3.5–4.8
	50	536	8.6	2190	135	4.0	
	60	635	9.8	2230	135	4.7	
18	50	558	8.7	2190	135	4.1	3.6–4.0
	60	620	9.9	2200	135	4.6	

5. Conclusions

The study indicates that for each value of thermal power and HFE-7100 flow rate, there is an optimum rotational speed of the scroll expander at which the electrical output power of the organic Rankine cycle (ORC) power system is maximised. In the research conducted, a maximum power of 635 W_e was obtained for a heat source power of 16 kW_t and a working fluid flow rate of 60 g/s.

It was found that, at the same working fluid flow rate, an increase in the thermal power of the heat source causes an increase in the voltage at the generator terminals for the same rotational speed. Consequently, at the same HFE-7100 flow rates, an increase in heat source power results in an increase in the electrical output power of the ORC system. Therefore, irrespective of the working medium flow rate, the inclination angles of the lines representing electrical power and voltage with respect to the expander's rotational speed axis increased as the thermal power of the heat source increased. Moreover, it was observed that, for each level of thermal power, there is an optimum generator load at which the electrical output power of the system is maximised.

Acknowledgements

This research was conducted as part of the project entitled ''Preliminary Studies of Thermodynamic Cycles Using the Low-Boiling Fluid 73DE'' (2023/07/X/ST8/01193), funded by the National Science Centre in Poland.

References

[1] Pesyridis, A., Alshammari, A.S., & Alzamil, A. (2025). Advanced energy conversion strategies using multistage radial turbines in organic Rankine cycles for low-grade heat recovery. *Case Studies in Thermal Engineering*, 69, 106034. doi: 10.1016/j.csite.2025.106034

[2] Montazerinejad, H., & Eicker, U. (2022). Recent development of heat and power generation using renewable fuels: A comprehensive review. *Renewable and Sustainable Energy Reviews*, 165, 112578. doi: 10.1016/j.rser.2022.112578

[3] Pielecha, I., & Szwajca, F. (2024). Experimental study and modelling of an air-cooled proton exchange membrane fuel cell stack in the static and dynamic performance. *Eksploatacja i Niezawodność – Maintenance and Reliability*, 26(2), 184232. doi: 10.17531/ein/184232

[4] Gunawan, G., Permana, D.I., & Soetikno, P. (2023). Design and numerical simulation of radial inflow turbine of the regenerative Brayton cycle using supercritical carbon dioxide. *Results in Engineering*, 17, 100931. doi: 10.1016/j.rineng.2023.100931

[5] Weerakoon, A.H.S., & Assadi, M. (2024). Generalized framework for micro gas turbine techno-economic assessment. *Energy Conversion and Management*, 316, 118820. doi: 10.1016/j.enconman.2024.118820

[6] Weerakoon, A.H.S., & Assadi, M. (2023). Trends and advances in micro gas turbine technology for sustainable energy solutions: A detailed review. *Energy Conversion and Management: X*, 20, 100483. doi: 10.1016/j.ecmx.2023.100483

[7] Krajewska, P., Dawidowicz, B., & Cieśliński, J.T. (2025). A concept of a micro-polygeneration system for zero-energy building. *Acta Mechanica et Automatica*, 19(1), 26−31. doi: 10.2478/ama-2025-0004

[8] Zhen, K., Shi, L., Zhang, Y., & Peng, B. (2024). Performance prediction and regression analysis of scroll expander based on response surface methodology. *Case Studies in Thermal Engineering*, 60, 104766. doi: 10.1016/j.csite.2024.104766

[9] Feng, Y.-Q., Wu, Y.-Z., Zhang, Q., Liu, Z.-N., Wang, X.-X., Hung, T.-Ch., Yu, H.-S., & He, Z.-X. (2025). Experiment investigation and machine learning prediction of a biomass-fired organic Rankine cycle combined heating and power system under various heat source temperatures and mass flow rates. *Energy*, 324, 135841. doi: 10.1016/j.energy.2025.135841

[10] Li, J., Gurgenci, H., Guan, Z., Li, J., Li, L., & Xue, Y. (2022). Multi-objective optimization of a small scale SCO_2 turbine rotor system with a shaft cooler. *Mechanics & Industry*, 23, 21. doi: 10.1051/meca/2022018

[11] Zhang, H.-H., Zhang, Y.-F., Feng, Y.-Q., Chang, J.-Ch., Chang, Ch.-W., Xi, H., Gong, L., Hung, T.-Ch., & Li, M.-J. (2023). The parametric analysis on the system behaviors with scroll expanders employed in the ORC system: An experimental comparison. *Energy*, 268, 126713. doi: 10.1016/j.energy.2023.126713

[12] Li, X., Lv, D., & Liu, Y. (2025). Optimization of organic Rankine cycle turbine expander based on radial basis function neural network and nondominated sorting genetic algorithm II. *Physics of Fluids*, 37, 035167. doi: 10.1063/5.0257260

[13] Serafino, A., Obert, B., & Cinnella, P. (2023). Multi-fidelity robust design optimization of an ORC turbine for high temperature waste heat recovery. *Energy*, 269, 126538. doi: 10.1016/j.energy.2022.126538

[14] Zhang, X., Wang, X., Cai, J., Wang, F., Bian, X., He, Z., & Tian, H. (2023). Operation strategy of a multi-mode Organic Rankine cycle system for waste heat recovery from engine cooling water. *Energy*, 263, 125934. doi: 10.1016/j.energy.2022.125934

[15] Daniarta, S., Imre, A.R., & Kolasiński, P. (2022). Thermodynamic efficiency of subcritical and transcritical power cycles utilizing selected ACZ working fluids. *Energy*, 254(A), 124432. doi: 10.1016/j.energy.2022.124432

[16] Belousov, A.E., & Ovchinnikov, E.S. (2022). Mathematical modeling of the operation of an expander-generator pressure regulator in non-stationary conditions of small gas pressure reduction stations. *Mathematics*, 10(3), 393. doi: 10.3390/math10030393

[17] Kruk-Gotzman, S., Ziółkowski, P., Iliev, I., Negreanu, G.-P., & Badur, J. (2023). Techno-economic evaluation of combined cycle gas turbine and a diabatic compressed air energy storage integration concept. *Energy*, 266, 126345. doi: 10.1016/j.energy.2022.126345

[18] Guan, Y., Li, W., Zhu, Y., Wang, X., Zhang, Y., & Chen, H. (2024). Energy loss analysis in two-stage turbine of compressed air energy storage system: Effect of varying partial admission ratio and inlet pressure. *Energy*, 305, 132214. doi: 10.1016/j.energy.2024.132214

[19] Kolasiński, P., & Daniarta, S. (2021). Sizing the thermal energy storage (TES) device for organic Rankine cycle (ORC) power systems. *MATEC Web of Conferences*, 345, 00018. doi: 10.1051/matecconf/202134500018

[20] Tauveron, N., Lhermet, G., Payebien, B., Caney, N., & Morin, F. (2024). an experimental study of an autonomous heat removal system based on an organic Rankine cycle for an advanced nuclear power plant. *Energies*, 17(20), 5069. doi: 10.3390/en17205069

[21] González, J., Llovell, F., Garrido, J.M., & Quinteros-Lama, H. (2023). A study of the optimal conditions for organic Rankine cycles coupled with vapour compression refrigeration using a rigorous approach based on the Helmholtz energy function. *Energy*, 285, 129554. doi: 10.1016/j.energy.2023.129554

[22] Hasan, A., Mugdadi, B., Al-Nimr, M.A., & Tashtoush, B. (2022). Direct and indirect utilization of thermal energy for cooling generation: A comparative analysis. *Energy*, 238(C), 122046. doi: 10.1016/j.energy.2021.122046

[23] Ahmed, A.M. (2024). Thermal efficiency investigation for organic Rankine cycle and trilateral flash cycle using hydrofluoroether working fluids. *Results in Engineering*, 21, 101648. doi: 10.1016/j.rineng.2023.101648

[24] Ahmed, A.M. (2022). Assessment of the thermal efficiency of subcritical power generation cycles using environmentally friendly fluids at various heat source temperatures. *Energy Science & Engineering*, 10(12), 4768−4781. doi: 10.1002/ese3.1307

[25] Witanowski, Ł. (2024). Multi-objective optimization of a small-scale ORC-VCC system using low-GWP refrigerants. *Energies*, 17(21), 5381. doi: 10.3390/en17215381

[26] Sanaye, S., & Ghaffari, A. (2023). Transient modeling and thermal analysis of an innovative dual-loop Rankine–organic Rankine heat recovery system integrated with a gas engine. *Journal of Thermal Analysis and Calorimetry*, 148, 10951−10971. doi: 10.1007/s10973-023-12435-3

[27] Di Battista, D., & Cipollone, R. (2023). Waste energy recovery and valorization in internal combustion engines for transportation. *Energies*, 16(8), 3503. doi: 10.3390/en16083503

[28] Kupka, D., Koloničný, J., & Pejchal, J. (2025). Development of an axial impulse turbine for a small-scale ORC system. *Results in Engineering*, 25, 103994. doi: 10.1016/j.rineng.2025.103994

[29] Feng, Y.-Q., Xu, K.-J., Liu, Z.-X., Yu, H.-S., Hung, T.-Ch., & He, Z.-X. (2024). Construction and preliminary test of a biomass-fired organic Rankine cycle system for heat and power system. *Energy*, 308, 133021. doi: 10.1016/j.energy.2024.133021

[30] Abdalhamid, A.M.K., & Eltaweel, A. (2024). Design and analysis of a single-stage supersonic turbine with partial admission. *Energy*, 309, 133100. doi: 10.1016/j.energy.2024.133100

[31] Hossain, M.S., Sultan, I., Phung, T., & Kumar, A. (2024). An optimum design for a fast-response solenoid valve: Application to a limaçon gas expander. *Dynamics*, 4(2), 457−474. doi: 10.3390/dynamics4020024

[32] Zaniewski, D., Klimaszewski, P., Klonowicz, P., Witanowski, Ł., Lampart, P., Jędrzejewski, Ł., & Suchocki, T. (2023). Organic Rankine cycle turbogenerator cooling – Optimization of the generator water jacket heat exchange surface. *Applied Thermal Engineering*, 223, 120041. doi: 10.1016/j.applthermaleng.2023.120041

[33] Ma, C., Yang, Q., Sun, X., Zhang, K., & Li, L. (2022). Performance analysis of externally pressurized gas journal bearing lubricated with vapor of R134a in centrifugal compressor. *Processes*, 10(10), 2067. doi: 10.3390/pr10102067

[34] Kaczmarczyk, T.Z., & Żywica, G. (2024). Experimental study of the effect of load and rotational speed on the electrical power of a high-speed ORC microturbogenerator. *Applied Thermal Engineering*, 238, 122012. doi: 10.1016/j.applthermaleng.2023.122012

[35] Aziz, F., Kamal, S.M., Perl, M., & Chetry, A. (2024). Increasing the load carrying capacity of hollow rotating disks by applying rotational autofrettage. *European Journal of Mechanics - A/Solids*, 105, 105231. doi: 10.1016/j.euromechsol.2024.105231

[36] Daniarta, S., Kolasiński, P., Imre, A.R., & Sowa, D. (2024). Artificial intelligence-driven performance mapping: A deep learning-based investigation of a multi-vane expander in retrofitted organic Rankine cycle. *Energy Conversion and Management*, 315, 118763. doi: 10.1016/j.enconman.2024.118763

[37] Li, Ch., Guo, Z., Guo, H., Bao, X., & Zhou, L. (2022). Influences of main design parameters on the aerodynamic performance of a micro-radial inflow turbine. *AIP Advances*, 12(10), 105012. doi: 10.1063/5.0090173

[38] Zhang, Y., Zhang, S., Peng, H., Tian, Z., Gao, W., & Yang, K. (2023). Thermodynamic analysis of Tesla turbine in organic Rankine cycle under two-phase flow conditions. *Energy Conversion and Management*, 276, 116477. doi: 10.1016/j.enconman.2022.116477

[39] Wu, T., Cai, S., Yao, Z., Yin, X., Ma, X., Gao, X., Xie, F., Yang, H., Shen, X., & Shao, L. (2024). Design and optimization of the radial inflow turbogenerator for organic Rankine cycle system based on the genetic algorithm. *Applied Thermal Engineering*, 253, 123749. doi: 10.1016/j.applthermaleng.2024.123749

[40] Witanowski, Ł., Klonowicz, P., Lampart, P., Klimaszewski, P., Suchocki, T., Jędrzejewski, Ł., Zaniewski, D., & Ziółkowski, P. (2023). Impact of rotor geometry optimization on the off-design ORC turbine performance. *Energy*, 265, 126312. doi: 10.1016/j.energy.2022.126312

[41] Wang, E., & Peng, N. (2023). A review on the preliminary design of axial and radial turbines for small-scale Organic rankine cycle. *Energies*, 16(8), 3423. doi: 10.3390/en16083423

[42] Rusanov, R., Kravchenko, I., Rusanov, A., Riznyk, S., Kukhtin, Y., Chugay, M., & Sukhanov, M. (2025). Development experience of the centripetal turbine flow part for an aviation engine air starter. *Aerospace Technic and Technology*, 1(201). doi: 10.32620/aktt.2025.1.04

[43] Peng, N., Wang, E., Meng, F., Zhang, W., Wang, Y., Zhang, B., Zhao, Y., & Yenga, E.Ch.Y. (2024). Experimental investigation on off-design performance of a small-scale two-stage counter-rotating impulse turbine. *International Journal of Energy Research*, 4623244, 21. 10.1155/2024/4623244

[44] Witanowski, Ł., Klonowicz, P., Lampart, P., & Ziółkowski, P. (2023). Multi-objective optimization of the ORC axial turbine for a waste heat recovery system working in two modes: cogeneration and condensation. *Energy*, 264, 126187. doi: 10.1016/j.energy.2022.126187

[45] Włodarski, W., & Piwowarski, M. (2024). A model modification for a microturbine set with partial admission stages. *Energies*, 17(8), 1792. doi: 10.3390/en17081792

[46] Sun, T., Liu, Y., Ma, Z., Shu, P., & Ye, Z. (2024). Numerical simulation of the relationship between steam flow excitation characteristics and coverage on the governing stage of marine steam turbine. *Ocean Engineering*, 314(1), 119526. doi: 10.1016/j.oceaneng.2024.119526

[47] Kaczmarczyk, T.Z., & Żywica, G. (2022). Experimental study of a 1 kW high-speed ORC microturbogenerator under partial load. *Energy Conversion and Management*, 272, 116381. doi: 10.1016/j.enconman.2022.116381

[48] Lu, Y., Guo, Z., Zheng, Z., Wang, W., Wang, H., Zhou, F., & Wang, X. (2023). Underwater propeller turbine blade redesign based on developed inverse design method for energy performance improvement and cavitation suppression. *Ocean Engineering*, 277, 114315. doi: 10.1016/j.oceaneng.2023.114315

[49] Witanowski, Ł., Ziółkowski, P., Klonowicz, P., & Lampart, P. (2023). A hybrid approach to optimization of radial inflow turbine with principal component analysis. *Energy*, 272, 127064. doi: 10.1016/j.energy.2023.127064

[50] Liaw, K.L., Kurnia, J.C., Lai, W.K., Ong, K.Ch., Zar, A.B.M.A., Muhammad, M.F.B., & Firmansyah. (2023). Optimization of a novel impulse gas turbine nozzle and blades design utilizing Taguchi method for micro-scale power generation. *Energy*, 282, 129018. doi: 10.1016/j.energy.2023.129018

[51] Peng, N., Wang, E., Wang, W., Lu, J., & Li, M. (2024). Aerodynamic analysis of a 1.5 kW two-stage counter-rotating partial-admission impulse turbine for small-scale power system with a high expansion pressure ratio. *Case Studies in Thermal Engineering*, 53, 103824. doi: 10.1016/j.csite.2023.103824

[52] Peng, N., Wang, E., & Wang, W. (2023). Design and analysis of a 1.5 kW single-stage partial-admission impulse turbine for low-grade energy utilization. *Energy*, 268, 126631. doi: 10.1016/j.energy.2023.126631

[53] He, S., Tong, Z., Tong, S., Chen, K., & Cao, X.E. (2025). Collaborative optimization of turbo-expander impellers and guide vanes to mitigate flow-induced vibrations. *Physics of Fluids*, 37(3), 035178. doi: 10.1063/5.0257754

[54] Mukherjee, A., & Seshadri, S. (2023). Numerical study on the effect of port geometry of intake manifold in a steam Wankel expander. *Thermal Science and Engineering Progress*, 37, 101621. doi: 10.1016/j.tsep.2022.101621

[55] Wei, J., Hua, Q., Yuan, L., Li, G., Wang, J., & Wang, J. (2023). A review of the research status of scroll expander. *Proceedings of the Institution of Mechanical Engineers, Part A: Journal of Power and Energy*, 237(1), 176−197. doi: 10.1177/09576509221109245

[56] Wołowicz, M., Kolasiński, P., & Badyda, K. (2021). Modern small and microcogeneration systems — A review. *Energies*, 14(3), 785. doi: 10.3390/en14030785

[57] Ping, X., Yang, F., Zhang, H., Wang, Y., Lei, B., & Wu, Y. (2022). Performance limits of the single screw expander in organic Rankine cycle with ensemble learning and hyperdimensional evolutionary many-objective optimization algorithm intervention. *Energy*, 245, 123254. doi: 10.1016/j.energy.2022.123254

[58] Gopal, V.V., & Seshadri, S. (2022). Effect of cut-off and compression ratio on the isentropic efficiency during off-design and part-load operations of a Wankel rotary steam expander used for small scale cogeneration. *Applied Thermal Engineering*, 207, 118212. doi: 10.1016/j.applthermaleng.2022.118212

[59] Ekwonu, M.C., Kim, M., Chen, B., Nasir, M.T., & Kim, K.C. (2023). Dynamic simulation of partial load operation of an organic Rankine cycle with two parallel expanders. *Energies*, 16(1), 519. doi: 10.3390/en16010519

[60] Kaczmarczyk, T.Z. (2021). Experimental research of a small biomass organic Rankine cycle plant with multiple scroll expanders intended for domestic use. *Energy Conversion and Management*, 244, 114437. doi: 10.1016/j.enconman.2021.114437

[61] Kaczmarczyk, T.Z. (2024). Experimental research of a pumping engine in a micro-ORC system with a low-boiling medium. *Archives of Thermodynamics*, 45(4), 125–140. doi: 10.24425/ather.2024.152002

[62] Kaczmarczyk, T.Z., Ihantowicz, E., Żywica, G., & Kaniecki, M. (2019). Experimental study of the prototype of a Roto-Jet pump for the domestic ORC power plant. *Archives of Thermodynamics*, 40(3), 83–108. doi: 10.24425/ather.2019.129995

[63] Sprouse, III C.E. (2024). Review of organic Rankine cycles for internal combustion engine waste heat recovery: Latest decade in review. *Sustainability*, 16(5), 1924. doi: 10.3390/su16051924

[64] Abbas, W.K.A., Baumhögger, E., & Vrabec, J. (2022). Experimental investigation of organic Rankine cycle performance using alkanes or hexamethyldisiloxane as a working fluid. *Energy Conversion and Management: X*. 15, 100244. doi: 10.1016/ j.ecmx.2022.100244

[65] Huo, E., Xin, L., & Wang, S. (2022). Thermal stability and pyrolysis mechanism of working fluids for organic Rankine cycle: A review. *International Journal of Energy Research*, 46, 19341–19356. doi: 10.1002/er.8518

[66] Colak, A.B., & Arslan, O. (2024). Numerical analysis-based performance assessment of the small-scale organic Rankine cycle turbine design for residential applications. *Thermal Science and Engineering Progress*, 51, 102626. doi: 10.1016/j.tsep.2024.102626

[67] Kottapallia, A., & Konijeti, R. (2022). Numerical and experimental investigation of nonlubricated air scroll expander derived from a refrigerant scroll compressor. *Frontiers in Heat and Mass Transfer*, 19(1), 1–11. doi: 10.5098/hmt.19.11

[68] Zhang, Y., Tsai, Y.-Ch., Ren, X., Tuo, Z., Wang, W., Gong, L., & Hung, T.-Ch. (2024). Experimental study of the external load characteristics on a micro-scale organic Rankine cycle system. *Energy*, 306, 132453. doi: 10.1016/j.energy.2024.132453

[69] Murthy, A.A., Norris, S., & Subiantoro, A. (2022). Performance of a four-intersecting-vane expander in a R134a refrigeration cycle. *Applied Thermal Engineering*, 209, 118244. doi: 10.1016/j.applthermaleng.2022.118244

[70] Sun, H., Li, H., Gao, P., Hou, F., Hung, T.-Ch., Chang, Y.-H., Lin, Ch.-W., & Qin, J. (2024). Numerical simulation and low speed experiment of a low partially admitted rate axial turbine for small scale organic Rankine cycle. *Applied Thermal Engineering*, 238, 122002. doi: 10.1016/j.applthermaleng.2023.122002

[71] Sun, J., & Peng, B. (2025). Experimental study on the influence of pump frequencies and oil flow rates on the performance of organic Rankine cycle systems. *Case Studies in Thermal Engineering*, 69, 106028. doi: 10.1016/j.csite.2025.106028

[72] Kaczmarczyk, T.Z., & Żywica, G. (2022). Experimental research of a micropower volumetric expander for domestic applications at constant electrical load. *Sustainable Energy Technologies and Assessments*, 49, 101755. doi: 10.1016/j.seta.2021.101755

Co-published by
Institute of Fluid-Flow Machinery
Polish Academy of Sciences
Committee on Thermodynamics and Combustion
Polish Academy of Sciences

Copyright©2026 by the Authors under licence CC BY-NC-ND 4.0

http://www.imp.gda.pl/archives-of-thermodynamics/

Safety enhancement of the Egyptian Second Research Reactor to reduce the effect of loss-off site power supply

Hesham Hassanin ElKhatib[a*], Asmaa Abo Elnoura[a], Ahmed Ramadan[a], Said Kotb[a], Magdy Zaky[b], Samy Dwidar[a]

[a]Egyptian Atomic Energy Authority, Nuclear Reactor Department, Inshas, Cairo 13759, Egypt
[b]Egyptian Atomic Energy Authority, Engineering and Scientific Instruments Department, Inshas, Cairo 13759, Egypt

Received: 07.05.2024; revised: 16.11.2025; accepted: 19.11.2025

Abstract

The studying and analysis of the nuclear abnormal conditions have become an important demand to achieve highly safety standards in the nuclear reactors (research or power), where the nuclear accidents have been a serious concern since the construction of the first nuclear reactor in 1954 and after the world faced some major nuclear accidents as Three Mile Island in 1979, Chernobyl in 1986 and Fukushima in 2011. This paper aims to analyse a failure in the natural circulation core cooling system that could lead to temperature rise during shutdown regime. According to this scenario, our study suggests a solution that involves the addition of a small pump to the core cooling circuit in case of flapper valve malfunction due to any reason. This potential scenario is applied theoretically in the ETRR-2 (Egyptian Testing and Research Reactor Number 2). The RELAP5-3D simulation code is used to simulate and model the thermal behaviour of the core condition during this abnormal scenario and to evaluate the proposed solutions. The proposed emergency pump may be designed and estimated to permit opening flapper valve as well. This approach resolves the issue of flapper valves malfunction, which makes the reactor shutdown safe.

Keywords: Nuclear reactors; Safety of research reactors; Loss of off-site power supply accident analysis; Modelling

Vol. 47(2026), No. 1, 137–144; doi: 10.24425/ather.2026.158665

Cite this manuscript as: ElKhatib, H.H., Elnoura, A.A., Ramadan, A., Kotb, S., Zaky, M., & Dwidar, S. (2026). Safety enhancement of the Egyptian Second Research Reactor to reduce the effect of loss-off site power supply. *Archives of Thermodynamics*, 47(1), 137–144.

1. Introduction

This paper suggests solutions to modify the core cooling system in a natural regime and to enhance the power supply operation to avoid core damage. An accident is modelled on ETRR-2 (Egyptian Testing Second Research Reactor) and the RELAP5 (Reactor Excursion and Leak Analysis Program) code is used to simulate the behaviour of the core cooling during the loss of off-site power supply, as well as to evaluate the proposed solutions. Accidents in research reactors may not have the same harmful risk level to the public as compared to accidents in power reactors. They may pose a greater hazard to operators; therefore, design limits of research reactors have been set to prevent the occurrence of accidents and mitigate their hazards. Most research reactors have a compact core structure with multi-parallel cooling channels. Due to the high heat flux and the low cooling capacity of the channels, the critical temperature of the heating surface is exceeded within a few seconds, affecting the fuel plates, which may be damaged. To detect the extent of damage resulting from accidents, many accidents should have been simulated and analysed to take precautions and find solutions to prevent their occurrences and their damages [1]. One of the important accidents is the loss of off-site power supply (LOPS), which leads to the shutdown of all the systems and automatic insertion of the absorbing rods into the core. As no electricity is available to operate the core cooling system, the pumps will coast down for 90 s and stop. Once the primary flow has been diminished, the natural convection mode is triggered mechanically to remove the residual decay heat by opening the flapper

Nomenclature

A – heat transfer area, m^2
C_p – specific heat at constant pressure, J/(kg K)
D – hydraulic diameter, m
E_{node} – energy content of the element, J/s
F – volume flow rate, m^3/s
g – gravitational acceleration, m/s^2
G – heat generated in element, W/m^3
h – convective heat transfer coefficient, $W/(m^2 K)$
K – conductive heat transfer coefficient, W/(m K)
L – channel length, m
m – mass of coolant, kg
ppf – power peaking factor
q – heat flux, W/m^2
Q – rate of heat transfer, J/s
Re – Reynolds number
t – time, s
T – temperature, °C, K
w – coolant mass flow rate, kg/s
x – thickness of control volume, m

Greek symbols

ρ – density, kg/m^3

Subscripts and Superscripts

c – coolant
cl – clad
$cond$ – conduction
f – fuel
i – inlet
o – outlet
p – pressure

Abbreviations and Acronyms

IAEA – International Atomic Energy Agency
ETRR – Egyptian Testing and Research Reactor
LOPS – loss of power supply
MTR – material testing reactor
SSR – steady state reactor
TTR – Tehran Research Reactor

valves installed on the primary pipe.

If LOPS happen and the flapper valves fail to open (stuck), the temperature of the water around the fuel will increase and the steam may be formed inside the coolant channel. At this moment, the core is in a dangerous situation, and this may lead to a severe accident. A severe accident refers to an event with an extremely low probability of occurrence, but that can cause significant damage to the reactor core [2]. There are many studies about the reasons, consequences and results of LOPS on the nuclear reactors, and how to enhance the emergency systems are investigated continuously [3]. The study in this paper focuses on loss of power supply accident during the reactor operation, which touches the beyond-design basis accident (failure of both flapper valves, which are responsible for the natural convection mode beginning). A beyond-design basis accident is a sequence of events that involves failures on the reactor protection system, the safety systems or engineered safety features, which lead to core damage [4]. This type of accident is studied and analysed to find solutions to prevent the resulting damages [5]. To evaluate the reactor performance during accidents, a thermal-hydraulic code may be used for simulating the transient behaviour of the core. The RELAP5 code is chosen for simulating the accidents and the proposed solutions, which are mentioned in this paper. The RELAP5 code is a best-estimate code, and this means that the accident simulation and the results are more realistic [6]. The RELAP5 code was developed at the Idaho National Laboratory (INL) for light water reactors during postulated accidents. It is based on a nonhomogeneous and non-equilibrium model for a two-phase system that is solved by a fast and partially implicit numerical scheme. It models the loss-of-coolant accidents, loss of off-site power, loss of feed water and loss of flow accidents [7]. The potential of the alternative sequence to cool down the reactor in the event of loss of off-site power supply was studied in [8]. It is interesting to integrate the alternative procedure into the reactor operation, in order to improve the reliability of the decay heat removal (DHR) function by adding a medium-strength safety defence line. The approach presented in [9] adapted both the deterministic and the probabilistic methods to determine the likelihood of the LOPS accident. Two applicable codes were used to model and investigate the LOPS accident: the probabilistic safety assessment package (PSAPACK) of the International Atomic Energy Agency (IAEA) and the TR22M21 code, which was developed by the author to simulate the reactor performance during an accident. The coolant system for a research reactor is designed and constructed to provide adequate cooling to the reactor core, where the primary cooling system is not designed for cooling the core after shutdown, and a reliable separate system shall be provided for the removal of residual heat. For the reactor systems that use flappers or equivalent systems for the transition from forced to natural circulation cooling, or for operation with natural circulation cooling, and for which this mode is part of the safety system (or is considered an engineered safety feature), the single failure criterion will be applied. Instrumentation to verify their functioning and to provide signals to the reactor protection system shall be provided [10,11]. The Serpent and DYN3D codes were extensively compared with a variety of static and burnup calculations as defined in the IAEA benchmark for a 10 MW pool-type material testing reactor (MTR) [12]. The safety classification of structures, systems and components (SSCs) for pool-type research reactors in Korean design is proposed based on the IAEA methodology [13]. It recommends that the SSCs of pool-type research reactors be categorised, classified and selected based on a graded approach. The Tehran Research Reactor (TRR) safety is studied with the second shutdown system (SSS) performing level one of probabilistic safety assessment (PSA) using the SAPHIRE (Systems Analysis Programs for Hands-on Integrated Reliability Evaluations) code, based on the selected initiating events [14]. It is seen that with the existence of the SSS, the failure rate of the reactor shutdown system decreases at least to 3.20×10^{-4} of its previous value. The core damage frequency conservatively turns out to decrease at least by half of the value previously reported to be 8.37×10^{-6}/y. In order to enhance the TRR, and the reactor personnel and other public safety,

equipping the TRR with an SSS is a rational plan. This engineered safety feature helps to avoid accidents. Study of MARIA Research Reactor, operated by the National Centre for Nuclear Research in Poland, provides the details of probabilistic analysis performed within the safety classification process [15]. It presents insight from the implementation of the procedure in the safety classification for the MARIA Research Reactor. The methods for common-cause failure (CCF) parameters estimation and mathematical models for estimation of the probability of occurrence of common cause events were studied for Romania-TRIGA Steady State (SSR) 14 MW Reactor [16]. It describes data collection and statistics referring to the potential common-cause failure for components of the reactor, which involve pumps, control rods, valves, fans, ejector, by taking into account the event attributes like root cause, coupling factor, detection method and corrective action taken. A fuzzy fault tree analysis (FFTA) to evaluate the performance of the primary cooling systems of the G.A. Siwabessy Multipurpose Research Reactor (RSG-GAS), which belongs to the National Nuclear Energy Agency of Indonesia (BATAN), is presented in [17]. Expert justifications were used to evaluate the failure occurrences of basic events in the primary cooling system of the RSG–GAS through questionnaires. The assessment by experts is in the form of qualitative data, which is then converted into quantitative data by applying FFTA. The development and application of the coupled neutron kinetics (NK) and thermal-hydraulic (TH) code THERMO-T to the analysis of protected reactivity insertion accidents and loss-of-flow accidents in a typical research reactor (RR) with standard materials testing reactor plate-type fuel elements is presented in [18]. The steady-state and transient neutron and thermo-hydraulic analysis of an MTR core defined in the IAEA 10 MW benchmark using Serpent2/SubChanFlow coupled code is carried out in [19]. The subchannel thermal hydraulic code SubChanFlow was extended and validated using relevant tests [20]. The SubChanFlow extension consists of the addition of a heat conduction module for a thin plate and the implementation of heat transfer correlations for rectangular channels. For the validation of the modified SubChanFlow code, temperature data from the RA-6 experiment obtained in a Reynolds range of $7\times10^3 < Re < 1.4\times10^4$ were used. The study in [21] deals with the extension of the thermal-hydraulic model of the CATHARE2 code to fast transient configurations. The extended CATHARE2 model is validated against experimental results from SPERT IV D-12/25: Benchmark.

2. Materials and research methods

2.1. Mathematical model

In this section, equations that govern the heat transfer by conduction in a symmetrical plane wall, using the energy balance approach from the core centreline to the coolant across the clad, are illustrated. The scheme used in RELAP5 follows the finite volume methodology. The energy balance method is based on subdividing the fuel plate into two control volumes and then applying an energy balance on each element, as shown in Fig. 1. This is done by first selecting nodes at which the temperatures are to be determined and then forming control volumes over the

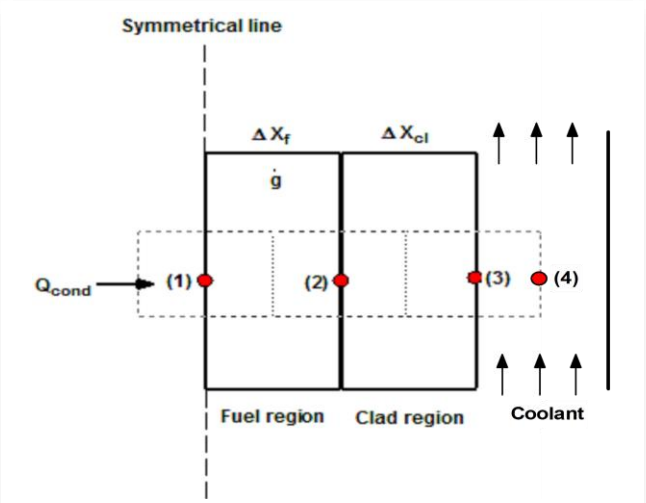


Fig. 1. Fuel plate model.

nodes. Fuel, cladding and coolant temperatures have been calculated using the equations below. Figure 1 shows a scheme of the different regions in the fuel plate adopted for calculation, including the fuel region and aluminium clad region.

The heat conduction equation in the fuel is [22]:

$$Q_{cond} = \frac{\Delta E_{node}}{\Delta t} + G, \tag{1}$$

where Q_{cond} is the rate of heat transferred by conduction, G is the heat generated from fuel per unit volume, E_{node} is the energy content of the element and t is the time.

The general differential equation is

$$\rho_f \, C_{pf} \frac{dT_f}{dt} = K_f \frac{d^2T_f}{dx^2} + G. \tag{2}$$

From the Taylor expansion theorem

$$T_{i+1} = T_i + \Delta x \frac{dT_i}{dx} + \frac{\Delta x^2}{2} \frac{dT_i^2}{dx^2} \tag{3}$$

The differential equation that describes the fuel centreline node, No. (1) and $i = N$, is expressed as

$$2K_f \frac{dT_i}{dx_f} + G \frac{\Delta x_f}{2} = \rho_f \, C_{pf} \, \Delta x_f \frac{dT_i}{dt}. \tag{4}$$

The differential equation of the fuel clad interface for the node No. (2), where $1 \leq i \leq N$, is:

$$K_f \frac{dT_i}{dx_f} + K_{cl} \frac{dT_i}{dx_{cl}} + G \frac{\Delta x_f}{2} = \left(\rho_f \, C_{pf} \frac{\Delta x_f}{2} + \rho_{cl} \, C_{pcl} \frac{\Delta x_{cl}}{2}\right) \frac{dT_i}{dt}, \tag{5}$$

$$C_{pc} \frac{dT_i}{dt} = h \, A \, (T_{i-1} - T_{i+1}) - wC_{pc} \, (T_{co} - T_{ci}), \tag{6}$$

where T is the temperature, K is the conductive heat transfer coefficient, h is the convective heat transfer coefficient, Δx is the thickness of the control volume, ρ is the density, m is the mass of coolant, w is the coolant mass flow rate and C_p is the specific heat at constant pressure. Subscripts *f*, *cl*, *ci* and *co* denote fuel, clad, coolant inlet and outlet, respectively.

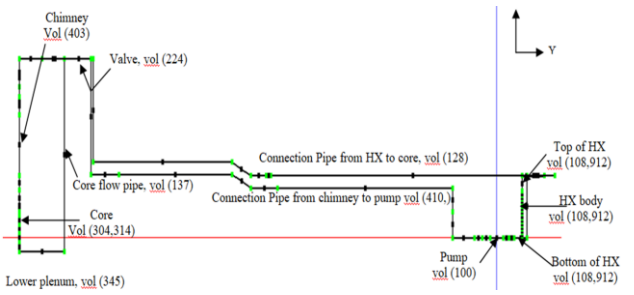


Fig. 2. RELAP5 nodalisation of cooling system;
HX – heat exchanger, vol – volumes of the node.

2.1.2. Nodalisation description

Nodalisation of the cooling system in RELAP5 is illustrated in Fig. 2. Component No. 100 represents the main pump. For simplification, it is modelled as a single volume, incorporating only the pump's geometric characteristics. Pipes 108 and 912 represent the internal structure of the heat exchanger. Each pipe is axially divided into 10 nodes, corresponding to the physical height of the heat exchanger. Pipes 128 and 137 model the internal connections from the heat exchanger outlet to the core inlet. These components are responsible for transporting the cooled water back to the core. Component 345 is a single-volume node that represents the lower plenum of the core. At this junction, the coolant flow splits into two streams: a larger portion directed to the average core channels and a smaller portion to the hot channel. Pipes No. 304 and 314 represent the hot and average core channels, respectively. Each channel is axially segmented into 21 nodes, representing the 0.8 m active length of the fuel elements. Radially, the channel is divided into six regions: two for cladding and four for fuel. Convective heat transfer boundary conditions are applied at the cladding surface. The coolant channel is modelled as a pair of half fuel plates, one from each side, forming a complete coolant passage.

3. Reactor description

Egyptian Second Research Reactor (ETRR-2) is an open pool type reactor, cooled and moderated by light water and reflected by beryllium. The nominal power is 22 MW. The reactor fuel is a plate-type fuel of 19.7% enrichment. The core is cooled by forced circulation upwards to avoid a cooling flow inversion in the case that the reactor is cooled by natural convection. The

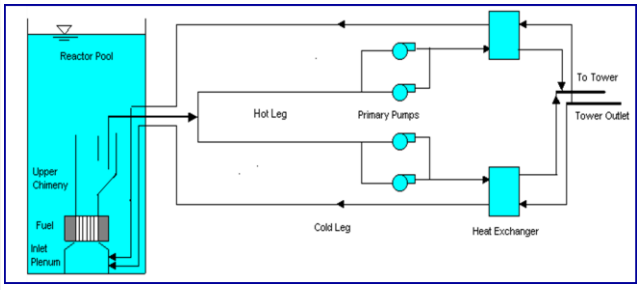


Fig. 3. Reactor core cooling system.

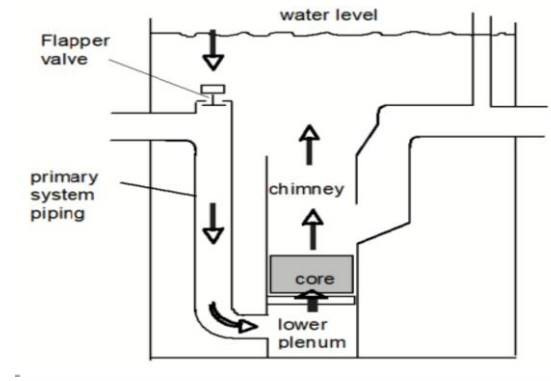


Fig. 4. Position of the flapper valve.

core coolant system with a flow rate of 1950 m^3/h is split into two 50% capacity branches; each branch has two 50% centrifugal pumps and one plate-type heat exchanger. Figure 3 shows the primary core cooling system [23]. The primary pipes have two flapper valves. These valves open by gravity forces in case there is no flow from primary pumps, as natural circulation cooling is established. Figure 4 shows the position and the working mechanism of a flapper valve. According to the quick reference of the emergency of ETRR-2, in case of a LOPS accident, the primary and secondary cooling systems will be stopped. The flapper valves must be opened after 90 s; otherwise, a malfunction may occur, but the operators can open them manually using operation tools. Flapper valves are mechanically designed to be closed under forced flow and opened by gravity; they may stack due to a failure in their seal part and cause a consequence of accident.

4. Results and discussion

4.1. Validation

The code is validated against core inlet temperature in normal operation, as shown in Fig. 5, and the reactor power status after shutdown − Fig. 6. It is shown from the two figures that the experimental values and the predicted values from RELAP5 are in good agreement [24].

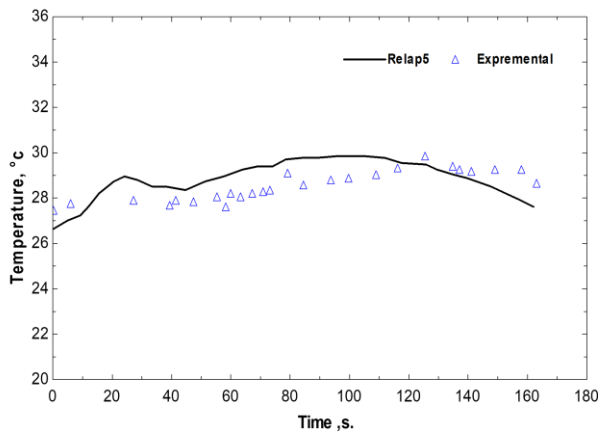


Fig. 5. Change in core inlet temperature over time.

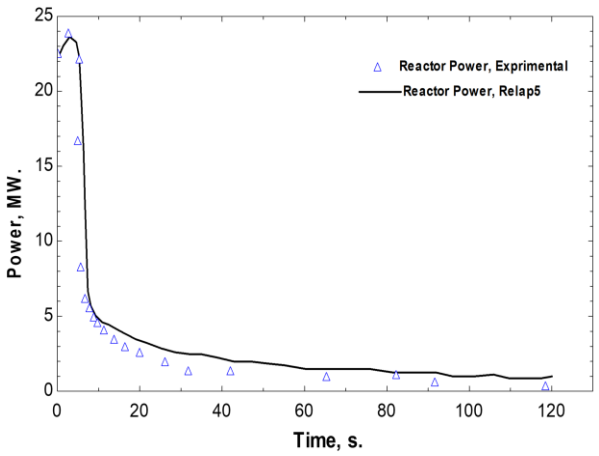


Fig. 6. Change of reactor power with time after shutdown.

4.2. Loss of power supply scenario

This event is analysed in an isolated manner; therefore, it would not be included as a cause of other events, where the absence of electric supply may be a contributor. Based on the safety analysis report, in a normal situation, if the external power supply is lost during the reactor operation, the primary and secondary pumps are stopped. At the same time, the reactor protection system (RPS) actuates the reactor shutdown system, which automatically inserts the control rods into the core, leading to a fast shutdown of the reactor in about 0.7 s. After the pumps tripped, the coast-down flow of the main pumps feeds the core with coolant for 90 s before it stops completely. Figure 7 shows the coast-down flow of the primary pump following the reactor shutdown.

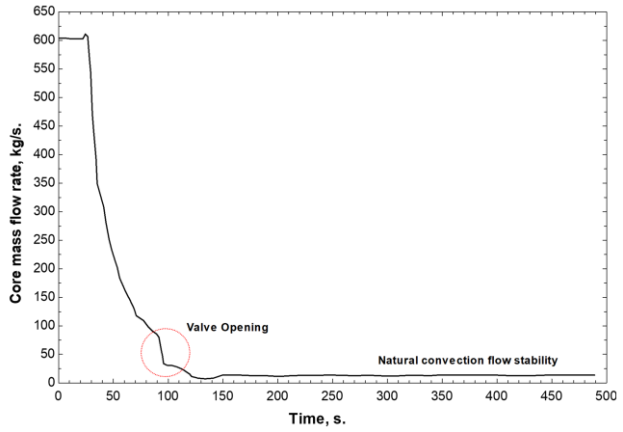


Fig. 7. Core flow after the pumps are tripped and the valves are opened.

Table 1. Sequence of events after LOPS accident.

Time (s)	Events
0.0 (initiative event)	• LOPS initiates • Core cooling system pump stops
0.7	• Fast shutdown (scram)
0.7–90	• Pump coast down
90	• Flapper valves opens and natural convection mode establishes

Normally, the flapper valves close during forced convection, but there is a special requirement that the valve should start to open when the pressure difference across it becomes less than 350 Pa. This condition is achieved 90 seconds after the pumps are tripped [18]. Table 1 shows the sequence of events after the LOPS event.

Figure 7 shows the core flow during normal conditions. After the flapper valves are opened, a marked drop in the core flow is observed, where the flow through the valve was initiated in an unexpected direction due to the pressure difference. After a while, natural circulation prevails in the expected direction (downwards inside the primary pipe) and the natural convection is established. The prediction obtained from the simulation carried out focuses on the hot channel, where it has the worst conditions in the core, and its safety means the core is safe. The hot channel is geometrically equal to a single fuel plate, the axial power is a cosine shape distribution, and the fraction of power allotted to hot channels was selected to produce a maximum allowable heat flux:

$$q_{max} = q_{ave}\,\text{ppf}, \tag{6}$$

where q_{max} is the maximum heat flux, q_{ave} is the average heat flux, and ppf is the power peaking factor (ppf ≤ 2.3).

Figure 8 shows the variability of the clad's hottest point temperature. As a result of the flow drop at the beginning of the valves' opening, the temperature of the hottest point of the clad increases to about 75°C, and it still does not exceed the safety limits, 125°C.

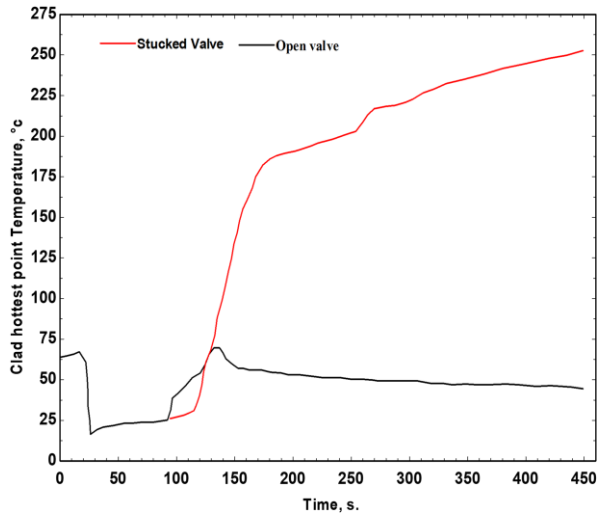


Fig. 8. Clad hottest point temperature.

4.3. LOPS scenario with flapper valves fail

If loss of power supply is followed by a failure of the flapper valves, the natural convection regime cannot be established, and the core flow will be zero. This situation is very serious because the coolant will heat up and the steam will be formed in a periodic way inside the coolant channels. In the first case, when the power drops below the threshold value after shutdown, the fuel will be cooled by a pulsed boiling mechanism, the steam is expelled, and

the water replenishes the coolant channel again. The second situation is for the powers above the threshold power. Then, the pulsed boiling mechanism is not enough to cool the fuel plate and it will burn out. This paper is focused on the second situation, where there is a risk of danger in the reactor, and diverse emergency plans must be found to avoid any surprising situations. Figure 6 shows the temperature of the clad compared with its temperature in the case of valve opening. Figure 8 shows that in the case of the valve failure, the fuel is heated up after the main pumps stop completely (after 90 s), and its temperature increases rapidly to a dangerous value exceeding the safety limits (≤ 125°C). According to safety objectives and engineering design requirements, the reactor is in a critical situation, and this issue must be solved before it occurs.

4.4 Proposed solutions

As a result of valve failure, the flow to the core is zero, and the temperature of the clad increases to critical values, as shown in Fig. 8, and these values are sufficient to boil the coolant. When the new pump starts to work, the temperature of the core drops slowly. After a while, the flow of the new pump becomes steady-state and the temperature of the core decreases rapidly.

A small pump is installed with a capacity of about 3.0 m^3/h on the primary line and operates after ensuring the failure of the flapper valve (at 90 s after immediate shutdown). Figure 9 shows the position of that small pump, which is called the emergency pump. As shown, it is installed parallel to the main pump. This pump is simulated to operate after 1 min, 2 min and 3 min from the failure of the valve. This simulation is important to determine the optimum time to operate the pump. The emergency pump runs with the flapper valves after 90 s of a shutdown. If the valve fails to open, the pump already runs in a diverse way. But the mechanism of valve opening depends on the pressure difference inside and outside the primary pipe (less than 350 kPa). Thus, the operation of the small pump at the time of the valve opening will not affect the valve function, because the pump is selected and designed to provide a head of water column below the head at the flapper valve position. Figure 10 illustrates the configuration, which permits the flapper valve to open and keep the circulation of coolant inside the cooling loop. If we suppose that the valve opens and the small pump runs at the same time, most of the pump flow will go through the cooling loop. This solution is also helpful, as shown in Fig. 11. Peaks of the curves shown in Figs. 12 and 13 indicate the start time of the pump operation, and the drop at the end of the curves indicates

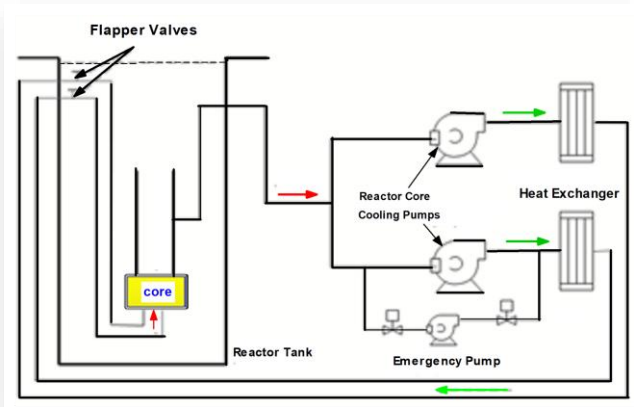


Fig. 9. Position of the emergency pump.

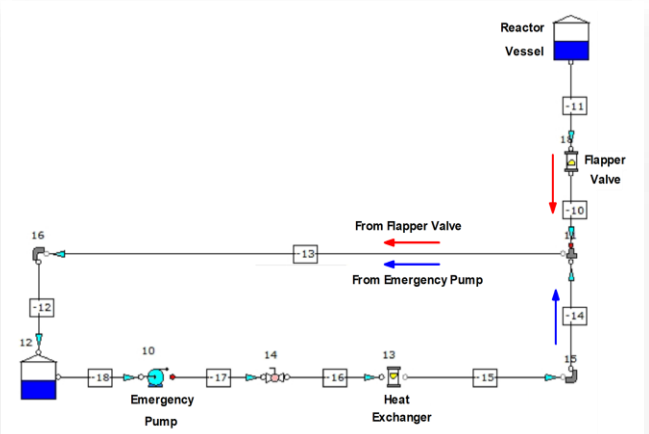


Fig. 10. Hydraulic layout of both the pump and the flapper valve.

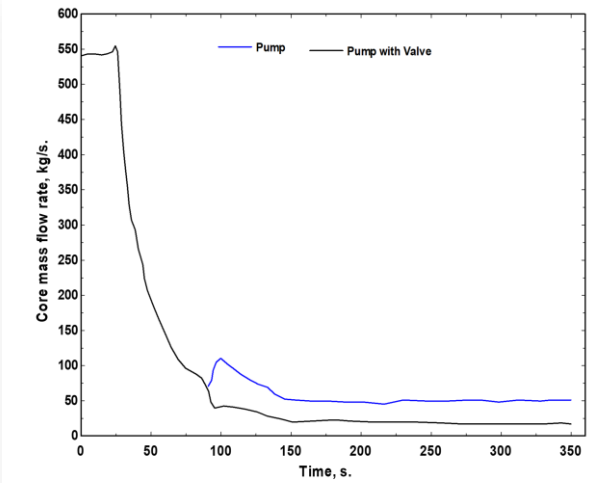


Fig. 11. Change in the outlet core coolant temperature over time for three cases.

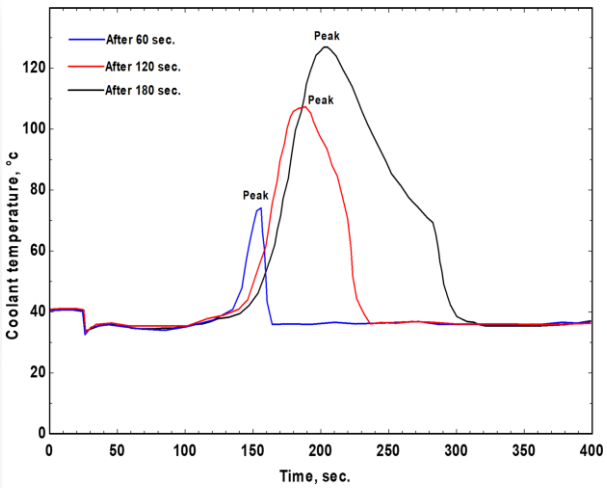


Fig. 12. Change in the coolant hottest temperature vs. time.

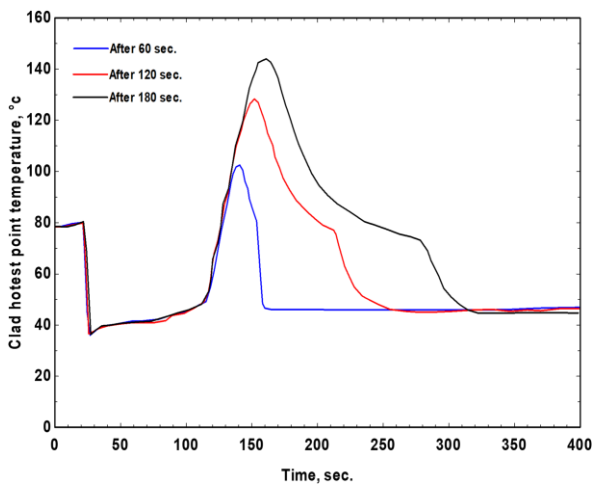


Fig. 13. Change in the clad hottest temperature vs. time.

the stability of the new pump flow. The peak values refer to the maximum core temperature reached in the different cases. It is found that, if the pump runs 1 min, 2 min and 3 min after the valve failure, the maximum core temperature does not exceed the safety values (125°C). Thus, it is recommended to operate the small pump after 1 min or 2 min of valve failure.

5. Conclusions

The reactor is capable of bringing and restoring a safe shutdown state by the passive natural convection safety system and inherent safety characteristics. If, for any reason, the passive and inherent safety systems have a malfunction, there is a need to use active safety systems. This situation is studied in this manuscript. It is supposed that the reactor is forced to shut down due to loss of power supply, and the flapper valve, which is responsible for natural convection, fails to open due to being stuck. It is recommended to install the proposed emergency small pump, with a capacity equal to that realised by a natural circulation laminar flow on the primary cooling system 50 m^3/h, to pressurise the core coolant after two minutes of the flapper valve failure. Modelling and simulation results indicate that the heat transfer and cooling are realised after the flapper valve is stuck with satisfactory temperatures prediction below safety limits, with a good margin. It is also recommended to connect an alternative power supply, such as a diesel generator, to run the emergency pump to guarantee its operation at any time.

References

[1] Dorsselaere, J.-P., Albiol, T., & Micaelli, J.-C. (2011). Research on severe accidents in nuclear power plants. In *Nuclear Power – Operation, Safety and Environment*. Intech, 155e182. doi: 10.5772/17552

[2] Volkanovski, A., Ballesteros Avila, A., Peinador Veira, M., Kančev, D., Maqua, M., & Stephan, J.-L. (2016). Analysis of loss of offsite power events reported in nuclear power plants. *Nuclear Engineering and Design*, 307, 234–248. doi:10.1016/j.nucengdes.2016.07.005

[3] Kim, S. H., Futami, T., Chang, S. H., & Jeong, Y. H. (2015). Safety Enhancements for PHWRs based on macroscopic losses of the Fukushima accident. *Science and Technology of Nuclear Installations*, 520756. doi: 10.1155/2015/520756

[4] Mohsendokht, M., Hadad, K. & Jabbari, M. (2018). Reducing the loss of off-site power contribution in the core damage frequency of a VVER-1000 reactor by extending the house load operation period. *Annals of Nuclear Energy*, 116, 303−313. doi: 10.1016/j.anucene.2018.01.030

[5] Gjorgiev, B., Volkanovski, A., Kancev, D., & Čepin, M. (2014). Alternative off-site power supply improves nuclear power plant safety. *Annals of Nuclear Energy*, 71, 304−312. doi: 10.1016/j.anucene.2014.04.011

[6] Petruzzi, A., & D'Auria, F. (2008). Thermal-hydraulic system codes in nuclear reactor safety and qualification procedures. *Science and Technology of Nuclear Installations*, 460795. doi: 10.1155/2008/460795

[7] RELAP5-3D Code Development Team. (2005). *RELAP5-3D code manual volume I: code structure, system models and solution methods*. INEEL-EXT-98-00834, Rev. 4.0.

[8] Grange, A., Marrel, A., Droin, J.B., Bertrand, F., Boutin, O., & Ferrasse, J. H. (2019). Loss of off-site power transient analysis for a sodium-cooled fast reactor equipped with a gas power conversion system and preliminary optimisation of its operation. *Nuclear Engineering and Design*, 355, 110315. doi: 10.1016/j.nucengdes.2019.110315

[9] International Atomic Energy Agency (2016). *Safety of research reactors: Specific safety requirements (IAEA Safety Standards Series No. SSR-3)*. IAEA, Vienna.

[10] International Atomic Energy Agency (2014). Safety of nuclear power plants. *Safety Reports Series*, 80. IAEA, Vienna.

[11] International Atomic Energy Agency (2016). Safety of nuclear power plants: Design, S*pecific Safety Requirements (No. SSR-2/1)*. IAEA, Vienna.

[12] Margulis, M., & Gilad, E. (2016). Monte Carlo and nodal neutron physics calculations of the IAEA MTR benchmark using Serpent/DYN3D code system. *Progress in Nuclear Energy*, 88, 118−133. doi: 10.1016/j.pnucene.2015.12.008

[13] Kim, T.-R. (2016). Safety classification of systems, structures, and components for pool-type research reactors. *Nuclear Engineering and Technology*, 48(4), 1015−1021. doi: 10.1016/j.net.2016.02.009

[14] Boustani, E., & Khakshournia, S. (2017). Enhancing Tehran Research Reactor safety through a second shutdown system: A probabilistic safety assessment. *Progress in Nuclear Energy*, 100, 380−388. doi: 10.1016/j.pnucene.2017.07.006

[15] Kałowski, J., & Kowal, K. (2023). An integrated risk-informed safety classification for unique research reactors. *Nuclear Engineering and Technology*, 55, 1814−1820. doi: 10.1016/j.net.2023.01.017

[16] Radu, G., Mladin, D., & Prisecaru, I. (2013). Analysis of potential common cause failure events for Romania−TRIGA 14 MW reactor. *Nuclear Engineering and Design*, 265, 164−173. doi: 10.1016/j.pnucene.2013.06.027

[17] Hermansya, H., Kumaraningrum, A.R., Purba, J.H., & Yohda, M. (2020). Safety analysis technique for systems with limited data: Case study of the multipurpose research reactor in Indonesia. *Energies*, 13(8), 1975. doi: 10.3390/en13081975

[18] Margulis, M., & Gilad, E. (2016). Development and verification of the dynamic system code THERMO-T for research reactor accident analysis. *Nuclear Technology*, 196(2), 377−395. doi: 10.13182/NT1623

[19] Almachi, J. C., Sánchez-Espinoza, V. H., & Imke, U. (2022). High-fidelity steady-state and transient simulations of an MTR research reactor using Serpent2/Subchanflow. *Energies*, 15(4), 1554. doi: 10.3390/en15041554

[20] Almachi, J. C., Sánchez-Espinoza, V., & Imke, U. (2021). Extension and validation of the SubChanFlow code for the thermos-hydraulic analysis of MTR cores with plate-type fuel assemblies. *Nuclear Engineering and Design*, 379, 111221. doi: 10.1016/j.nucengdes.2021.111221

[21] Labit, J.-M., Seiler, N., Clamens, O., & Merle, E. (2021). Thermal-hydraulic two-phase modeling of reactivity-initiated transients with CATHARE2 − Application to SPERT-IV simulation. *Nuclear Engineering and Design*, 381, 111310. doi: 10.1016/j.nucengdes.2021.111310

[22] Bergman, T.L., Lavine, A.S., Incropera, F.P., DeWitt, D.P. (2011). *Fundamentals of heat and mass transfer* (7th ed.). Wiley & Sons.

[23] INVAP S.E. (1996). *ETRR-2 Detail Engineering Design*, NC-NSRC, Atomic Energy Authority, Cairo, Egypt.

[24] Abdelrazek, I., Abo Elnour, A.G., & Gaheen, M.A. (2015). Thermal hydraulic analysis of ETRR-2 using RELAP5 code. *Kerntechnik*, 80(1), 32−39. doi.org/10.3139/124.110475

Co-published by
Institute of Fluid-Flow Machinery
Polish Academy of Sciences
Committee on Thermodynamics and Combustion
Polish Academy of Sciences

Copyright©2026 by the Authors under licence CC BY-NC-ND 4.0

http://www.imp.gda.pl/archives-of-thermodynamics/

Review of the Modified Kalina Cycle for Cogeneration Systems (MKCS)

Mohammed Wahody Eraiby*, Abdulkhodor Kathum Nassir

College of Engineering, Mechanical Engineering Department, University of Babylon, Babylon City 51001, Hilla, Iraq
*Corresponding author email: eng895.mohammed.whwdy@student.uobabylon.edu

Received: 27.10.2024; revised: 18.12.2025; accepted: 04.01.2026

Abstract

The increasing demand for electricity and cooling, resulting from accelerating urban growth, growing economies and the integration of technology into daily life, leads to continued research and study of theories related to the optimal exploitation of energy sources, including those with low temperatures, for a sustainable environment free of CO_2. The authors regard the Kalina cycle, which uses ammonia and water as its working fluid, as the most efficient system in this field. This manuscript presents a comprehensive review of the published literature on the modified Kalina cycle, a cogeneration system that simultaneously produces electricity and cooling. It also provides an overview of the original Kalina cycle, other types of Kalina cycles, and their various applications. We also discuss the properties of the binary solution, which the cycle uses as a working fluid. Discuss the boiling and freezing points to maintain the fluidity of the working fluid through the cooling process. Additionally, we discuss the corrosion-related aspects of applying the Kalina cycle, specifically the reaction between ammonia and metal components, as well as strategies for mitigating this corrosion, as previously mentioned in the literature.

Keywords: Modified Kalina cycle; Generation power and cooling; Boiling and freezing points; Low-temperature source; Ammonia-water fluids.

Vol. 47(2026), No. 1, 145–160; doi: 10.24425/ather.2026.158666

Cite this manuscript as: Eraiby, M.W., & Nassir, A.K. (2026). Review of the Modified Kalina Cycle for Cogeneration Systems (MKCS). *Archives of Thermodynamics*, 47(1), 145−160.

1. Introduction

Providing electricity and cooling is critical, particularly during summer, due to high energy consumption. Studies emphasise the considerable impact of cooling requirements on electricity consumption, with operating cooling representing a substantial portion of electricity use during hot seasons. Therefore, planning for cogeneration power and cooling is a better way to solve the energy deficiency, especially when providing cooling without affecting or reducing electricity production. The original and modified Kalina cycle system (MKCS) has emerged as a promising cogeneration system, enhancing energy efficiency, environmental sustainability, and economic viability in various applications. The system utilises various energy sources, including low-grade heat sources (373 K − 473 K), such as wind, geothermal, solar and waste heat, to generate power, cooling and heating. Research has demonstrated that the Kalina cycle (KC) excels in operating with low-heat sources, making it a perfect choice for obtaining energy from these sources [1]. In Kumar et al. [2], the working solution of the Kalina cycle is a non-zeotropic mixture of NH_3-H_2O. These binary mixture properties improve the thermal match between the heating source, which has a low temperature, and the working fluid, leading to more efficient low-heat source utilisation. Optimising the operational

Nomenclature

$\dot{E}$ – exergy rate, kW
h – specific enthalpy, kJ kg^{-1}
$\dot{m}$ – mass flow rate, kg·s^{-1}
P – pressure, kPa
Q – heat rejected, kW
Qr – cooling capacity, kW
s – specific entropy, kJ kg^{-1} K
$\dot{W}$ – rate of work, kW
W – output power, kW
x – dryness fraction

Greek symbols

η_{th} – thermal efficiency, %
η_{exe} – exergy efficiency, %
$(\eta_{pump})_{isent}$ – isentropic efficiency of the pump
$(\eta_t)_{isent}$ – isentropic efficiency of the turbine

Subscripts and Superscripts

con – condenser
d – destruction
exe – exergy
exh – exhaust
gen – generator
isent – isentropic
max – maximum
min – minimum
sep – separator
tot – total
t – turbine
th – thermal
thr – throttle valve

Abbreviations and Acronyms

ACH – absorption chiller
AHP – absorption heat pump
ARC – absorption refrigeration cycle
AWKRC – ammonia-water Kalina Rankine cycle
BTC – bottom cycle
CCP – collected cooling and power
DF – dryness fraction
DNI – direct normal irradiance
DC – direct current
ERC – ejector refrigeration cycle
GEN – generator
HGH – high-grade heat cycle
HRVG – heat recovery vapour generator
HE – heat exchanger
KC – Kalina cycle
KCS – Kalina cycle system
KFC – Kalina flash cycle
KLPCCS – Kalina lithium power-cooling cycle system
LGH – low-grade heat cycle
LiBr – lithium bromide
LNG – liquefied natural gas
MKCS – modified Kalina cycle system
NH_3-H_2O – ammonia-water
ORC – organic Rankine cycle
PPR-KC – parallel cogeneration of power and refrigeration–Kalina cycle
PTSC – parabolic through solar collector
SGS – separate generation system
TIT – turbine inlet temperature
TEG – thermoelectric generator
VAS – vapour absorption system

conditions and the composition of the working fluid can enhance the performance of the Kalina cycle. Esmailzadeh et al. [3] added a Kalina cycle with a polymer membrane fuel cell and a vacuum heat tube collector, improving the energy efficiency and exergy efficiency by 13.12% point and 10.35% point, respectively.

2. Glance of Kalina cycle

The rapid expansion of cities and the rapid rise in global population have posed significant challenges to the global energy system. To address these challenges, it is crucial to prioritise waste heat recovery technology and reduce greenhouse gas emissions and fossil fuel consumption for a sustainable future [4]. The Rankine cycle received the first nomination for the use of this low-temperature heat energy, but its efficiency in this area is very low. The second nominee was the organic Rankine cycle (ORC), in which the selection of working fluid and the turbine design (or expander in ORC) are important problems. Dr. Alexander Kalina (1983) first presented the Kalina cycle as in Fig. 1, using a non-azeotropic pair mixture (NH_3-H_2O) working fluid, and compared the three cycles in power generation and for cogeneration application. The Kalina cycle exhibits greater efficiency when operating at maximum fluid pressure due to the fluid mixture's variable boiling temperature [5,6]. The available literature has broadly discussed different Kalina cycles and their applications, as shown in Table 1 [7,8].

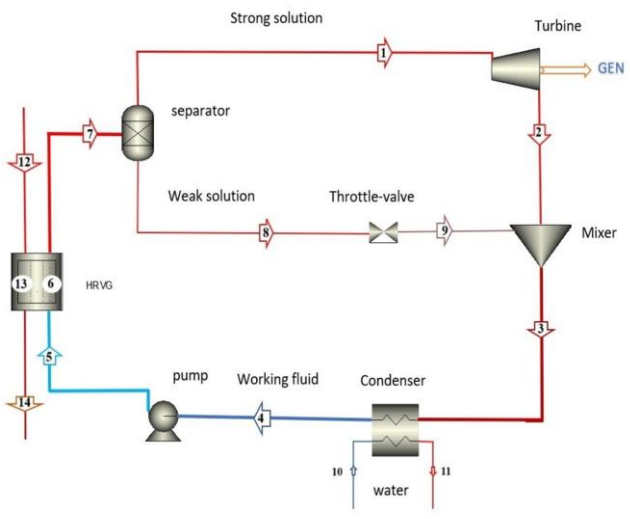


Fig. 1. Original Kalina cycle (drawn after [9]).

Table 1. Different types of Kalina cycle [7,8].

System	Application	Net output power ratio (KC/RC)	Cycle efficiency ratio (KC/RC)	State of development
KCS0	Used for a one heat exchanger plant below 1 MW	-	-	Design completed
KCS1	Bottoming cycle small plant about 8 MW	(49.5/46.0) = 1.07[a]	(32.0/26.6) = 1.2	Design completed
KCS2	Low-temperature geothermal plant for heat source under 623 K	(17.6/10.3) = 1.71[b, c]	(20.5/13.1) = 1.56[a]	Design completed
KCS3	High-temperature geothermal and industrial waste			Under development
KCS4	Cogeneration			Planned
KCS5	Direct-fired for coal and other solid fuels	(40.9/34.6) = 1.18[d]	(48.6/42.2) = 1.15	Design completed
KCS5n	High-temperature gas-cooled nuclear reactor	(46.0/36.0) = 1.28	(46.0/36.0) = 1.28	Design completed
KCS6	Bottoming for a utility combined cycle above 20 MW	(56.4/51.0) = 1.11[a]	(37.8/28.7) = 1.32	Design completed
KCS7	Direct-fired, split cycle	(42.4/34.6) = 1.22[d]	(50.0/42.2) = 1.19	Under development
KCS8	Bottoming cycle, split cycle	(56.67/51.0) = 1.11[a]	(39.0/28.7) = 1.36	Under development
KCS9	Retrofit subsystem for the existing plant	(40.4/34.6) = 1.17[d]	N/A	Under development
KCS11	Bagasse-fired cogeneration plant of the sugar industry, for heat source temperature range 394 – 477 K			Under development
KCS12	Low-temperature geothermal	(16.5/10.3) = 1.6[b, c]	(19.2/13.1) = 1.47	Design completed
KCS34	Cascade utilisation of low-grade waste heat, combined power system	N/A	N/A	Design completed
KCS34g	Low temperature small size plant	N/A	N/A	Design completed
KCSCS	Biomass chip plants	N/A	N/A	Design completed
KCS17	Double-flash geothermal system (hybrid cycle)	N/A	N/A	Design completed

[a]For the entire combined cycle.
[b]Compared to the Heber plant binary cycle
[c]Includes losses due to injection pumps and other auxiliaries.
[d]Includes losses from fuel handling and plant auxiliaries.

3. Modified Kalina cycle for cogeneration

The Kalina cycle is a thermodynamic cycle that is useful for the generation of electricity and cooling at the same time. As a co-generator, the primary aim is to produce additional energy. You can achieve this by either obtaining additional electricity from the same waste heat input source, which you can then use to operate a separate cooling cycle (traditional compression cooling), or using waste heat from the power generation of the Kalina cycle to provide heating or cooling. The type of collected cooling and power (CCP) is effective for large cooling needs in hot places, industrial facilities that generate a significant amount of waste heat, or for a plant that produces both power and cooling [10]. By integrating the Kalina cycle system (KCS) and the system of vapour absorption (VAS), you can seamlessly combine power with other applications, such as water and hydrogen production. This approach enables you to select double, triple or even more services in a single step [11]. Seçkin [12] studied a combined power and cooling system, as shown in Fig. 2. The system comprises the Kalina cycle (KC), which uses aqua-ammonia working fluid for power generation, and the ejector refrigeration cycle (ERC), which uses R-134a working fluid for cooling. The results indicate an enhancement in both thermal and exergy efficiencies with an increase in maximum pressure. However, an increase in the turbine entrance temperature adversely affects only the exergy efficiencies. Shankar et al. [13] looked into a cogeneration cycle that uses the Kalina cycle to make electricity and cool the air, as seen in Fig. 3. The condenser, situated after the turbine, transforms the ammonia vapour into a liquid state, which then expands through the sub-cooler with a constant heat content to generate refrigeration. The results show that when the source temperature was 383 K for a 0.25 of the ammonia mass fraction, the coefficient of performance (COP) was 0.16.

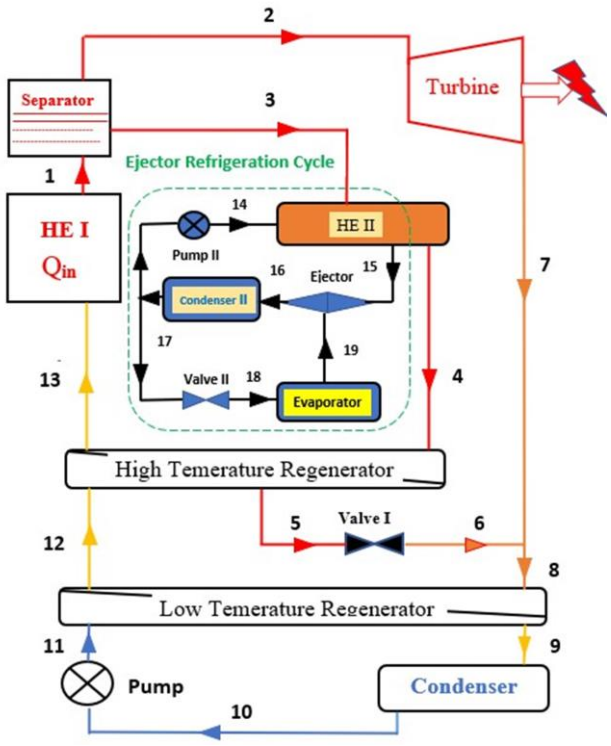


Fig. 2. Combined cycle with a Kalina sub-cycle with ejector refrigeration cycle ERC (drawn after [12]).

Karaali [14] studied a cogeneration aqua-ammonia cycle (Kalina cycle) to generate power and refrigeration. A turbine expands a strong solution and generates power. The ammonia vapour that leaves the turbine is used to produce cooling. The results show that raising the turbine entrance pressure reduced energy, exergy efficiencies and output power. Abam et al. [15]

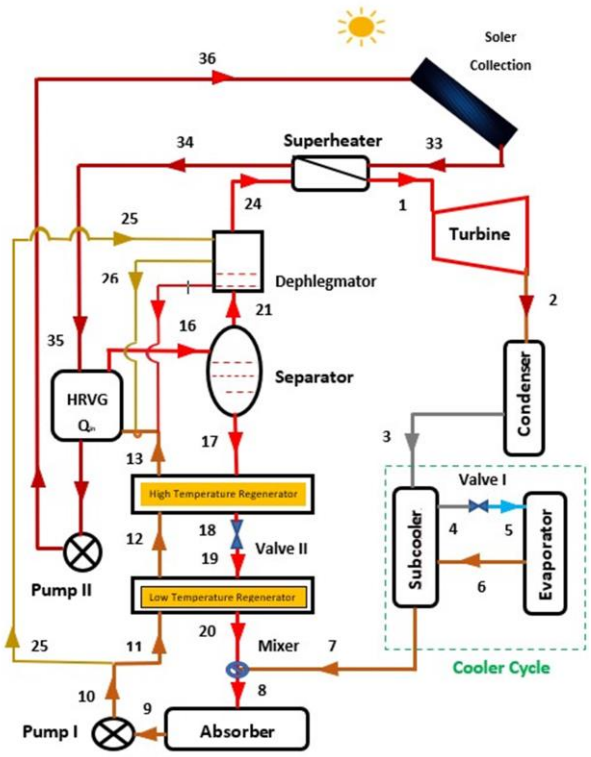


Fig. 3. Combined power and cooling cycle (drawn after [13]).

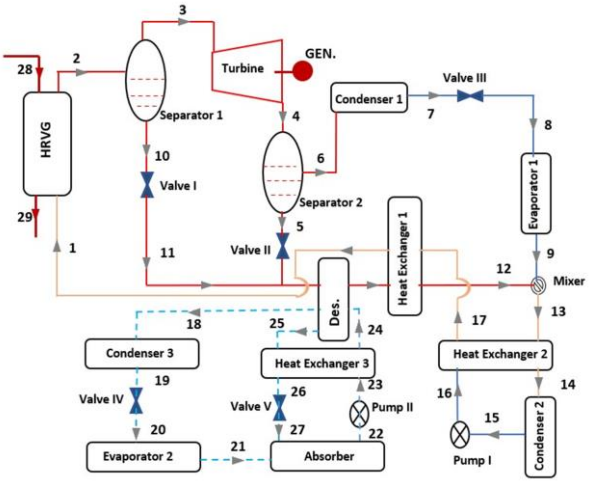


Fig. 4. Modified Kalina cycle for the combined power-cooling plant KLPCC (drawn after [15]).

looked into a cogeneration system called the Kalina lithium power-cooling cycles system (KLPCCS), as seen in Fig. 4.

This system has a top cycle (TPC) that uses aqua-ammonia as a working fluid to make electricity and a bottom cycle (BTC) that uses the vapour absorption cooling system (VAB) with LiBr as the working fluid. Kim [16] studied a combined system of Kalina cycles (KCS11) to produce power, using NH_3/H_2O as the working fluid and an absorption chiller for cooling. The results indicated that as the source temperature rises, the power increases, but the cooling capacity reduces. Zhang et al. [17] studied a Kalina cycle (KCS1-2) in parallel cogeneration of power and refrigeration (PPR-KC), which generates both electricity and cooling, as illustrated in Fig. 5.

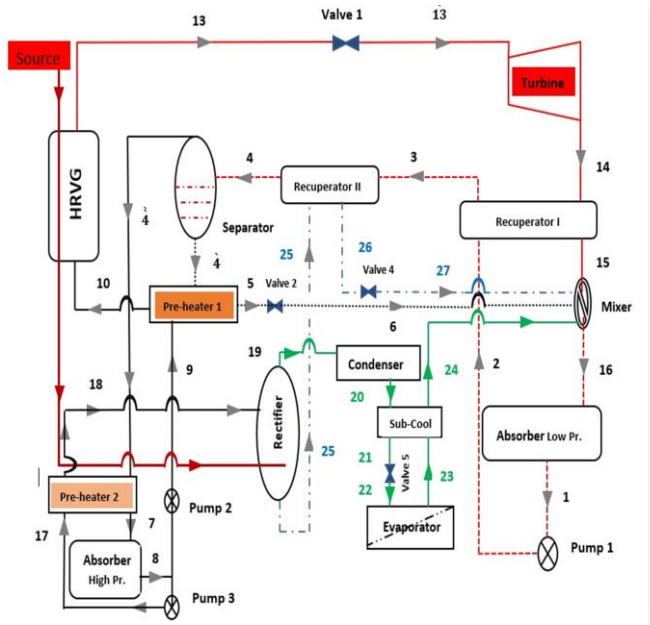


Fig. 5. Kalina cycle with parallel cogeneration of power and refrigeration PPRKC (drawn after [17]).

The cooling circuit is integrated with the power circuit, ensuring simultaneous efficiency. The proposed cycle significantly improves heat-waste recovery efficiency to 27.2%, compared to the reference cycle KCS1-2 of approximately 22.62% efficiency. Hua et al. [18] provided a new cogeneration cycle, including a modified Kalina cycle (ammonia-water) to generate power and an absorption chiller for air conditioning with low-grade temperature sources. The results indicate that energy and exergy efficiencies increase by 3.19%-points and 3.64%-points, respectively, as compared to the reference Kalina power cycle. Cao et al. [19] worked on a proposed combined system including the absorption refrigeration cycle and a Kalina cycle, as illustrated in Fig. 6. Next, they compared it to a system that generates electricity under identical conditions, and powers a DC

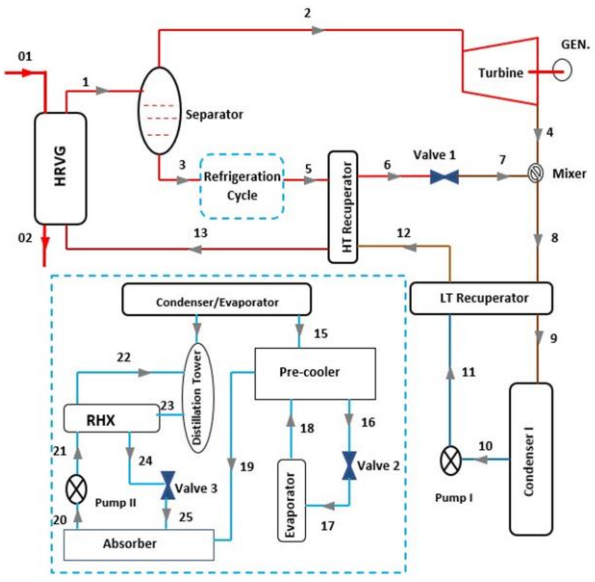


Fig. 6. Kalina-based CCP cycle (drawn after [19]).

cooling unit. The results indicated that the proposed cycle outperformed the separate generation system (SGS). Furthermore, the separate generation system consumed an additional 12.54 kW of energy compared to the suggested cycle, specifically for operating the cooling unit's compressor. Wang et al. [20] suggested a system that integrates a Kalina cycle for electricity generation with an ammonia-water absorption refrigeration cycle (AWARC). This system extracts purer ammonia vapour from the exhaust of the ammonia-water turbine using a second separator. The purer vapour is then condensed and throttled before entering the evaporator to produce cooling output. The outcomes reveal that an increased first separator pressure increases the system thermal and exergy efficiencies. The system provides electricity and cooling output simultaneously, minimising redundancy in certain components across both cycles, which leads to reduced costs and a smaller size. Seçkin [21] looked into a system that integrates both the Kalina cycle (KC) for power generation, which utilises ammonia and water as working fluids, and the ejector refrigeration cycle (ERC), which employs refrigerants such as R290, R134a, and R152a. ERC is installed at the weak solution stream of KC. The results indicated that R290 achieved the highest thermal efficiency, while R134 attained the highest exergy efficiency, respectively. Seckin [22] proposed combining the Kalina cycle (using ammonia solution) with the ejector refrigeration cycle (ERC) using R134a as a coolant to produce electricity and cooling. The process of burning biomass (organic waste) drives this combined cycle. The results indicate that an increase in the evaporator temperature of ERC leads to an increase in overall thermal efficiency, gross power output, and cooling capacity. Additionally, the energy efficiency of the proposed cycle is dependent on the Kalina cycle efficiency. Zhang et al. [23] utilised a system that operates with ammonia-water, known as the Kalina-Rankine cycle (AWKRC); this system employs a valve to switch between the Rankine and Kalina cycles. In the winter, the Rankine cycle functions as a cogeneration plant that provides power and heating water, while during the rest of the year, the Kalina cycle operates solely to produce electricity. As illustrated in Fig. 7, with the Kalina cycle, an increase in ammonia concentration slightly enhances the heating recovery efficiency.

A summary of the conducted study on the application of the modified Kalina cycle for combined power, cooling and heating is presented in Table 2.

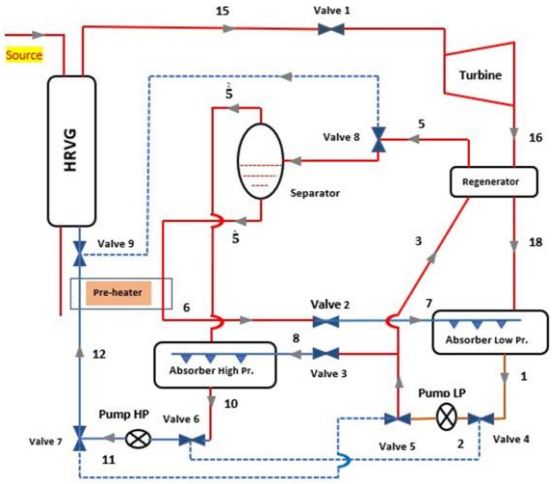


Fig. 7. Kalina cycle in non-heating application (drawn after [23]).

Table 2. Modified Kalina cycles for cogeneration.

Articles	Type of cycle	Cycle specifications	η_{th}, %	η_{exe}, %	Remarks
Wang et al. [10]	KC + ARC	TIT:473 K, P_{max}= 5 MPa	24.62	11.52	Both cycles working with the ammonia-water mixture.
Abam et al. [11]	KC+ VAS	TIT= 1350 K	53.48	50.05	The power output and flow rate of hydrogen are 86.320 MW and 0.1524 kg/h, respectively.
Seçkin [12]	KC+ ERC	P_{max}= 2.5 MPa P_{max}= 4 MPa TIT= 388 K TIT= 413 K	10.8 11.88 11.5 19.55	45 76.5 75 44.25	The refrigeration capacity of ERC remained constant at about 44.65 kW with ammonia-water as the working fluid.
Shankar et al. [13]	MKCS	TIT= 383 K, x=0.25	3.6	-	At TIT=398 K, the highest power output of 1.8 kW and 2.2 TR of cooling.
Karaalı [14]	MKCS	P_{max}= 4 MPa, x=0.54	23	68	The mechanical power and cooler heat energy were 197 kW and 26 kW, respectively.
Abam et al. [15]	KC+ VAS	TIT= 453 K P_{max}= 2 MPa	8.15	16.97	A reach of about 1077 kW of refrigeration was produced, and power output was 291 kW.
Kim [16]	KC+ARC	TIT= 393 K P_{max}= 3.6 MPa Output power 16.9 kW	60	-	The maximum cooling capacity is 64.7 kW at TIT= 393 K and pressure of 1600 kPa.
Zhang et al. [17]	PPR-KC KCS1-2	TIT= 673 K x=0.5	27.96 27.19	-	The system recorded approximately 699.2 kW in net output power, whereas the cooling output system recorded 299.9 kW.
Hua et al. [18]	Chilling cogeneration	P_{max}= 2.74 MPa TIT= 468 K	16.4	48.3	At a chilling fraction of about 5%, specific cooling capacity is 119.53 kJ/kg, and specific output power is 139.1 kJ/kg
Cao et al. [19]	KC+ ARC SGS	TIT= 413 K P_{max}= 4 MPa	-	25.76 23.44	The combined system recorded approximately 89.59 kW, whereas SGS recorded 77.81 kW in net output power.
Wang et al. [20]	KC+ AWARC	TIT= 453 K P_{max}= 2 MPa	13.72	5.40	A reach of about 75.12 kW of refrigeration was produced, and power output was 37.63 kW.
Seçkin [21]	KC+ ERC	R290 as a working fluid R134a as a working fluid R152a as a working fluid	16.7 15.5 15	26 30 28	At 415 kPa, the maximum cooling capacity is approximately 120 kW when using R290, while the net output power is around 95 kW with R134
Seçkin [22]	KC+ ERC	P_{max}= 3.25 MPa x=0.7	1.2	-	With an evaporator temperature of 283 K in ERC, the cooling capacity and net output power are 53 kW and 95 kW, respectively.
Zhang et al. [23]	KC-system RC-system	TIT=553 K P_{max}= 6 MPa	20.85 17.09	-	With a heating recovery efficiency of 55.3% to generate heating water in the winter season by RC.

4. Adjusted Kalina cycles for Integration with other systems and applications

One of the greatest operant exploits of energy is cogeneration. But that's not all that's needed. Other aspects need work. The available literature has broadly discussed the modified Kalina cycles and their applications in this scope; we mention them as examples, not as exclusives.

4.1. Cycles integrated with solar heat and geothermal energy

The Kalina cycle effectively utilises low- and medium-temperature heat sources and can be integrated with solar heat and geothermal energy to enhance power generation efficiency and sustainability, resulting in higher efficiency and lower emissions than traditional cycles. Khanmohammad et al. [24] utilised the waste heat from a solar collector (PTSC) to drive a Kalina cycle, generating the power needed to operate reverse osmosis desalination (RO) to produce drinking water, which is connected to a unit of a thermoelectric generator (TEG) to cogenerate electricity. The results show that increasing either the direct normal irradiance (750–1000 W/m^2) or the pressure of the turbine inlet, both the gross power output and desalinated water output will increase. Qu et al. [25] suggested a system that uses concentrating photovoltaics and the Kalina cycle, equipped with an absorption chiller cycle; this absorption chiller cycle can recover waste heat from photovoltaic cells to cool the working fluid of the Kalina cycle at the turbine's exit. As illustrated in Fig. 8, the findings suggest that the proposed cycle improves the efficiency of heat loss recovery from the photovoltaic cell compared to the Kalina cycle, which does not utilise a chiller.

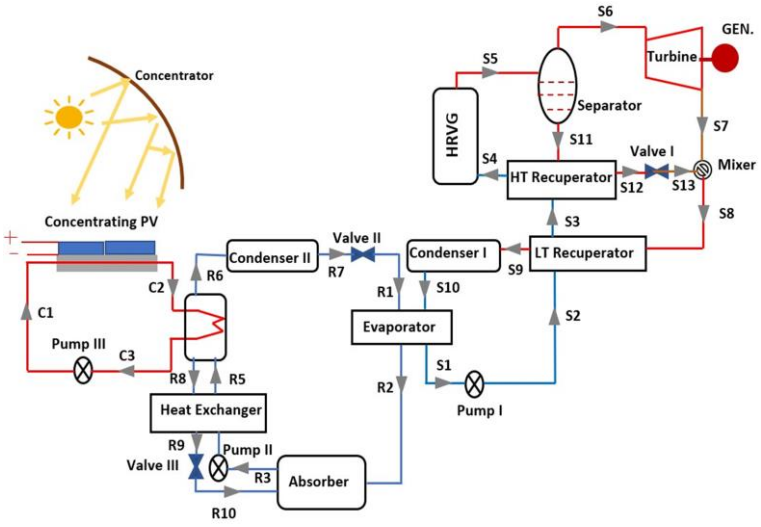


Fig. 8. Concentrating photovoltaic/thermal and Kalina cycle combined system (drawn after [25]).

Lei et al. [26] proposed to utilise the modified Kalina cycle (MKC) for recovering energy from geothermal well water and enhancing the net output power. Taking the geothermal parameters of the Husavik Power Plant in Iceland, where the geothermal well temperature is approximately 395 K and the well water temperature is around 353 K, the results indicated that the gross power extracted by MKC was enhanced compared to that of the reference KC.

A summary of studies that focus on the integration of KCS with solar heat and geothermal energy is presented in Table 3.

Table 3. Cycle integrated with solar heat and geothermal energy.

Articles	Type of heat source and connected cycle	η_{th}, %	η_{exe}, %	Remarks
Khanmohammadi et al. [24]	PTSC with KCS	24.3	–	The system can generate a gross power output of 372.1 kW and a drinking water output of 48.09 m^3/h as DNI increases to 1000 W/m^2.
Qu et al. [25]	Photovoltaic cells: - with absorption - without absorption	 24 4.2	 41	Able to exploit a waste heat temperature range (333 – 343 K) Increase the Kalina cycle energy efficiency by 2 – 3%.
Lei et al. [26]	Geothermal well water: - with MKCS, - with KCS	13.43 9.42	–	The gross power of MKC and KC is approximately 2329 kW, 2108 kW and 9.4 kW, respectively.

4.2. Contribution to internal combustion engines

Kalina cycle's integration with internal combustion engines (ICE) can enhance energy efficiency and reduce environmental impact by recovering waste heat from exhaust gases from ICEs. Studies of Gao and Chen [27] focused on integrating a Kalina cycle as a subsystem with an internal combustion engine (ICE) to utilise exhaust gases for energy production. The outcomes indicate that the increase in energy efficiency exceeds 10% across all operating loads of ICE while also contributing to a reduction

in greenhouse gas emissions. Larsen et al. [28] suggested a unique type of Kalina split-cycle that utilises hot flue gases from large marine diesel engines as a low heat source. In this innovative cycle, the concentrations of the binary solution can be varied during the HRVG process to better match the temperatures of the heat source and binary solution. Results show that the suggested cycle process can improve thermal efficiency when using reheat, as compared to a traditional cycle. Table 4 summarises the most important findings related to the contribution of KCS in internal combustion engines.

Table 4. Contribution of KCS to internal combustion engines.

Articles	Condition specifications	η_{th}, %	η_{exe}, %	Remarks
Gao & Chen [27]	ICE operates at full load	46.94	74	The energy and exergy efficiencies of KC exceed those reported in other articles for all ICE loads.
Larsen et al. [28]	Kalina split-cycle Traditional cycle	23.2 20.8	-	When reheating in both cycles.

4.3. Contribution to enhancing the power production

By utilising a binary mixture as a working fluid, the Kalina cycle enhances efficiency compared to conventional cycles and significantly boosts power production. Akimoto et al. [29] investigated a combination of Kalina cycles and absorption heat pumps to produce power in multiple stages, utilising the Kalina cycle to produce power. When the heat rejected from the first cycle is insufficient to drive another Kalina cycle (KC), use an absorption heat pump (AHP) to increase the heat rejected. This enables the system to reproduce the power from a second Kalina cycle, and so on, for the entire chain of Kalina cycles, while also utilising an absorption heat pump to handle multiple electric heat energies. The result is an 81% increase in net power compared to the traditional Kalina cycle.

Zhang and Li [30] suggested a dual modification for the three Kalina cycles KCS 11, 34 and 34g by substituting the throttle valve with a single-screw expander (SSE). SSE is located between the absorber and the regenerator in the I-recomposition cycle. The II-recomposition cycle places SSE between the regenerator and the separator. The results show enhancements in the energy efficiency, net power and exergy efficiency of two recomposition cycles compared to their reference KCS. The II-recomposition cycle performs better than the I-recomposition cycle. Nassir and Shahad [31] suggested two modifications to the original Kalina cycle (KC). As shown in Fig. 9, the first adjustment (MKCS1) consists of adding a heat exchanger (HE1) before the throttle valve, while the second adjustment (MKCS2) consists of adding a heat exchanger (HE2) after the turbine. The Kalina cycle uses aqua-ammonia as a working fluid. The results demonstrate an enhancement in the maximum efficiencies for both adjustments, MKCS1 and MKCS2, when compared to the original reference cycle.

Kim et al. [32] looked into a Kalina flash cycle (KFC) that incorporates an additional flash vessel in the stream of weak ammonia solution from the original cycle. This vessel generates both a strong and weak solution; the strong solution powers a second turbine, increasing the cycle's power output (Fig. 10).

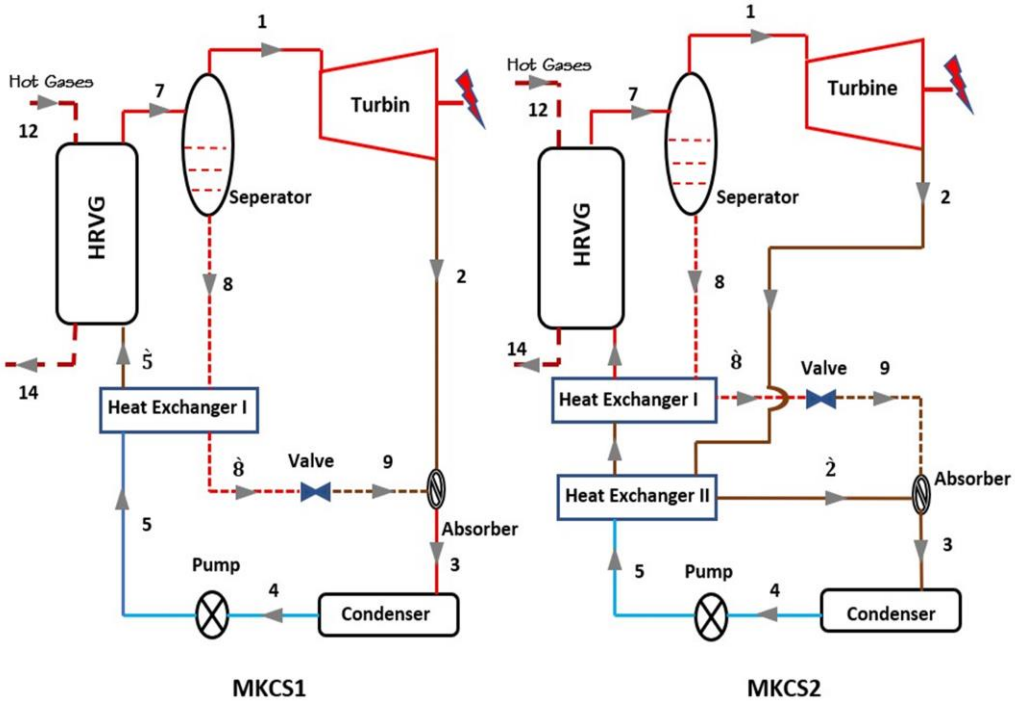


Fig. 9. Two modifications of Kalina cycle system (drawn after [31]).

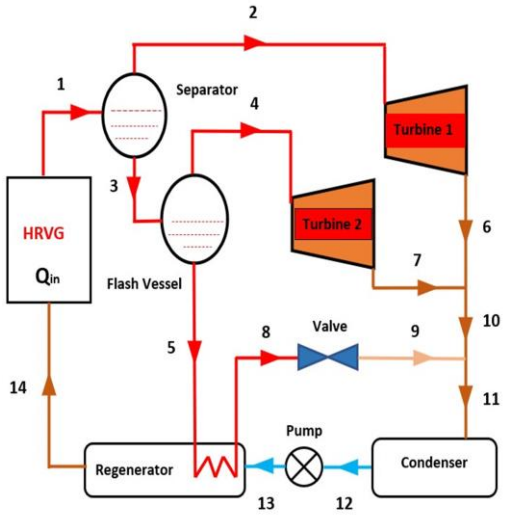


Fig. 10. Kalina flash cycle (drawn after [32]).

The outcomes indicate that the net power in both cycles (KFC and KC) increases as the ammonia concentration (x) decreases from 0.8 to 0.4; however, the higher power output from KC remains lower than that of KFC under the same conditions. He et al. [33] studied two modified versions of Kalina cycle 11 (KCS11) with a replacement for the throttling valve by an expander in the ammonia-weak stream loop of the Kalina cycle: (I-modified cycle) the expander is located between the regenerator and the absorber; (II-modified cycle) the expander is located between the separator and the regenerator. The outcomes indicated the II-modified cycle has a better thermodynamic impact than the I-modified cycle and the KCS 11, and the best performance at an ammonia concentration of approximately 0.875. Li et al. [34] studied an ejector Kalina cycle (EKalina) that uses an ejector instead of a throttle valve and absorber in the Kalina cycle (KCS 11). This adjustment decreases the expander output pressure, leading to an increase in the working pressure difference and, consequently, the cycle's power output. The outcomes indicate that the E Kalina cycle exhibits a higher net power output and thermal efficiency compared to the original Kalina cycle when the ammonia concentration is 0.55 and the source heat temperature is 383 K. Dubey and Sharma [35] worked on a review of several Kalina cycle adjustments, such as using an ejector, a distillation column, a split unit, sliding condensation pressure, double pressure, and composition-adjustable. These modifications have several advantages for Kalina power systems, such as improved power, enhanced performance and lower losses. Table 5 summarises the key findings regarding the contribution of KCS to enhancing the power production application.

Table 5. Contribution of KCS to enhance the power production.

Articles	Type of cycle	η_{th}, %	η_{exe}, %	Remarks
Akimoto et al. [29]	KC KC+AHP KC+AHP+KC	2.2 3 3	8.9 11.5 11.5	KC+AHP+KC achieved greater economic efficiency above a source temperature of 353 K.
Zhang & Li [30]	II-KCS 34 II- KCS 11 II-KCS 34g	11.44 11.14 10.85	56.59 55.4 53.7	Also, at an ammonia concentration exceeding 0.75 and a maximum pressure of 3 MPa, the highest recorded net power was 5.42 kW with KCS34.
Nassir & Shahad [31]	KC MKCS1 MKCS2	8.64 12.7 18.85	34.21 51.92 75.34	Operating at P_{max} = 3500 kPa, P_{min} = 300 kPa and x = 0.85.
Kim et al. [32]	KC KFC	11.4 11.6	41 41.5	The highest net power of KFC for P_{max} = 2.4 MPa and x = 0.40 is approx. 5.05 kW, which is greater than that of KC at P_{max} = 4 MPa and x = 0.8.
He et al. [33]	KCS11 I-modified cycle II-modified cycle	10.23 10.24 10.51	50.61 50.65 52	The highest net power of cycles is approximately 4.83 kW, 4.83 kW and 4.96 kW, respectively, at 3 MPa.
Li et al. [34]	KCS11 Ejector Kalina cycle	8.16 8.36	–	The highest net power of ejector Kalina cycle is approximately 13.11 kW greater than 12.48 kW of KCS11 at the same operating conditions.

4.4. Kalina cycle integrated with traditional cycles

The incorporation of the Kalina cycle with conventional power cycles, such as the Rankine cycle, the Organic Rankine cycle, and other combined cycles, provides significant advantages across a variety of applications. Liu et al. [36] use a combined system that incorporates an absorption chiller with a lithium bromide-water mixture ACH(LiBr-H_2O), utilising the heat rejected by the Kalina cycle (KCS-34) from the ammonia solution before the pump's entrance, which also aids in cooling the ammonia solution. As shown in Fig. 11, the outcomes indicate that the net power output is rising with the suggested cycle and higher ammonia concentrations. Ayou and Eveloy [37] studied a system that combines cold (heat), electricity and liquefied natural gas using a Kalina cycle (KC-CP-LNG), which generates electricity with aqua-ammonia, and an open Rankine cycle that uses LNG heated by waste heat from the KC condenser to turn it into gas. The gas then goes into a turbine that powers a DC chiller cycle to cool the air. The bottom cycle feeds this vapour into the turbine, which operates a DC chiller cycle to cool the air. As shown in Fig. 12, it was found that natural gas provided about 561 kJ of cooling and 151 kJ of output power at a 403 K heat source. Khankari and Karmakar [38] suggested a combined system that includes the main-cycle coal-fired steam power plant according to the Rankine cycle, and the sub-system is the Kalina power cycle (KCS11), which uses an NH_3/H_2O working fluid mixture. The study found that replacing the main cycle condenser with the KC evaporator enhanced the energy and exergy efficiency of the 500 MW independent power plant. Mirjavadi et al. [39] suggested two systems with various bottom cycles. The first cy-

cle utilised the organic Rankine cycle (ORC), while the second cycle employed the Kalina cycle (KC), with a fixed top cycle that used a steam Rankine cycle (SRC) powered by solar energy. The outcomes indicated that KC outperformed ORC as a bottom cycle, and therefore, the overall efficiency of the second system was better than that of the first system. Okten et al. [40] proposed a system to exploit renewable sources stored by connecting a Kalina cycle (KC) to a thermal integral pump for a thermal energy storage (TI-PTES) system; it includes a heat pump circuit, which links both a low-grade heat cycle (LGH) and a high-grade heat cycle (HG). Each circuit relies on water circulating between the hot tank and cold tank to maintain and regulate a consistent heat level in the heat pump circuit. As shown in Fig. 13, the outcomes indicate that increasing the evaporator entrance temperature of the heat pump cycle enhances the exergy efficiency of the system.

A summary of all important results of integrating the Kalina cycle with traditional cycles in this section is given in Table 6.

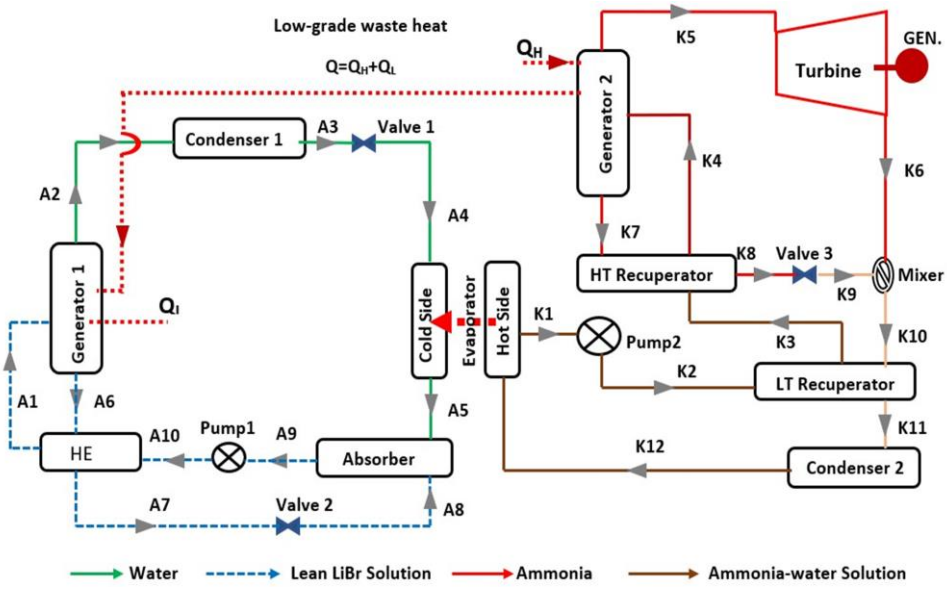


Fig. 11. Coupled LiBr-H_2O absorption chiller/Kalina cycle (drawn after [36]).

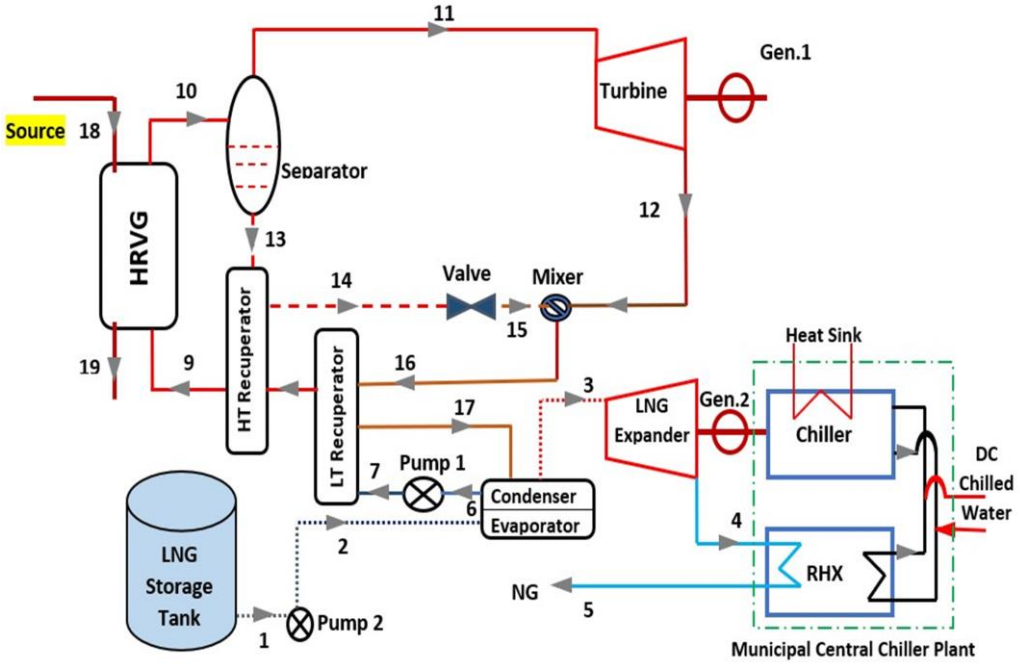


Fig. 12. Polygeneration system based on the Kalina cycle (KC) and aided by liquefied natural gas (LNG) for the production of electricity, vaporisation of LNG and municipal air conditioning (drawn after [37]).

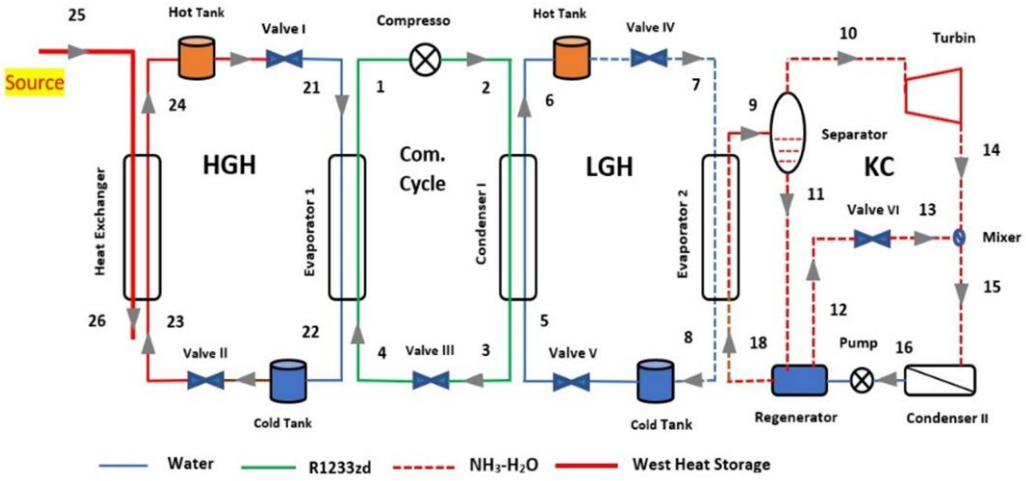


Fig. 13. Kalina cycle with TI-PTES system (drawn after [40]).

Table 6. Kalina cycle integrated with traditional cycles.

Articles	Type of Cycle	η_{th}, %	η_{exe}, %	Remarks
Liu et al. [36]	KC+ACH(LiBr/H_2O)	16.78	-	The gross power output of KC is increased by about 45% with respect to the reference cycle (KCS-34).
Ayou & Eveloy [37]	KC-CP-LNG	33	35	The net power gained yearly is approximately 74 GWh in comparison to the energy consumed by standard air conditioning, power and gas.
Khankari & Karmakar [38]	Coal-fired steam cycle (RC) Combine cycle	39.68 40.5	35.46 36.2	Able to reduce approximately 2.02 tons of CO_2 emissions per hour by generating an additional 5.14 MWe of electricity.
Mirjavadi et al. [39]	RC+ ORC RC+ KC	29.85 31.24	- -	As the ORC energy efficiency was recorded at 9.51%, while KC was approximately 11.3% at a bottom cycle turbine input pressure of 3.5 MPa.
Okten et al. [40]	KC+ TI-PTES	-	48.5	As the hot tank entrance temperature in the LGH cycle increased from 373 K to 393 K, the gross power rose from 650 kW to 750 kW.

5. The working fluid

5.1. Binary fluid properties

Two solutions combine to form the binary fluid system, which possesses the desired properties for successful system operation. The binary mixture system holds the qualities of the two fluids. Below are the pros and cons of the binary solution system [41]:

- **Benefits**
  1. A binary fluid system is possible to run with a low-grade heat source.
  2. The phase change takes place at a wide range of different temperatures.
  3. Any system that uses a binary fluid that is highly adaptable to a heat source to generate the required energy.
- **Drawbacks (defects)**
  1. The system requires additional components, such as separators and mixers, thereby necessitating more space for installation.
  2. It may be challenging to create a homogenous mixture when the components are mostly immiscible.
  3. The variant molecular weight of the members may lead to coalescence and flocculation.
  4. The corrosion or reaction of some binary fluids with the vessel's materials may take place.

5.2. Type of a binary fluid (binary solution) as the working fluid

Several pairs of working fluids have been studied in research and industrial settings. These include NH_3-H_2O, LiBr-H_2O, CH_4O-H_2O, C_2H_6O-H_2O, C_3H_8O-H_2O, and other. Every pair consists of a refrigerant and an absorbent. This binary fluid comes back with more benefits than a single fluid in a cycle by allowing for a closer temperature match between the working fluid and the heat source, which improves energy efficiency and power output, making the Kalina cycle a future technology for several heat source applications [42]. It is important to choose a binary fluid having suitable properties, that is, one that is homogeneous in components and has a good temperature gradient (the difference in temperature between the boiling point and the dew point), which provides the possibility of changing the phase of the fluid with a change in temperature of the heat source, thus changing the ammonia concentration; in other words, for every ammonia concentration there is a certain temperature gradient of the phase change of the binary fluid. The key classified binary solutions below include [43], to name a few:

1. The alcohol group offers good dissolubility in water, and for this reason, the focus is on alcohol-water mixtures. The mix of alcohol with water declines with the increasing number of carbon atoms in it. Until three carbon atoms, it is a good mix in water; with four and five atoms, it is only

partially soluble in water, and greater than 5 atoms do not mix, see Table 7.

2. Binary alcohol-alcohol fluid refers to a mixture of a lower alcohol content (up to three carbon atoms) and a higher alcohol content (more than five carbon atoms).
3. Ammonia-water is a non-azeotropic working fluid.
4. Lithium bromide (LiBr) is a salt whose density is 3464 g/cm^3 that can be soluble in water to form a solution with new thermo-physical properties. Possesses varying makeup with the heating and cooling process, allowing for the best exploitation of lower-grade heat sources. Its good vapour-liquid balance makes the Kalina cycle more thermodynamically efficient, especially when it comes to recovering waste heat and cooling. However, the use of LiBr solutions presents issues with erosion and crystallisation; thus, only certain concentrations in water are used, which are considered non-flammable. Although it is considered non-toxic, it has a potential to cause health problems [44].

Table 7. The alcohol group [43].

Alcohol	Formula	Type	Water dissolubility
Methanol	CH_4O	Low alcohol	Complete
Ethanol	C_2H_6O	Low alcohol	Complete
Propanol	C_3H_8O	Low alcohol	Complete
Butanol	$C_4H_{10}O$	Medium alcohol	Partial
Pentanol	$C_5H_{12}O$	Medium alcohol	Partial
Hexanol	$C_6H_{14}O$	High alcohol	No
Heptanol	$C_7H_{16}O$	High alcohol	No

5.3. Why ammonia-water as the working fluid?

As previously mentioned, the Kalina cycle utilises ammonia-water as a working fluid, making it unique because it includes two distinct ingredients, each having a different boiling and freezing point. Given that a two-ingredient binary fluid allows for ratio changes in different applications and can boil and condense at various temperatures, it is considered unique and consequently leads to improved thermodynamic efficiency. Additional features are listed below [8]:

1. The binary fluid is a new type of working fluid with unique properties.
2. Ammonia's molecular weight (17.03074 gram/mol) is quite similar to that of water (18.0157 gram/mol).
3. This binary fluid has high miscibility.
4. It is characterised by higher heat transfer coefficients.
5. Water containing ammonia does not freeze at 0°C; the freezing point varies with ammonia concentration in the solution.
6. Both are ecologically benign and available in nature.
7. No deposits occur in the binary fluid under the operating condition.
8. The solution has varying boiling point and dew point temperatures.
9. Because of the advantages of the binary fluid, KC recovers a greater amount of waste heat than ORC. However, the volume flow rate of the binary solution is lower in KC.
10. Ammonia is considered less amenable to flame and less hazardous compared to standard working fluids used in ORC, such as toluene, xylene, n-pentane, n-butane, R-11, R-22 and R-248fa, and it is self-alarming due to its odour, but there remains the issue of toxicity.
11. The temperature of a miscible substance can be low.
12. The ammonia has a high latent heat of evaporation.

6. Cycle thermodynamics analysis, assumptions, and *T–s* diagram

The mass, energy, and exergy conservation equations are needed to make the thermodynamic analysis of each part of the original Kalina cycle (KS) presented in Fig. 1. The balance equations for the components that make up the original Kalina cycle, including an HRVG, a separator, a turbine, a throttle valve, a mixer (also called an absorber), a condenser and a pump, can be found in Table 8.

Table 8. Governing equations for each component [45].

Component	Total mass	Ammonia mass	Energy balance	Exergy balance	Power and efficiency
HRVG	$\dot{m}_{exh} = \dot{m}_{fuel} + \dot{m}_{air}$ $\dot{m}_{12} = \dot{m}_{14}$ $\dot{m}_{tot} = \dot{m}_7 = \dot{m}_5$	$x_5 = x_7$	$\dot{Q}_{in} = \dot{m}_{exh} cp_{exh}(T_{12} - T_{14})$ $\dot{Q}_{in} = \dot{m}_{tot}(h_7 - h_5)$	$(\dot{E}_d)_{gen} = (\dot{E}_{12} - \dot{E}_{14})$ $-(\dot{E}_7 - \dot{E}_5)$	
Separator	$\dot{m}_7 = \dot{m}_1 + \dot{m}_8$	$\dot{m}_7 x_7 = \dot{m}_1 x_1 + \dot{m}_8 x_8$	$\dot{m}_7 h_7 = \dot{m}_1 h_1 + \dot{m}_8 h_8$	$(\dot{E}_d)_{sep} = \dot{E}_7 - (\dot{E}_1 + \dot{E}_8)$	
Turbine	$\dot{m}_1 = \dot{m}_2$	$x_1 = x_2$		$(\dot{E}_d)_t = (\dot{E}_1 - \dot{E}_2) - \dot{W}_t$	$\dot{W}_{t_{isent}} = \dot{m}(h_1 - h_2)$ $(\eta_t)_{isent} = \frac{h_1 - h_2}{h_1 - h_2}$
Throttle-valve	$\dot{m}_8 = \dot{m}_9$	$x_8 = x_9$	$h_8 = h_9$	$(\dot{E}_d)_{thr} = \dot{E}_8 - \dot{E}_9$	$\eta_{exe} = \frac{W_{net}}{(\dot{E}_{in} - \dot{E}_{out})}$ $\eta_{th} = \frac{W_{net}}{\dot{Q}_{in}}$
Mixer (absorber)	$\dot{m}_2 + \dot{m}_9 = \dot{m}_3$	$\dot{m}_2 x_2 + \dot{m}_9 x_9 = \dot{m}_3 x_3$	$\dot{m}_2 h_2 + \dot{m}_9 h_9 = \dot{m}_3 h_3$	$(\dot{E}_d)_{abs} = (\dot{E}_2 + \dot{E}_9) - \dot{E}_3$	
Condenser	$\dot{m}_3 = \dot{m}_4$	$x_3 = x_4$	$\dot{Q}_{con} = \dot{m}_3(h_4 - h_3)$	$(\dot{E}_d)_{con} = (\dot{E}_3 - \dot{E}_4)$ $-(\dot{E}_{11} - \dot{E}_{10})$	
Pump	$\dot{m}_4 = \dot{m}_5$	$x_4 = x_5$	$h_5 = h_4 + v_f(P_5 - P_4)$	$(\dot{E}_d)_{pump} = (\dot{E}_5 - \dot{E}_4) - \dot{W}_P$	$W_p = \dot{v}_f(P_5 - P_4)$ $W_p = \dot{m}_5(h_6 - h_5)$ $(\eta_{pump})_{isent} = \frac{h_5 - h_4}{h_5 - h_4}$

Additionally, the mathematical analysis relies on certain assumptions, such as those outlined in [45]:

1. Each component of the system is steady.
2. The pressure and heat losses are ignored.
3. The cycle is an adiabatic process.
4. The strong solution at the turbine entrance represents a dry saturated vapour, DF = 1.
5. A saturated liquid with DF = 0 represents the weak solution at the separator outlet.
6. We ignore the changes in kinetic energy (KE) and potential energy (PE) in the components.
7. Working fluid exits the condenser in a saturated liquid state.
8. Working fluid exits the absorber in a wet vapour state.
9. The throttling process is isenthalpic.
10. The binary mixture is a wet vapour at the separator inlet.
11. The effectiveness of heat recovery vapour generation and the condenser is equal ($\epsilon = 1$).

The *T*–*s* diagram is an important relation for imaging the efficiency and energy distribution of the Kalina cycle. Each point on the figure represents a specific thermodynamic state (temperature, entropy and pressure) of the ammonia-water mixture at a given moment in the cycle. The heat is added and rejected at variable temperatures in the mixed-phase region cycle due to the use of a binary fluid (shown as lines 5–7 and 3–4). As temperature increases in the Kalina cycle, entropy also increases as the fluid absorbs heat and transitions from liquid to wet vapour (lines 5–7). Generally, increased temperatures at the turbine inlet increase the output work (line 1–2).

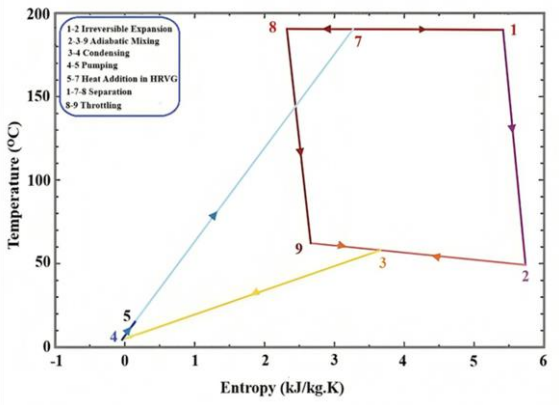


Fig. 14. *T*–*s* diagram for the original Kalina cycle (drawn after [46]).

7. The boiling and freezing points of ammonia-water mixtures

Ammonia solution (NH_3-H_2O) has gained interest as a working fluid in alternative energy cycles and is also being used in the cooling industry. Varying this mixture's thermodynamic properties is crucial to improve the required processes. Their composition and thermodynamic properties affect ammonia solutions' boiling and freezing points. The ammonia and water mixtures show a non-azeotropic manner, meaning their boiling and freezing points vary with different ammonia concentrations. This means that these properties are important for implementations in power and refrigeration production. The pure parts of this mixture are polar substances that are very similar to each other. For example, they have the same molecular structure and mass, even though hydrogen bonding makes them weaker in ammonia than in water [47]. Also, they have considerably different boiling points and critical points. So, at atmospheric pressure (99.75 kPa), the boiling point (*Tb*) of a mixture of ammonia and water with 0.04 NH_3 and 0.96 H_2O is 358.5 K [48]. Kherris et al. [49] examined the thermodynamic properties of ammonia-water mixtures used in absorption refrigeration systems. They did this by using theoretical modelling to look at high wet vapour equilibrium pressures of up to 11000 kPa and temperatures from 230 to 600 K. The results show that boiling points can vary greatly with pressure, with higher pressures leading to higher boiling temperatures. If the ammonia mass fraction is higher, the mixture's freezing point can reach about 197 K, which is closer to the freezing point of pure ammonia. If the ammonia mass fraction is very low, the mixture's freezing point can be closer to that of pure water. Ganesh and Srinivas [50] conducted a study on the ammonia-water binary solution to increase the overall efficiency of the Kalina cycle (KC) and vapour absorptive refrigeration (VAR) system. Evaluating the thermodynamic properties of the binary solution necessitates known mixture concentrations. As a result, the water exhibits favourable characteristics at high temperatures, while the ammonia demonstrates favourable characteristics at low temperatures. Ammonia freezes at a very low temperature, as it has a low freezing point (195.2 K). At a concentration of approximately 25% of ammonia in the binary solution, the freezing point can be as low as –40°C. Friend et al. [51] studied the properties of the ammonia solution, which are crucial as a working fluid in many energy cycles and for cooling applications. Research is limited to the thermodynamic properties of ammonia-rich fluids at pressures of 3500 kPa. It turns out that the boiling point varies with pressure as well. An increased pressure results in higher boiling points, and some studies have indicated that boiling points can reach up to 450 K, which is suitable for geothermal use. The main purpose of the study of Chettiyankandy et al. [52] was to investigate the impact of the ammonia mass fraction on the water's hydrogen bonding structure in the ammonia solution and, consequently, on the boiling and freezing behaviour of the mixture. Changing the ammonia mass fraction from $x_{NH3} = 0.02$ to 0.30, and changing the pressure on the concentrated ammonia solution ($x_{NH3} = 0.30$) from $P = 0.1$ MPa to 8 MPa is done at 293 K. The outcomes show that when the ammonia mass fraction increases, the hydrogen ties in the water increase more than the water-ammonia ties, and the last increase is greater than the ammonia-ammonia hydrogen ties in the solution. Therefore, the transition and diffusion of ammonia molecules is quicker than that of water molecules in the solution. Hence, the boiling and condensing points in ammonia-water are lower than those of water. Tables in the book of Srinivas et al. [53] show different properties of ammonia and water. These tables can be used to figure out a lot of facts, but the most important one is that the boiling and freezing points of the ammonia-water mixture drop as the ammonia concentration goes up. At 15 kPa with a 0.3 dryness fraction, the

boiling points for 0.3 and 0.7 ammonia concentrations are 278.47 K and 242.23 K, respectively. Additionally, at a constant mass and dryness fraction, increasing the pressure raises both the boiling and condensing points. This is evidenced at a 0.5 ammonia concentration and 0.3 dryness fraction, where increasing the pressure from 40 kPa to 100 kPa raises the boiling point from 274.47 K to 294.06 K. Kargel [54], as in much previous published research, used the diagram of the freezing point of aqueous ammonia to illustrate and discuss the solid-liquid phase equilibria in the system H_2O-NH_3 at a pressure of 1 atm (~1 bar), as shown in Fig. 15. The freezing points of pure water and pure ammonia, along with the varying freezing temperatures of their mixture based on ammonia concentration in the binary fluid, thus form the freezing point curve. Within this curve, three distinct eutectic points (three hydrates I, II, and III) are prominent. Understanding these properties is essential for managing the state of the working solution and ensuring fluidity in refrigeration applications.

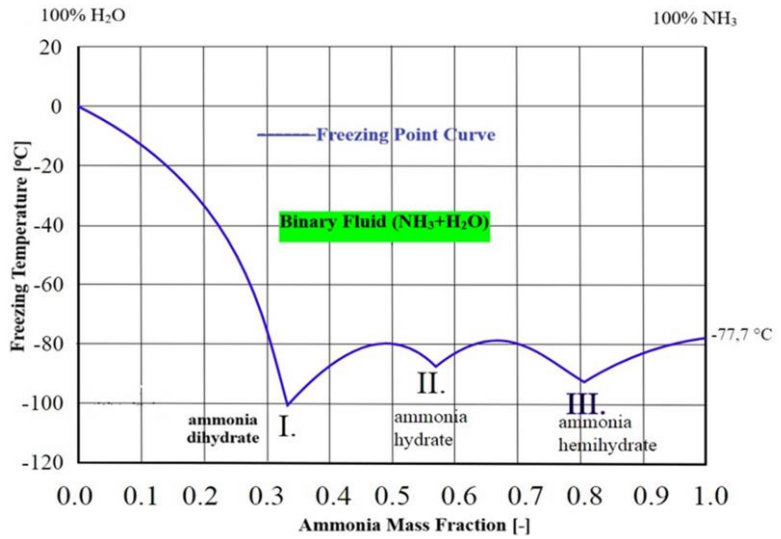


Fig. 15. Freezing points curve (solid-liquid separation curve) for the aqua-ammonia mixture (drawn after [54,55]).

Conde [55] explained the diagram of the freezing point and how the increasing ammonia concentration decreases the freezing point of the aqua-ammonia mixture. The curve shows the freezing points corresponding to the ammonia concentrations within the aqua-ammonia mixture. From zero ammonia concentration to 100%, pure water has a freezing point of 273 K (0°C). As the ammonia concentration increases, the freezing point of the mixture at first becomes lower, as shown in the freezing point curve. When the mixture contains 33.5% ammonia, its freezing point rapidly decreases, reaching 373 K (100°C), as indicated by point (I). When the ammonia concentration exceeds 33.5%, the aqua-ammonium mixture also reaches two low freezing points (II, III); generally, the freezing point remains in the range of 173 K to 199.7 K (−100°C to −73.3°C). When the ammonia concentration is 100%, the freezing point in anhydrous state is 195.4 K (−77.6°C).

8. Corrosion-related aspects in applying the Kalina cycle

This section aims to discuss material selection and protection for Kalina cycle plants. Therefore, the corrosion problem in the Kalina cycle, which utilises an aqueous ammonia (NH_3-H_2O) mixture as a working solution, poses significant challenges in planning, execution and maintenance due to the formation of corrosive species. Zhang et al. [56] explained that the working fluids can accelerate corrosion, leading to material spoilage and failure, especially at high temperatures. Materials like low nickel-iron alloys, hastelloy and alloys with cobalt can motivate this reaction. Due to their characteristics, some of the most endangered parts of the Kalina cycle are the turbine, condenser, heat recovery vapour generation (HRVG) and heat exchanger. Whittaker [57] studied the effect of ammonia-water working fluid on parts of the Kalina cycle to produce geothermal energy in Húsavík, Iceland. The results show that aluminium and mild steel are not good materials for Kalina cycle systems. On the other hand, 316, 304, nitronic 60, duplex and many types of stainless steel, as well as 6Al-4V titanium, do not seem to corrode. Wear of the stainless-steel spacer ring was most likely caused by erosion due to the high speed of the working fluid. Kim et al. [58] looked at how ammonia changed the manner in which a titanium-aluminium-zirconium alloy was worn down, and tested it under pressurised water at 633 K for 20 months. The erosion examination outcomes indicated that adding ammonia accelerated the erosion and hydrogen freedom rates. Murugan and Subbarao [59] mentioned that utilising ammonia-water solution at a temperature higher than 673 K is not favourable since at higher temperatures ammonia becomes unstable and the conversion of ammonia into hydrogen and nitrogen is potential, which leads to nitride erosion. Hannon et al. [60] looked into a project to make a new method for stopping erosion on the carbon steel surfaces of aqua-ammonia absorption heat pumps and chillers that use rare metal salt compounds. These results show that cerium nitrate works better than chromate composites as an erosion inhibitor in high-temperature tests. Chromate composites are harmful to both people and the environment. Thorin

[61] studied a mixture with ammonia at a concentration of 0.8 for 24 hours, which was kept in a reactor at a temperature of about 823 K and a pressure of about 10 MPa. Three experiments exposed the mixture to incoloy 800 and 316 stainless steel materials. The examination revealed no traces of nitrogen or hydrogen. Shan and Nihaj [62] mentioned in a review that the Kalina cycle plant using aqua-ammonia as a working fluid presents different material issues compared to other energy plants. The oxidation of Kalina cycle parts through the power cycle is least likely due to deficient levels of oxygen inside the working fluid. Despite that, nitridation of high-temperature ingredients is a concern to keep in mind when additional heat exchangers, superheaters, reheaters and high-temperature turbine units are involved.

9. Summary of the benefits and drawbacks of the present versions of the Kalina cycle

Systems that utilise a binary solution possess all the advantages and disadvantages of the binary mixture that were mentioned and discussed in a previous section. The primary benefits and drawbacks of this cycle are outlined in Table 9.

Table 9. The main advantages and disadvantages of versions of the Kalina cycle.

Advantages
1. Cogeneration systems provide electricity and cooling at a single site.
2. Cogeneration reduces certain recurring components shared between the two cycles of the system.
3. It can exploit more of the recovery wasted heat to generate cooling without impacting electrical energy production.
4. It simultaneously produces electricity and refrigeration with greater efficiency (absorption cycle).
5. It works better with renewable energy sources, including geothermal, biomass and ray insolation heat.
6. It reduces greenhouse gas emissions compared to conventional cycles.
7. It makes it possible to work with low-temperature sources (373 − 473 K).
8. The Kalina cycle uses a binary working fluid with a regulable concentration ratio to control its freezing point and match it to a low heat source.
Disadvantages
1. More complex than standard cogeneration setups.
2. Power cycle design may be more complex than conventional cycles, leading to higher initial installation costs.
3. It requires skilled management for controls and operational expertise in power and cooling.
4. Requires materials that can withstand ammonia's corrosive effects, which may increase maintenance and replacement costs.
5. Dealing with ammonia presents potential safety hazards because of its toxicity and flammability.

10. Conclusions

1. The original Kalina cycle has a better efficiency than ORC. Also, the modified Kalina cycle has a better efficiency than the original Kalina cycle system under the same operating conditions [2].
2. The cycle to produce power and cooling together has been more efficient than the single power or cooling-only, and in exploiting the waste heat sources or low-temperature sources.
3. When comparing the results, we found that the cogeneration in the Kalina cycle, which produces both power and cooling, has a higher energy efficiency than the Kalina cycle of the power generating system, which drives a separate cooling cycle to produce the same amount of refrigeration. The efficiency of these cycles was found 25.76% and 23.44%, respectively, under the same operating conditions [19].
4. We investigated and discussed several different applications of the Kalina cycle, including its use in solar collection, multi-absorption heat pumps, the Rankine cycle, the organic Rankine cycle, the Brayton cycle, exhaust gases, gasoline engines, geothermal well water, and other systems. The Kalina cycle improves all these applications by adding new power by recovering more waste heat from these systems.
5. As the ammonia mass fraction in a mixture increases, the boiling and freezing points decrease; the following trends have been observed:
   – for the mass fraction (0–10% NH_3), the freezing point is fairly high, about 268 K to 263 K; refrigeration is then considered not effective [51],
   – for the mass fraction (20–30% NH_3), the freezing point declines from 258 K to 253 K, promoting the effectiveness of refrigeration [52],
   – for the mass fraction (50–70% NH_3), the freezing point will decline to 243 K or less, benefiting low-temperature applications [49,50],
   – near pure ammonia (more than 90% NH_3), the freezing point reaches 196 K, indicating a sharp decline that makes it suitable for extreme cooling applications [51].
6. Some materials, like stainless steels (316, 304, nitronic 60, and duplex), carbon steel and 6A1-4V titanium, can be used with aqua-ammonia as the working mixture in the Kalina cycle. Others, such as mild steel, aluminium and copper alloys are unsuitable due to their rust [56−59,62].

References

[1] Deepak, K., Sreeramulu, M., & Durga Prasad, P.V. (2022). Thermodynamic analysis of power and cooling Kalina cycle system. *AIP Conference Proceedings*, 2648(1). AIP Publishing. doi: 10.1063/5.0116475

[2] Kumar, N.P., Wanve, S., Maheshwari, A., & Kumar, M. (2018). Kalina Cycle (waste heat recovery applications) – A Review. *International Journal of Advanced in Management, Technology and Engineering Sciences*, 8(3), 1369−1376.

[3] Esmailzadeh, H., Daghigh, R., & Khayyam, H. (2022). Integrated Kalina cycle in a combined polymer membrane fuel cell and evacuated heat pipe collector for a new power generation system. *Process Safety and Environmental Protection*, 167, 146−161. doi: 10.1016/j.psep.2022.09.013

[4] Zhang, X., Li, Z., Wang, J., Wu, Y., & Ma, C. (2021). Performance Improvement of KCS (Kalina Cycle System) 34 by Replacing Throttle Valve with Single-Screw Expander. *Frontiers in Energy Research*, 9, 741704. doi:10.3389/fenrg.2021.741704

[5] Ahmad, M., & Karimi, M.N. (2016). Thermodynamic analysis of Kalina cycle. *International Journal of Science and Research*, 5(3), 2244−2249. https://www.researchgate.net/publication/300290650 [accessed 10 July 2025].

[6] Amorim, G.S., Sato, A.I., Souza, A.B., & Rodrigues V.M. (2022). Study of a solar energy Kalina cycle applied in Bom Jesus da Lapa-Bahia. *Engenharia Térmica (Thermal Engineering)*, 21(3), 30−36. doi: 10.5380/reterm.v21i3.89667

[7] Cruz, G.E.E.D., & Manuel, M.C.E. (2022). A Literature Review of the Kalina Cycle and Trends. *IOP Conference Series: Earth and Environmental Science*, 1046(1), 012011. IOP Publishing. doi: 10.1088/1755-1315/1046/1/012011

[8] Nassir, A.K., & Shahad, H.A. (2023). Kalina cycle system (a state of the art). *4th International Scientific Conference of Alkafeel University*, 20−21 December, Najaf, Iraq. *AIP Conference Proceedings*, 2977(1). doi: 10.1063/5.0182275

[9] Nassir, A.K., & Shahad, H.A. (2023). Thermodynamic analysis of ammonia mass fraction effect on simple Kalina cycle system performance. *4th International Scientific Conference of Alkafeel University*, 20−21 December, Najaf, Iraq. *AIP Conference* Proceedings, 2977(1). doi: 10.1063/5.0182273

[10] Wang, H., Wang, J., Liu, Z., Chen, H., & Liu, X. (2022). Thermodynamic analysis of a new combined cooling and power system coupled by the Kalina cycle and ammonia–water absorption refrigeration cycle. *Sustainability*, 14(20), 13260. doi: 10.3390/su142013260

[11] Abam, F., Umeh, V., Ekwe, E.B., Effiom, S.O., Egbe, J., Anyandi, A.J., Enyia, J., Ubauike, U.H., & Ndukwu, M.C. (2024). Thermodynamic and environmental performance of a Kalina-based multigeneration cycle with biomass ancillary firing for power, water and hydrogen production. *Future Technology*, 3(1), 40−55. doi: 10.55670/fpll.futech.3.1.5

[12] Seçkin, C. (2023). Energy and exergy analysis of an innovative power/refrigeration cycle: Kalina cycle and ejector refrigeration cycle. *International Journal of Advances in Engineering and Pure Sciences*, 35(2), 193−202. doi: 10.7240/jeps.1203686

[13] Shankar, R., Srinivas, T., Anand, B., Murugavelh, S., & Rivera, W. (2020). Design and analysis of cooling co-generation cycle using aqua-ammonia as working fluid. *Thermal Science and Engineering Progress*, 20, 100744. doi: 10.1016/j.tsep.2020.100744

[14] Karaali, R. (2016). Exergy analysis of a combined power and cooling cycle. *Acta Physica Polonica A*, 130(1), 209−213. doi: 10.12693/APhysPolA.130.209

[15] Abam, F.I., Briggs, T.A., Diemuodeke, O.E., Ekwe, E.B., Ujoatuonu, K.N., Isaac, J., & Ndukwu, M.C. (2020). Thermodynamic and economic analysis of a Kalina system with integrated lithium-bromide-absorption cycle for power and cooling production. *Energy Reports*, 6, 1992−2005. doi: 10.1016/j.egyr.2020.07.021

[16] Kim, K.H. (2019). Thermodynamic analysis of Kalina based power and cooling cogeneration cycle employed once through configuration. *Energies*, 12(8), 1536. doi: 10.3390/en12081536

[17] Zhang, S., Chen, Y., Wu, J., & Zhu, Z. (2018). Thermodynamic analysis on a modified Kalina cycle with parallel cogeneration of power and refrigeration. *Energy Conversion and Management*, 163, 1−12. doi: 10.1016/j.enconman.2018.02.035

[18] Hua, J., Chen, Y., Wang, Y., & Roskilly, A.P. (2014). Thermodynamic analysis of ammonia–water power/chilling cogeneration cycle with low-grade waste heat. *Applied Thermal Engineering*, 64(1−2), 483−490. doi: 10.1016/j.applthermaleng.2013.12.043

[19] Cao, L., Wang, J., Wang, H., Zhao, P., & Dai, Y. (2017). Thermodynamic analysis of a Kalina-based combined cooling and power cycle driven by low-grade heat source. *Applied Thermal Engineering*, 111, 8−19. doi: 10.1016/j.applthermaleng.2016.09.088

[20] Wang, J., Wang, J., Zhao, P., & Dai, Y. (2016). Thermodynamic analysis of a new combined cooling and power system using ammonia–water mixture. *Energy Conversion and Management*, 117, 335−342. doi: 10.1016/j.enconman.2016.03.019

[21] Seçkin, C. (2020). Effect of operational parameters on a novel combined cycle of ejector refrigeration cycle and Kalina cycle. *Journal of Energy Resources Technology*, 142(1), 012001. doi: 10.1115/1.4044220

[22] Seçkin, C. (2019). Performance analysis of a biomass-fired cooling/power combined cycle (Ejector Refrigeration and Kalina cycle). *2019 International Conference on Power Generation Systems and Renewable Energy Technologies* (pp. 1−6), 26-27 August, Istanbul, Turkey. doi: 10.1109/PGSRET.2019.8882691

[23] Zhang, Z., Guo, Z., Chen, Y., Wu, J., & Hua, J. (2015). Power generation and heating performances of integrated system of ammonia–water Kalina–Rankine cycle. *Energy Conversion and Management*, 92, 517−522. doi: 10.1016/j.enconman.2014.12.084

[24] Khanmohammadi, S., Genceli, H., Pakseresht, A., & Bellotti, D. (2024). Optimal design of a solar-driven Kalina system for combined power and desalination purposes. *Solar Energy*, 268, 112277. doi: 10.1016/j.solener.2023.112277

[25] Qu, W., Hong, H., Su, B., Tang, S., & Jin, H. (2018). A concentrating photovoltaic/Kalina cycle coupled with absorption chiller. *Applied Energy*, 224, 481-493. doi: 10.1016/j.apenergy.2018.04.093

[26] Lei, G., Zhou, J., Shi, S., Qi, F., Xu, J., Peng, J., Zhang, J., Liu, D., & Meng, Q. (2021). Simulation and parametric study on a novel modified Kalina cycle. *Turkish Journal of Earth Sciences*, 30(9), 1151−1161. doi: 10.3906/yer-2105-13

[27] Gao, H., & Chen, F. (2018). Thermo-economic analysis of a bottoming Kalina cycle for internal combustion engine exhaust heat recovery. *Energies*, 11(11), 3044. doi: 10.3390/en11113044

[28] Larsen, U., Nguyen, T.V., Knudsen, T., & Haglind, F. (2014). System analysis and optimisation of a Kalina split-cycle for waste heat recovery on large marine diesel engines. *Energy*, 64, 484−494. doi: 10.1016/j.energy.2013.10.069

[29] Akimoto, R., Yamaki, T., Nakaiwa, M., & Matsuda, K. (2021). Evaluation of a power generation system that integrates multiple Kalina cycles and absorption heat pumps. *Case Studies in Thermal Engineering*, 28, 101363. doi: 10.1016/j.csite.2021.101363

[30] Zhang, X., & Li, Z. (2022). Performance of Kalina cycle with single-screw expander for low-temperature geothermal energy utilization. *Applied Thermal Engineering*, 210, 118364. doi: 10.1016/j.applthermaleng.2022.118364

[31] Nassir, A.K., & Shahad, H.A. (2022). Effect of operating conditions on modified Kalina cycle performance. *International Journal of Heat and Technology*, 40(5), 1186−1195. doi: 10.18280/ijht.400509

[32] Kim, K.H., Han, C.H., & Ko, H.J. (2018). Comparative thermodynamic analysis of Kalina and Kalina flash cycles for utilizing low-grade heat sources. *Energies*, 11(12), 3311. doi: 10.3390/en11123311

[33] He, J., Liu, C., Xu, X., Li, Y., Wu, S., & Xu, J. (2014). Performance research on modified KCS (Kalina cycle system) 11 without throttle valve. *Energy*, 64, 389−397. doi: 10.1016/j.energy.2013.10.059

[34] Li, X., Zhang, Q., & Li, X. (2013). A Kalina cycle with ejector. *Energy*, 54, 212−219. doi: 10.1016/j.energy.2013.03.040

[35] Dubey, A.M., & Sharma, M. (2021, July). High-efficiency thermodynamic cycles for Kalina power generation systems: A comprehensive review. *International E-Conference on "Cutting Edges in Mechanical Engineering",* 20th February, Greater Noida, India. *IOP Conference Series: Materials Science and Engineering*, 1168(1), 012030. doi: 10.1088/1757-899X/1168/1/012030

[36] Liu, Z., Xie, N., & Yang, S. (2020). Thermodynamic and parametric analysis of a coupled LiBr/H_2O absorption chiller/Kalina

cycle for cascade utilization of low-grade waste heat. *Energy Conversion and Management*, 205, 112370. doi: 10.1016/j.enconman.2019.112370

[37] Ayou, D.S., & Eveloy, V. (2020). Integration of municipal air-conditioning, power, and gas supplies using an LNG cold exergy-assisted Kalina cycle system. *Energies*, 13(18), 4599. doi: 10.3390/en13184599

[38] Khankari, G., & Karmakar, S. (2018). Improvement of efficiency of coal-fired steam power plant by reducing heat rejection temperature at condenser using Kalina cycle. *International Journal of Engineering, Transactions A: Basics*, 31(10), 1789−1795. doi: 10.5829/ije.2018.31.10a.23

[39] Mirjavadi, K., Pourfayaz, F., Pourmoghadam, P., & Kasaeian, A. (2022). A comparison of using organic Rankine and Kalina cycles as bottom cycles in a solar-powered steam Rankine cycle. *Energy Science and Engineering*, 10(8), 2714−2731. doi: 10.1002/ese3.1161

[40] Ökten, K., Natesan, K., & Biyikoğlu, A. (2022). Thermodynamic analysis of Kalina cycle with TI-PTES system. *Third International Conference on "Emerging Research in Civil, Aeronautical & Mechanical Engineering"*, 16–17 December, Bangalore, India. *AIP Conference Proceedings*, 2615(1). doi: 10.1063/5.0116271

[41] Srinivas, T. (2023). Binary Fluid Properties and Processes. In *Thermal Polygeneration* (pp. 56−90). Cham: Springer Nature Switzerland. doi: 10.1007/978-3-031-37886-7_3

[42] Nassir, A.K., & Shahad, H.A. (2024). Experimental Investigation of a Regenerative Kalina Cycle for Electrical Power Generation Using Waste Heat. *Journal of Petroleum Research and Studies*, 14(4), 154−169. doi: 10.52716/jprs.v14i4.899

[43] Eller, T., Heberle, F., & Brüggemann, D. (2017). Techno-economic analysis of novel working fluid pairs for the Kalina cycle. *Energy Procedia*, 129, 113−120. doi: 10.1016/j.egypro.2017.09.175

[44] Zhu, Y., Yan, M., Liu, Z., Li, S., & Li, W. (2024). Study on Thermophysical Properties of Lithium Bromide-Water (LiBr/H_2O) Solution1 with Property Balanced Regression Equations. *SSRN*, 4707784. doi: 10.2139/ssrn.4707784

[45] Eraiby, M.W., & Mak, D.F. (2025). The Effect of Temperature at Turbine Entrance on the Situation of Working Fluid at the Modified Kalina Cycle Condenser Exit. *International Journal of Heat and Technology*, 43(2), 513–520. doi: 10.18280/ijht.430213

[46] Nassir, A.K., & Shahad, H.A. (2022). Energy and Exergy Performance Analysis of Different Kalina Cycle Configurations. *International Journal of Heat and Technology*, 40(6), 1454–1461. doi: 10.18280/ijht.400613

[47] Ganesh, N.S., & Srinivas, T. (2011). Evaluation of thermodynamic properties of ammonia-water mixture up to 100 bar for power application systems. *Journal of Mechanical Engineering Research*, 3(1), 25−39.

[48] Reiner, R.H., & Zaltash, A. (1993). *Densities and viscosities of ternary ammonia/water fluids*. (No. CONF-931121-9). Oak Ridge National Laboratory, TN (United States).

[49] Kherris, S., Makhlouf, M., Zebbar, D., & Sebbane, O. (2013). Contribution study of the thermodynamics properties of the ammonia-water mixtures. *Thermal Science*, 17(3), 891−902. doi: 10.2298/TSCI110206083K

[50] Ganesh, N.S., & Srinivas, T. (2017). Development of thermophysical properties of aqua ammonia for Kalina cycle system. *International Journal of Materials and Product Technology*, 55(1−3), 113−141. doi: 10.1504/IJMPT.2017.084955

[51] Friend, D.G., Olson, A.L., & Nowarski, A. (1994). Standard thermophysical properties of the ammonia-water binary fluid. In *Physical chemistry of aqueous systems: meeting the needs of industry* (pp. 854–861). Begell House. doi: 10.1615/ICPWS-1994.1070

[52] Chettiyankandy, P., Ghosh, R., & Chowdhuri, S. (2020). Effects of concentration and pressure on the aqueous solvation structure of ammonia and composition dependent ion solvation scenario in water-ammonia mixtures. *Fluid Phase Equilibria*, 511, 112507. doi: 10.1016/j.fluid.2020.112507

[53] Srinivas, T., Ganesh, N.S., & Shankar, R. (2019). *Flexible Kalina Cycle Systems* (1st ed.). Apple Academic Press, New York. doi: 10.1201/9780429487774

[54] Kargel, J.S. (1992). Ammonia-water volcanism on icy satellites: Phase relations at 1 atmosphere. *Icarus*, 100(2), 556−574. doi: 10.1016/0019-1035(92)90118-Q

[55] Conde, M. (2006). *Thermodynamic properties of {NH_3+ H_2O} mixtures for the industrial design of absorption refrigeration equipment*. http://www. mrc-eng. com/ [accessed 10 July 2025].

[56] Zhang, X., He, M., & Zhang, Y. (2012). A review of research on the Kalina cycle. *Renewable and Sustainable Energy Reviews*, 16(7), 5309−5318. doi: 10.1016/j.rser.2012.05.040

[57] Whittaker, P. (2009). *Corrosion in the Kalina cycle: An investigation into corrosion problems at the Kalina cycle geothermal power plant in Húsavík, Iceland*. PhD Thesis, the School for Renewable Energy Science in affiliation with University of Iceland and University of Akureyri. Akureyri, Iceland.

[58] Kim, T.K., Baek, J.H., Choi, B.K., & Jeong, Y.H. (2007). Influence of ammonia on the corrosion behavior of Ti− Al− Zr alloy in 360 °C water. *Metals and Materials International*, 13, 47−52. doi: 10.1007/BF03027822

[59] Murugan, R., & Subbarao, P. (2008). Thermodynamic analysis of Rankine-Kalina combined cycle. *International Journal of Thermodynamics*, 11(3), 133−141.

[60] Hannon, C.L., Gerstmann, J., Mansfeld, F.B., & Sun, Z.N. (2000). Development of Improved Corrosion Inhibitors for Ammonia-Water Absorption Heat Pumps. *ASME International Mechanical Engineering Congress and Exposition*, IMECE2000-1294, 35−46. November 5–10, Orlando, Florida, USA. doi: 10.1115/IMECE2000-1294

[61] Thorin, E. (2000). *Power cycles with ammonia-water mixtures as working fluid. Analysis of Different Applications and the Influence of Thermophysical Properties.* PhD Thesis, Royal Institute of Technology, Department of Chemical Engineering and Technology/Energy Processes, Stockholm, Sweden.

[62] Nihaj Uddin Shan, A.N.M. (2020). A review of Kalina cycle. *International Journal of Smart Energy Technology and Environmental Engineering*, 1(1), 77−107.

Co-published by
Institute of Fluid-Flow Machinery
Polish Academy of Sciences
Committee on Thermodynamics and Combustion
Polish Academy of Sciences

Copyright©2026 by the Authors under licence CC BY-NC-ND 4.0

http://www.imp.gda.pl/archives-of-thermodynamics/

Parametric Analysis of Heat Transfer and Flow Characteristics of the Cross-Flow Heat Exchanger with a Backwards Splitter Plate Using the Computational Fluid Dynamics (CFD) Model

Sachin Kaushik[a], Subash Chandra Ram[b*], Chandra Kishor[a], Sunii Chamoli[c]

[a]Department of Mechanical Engineering, Graphic Era University, Dehradun 248002, Uttarakhand, India
[b]Department of Mechanical Engineering, Tula's Institute, Dehradun 248011, Uttarakhand, India
[c]Department of Mechanical Engineering, GBPIET, Pauri, Garhwal 246194, Uttarakhand, India
*Corresponding author email: subh.mtech07@yahoo.com

Received: 08.07.2025; revised: 26.01.2026; accepted: 30.01.2026

Abstract

This article investigates the parametric effects on heat transfer in cross-flow heat exchangers integrated with a backward splitter plate to enhance the coefficient of performance in a solar assisted vapour absorption refrigeration system. The system replaces conventional electric energy with solar energy, utilising a solar energy collector to heat water between 50 − 80°C. This heated water vaporises aqueous ammonia in a generator designed as a double pipe heat exchanger. The primary objective is to facilitate efficient heat transfer from the solar energy collector to the solar assisted vapour absorption refrigeration system and evaluate the cooling performance at varying water mass flow rates. Computational fluid dynamics has been used to solve the governing equations under appropriate boundary conditions. While second-order discretisation has been used for momentum and energy equations, coupled equations have been used to address velocity and pressure coupling. Convergence criteria of 10^{-6} for velocity and continuity, and 10^{-8} for energy, were employed. Thermal modelling was conducted to find out component-specific heat transfer rates and estimate the cumulative coefficient of performance. A small-capacity (1.5 ton or 5.25 kW) solar vapour absorption cooling system was tested. The study found that increasing the L/D ratio enhances heat transfer; for instance, at Re = 12000 and L/D = 2, the Nusselt number increased by 90% compared to Re = 2000. However, the pressure dropped significantly at L/D = 3, suggesting an optimal design trade-off. Additionally, the impact of key parameters such as absorber, condenser, generator and evaporator temperatures on the system's coefficient of performance was thoroughly analysed.

Keywords: Parametric analysis; Cross flow heat exchanger; Heat transfer; Back splitter plate

Vol. 47(2026), No. 1, 161–176; doi: 10.24425/ather.2026.158667

Cite this manuscript as: Kaushik, S., Ram, S.C., Kishor, C., & Chamoli, S. (2026). Parametric Analysis of Heat Transfer and Flow Characteristics of the Cross-Flow Heat Exchanger with a Backwards Splitter Plate Using the Computational Fluid Dynamics (CFD) Model. *Archives of Thermodynamics*, 47(1), 161−176.

1. Introduction

The application of the solar vapour absorption technique remains the most feasible choice, given the rapidly changing global energy landscape and the increasing focus on environmental preservation and energy conservation. Solar vapour absorption cooling is a solution to the growing expense of electricity, the worsening power situation, and the increasing emissions of chlorofluorocarbons (CFCs) pollutants. Non-traditional energy sources, including hydropower, geothermal, wind and solar are crucial for mitigating biodiversity loss for a broad spectrum of reasons. When operating, unconventional energy sources emit little or no greenhouse gases (GHGs). The practical application of solar energy has grown significantly over the past few years among unconventional energy sources. In areas that have consistently high levels of sunshine throughout the year, solar

Nomenclature

h – enthalpy, kJ/kg
L/D – length of splitter plate to diameter of tube ratio
$L\times W\times H$– length × width × height (geometrical dimensions)
$\dot{m}$ – mass flow rate, kg/s
Nu – Nusselt number
P – pressure
Pr – Prandtl number
Q_a – total heat transfer rate, kW
Q_{HX} – heat exchanger heat transfer rate, kW
Re – Reynolds number
SD/D – diagonal spacing
SL/D – longitudinal spacing
ST/D – transverse spacing
T – temperature, K
$T_{a,o}$ – outlet air temperature
$T_{a,i}$ – inlet air temperature

Greek symbols

α – inclination angle of splitter plate, °
λ – circulation ratio
ξ – concentration

Abbreviations and Acronyms

CFCs– chlorofluorocarbons
CFD – computational fluid dynamics
CHPC– combined heat, power and cooling
COP – coefficient of performance
GHGs– greenhouse gases
H_2O – water
LHTES– latent heat thermal energy storage
LiBr – lithium bromide
SAVAR– solar assisted vapour absorption refrigeration
SEC – solar energy collector

energy has become a necessity and a daily need. Solar energy consumption is particularly important in these places due to the regularity and amount of sunlight [1−5].

A type of cooling agent is used in the vapour absorption cycle to both absorb and release heat during the condensation and evaporation processes. This process often requires heat, which can be obtained from a variety of fuels or eco-friendly sources like solar energy. A solar-powered vapour absorption refrigeration unit employs solar thermal collectors to provide the heat required to power the absorption cycle, making it more environmentally friendly and energy-efficient than conventional electrically-driven refrigeration systems. Fan et al. [6] claim that an absorption cycle is comparable to a vapour compression cycle, and is predicated on the evaporation or absorption effects that occur when a substance's liquid and gaseous phases interact, each of which has a different vapour pressure. Heat loss to the surroundings is a serious issue with the hot water storage tank. The actual heat loss coefficient, as reported by Jacobsen [7], was 1.65 W/(m^2·K), over 50% higher than the expected value of 1.19 W/(m^2·K). Sometimes, the heat loss through the boiling water storage tank is equivalent to two hours of daily operation of the solar air conditioner. Developing the construction of the lithium bromide solution (LiBr-H_2O) absorption refrigerator with a nominal capacity of 1 kW was considered by Kalogiro and Florides [8]. Absorption refrigerators are machines without moving parts that generate cooling through the use of heat energy.

One of the earliest innovations of the refrigeration system, which is now the most important use of solar energy for cooling, was the vapour absorption cycle. Furthermore, researchers are becoming increasingly interested in the ongoing development of absorption refrigeration systems due to the need for high-grade energy to operate mechanical vapour compression refrigeration systems. Experiments with high LiBr concentrations, extremely close to the solution's crystallisation limit, have been carried out by Charters and Chen [9]. It was observed that crystals would form and the system would "shut down" if the generator's temperature dropped suddenly. It was proposed that to solve this issue; the LiBr-H_2O solution must contain certain salts (such as LiSCN) in order to reduce the solution's vapour pressure and enhance the solution's properties for usage in an air-cooled system. The absorption refrigeration system is more appealing to researchers because it can generate a cooling effect using low-grade energy. Systems based on vapour compression are currently the most widely used air conditioning and refrigeration systems. Because of their proven technology, dependability and affordability, these systems are frequently used. However, in order to function, these systems need high-grade energy, either electrical or mechanical. In addition, scientists have been compelled to explore alternative cooling systems as it was recently discovered that the traditional working fluids of vapour compression systems are contributing to ozone layer depletion and greenhouse effects. The absorption system, which operates mostly on thermal energy, is the obvious substitute. Additionally, these systems operating fluids are environmentally improved.

Choosing the right working fluid is arguably the most crucial component of any refrigeration system. The cycle efficiency and performance characteristics of the absorption refrigeration system are determined by the properties of the absorbent, refrigerant and their combinations. Additionally, absorbent and refrigerant vapour pressure, solvent solubility, solution heat capacity, heat of vaporisation, heat of solution and solution viscosity all affect cycle efficiency. The two most important thermo-physical properties of the solution are its surface tension and thermal conductivity. In addition, toxicity, chemical stability and corrosivity are further selection factors for the working fluids. The energy efficiency of systems like cogeneration or combined heat, power and cooling (CHPC) is increased with the use of absorption chillers. Because absorption chillers have nearly zero running costs when waste heat energy is the source, they are widely used in industries such as textiles, synthetic fibre, chemicals, pharmaceuticals, electronics, beverage cooling, brewing, tobacco and more.

Using the first as well as the second laws of thermodynamics, Mansoori and Patel [10] have established upper and lower constraints for the coefficient of performance (COP) of absorbent cooling cycles. It is shown that these upper and lower limitations are dependent not only on the ambient temperatures of

the cycle's component sections but also on the thermodynamic properties of refrigerants, absorbents and their mixtures. A quantitative comparison of various refrigerant-absorbent combinations can be conducted using these upper and lower bounds of COP. The H_2O-NH_3, NH_3-NaSCN and LiBr-H_2O combinations, all of which are viable choices for solar absorption cooling cycles, are compared using the developed approach. Vapour absorption refrigeration/cooling systems belong to the same class of vapour cycles as vapour compression refrigeration systems. However, absorption systems require heat as an input, in contrast to vapour compression refrigeration systems. As a result, these systems are often known as thermal energy-driven or heat-operated systems. Both vapour compression and absorption refrigeration cycles remove heat by allowing a refrigerant to evaporate at low pressure and reject heat by allowing the refrigerant to condense at a higher pressure. The main difference is that a vapour compression technology uses a mechanical compressor, whereas an absorption method uses a heat source to create the pressure differences needed to circulate the refrigerant. Because of these distinctions, an absorption system needs little to no work input, but heat must be supplied as energy. The system becomes more attractive when there is a low-cost heat source, such as solar heat or waste heat from power or heat generation.

Zhang et al. [11] conducted a comprehensive review of previous studies on the use of heat transfer enhancement strategies in plate heat exchangers, with a focus on passive surface methods and the use of nanofluids. The study showed that the thermal-hydraulic capabilities of the investigations employing different parameters of geometry and augmentation procedures are frequently higher for relatively small Reynolds numbers. Similarly, Awad and Muzychka [12] analysed and investigated the thermal-hydrodynamic characteristics of air-cooled tiny wavy fin heat exchangers. They released new models that facilitate the prediction of the Fanning and Colburn friction factors. To enhance the system's functionality, since energy losses are the cause of system performance decline, the irreversible nature should be assessed during the cycle. The COP is commonly used to assess a vapour compression system's effectiveness.

COP does not reveal the system component elements' thermodynamic equilibrium deterioration. The losses of energy in vapour compression refrigeration systems can be measured with the use of exergy evaluation. As the temperature differential between the system and its surroundings increases, so do the energy losses [13]. Ghamati et al. [14] investigated the flow patterns and energy transmission of natural convection using nanofluid technology in enclosed areas that are square, circular and hexagonal in shape. The study's findings demonstrated that the final equations were validated through prior research and solved numerically. For a variable that stays constant in the temperature index (n), the results showed that increasing the Prandtl number (Pr) from about 0.1 to 2 reduces the skin friction coefficient by approximately 32% and the velocity at its maximum by slightly more than a half. Because the temperature that is dimensionless drops to zero faster in this case, the thermal boundary layer thickness falls, and the Nusselt number (Nu) rises. The effective COP for heat exchangers with a finned backward splitter plate was shown to be lower for solar-assisted vapour absorption refrigeration (SAVAR) systems, which is an intriguing area of scientific study.

Beyond the general literature, several focused studies have explored performance improvements in LiBr–water absorption cooling systems. One such study examined the use of a plate heat exchanger as a pre-cooler for the absorber, showing that this setup could reduce absorber size by 6–14%. Notably, channelling just 20% of the total cooling water flow through the pre-cooler was enough to yield significant efficiency gains [15]. Another study developed a simulation model of a solar-powered LiBr–water absorption system with auxiliary heating, analysing the effects of changes in the atmospheric clearness index. A decrease in the index from 0.63 to 0.52 resulted in a 67% increase in the auxiliary heat requirement to maintain consistent cooling performance [16]. In recent years, both experimental and theoretical work has advanced in the field of solar-assisted absorption and adsorption refrigeration (AR) systems. For example, Sumathy and Li [17] experimentally investigated a solar-driven adsorption system using an activated carbon–methanol pair. Their setup, which utilised a flat plate solar collector with an exposed surface area of 0.92 m^2, achieved a COP between 0.10 and 0.12. Similarly, Pons and Guilleminot [18] conducted experiments on a solar-powered adsorption chiller using the same activated carbon–methanol working pair, achieving a COP of approximately 0.12. Dawoud [19] developed a hybrid solar-assisted adsorption cooling system tailored for vaccine storage applications. In another study, Ghali et al. [20] evaluated the hourly performance of a hybrid cooling system incorporating a desiccant wheel for air conditioning in a typical auditorium. Their work included a comparative analysis with conventional air conditioning systems under the climatic conditions of Beirut. The system included a 1.5 m^3 thermal storage tank, a vacuum flat-plate solar collector with a total aperture area of approximately 42.2 m^2 and a 25 kW plate heat exchanger. Additionally, Abu Ein et al. [21] conducted a thermodynamic assessment of a 10 kW solar-powered ammonia–water absorption chiller, utilising both first and second law analyses to evaluate its performance. Further research has also explored the integration of thermal energy storage in LiBr-H_2O absorption systems to mitigate mismatches between thermal energy supply and cooling demand. Various system configurations have been investigated, focusing on performance metrics such as COP and energy storage density (ESD). Important findings showed that under ideal circumstances, ESD values ranged from roughly 119.6 kWh/m^3 to 444.3 MJ/m^3, and COP values ranged from 0.69 to 0.99 [22]. Low-temperature-driven LiBr–water absorption heat pumps have also been developed with innovative modular designs, namely, "Bee", "Bumblebee" and "Hornet". Operating at driving water temperatures around 90°C, these systems achieved thermal COPs of approximately 0.8 while maintaining a compact form factor. Several commercial models have been deployed in pilot-scale solar cooling applications [23]. In a separate study, a compact cross-flow heat exchanger was assessed as an air heater in a solar tunnel dryer. The device enabled heat transfer between ambient air and hot water supplied by a parabolic trough collector. Findings showed that increasing the air mass

flow rate improved the heat transfer rate but simultaneously decreased the overall effectiveness of the heat exchanger [24]. Additional research explored the impact of solar radiation on the thermal performance of a cross-flow wet cooling tower under hot climate conditions. It was observed that the use of a sunshade led to significant performance improvements, with outlet water temperature, temperature range and thermal efficiency increasing by up to 37% [25]. This study has explored the impact of incorporating a backward splitter plate within a cross-flow heat exchanger on heat transfer characteristics and the overall enhancement of the COP in a SAVAR system. In this configuration, conventional electrical energy has been substituted with solar energy via a solar energy collector (SEC), which heats water within the range of 50 – 80°C. The resulting thermal energy is used to vaporise aqueous ammonia in a double-pipe heat exchanger serving as the generator. The primary aim is to optimise heat transfer and assess the cooling performance of the system across varying water mass flow rates. Additionally, the study presents a comparative evaluation of three refrigerant-absorbent pairs: H_2O-NH_3, NH_3-NaSCN and LiBr-H_2O to determine their suitability for use in solar absorption cooling systems. Unlike conventional vapour compression systems, which depend on mechanical energy input, absorption systems are driven by thermal energy, making them particularly suitable for integration with low-cost energy sources such as solar or industrial waste heat.

Although prior research has examined solar-assisted absorption systems, several critical gaps remain. Notably, the influence of geometric modifications such as the addition of a backward splitter plate on internal flow distribution and thermal performance within heat exchangers has not been comprehensively addressed. Furthermore, the system's performance under dynamic solar radiation conditions and its long-term efficiency across seasonal variations are under-investigated. Finally, while refrigerant absorbent combinations are often assessed based on thermal performance, there is a lack of multi-objective optimisation studies that consider economic feasibility, environmental impact and operational reliability factors essential for the widespread practical adoption of these systems. The system's thermodynamic analysis was carried out to determine which components were subject to heat transfer. The system performance was then calculated, and COP was enhanced. The present experimental research has used a solar energy vapour absorption cooling system with a small capacity (1.5 ton or 5.25 kW). Additionally, the impact of variables affecting the system COP, such as the temperature of the condenser, generator, absorber and evaporator, was examined.

These heat exchangers can be designed and analysed through numerical analysis, experimentation or the use of computational fluid dynamics (CFD) software. The science of CFD uses digital computers to generate quantitative forecasts of fluid-flow phenomena based on the mass, momentum and energy conservation laws that govern fluid motion. The majority of CFD software tools, which were created to aid in the rapid resolution of heat exchangers, can forecast heat distributions and boost flow system efficiency. CFD methods have been used in a number of studies on cross-flow heat exchanger performance. Computational fluid dynamics simulation can also be used to improve the performance of an existing heat exchanger even when it has heat pipes. The CFD simulation was used to examine how altering the pipe diameter and the angle between the pipes could improve performance, which was then applied to the heat exchanger under study. This method's high adaptability and reduced simulation time make it a viable option for other heat exchanger designs that incorporate heat pipes [26,27].

It has been demonstrated that using splitters to manage the separated wake downstream of the pin-fins is beneficial [28]. Ul-Islam et al. [29] investigated the effects of the length of dual splitter plates positioned at the front and rear sides of two adjacent square cylinders on flow characteristics and fluid force reduction. It was found that the splitter plate placed behind the cam-shaped cylinder functions as an appropriate passive control mechanism to successfully limit vortex shedding and lower drag. This device can be used to minimise drag in bluff bodies and cam-shaped cylinders [30]. Tu et al. [31] predicated on the impact of the centre cylinder in a five-cylinder array, which has been illustrated by altering the spacing ratio. Elmekawy et al. [32] investigated on cross-flow staggered tube banks of cylinders with splitter plates attached to the tubes. Their study demonstrated an improvement in thermal performance by providing a more streamlined flow through the splitter plates in the downstream section of the tubes. This design reduces the interactions and intensities of vortices and eddies, as well as energy losses. However, a 16–20% rise in pressure drop was reported [32].

Hishikar et al. [33] investigated that the multi-cylinder arrangement enhances the rate of heat transfer by allowing for vortex shedding and turbulence to occur in the spaces between the cylinders. Another research was on creating a computational fluid dynamics model to describe the heat transfer in a boosted diesel engine cross-flow plate heat exchanger [34]. Pressure distributions, vorticity and pathline structures were used to comprehend the phenomena of heat transfer and flow, while an analysis of drag, lift and the Nusselt number was conducted. Heat transfer by two distinct clusters of nine circular cylinders was analysed using two-dimensional unsteady calculations. The cylinders were exposed to a cross-flow of air in ambient conditions while being kept at constant-heat-flux wall conditions [35]. Heat exchangers, nuclear reactors and electronic circuit boards are just a few examples of engineering devices that display flow separation and reattachment. These device components, which resemble stepped channel designs, are designed to lessen the effects of thermal stress. Another research was reported on the properties of heat transfer and fluid flow using a double backwards-facing step with elliptic obstacles placed after each step. An internal code based on the streamline upwind/Petrov-Galerkin finite element method is used to solve the equations governing fluid flow and heat transfer in a Cartesian framework for this purpose [36].

The performance of heat transfer and the flow structure of a swirling jet on a flat target surface are the main topics of the study. The analysis is performed by varying the number of vanes with Reynolds numbers between 11 200 and 35 600, using helicoid inserts with the swirl number S = 1.3. The performance of swirling and circular jets in terms of heat transfer is compared. According to the heat transfer results, the triple helicoids' axial

recirculation zone at Re = 29 800 and Re = 35 600 has an impact on the uniformity of heat transfer distribution [37]. The flow regime transitions around two adjacent square cylinders under the influence of attached upstream splitters were analysed computationally. The lattice Boltzmann method is employed as a numerical technique for this work. The effect of two influencing factors, the splitters' length (SL) and the cylinder spacing ratio (SR), is highlighted. At a fixed Reynolds number of 150, both parameters are varied between 1 and 4 times the characteristic length (d). In contrast to the situation of two side-by-side cylinders without splitters, the results show an early transition to a synchronised flow regime because of splitters [38].

This study introduces the novel incorporation of a splitter plate within the flow domain of the generator or absorber in a SAVAR system. The geometric modification strategically alters fluid flow patterns, enhancing heat and mass transfer processes critical to the absorption cycle. The presence of the splitter plate promotes more uniform flow distribution and suppresses thermal stratification. This leads to improved heat exchange efficiency between the working fluid and the heat source (solar energy), optimising the energy input required for desorption in the generator. Comparative simulations and experiments demonstrate that the inclusion of the splitter plate results in a noticeable increase in COP of the SAVAR system. This improvement is attributed to better thermal energy utilisation and reduced irreversibilities in the absorption-desorption cycle. Unlike conventional enhancement techniques that require additional mechanical or control systems, the splitter plate serves as a passive method to control flow dynamics, offering a cost-effective and energy-efficient design enhancement. By boosting the performance of solar-assisted vapour absorption systems, this work contributes toward more sustainable and energy-efficient refrigeration technologies, aligning with the global goals of reducing reliance on fossil fuels and minimising environmental impact.

2. Experimental procedure

In this study, CFD simulations and the renormalisation group (RNG) k–ε turbulence model have been employed. This model was chosen due to its enhanced accuracy and reliability in capturing the effects of turbulence in recirculating and swirling flows, which are common in heat exchanger and thermal system applications, particularly in SAVAR systems. The renormalisation group (RNG) k–ε model offers several advantages over the standard k–ε model:

- It incorporates an additional term in the ε equation to account for the interaction between turbulence dissipation and mean shear, which improves performance in rapidly strained and curved flows.
- It provides better predictions for low Reynolds number and near-wall flows compared to the standard model.
- It is computationally more efficient than more complex models like k–ω SST, making it suitable for simulations involving large domains or long transient runs.

2.1. Design of the solar assisted vapour absorption refrigeration system

The general design process involves determining crucial factors such as the component's diameter, length, heat transfer area, and transfer coefficients. When determining a component's performance, the design phase seems to be the most crucial phase before the measurement of experimental data and applications.

Every component must be planned before it is fabricated, and the accuracy and precision of the design determine how well the component will function in real life. The primary goal of the design created for this study was to understand the specifics of each component, as seen in Fig. 1.

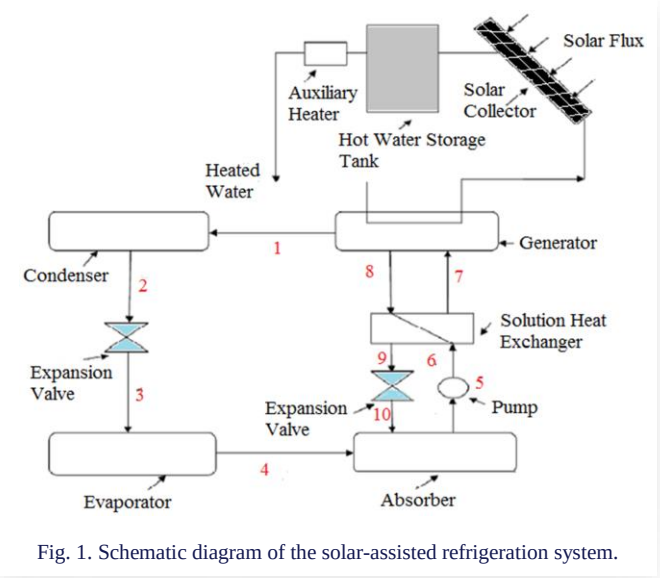


Fig. 1. Schematic diagram of the solar-assisted refrigeration system.

First, the collector collected the solar energy, which was then stored in the storage tank. The generator then boils water vapour using a solution of lithium bromide and water, using the hot water within the storage tank. The condenser cools the water vapour, which then moves to the evaporator, where it evaporates again at low pressure to cool the required area. Once the strong liquid evacuates the generator and flows to the absorber, a heat exchanger warms the weaker solution coming into the generator. The absorber absorbs the water vapour exiting the evaporators into the strong solution. The ventilated tower's cold water mixes and condenses to remove heat. When solar energy is insufficient to heat the water to the temperature required by the generator, an additional energy source supplies the hot water.

2.2. Thermodynamic analysis of the system

To perform the thermodynamic analysis of the system, key parameters such as enthalpy, mass and heat transfer rates are required to determine the system's coefficient of performance (COP). Initially, a set of thermodynamic mathematical models is developed based on mass flow rates and enthalpy, using energy and mass balance equations for each component. To determine the system's COP, operating conditions such as temperatures, pressures and enthalpies are input into the mathematical models. The thermodynamic analysis of the system is based on the following assumptions:

i. Constant flow and stable state,
ii. No friction-related pressure drops,
iii. In the generator, only pure refrigerant boils.

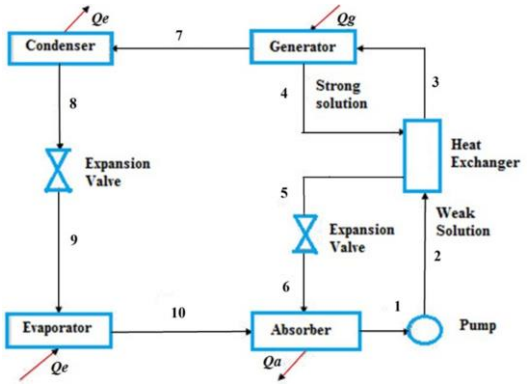


Fig. 2. Block diagram of the absorption vapour refrigeration system.

2.3. Cross-flow heat exchangers with integration of backward splitter plate

We created the geometry using ANSYS Design Modeler and adjusted the mesh to ensure high resolution in flow areas such as the tube surfaces and splitter plate edges. Splitter plate length-to-diameter ratios (L/D) of 0, 0.5, 2 and 3 were taken into consideration in this investigation. Furthermore, the splitter plates have been examined with clockwise rotational inclinations of 15° and 30°, see Table 1. As shown in Fig. 3, the rectangular channel under consideration in this study has dimensions of $L \times W \times H$ of 600 mm, 150 mm and 150 mm, respectively. The cylinder diameter of 25 mm is taken for the study.

Table 1. Range of parameters of the present research work.

Parameter	Parameter details
Length of splitter plate to diameter of tube (L/D) ratio	0.5, 1, 2, 3
Inclination of the splitter plate	+30°, +15°, 0, -30°, -15°
Reynolds number (Re)	2000 – 12 000

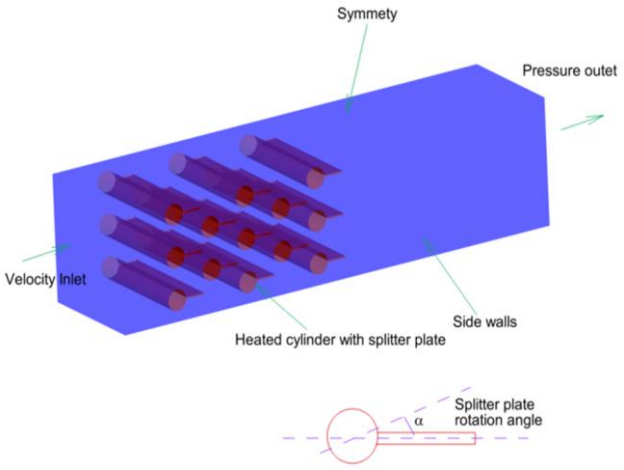


Fig. 3. Computational domain of the present study.

The computational model is depicted in Fig.3. The splitter plate is considered at different inclination angles. The air is considered with a velocity inlet boundary condition and an outlet with a pressure outlet. The cylinder with a splitter is heated with a constant temperature of 350 K. The top and bottom walls are considered symmetry boundary conditions, and the side walls are given adiabatic boundary conditions.

ANSYS Fluent, which depends on the finite volume approach, solves the governing equations by applying the proper boundary conditions. The coupled algorithm resolves the velocity and pressure coupling. The momentum and energy equations are discretised using a second-order upwind approach. While the velocity and continuous residuals must satisfy the convergence requirement of 10^{-6}, the energy residual has to overcome the barrier of 10^{-8}. The mesh that is used for the computational domain, shown in Fig. 4, is created using fluid meshing. The analysis that is currently available uses a tetrahedral mesh with hex core volume meshing.

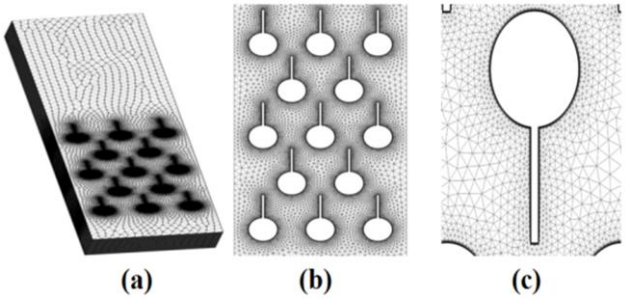


Fig. 4. Mesh at L/D = 2 and α = 15°: (a) computational domain, (b) side view of mesh domain, and (c) enlarged view of meshing of cylinder with splitter plate.

2.3.1. Heat exchanger modelling approach

The heat exchanger was modelled using a 2D steady-state CFD framework to capture flow and temperature distribution within the fluid channels. The governing equations for mass, momentum and energy conservation were solved using the finite volume method. Turbulence effects were captured using the RNG k–ε model, which provides a good balance between accuracy and computational efficiency for internal flows.

2.3.2. Role of the backwards splitter plate

The backward splitter plate was introduced in the design to enhance thermal performance by inducing flow separation and promoting secondary vortices downstream. This geometry forces the fluid to reattach further along the channel, thereby increasing the thermal boundary layer disruption and enhancing convective heat transfer. The position and length of the splitter plate were optimised to avoid excessive pressure drop while maximising thermal enhancement. The backward orientation specifically delays the flow reattachment point and increases residence time in the high-shear region.

2.3.3. Comparison with established correlations

To validate the CFD results, the Nusselt number (Nu) and friction factor (f) obtained from simulations were compared to standard empirical correlations for laminar and turbulent flow in ducts with and without flow disturbances:

- for a smooth channel, the Dittus-Boelter correlation was used for turbulent flow:

$$Nu=0.023Re^{0.8}\,Pr^{0.4},$$

- for laminar flow, the Sieder-Tate correlation was referenced:

$$Nu=1.86(Re\cdot Pr\cdot d\,L)^{1/3}.$$

2.3.4. Computational details, geometry parameters, and mesh independence

The thermal performance and pressure fluctuations in a cross-flow heat exchanger with a grid like circular tube configuration are numerically analysed in this work. To improve heat transfer and control wake dynamics, each tube has a trailing-edge splitter plate. A rectangular duct with 13 circular tubes arranged in a staggered configuration makes up the computing domain (Fig. 5). The industrial applications and design parameters were chosen from the available database for system's heat and mass transfer evaluation. Important characteristics include a 16.4 mm tube diameter, 34.3 mm longitudinal spacing ($SL/D \approx 2.09$), 31.3 mm transverse spacing ($ST/D \approx 1.91$) and 37.7 mm diagonal spacing ($SD/D \approx 2.30$). The ducts 95.4 mm height allow for the accommodation of three rows of tubes across the transverse plane. The overall duct dimensions (190.8 mm in length and width) result in a 2:1 aspect ratio, which ensures controlled flow conditions while maintaining computational efficiency. A rectangular splitter plate that is parallel to the flow direction and has dimensions equal to the tube diameter (16.4 mm) and thickness of 1.75 mm is fastened to the trailing edge of each tube.

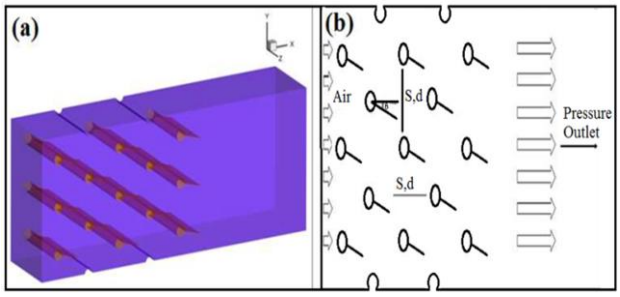


Fig. 5. Schematic view of the computational domain at $L/D = 2$ and $\alpha = 15^{o}$ used in the present study: (a) 3D view, (b) 2D view.

In order to observe wake behaviour and pressure recovery, the computational domain extends 14 tube diameters (229.6 mm) downstream from the first row and two tube diameters (32.8 mm) upstream for appropriate flow development. Four split-tube structures that enforce periodic flow conditions are included in the lateral boundaries to simulate an endless tube bank layout. ANSYS Design Modeler was used to design the geometry, and fine-tuning the meshing ensured good resolution at crucial flow areas like splitter plate edges and tube surfaces. Splitter plate length-to-diameter ratios (L/D) of 0, 0.5, 2 and 3 were taken into consideration in this investigation. Furthermore, the splitter plates have been examined with clockwise rotational inclinations of 15º and 30º. These differences enable a thorough analysis of how splitter plate sizes and orientations affect pressure loss, heat transfer effectiveness and wake dynamics. ANSYS Fluent Meshing was used to perform the meshing process using an unstructured poly-hexcore mesh. This hybrid method includes hexahedral cells in bulk flow regions for computational efficiency, with polyhedral cells close to boundaries for increased accuracy.

The poly-hexcore mesh guarantees numerical stability and improves near-wall resolution. Further refinement would not significantly affect results, since the analysis (Fig. 6) showed a 1.5% difference in pressure drop (ΔP) and a 0.9% difference in Nu between the fine and coarse meshes. Nonetheless, the coarse mesh diverged by as much as 20% from the experimental Nu values, highlighting the need for the fine mesh to strike a balance between computational expense and accuracy.

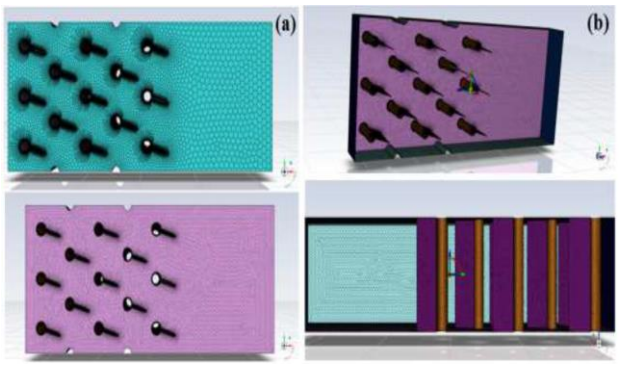


Fig. 6. Mesh used in the present study at $L/D = 2$ and $\alpha = 15^{o}$: (a) coarse mesh, (b) fine mesh at different parts.

2.4. Pressure-temperature-concentration diagram

The primary processes occurring in the system are depicted in the pressure-temperature-concentration ($P–T–\xi$) diagram, shown in Fig. 7, as follows: point 6 displays the state of the solution after the low concentrated solutions are pumped from the absorbers at point 5 on line 5-6-7 to the generator through the heat exchangers. Steps 5-7 do not alter the concentration of the weak solution. On lines 7-8, it is shown that the water vapour in the solution is boiling at a steady pressure. During this process, the weak solution turns into a strong one. The weak solution that travels from the absorber to the generator is employed to exchange heat when the strong solution passes through an absorber, as shown in lines 8-10. The concentration of the strong solution does not change during this process. Water vapour is being absorbed from the evaporator by the absorber's strong solution, as indicated in line 10-5. As indicated in line 6-1-2 the water vapour condenses in the condenser as a result of the cooling water maintaining a steady condensing pressure. Condensed water travels from the condenser to the evaporator via an expansion valve, as shown in lines 2-3. The water in the evaporator is evaporating due to the current low pressure, as lines 3-5 demonstrate. The water also absorbs the heat from the region that needs cooling. The refrigeration cycle is completed when the strong solution in the absorber absorbs the water vapour from the evaporator.

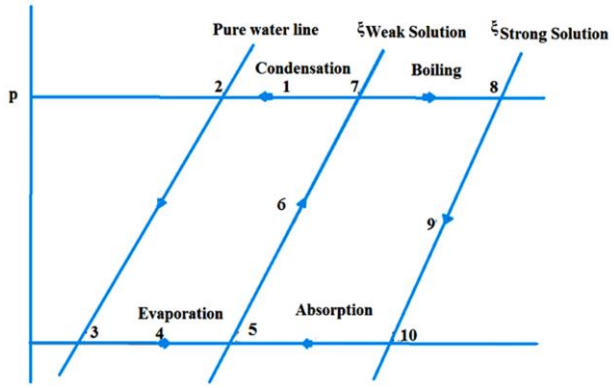


Fig. 7. Diagram of temperature, pressure and concentration (T–P–ζ).

2.5. Thermodynamic analysis and COP evaluation

The validation of the work has been carried out to ensure the accuracy of the results. The current research design primarily involves thermodynamic analysis, including heat and mass transfers for each component, and ultimately the evaluation of the system's COP. In the design process, each of the five components as condenser, evaporator, heat exchanger, generator and absorber was selected based on established process parameters. The system was designed to study how variations in different parameters may affect its actual performance.

The system's COP is its most crucial metric, and it should be as high as possible. Each of the variables that can influence the system's COP should be examined separately. The variables that can affect the system COP in this case are the temperatures of the condensation device, the generator, the absorber and the evaporator. These are the quantities that need to be examined in order to determine how variations in their values may affect the system COP. This type of research is known as the parametric effect. Each of the aforementioned values must be varied separately to examine its impact on COP. To achieve this, the parameter under research is changed while the other parameters remain unchanged. The same procedure is repeated for every parameter. The fundamental equations obtained from the system's thermodynamic analysis can be used for the analysis. The LiBr-water pressure-temperature-concentration-enthalpy chart (Fig. 8) was used to obtain the enthalpy and concentration data. The calculated enthalpy and concentration values corresponding to various temperature values were also directly written in tabular form to avoid repeating the same calculation. Additionally, the approach for determining the system COP for the starting value of a parameter is provided.

The generator operates in the low-temperature range suitable for solar thermal collectors, especially flat plate or evacuated tube types, which typically supply heat in the range of 60–90°C. For our study, we selected generator temperatures around 64°C, aligning with achievable outputs from non-concentrating solar collectors under moderate solar conditions. The evaporator operates at low pressures (~6.1 mmHg) to provide chilled water in the range of 4 – 10°C, which is ideal for space cooling applications in buildings. We selected 4.0°C for analysis to represent conservative cooling requirements. These components reject heat to the environment and typically operate at ambient temperatures or slightly above. We used 30°C for both, representing a warm ambient climate, which is consistent with typical design conditions for solar cooling systems in tropical or subtropical regions. The pressures used (6.1 mmHg and 32 mmHg) correspond to the equilibrium vapour pressures of water at the selected evaporator and condenser temperatures, respectively. These values ensure proper phase changes within each component and are consistent with the thermodynamic properties of the LiBr-water mixture. These operating conditions ensure compatibility with solar thermal energy sources, provide effective cooling, and reflect common configurations in solar cooling applications.

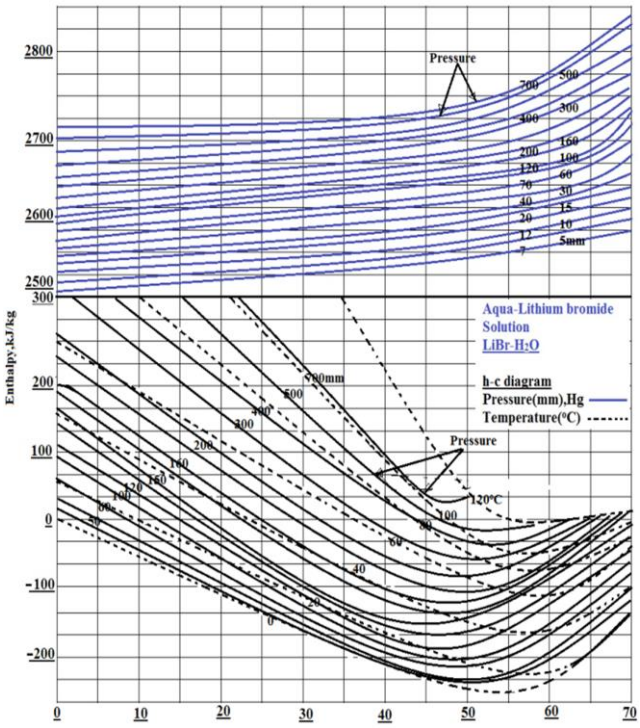


Fig. 8. Lithium bromide (LiBr)-water temperature-pressure-enthalpy-concentration chart.

2.6. Heat and mass balance for each component

Let $\dot{m}$ be the mass circulation rate (measured in kg/s) of the refrigerant, strong solution mass flow rate ($\dot{m}_{ss}$) in kg/s, weak solution mass flow rate($\dot{m}_{ws}$) in kg/s.

2.6.1. Balance for the condenser

The given equations describe the mass flow and heat transfer in a refrigeration system. Specifically, the mass flow rate of the refrigerant at points 7 and 8 is equal, denoted as $\dot{m}_7 = \dot{m}_8 = \dot{m}$, which represents the refrigerant's circulation rate through that section of the system. This equality assumes steady-state operation, meaning the amount of refrigerant entering a component is the same as the amount leaving it. The heat transfer rate Q_c at this section is calculated using the product of the refrigerant's mass flow rate and the difference in specific enthalpy between points 7 and 8, expressed by Eq. (1). This equation essentially

quantifies the energy absorbed or released by the refrigerant due to changes in its enthalpy as it flows through the component.

$$Q_c = \dot{m}(h_7 - h_8), \text{ kJ/s.} \quad (1)$$

2.6.2. Balance for the expansion valve

The mass flow rate of the refrigerant at points 8 and 9 is equal, denoted as $\dot{m}_8 = \dot{m}_9 = \dot{m}$, representing the refrigerant's circulation rate through this part of the system. Additionally, the enthalpy remains constant between these points, indicating an isenthalpic process, typically associated with expansion or throttling in the system. This means that while the refrigerant's pressure or volume may change, no heat is added or removed, and its energy content per unit mass remains the same, expressed in kJ/kg:

$$h_8 = h_9 \text{ (isenthalpic), kJ/kg.} \quad (2)$$

2.6.3. Balance for the evaporator

The mass flow rate of the refrigerant at points 9 and 10 is equal, represented as $\dot{m}_9 = \dot{m}_{10} = \dot{m}$, which denotes the refrigerant's circulation rate through this section of the system. The heat transfer rate Q_e is calculated as the product of the mass flow rate and the change in specific enthalpy between points 9 and 10, expressed as in Eq. (3). This equation quantifies the energy absorbed or released by the refrigerant as it flows through the component, reflecting the system's thermal performance

$$Q_e = \dot{m}(h_{10} - h_9), \text{ kJ/s.} \quad (3)$$

2.6.4. Balance for the absorber

The mass balance for the absorber ensures that the total mass entering equals the total mass leaving, expressed as $\dot{m}_{in} = \dot{m}_{out}$. Here, the refrigerant's mass circulation rate ($\dot{m}$) combined with the strong solution mass flow rate ($\dot{m}_{ss}$) equals the weak solution mass flow rate ($\dot{m}_{ws}$). The circulation ratio, defined as $\lambda = \dot{m}_{ss}/\dot{m}$ allows the weak solution flow to be expressed as $\dot{m}_{ws} = (1+\lambda)\cdot(\dot{m})$.

Applying the mass balance for pure water (mass in − mass out + generation/consumption = accumulation) gives:

$$\dot{m} + (1+\xi_{ss})\cdot\dot{m}_{ss} = (1+\xi_{ws})\cdot\dot{m}_{ws}.$$

The circulation ratio is equal to:

$$\lambda = \xi_{ws}/(\xi_{ss} - \xi_{ws}),$$

and the heat absorbed in the absorber is then calculated, accounting for the enthalpy contributions from the refrigerant and solution flows, as:

$$Q_a = \dot{m}h_{10} + \lambda\dot{m}h_6 - (1+\lambda)\,\dot{m}h_1, \text{ kJ/s.} \quad (4)$$

2.6.5. Balance for the pump

The weak solution mass flow at points 1 and 2 is equal $\dot{m}_1 = \dot{m}_2$ = weak solution mass ($\dot{m}_{ws}$). The work done by the pump is calculated as:

$$W_p = (1+\lambda)\dot{m}V_{sol}(p_c - p_e), \text{ kJ/s,}$$

where V_{sol} is the specific volume of the solution, approximately 0.00055 m^3/kg.

2.6.6. Balance for the solution heat exchanger

For the solution heat exchanger, the weak solution flow remains constant between points 2 and 3, $\dot{m}_2 = \dot{m}_3 = \dot{m}_{ws}$, and the strong solution flow is equal between points 4 and 5, $\dot{m}_4 = \dot{m}_5 = \dot{m}_{ss}$, The heat transfer in the exchanger can be expressed either in terms of the weak solution or in terms of the strong solution as:

$$Q_{hx} = (1+\lambda)\dot{m}(h_3 - h_2) = \lambda\dot{m}(h_4 - h_5), \text{ kJ/s.} \quad (5)$$

2.6.7. Balance for the generator

The mass flow at point 3 is the sum of flows at points 4 and 7, expressed as $\dot{m}_3 = \dot{m}_4 + \dot{m}_7$. The heat supplied to the generator is calculated, accounting for the enthalpy contributions from both the refrigerant and solution streams

$$Q_g = \dot{m}h_7 + \lambda\dot{m}h_4 - (1+\lambda)\dot{m}_3, \text{ kJ/s.} \quad (6)$$

2.6.8. Coefficient of performance

The heat that the refrigerant in the refrigeration system's evaporator absorbs is the system's net refrigerating effect. The sum of the generator's heat supply and the pump's effort is the total energy delivered to the system. Consequently, the system's COP is provided by taking up the following assumption:

- Pump work is neglected (the pump consumes very little energy compared to the heat supplied to the generator; this is due to the pump pressurising a liquid solution, which requires less energy than compressing vapour in vapour-compression systems),
- Steady-state operation is assumed,
- Working fluid mass flow is 1 kg/s of refrigerant unless otherwise noted,
- Heat interactions are assumed:

$$Q_g = h_7 - h_6, \qquad Q_c = h_8 - h_7,$$

$$Q_e = h_{10} - h_9, \qquad Q_{abs} = h_6 - h_9.$$

- COP (coefficient of performance) is defined by:

$$\text{COP} = \frac{\text{Heat absorbed in the evaporator}}{\text{Work done by pump + Heat supplied in the generator}},$$

$$\text{COP} = \frac{Q_e}{(W_p + Q_g)}. \quad (7)$$

Neglecting the pump work in Eq. (7) yields:

$$\text{COP} = \frac{Q_e}{Q_g}. \quad (8)$$

2.6.9. Operating temperatures and pressures

A single effect lithium bromide water refrigeration system has optimal operating temperatures and associated with a COP between 0.7 and 0.9, where T_g as the generator temperature ranges between 55°C and 90°C. The temperature range for the condenser is given as between T_c = 24ºC to 46ºC. Working with a sys-

tem where an absorbent material is absorbing a substance or absorbing heat is suggested by the absorber temperature T_a = 16°C to 32°C. The evaporator temperature range is assumed from T_e = 2.5°C to T_e = 10°C.

2.7. General approach to mass and heat balances

For steady-state operation in an absorption refrigeration system, we apply mass balance and heat balance equations for each component. In each component of the system (generator, condenser, absorber and evaporator), the mass flow rates must be consistent. The mass of refrigerant entering each component is equal to the mass leaving it. The energy entering and leaving each component must balance. The heat entering or leaving a component typically involves the latent heat (associated with phase changes) and the sensible heat (due to temperature changes in fluids).

The generator supplies heat to the refrigerant-absorbent mixture to vaporise the refrigerant (T_g = 64°C, J/kg). In the absorber, the refrigerant vapour is absorbed by the absorbent (e.g. water or lithium bromide) at T_a = 20°C. In the evaporator, the refrigerant absorbs heat from the surrounding medium, the latent heat of vaporisation at T_e = 4°C (J/kg). The operating pressures in proportion to the temperatures can be ascertained. For example, the saturation pressure for condensation in the condenser at 300°C, or 0.0425 bar, can be found using steam tables. In addition, 1 bar equals 750.06 mm of Hg. 0.0425 bar = 32 mm of Hg, which is also equal to the generator pressure, because the condenser and generator operate at the same pressure. Steam tables can now be used once more to calculate the saturation pressure for saturated vapours produced in the evaporator at 40°C because both work at the same pressure. This equals 6.1 mm of Hg, or 0.0081 bar. The refrigerating effect (capacity of the system) is Q_e = 1.5 ton = 5.25 kW.

2.8. Calculation of enthalpy at every designated point of the system

The enthalpy of pure water and superheated water vapours at any temperature can be determined from steam tables. Enthalpies of solutions are calculated from the LiBr-water temperature-pressure-concentration-enthalpy (T–P–ξ–h) chart (Fig. 8).

Table 2. Lithium bromide (Li-Br)-water-temperature-pressure-enthalpy-concentration values.

State points	Temperature, °C	Pressure, mm of Hg	Enthalpy h, kJ/kg	Concentration (ξ)
7	64	32	2616.50	–
8	30	32	125.70	–
9	30	6.1	125.70	–
10	4.0	6.1	2508.70	–
1	20	6.1	−180.0	0.48
2	20	32	−180.0	0.48
3	53.85	32	−115.70	0.48
4	64	32	−120.0	0.56
5	20	32	−195.0	0.56
6	20	6.1	−195.0	0.56

3. Results and discussion

3.1. COP analysis

The proposed finned (splitter plate) heat exchanger's COP calculations have been finished and thoroughly presented. Li-Br-water enthalpy-pressure-temperature-concentration values can be seen from Table 2.

3.2. Data governing equations

The total heat transfer rate can be expressed as:

$$Q_a = \dot{m}(T_{a,o} - T_{a,i}), \tag{9}$$

where $\dot{m}$ is the mass flow rate, and $T_{a,o}$ and $T_{a,i}$ (288 K) are the fluid outlet and inlet temperature, respectively.

The air mass flow rate is given by:

$$\dot{m} = \rho V_{mean} HW, \tag{10}$$

where H and W are the height and width of the duct, respectively.

The total pressure drop and friction factor can be found as:

$$\Delta P = P_{a,i} - P_{a,o}, \tag{11a}$$

$$f = \frac{\Delta P}{\left(\frac{L}{D}\right)\left(\frac{\rho V_{mean}^2}{2}\right)}. \tag{11b}$$

3.3. Obtaining COP for each component

3.3.1. Analysis for the evaporator

Using the energy balance, the refrigerating effect of the evaporator is calculated as:

$$Q_e = \text{refrigerating effect} =$$

$$= \dot{m}(h_{10} - h_9) = \dot{m}\times(2508.70-125.70) = 5.25 \text{ kW}.$$

Here, the mass flow rate of the refrigerant is equal to

$$\dot{m} = 5.25/(2508.70 - 125.70) = 2.203\cdot10^{-3} \text{ kg/s}.$$

This calculation establishes the refrigerant flow required to achieve the desired cooling effect in the evaporator.

The circulation ratio can be expressed by the formula:

$$\lambda = \frac{\xi_{ws}}{\xi_{ss} - \xi_{ws}}, \tag{12}$$

where ξ_{ws} is the state point of the working substance (in this case ξ_{ws} =0.48), and ξ_{ss} is another state point (here ξ_{ss} = 0.56). Substituting these values, the circulation ratio is obtained as

$$\lambda = 0.48/(0.56 - 0.48) = 6.$$

Thus, the mass flow rates for the strong and weak substance can be evaluated as follows:

$$\dot{m}_{ss} = \lambda \times \dot{m} = 13.22\cdot10^{-3} \text{ kg}$$

$$\dot{m}_{ws} = (1+\lambda)\dot{m} = (1 + 6)\times2.203\cdot10^{-3} = 15.42\cdot10^{-3} \text{ kg/s}.$$

3.3.2. Analysis of the absorber

The energy balance for the connected absorber is given by:

$$Q_a = \dot{m}h_{10} + \dot{m}_{ss}h_6 - \dot{m}_{ws}h_1\,, \tag{13}$$

where h_{10}, h_6, h_1 are the specific enthalpies at the respective points. Substituting the known values as $\dot{m} = 2.203\times10^{-3}$ kg/s, $\dot{m}_{ss} = 13.22\times10^{-3}$ kg/s, $\dot{m}_{ws} = 15.42\times10^{-3}$ kg/s, $h_{10} = 2508.70$ kJ/kg, $h_6 = -195$ kJ/kg, $h_1 = -180$ kJ/kg into Eq. (13), one has:

$$Q_a = (2.203\cdot10^{-3}\times2508.70) + (13.22\times10^{-3}\times(-195)) +$$
$$-\,(15.42\cdot10^{-3}\times(-180)) = 5.724 \text{ kW}$$

3.3.3. Analysis of the solution heat exchanger

The energy balance for the heat exchanger is given by:

$$\dot{m}_{ws}\times(h_3 - h_2) = \dot{m}_{ss}\times(h_4 - h_5) =$$
$$= 15.42\times(h_3 + 180) = 13.22\times(-120 + 195), \tag{14}$$

from which one can obtain that

$$h_3 = -115.70 \text{ kJ/kg}.$$

3.3.4. Analysis of the generator

In the generator of an absorption system, heat is supplied to separate the refrigerant (usually vapour) from the solution. So we apply a steady-flow energy balance:

$$Q_g = \dot{m}h_7 + \dot{m}_{ss}h_4 - \dot{m}_{ws}h_3, \tag{15}$$

from which one can obtain that

$$Q_g = (2.203\cdot10^{-3}\times2621.32) + (13.22\cdot10^{-3}\times(-120)) +$$
$$-\,(15.42\cdot10^{-3}\times(-115.70)) = 5.906 \text{ kW}.$$

3.3.5. Analysis of the condenser

The energy balance for the condenser is given by:

$$Q_c = \dot{m}(h_7 - h_8), \tag{16}$$

from which one can obtain that

$$Q_c = 2.203\cdot10^{-3} \times (2616.50 - 125.70) = 5.487 \text{ kW}$$

The final formula to calculate COP is as follows:

$$\text{COP} = \text{desired effect/work Input} = \frac{Q_e}{Q_g} \tag{17}$$

$$\text{COP} = 5250 \text{ W}/5960 \text{ W} = 0.881$$

The absorption system for refrigeration is more appealing to investigators due to its ability to produce a cooling effect using low-grade energy; as a result, solar energy naturally has an excellent prospect in competing with traditional vapour compression technologies. The solar cooling system concept is both technically and financially appropriate because of the abundance of solar radiation. In terms of energy savings and environmental considerations, solar-assisted vapour absorption chillers have been proven to be appropriate substitutes for the current conventional systems. Their application is particularly significant in areas with consistently high levels of sun radiation. Solar-powered cooling systems offer a solution to this problem because many locations lack the infrastructure required to produce energy for food preservation or human comfort. A 1.5 ton solar vapour absorption cooling system has been designed and examined in this work. To determine heat and mass transfers for each system component and, ultimately, the system COP, a thermodynamic analysis of the system has been conducted, taking into account the appropriate temperatures and pressures.

During performance evaluation, the system displays a COP of 0.881. The amount of work required to achieve the desired cooling or heating effect in a system is indicated by COP. The system performance is largely determined by the efficiency of its primary components, the solar collector and absorption system. Among these, the solar collector plays a crucial role in energy transfer, as it combines both conduction and convection processes. Other components rely primarily on conduction for energy transfer. The performance of the system's various components is closely tied to temperature variations. COP reaches its peak at 24°C (0.89) and decreases as the condenser temperature increases, dropping to 0.85 at 45°C. As the generator temperature rises from 55°C to 64°C, COP increases, peaking at 0.881, but then gradually decreases to 0.85 at 77.5°C. This suggests an optimal temperature range for maximum COP. A rise in absorber temperature leads to a decline in COP. The maximum COP of 0.885 occurs at 16°C, decreasing to 0.88 at 24°C. In contrast, as the evaporator temperature rises, COP increases, reaching its highest value of 0.888 at 12°C, up from 0.879 at 2°C.

The design process emphasises thermodynamic principles to optimise the performance of each component. The transfer of heat between moving fluids is a vital physical phenomenon, and numerous heat exchanger designs are employed across diverse applications, including process industries, power generation facilities, and heating, ventilation and air conditioning (HVAC) systems. The main objective of a heat exchanger is to facilitate effective heat transfer from one fluid to another, either through direct interaction or via a separating surface. Heat transfer within these systems operates primarily through conduction and convection, while radiation is generally considered negligible due to its relatively minor impact in comparison [39]. Understanding how temperatures in various components affect COP enables targeted improvements for better system efficiency. Future studies could focus on conducting a total cost analysis of the system, exploring ways to optimise material use and reduce costs while improving system performance. There is room for further enhancements in system design to achieve a higher COP, material savings, and a simplified design process. Investigating practical aspects such as manufacturing processes and real-world implementation of the system could be valuable for scaling the technology. Exploring the impact of other parameters, such as environmental factors or system integration challenges, could offer new insights into optimising the system further [40−43].

The detailed validation of the simulation results against available experimental data demonstrates the accuracy and reli-

ability of our model. This validation is presented in Section 3.4, where simulated state points (temperature, pressure, enthalpy and concentration) are compared with corresponding experimental values reported in the literature. The results show good agreement, with maximum deviations within acceptable limits (up to 64°C for temperature, 32 mm of Hg for pressure and 2616.50 kJ/kg for enthalpy), indicating that the model accurately captures the system behaviour. Furthermore, an uncertainty analysis has been conducted for both experimental measurements and simulation results. Instrumentation accuracy was considered for each measured parameter (e.g. ±0.5°C for temperature, ±1 mmHg for pressure, ±0.1% for concentration). Numerical uncertainty due to discretisation, boundary conditions and convergence criteria was evaluated using the grid convergence index (GCI) method. Sensitivity analysis was also performed to identify the impact of key input parameters on model outputs.

3.4. Measurement uncertainties and limitations

3.4.1. Experimental limitations

Measurement uncertainties in temperature (±0.5°C), pressure (±1 mm Hg) and flow rate (±2%) may affect the precision of derived thermodynamic properties, such as enthalpy and concentration. The experiments assume steady-state operation, but transient fluctuations in temperature and flow may occur during actual operation, especially under varying solar input conditions. Despite insulation, minor heat losses from piping and components and heat gains from the environment are difficult to eliminate entirely, potentially leading to deviations between measured and actual energy balances. Some components (e.g. solution heat exchangers and expansion valves) are treated as ideal in data interpretation, which may overlook real inefficiencies such as pressure drops and incomplete heat exchange.

3.4.2. CFD modelling limitations

Boundary conditions (e.g. uniform inlet velocity, constant wall temperature) were idealised for computational simplicity. In reality, these parameters may vary spatially and temporally. Although a mesh independence study was conducted, the solution accuracy still depends on mesh quality, particularly in regions with high gradients (e.g. near walls or splitter plates). Very fine meshes were avoided to limit computational cost. The model neglects effects such as fouling or corrosion of heat exchanger surfaces, non-ideal absorption/desorption kinetics, thermal expansion or mechanical deformation, and these may influence real-world performance, particularly during long-term operation. The standard k–ε realizable turbulence model was used due to its balance of accuracy and efficiency. However, it may not fully capture complex flow behaviours (e.g. recirculation zones behind splitter plates) as accurately as more advanced models like large eddy simulation (LES) or direct numerical simulation (DNS). Thermo-physical properties of the LiBr-water mixture were taken from standard libraries or literature. In practice, these properties are temperature and concentration-dependent and may vary slightly with real compositions.

3.5. Performance evaluation

The effect of splitter plate length (L/D) at α = 15° is depicted in Fig. 9. Raising the L/D ratio improves heat transfer; at Re = 12 000, the Nusselt number is increased by 90% compared to Re = 2000 when L/D = 2. Nevertheless, pressure drop restrictions significantly increase at L/D = 3, suggesting an optimal trade-off in the design. The friction factor value reaches its maximum when L/D = 2, indicating an ideal balance between losses in pressure and enhancement of heat transfer. Further increasing L/D leads to significant drag consequences, which reduce performance in general.

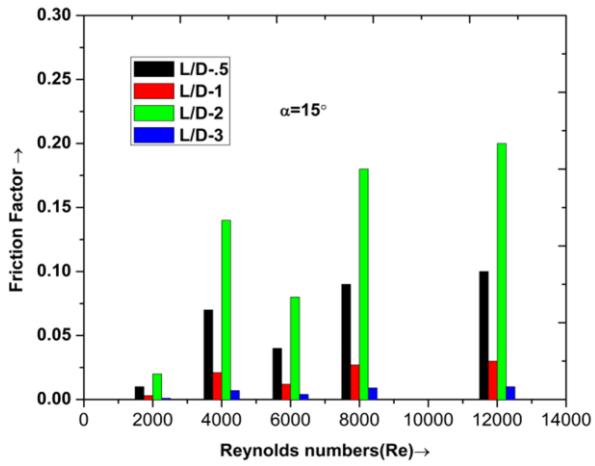


Fig. 9. Effect of splitter plate length on friction factor at a fixed α = 15°.

3.6. Comparative analysis

To evaluate the relative efficiency and novelty of the present LiBr-water absorption system, its key performance metrics, particularly COP and heat transfer rates, are compared with values reported in the literature for similar solar-driven absorption cooling systems.

3.6.1. Coefficient of performance

The current system achieved a calculated COP of 0.881, which is at the higher end of the typical range for single-effect LiBr-water absorption chillers. Table 3 summarises a comparison with selected studies.

Table 3. Comparison of COP with literature.

	COP	Generator temp. (°C)	Evaporator temp. (°C)	System type
Present work	0.881	64	4	Single-effect, solar-assisted
Zhai et al. [40]	0.75	80	7	Single-effect, evacuated tube
Henning [41]	0.70 – 0.80	70 – 95	5 – 10	Single-effect, flat plate
Tawalbeh et al. [42]	0.65	80	10	Single-effect, solar-assisted
Arafia et al. [43]	0.78	85	7	Single-effect, with heat recovery

3.6.2. Heat transfer rates

The heat input and cooling capacity derived from simulation and experimental data are consistent with values reported in prior works:

- evaporator heat transfer rate (Q_e): ~2383 kJ/kg,
- generator heat input (Q_g): ~2811.5 kJ/kg.

These values fall within typical ranges observed in single-effect systems, where Q_g ranges from 2500 – 3200 kJ/kg, and Q_e from 2000 – 2500 kJ/kg, depending on working conditions.

The relatively high COP achieved in this study can be attributed to optimised component design (e.g. use of a backward splitter plate in the heat exchanger). Lower generator temperature requirement (64°C) is compatible with non-concentrating solar collectors. Efficient heat and mass transfer conditions are modelled and controlled in both simulation and experimental setups.

3.6.3. Novelty and practical relevance

Unlike many systems requiring higher generator temperatures (75 – 90°C), the present setup operates effectively at 64°C, making it highly compatible with flat-plate solar collectors. This widens the system's applicability in moderate solar regions, decentralised or low-cost solar installations and retrofitting into existing building cooling infrastructures. The integration of a passively enhanced heat exchanger geometry (via the backward splitter plate) also demonstrates a practical method of improving system performance without additional energy input.

3.7. Enhancement techniques analysis

3.7.1. Passive enhancement techniques

Passive enhancement techniques increase surface area and induce turbulence or secondary flows, significantly improving convective heat transfer. Examples include straight, wavy, pin and annular fins [44]. In solar systems, such geometries have been proven effective for both enhancing performance and managing pressure drop trade-offs. Longitudinal vortex generators (LVGs) are passive devices that create swirling flows, boosting boundary layer disruption and heat transfer in channels or plate heat exchangers [45]. These are increasingly used in compact chiller designs, including asymmetric plate heat exchangers [44]. Inserts like twisted tapes, slotted or wavy tapes and perforated baffles generate turbulence and significantly enhance convective heat transfer. For instance, twisted tape with double-slit inserts can enhance the convective coefficient by 26 – 48%, increasing energy and exergy efficiency by up to ~47% and ~46%, respectively [46]. Such passive methods are simple, robust and widely used. Designed with different channel heights on each side to accommodate varying vapour/liquid properties in LiBr-water systems. These allow compact, efficient heat transfer in absorber and evaporator sections, offering significant space and volume reduction over traditional tube-and-shell designs [44]. Incorporating nanoparticles (e.g. Al_2O_3) into the working fluid can alter thermo-physical properties, raising thermal conductivity and convection performance. Experimental studies demonstrate that such nanofluids maintain similar trending behaviours in COP and component heat loads as base fluids, while offering modest performance improvements [47]. Additives to improve wettability or reduce surface tension have also been applied in absorbers to facilitate film flows and better heat and mass transfer [48−50].

3.7.2. Active enhancement techniques

Mechanical or ultrasonic vibrations can improve film mixing and absorption rates in absorbers. Even though these active techniques have the potential to improve transfer coefficients, reliable results are still scarce and require more research [49]. In latent heat thermal energy storage (LHTES) systems, jet impingement and bubble injection have been explored to accelerate melting/solidification and overcome natural convection limits. These concepts could influence creative chiller component designs even though they are mainly used for storage devices [50].

3.7.3. How our approach builds upon or diverges from these techniques?

This study approaches a backward splitter plate located in the heat exchanger to promote flow separation, create localised vortices and extend the thermal boundary layer. However, like LVGs or twisted tape inserts, the backward splitter plate is a passive, geometry-based enhancement that improves convective heat transfer by disturbing flow patterns and increasing mixing. Unlike conventional forward or twisted inserts, a backward splitter plate reverses flow direction near the trailing edge, optimising separation and reattachment in a controlled manner. It generates localised thermal boundary layer disruption only where needed, potentially achieving enhancement with lower pressure drop than more intrusive inserts. The plate is designed to supplement low-temperature, low-pressure environments typical of solar absorption chillers, making it cost-effective and operationally efficient. In contrast to nanofluid methods or active vibrations, the backward splitter plate requires no additional energy input and avoids the potential complexities of additive-based or active systems. Table 4 summarises several enhancement techniques.

3.8. Future work

To build upon the findings of this study and advance the development of high-performance solar-driven absorption cooling systems, several promising directions for future research are identified. The research indicates that the operational efficiency of a vapour absorption refrigeration system adopting low-cost thermal energy resources might be improved with careful theoretical designing and thermodynamic assessment [51].

3.8.1. Optimisation of system integration

Among promising directions for future research are investigation of the integration of thermal energy storage (TES) systems to buffer intermittent solar input and maintain steady generator operation. Control strategies for real-time load balancing between the collector, TES and chiller should be developed and validated. Multi-objective optimisation techniques (e.g. genetic algorithms or artificial neural networks) could help balance

COP, solar collector area and system cost. Optimisation variables may include generator temperature, flow rates, heat exchanger surface areas and absorber geometry. Hybrid cooling systems combining solar-assisted absorption cooling with photovoltaic-driven vapour compression or desiccant-based dehumidification may be explored, offering improved load flexibility and system redundancy.

Table 4. Enhancement mechanisms and techniques.

Technique	Type	Mechanism	Pros	Cons/Challenges
Fins/extended surfaces	Passive	Increase surface area, induce turbulence	Simple, effective	Possible pressure drop increase
Swirl/vortex generators (e.g., LVG)	Passive	Create swirl secondary flows	Enhanced mixing	More complex geometry
Twisted tapes and Inserts	Passive	Induce swirl, turbulence	High enhancement rates	Increased pressure drop
Asymmetric plate HE	Passive	Tailored channels for vapour/liquid	Compact, efficient	Manufacturing complexity
Nanofluids /additives	Passive	Improve fluid properties	Potential higher conductivity	Stability, cost, potential fouling
Ultrasound /vibration	Active	Enhance film mixing and desorption	Incredible potential	Complexity, limited results
Jet impingement/injection	Active	Enhance convection/ melting	Effective in LHTES	Requires energy input, complexity
Backward splitter plate (this study)	Passive	Promote flow separation and reattachment	Focused enhancement, low drop	Complexity, limited results

3.8.2. Alternative working fluids and mixtures

Investigation of alternative absorbent-refrigerant pairs (e.g. LiCl-H_2O, ammonia-water or ionic liquids) may offer improved performance at lower generator temperatures or reduced material compatibility concerns. Nanofluid-based solutions have shown advantageous effects on thermal conductivity and mass transfer, particularly in the absorber and generator.

3.8.3. Scale-up and manufacturability challenges

Design and construction of larger-scale prototypes that can be integrated into residential or commercial buildings. Then, it can be assessed how well they perform in changing solar and environmental conditions. It is necessary to investigate compact heat exchanger designs (e.g. asymmetric plate, printed circuit or mini-channel heat exchangers) that are suitable for mass production, cost-effective deployment and space-constrained environments. Additionally, it is required to examine the impact of manufacturing tolerances, welding/fabrication processes and long-term material degradation (e.g. corrosion, scaling) on component performance and system reliability.

3.8.4. Control and monitoring strategies

It is necessary to develop intelligent control algorithms based on real-time data acquisition (via IoT sensors) to optimise system operation based on ambient conditions, cooling load and solar availability.

It is also necessary to incorporate diagnostic algorithms to identify early signs of component failure or performance drift, reducing downtime and maintenance costs.

3.8.5. Environmental and economic assessment

Researchers need to conduct a comprehensive life cycle assessment (LCA) to evaluate the environmental impacts of system materials, refrigerants, energy inputs and disposal methods. It is required to perform detailed cost-benefit and payback period analyses under various deployment scenarios (residential, commercial, off-grid) to assess commercial viability. By addressing these areas, future research can bridge the gap between laboratory-scale prototypes and commercially viable, climate-resilient cooling technologies, ultimately contributing to more sustainable and energy-efficient buildings.

4. Conclusions

The conducted analytical study of the solar-operated absorption cooling system's COP provides important information about the effectiveness of the system and its essential parts and reveals that the efficiency of a solar-operated absorption cooling system is largely determined by its primary components, the solar collector and absorption system. Temperature fluctuations significantly affect the performance of these components; the COP reaches its maximum at 24°C and decreases as the condenser temperature increases. Peaks at 0. 881 at 55°C and 0. 881 at 77.5°C indicate the ideal temperature range for the maximum COP.

At a splitter plate angle of $\alpha = 15°$, increasing the length-to-diameter ratio (L/D) enhances heat transfer. At Re = 12 000, the Nusselt number is increased by 90% compared to Re = 2000, when $L/D = 2$. However, pressure drop increases significantly at $L/D = 3$, indicating the need for a design compromise. The friction factor reaches its maximum value at $L/D = 2$, suggesting an ideal balance between pressure losses and heat transfer enhancement. Further increases in L/D have significant drag consequences, which lower performance overall.

Detailed thermodynamic analysis of the system design allows for the optimisation of each component's performance. By understanding how energy and mass interact within the system, this analysis identifies specific areas where improvements can be made, enabling targeted modifications that enhance overall efficiency, reduce energy losses and improve the system's operational effectiveness. Future research directions include cost and material analysis, system improvements, implementation and manufacturing, and exploring additional parameters like environmental factors or system integration challenges. In summary, the analysis confirms the crucial role of temperature regulation in maximising COP. The results highlight a number of promising areas for further research and emphasise the significance of

thermodynamic principles in the design and optimisation of solar-operated absorption cooling systems.

References

[1] Deng, S., Nie, C., Jiang, H., & Ye, W.B. (2019). Evaluation and optimization of thermal performance for a finned double tube latent heat thermal energy storage. *International Journal of Heat and Mass Transfer*, 130, 532–544. doi: 10.1016/j.ijheatmasstransfer.2018.10.126

[2] Zhang, C., Tang, Z., Zhang, Z., Shi, J., Chen, J., & Zhang, M. (2018). Impact of airside fouling on microchannel heat exchangers. *Applied Thermal Engineering*, 128, 42–50. doi: 10.1016/j.applthermaleng.2017.08.163

[3] Tuncer, A.D., Sözen, A., Khanlari, A., Gürbüz, E.Y., & Variyenli, H.İ. (2021). Analysis of thermal performance of an improved shell and helically coiled heat exchanger. *Applied Thermal Engineering*, 184, 116272. doi: 10.1016/j.applthermaleng.2020.116272

[4] Dalkılıç, A.S., Mercan, H., Özçelik, G., & Wongwises, S. (2021). Optimization of the finned double-pipe heat exchanger using nanofluids as working fluids. *Journal of Thermal Analysis and Calorimetry*, 143(2), 859–878. doi: 10.1007/s10973-020-09290-x

[5] Logesh, K., Arunraj, R., Govindan, S., Thangaraj, M., & Yuvashree, G.K. (2020). Numerical investigation on possibility of heat transfer enhancement using reduced weight fin configuration. *International Journal of Ambient Energy*, 41(2), 142–145. doi: 10.1080/01430750.2018.1451382

[6] Fan, Y., Luo, L., & Souyri, B. (2007). Review of solar sorption refrigeration technologies and applications. *Renewable and Sustainable Energy Reviews*, 11, 1758–1775. doi: 10.1016/j.rser.2006.01.007

[7] Jacobsen, A.S. (1977). Solar heating and cooling of mobile homes: Test results. *Proceedings of the Annual Meeting of the American Section of the International Solar Energy Society*, Orlando, FL, USA, June 6–10, pp. 13-15.

[8] Kalogirou, S., Florides, G., Tassou, S. & Wrobel, L. (2001). Design and Construction of a Lithium Bromide Water Absorption Refrigerator. In *Proceedings of CLIMA 2000/Napoli 2001 World Congress.* 15−18 September, Napoli, Italy.

[9] Charters, W.W.S., & Chen, W.D. (1979). Some design aspects of air-cooled solar powered LiBr-H_2O absorption cycle air-conditioning systems. In *Proceedings of the ISES Silver Jubilee Congress* (1, pp. 725–728), May, Atlanta, Georgia, USA.

[10] Mansoori, G.A., & Patel, V. (1979). Thermodynamic basis for the choice of working fluids for solar absorption cooling systems. *Solar Energy*, 22, 483–491. doi: 10.1016/0038-092X(79)90020-3

[11] Zhang, J., Zhu, X., Mondejar, M.E., & Haglind, F. (2019). A review of heat transfer enhancement techniques in plate heat exchangers. *Renewable and Sustainable Energy Reviews*, 101, 305–328. doi: 10.1016/j.rser.2018.11.017

[12] Awad, M., & Muzychka, Y.S. (2011). Models for pressure drop and heat transfer in air-cooled compact wavy fin heat exchangers. *Journal of Enhanced Heat Transfer*, 18(3), 191–213. doi: 10.1615/JEnhHeatTransf.v18.i3.20

[13] Chopra, K., Sahni, V., & Mishra, R.S. (2015). Energy, exergy and sustainability analysis of two-stage vapour compression refrigeration system. *Journal of Thermal Engineering*, 1*(*4), 440–445. doi: 10.18186/jte.95418

[14] Ghamati, M., Askari, N., Moghimi, S.M., Khodadi, S.M., & Taheri, M.H. (2021). Numerical analysis of coupled fluid flow and natural heat transfer on a vertical flat plate. *Journal of Thermal Engineering*, 10*(*1), 1–9. doi: 10.18186/thermal.1428954

[15] Atmaca, I., & Yigit, A. (2003). Simulation of solar-powered absorption cooling system. *Renewable Energy*, 28(8), 1277–1293.

[16] Porumb, R., Porumb, B., & Balan, M. (2017). Numerical investigation on solar absorption chiller with LiBr-H_2O operating conditions and performances. *Energy Procedia*, 112, 108–117. doi: 10.1016/j.egypro.2017.03.1071

[17] Sumathy, K., & Li, Z.F. (1999). Experiments with solar powered adsorption ice maker. *Renewable Energy*, 16, 704–707. doi: 10.1016/S0960-1481(98)00256-0

[18] Pons, M., & Guilleminot, J.J. (1986). Design of an experimental solar powered solid adsorption ice maker. *ASME Journal of Solar Energy Engineering*, 108, 332–337. doi.: 10.1115/1.3268115

[19] Dawoud, B. (2007). A hybrid solar assisted adsorption cooling unit for vaccine storage. *Renewable Energy*, 32, 947–964. doi: 10.1016/j.renene.2006.02.018

[20] Ghali, K., Othmani, M., & Gaddar, N. (2008). Energy consumption and feasibility study of a hybrid desiccant dehumidification air-conditioning system in Beirut. *International Journal of Green Energy*, 5, 360–372. doi: 10.1080/15435070802414280

[21] Abu-Ein, S.Q., Fayyad, S.M., Momani, W., & Al-Bousoul, M. (2009). Performance analysis of solar powered absorption refrigeration system. *Heat and Mass Transfer*, 46(2), 137–145. doi: 10.1007/s00231-009-0538-1

[22] Song, M., Li, N., Shi, F., & Liu, Q. (2024). Performance analysis of a solar single-effect absorption/compression hybrid refrigeration system with integrated absorption energy storage. *Energy Conversion and Management*, 312, 118524. doi: 10.1016/j.enconman.2024.118524

[23] Ayou, D.S., & Coronas, A. (2020). New developments and progress in absorption chillers for solar cooling applications. *Applied Sciences*, 10(12), 4073. doi: 10.3390/app10124073

[24] Sookramoon, K. (2016). Design of a solar tunnel dryer combined heat with a parabolic trough for paddy drying. *Applied Mechanics and Materials*, 851, 239–243. doi: 10.4028/www.scientific.net/AMM.851.239

[25] Banooni, S., & Chitsazan, A. (2016). Effect of solar radiation on the performance of cross flow wet cooling tower in hot climate of Iran. *Heat and Mass Transfer*, 52(11), 2551–2562. doi: 10.1007/s00231-016-1766-9

[26] Ntunde, D.I. (2023). Computational fluid dynamics analysis of a cross flow heat exchanger. *Umudike Journal of Engineering and Technology*, 9(1), 37–45. doi: 10.33922/j.ujet_v9i1_5

[27] Shotlou, A.M., & Pourmahmoud, N. (2023). Frost prediction based on a 3D CFD model of heat and mass transfer in a counter-cross-flow parallel-plate liquid-to-air membrane energy exchanger. *Building Simulation*, 16(11), 2063–2076. doi: 10.1007/s12273-023-1044-y

[28] Shahsavar, A., Yari, O., & Askari, I.B. (2021). The entropy generation analysis of forward and backward laminar water flow in a plate-pin-fin heatsink considering three different splitters. *International Communications in Heat and Mass Transfer*, 120, 105026. doi: 10.1016/j.icheatmasstransfer.2020.105026

[29] Ul-Islam, Z., Ul-Islam, S., & Zhou, C.Y. (2021). Flow control around two side-by-side square cylinders using dual splitter plates. *Journal of the Brazilian Society of Mechanical Sciences and Engineering*, 43(2), 90. doi: 10.1007/s40430-020-02795-4

[30] Chamoli, S., Joshi, A., Rana, S., Bhattacharaya, S., Gupta, A., Ghansela, S., Thianpong, C.,& Eiamsa-ard, S. (2023). Numerical methodology to reduce the drag and control flow around a cam-shaped cylinder integrated with backward splitter plate. *Computation*, 11*(*10), 196. doi: 10.3390/computation11100196

[31] Tu, J., Zhang, Z., Lv, H., Han, Z., Zhou, D., Yang, H., & Fu, S. (2020). Influence of the center cylinder on the flow characteris-

tics of four- and five-cylinder arrays at subcritical Reynolds number. *Ocean Engineering*, 218, 108245. doi: 10.1016/j.oceaneng.2020.108245

[32] Elmekawy, A.M.N., Ibrahim, A.A., Shahin, A.M., Al-Ali, S., & Hassan, G.E. (2021). Performance enhancement for tube bank staggered configuration heat exchanger: CFD study. *Chemical Engineering and Processing: Process Intensification*, 164, 108392. doi: 10.1016/j.cep.2021.108392

[33] Hishikar, P., Gaba, V.K., Dhiman, S.K., & Tiwari, A.K. (2023). Thermal performance of four cylinders in different layouts of spacing ratios under cross-flow at Reynolds number of 35000. *Ocean Engineering*, 281, 114834. doi: 10.1016/j.oceaneng.2023.114834

[34] Duong, C.Q., Luong, T.D., Nguyen, Q.Q., Phung, D.V., & Pham, P.X. (2023). Developing a computational fluid dynamics model for characterizing the heat transfer for a cross-flow plate heat exchanger in a boosted diesel engine. *SAE Technical Paper* 2023-01-5020. doi: 10.4271/2023-01-5020

[35] Hishikar, P., Gaba, V., Dhiman, S., & Tiwari, A. (2025). Heat transfer analysis of nine cylinders arranged inline and staggered at subcritical Reynolds number. *Numerical Heat Transfer, Part A: Applications*, 86(24), 8795–8816. doi: 10.1080/10407782.2024.2363495

[36] Mohankumar, V., & Prakash, K.A. (2024). Numerical investigation of fluid flow and heat transfer characteristics over double backward-facing step with obstacles. *Heat Transfer Engineering*, 45(9), 779–799. doi: 10.1080/01457632.2023.2220474

[37] Rahman, H. (2025). Reduction of drag force for flow around two side-by-side square cylinders through attached upstream splitters. *Journal of the Brazilian Society of Mechanical Sciences and Engineering*, 47(11), 540. doi: 10.1007/s40430-025-05876-4

[38] Illyas, S.M., MuthuManokar, A., & Kabeel, A.E. (2022). Experimental and computational study on effect of vanes on heat transfer and flow structure of swirling impinging jet. *Journal of Applied Fluid Mechanics*, 16(2), 205–221. doi: 10.47176/jafm.16.02.1296

[39] Chauhan, G., Bisht, V.S., Bhandari, P., Singh, S., Shukla, R., Ranakoti, L., & Bist, A.S. (2025). Numerical investigation of heat transfer enhancement in a double pipe heat exchanger using tangential perforated ring turbulators. *Archives of Thermodynamics*, 177–184. doi: 10.24425/ather.2025.154191

[40] Zhai, X.Q., & Wang, R.Z. (2009). A review for absorption and adsorption solar cooling systems in China. *Renewable and Sustainable Energy Reviews*, 13(6–7), 1523–1531. doi: 10.1016/j.rser.2008.09.022

[41] Henning, H.M. (2007). Solar assisted air conditioning of buildings – An overview. *Applied Thermal Engineering*, 27(10), 1734–1749. doi: 10.1016/j.applthermaleng.2006.07.021

[42] Tawalbeh, M., Salameh, T., Albawab, M., Al-Othman, A., El Haj Assad, M., & Alami, A.H. (2020). Parametric study of a single effect lithium bromide–water absorption chiller powered by a renewable heat source. *Journal of Sustainable Development of Energy, Water and Environment Systems*, 8(3), 464–475. doi: 10.13044/j.sdewes.d7.0290

[43] Arafia, M., Soliman, A., & Ossama, A. (2020). A simulation study of n-butane absorption refrigeration system using commercial hydrocarbons as absorbents. *International Journal of Refrigeration*, 112, 110–124. doi: 10.1016/j.ijrefrig.2020.01.004

[44] Ayou, D.S., & Coronas, A. (2020). New developments and progress in absorption chillers for solar cooling applications. *Applied Sciences*, 10(12), 4073. doi: 10.3390/app10124073

[45] He, Y.L., & Zhang, Y. (2012). Advances and outlooks of heat transfer enhancement by longitudinal vortex generators. In: Hewitt, G.F. (Ed.) *Advances in Heat Transfer* (44, pp. 119–185), Elsevier.

[46] Vengadesan, E., & Senthil, R. (2022). Experimental performance enhancement of a flat plate solar collector using straight and twisted flow inserts. *Environmental Science and Pollution Research*, 29(42), 64232–64243. doi: 10.1007/s11356-022-22223-5

[47] Sözen, A., Özbaş, E., Menlik, T., Çakır, M.T., Gürü, M., & Boran, K. (2014). Improving the thermal performance of diffusion absorption refrigeration system with alumina nanofluids: An experimental study. *International Journal of Refrigeration*, 44, 73–80. doi: 10.1016/j.ijrefrig.2014.04.018

[48] Wang, P., Yoon, S., Yu, Y., & Shen, Z. (2019). Experimental study on the active enhancement mechanisms of heat and mass transfer in an absorption chiller (RP-1462). *Science and Technology for the Built Environment*, 25(1), 58–68. doi: 10.1080/23744731.2018.1498668

[49] Raul, R.B., Panda, S.K. (2021). Heat and Mass Transfer-Enhancement Technique Used for Vapour Absorption Refrigeration System. In: Ramgopal, M., Rout, S.K., Sarangi, S.K. (Eds.) *Advances in Air Conditioning and Refrigeration. Lecture Notes in Mechanical Engineering*. Springer, Singapore. doi: 10.1007/978-981-15-6360-7_33

[50] Shank, K., & Tiari, S. (2023). A review on active heat transfer enhancement techniques within latent heat thermal energy storage systems. *Energies*, 16, 4165. doi: 10.3390/en16104165

[51] Ghodeshwar, A., & Sharma, P. (2018). Thermodynamic analysis of lithium bromide–water (LiBr-H_2O) vapor absorption refrigeration system based on solar energy. *International Research Journal of Engineering and Technology*, 5(1), 1365–1371.

Co-published by
Institute of Fluid-Flow Machinery
Polish Academy of Sciences
Committee on Thermodynamics and Combustion
Polish Academy of Sciences

Copyright©2026 by the Authors under licence CC BY-NC-ND 4.0

http://www.imp.gda.pl/archives-of-thermodynamics/

Heat and Mass Transfer with Entropy Generation in Immiscible Fluid Flow through a Vertical Channel under Slip and Non-Uniform Thermal Conditions

Santhosh Kasula[a*], M.N. Raja Shekar[b]

[a]Sreyas Institute of Engineering and Technology, Hyderabad 500068, Telangana, India
[b]JNTUH University College of Engineering Science and Technology, Hyderabad 500068, Telangana, India
*Corresponding author email: kasula.santhosh54506@gmail.com

Received: 22.10.2025; revised: 19.12.2025; accepted: 04.01.2026

Abstract

The collective influence of slip and asymmetric heating is of great importance in many industries involving micro and macro-scale thermal systems, as it is directly related to flow resistance, thermal gradients and entropy generation. These effects are particularly relevant in channels with immiscible fluids, where wall fluid interactions and spatially varying boundary conditions govern the overall transfer behaviour. So the novelty of this work is a numerical analysis of entropy generation and heat and mass transfer in a vertical channel filled with two immiscible fluids, under a non-uniform heat, along with the influence of velocity slip. The system of governing equations of momentum, energy and diffusion is made non-dimensional using relevant variables, and then solved numerically using the Runge-Kutta method. The momentum, temperature and diffusion variations are presented in a graphical mode using data visualisation and smoothing via interpolation in Python for better visibility of the variations. The momentum, heat and mass transfer rates on both plates of the channel are also made non-dimensional. The other important parameter, entropy, is also calculated in the defined domain, and the obtained values are tabulated. The study found that all parameters, including slip effect, have a significant impact. In particular, the temperature, entropy generation and velocity are strongly affected by buoyancy forces and magnetic fields. The increase in Grashof number and molecular Grashof number improves fluid motion and reduces entropy. Both the increasing Reynolds number and magnetic parameter contribute to an increase in entropy generation. Shear stress analysis reveals two flow layers affected by buoyancy and magnetic damping.

Keywords: Heat and mass transfer; Non-uniform heat; Vertical channel; Entropy; Slip effects

Vol. 47(2026), No. 1, 177–194; doi: 10.24425/ather.2026.158668

Cite this manuscript as: Kasula, S., & Raja Shekar, M.N. (2026). Heat and Mass Transfer with Entropy Generation in Immiscible Fluid Flow through a Vertical Channel under Slip and Non-Uniform Thermal Conditions. *Archives of Thermodynamics*, 47(1), 177−194.

1. Introduction

Heat and mass transfer are fundamental processes that govern the movement of thermal energy and matter within physical systems. Heat flows due to temperature differences, while mass moves from high to low concentration regions. These mechanisms are vital in nature and industry, from climate systems to chemical reactors. Understanding them helps improve efficiency, reduce energy loss, and design better technologies. Fathima et al. [1] investigate the transfer of heat and mass in a two-layer viscous fluid flow affected by buoyancy motion. Profiles of temperature, velocity and concentration are acquired. Reddy et al. [2] explain the flow and heat transfer behaviour of fluids across an elongating surface under the influence of magnetic fields and thermal radiation. The results indicate that the fluid within the geometry exhibits a higher velocity. Srinivasulu and Goud [3] statistically analyse heat and mass transfer in Williamson nanofluid flow across a stretching surface with convective boundary conditions and an aligned magnetic field. Govindarajan et al. [4] analyse heat and mass transfer between two stratified immiscible fluids, focusing on interfacial oscillations and their impact on flow characteristics. They formulate equa-

Nomenclature

b_1, b_2 – thermal and solutal expansion ratios, $b_1 = \beta_{1T}/\beta_{2T}$, $b_2 = \beta_{1C}/\beta_{2C}$
B_0 – magnetic field strength, T
c_i – dimensionless concentration, $c_i = (C_i - C_*)/\Delta C$
C_i – concentration in fluid regions kg m^{-3}
C_*, C_L, C_R– reference and wall concentrations kg m^{-3}
D – mass diffusivity ratio, $D = D_1/D_2$
D_1, D_2 – mass diffusivities, m^2 s^{-1}
Du – Dufour number, Du = $D_1 \cdot K_{T1} \cdot \Delta C/(C_P \cdot C_{S1} \cdot \nu_1 \cdot \Delta T)$
Ec – Eckert number, Ec = $U_0^2/(C_{p1}\Delta T)$
g – acceleration due to gravity, m^2 s^{-1}
Gc – solutal Grashof number, Gc = $g \cdot \beta_{1C} \cdot \Delta C \cdot h_1^3/\nu_1^2$
Gr – thermal Grashof number, Gr = $g \cdot \beta_{1T} \cdot \Delta T \cdot h_1^3/\nu_1^2$
h – height ratio of the two fluid layers, $h = h_1/h_2$
h_1, h_2 – half widths of region 1 and region 2, m
k – micro polar fluid material parameter, $k = K/\mu_1$
K – vortex (spin) viscosity, Pa s
K_{T1}, K_{T2}–thermal conductivities, W m^{-1} K^{-1}
K_T – thermal conductivity ratio, $K_T = K_{T1}/K_{T2}$
m – dynamic viscosity ratio, $m = \mu_1/\mu_2$
M – magnetic interaction (Hartmann) parameter, $M = \sigma \cdot B_0^2 \cdot h_1^2/\mu_1$
n – dimensionless micro-rotation, $n = (h_1/u_0) \cdot N$
N – micro-rotation, s^{-1}
Pr – Prandtl number, Pr = ν_1/α_1
R – Reynolds number, $R = U_0 h_1/\nu_1$
Sc – Schmidt number, Sc = ν_1/D_1
Sr – Soret number, Sr = $D_1 \cdot K_{T1} \cdot \Delta T/(T_m \cdot D_1 \cdot \Delta C)$
T_i – fluid temperature, K
T_*, T_L, T_R–reference and wall temperatures, K
u_i – dimensionless axial velocity, $u_i = U_i/U_0$
U_0 – reference (mean) velocity, m s^{-1}
U_i – axial velocity in regions, m s^{-1}
y – dimensionless transverse coordinate in each region, $y = Y/h_i$
Y – transverse coordinate, m

Greek symbols

α – thermal conductivity ratio, $\alpha = k_1/k_2$
β – variable thermal conductivity parameter
β_{1T}, β_{2T}– thermal expansion coefficients, K^{-1}
β_{1C}, β_{2C}– solutal expansion coefficients, kg^{-1} m^{-3}
θ_i – dimensionless temperature $\theta_i = (T_i - T_*)/\Delta T$
θ_r – variable viscosity parameter
μ_1, μ_2 – dynamic viscosity, Pa s
$\mu\xi$ – dimensionless velocity slip parameter, $\mu\xi = \mu\xi^*/h_1$
$\mu\xi^*$ – dimensional velocity slip parameter, m
ρ_0 – reference density, kg m^{-3}
ρ_1, ρ_2 – fluid densities, kg m^{-3}
σ – electrical conductivity, S m^{-1}
ψ – dimensionless concentration ratio, $\psi = C_L/\Delta C$
ω, η – frequency parameters for thermal modulation, $\omega = \omega^*/h_1$, $\eta = \eta^*/h_2$
ω^*, η^* – dimensional frequency parameters, s^{-1}
Ω – dimensionless temperature ratio, $\Omega = T_L/\Delta T$

tions for mass, momentum, energy and concentration, examining parameters affecting the Nusselt and Sherwood numbers. Rabha and Deka [5] focus on heat and mass transfer in a porous medium with variable temperature and mass diffusion, specifically in the context of an accelerated plate. Nurni et al. [6] discuss heat and mass transfer in dynamic process systems, emphasising that simultaneous consideration of both transfers is essential, particularly during state transitions. Jan et al. [7] investigate the magnetohydrodynamic squeezing flow of an incompressible fluid through porous media exhibiting viscous dissipation, generated by converging parallel plates. The response surface methodology can help make important factors like magnetic strength, porosity and Eckert number better for predicting skin friction and heat transfer. Research helps to reduce drag and improve heat transfer in magnetohydrodynamic generators, extrusion processes and lubrication systems. Kumaraswamy et al. [8] consider internal heat sources, thermal conductivity, thermal slip and changing viscosity. They look at shear stress, Nusselt number, Sherwood number, temperature, diffusion profiles and velocity and angular velocity. The findings provide insights for engineering optimisation by highlighting the ways in which heat source intensity affects flow behaviour and transfer rates. Baithalu et al. [9] examine heat and mass transfer across an expanding surface within porous media, considering many effects. Based on their findings, using similarity transformations, the velocity and shear rate were diminished, whereas the fluid temperature rose with the increasing Eckert number.

Heat and mass transfer in a vertical channel involves the simultaneous flow of thermal energy and substances across vertical surfaces. This flow is driven by temperature and concentration differences. Natural convection and diffusion play a role in this process. It is essential in areas such as cooling systems, chemical processing and solar energy technologies. The interaction between thermal and solutal effects can either promote or hinder flow stability. Understanding these mechanisms is vital for the effective design and operation of engineering systems. Ouedraogo et al. [10] describe heat and mass transfer in a vertical channel under laminar forced convection, emphasising the significant impact of inlet fluid temperature on flow patterns and hydrodynamic fields, with latent heat transfer as the primary mode. Kalyan et al. [11] explore the heat and mass flow of two immiscible Jeffrey fluids within a vertical channel. Kemparaju et al. [12] investigate thermosolutal flow and heat mass transfer in a vertical porous annulus with localised vertical heating and insulated horizontals. In-line source-sink configurations optimise the circulation compared to alternatives; thermal mass dissipation is the highest through the upper source in counter-flow or through the lower inner source in other scenarios. A study by Baluguri et al. [13] offers a mathematical model for convective heat and mass transfer of two immiscible fluids in a vertically varying channel, considering diffusion-thermal effects and thermo-diffusion.

In a vertical channel with immiscible fluids, heat and mass transfer refers to the simultaneous motion of materials and thermal energy between two vertical surfaces that have two immiscible liquid layers. The interface between the fluids is essential, as variations in density, viscosity, thermal conductivity and diffusivity influence convection and diffusion processes. These systems are prevalent in applications like liquid heat exchangers, petroleum processing and environmental flows, where interfacial tension and buoyancy-driven motion govern the overall transfer properties. Comprehending these interconnected sys-

tems is crucial for enhancing performance and ensuring stability in both industrial and natural processes. The effects of Grashof numbers, viscosity ratio and heat generation on fluid flow and heat transfer are examined by Kandagal and Kempepatil [14] in their investigation of heat and mass transfer in vertical channels with immiscible fluid flow through a porous matrix. Kumar et al. [15] investigate the influence of radiation, Soret and Dufour effects on the laminar flow of a rotating fluid over a permeable plate amid chemical processes. The finite element method and similarity transformations are used to figure out the profiles of velocity, temperature and concentration. Gosty et al. [16] investigate heat and mass transfer in a vertical channel with immiscible fluids, focusing on slip effects. They analyse how variations in thermal conductivity and viscosity influence fluid dynamics, revealing significant interactions among slip mecha-nisms and engineering parameters like the Nusselt and Sherwood numbers. Srinivas et al. [17] explain heat and mass transfer in a vertical channel with immiscible fluids, focusing on variable viscosity and velocity slip. They reveal significant correlations affecting velocity, angular velocity, temperature and diffusion. Umavathi and Sheremet [18] analysed mixed convection in vertical channels, where a viscous fluid is sandwiched between nanofluids in a porous medium. The effects of the Grashof and Brinkman numbers, solid volume fraction and porous parameter on the velocity and temperature fields are investigated. Suresh et al. [19] investigate thermal slip's impact on heat and mass transfer in immiscible fluid flow within a vertical channel, highlighting that increased thermal slip decreases velocity and temperature profiles, while the Grashof and molecular Grashof numbers enhance fluid dynamics.

When two non-mixing liquids exchange thermal energy and species, heat and mass are transmitted along a vertical conduit filled with immiscible fluids, and entropy is created. This process is affected by interfacial phenomena and variations in characteristics. Entropy generation, arising from heat conduction, mass diffusion and viscous dissipation, quantifies irreversibility. It also enhances efficiency in thermal fluid systems. Naseem et al. [20] examine the generation of entropy in magnetohydrodynamic viscous flow across a permeable, radially extending disk, integrating Joule heating and radiative effects. Suction slows down the flow and heat transfer, while injection speeds them up. Magnetic fields reduce entropy near the disk, but their effects are weaker at greater distances.

Ghasemi and Ranjbar [21] numerically analyse entropy generation in a water-based alumina nanofluid flowing through vertical channels, considering the simultaneous effects of both forced and natural convection in a vertical channel with immiscible fluids. In a vertical channel with immiscible fluids, Suresh Babu et al. [22] explore heat and mass transmission, highlighting the impact of slip effects. They investigate the effects of viscosity and thermal conductivity variations on entropy generation, revealing complex interactions resulting from various thermal distributions and slip circumstances. Abdel et al. [23] investigate entropy generation in a micropolar fluid flowing through a corrugated channel, considering convective and slip boundary conditions. Mebarek-Oudina et al. [24] examine the magnetohydrodynamic flow of Burgers' fluid over a stretching cylinder, focusing on internal heat generation and absorption as well as temperature-dependent heat sources. Using similarity variables, the boundary layer equations are turned into ordinary differential equations. The BVP4C method is then used to find the velocity and temperature profiles.

In their study of entropy formation in the flow of a micropolar fluid via a vertical microchannel, Usha and Gireesha [25] took into consideration the combined effects of thermal radiation, viscous dissipation and Joule heating. In order to give a thorough grasp of the thermodynamic irreversibility in the system, the study additionally included convective boundary conditions. Kumar and Yadav [26] focus on analysing the entropy production characteristics of two non-miscible fluids, specifically couple stress and Newtonian fluids within an inclined porous channel. Govindarajulu et al. [27] investigate the entropy generation within a magnetohydrodynamic pulsatile flow of a third-grade hybrid nanofluid. The study focuses on the flow occurring between two vertical porous walls, considering several influencing factors, and analysing their effects on various physical quantities. Nayak et al. [28] conduct a computational analysis of the effects of the interfacial layer and shape on the Darcy-Forchheimer magnetohydrodynamic flow of single-walled and multi-walled carbon nanotube water nanofluids, including nonlinear thermal radiation and chemical processes. Enhanced nanoparticle form factors accelerate axial and radial flows while impeding tangential flow between disks, thereby affecting temperature, concentration, skin friction, Nusselt number, entropy and Bejan number profiles. Reddy et al. [29] investigate the complex behaviour of cross-flow fluid flow within microchannels, focusing on thermal and entropy generation aspects under specific conditions. The formation of entropy in the flow of Newtonian and immiscible micropolar fluids through a conduit was examined by Yadav et al. [30]. The investigation emphasised the impact of immiscibility of the micropolar and Newtonian viscous fluids on overall flow behaviour by looking at thermal properties, entropy production, flow velocity and Bejan number profiles. Prasad et al. [31] formulate a mathematical model for melting heat transmission in nanofluid flow using chemical processes and Joule heating. Complex nonlinear partial differential equations are simplified to ordinary differential equations by similarity transformations.

Khan et al. [32] explain Caputo fractional derivatives to elucidate memory effects in unsteady mixed convection within porous concentric cylinders. The temperature-dependent viscosity model is addressed by an implicit finite difference method, and the production of entropy from heat transfer, friction and porous resistance is analysed.

Shamshuddin and Ibrahim [33] examine the constant electromagnetohydrodynamic flow of a reactive Casson micropolar nanofluid between rotating parallel plates. The finite element method is employed to statistically resolve the issue while considering the influences of electric and magnetic forces. Madhuri et al. [34] examine heat transmission and nanofluid flow over a porous rotating disc influenced by buoyancy forces, incorporating thermal radiation effects via the Rosseland and Boussinesq approximations. Finite element study indicates that, although thermal radiation significantly influences temperature distribution, augmenting the volume fraction of nanoparticles enhances heat transfer efficiency. To optimise heat transmis-

sion, buoyancy forces alter flow topologies, impacting the thermal and velocity boundary layers.

Jan et al. [35] incorporate viscous dissipation and Ohmic heating while analysing boundary layer flow, thermal dynamics and hydrodynamic behaviour in battery systems utilising nanoparticles under cross non-Newtonian fluid conditions. Artificial neural networks in machine learning utilise numerical information to predict temperature distribution, heat transfer rates and energy efficiency, considering shear-thinning and thickening processes.

From the reviewed literature, it is observed that the present concept has not been previously addressed, i.e. entropy analysis in immiscible fluids in a vertical channel, considering the velocity slip. This study examines heat and mass transfer and entropy generation in a vertical channel containing immiscible fluids under non-uniform thermal distribution, considering the slip effect on the left wall. Entropy production, transfer rates and flow dynamics are all impacted by the interplay between fluid layers and temperature changes. To examine thermodynamic irreversibility and system performance, governing equations are solved. The findings demonstrate how important parameters affect the efficiency of heat and mass transfer. Entropy analysis sheds light on optimisation techniques and energy loss. The results help improve multi-fluid systems' thermal management.

2. Mathematical formulation

As shown in Fig. 1, the geometry is regarded as a vertical channel with two plates located at $Y = -h_1$ and $Y = h_2$ to investigate the entropy generation, heat and mass transfer in a vertical channel with immiscible fluids and non-uniform thermal distribution. The flow is thought to be fully formed. There are two regions in the channel: 0 to $-h_1$ and 0 to h_2. One of these regions is filled with micropolar fluid, while the other is filled with viscous fluid. Angular momentum characteristics are added to examine the nature of the system in the first region, which has micro-rotation. The system is assumed to satisfy the Boussinesq approximation.

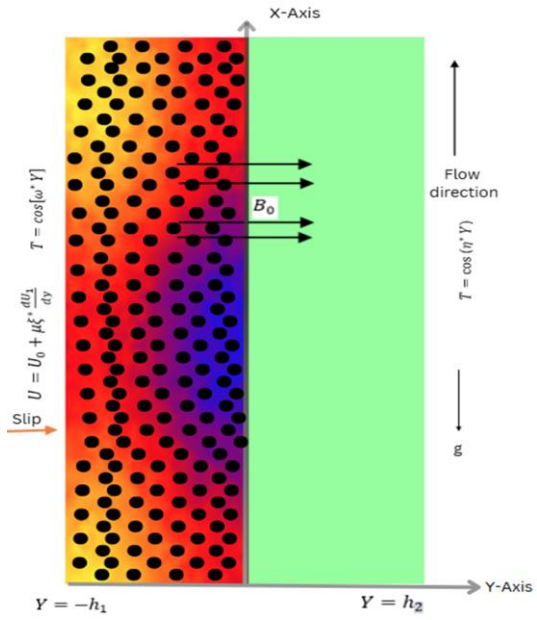


Fig. 1. Schematic diagram of the investigated system.

2.1. Governing equations

The governing equations for momentum, energy and species diffusion are derived based on the assumptions outlined in the mathematical formulation.

$$\frac{\partial U_1}{\partial Y} = 0, \frac{\partial U_2}{\partial Y} = 0, \tag{1}$$

$$\rho_1 = \rho_0[1 - \beta_{1T}(T_1 - T_*) - \beta_{1C}(C_1 - C_*)],$$

$$\rho_2 = \rho_0[1 - \beta_{2T}(T_2 - T_*) - \beta_{2C}(C_2 - C_*)], \tag{2}$$

$$\left(\mu_1 + \frac{K}{2}\right) {h_1}^2 \frac{\partial^2 N}{\partial Y^2} - K\left(2N + \frac{\partial U_1}{\partial Y}\right) = 0, \tag{3}$$

$$\frac{1}{\rho_1}\frac{\partial}{\partial Y}(\mu_1 + K)\frac{\partial U_1}{\partial Y} + \frac{K}{\rho_1}\frac{\partial N}{\partial Y} + g\beta_{1T}(T_1 - T_*) +$$

$$+ g\beta_{1C}(C_1 - C_*) - \sigma\frac{B_0^2 U_1}{\rho_1} = 0, \tag{4}$$

$$\frac{1}{\rho_2}\frac{\partial}{\partial Y}\left(\mu_2\frac{\partial U_2}{\partial Y}\right) + g\beta_{2T}(T_2 - T_*) +$$

$$+ g\beta_{2c}(C_2 - C_*) - \sigma\frac{B_0^2 U_2}{\rho_2} = 0, \tag{5}$$

$$\frac{\partial}{\partial Y}(K_{T1}\frac{\partial T_1}{\partial Y}) + \mu_1\left(\frac{\partial U_1}{\partial Y}\right)^2 + \frac{\rho_1 D_1 K_{T1}}{C_{s1}}\frac{\partial^2 C_1}{\partial Y^2} = 0, \tag{6}$$

$$\frac{\partial}{\partial Y}(K_{T2}\frac{\partial T_2}{\partial Y}) + \mu_2\left(\frac{\partial U_2}{\partial Y}\right)^2 + \frac{\rho_2 D_2 K_{T2}}{C_{s2}}\frac{\partial^2 C_2}{\partial Y^2} = 0, \tag{7}$$

$$D_1\frac{\partial^2 C_1}{\partial Y^2} + \frac{D_1 K T_1}{T_m}\frac{\partial^2 T_1}{\partial Y^2} = 0, \tag{8}$$

$$D_2\frac{\partial^2 C_2}{\partial Y^2} + \frac{D_2 K_{T2}}{T_m}\frac{\partial^2 T_2}{\partial Y^2} = 0. \tag{9}$$

2.2. Entropy generation

The dimensional entropy production for the current problem is derived as given by Bejan [36]:

$$E_{gen} = E1_{gen} + E2_{gen} \tag{10}$$

where:

$$E1_{gen} = \frac{1}{h_1 T_L}\int_{-h_1}^{0}[\mu_1 + K]\left(\frac{dU_1}{dY}\right)^2 dY +$$

$$+ \frac{1}{{h_1}{T_L}^2}\int_{-h_1}^{0} K_{T_1}\left(\frac{dT_1}{dY}\right)^2 dY + \frac{1}{h_1}\int_{-h_1}^{0}\frac{\sigma {B_0}^2 {U_1}^2}{T_L} dY +$$

$$+ \frac{1}{{C_L}^2 h_1}\int_{-h_1}^{0} D_1\left(\frac{dC_1}{dY}\right)^2 dY,$$

$$E2_{gen} = \frac{1}{h_2 T_R}\int_{0}^{h_2}\mu_2\left(\frac{dU_2}{dY}\right)^2 dY + \frac{1}{{h_2}{T_R}^2}\int_{0}^{h_2} K_{T_2}\left(\frac{dT_2}{dY}\right)^2 dY +$$

$$+ \frac{1}{h_2}\int_{0}^{h_2}\frac{\sigma {B_0}^2 {U_2}^2}{T_R} dY + \frac{1}{{C_R}^2 h_2}\int_{0}^{h_2} D_2\left(\frac{dC_2}{dY}\right)^2 dY.$$

2.3. Boundary and interface conditions

The flow domain consists of two immiscible fluid layers confined between two vertical plates separated by a total width of $h_1 + h_2$. The left wall $Y = -h_1$ is maintained at a prescribed oscillatory temperature distribution, and allows velocity slip and

thermal modulation. At the interface $Y = 0$, both the velocity and the stress are continuous, as are the temperature, heat flux, concentration and mass flux. The right wall $Y = h_2$ is also maintained with thermal modulation controlled by another parameter.

2.3.1. Dimensional form

At $Y = -h_1$ we have:

$$U = U_0 + \mu\xi^* \frac{dU_1}{dy}, \quad T = \cos(\omega^* Y), \quad C = C_*, \quad N = 0. \quad (11a)$$

At $Y = 0$:

$$U_1 = U_2, \quad \frac{dN}{dY} = 0, \quad T_1 = T_2, \quad C_1 = C_2, \quad \mu_1 \frac{dU_1}{dY} = \mu_2 \frac{dU_2}{dY},$$
$$k_{T1} \frac{dT_1}{dY} = k_{T2} \frac{dT_2}{dY}, \quad D_1 \frac{dC_1}{dY} = D_2 \frac{dC_2}{dY}. \quad (11b)$$

At $Y = h_2$:

$$U = 0, \qquad T = \cos(\eta^* Y), \qquad C = C_*. \quad (11c)$$

2.3.2. Non-dimensional form

At $y = -1$ we have:

$$u_1 = 1 + \mu\xi \frac{du_1}{dy}, \quad \theta_1 = \cos(\omega y), \quad n = 0, \quad c_1 = 1. \quad (12a)$$

At $y = 0$:

$$u_1 = u_2, \quad \frac{dn}{dy} = 0, \quad \theta_1 = \theta_2, \quad c_1 = c_2, \quad \frac{du_2}{dy} = mh \frac{du_1}{dy},$$
$$\frac{d\theta_2}{dy} = h\,\alpha \frac{d\theta_1}{dy}, \quad \frac{dc_2}{dy} = Df \frac{dc_1}{dy}. \quad (12b)$$

At $y = 1$:

$$u_2 = 0, \qquad \theta_2 = \cos(\eta y), \qquad c_2 = 0. \quad (12c)$$

2.3.3. Physical interpretation

The boundary condition on the right wall incorporates a velocity slip effect governed by the dimensionless parameter $\mu\xi$. For $\mu\xi = 0$, the surface behaves as a classical no-slip wall, whereas increasing $\mu\xi > 0$ allows partial fluid slippage, accounting for rarefaction effects, micro layer formation, or surface coatings that reduce shear resistance. The temperature at each wall varies periodically with Y to simulate thermal oscillations or uneven wall heating. At the fluid interface ($y = 0$), continuity of velocity, temperature and concentration ensures smooth transfer of momentum, heat and mass between the two immiscible layers, while equality of their respective fluxes ensures conservation across the interface.

2.4. Non-dimensional system

The governing equations and the respective boundary conditions are converted into non-dimensional forms as follows, which are given in region 1 and region 2:

$$\frac{d^2 n}{dy^2} - \frac{2k}{2+k}\left(2n + \frac{du_1}{dy}\right) = 0, \quad (13)$$

$$k\frac{dn}{dy} + \frac{\theta_r}{(\theta_1-\theta_r)^2}\frac{d\theta_1}{dy}\frac{du_1}{dy} - \frac{\theta_r}{\theta_1-\theta_r}\frac{d^2u_1}{dy^2} + $$
$$+\frac{\mathrm{Gr}}{\mathrm{R}}\theta_1 + \frac{\mathrm{Gc}}{\mathrm{R}}c_1 - Mu_1 = 0, \quad (14)$$

$$\beta\left(\frac{d\theta_1}{dy}\right)^2 + (1+\beta\theta_1)\frac{d^2\theta_1}{dy^2} - \mathrm{PrEc}\frac{\theta_r}{\theta_1-\theta_r}\left(\frac{du_1}{dy}\right)^2 + \mathrm{Du}\frac{d^2c_1}{dy^2} = 0, \quad (15)$$

$$\frac{1}{\mathrm{Sc{\cdot}R}}\frac{d^2c_1}{dy^2} + \mathrm{Sr}\frac{d^2\theta_1}{dy^2} = 0, \quad (16)$$

$$\frac{\theta_r}{(\theta_2-\theta_r)^2}\frac{d\theta_2}{dy}\frac{du_2}{dy} - \frac{\theta_r}{(\theta_2-\theta_r)}\frac{d^2u_2}{dy^2} + \frac{1}{a{\cdot}b{\cdot}f^2}\frac{\mathrm{Gr}}{\mathrm{R}}\theta_2 + $$
$$+\frac{1}{a{\cdot}b{\cdot}f^2}\frac{\mathrm{Gc}}{\mathrm{R}}c_2 - Mu_2 = 0, \quad (17)$$

$$\beta\left(\frac{d\theta_2}{dy}\right)^2 + (1+\beta\theta_2)\frac{d^2\theta_2}{dy^2} - a\,\mathrm{Pr\,Ec}\left(\frac{\theta_r}{\theta_2-\theta_r}\right)\left(\frac{du_2}{dy}\right)^2 +$$
$$+\mathrm{Du}\frac{d^2c_2}{dy^2} = 0, \quad (18)$$

$$\frac{f}{d\,\mathrm{Sc\,R}}\frac{d^2c_2}{dy^2} + \frac{f{\cdot}\mathrm{Sr}}{K_T{\cdot}d}\frac{d^2\theta_2}{dy^2} = 0. \quad (19)$$

The non-dimensional transfer rates on the boundaries using the non-dimensional variables are obtained as:

– shear stress on the channel's left plate:

$$st_1 = \left[\frac{du_1}{dy}\right]_{y=-1}, \quad (20a)$$

– shear stress on the channel's right plate:

$$st_2 = \left[\frac{du_2}{dy}\right]_{y=1}, \quad (20b)$$

– Nusselt number on the channel's left plate:

$$\mathrm{Nu}_1 = \left[\frac{d\theta_1}{dy}\right]_{y=-1}, \quad (20c)$$

– Nusselt number for the channel's right plate:

$$\mathrm{Nu}_2 = \left[\frac{d\theta_2}{dy}\right]_{y=1}, \quad (20d)$$

– Sherwood number on the channel's left plate:

$$\mathrm{Sh}_1 = \left[\frac{dc_1}{dy}\right]_{y=-1}, \quad (20e)$$

– Sherwood number on the channel's right plate:

$$\mathrm{Sh}_2 = \left[\frac{dc_2}{dy}\right]_{y=1}. \quad (20f)$$

Entropy in the considered domain is obtained in the non-dimensional form as:

$$e_{gen} = e1_{gen} + e2_{gen}, \quad (21)$$

where:

$$e1_{gen} = \mathrm{PrEc}\int_{-1}^{0}\left[\frac{\theta_r - k(\theta_1-\theta_r)}{\theta_1-\theta_r}\left(\frac{du_1}{dy}\right)^2\right]dy +$$
$$+\frac{1}{\Omega}\int_{-1}^{0}\left[(1+\beta\theta_1)\left(\frac{d\theta_1}{dy}\right)^2\right]dy + \frac{1}{\mathrm{Sc}\,\psi^2}\int_{-1}^{0}\left(\frac{dc_1}{dy}\right)^2 dy +$$
$$+M{\cdot}\mathrm{Pr}{\cdot}\mathrm{Ec}\int_{-1}^{0}({u_1}^2)\,dy,$$

$$e2_{gen} = \frac{h\,\mathrm{PrEc}\,\alpha}{m}\int_0^1 [(\frac{\theta_r - k(\theta_2-\theta_r)}{\theta_2-\theta_r})\left(\frac{du_2}{dy}\right)^2]\,dy +$$

$$+\frac{h}{\Omega}\int_0^1 [(1+\beta\,\theta_2)\left(\frac{d\theta_2}{dy}\right)^2]\,dy + \frac{d}{\mathrm{Sc}\psi^2}\int_0^1 \left(\frac{dc_2}{dy}\right)^2 dy +$$

$$+\frac{MPr\mathrm{Ec}\,\alpha}{h}\int_0^1 (u_2{}^2)\,dy.$$

3. Solution of the problem

The non-dimensional system of Eqs. (13) to (19), subjected to boundary conditions Eqs. (12a−12c), are solved using the Mathematica package under the ND Solve technique. Using an integrated shooting strategy, the boundary value problem will be transformed into an initial value problem. The required coefficients will then be computed until the required precision of 10^{-5} is achieved. The method's convergence is confirmed by meeting the boundary requirements. Utilising the formulas found in Eqs. (20a−20f), the rates of mass and heat transmission are determined. The entropy is also calculated from the obtained non-dimensional Eq. (21). All the governing parameter values are considered in possible combinations to analyse the variations in the form of graphs.

4. Results and discussion

The effects of important physical factors, such as the Grashof number (Gr), molecular Grashof number (Gc), magnetic field parameter (M), Reynolds number (R), material parameter (k), variable viscosity parameter (θ_r), velocity slip parameter ($\mu\zeta$), Soret number (Sr), Schmidt number (Sc), dimensionless temperature ratio (Ω), dimensionless concentration ratio (ψ), Eckert number (Ec), Dufour number (Du), variable thermal conductivity (β) and frequency parameters (ω, η) were carefully examined and presented in graphical mode using data visualisation and smoothing via interpolation in Python for better visibility of the variations.

4.1. Analysis of velocity, angular velocity, temperature, and concentration

Figures 2−7 depict the variations of velocity with respect to Grashof number (Gr), molecular Grashof number (Gc), magnetic field (M), Reynolds number (R), material parameter (k) and velocity slip parameter ($\mu\zeta$). The increase in molecular Grashof number (Gc) provides a modest enhancement in velocity due to mass transfer effects, but elevated Grashof numbers (Gr) and material parameters (k) significantly enhance the flow by augmenting buoyancy forces and favourable material characteris-

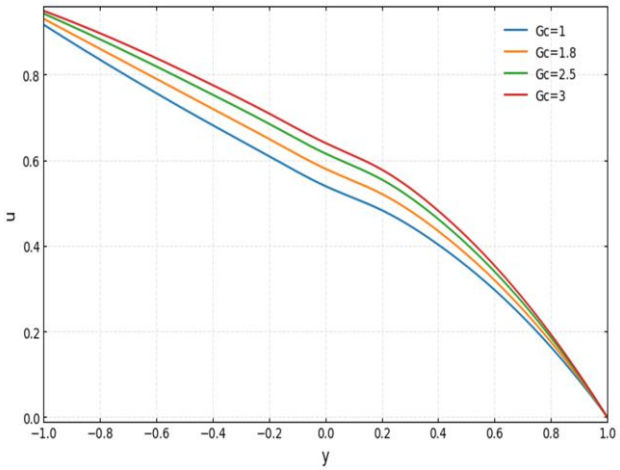


Fig. 3. Change of velocity with respect to molecular Grashof number (Gc).

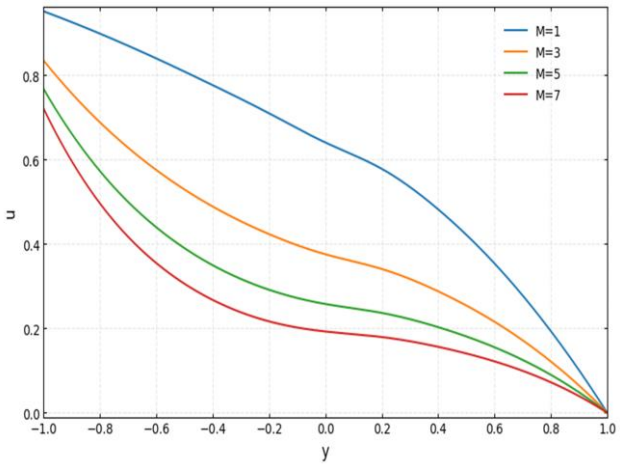


Fig. 4. Change of velocity with respect to the magnetic field (M).

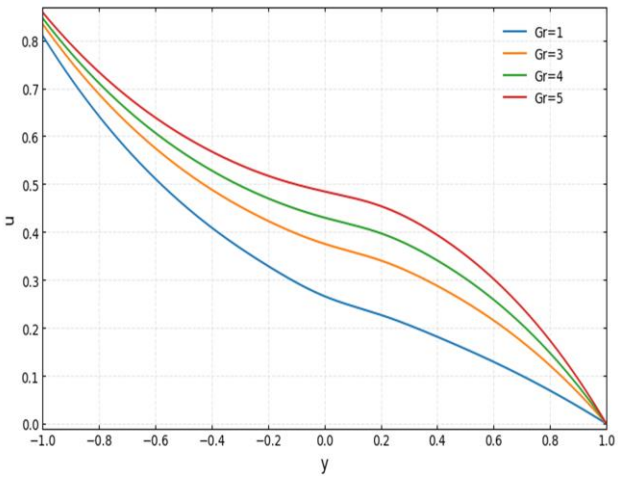


Fig. 2. Change of velocity with respect to Grashof number (Gr).

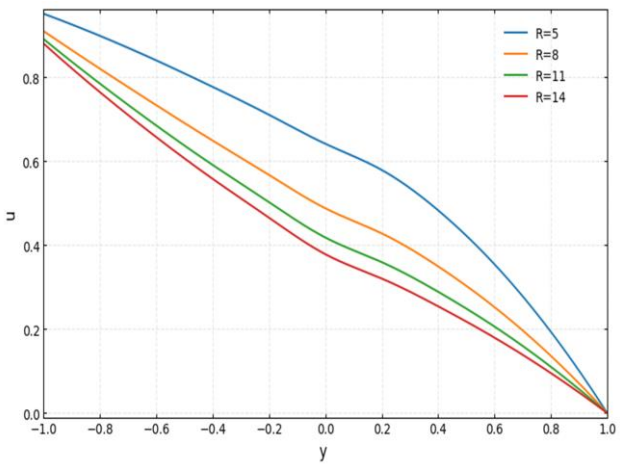


Fig. 5. Change of velocity with respect to Reynolds number (R).

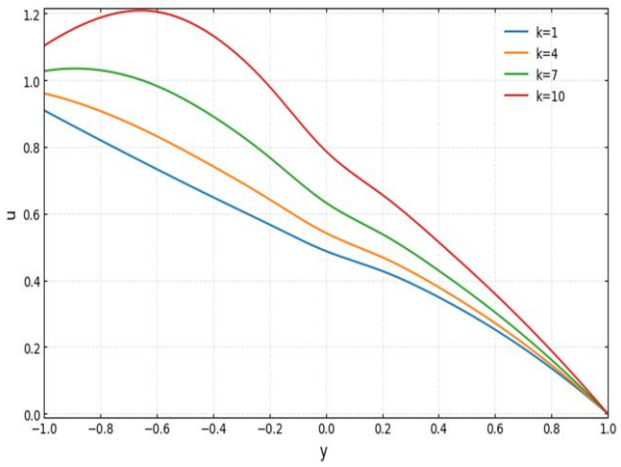


Fig. 6. Change of velocity with respect to the material parameter (k).

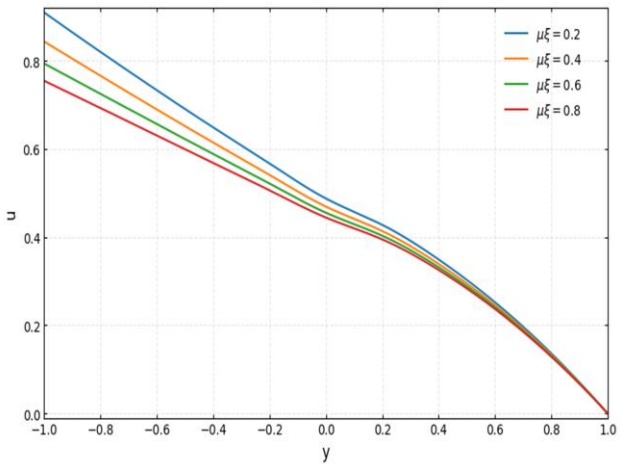


Fig. 7. Change of velocity with respect to the velocity slip parameter ($\mu\xi$).

tics. The effect of buoyancy forces is significant on both thermal and solutal Grashof numbers. Conversely, inertial forces tend to resist the flow. The presence of a magnetic field further suppresses the velocity due to the Lorentz force. Consequently, an increase in the Reynolds number (R) and magnetic parameter (M) leads to a marked reduction in velocity. However, the velocity slip parameter ($\mu\xi$) exhibits comparatively weaker damping, while higher viscosity increases flow resistance under slip conditions.

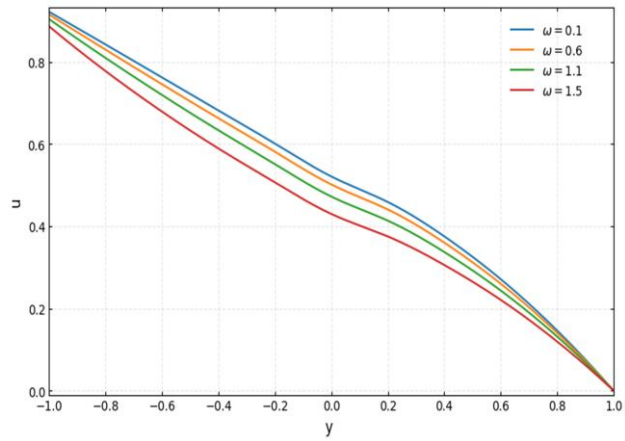


Fig. 8. Change of velocity with respect to frequency parameter (ω).

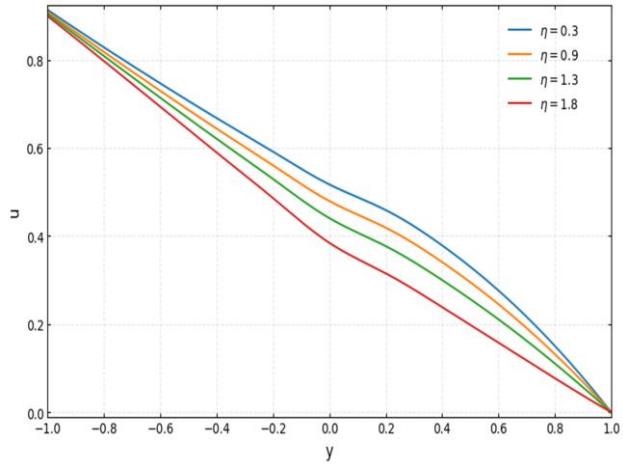


Fig. 9. Change of velocity with respect to frequency parameter (η).

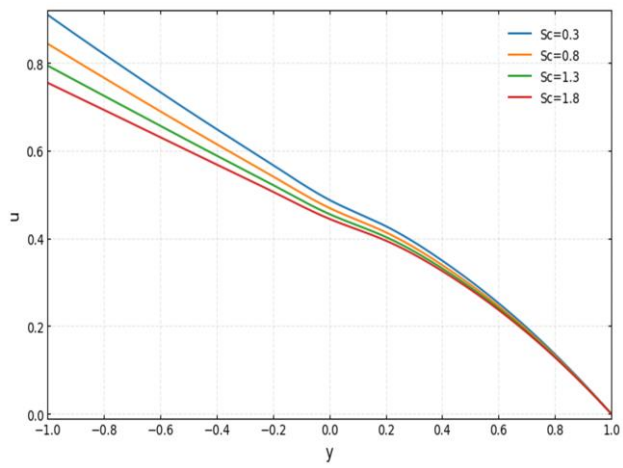


Fig. 10. Change of velocity with respect to Schmidt number (Sc).

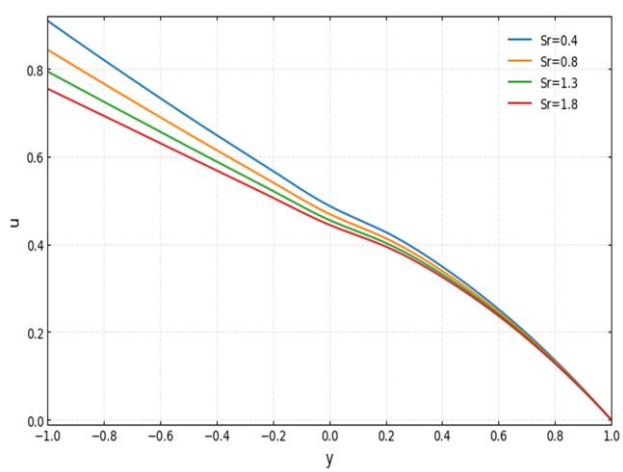


Fig. 11. Change of velocity with respect to Soret number (Sr).

In Figs. 8–13, it is demonstrated that when any of the parameters like frequency parameters (η, ω), Schmidt number (Sc),

Soret number (Sr), dimensionless temperature ratio (Ω) and dimensionless concentration ratio (ψ) increases, then a decrease in velocity is observed across the whole domain.

Since the increased viscosity decreases the mobility of fluids, this reduction becomes more apparent with the increasing values of frequency. This is due to oscillatory or time-dependent forcing effects on the fluid. Simultaneously, additional variables reduce velocity by increasing the mass diffusivity, altering heat diffusion, and quickening the rates of concentration. This effect is due to the increased momentum diffusivity to mass diffusivity ratio. Also, the thermophoresis effect on velocity is significant. So, upon the variation of the Soret number, these pertinent parameters vary. The dimensionless temperature ratio represents the relative temperature difference between the channel walls or fluid layers, and the dimensionless concentration ratio reflects the relative concentration difference between the plates or fluid layers. Since the non-uniform heating is applied, these effects are significant.

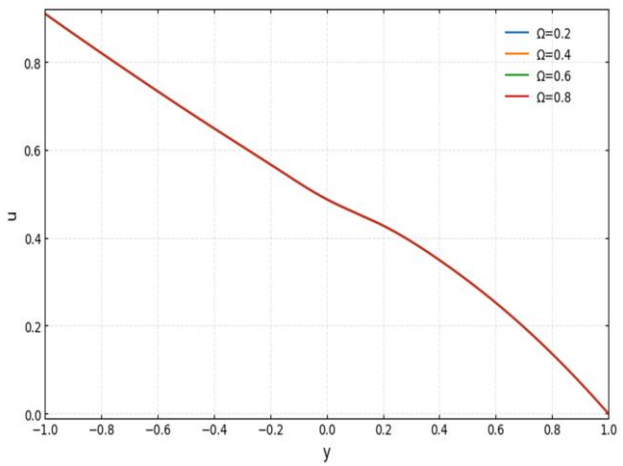


Fig. 12. Change of velocity with respect to dimensionless temperature ratio (Ω).

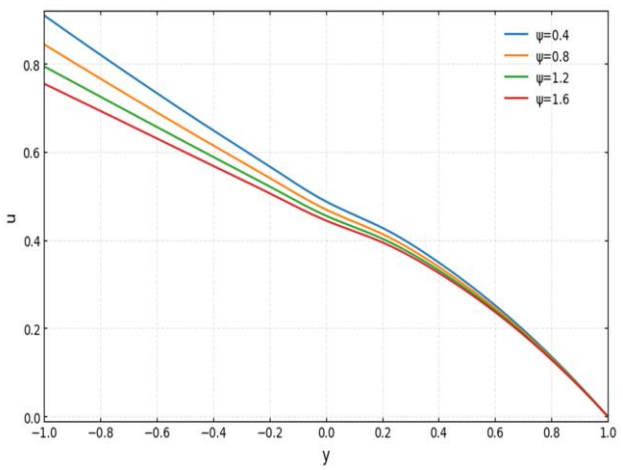


Fig. 13. Change of velocity with respect to dimensionless concentration ratio (ψ).

The temperature profiles (Figs. 14–19) illustrate the different effects of various parameters on the thermal behaviour of the fluid. Increased buoyant forces that enhance heat transfer result in a small temperature increase in the core region as the Grashof number (Gr) escalates. Magnetic damping reduces the velocity and allows for more heat accumulation, leading to a gradual yet consistent increase in temperature with a higher magnetic field value (M). Elevated Reynolds numbers (R) signify poorer convective cooling at reduced velocities, resulting in increased temperatures. As the material parameter (k) increases, the tempera-

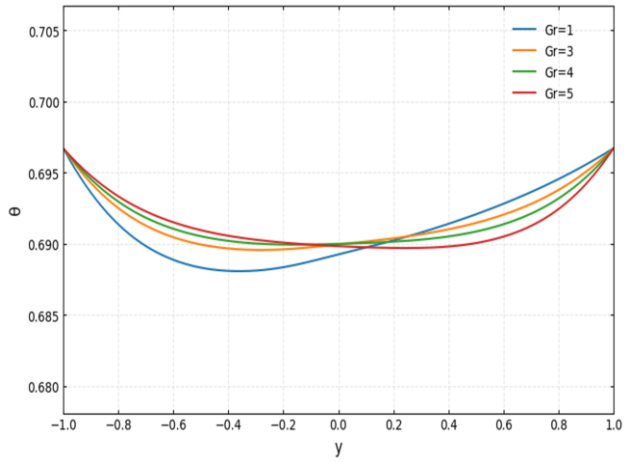


Fig. 14. Change of temperature with respect to Grashof number (Gr).

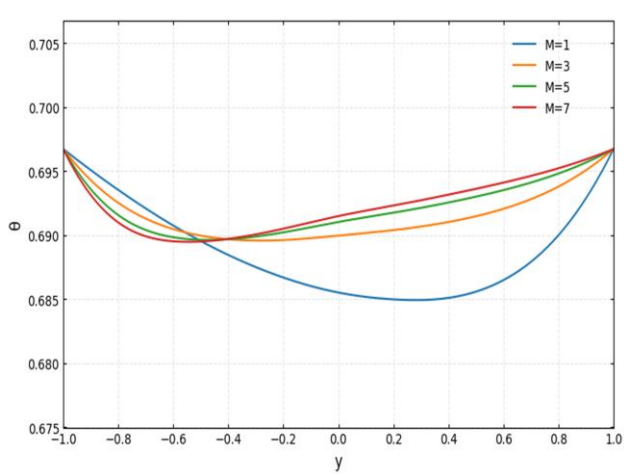


Fig. 15. Change of temperature with respect to magnetic field (M).

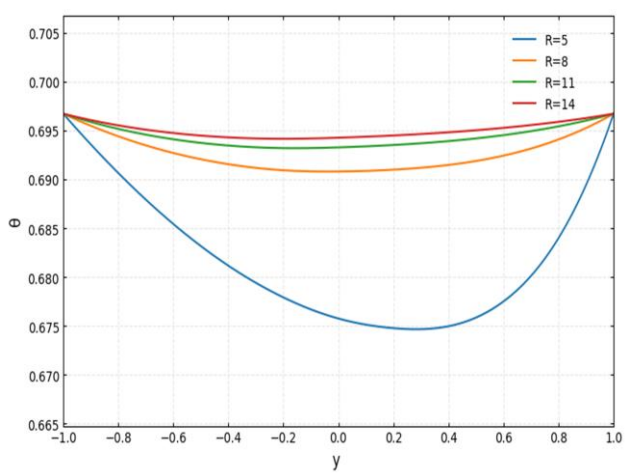


Fig. 16. Change of temperature with respect to Reynolds number (R).

ture decreases, indicating enhanced thermal conductivity that facilitates heat dissipation.

An increase in the variable viscosity parameter (θ_r) leads to a slight rise in temperature, indicating additional heat generation within the system. As the Eckert number (Ec) rises, the temperature profile diminishes, indicating heightened viscous dissipation effects that facilitate localised cooling in the core and convert kinetic energy into thermal energy. The temperature increases with factors that enhance heat retention, whereas its distribution is significantly influenced by mechanisms that promote heat loss or induce thermal fluctuations.

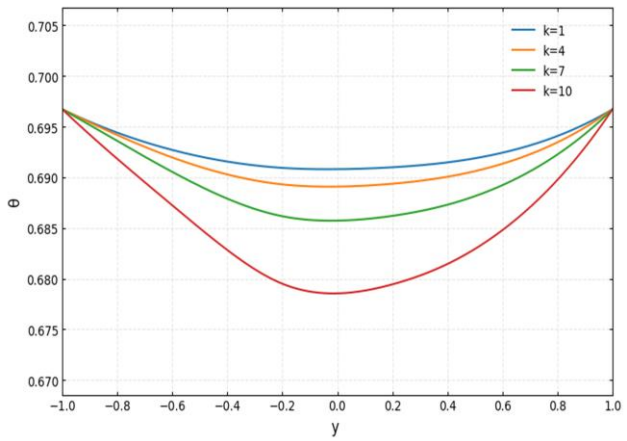


Fig. 17. Change of temperature with respect to material parameter (k).

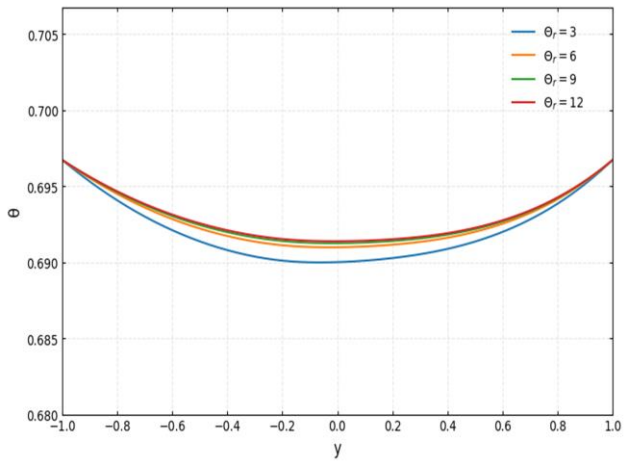


Fig. 18. Change of temperature with respect to viscosity parameter (θ_r).

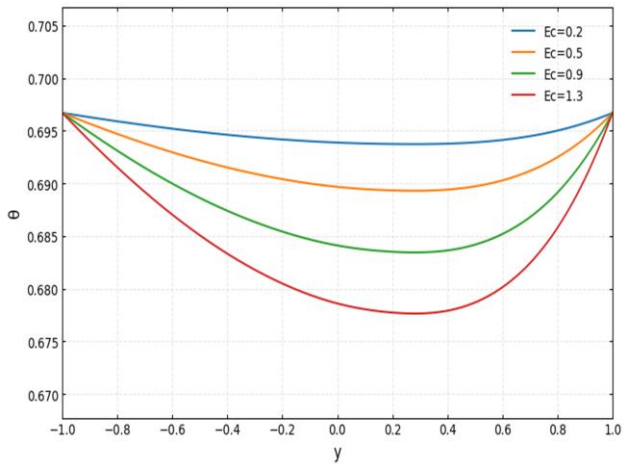


Fig. 19. Change of temperature with respect to Eckert number (Ec).

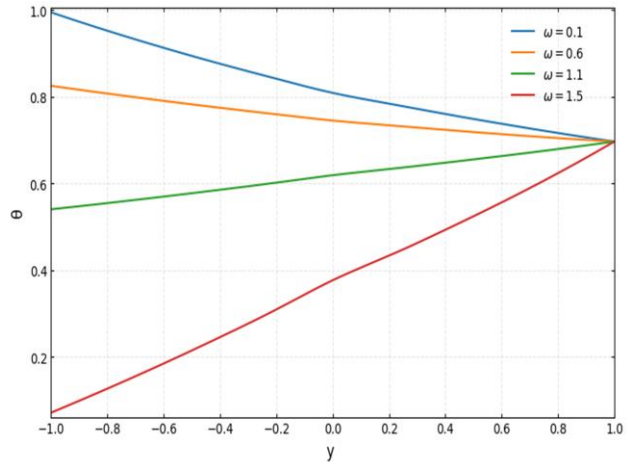


Fig. 20. Change of temperature with respect to non-uniform temperature amplitude (ω).

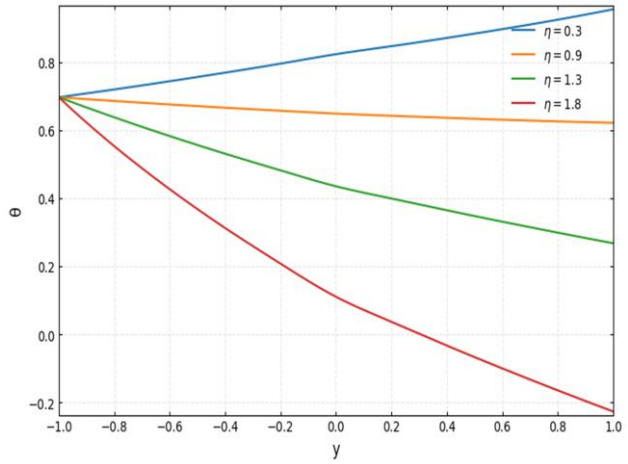


Fig. 21. Change of temperature with respect to non-uniform temperature amplitude (η).

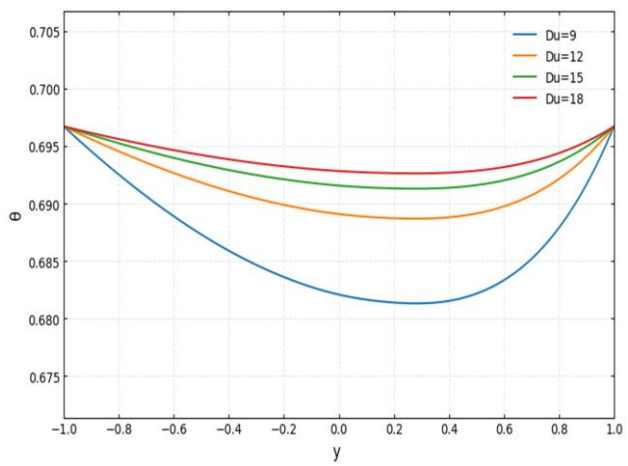


Fig. 22. Change of temperature with respect to Dufour number (Du).

The impact of different parameters on the thermal behaviour of the system is depicted in the temperature profiles in Figs. 20−28. The temperature profile is significantly influenced by the frequency parameter (ω). Elevated values markedly alter the distribution and slope, signifying pronounced thermal oscillations. The temperature distribution is significantly influenced by an increase in the frequency parameter (η), since elevated η markedly reduces the temperature in certain areas of the domain due to increased thermal non-uniformity. The significance of thermal mass diffusion coupling is further underscored by the observation that an increased Dufour number (Du) results in a temperature decrease at the centre, and in a small increase towards the walls. The minimal variation in the Schmidt number (Sc) and Soret number (Sr) indicates that mass diffusivity and thermodiffusion exert a diminished influence on temperature.

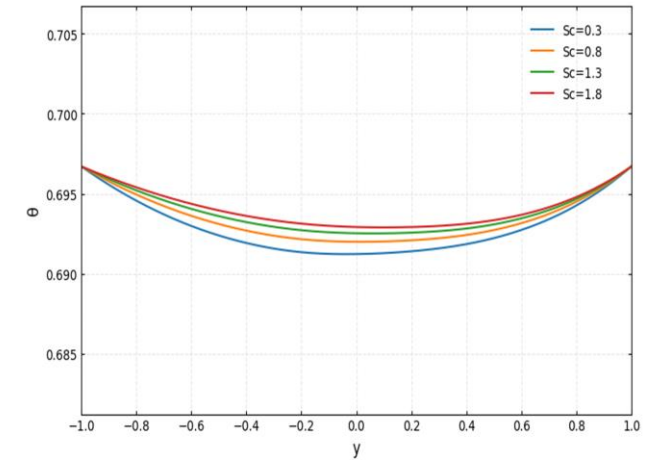


Fig. 23. Change of temperature with respect to Schmidt number (Sc).

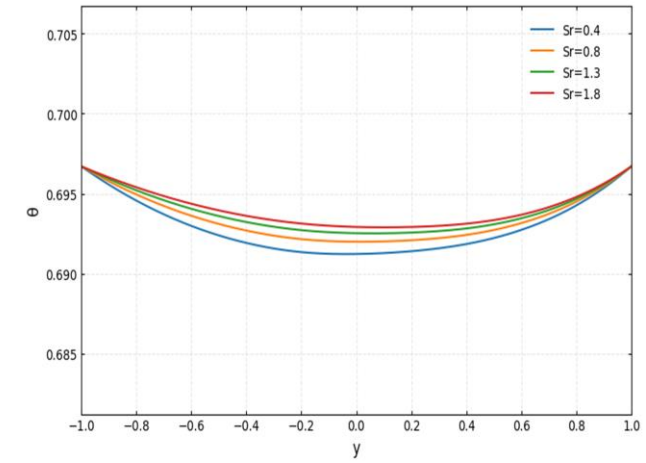


Fig. 24. Change of temperature with respect to Soret number (Sr).

As it ascends, variable thermal conductivity (β) diminishes the temperature, signifying enhanced thermal conduction or related physical resistance. An increase in the velocity slip parameter $\mu\xi$ causes a small increase in the temperature profile, which then becomes more uniform throughout the entire region. More slip at the wall reduces thermal gradients, leading to a more uniform distribution of temperature. Different values of the dimensionless temperature ratio (Ω) are shown by different temperature profiles (Ω), which are almost the same and do not change much as Ω goes up. Finally, for elevated values, the dimensionless concentration ratio (ψ) increases the temperature marginally, presumably due to contributions from exothermic reactions.

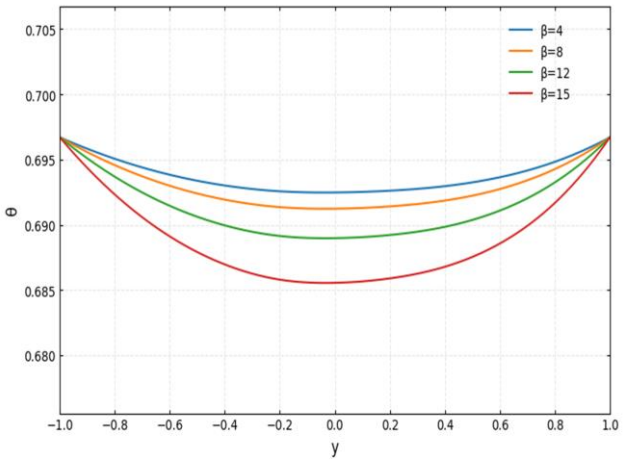


Fig. 25. Change of temperature with respect to variable thermal conductivity (β).

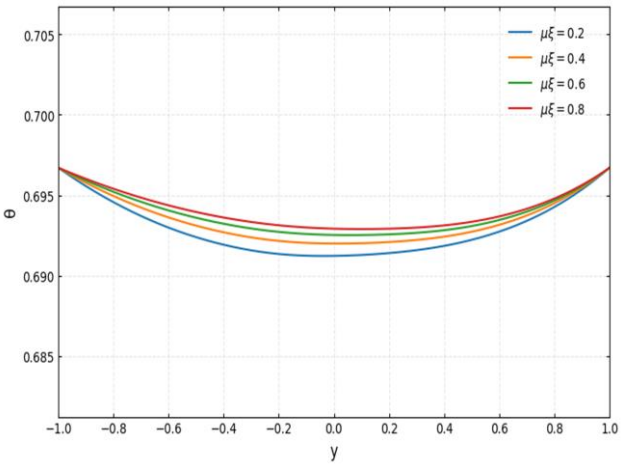


Fig. 26. Change of temperature with respect to the velocity slip parameter ($\mu\xi$).

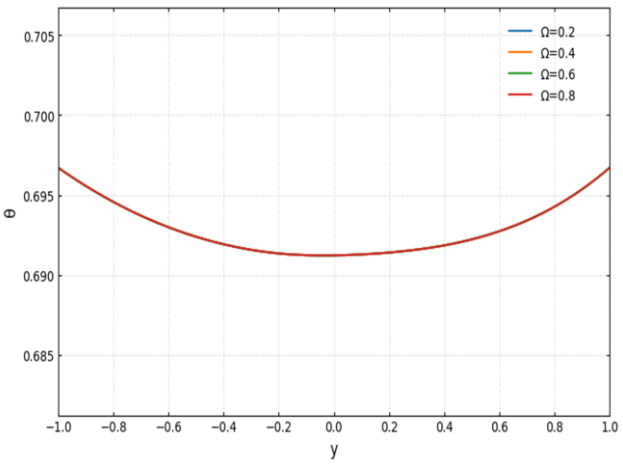


Fig. 27. Change of temperature with respect to the dimensionless temperature ratio (Ω).

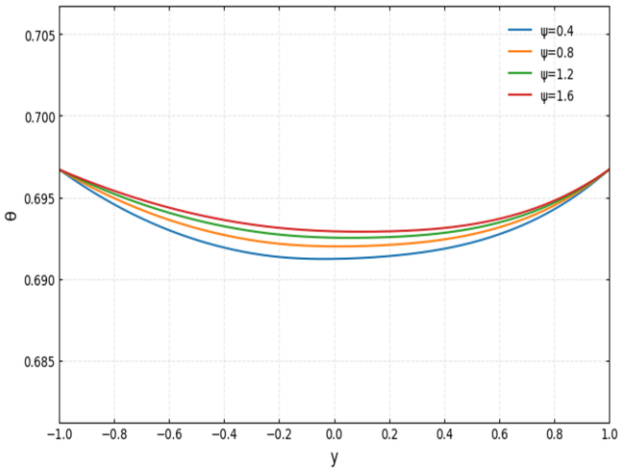


Fig. 28. Change of temperature with respect to dimensionless concentration ratio (ψ).

The angular momentum profiles in Figs. 29–38 show that different parameters have varying effects on the distribution of momentum. The angular momentum is increased throughout the domain by increasing the Reynolds number (R) and the magnetic field parameter (M). The effect is more significant for greater M due to the influence of magnetic forces on rotational flow, and for bigger R because of the augmented inertial effects. Beneficial material qualities enhance rotational motion, as demonstrated by the significant positive impact of the material parameter (k), with the angular momentum markedly increasing for elevated values of k. The variable viscosity parameter (θ_r) leads to a minor enhancement in angular momentum, suggesting that alterations in viscosity slightly affect rotational characteristics. The angular momentum experiences a minor rise with an elevation in the frequency parameter ω, whereas the frequency parameter η exerts a more pronounced positive influence, perhaps due to enhanced thermal gradients that facilitate rotational motion. When the dimensionless temperature ratio (Ω) increases, the value of angular momentum rises gradually, but the overall change remains very small. This shows that varying Ω has only a minor effect on angular momentum within the domain.

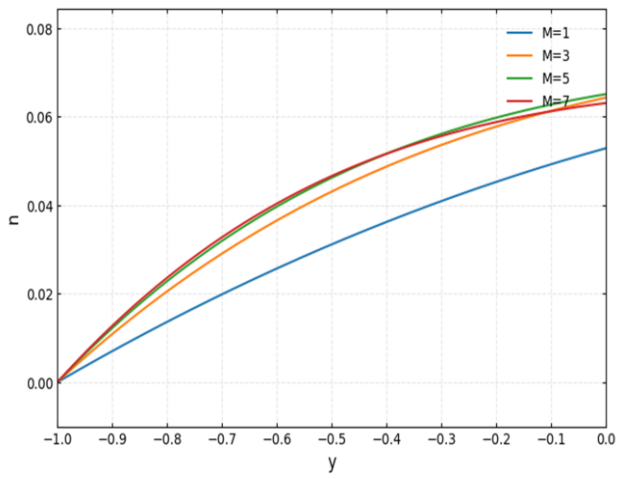


Fig. 29. Change of angular momentum with respect to magnetic field (M).

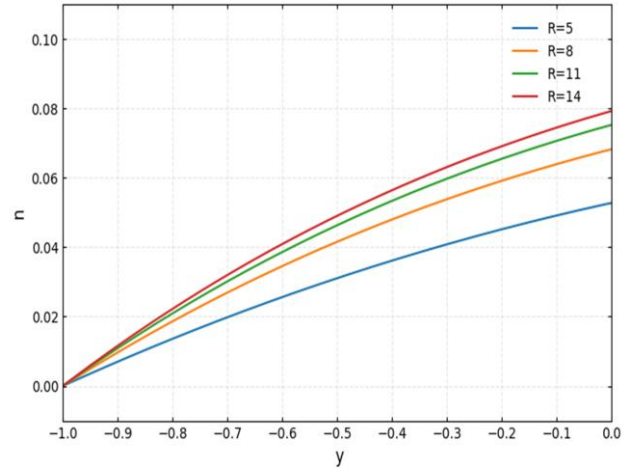


Fig. 30. Change of angular momentum with respect to Reynolds number (R).

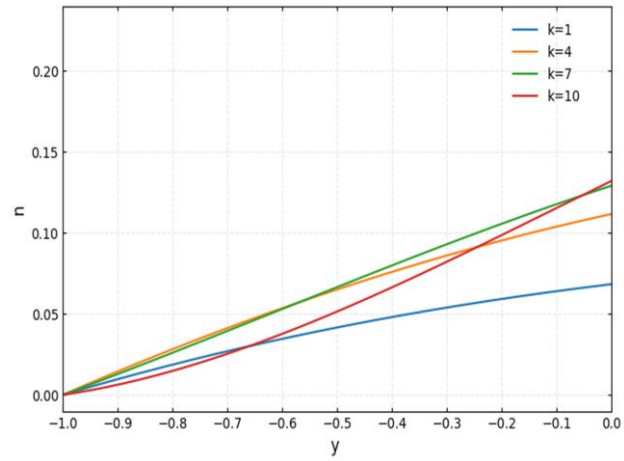


Fig. 31. Change of angular momentum with respect to material parameter (k).

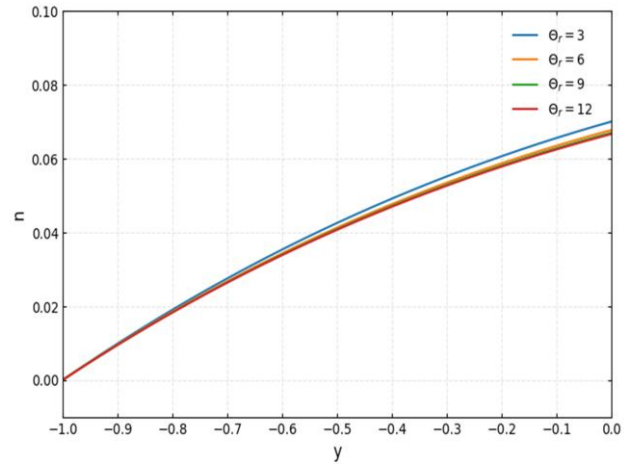


Fig. 32. Change of angular momentum with respect to viscosity parameter (θ_r).

A higher Schmidt number (Sc), dimensionless concentration ratio (ψ) and velocity slip parameter ($\mu\xi$) collectively diminish the angular momentum, indicating that the enhanced resistance

to mass diffusivity, reaction rates, and viscosity effects hinder rotational flow.

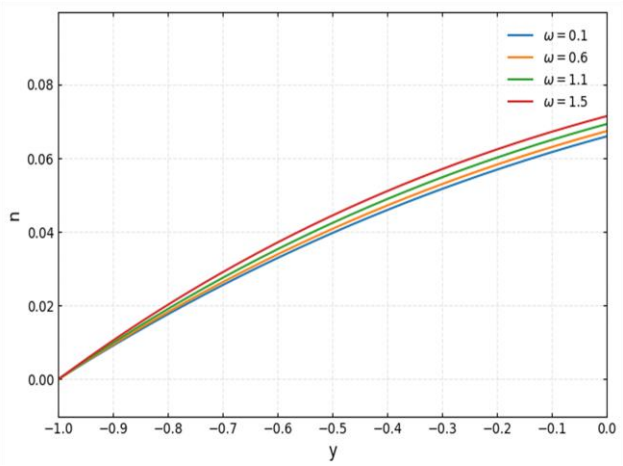


Fig. 33. Change of angular momentum with respect to non-uniform temperature amplitude (ω).

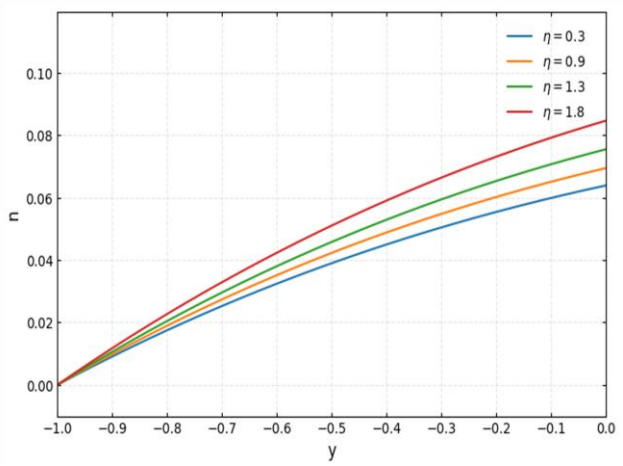


Fig. 34. Change of angular momentum with respect to non-uniform temperature amplitude (η).

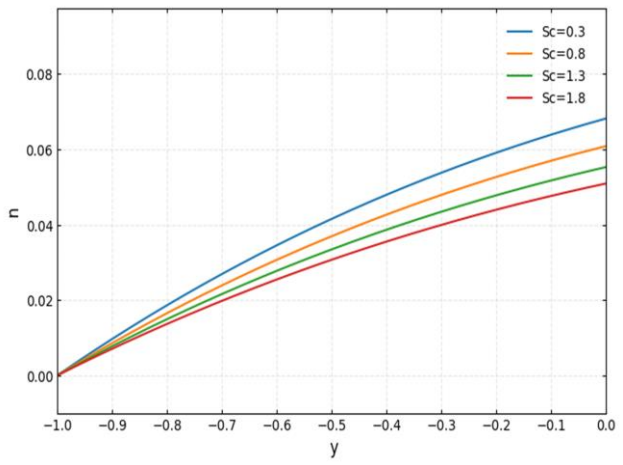


Fig. 35. Change of angular momentum with respect to Schmidt number (Sc).

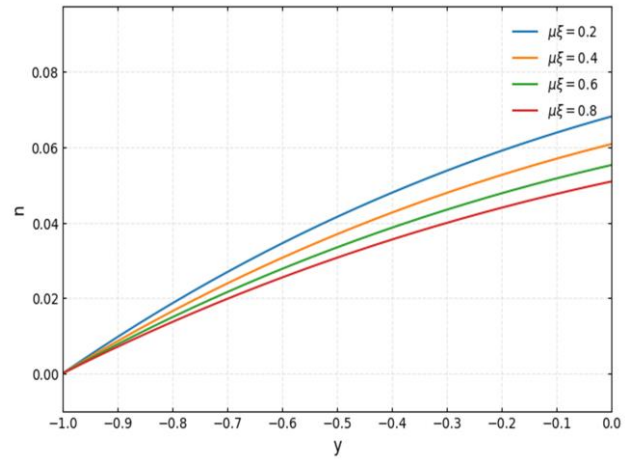


Fig. 36. Change of angular momentum with respect to the velocity slip parameter ($\mu\zeta$).

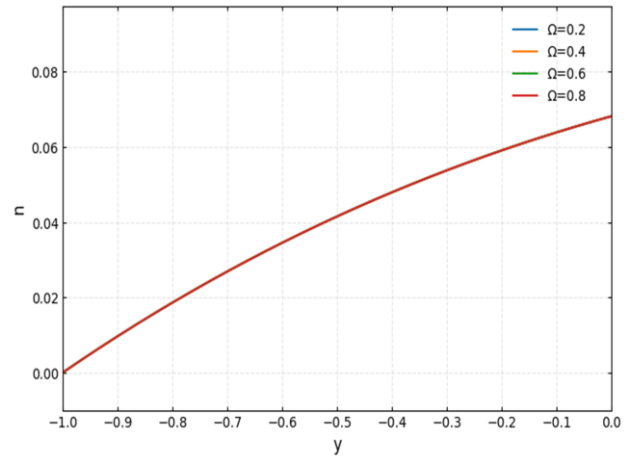


Fig. 37. Change of angular momentum with respect to dimensionless temperature ratio (Ω).

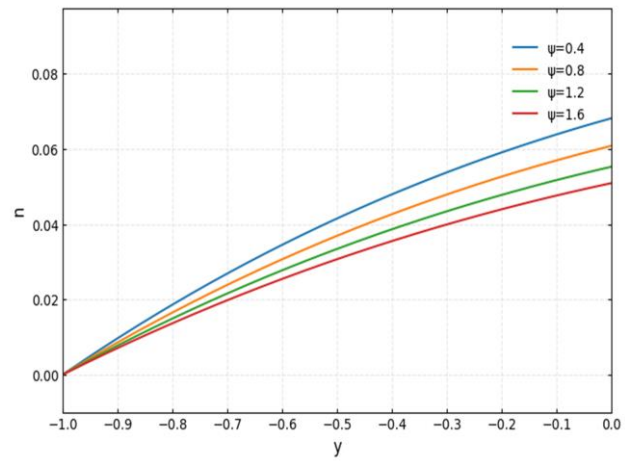


Fig. 38. Change of angular momentum with respect to dimensionless concentration ratio (ψ).

The concentration profiles illustrated in Figs. 39–45 indicate that, except for frequency parameters (ω, η), which produce more significant alterations, many parameters exert only a neg-

ligible influence on species concentration. An insignificant reduction in concentration occurs with an increase in Reynolds number (R) and material parameter (k), suggesting a marginal enhancement in mixing and heat transfer.

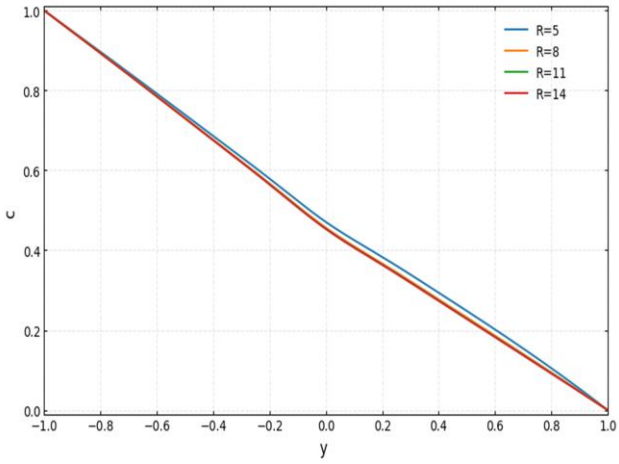


Fig. 39. Change of diffusion with respect to Reynolds number (R).

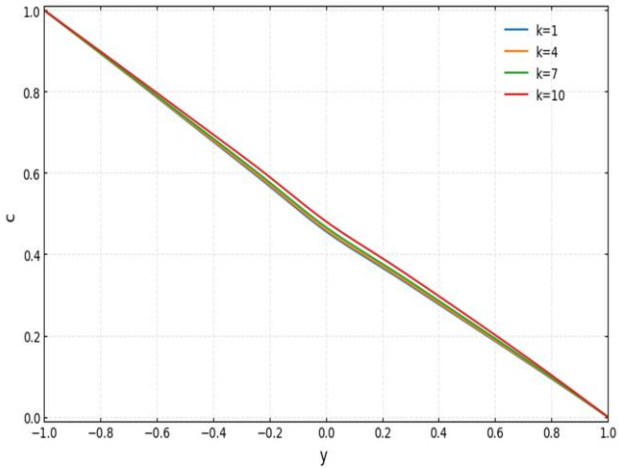


Fig. 40. Change of diffusion with respect to material parameter (k).

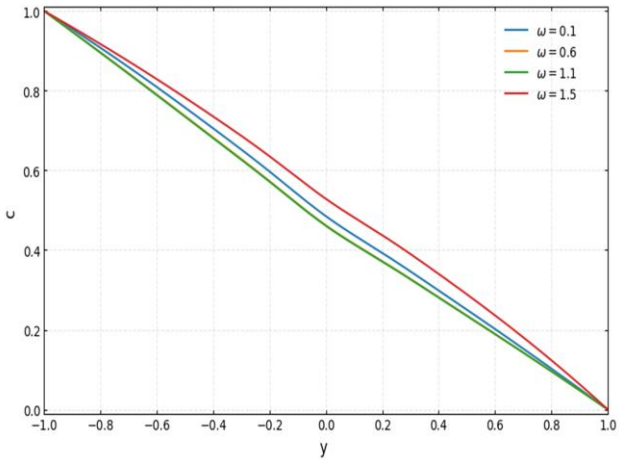


Fig. 41. Change of diffusion with respect to non-uniform temperature amplitude (ω).

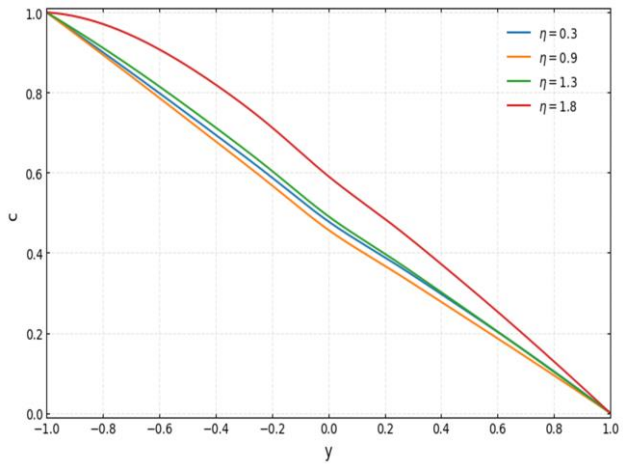


Fig. 42. Change of diffusion with respect to non-uniform temperature amplitude (η).

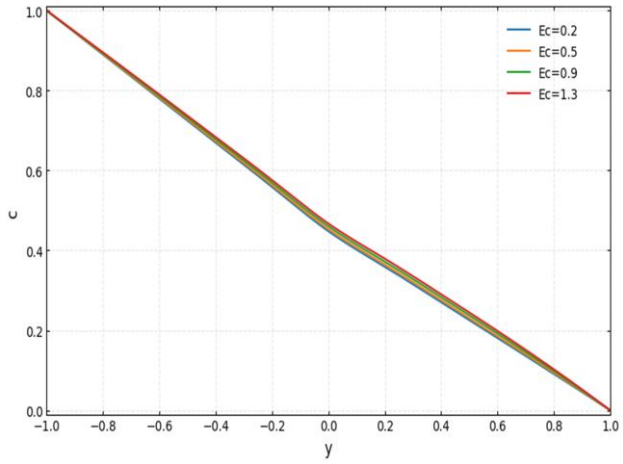


Fig. 43. Change of diffusion with respect to Eckert number (Ec).

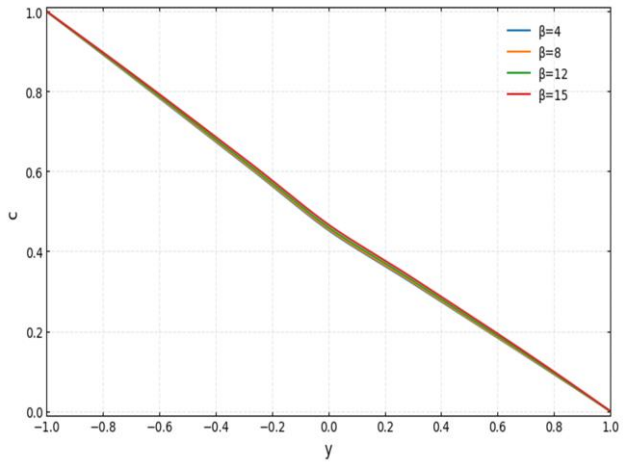


Fig. 44. Change of diffusion with respect to variable thermal conductivity (β).

The increased η significantly elevates concentration in certain areas of the domain due to enhanced thermal non-uniformity, facilitating mass transfer, while the elevated ω marginally raises concentration near the left border. In this context, vis-

cous heating and its related effects exert a minimal impact on concentration, as seen by the insignificant influence of the β parameter and Eckert number (Ec). For all values of the velocity slip parameter $\mu\xi$, the value of c decreases steadily from left to right without much difference between the curves. This indicates that changing $\mu\xi$ has almost no effect on diffusion over the entire domain. The distribution can be substantially altered by η and ω, while other factors induce only minor variations.

4.2. Analysis of the heat transfer rate

The non-dimensional transfer rates on the boundaries obtained using Eq. (20) are presented in the form of bar charts. Figures 46a and 46b depict the variations of Nusselt number for various pertinent parameters. It is very clear that the rate of transfer on both boundaries is largely influenced by these parameters, particularly in the presence of magnetic fields, heat loss, temperature and concentration fluctuations. According to the variations in the Nusselt number, for most parameters, Nu_1 and Nu_2 move in opposition to one another, which means that Nu_1 decreases and Nu_2 increases. The thermal and buoyancy factors (Gr), (Gc), and (M) have a significant impact on enhancing heat transmission, as seen in Fig. 46a, with Nu_2 displaying large positive peaks. Figure 46b demonstrates that the most significant parameter is always Nu_2, while slip and thermal conductivity parameters have a minimal impact on convective heat transfer. This indicates that in these circumstances, thermal performance is improved.

According to the shear stress profiles, for most parameters, both st_1 and st_2 exhibit negative trends. In other words, the flow zone has an increased wall resistance. Shear stress behaviour is influenced by buoyancy and magnetic factors, as seen by changes in wall drag intensity in Fig. 47a. The distribution of shear stress is altered by permeability and slip parameters, as seen in Fig. 47b. Wall friction tends to decrease with increasing slip conditions, allowing fluid to flow more easily close to the edges.

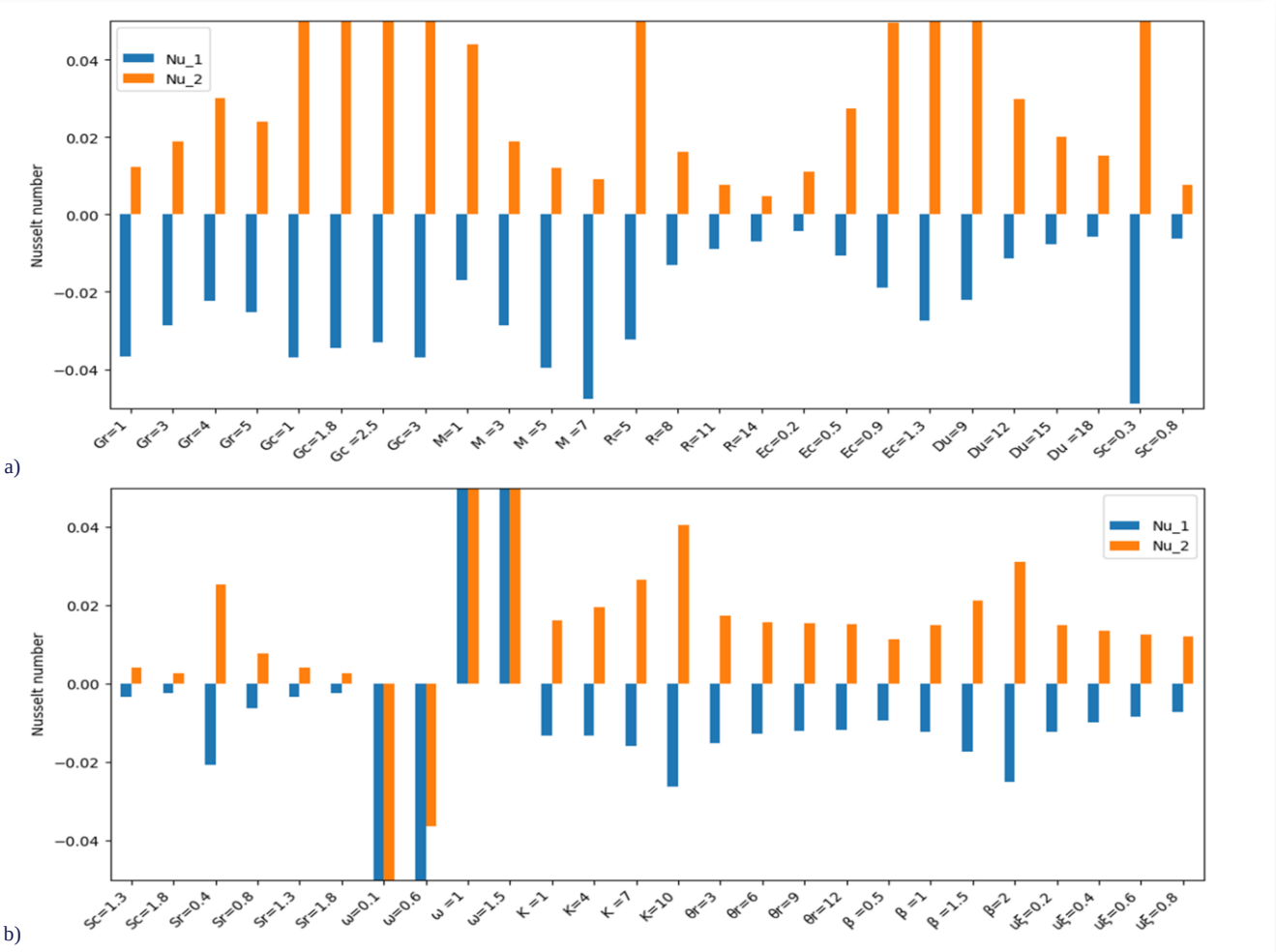


Fig. 46. Nusselt number variations for different parameters.

The Sherwood number distributions demonstrate that Sh_1 and Sh_2 remain almost constant with relatively minor variations across all values. This implies that the features of mass transmission remain unchanged. Buoyancy and magnetic-related parameters have a minor impact on concentration gradients in Fig. 48a, which implies that they have a minor impact on diffusion rates. Small variations in Sherwood numbers are caused by permeability and slip effects, as seen in Fig. 48b. Consequently, there is a little reduction in mass transfer at the channel walls due to improved slip conditions.

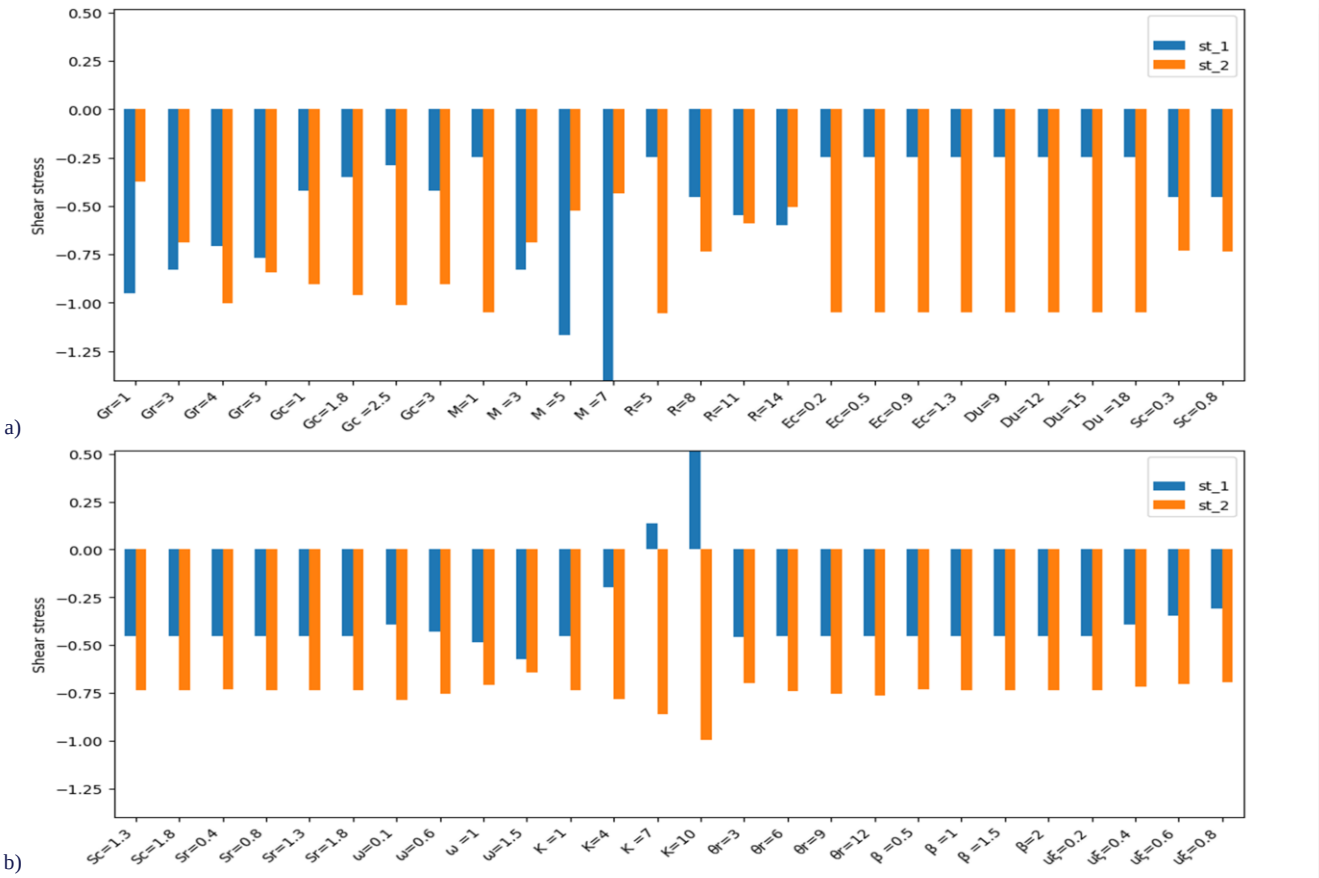


Fig. 47. Shear stress number variations for different parameters.

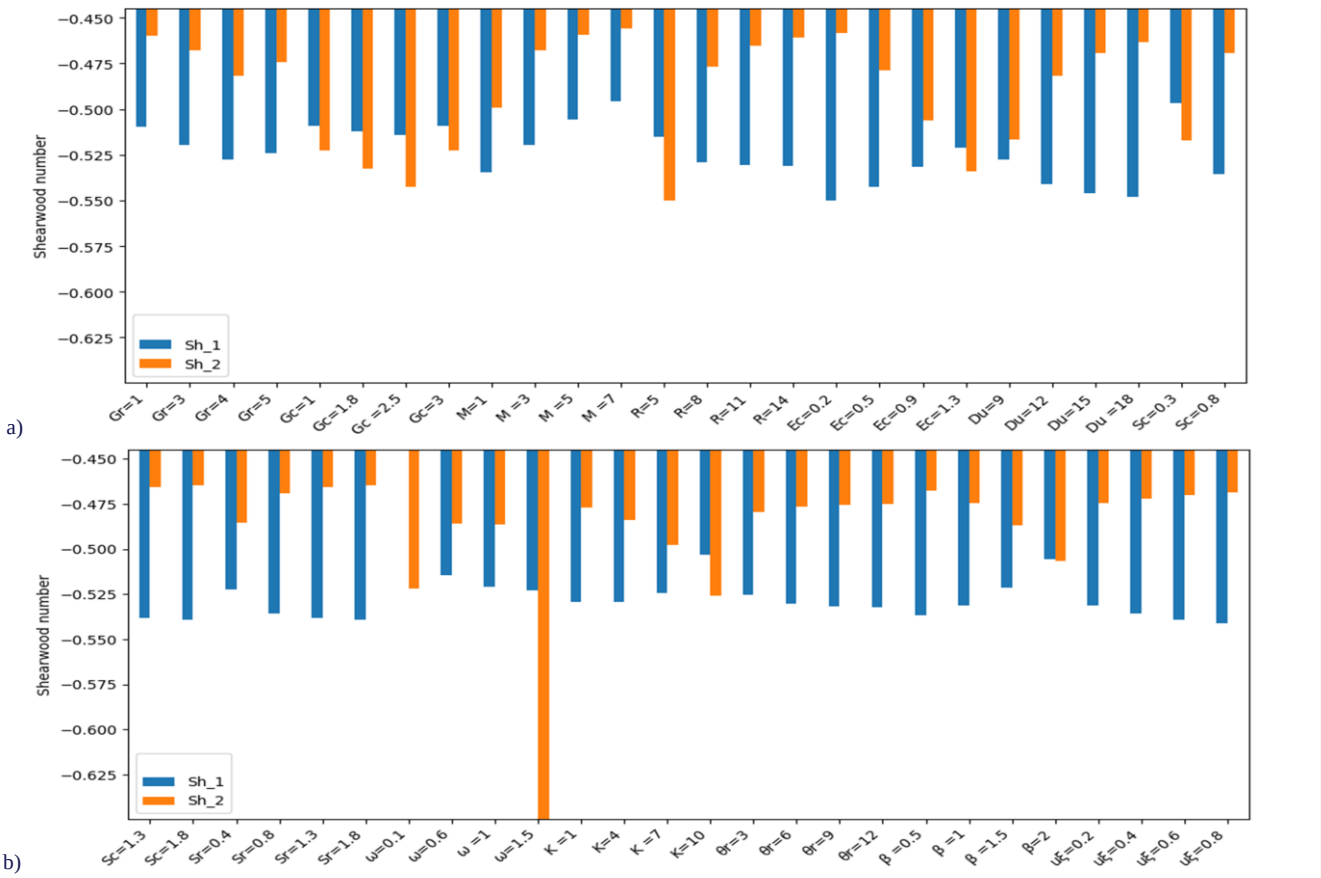


Fig. 48. Shearwood number variations for different parameters.

4.3. Analysis of entropy values

The entropy values obtained using Eq. (21) are presented in Table 1. Entropy study indicates that the molecular Grashof number (Gc) results in a gradual reduction of entropy, while the Grashof number (Gr) leads to an increase. The material parameter (k) significantly reduces entropy formation, signifying enhanced thermal efficiency, whereas the magnetic field strength (M) elevates it due to the Lorentz force effects. At elevated values, the Dufour number (Du) leads to an increased entropy, but the Reynolds number (R) shows minimal fluctuations. The Soret number (Sr) marginally elevates the entropy, whereas the Schmidt number (Sc) significantly diminishes it. The frequency parameter (ω) exhibits a non-monotonic trend, with the entropy increasing under certain situations and decreasing under others. The dimensionless concentration ratio (ψ) markedly decreases the entropy, whereas the velocity slip parameter ($\mu\xi$) shows minimal alteration. The variable viscosity parameter (θ_r) and variable thermal conductivity parameter (β) exert a minimal influence. Entropy generation is typically augmented by Gr, M and Du, whereas it is mitigated by elevated k, Sc and ψ.

Table 1. Generated entropy values.

Parameter	Entropy	Parameter	Entropy	Parameter	Entropy
Gr = 1	5.05726	Du = 9	4.859	θ_r = 3	4.90557
Gr = 3	5.28402	Du = 12	5.00979	θ_r = 6	4.96241
Gr = 4	5.37617	Du = 15	5.06475	θ_r = 9	4.97643
Gr = 5	5.34659	Du = 18	5.09302	θ_r = 12	4.98265
Gc = 1	4.86612	Sc = 0.3	7.74489	β = 0.5	5.01018
Gc = 1.8	4.83861	Sc = 0.8	3.20877	β = 1	4.96761
Gc = 2.5	4.7892	Sc = 1.3	2.068	β = 1.5	4.89166
Gc = 3	4.86612	Sc = 1.8	1.55738	β = 2	4.78118
M = 1	4.93146	Sr = 0.4	4.90236	Ω = 0.2	4.9681
M = 3	5.28402	Sr = 0.8	5.00063	Ω = 0.4	4.96736
M = 5	5.38571	Sr = 1.3	5.02133	Ω = 0.6	4.96712
M = 7	5.83279	Sr = 1.8	5.02894	Ω = 0.8	4.96699
R = 5	4.7392	ω = 0.1	6.03763	ψ = 0.4	7.63652
R = 8	4.95292	ω = 0.6	5.11414	ψ = 0.8	2.07629
R = 11	4.89488	ω = 1	5.06474	ψ = 1.2	1.04662
R = 14	4.82817	ω = 1.5	5.65689	ψ = 1.6	0.686233
Ec = 0.2	4.93593	K = 1	4.95292	$\mu\xi$ = 0.2	4.96761
Ec = 0.5	4.9332	K = 4	4.70198	$\mu\xi$ = 0.4	4.97675
Ec = 0.9	4.93121	K = 7	4.04358	$\mu\xi$ = 0.6	4.97886
Ec = 1.3	4.93157	K = 10	0.549262	$\mu\xi$ = 0.8	4.97759

4.4. Validation section

The non-dimensional system of equations was solved by the Runge-Kutta method under the ND Solve technique in the Mathematica package. The numerical computations were performed up to the accuracy of 10^{-5}. The variations of velocity, angular velocity, temperature and diffusion were validated with the studies of Kumaraswamy et al. [8], Gosty et al. [16], Suresh et al. [19], and found to be in good agreement.

5. Conclusions

The impact of various physical parameters on the entropy generation, heat and mass transfer in a vertical channel with immiscible fluids and non-uniform thermal distribution with slip effects is examined in this thorough investigation.

- The findings show that the transfer of momentum, thermal energy and solute concentrations under various circumstances exhibit consistent behaviour.
- It is confirmed that buoyancy forces (via increasing Gr and Gc) greatly improve heat/mass transfer and velocity profiles while simultaneously decreasing the angular velocity, demonstrating the stabilising function of strong convective flows. The distribution of shear stress is also significantly influenced by these parameters, indicating the development of two-layered boundary structures with opposing near-wall and far-field velocity gradients.
- It is shown that Reynolds number (R) and magnetic field strength (M) are the main damping factors for angular motion and velocity. While M prevents flow through magnetic resistance, R enhances momentum transfer while reducing rotational persistence. Their influence is especially apparent in shear stress and entropy formation, indicating their critical function in energy dissipation.
- The Nusselt number, which measures heat transfer trends, exhibits asymmetrical behaviour across surfaces. While Nu_2 turns positive under high ω, η, or Ec, indicating dominant outward heat flux in dynamic or dissipative regimes, persistently negative Nu_1 values suggest backward diffusion or surface absorption. This emphasises how rotational effects and porous media can improve heat transfer away from the core domain.
- On the other hand, diffusion-driven solute absorption is reflected in mass transfer (Sherwood numbers), which is mostly negative and constant. The fact that Du and Sr have little effect on Sh values indicates that mass transfer is more dependent on molecular diffusion and boundary layer thickness and less susceptible to dynamic forces.
- The system exhibits notable irreversibility trends, as revealed by the entropy analysis. While parameters like M, R and k increase entropy generation, indicating their dissipative influence, Gr and Gc help to lower entropy, exhibiting organised flow behaviour. It is interesting to note that Ec and Du show secondary and nonlinear effects, while β and Ω contribute relatively little. This implies that system-scale fluid dynamics, as opposed to localised diffusion mechanisms, control the entropy.
- Higher Nusselt numbers indicate that buoyancy, magnetic and slide phenomena all improve heat transfer. Shear stress decreases as slip and permeability increase. Wall friction decreases as a result. Mass transfer is stable under all conditions since Sherwood number variations are still quite tiny.
- Limitations of the work: The limitations of the work are the steady-state assumption, constant thermo-physical properties and simplified interfacial conditions.

- Future work: The present work can be extended to transient and time-dependent analysis on different geometries.

References

[1] Fatima, N., Nisar, K.S., Shaheen, S., Arain, M.B., Ijaz, N., & Muhammad, T. (2023). A case study for heat and mass transfer of viscous fluid flow in double layer due to ciliated channel. *Case Studies in Thermal Engineering*, 45, 102943. doi: 10.1016/j.csite.2023.102943

[2] Reddy, M.V., Meenakumari, R., Sucharitha, G., Ali, F., Zafar, S.S., & Lakshminarayana, P. (2024). Heat and mass transfer analysis of conducting non-Newtonian nanofluid flows over an elongating sheet with a non-uniform heat source. *Modern Physics Letters B*, 38(35), 2450349. doi: 10.1142/s0217984924503494

[3] Srinivasulu, T., & Goud, B.S. (2021). Effect of inclined magnetic field on flow, heat and mass transfer of Williamson nanofluid over a stretching sheet. *Case Studies in Thermal Engineering*, 23, 00819. doi: 10.1016/j.csite.2020.100819

[4] Govindarajan, A.G., Sasikumar, J., & Vaidehi, P. (2022). Heat and mass transfer effect on unsteady flow of two stratified immiscible fluids with thermal radiation. *2nd International Conference on Mathematical Techniques and Applications*, 24–26 March, Kattankulathur, India. *AIP Conference Proceedings* 2516(1), 170013. doi: 10.1063/5.0109222

[5] Rabha, R., & Deka, R. (2024). Heat And Mass Transfer on Flow Past an Accelerated Plate Through Porous Medium with Variable Temperature and Mass Diffusion in Presence of Heat Source/Sink. *East European Journal of Physics*, 1, 269−277. doi: 10.26565/2312-4334-2024-1-23

[6] Nurni, V.N., Ballal, B.N., Ghosh, S., & Vaughan, J. (2024). Heat, Mass, Momentum and Charge Transport. In *Treatise on Process Metallurgy. Volume 1: Process Fundamentals* (pp. 565–679). Elsevier. doi: 10.1016/b978-0-323-85935-6.00018-0

[7] Jan, A., Farooq, U., Khan, M.I., & Aslam, F. (2025). Applications of neural networking analysis on drag reduction and heat transfer rate of non-Newtonian fluid flows in energy storage systems. *International Communications in Heat and Mass Transfer*, 169, 109569. doi: 10.1016/j.icheatmasstransfer.2025.109569

[8] Kumaraswamy, P., Ramakrishna Goud, T., Suresh Babu, B., Gosty, V., Srinivas, G., Haripriya, T., & Makinde, O.D. (2025). Numerical analysis on heat and mass transfer of immiscible fluids in a vertical channel with diffusion effects. *Partial Differential Equations in Applied Mathematics*, 13, 101139. doi: 10.1016/j.padiff.2025.101139

[9] Baithalu, R., Mishra, S.R., Pattnaik, P.K., & Panda, S. (2024). Analysis of heat and mass transfer rates in conducting Casson fluid flow over an expanding surface considering Ohmic heating and Darcy dissipation effects. *Partial Differential Equations in Applied Mathematics*, 12, 100972. doi: 10.1016/j.padiff.2024.100972

[10] Ouedraogo, R.W., Namoano, D., Ilboudo, J.M., Igo, W.S., Sawadogo, G.L., & Ouedraogo, D. (2025). Modeling Heat and Mass Transfer in Laminar Forced Convection in A Vertical Channel: Influence of Inlet Fluid Temperature. *IRA-International Journal of Applied Sciences*, 19(4), 89–106. doi: 10.21013/jas.v19.n4.p1

[11] Kalyan, S., Sharan, A., & Chamkha, A.J. (2023). Heat and mass transfer of two immiscible flows of Jeffrey fluid in a vertical channel. *Heat Transfer*, 52(1), 267−288. doi: 10.1002/htj.22694

[12] Kemparaju, S., Swamy, H.K., Sankar, M., & Mebarek-Oudina, F. (2022). Impact of thermal and solute source-sink combination on thermosolutal convection in a partially active porous annulus. *Physica Scripta*, 97(5), 055206. doi: 10.1088/1402-4896/ac6383

[13] Babu, B.S., Santhosh, K., Kumari, G., & Srinivas, G. (2022). Numerical solution of MHD free convective Jeffrey fluid of variable viscosity with chemical reaction and heat source. *Materials Today: Proceedings*, 66, 2636−2641. doi: 10.1016/j.matpr.2022.07.226

[14] Kandagal, M., & Kempepatil, R. (2024). An investigation of the heat and mass transfer effects in vertical channels with immersible fluid flow through a porous matrix. *Journal of Applied Mathematics and Mechanics*, 104(10). doi: 10.1002/zamm.202300998

[15] Kumar, M.A., Mebarek-Oudina, F., Mangathai, P., Shah, N.A., Vijayabhaskar, C., Venkatesh, N., & Fouad, Y. (2025). The impact of Soret Dufour and radiation on the laminar flow of a rotating liquid past a porous plate via chemical reaction. *Modern Physics Letters B*, 39(10), 2450458. doi: 10.1142/S021798492450458X

[16] Gosty, V., Srinivas, G., & Suresh Babu, B. (2024). Numerical investigation of slip effects on heat and mass transfer in a vertical channel with immiscible micropolar and viscous fluids of variable viscosity. *Heat Transfer*, 53(7), 3987−4012. doi: 10.1002/htj.23120

[17] Gosty, V., Srinivas, G., Babu, B.S., Goud, B.S., Hendy, A.S., & Ali, M.R. (2024). Influence of variable viscosity and slip on heat and mass transfer of immiscible fluids in a vertical channel. *Case Studies in Thermal Engineering*, 58 doi: 10.1016/j.csite.2024.104368

[18] Umavathi, J.C., & Sheremet, M.A. (2021). Heat transfer of viscous fluid in a vertical channel sandwiched between nanofluid porous zones. *Journal of Thermal Analysis and Calorimetry*, 144(4), 1389–1399. doi: 10.1007/S10973-020-09664-1

[19] Suresh Babu, B., Srinivas, G., & Srikanth, G.V.P.N. (2022). Finite element analysis of diffusion effects on convective heat and the mass transfer of two fluids in a vertical channel. *International Journal of Automotive and Mechanical Engineering*, 14(1), 3998−4012. doi: 10.15282/ijame.14.1.2017.14.0324

[20] Naseem, T., Mebarek-Oudina, F., Vaidya, H., Bibi, N., Ramesh, K., & Khan, S. (2025). Numerical analysis of entropy generation in Joule heated radiative viscous fluid flow over a permeable radially stretching disk. *Computer Modeling in Engineering and Sciences*, 143(1), 351−371. .doi: 10.32604/cmes.2025.063196

[21] Ghasemi, S.E., & Ranjbar, A. (2025). Entropy Generation Study on Natural and Forced Convection of Nanofluid Flow in Vertical Channels. *Engineering Reports*, 7, e13096. doi: 10.1002/eng2.13096

[22] Suresh Babu, B., Srinivas, G., & Srikanth, G.V.P.N. (2018). Finite element study of convective heat and mass transfer of two fluids in a vertical channel of variable width with Soret and Dufour effects. In *Numerical Heat Transfer and Fluid Flow. Lecture Notes in Mechanical Engineering* (pp. 537−546). Singapore: Springer Singapore. doi: 10.1007/978-981-13-1903-7_62

[23] Abdel-wahed, M.S., Ahmed, S.I., Mekheimer, K.S., & Sayed, A.Y. (2024). Entropy generation analysis of a micropolar fluid in a corrugated channel with convective and slip conditions. *Case Studies in Thermal Engineering*, 57 104283. doi: 10.1016/j.csite.2024.104283

[24] Mebarek-Oudina, F., Dharmaiah, G., Prasad, J.R., Vaidya, H., & Kumari, M.A. (2025). Thermal and flow dynamics of magneto-hydrodynamic Burgers' fluid induced by a stretching cylinder with internal heat generation and absorption. *International Journal of Thermofluids*, 25, 100986. doi: 10.1016/j.ijft.2024.100986

[25] Usha, B., & Gireesha, B.J. (2025). Entropy generation analysis of micropolar fluid flow through a vertical microchannel under the combined effect of Joule heating, viscous dissipation, and thermal radiation with convective boundary conditions. *International*

Journal of Modelling and Simulation, 45(6) 1932−1944. doi: 10.1080/02286203.2024.2306088

[26] Kumar, A., & Yadav, P.K. (2023). Entropy generation analysis of non-miscible couple stress and Newtonian fluid in an inclined porous channel with variable flow properties: HAM Analysis. *International Journal of Modern Physics B*, 38(28), 2450390. doi: 10.1142/s0217979224503909

[27] Govindarajulu, K., Reddy, A.S., Jagadeshkumar, K., Srinivas, S., Kumar, B.R., & Vajravelu, K. (2023). Entropy generation on MHD pulsatile flow of third grade hybrid nanofluid in a vertical porous channel with nonuniform heat source/sink, variable viscosity, thermal conductivity, and Joule heating: A numerical study. *Numerical Heat Transfer Part A: Applications*, 85(24), 4184−4203. doi: 10.1080/10407782.2023.2255929

[28] Nayak, M.K., Shaw, S., Ijaz, K.M., Makinde, O.D., Chu, Y.-M., & Khan, S.U. Interfacial layer, and shape effects of modified Hamilton's Crosser model in entropy optimized Darcy-Forchheimer flow. *Alexandria Engineering Journal*, 60(4), 4067−4083, doi: 10.1016/j.aej.2021.02.010

[29] Reddy, C.S., Mahanthesh, B., Rana, P., & Muhammad, T. (2023). Entropy generation and thermal analyses of a Cross fluid flow through an inclined microchannel with non-linear mixed convection. *Journal of Applied Mathematics and Mechanics*, 103(8). doi: 10.1002/zamm.202100364

[30] Yadav, P., Kumar, A., & Filippov, A.N. (2023). Analysis of entropy production of immiscible micropolar and Newtonian fluids flow through a channel: effect of thermal radiation and magnetic field. *Colloid Journal*, 85(1), 101–121. doi: 10.31857/s0023291222700033

[31] Prasad, J.L.R., Mebarek-Oudina, F., Dharmaiah, G., Rao, P.B., & Vaidya, H. (2024). Melting Flow Analyzation of Radiative Riga Plate Two-Phase Nano-Fluid Across Non-Flatness Plane with Chemical Reaction. *Frontiers in Heat and Mass Transfer*, 22(5), 1515−1532. doi: 10.32604/fhmt.2024.057854

[32] Khan, Z.H., Makinde, O.D., Usman, M., Ahmad, R., & Khan, W.A. (2025). Fractional order unsteady mixed convection in porous-filled concentric pipes: Entropy analysis. *Alexandria Engineering Journal*, 129, 483−503. doi: 10.1016/j.aej.2025.06.047

[33] Shamshuddin, M.D., & Ibrahim, W. (2022). Finite element numerical technique for magneto-micropolar nanofluid flow filled with chemically reactive Casson fluid between parallel plates subjected to rotatory system with electrical and Hall currents. *International Journal of Modelling and Simulation*, 42(6), 985−1004. doi: 10.1080/02286203.2021.2012634

[34] Madhuri, N.J.P., Shamshuddin, M.D., & Salawu, S.O. (2025). Exploring radiative heat transfer and buoyancy effects on Tiwari-Das nanofluid flow model in permeable rotating disc: Finite element study. *Thermal Science and Engineering Progress*, 65, 103855. doi: 10.1016/j.tsep.2025.103855

[35] Jan, A., Khan, M.I., Farooq, U., Aslam, F., & Adnan, R. (2026). Response surface method base multi objective analysis of drag reduction and heat transfer rate in magnetized squeezing channel flow with ohmic heating and viscous dissipation. *International Communications in Heat and Mass Transfer*, 170, 110024. doi: 10.1016/j.icheatmasstransfer.2025.110024

[36] Bejan, A. (1995). *Entropy generation minimization. The method of thermodynamic optimization of finite-size systems and finite-time processes* (1st. ed.). Boca Raton, CRC Press. doi: 10.1201/9781482239171

Co-published by
Institute of Fluid-Flow Machinery
Polish Academy of Sciences
Committee on Thermodynamics and Combustion
Polish Academy of Sciences

Copyright©2026 by the Authors under licence CC BY-NC-ND 4.0

http://www.imp.gda.pl/archives-of-thermodynamics/

Energy consumption prediction and energy-saving retrofit design for office buildings in climate adaptation

Yining Shen

Department of Architecture Engineering, Shijiazhuang College of Applied Technology, 226/227 Tianning Road, Shijiazhuang 050800, China
Author email: 2017010854@sjzpt.edu.cn

Received: 27.06.2025; revised: 15.10.2025; accepted: 08.12.2025

Abstract

In order to accurately predict the energy consumption and design energy-saving retrofits for office buildings, this study proposes a climate adaptation-based energy consumption prediction method by combining depthwise separable convolution and frequency-guided two-dimensional tensorisation algorithm. A multi-objective optimisation retrofit design model is then constructed using the non-dominated sorting genetic algorithm III and ideal point method. Experimental results show that the prediction method achieves the highest accuracy of 96.3% and the lowest error rate of 5.9% under various climate conditions, outperforming comparison algorithms. In practical applications, the retrofit design model responds in as little as 7.3 s and consumes a minimum memory of 189 MB. With a 30% increase in electricity prices, the payback period is only 6.05 years, and the carbon reduction rates for air conditioning and lighting are 59.9% and 58.6%, respectively. The results indicate that the proposed model provides a design solution with high prediction accuracy, robustness and cost-effectiveness, improving the feasibility of office buildings' low-carbon transformation.

Keywords: Depthwise separable convolution; Frequency-guided two-dimensional tensorisation algorithm; Multi-objective optimisation; Energy-saving; Energy consumption prediction

Vol. 47(2026), No. 1, 195–204; doi: 10.24425/ather.2026.158669

Cite this manuscript as: Shen, Y. (2026). Energy consumption prediction and energy-saving retrofit design for office buildings in climate adaptation. *Archives of Thermodynamics*, 47(1), 195–204.

1. Introduction

With the increasing severity of global climate change and the frequent occurrence of extreme weather events, energy conservation and emission reduction have become urgent issues facing the world. Office buildings, as major contributors to urban energy consumption, account for approximately 40% of total urban energy use. It is essential to retrofit these buildings to reduce carbon emissions [1]. Before implementing energy-saving retrofits in office buildings, energy consumption prediction is required to develop targeted retrofit plans. However, traditional energy consumption prediction methods often rely on static climate parameters and fail to account for inter-periodic climate variations. This results in significant deviations between predicted and actual outcomes, leading to suboptimal retrofit effects [2,3]. The frequency-guided two-dimensional tensorisation algorithm (FGTTA) improves the energy consumption prediction accuracy under dynamic climate conditions by considering both intra-seasonal and inter-seasonal variations through higher-order tensor decomposition and feature mapping [4]. Depthwise separable convolution (DSC) reduces computational complexity while maintaining comprehensive feature extraction [5]. Therefore, this study combines depthwise separable convolution and frequency-guided two-dimensional tensorisation algorithm to propose a climate adaptation-based energy consumption prediction algorithm, named DSC-FGTTA.

Nomenclature

Abbreviations and Acronyms

AECOSIM – architecture, engineering, construction and operations integrated simulation model
BIM – building information modelling
DSC – depthwise separable convolution
ECP-RD – energy consumption prediction and retrofit design
FGTTA – frequency-guided two-dimensional tensorisation algorithm
IPM – ideal point method
IR – inverted residuals
MEA-BP – mind evolutionary algorithm-back propagation neural network
NSGA-III – third-generation non-dominated sorting genetic algorithm
NZEB – net zero energy building
PSO-SVM – particle swarm optimisation-support vector machine
TFEU – tensor feature extraction unit
XAI – explainable artificial intelligence

Multi-objective optimisation algorithms can simultaneously address energy saving, long-term costs and indoor comfort, maximising the benefits and optimising the resource allocation of retrofit plans [6,7]. Based on DSC-FGTTA, this study introduces the third-generation non-dominated sorting genetic algorithm (NSGA-III) and ideal point method (IPM) to design energy-saving retrofit plans for office buildings, constructing an energy consumption prediction and retrofit design (ECP-RD) model that considers long-term costs and indoor comfort. This model aims to couple data-driven methods with physical mechanisms, such as the thermodynamics of building envelope structures and the dynamic interaction process between the indoor environment and external climate, in order to improve the accuracy of predictions. It provides decision-makers with a clear and interpretable energy-saving transformation solution, based on the principle of energy transfer and conversion.

Compared with existing research in the field of building energy consumption prediction methods, the main innovation of this study lies in: (1) Combining depthwise separable convolution with frequency guided two-dimensional tensorisation algorithm to propose a climate adaptive energy consumption prediction model DSC-FGTTA, which effectively captures multi period dynamic climate characteristics and overcomes the shortcomings of traditional static models in cross period trend analysis; (2) At the same time, NSGA-III multi-objective optimisation and ideal point method were introduced to construct an energy-saving renovation design (ECP-RD) model that integrates energy consumption, cost and comfort, achieving integrated optimisation from prediction to renovation strategy generation, significantly improving the scientificity and practicality of decision-making.

2. Related works

The frequency-guided two-dimensional tensorisation algorithm, due to its structured data-carrying capacity and flexible mathematical operations, has become a core tool in data processing. Experts and scholars worldwide have explored and studied its applications. For example, the research team led by Zheng proposed a semi-blind thick cloud removal method based on the two-dimensional tensor algorithm, solving the issues of incomplete information recovery and colour distortion in traditional thick cloud removal methods in remote sensing image processing. The final experimental results verified the effectiveness of the method [8]. Wang et al. [9], in order to address the inefficiency caused by high computational and storage complexity in modelling high-dimensional nonlinear autoregressive exogenous systems, proposed a new hybrid modelling and recognition algorithm by combining two-dimensional tensor networks and recursive algorithms. Numerical experiments confirmed the superiority of this algorithm.

The depthwise separable convolution, due to its low computational and parameter requirements and high operational efficiency, has become a favoured method for scholars across various fields. For instance, Asker et al. [10] addressed the issues of large parameter quantities and insufficient feature representation in classifying hyperspectral images using a traditional convolutional neural network. By utilising DSC in the network architecture, they reduced the number of parameters while maintaining both classification accuracy and computational complexity. Due to the inability of standard convolutional networks to accurately classify fisheye freshness based on subtle features, Prasetyo's research team enhanced the model's ability to express subtle features through an improved DSC, thereby improving the accuracy of fisheye freshness classification [11]. Multi-objective optimisation algorithms can simultaneously balance multiple optimisation objectives, making them highly practical in real-world production and daily life. As a result, many scholars have explored the application of these algorithms. For example, to address the problem of traditional feature selection methods struggling to balance the efficiency and accuracy of feature extraction in data processing, Abdollahzadeh et al. [12] proposed a multi-objective hybrid optimisation algorithm, which achieved improvements in both efficiency and accuracy.

Accurate building energy consumption prediction is of significant importance for building retrofitting. Therefore, experts and scholars worldwide have conducted extensive research on energy consumption prediction for buildings. For instance, to address the issue of data sparsity in building energy consumption prediction, Qiao et al. [13] improved the traditional prediction method's feature extraction approach using multivariate packaging methods. Experimental results demonstrated the good accuracy and robustness of this method. Buturache et al. [14] tackled the issue of low historical data utilisation in practical building energy consumption predictions by integrating data preprocessing strategies and hyperparameter optimisation techniques. They developed a method capable of balancing trade-offs, and their final experiments showed that the method could balance the performance and flexibility in building energy consumption prediction.

Energy-saving retrofitting of buildings not only alleviates energy and environmental pressures but also has economic significance. As a result, experts and scholars around the world have conducted in-depth research on this topic. For example, Li

et al. [15] addressed the high energy consumption in mountainous campus buildings by applying computational fluid dynamics wind environment simulation technology and ergonomic programming systems combined with composite insulation layer façade retrofitting technology. The energy-saving rate of the retrofitted campus buildings reached 24%. Borràs et al. [16], through experiments, compared the energy-saving effects of only retrofitting the roof versus retrofitting the entire thermal envelope of buildings, revealing the impact of building roofs on energy savings. This study provides more reference for selecting energy-saving retrofit solutions in buildings.

In conclusion, while there have been some improvements in the prediction accuracy of building energy consumption methods, issues such as not considering climate factors and computational complexity remain. Regarding the exploration of building energy-saving retrofit design methods, most studies still focus only on energy-saving effects, without considering costs and comfort. In light of this, the study combines FGTTA and DSC to propose a climate-adaptation-based building energy consumption prediction method that balances prediction accuracy and computational load. The energy consumption data output by the above prediction method was used as the optimisation input, and the NSGA-III multi-objective optimisation algorithm was further introduced to construct a building energy-saving renovation design model, in order to seek the optimal balance between multiple objectives. It is expected that this model will provide more practical and excellent retrofit solutions for building energy-saving retrofits.

3. Climate-adaptive energy prediction and energy-saving model for office buildings

3.1. Design of energy consumption prediction algorithm for office buildings

For building energy consumption prediction, traditional models only analyse single-period trends, ignoring the longitudinal correlations of data across different periods. This leads to an insufficient capture of energy consumption fluctuations caused by factors such as climate, increasing the prediction error rate. This study conceptualises an office building as a dynamic thermodynamic system, whose energy consumption and comfort state fundamentally depend on the thermal performance of the building envelope, indoor and outdoor climate boundary conditions and the dynamic balance of internal thermal disturbances. The proposed mathematical architecture of the prediction and optimisation model aims to accurately describe the operating laws of this physical system and to use climate parameters as the core physical driving variables to ensure that the model output results have a solid physical foundation. The frequency-guided two-dimensional tensorisation algorithm can capture both seasonal variations within the same period and corresponding changes across different periods through its multi-layered network structure [17]. Therefore, this study uses FGTTA to extract multi-level seasonal features of energy consumption data from office buildings.

The algorithm structure is shown in Fig. 1. As shown in the figure, FGTTA consists of multiple two-dimensional tensor feature extraction units (TFEUs). Taking one two-dimensional TFEU as an example, the energy consumption data is first mapped to one-dimensional deep features. Then, the one-dimensional data is mapped to a two-dimensional space, obtaining a set of two-dimensional tensors. Convolutional neural networks perform convolution operations on the two-dimensional tensor group, which is then converted back to a one-dimensional tensor. Finally, the one-dimensional vectors are concatenated to obtain the final prediction result. The mapping of the one-dimensional energy consumption data to deep features, resulting in a one-dimensional time series, is expressed by the equation

$$X_{1\mathrm{D}}^{h} = \mathrm{TFEU}\left(X_{1\mathrm{D}}^{h-1}\right) + X_{1\mathrm{D}}^{h-1}, \tag{1}$$

where h represents the layer of TFEU, and $X_{1\mathrm{D}}^{h-1}$ and $X_{1\mathrm{D}}^{h}$ represent the input and output values. After the one-dimensional time series $X_{1\mathrm{D}}^{h-1}$ is tensorised into a two-dimensional tensor group $X_{2\mathrm{D}}^{h,i}$, convolution is applied to $X_{1\mathrm{D}}^{h-1}$, as shown in the equation

$$\hat{X}_{2\mathrm{D}}^{h,i} = \mathrm{Re\,Lu}\left\{\mathrm{BN}\left[\mathrm{Conv2D}\left(X_{2\mathrm{D}}^{h,i}\right)\right]\right\},\ i \in \{1, \ldots, k\}, \tag{2}$$

where $\mathrm{Conv2D}(\cdot)$, $\mathrm{BN}(\cdot)$, and $\mathrm{ReLu}(\cdot)$ represent the convolution layer, batch normalisation layer, and activation function layer, respectively, and $\hat{X}_{2\mathrm{D}}^{h,i}$ is the two-dimensional tensor obtained after the convolution operation. The sequence is then truncated, and the amplitude corresponding to the relative importance of the two-dimensional tensor is calculated. Based on this relative importance, the two-dimensional vector is dynamically concatenated to form a one-dimensional tensor. This process is expressed as follows

$$\begin{cases} \hat{X}_{1\mathrm{D}}^{h,i} = \mathrm{Tru}\left[\mathrm{Re\ factor}_{1,(f_i \times \tau_i)}\left(\hat{X}_{2\mathrm{D}}^{h,i}\right)\right], \ i \in \{1, \ldots, k\}, \\ \hat{A}_{f_1}^{h-1}, \ldots, \hat{A}_{f_k}^{h-1} = \mathrm{Soft\,max}\left(A_{f_1}^{h-1}, \ldots, A_{f_k}^{h-1}\right), \\ X_{1D}^{h} = \sum_{i=1}^{k} \hat{A}_{i}^{h-1} \times \hat{X}_{1\mathrm{D}}^{h,i}, \end{cases} \tag{3}$$

where $\mathrm{Tru}(\cdot)$ represents the truncation operation, $\hat{X}_{1\mathrm{D}}^{h,i}$ represents the converted one-dimensional time series, and f_i and τ_i represent the row and column numbers of the two-dimensional tensor.

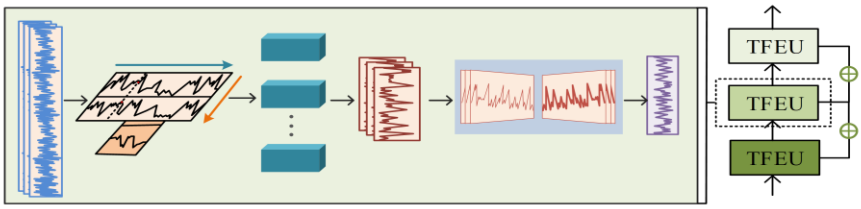


Fig. 1. Schematic diagram of FGTTA structure.

Variable A represents the amplitude strength of the frequency domain components obtained through the Fourier transform, k represents the first largest frequency domain components, $\hat{A}_{f_k}^{h-1}$ represents the amplitude weights of $A_{f_k}^{h-1}$ calculated by the Softmax function, and X_{1D}^{h} represents the final concatenated one-dimensional sequence.

The frequency-guided two-dimensional tensorisation algorithm improves the accuracy of long-term energy consumption prediction by analysing both single-period and cross-period energy trends. However, the time complexity increases, affecting the prediction efficiency. The depthwise separable convolution reduces computation and model parameters while maintaining feature extraction performance through depthwise and pointwise convolutions [18,19]. The inverted residuals (IR) network can not only overcome the data loss limitation of traditional residual networks, but also reduce the computational resources required. Therefore, this study proposes a feature extraction network combining DSC and IR, named DSC-IR, as shown in Fig. 2.

As shown in Fig. 2, the DSC-IR network consists of multiple convolution stages and pooling layers. The convolution stages are composed of inverted residual modules, which first increase the channel count through a convolution layer, then use depthwise separable convolutions to extract feature map features, and finally reduce the channel count through another convolution layer. By using different numbers of inverted residual modules at different stages, features at various levels and scales can be captured. After efficiently extracting features through the convolution stages, the pooling layers further reduce the dimensions of the feature maps. The depthwise separable convolution extracts spatial features from each channel, with each channel's depthwise convolution represented by the equation

$$\hat{G}_{k,l,m} = \sum_{i,j} \hat{k}_{i,j,m} \cdot F_{k+i-1,l+j-1,m}, \quad (4)$$

where $\hat{k}$ represents the depth convolution kernel of size $D_K \times D_K \times M$, m in $\hat{k}_{i,j,m}$ represents the m-th convolution kernel, and m in $F_{k+i-1,l+j-1,m}$ and $\hat{G}_{k,l,m}$ represents the m-th channel in the input feature and output feature, respectively. The computational cost of depth convolution is expressed as

$$C_1 = D_K \times D_K \times M \times D_F \times D_F, \quad (5)$$

where M represents the number of input channels and D_F represents the width and height of the input feature map. After extracting spatial features from the feature map through depthwise convolution, a pointwise convolution is applied to fuse the features, forming new features. The computational cost of the final depthwise separable convolution after pointwise convolution is expressed as

$$C_2 = D_K \times D_K \times M \times D_F \times D_F + N \times M \times D_F \times D_F, \quad (6)$$

where N represents the number of output channels.

The DSC-IR network effectively reduces computation while maintaining stable feature extraction performance, balancing both performance and efficiency. To further enhance the algorithm's predictive performance, the study replaces the convolutional neural network part of the two-dimensional tensorisation algorithm with the deep separable inverted residual network,

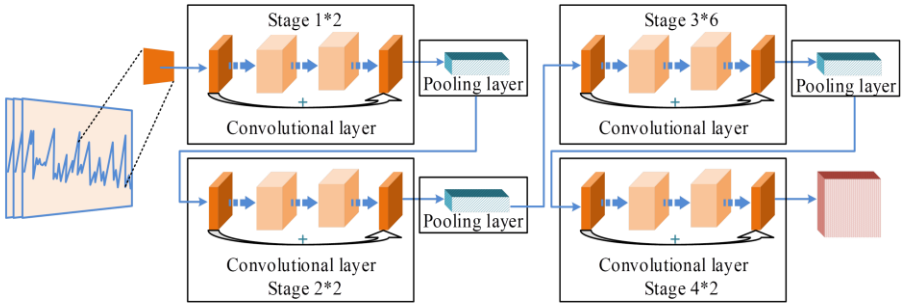


Fig. 2. The DSC-IR network structure.

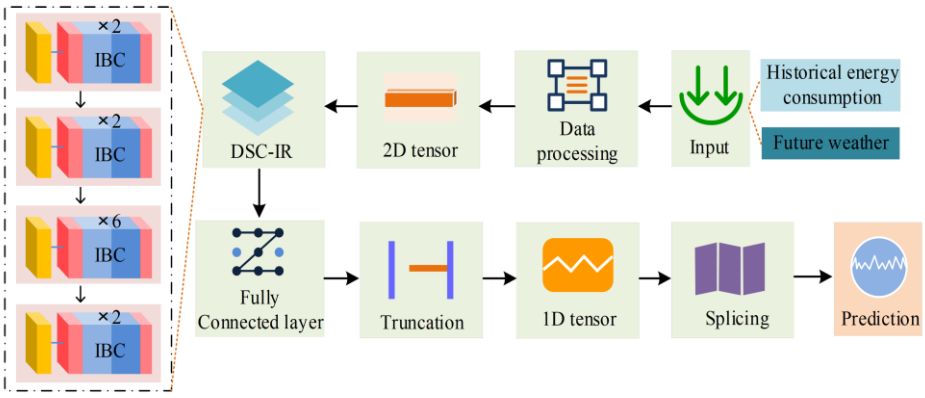


Fig. 3. The DSC-FGTTA flowchart.

proposing a DSC-FGTTA-based energy prediction algorithm for office buildings.

As shown in Fig. 3, which illustrates the prediction flow, in the DSC-FGTTA, historical energy consumption and future weather data are input and standardised to eliminate scale differences, then converted into two-dimensional spatial tensors. Next, the DSC-IR module performs multi-stage convolution and pooling operations to extract features and reduce dimensions. The processed feature data is returned to the fully connected layer of FGTTA, where different features are integrated to obtain a global description of the data. The energy consumption features are then truncated to form a fixed-length one-dimensional tensor, and weighted concatenation is applied to construct the final prediction sequence. Finally, future energy consumption is predicted based on the final tensor sequence. DSC-FGTTA effectively captures short-term and long-term energy consumption trends from historical data, enabling accurate predictions of seasonal fluctuations.

3.2. Prediction and energy-saving model based on multi-objective optimisation algorithm

After predicting the energy consumption of the target office building using DSC-FGTTA, it is necessary to design a targeted renovation plan to minimise future energy consumption and achieve energy savings. However, the renovation of office buildings does not only consider energy consumption, but also takes into account long-term costs and indoor comfort. NSGA-III can continuously approach the optimal solution by evaluating fitness and eventually obtain a set of non-dominated pre-optimal solutions [20]. Therefore, this study uses NSGA-III to determine the optimal renovation plan based on the prediction results from DSC-FGTTA, as illustrated in Fig. 4. As shown in the figure, NSGA-III first defines the target problem as a reference point, then initialises a set of random solutions and calculates their fitness. Afterwards, a subset of high-fitness random solutions is selected as parents. These parent solutions undergo crossover to generate new solutions, and mutation operations are applied to introduce additional solutions. The newly generated and introduced solutions are added to the current solution set. The iteration process continues until the maximum number of iterations is reached or the solution and fitness meet the preset criteria; then the iteration stops, and the final results are output. This

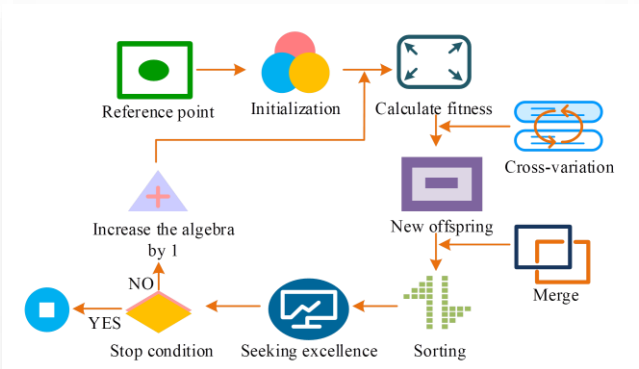


Fig. 4. The NSGA-III implementation flowchart.

study sets the maximum number of iterations to 200, and the preset convergence threshold is that the improvement of the optimal solution of the population within 20 consecutive generations is less than 0.0001. If the conditions are not met, fitness evaluation continues until the stopping conditions are reached. In the NSGA-III process, starting from the physical characteristics of the building, the energy consumption predicted by DSC-FGTTA, as well as the average predicted dissatisfaction and renovation cost determined by building thermal engineering and human thermal comfort theory, are jointly set as optimisation objectives.

As shown in the equation, the objective function is formed by the building energy consumption ($e_c(\bar{x})$), average predicted dissatisfaction ($R_{\mathrm{D}}(\bar{x})$) and renovation cost ($c(\bar{x})$):

$$G(\bar{x}) = G[(e_c(\bar{x}), R_{\mathrm{D}}(\bar{x}), c(\bar{x}))], \tag{7}$$

where $\bar{x}$ represents the optimisation variable. The study uses the average thermal sensation index to evaluate average prediction dissatisfaction, which is expressed as follows:

$$R_{\mathrm{D}} = \frac{1}{n}\sum_{i=1}^{n} \bar{R}_{\mathrm{D},i}, \tag{8}$$

where n represents the number of thermal zones in the target building and $\bar{R}_{\mathrm{D},i}$ stands for the average predicted dissatisfaction with the thermal environment. The predicted renovation cost is expressed as follows:

$$c = \frac{1}{A}\sum_{i=1}^{i} C_i = \frac{1}{A}\sum_{i=1}^{i} A_i \times c_{p,i}, \tag{9}$$

where C_i and A_i denote the incremental renovation cost and renovation area for each part of the building, respectively, and $c_{p,i}$ is the unit area cost of renovation materials. Additionally, to ensure that all design parameters comply with relevant standards, constraints are applied:

$$\begin{cases} {x^1}_{\min} < {x^1}_i < {x^1}_{\max} \\ {x^2}_{\min} < {x^2}_i < {x^2}_{\max} \\ {x^3}_{\min} < {x^3}_i < {x^3}_{\max} \end{cases}, \tag{10}$$

where ${x^1}_i$, ${x^2}_i$, and ${x^3}_i$ represent building energy consumption, dissatisfaction and renovation cost, respectively, and ${x^1}_{\min}$, ${x^2}_{\min}$, and ${x^3}_{\min}$ represent the lower limits of design parameters, while ${x^1}_{\max}$, ${x^2}_{\max}$, and ${x^3}_{\max}$ represent the upper limits of design parameters. The optimal solution set obtained through NSGA-III includes several equally valid renovation methods. However, in practical applications, only one renovation plan is typically chosen. Therefore, after obtaining the optimal solution set from NSGA-III, it is necessary to select the best solution as the final renovation plan. The ideal point method evaluates the solutions by comparing the difference between each solution and the ideal point, thus selecting the optimal solution [21].

The study adopts the IPM as the multi-objective decision-making method, combined with NSGA-III to form the optimal renovation plan determination method, named NSGA-III-IPM. The implementation process of this method is shown in Fig. 5. As seen from the figure, the NSGA-III-IPM first defines the objective and constraint functions. The study uses building energy

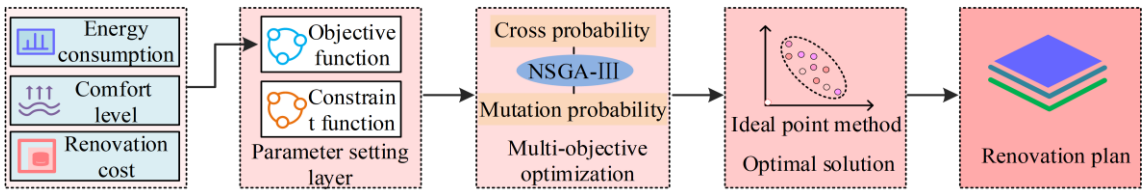


Fig. 5. The NSGA-III-IPM flowchart.

consumption, comfort and renovation cost as optimisation objectives. Then, NSGA-III is used to obtain the feasible optimal solution set. The best solution is then selected from the set of alternative optimal solutions to form the target building's renovation plan. The difference between each alternative optimal solution and the ideal solution is determined using the Euclidean distance:

$$U_n = \left[\left(\frac{\eta_{\text{Pareto}} - \eta_{\text{E}_{\text{point}}}}{\eta_{E_{point}}}\right)^2 + \left(\frac{Z_{\text{Pareto}} - Z_{\text{E}_{\text{point}}}}{Z_{\text{E}_{\text{point}}}}\right)^2\right]^{\frac{1}{2}}, \quad (11)$$

where $(\eta_{\text{Pareto}}, Z_{\text{Pareto}})$ and $(\eta_{\text{E}_{\text{point}}}, Z_{\text{E}_{\text{point}}})$ represent the coordinates of the alternative optimal solution (a Pareto optimal solution) and the ideal point. After calculating the distance between all solutions in the optimal solution set and the ideal solution, the solution closest to the ideal solution is selected:

$$U_{\text{opt}} = \min(U_n), \quad (12)$$

where U_{opt} denotes the final selected optimal solution. Finally, this study captured the dynamic physical response of buildings to external climate using the DSC-FGTTA and utilised the NSGA-II-IPM to seek the optimal solution while satisfying multiple physical and comfort constraints, thus forming a complete office building renovation design model (i.e. ECP-RD) from physical mechanism analysis to optimisation decision-making.

The overall framework of the ECP-RD model is shown in Fig. 6. In the ECP-RD model, energy consumption prediction is performed by DSC-FGTTA to extract features from historical energy consumption data and future weather, and climate-adapted energy consumption prediction results are obtained based on these features. The predicted energy consumption values are then used as one of the optimisation objectives in the renovation design part, along with comfort and renovation cost, forming the optimisation function. The NSGA-III is then applied to obtain the optimal solution set. Finally, IPM is used to determine the solution closest to the ideal solution as the optimal solution, which is the final renovation plan.

4. Performance validation of the ECP-RD energy prediction and retrofit design model

4.1. Performance validation of the DSC-FGTTA algorithm

To evaluate the energy conservation and retrofit design model proposed in this study, both algorithm performance verification experiments and practical application experiments were conducted to assess the building energy consumption prediction and renovation design performance. The comparative algorithms used in the algorithm performance verification experiments were mind evolutionary algorithm-back propagation neural network (MEA-BP), explainable artificial intelligence (XAI) and particle swarm optimisation-support vector machine (PSO-SVM). The comparative models used in the practical application experiments were building information modelling (BIM), net zero energy building (NZEB), and architecture, engineering, construction, and operations integrated simulation model (AECOSIM).

The study selected an office building in Chengdu as the target object. This building consists of 15 floors, with a standard floor height of 3 m, and integrates commercial, office and hotel functions. It uses a split air-conditioning system. The experiment used the Building Energy and Climate Database (BECD) as the dataset, which includes basic building data, equipment system information, and historical weather records. The experimental environment is shown in Table 1.

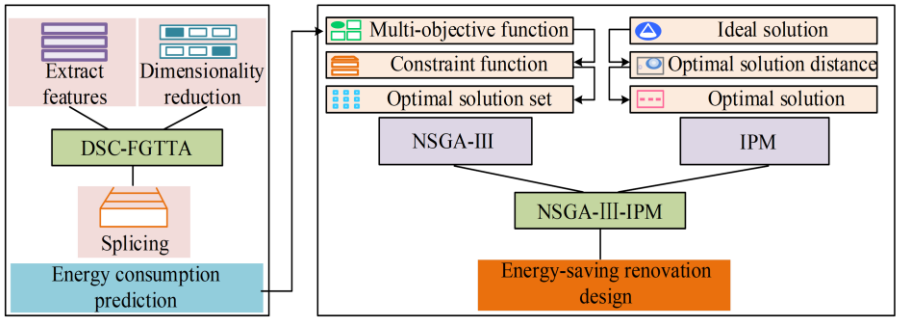


Fig. 6. The ECP-RD model structure.

Table 1. Experimental environment and configuration parameters.

Parameter	Configuration
CPU	AMD Ryzen 5
Memory	32GB
IDE	VS Code
Operating system	Windows 10
Programming language	Python 4.0
GPU	NVIDIA RTX 3090

Based on the experimental environment, the study first conducted a comparison experiment on the electrical consumption prediction methods. The experimental results are shown in Fig. 7.

As shown in Fig. 7a, when the target is the building's summer electricity consumption, the prediction accuracy of MEA-BP was 93.2%, while XAI and PSO-SVM had prediction accuracies of 91.3% and 89.5%, respectively. The prediction accuracy of DSC-FGTTA was 95.6%. As depicted in Fig. 7b, for the winter electricity consumption prediction experiment, the prediction accuracies of MEA-BP, XAI, PSO-SVM and DSC-FGTTA were 94.1%, 92.5%, 90.3% and 96.3%, respectively. From these experimental results, it can be concluded that DSC-FGTTA demonstrated higher accuracy in predicting building energy consumption across different climates, indicating that the method can adapt to dynamic climate changes. To further verify the robustness of the energy consumption prediction method, the study conducted an experiment to assess the prediction error rate under extreme weather conditions. The results are presented in Fig. 8.

As shown in Fig. 8a, during extremely hot weather, the highest and lowest error rates for the MEA-BP method were 20.6% and 15.8%, respectively. For XAI, the highest and lowest error rates were 23.4% and 15.1%, respectively. The highest and lowest error rates for PSO-SVM were 15.9% and 13.8%, respectively. For DSC-FGTTA, the highest and lowest error rates were 7.2% and 5.9%, respectively. According to Fig. 8b, during extreme weather with continuous rainfall, the highest error rates for MEA-BP and XAI were 18.1% and 23.8%, with the lowest error rates at 14.8% and 19.1%, respectively. The highest and lowest error rates for PSO-SVM were 14.9% and 12.1%, respectively. The highest and lowest error rates for DSC-FGTTA were 9.8% and 6.9%, respectively. From these data, it can be observed that under both extreme weather conditions, the prediction error rates for DSC-FGTTA remained below 10%, outperforming the comparative models. This experiment demonstrated that the DSC-FGTTA energy consumption prediction method has high prediction accuracy and excellent robustness.

4.2 Practical application of the ECP-RD model

The validation experiment of the DSC-FGTTA energy consumption prediction algorithm confirmed the high prediction accuracy and excellent robustness of the algorithm when applied to climate adaptation. It demonstrated that the DSC-FGTTA energy consumption prediction algorithm could provide a reliable

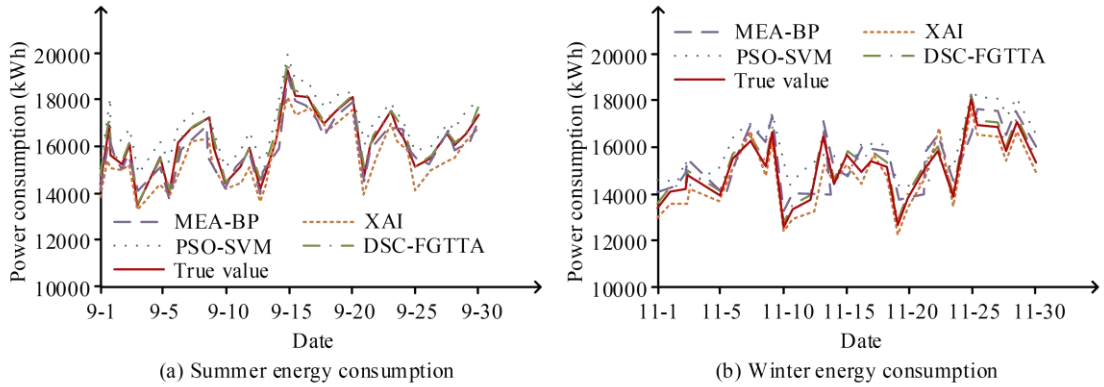


Fig. 7. Results of the electrical consumption prediction experiment.

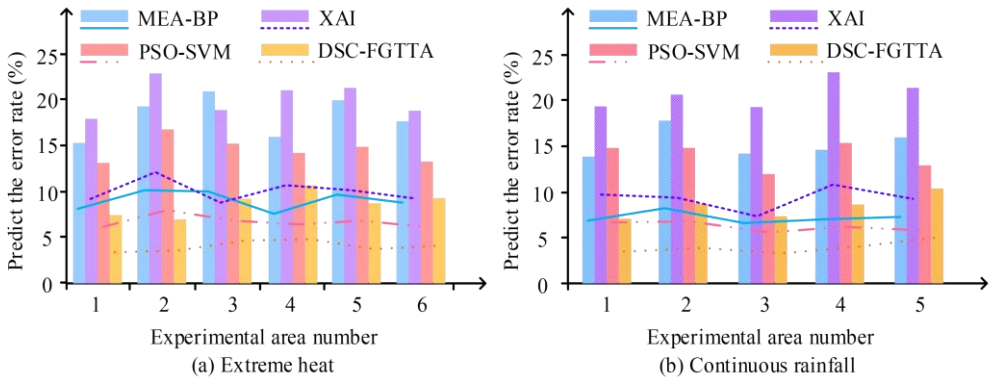


Fig. 8. Prediction error rate under extreme weather.

data source for the ECP-RD model. To further verify the practical application performance of the ECP-RD model in building energy-saving renovation design, the study first conducted experiments on the response time and memory usage of the model to evaluate its practicality. The experimental results are shown in Fig. 9.

As seen in Fig. 9a, in the response time experiment, the fastest response time for NZEB was 15.1 s, with an average response time of 15.3 s. For BIM, the fastest and average response times were 9.9 s and 11.3 s, respectively, whereas for AECOSIM, these response times were 10.4 s and 13.6 s, respectively. For the ECP-RD model proposed by the study, the fastest and average response times were 7.3 s and 10.2 s, respectively. As shown in Fig. 9b, in the memory usage experiment, the average memory usage for NZEB, AECOSIM and BIM during operation was 358 MB, 326 MB and 223 MB, respectively, while the average memory usage for ECP-RD was 189 MB.

In summary, in both the response time and memory usage experiments, ECP-RD outperformed the other three comparative models, indicating that ECP-RD has excellent practicality. After verifying the practicality of the ECP-RD model, the study continued to assess its economic benefits. The experiment used the payback period as the performance indicator, and the experimental results are shown in Fig. 10. According to Fig. 10a, when the electricity price increase was 5%, the payback periods for NZEB, BIM and AECOSIM were 8.03 years, 6.91 years and 7.06 years, respectively. The payback period for ECP-RD was 5.73 years. When the electricity price increase was 30%, the payback periods for NZEB, BIM, AECOSIM and ECP-RD increased by 1.11 years, 0.41 years, 0.75 years and 0.32 years, respectively, compared to the 5% price increase. As shown in Fig. 10b, when the equipment degradation rate reached 50%, the payback periods for the four models were 8.94 years, 5.95 years, 7.12 years and 5.62 years, respectively.

In summary, under both electricity price increase and equipment degradation, the ECP-RD model showed the shortest payback period and the smallest increase, indicating that the renovation plan provided by ECP-RD delivers excellent economic benefits.

Finally, the study conducted experiments on the energy-saving effects of the ECP-RD model. The experimental results are shown in Fig. 11. Figures 11a and b show the carbon reduction rates for air conditioning and lighting, respectively. As shown in Fig. 11a, the average carbon reduction rates for BIM, NZEB, AECOSIM and ECP-RD were 35.6%, 28.6%, 42.6% and 59.9%, respectively. In Fig. 11b, for lighting equipment, the average carbon reduction rates for NZEB, BIM, AECOSIM and ECP-RD were 30.55%, 40.9%, 43.6% and 58.6%, respectively. These experimental results clearly demonstrate that the ECP-RD model significantly outperformed the comparative models in

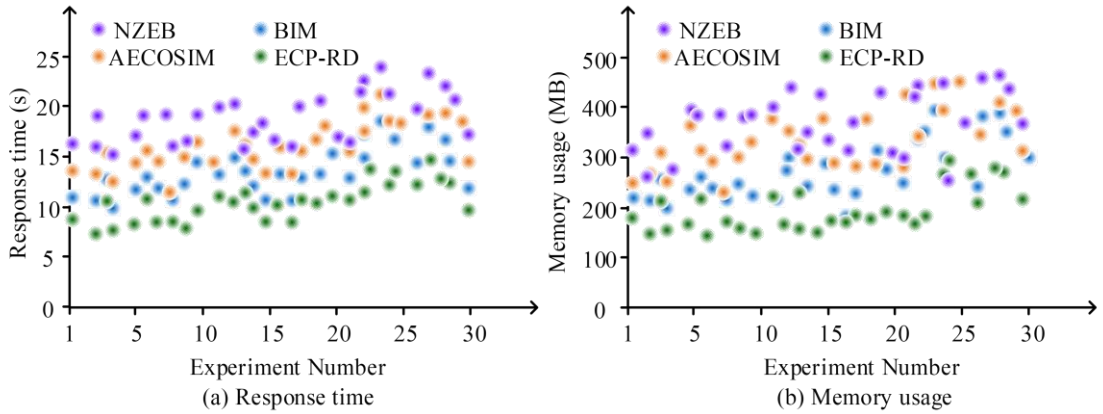


Fig. 9. Results of the response time and memory usage experiments.

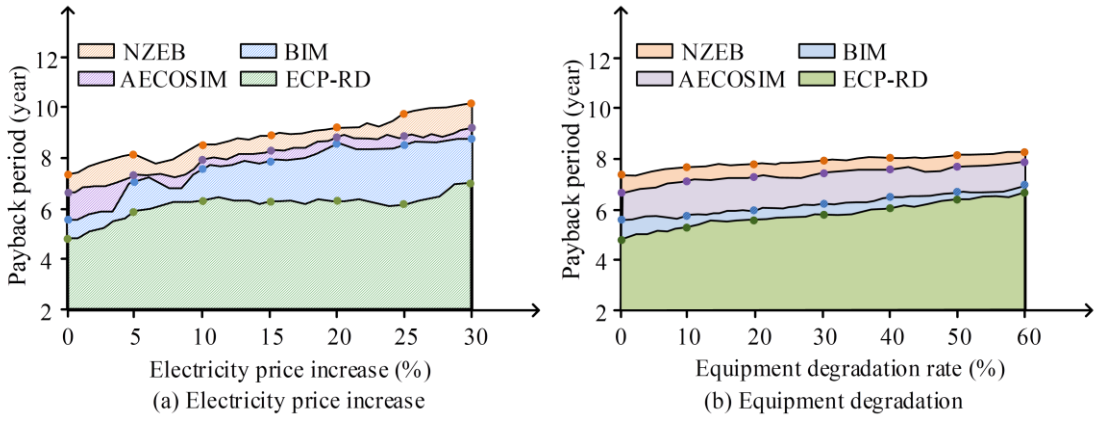


Fig. 10. Payback period experimental results.

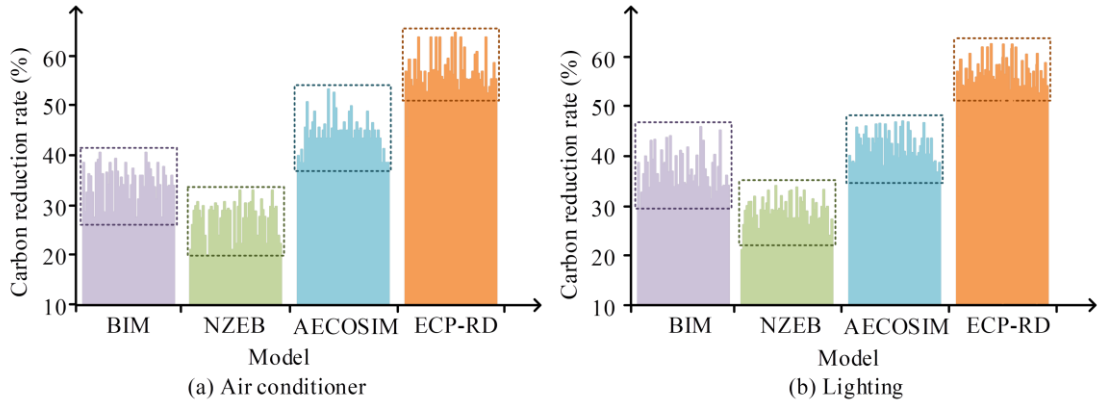


Fig. 11. Carbon reduction rate experimental results.

terms of carbon reduction, indicating that the renovation plan provided by ECP-RD can help the target building achieve substantial energy-saving effects.

6. Conclusions

In response to the energy consumption prediction and energy-saving renovation needs of office buildings facing dynamic climate changes, the study proposed a hybrid model based on depthwise separable convolution, frequency-guided two-dimensional tensorisation algorithm and multi-objective optimisation algorithms. This model integrates both building energy consumption prediction and energy-saving renovation design.

The final model performance verification results showed that the prediction accuracy for energy consumption was 95.6% in summer and 96.3% in winter, with the error rate as low as 5.9% under extreme weather conditions. These experimental data indicate that the model can accurately predict the energy consumption of the target building.

In the energy-saving renovation experiments, the model outperformed the comparative models in terms of both response time and memory usage, with an average response time of 10.2 s and memory usage of 189 MB. When the electricity price increased by 30%, the payback period was only 6.05 years, and the carbon reduction rates for air conditioning and lighting were 59.9% and 58.6%, respectively. These experimental data demonstrate that the proposed building energy consumption prediction and energy-saving renovation model has excellent prediction accuracy and robustness, helping decision-makers develop reasonable energy-saving renovation plans. This is mainly due to its core algorithm, effectively capturing and quantifying the dynamic response laws of the building thermodynamic system to external climate stimuli. Compared to pure mathematical fitting, the proposed model provides decision-makers with not only optimised results, but also clear physical mechanisms through in-depth exploration of key physical processes, such as thermal performance of building envelope structures and dynamic characteristics of air conditioning systems. However, the model currently relies heavily on the quality of historical data, and its applicability is limited in buildings with insufficient data.

References

[1] Röck, M., Balouktsi, M., & Saade, M.R.M. (2023). Embodied carbon emissions of buildings and how to tame them. *One Earth*, 6(11), 1458−1464. doi: 10.1016/j.oneear.2023.10.018

[2] Usman, A.M., & Abdullah, M.K. (2023). An assessment of building energy consumption characteristics using analytical energy and carbon footprint assessment model. *Green and Low-Carbon Economy*, 1(1), 28−40. doi: 10.47852/bonviewGLCE3202545

[3] Li, J., Zhang, C., Zhao, Y., Qiu, W., Chen, Q., & Zhang, X. (2022). Federated learning-based short-term building energy consumption prediction method for solving the data silos problem. Building Simulation. *Building Simulation*, 15(6), 1145−1159. doi: 10.1007/s12273-021-0871-y

[4] Zhang, Q., Kong, J., Jiang, M., & Liu, T. (2023). Building energy consumption prediction based on temporal-aware attention and energy consumption states. *Journal of Electrical Engineering & Technology*, 18(1), 61−75. doi: 10.1007/s42835-022-01159-3

[5] Bañuls, M.C. (2023). Tensor network algorithms: A route map. *Annual Review of Condensed Matter Physics*, 14(1), 173−191. doi: 10.1146/annurev-conmatphys-040721-022705

[6] Nguyen, X.T., & Tran, G.S. (2024). Hyperspectral image classification using an encoder-decoder model with depthwise separable convolution, squeeze and excitation blocks. *Earth Science Informatics*, 17(1), 527−538. doi: 10.1007/s12145-023-01181-7

[7] Sharma, S., & Kumar, V. (2022). A comprehensive review on multi-objective optimization techniques: Past, present and future. *Archives of Computational Methods in Engineering*, 29(7), 5605−5633. doi: 10.1007/s11831-022-09778-9

[8] Zheng, W.J., Zhao, X.L., Zheng, Y.B., Lin, J., Zhuang, L., & Huang, T.Z. (2023). Spatial-spectral-temporal connective tensor network decomposition for thick cloud removal. *ISPRS Journal of Photogrammetry and Remote Sensing*, 199(1), 182−194. doi: 10.1016/j.isprsjprs.2023.04.006

[9] Wang, Y., Tang, S., & Deng, M. (2022,).Modeling nonlinear systems using the tensor network B-spline and the multi-innovation identification theory. *International Journal of Robust and Nonlinear Control*, 32(13), 7304−7318. doi: 10.1002/rnc.6221

[10] Asker, M.E. (2023). Hyperspectral image classification method based on squeeze-and-excitation networks, depthwise separable convolution and multibranch feature fusion. *Earth Science Informatics*, 16(2), 1427−1448. doi: 10.1007/s12145-023-00982-0

[11] Prasetyo, E., Purbaningtyas, R., Adityo, R.D., Suciati, N., Fatichah, C. (2022). Combining MobileNetV1 and Depthwise Separable convolution bottleneck with Expansion for classifying the

freshness of fish eyes. *Information Processing in Agriculture*, 9(4), 485−496. doi: 10.1016/j.inpa.2022.01.002

[12] Abdollahzadeh, B., & Gharehchopogh, F.S. (2022) A multi-objective optimization algorithm for feature selection problems. *Engineering with Computers*, 38(Suppl. 3), S1845−S1863.

[13] Qiao, Q., Yunusa-Kaltungo, A., & Edwards, R.E. (2022). Feature selection strategy for machine learning methods in building energy consumption prediction. *Energy Reports*, 8(1), 13621−13654. doi: 10.1016/j.egyr.2022.10.125

[14] Buturache, A.N, & Stancu, S. (2022). Building energy consumption prediction using neural-based models. *International Journal of Energy Economics and Policy*, 12(2), 30−38. doi: 10.32479/IJEEP.12739

[15] Li, Y., Chen, H., & Yu, P. (2024). Green campus transformation in smart city development: A study on low-carbon and energy-saving design for the renovation of school buildings. *Smart Cities*, 7(5), 2940−2965. doi: 10.3390/smartcities7050115

[16] Borràs, J.G., Lerma, C., Mas, Á., Vercher, J., & Gil, E. (2022). Contribution of green roofs to energy savings in building renovations. *Energy for Sustainable Development*, 71(3), 212−221. doi: 10.1016/j.esd.2022.09.020

[17] Menczer, A., & Legeza, O. (2024). Tensor network state algorithms on AI accelerators. *Journal of Chemical Theory and Computation*, 20(20), 8897−8910. doi: 10.1021/acs.jctc.4c00800

[18] Asif, S., Zhao, M., Chen, X., & Zhu, Y. (2023). StoneNet: An efficient lightweight model based on depthwise separable convolutions for kidney stone detection from CT images. *Interdisciplinary Sciences: Computational Life Sciences*, 15(4), 633−652. doi: 10.1007/s12539-023-00578-8

[19] Zhang, K., Bello, I.M., Su, Y., Wang, J., & Maryam, I. (2022). Multiscale depthwise separable convolution based network for high-resolution image segmentation. *International Journal of Remote Sensing*, 43(18), 6624−6643. doi: 10.1080/ 01431161.2022.2142081

[20] Pereira, J.L.J., Oliver, G.A., Francisco, M.B., Cunha Jr, S.S., & Gomes, G.F. (2022). A review of multi-objective optimization: Methods and algorithms in mechanical engineering problems. *Archives of Computational Methods in Engineering*, 29(4), 2285−2308. doi: 10.1007/s11831-021-09663-x

[21] Fallahnejad, R., Wanke, P.F., Mozaffari, M.R., & Tan, Y. (2024). A modification of double frontier ideal point method for Malmquist productivity index in the investigation of eco−innovation in transportation industry. *International Journal of Shipping and Transport Logistics*, 18(2), 191−222. doi: 10.1504/ IJSTL.2024.137894

Co-published by
Institute of Fluid-Flow Machinery
Polish Academy of Sciences
Committee on Thermodynamics and Combustion
Polish Academy of Sciences

Copyright©2026 by the Authors under licence CC BY-NC-ND 4.0

http://www.imp.gda.pl/archives-of-thermodynamics/

Physical modelling in heat and fluid flow

Jarosław Mikielewicz[a], Dariusz Mikielewicz[b*]

[a]Institute of Fluid-Flow Machinery, Polish Academy of Sciences, Fiszera 14, Gdańsk 80-231, Poland
[b]Gdańsk University of Technology, Gabriela Narutowicza 11/12, 80-233 Gdańsk, Poland
*Corresponding author email: Dariusz.Mikielewicz@pg.edu.pl

Received: 29.11.2025; revised: 13.02.2026; accepted: 25.02.2026

Abstract

Experimental research, especially physical modelling, is vital when direct study of real systems is impractical. By applying similarity theory and dimensionless variables, models allow reliable analysis of results. While experiments alone are often qualitative and time-consuming, combining them with theoretical modelling yields stronger quantitative insights. Careful planning, computer-based data collection, and awareness of measurement errors ensure precision and efficiency. The theory of similarity defines the criteria under which the behaviour of a model can be considered representative of the real system. By satisfying these criteria, experimental results obtained from the model can be reliably extrapolated to the actual phenomenon. The present paper aims to present Authors' up-to-date experiences in advanced research using scaled models based on similitude theory, ever since its establishment as a branch of the engineering science to convince the reader about the benefits of physical modelling in comparison to advanced computer based methods governing the contemporary research.

Keywords: Experiment planning; Modelling; Energy; Entropy

Vol. 47(2026), No. 1, 205–212; doi: 10.24425/ather.2026.158670

Cite this manuscript as: Mikielewicz, J. & Mikielewicz, D. (2026). Physical modelling in heat and fluid flow. *Archives of Thermodynamics*, 47(1), 205−212.

1. Introduction

One of the fundamental methods for solving problems in science and engineering is experimental research, particularly through physical modelling of phenomena and processes. Careful planning of the experiment can provide a significant amount of required information at a moderate effort. In many cases, direct investigation of a real device is impractical due to high costs, safety concerns, or the scale of the system. In such situations, studies are conducted using physical models that replicate key aspects of the original system.

Physical models enable comprehensive investigations of technical devices or isolated phenomena under controlled laboratory conditions. The theory of similarity defines the criteria under which the behaviour of a model can be considered representative of the real system. By satisfying these criteria, experimental results obtained from the model can be reliably extrapolated to the actual phenomenon.

Physical modelling serves as a tool for acquiring new experimental data in cases where no reliable mathematical model exists or where available data are insufficient to validate existing theoretical models. This approach relies on inductive reasoning, involving observation, experimentation, data collection and inference. When supported by the theory of similarity, experimental findings can be generalised to other systems governed by the same dimensionless differential equations and boundary conditions.

However, research based solely on experimentation is often

Nomenclature

a – thermal diffusivity, m^2/s
c_p – specific heat, J/(kg·K)
F – force, N
g – gravitational acceleration, m^2/s
l – characteristic dimension, m
p – pressure, Pa
q – unit heat, J/kg
T – temperature, K
w – velocity, m/s
x, y, z – coordinates, m

Greek symbols
α – heat transfer coefficient, $W/(m^2 \cdot K)$
β – coefficient of volumetric expansion, 1/K
λ – thermal conductivity, W/(m·K)
ρ – density, kg/m^3
ν – kinematic viscosity, m^2/s
τ – time, s

Subscripts
0 – reference
v – volumetric

Superscripts
+ – non-dimensional

time-consuming and typically yields qualitative insights. Combining experimental methods with theoretical modelling – formulating mathematical models based on empirical data – leads to more robust, quantitative conclusions.

Modern experimental research is guided by a well-established methodology that facilitates the design, execution and interpretation of experiments. The preparatory phase includes a literature review, identification of independent and dependent variables, design of the experimental setup, selection of measurement techniques, and acquisition or fabrication of instrumentation. Each step requires a deep understanding of the phenomenon and substantial research experience.

To streamline the research process, variables are commonly expressed in dimensionless form, which reduces their number and simplifies analysis. The principles of similarity, modelling strategies and the formulation of dimensionless variables will be discussed later in detail.

Careful planning of experimental or numerical studies helps minimise effort and cost while maintaining the desired level of precision. Data acquisition and processing are typically performed using computer systems equipped with specialised software and sensor interfaces. All measurements are subject to error, stemming from limitations of both instruments and human perception. Although a detailed statistical analysis of measurement uncertainty is beyond the scope of this paper, it is worth noting that heat and flow measurements are often single-instance observations, which do not require extensive treatment of random error as in other experimental contexts.

The present paper aims to present Authors' up-to-date experiences in advanced research using scaled models based on similitude theory, ever since its establishment as a branch of engineering science, to convince the reader about the benefits of physical modelling in comparison to advanced computer based methods governing the contemporary research. Advances in computational power have also encouraged hybrid strategies that integrate similitude principles with finite element modelling. These methods allow researchers to construct reduced-scale models of highly complex structures with greater fidelity, positioning them as one of the most promising directions for future research. Collectively, the reviewed methodologies highlight both the progress achieved and the challenges that remain in establishing robust similitude frameworks for modern engineering structures. Presented are also the capabilities of physical modelling in application to complex flows.

2. Theory of similarity and principles of physical modelling

Interest in the similarity of physical phenomena dates back centuries. The work presented by Rayleigh [1] is consensually recognised as the first presentation of the use of scientific models, based on dimensional analysis. Research on this topic has been ongoing since the earliest mathematical descriptions of physical processes. Considerations related to similarity were already undertaken by Galileo, Reynolds, Fourier [2], Carnot [3] and others.

Research on reduced-scale models continues to expand as engineers seek reliable methods for predicting the behaviour of complex systems, identifying areas requiring further investigation. Historically, dimensional analysis has served as the dominant methodology, originating from the foundational work of Goodier and Thomson [4]. Although widely presented in academic literature through simplified examples, its successful application in aerospace case studies demonstrates its capability to address highly complex structural configurations. Nevertheless, the method demands meticulous selection of all relevant physical quantities and careful construction of non-unique dimensionless groups, making its practical use both labour-intensive and dependent on expert judgment.

In contrast, Kline's [5] formulation introduced a more intuitive approach based on governing differential equations that explicitly describe system response. Subsequent research has followed two paths: employing the solutions of these equations or using the equations directly to derive similitude conditions. While the latter avoids the need for analytical solutions, it requires complete knowledge of the physics and availability of governing equations – conditions rarely met for structures more complex than plates or shells. A derivative of this approach has been applied in modelling of complex flows presented as examples later.

To address this limitation, a recent work by De Rosa et al. [6] proposes an energy-distribution-based methodology formulated in modal coordinates. Since 2008, this approach has enabled detailed analysis of dynamic and acousto-elastic systems, offering a promising alternative where governing equations are incomplete or unavailable. Despite its mathematical complexity, it represents a significant step toward extending similitude theory to intricate structural assemblies.

Work in this area continues to evolve, with significant contributions such as those by Macagno [7] or Mikielewicz [8].

The principles of similarity are applied in:

- the search for analytical solutions,
- interpretation of experimental research results,
- modelling of phenomena and systems when direct investigation of the real object is impractical.

Similarity is generally an abstract property that may or may not be present in the analysed phenomena or systems. It is most commonly associated with geometric similarity, which is a limited concept that does not encompass the physical similarity of phenomena. Physically similar phenomena do not necessarily exhibit geometric similarity.

In a broader sense, geometric similarity includes the following types of geometric transformations:

- **uniformity**, involving proportional scaling of all geometric dimensions (uniform scale),
- **affinity**, involving transformations with different scaling factors in different directions,
- **affine transformation**, involving arbitrary linear transformations of geometric dimensions (defined by a transformation matrix).

Geometric similarity exists between objects if a unique transformation of geometric dimensions can be established between them. Such a transformation is referred to as a *geometric mapping*. Examples of geometric similarity are illustrated in Fig. 1.

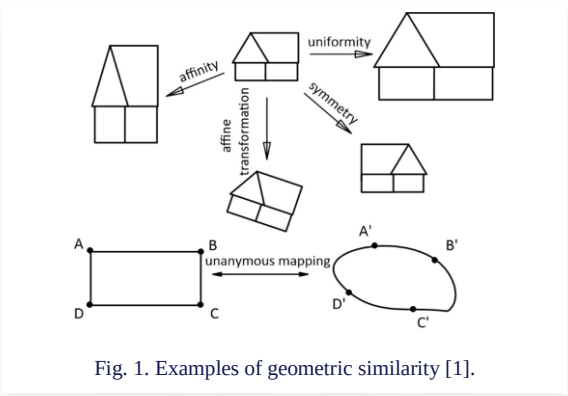


Fig. 1. Examples of geometric similarity [1].

However, geometric similarity alone does not guarantee similarity of physical phenomena – such as fields of physical quantities or the functioning of devices. If it did, a human being geometrically similar to an ant would be able to lift a piano with ease, and a flea scaled to human dimensions would be capable of jumping hundreds of meters. This is not the case, because physical quantities such as force scale with the cross-sectional area of muscles (proportional to the square of a linear dimension), while weight scales with volume (proportional to the cube of a linear dimension). As a result, actions such as lifting are not directly similar.

Phenomena or device behaviours are considered similar if the behaviour of one system allows the prediction of the other. Mathematically, this means that under joint geometric and physical similarity, the vector describing a point in space-time and its physical parameters are uniquely reproduced in the second, similar system. Such a mapping exists if both systems are governed by the same dimensionless set of equations and boundary conditions. In the most general case, these equations form a system of differential-integral equations with uniqueness conditions.

It follows that the criteria for similarity are most easily identified when a mathematical description of the phenomena is available. However, a complete description is not always possible. Therefore, various methods are used to determine similarity criteria, depending on the available information:

- analysis of differential-integral equations describing the phenomena,
- analysis of global balance equations (e.g. forces or energy) – partial analysis,
- dimensional analysis, based on the dimensions of selected physical and geometric parameters.

The reliability of these methods depends on the amount and quality of information available to the researcher. Dimensional analysis is considered the least reliable among them.

These methods will be discussed in more detail later in this paper. Regardless of the method used, the resulting similarity criteria can be applied in physical modelling of phenomena or devices. Depending on the degree to which the criteria are satisfied, modelling may be complete, approximate or partial.

2.1. Analysis of the mathematical description of similar phenomena

As mentioned in the introduction, similar phenomena are governed by the same system of differential-integral equations expressed in dimensionless form. Determining similarity criteria based on the mathematical description relies on the following principles [9−13]:

- Similar phenomena are described by dimensionless differential-integral equations along with appropriate boundary conditions,
- The solutions to these equations are expressed in terms of dimensionless parameters – known as *similarity numbers* – which appear both in the equations and in boundary conditions,
- These similarity numbers, formed as combinations of physical parameters, must have identical values for similar phenomena. The similarity criteria are constructed from independent similarity numbers.

The core task is therefore to transform the dimensional (physical) equations describing the phenomena into a dimensionless form, and then derive the similarity criteria from the resulting mathematical equations.

Dimensional (physical) equations are homogeneous with respect to physical dimensions, meaning that each term in the equation has the same dimensional unit. The process of converting a physical equation into a mathematical (dimensionless) one involves:

- Defining the relevant dimensions and characteristic values,
- Introducing dimensionless variables into the physical equations.

As a result, each term in the equation can be expressed as a product of two components: one dimensional (constructed from characteristic quantities and units), and one dimensionless

(constructed from non-dimensional variables). This transformation follows from *Bridgman's theorem*. By dividing the entire equation by one of the dimensional components – since all such components share the same dimension – a fully dimensionless equation is obtained.

This method will be applied to a system of equations describing thermo-fluid processes. For the purpose of analysis, we consider a general system of conservation equations, where the equation of motion is represented by the Navier–Stokes equation, and the energy equation by the Fourier–Kirchhoff equation [10].

According to the presented method, let us define the characteristic quantities:

a_0 – characteristic thermal diffusivity,
l_0 – characteristic dimension,
τ_0 – characteristic time,
T_0 – characteristic temperature,
ΔT_0 – characteristic temperature drop,
λ_0 – characteristic thermal conductivity coefficient,
c_{p0} – characteristic specific heat,
ρ_0 – characteristic density,
q_{v0} – characteristic intensity of heat sources,
F_0 – characteristic mass force,
Δp_0 – characteristic pressure drop,
ν_0 – characteristic kinematic viscosity,
w_0 – characteristic speed.

Using characteristic quantities, let us define dimensionless quantities:

$x^+ = x/l$, $y^+ = y/l$, $z^+ = z/l$ – dimensionless coordinates,
$\tau^+ = \tau/\tau_0$ – dimensionless time,
$T^+ = T/\Delta T_0$ – dimensionless temperature,
$w^+ = w/w_0$ – dimensionless speed,
$\lambda^+ = \lambda/\lambda_0$ – dimensionless thermal conductivity coefficient,
$c_p{}^+ = c_p/c_{p0}$ – dimensionless specific heat,
$\rho^+ = \rho/\rho_0$ – dimensionless density,
$q_v{}^+ = q_v/q_{v0}$ – dimensionless intensity of internal heat sources,
$F^+ = F/F_0$ – dimensionless force acting on a unit of mass,
$p^+ = p/\Delta p_0$ – dimensionless pressure,
$\nu^+ = \nu/\nu_0$ – dimensionless coefficient of kinematic viscosity.

Moreover, dimensionless spatial differentiation operators should be introduced. Operations ∇ and ∇^2 have a dimension and are related to the adopted scale defined by the characteristic dimension l_0. Therefore, the operators can be written:

$\nabla^+ = l_0 \nabla$ – dimensionless Hamiltonian operator,
$\nabla^{+2} = l_0^2 \nabla^2$ – dimensionless Laplace operator.

By introducing the above relationships into the balance equations for incompressible fluids, we obtain:

– for the mass balance:

$$\frac{w_0}{l_0}\nabla^+ w^+ = 0, \tag{1}$$

– for the Navier-Stokes equation:

$$\frac{w_0}{\tau_0}\frac{\partial w^+}{\partial \tau^+} + \frac{w_0}{l_0^2} w^+\nabla^+ w^+ = F_0 F^+ - \frac{\Delta p_0}{l_0 \rho_0}\frac{\nabla^+ p^+}{\rho^+} + \frac{\nu_0 w_0}{l_0^2}\nu^+\nabla^{+2} w^+, \tag{2}$$

– for the Fourier-Kirchhoff equation:

$$\frac{\Delta T_0}{\tau_0}\frac{\partial T^+}{\partial \tau^+} + \frac{w_0 \Delta T_0}{l_0} w^+\nabla^+ T^+ = \frac{\lambda_0 \Delta T_0}{l_0^2 c_{p0}\rho_0}\frac{\nabla^+(\lambda^+\nabla^+ T^+)}{c_p^+\rho^+} + \frac{q_{v0} q_v}{c_{p0}\rho_0 c_p^+\rho^+}. \tag{3}$$

In Eqs. (1)–(3), the relations between scales, called dimensional factors, present in each term of the equations must be equal to each other in order to be used in modelling between the model equation and a modelled equation. Dividing both sides of the equations by the dimensional factor gives:

$$\nabla^+ w^+ = 0, \tag{4}$$

$$\frac{l_0^2}{\tau_0 \nu_0}\frac{\partial w^+}{\partial \tau^+} + \frac{w_0 l_0}{\nu_0} w^+\nabla^+ w^+ = F_0 \frac{l_0^3}{\nu_0^2}\frac{\nu_0}{w_0 l_0} F^+ + - \frac{\Delta p_0}{w_0^2 \rho_0}\frac{w_0 l_0}{\nu_0}\frac{\nabla^+ p^+}{\rho^+} + \nu^+\nabla^{+2} w^+, \tag{5}$$

$$\frac{\partial T^+}{\partial \tau^+} + \frac{w_0 \tau_0}{l_0} w^+\nabla^+ T^+ = \frac{\lambda_0 \tau_0}{l_0^2 c_{p0}\rho_0}\frac{\nabla^+(\lambda^+\nabla^+ T^+)}{c_p^+\rho^+} + \frac{q_{v0} q_v \tau_0}{\Delta T_0 c_{p0}\rho_0 c_p^+\rho^+}. \tag{6}$$

The mass balance equation does not provide dimensionless parameters. The equation of motion, however, has dimensionless complexes:

1. $$\frac{l_0^2}{\tau_0 \nu_0} = \frac{l_0^2}{\tau_0 a_0}\frac{a_0}{\nu_0} = \frac{1}{\mathrm{PrFo}}, \tag{7a}$$

2. $$\frac{w_0 l_0}{\nu_0} = \mathrm{Re}, \tag{7b}$$

3. $$F_0 \frac{l_0^3}{\nu_0^2}\frac{\nu_0}{w_0 l_0} = F_0 \frac{l_0^3}{\nu_0^2}\mathrm{Re}^{-1}, \tag{7c}$$

4. $$\frac{\Delta p_0}{w_0^2 \rho_0}\frac{w_0 l_0}{\nu_0} = \mathrm{Eu}\,\mathrm{Re}, \tag{7d}$$

which are expressed by known dimensionless numbers.

The third dimensionless number $F_0 \frac{l_0^3}{\nu_0^2}$ can appear in different forms depending on the nature of the force F_0 in the Navier-Stokes equation. These mass forces can result from the existence of different fields: gravitational, electric, magnetic and others. Let us define this number in the case of the existence of a gravitational field.

Let a body of volume V and density ρ_0 be in a medium of density that differs by $\Delta\rho_0$ from the body's density. Then, according to Archimedes' principle, the body is subjected to a buoyant force:

$$Vg\Delta\rho_0 = Vg(\rho_0 - \rho). \tag{8}$$

In the case of gravitational field, its intensity is defined by the magnitude of the unit force F_0, that is the ratio of the buoyancy force $Vg\Delta\rho_0$ and the mass of the body, i.e. $V_0\rho_0$:

$$F_0 = g\frac{\Delta\rho_0}{\rho_0}. \tag{9}$$

Substituting Eq. (9) into Eq. (7c), the Archimedes number is obtained:

$$\mathrm{Ar} = \frac{g l_0^3}{\nu_0^2}\frac{\Delta\rho_0}{\rho_0} \tag{10}$$

If the density of the medium is negligible in relation to the density of the body, i.e. $\Delta\rho_0 \approx \rho_0$, then Archimedes' number is equal to Galileo's number:

$$\mathrm{Ga} = \frac{g l_0^3}{\nu_0^2}. \tag{11}$$

A special case of buoyancy forces are the forces resulting from thermal expansion or compressibility of the medium. The change in density $\Delta\rho_0$ is defined by the relationship:

$$\Delta\rho_0 = \beta\rho_0\Delta T_0. \tag{12}$$

Substituting the relationship (11) into (9), the Grashof number is obtained:

$$\mathrm{Gr} = \frac{g l_0^3 \beta \Delta T_0}{\nu_0^2}. \tag{13}$$

Let us return to the last of the dimensionless numbers appearing in the equation of motion – Eq. (5). It is called the Euler number:

$$\mathrm{Eu} = \frac{\Delta p_0}{\rho_0 w_0^2}. \tag{14}$$

In turn, the product of Grashof and Prandtl numbers is called the Rayleigh number:

$$\mathrm{Ra} = \frac{g l_0^3 \beta \Delta T_0}{\nu_0 a_0} = \frac{g l_0^3 \beta \Delta T_0}{\nu_0^2}\frac{\nu_0}{a_0} = \mathrm{Gr}\,\mathrm{Pr}. \tag{15}$$

The solution to the equation of motion is therefore described by the following relationship, which includes all dimensionless numbers occurring in the fluid flow:

$$\mathrm{Eu} = \mathrm{Eu}\left(\mathrm{Pr}, \mathrm{Fo}, \mathrm{Re}, \frac{F_0 l_0^3}{\nu_0^2}\right), \tag{16}$$

and defining the similarity of the velocity fields.

There are three complexes of dimensionless numbers in the energy equation:

$$\frac{\partial T^+}{\partial \tau^+} + \frac{w_0\tau_0}{l_0} w^+\nabla^+ T^+ = \frac{\lambda_0\tau_0}{l_0^2 c_{p0}\rho_0}\frac{\nabla^+(\lambda^+\nabla^+ T^+)}{c_p^+\rho^+} + \frac{q_{v0}q_v\tau_0}{\Delta T_0 c_{p0}\rho_0 c_p^+\rho^+},$$

1. $$\frac{w_0\tau_0}{l_0} = \frac{w_0 l_0}{a_0}\frac{a_0\tau_0}{l_0^2} = \mathrm{Pe}\,\mathrm{Fo}, \tag{17a}$$
2. $$\frac{\lambda_0\tau_0}{l_0^2 c_{p0}\rho_0} = \frac{a_0\tau_0}{l_0^2} = \mathrm{Fo}, \tag{17b}$$
3. $$\frac{q_{v0}\tau_0}{\Delta T_0 c_{p0}\rho_0} = \frac{q_{v0} l_0^2}{\lambda_0\,\Delta T_0}\mathrm{Fo}, \tag{17c}$$

and a dimensionless number characterising the internal heat source: $\frac{q_{v0} l_0^2}{\lambda_0\,\Delta T_0}$. From the above, it turns out that the temperature field depends on:

$$\frac{T}{\Delta T} = T^+\left[x_i^+, \mathrm{Fo}, \mathrm{Pe}, \frac{q_{v0} l_0^2}{\lambda_0\,\Delta T_0}\right]. \tag{18}$$

The similarity of temperature fields results in the similarity of temperature gradients at the wall. From the boundary condition – $\lambda\nabla T = \alpha\nabla T$, the Nusselt number can be derived:

$$\mathrm{Nu} = \frac{\alpha l_0}{\lambda_0} = \frac{\alpha\,\Delta T^+}{\lambda_0\Delta^+ T^+}. \tag{19}$$

From Eq. (19), it follows that the Nusselt number is a function of the temperature field; taking into account Eq. (18), we have:

$$\mathrm{Nu} = \mathrm{Nu}(T^+) = \mathrm{Nu}\left[x_i^+, \mathrm{Fo}, \mathrm{Pe}, \frac{q_{v0} l_0^2}{\lambda_0\,\Delta T_0}\right]. \tag{20}$$

Summarising the above considerations, it can be stated based on Eqs. (16) and (20) that in problems in which, in addition to geometric similarity, there is a similarity of temperature and velocity fields, the dependent Nusselt number can be expressed in the form:

$$\mathrm{Nu} = \mathrm{Nu}(T^+) = \mathrm{Nu}\left[x_i^+, \mathrm{Fo}, \mathrm{Re}, \mathrm{Pr}, \frac{q_{v0} l_0^2}{\lambda_0\,\Delta T_0}, \frac{F_0 l_0^3}{\nu_0^2}\right], \tag{21}$$

where $\frac{F_0 l_0^3}{\nu_0^2}$ may be the Archimedes, Galileo or Grashof number.

If the fluid is compressible, the velocity field and temperature field will also be influenced by the Mach number:

$$\mathrm{Ma} = \frac{w}{w_s}, \tag{22}$$

where w_s is the speed of sound in a given medium.

2.2. Partial analysis of similar phenomena

If we do not have a full mathematical description of the phenomenon, we can rely on the balances of global forces or energy when establishing the similarity criteria.

The following forces related to the unit mass can be distinguished:

- inertia: $F_b \approx \frac{w_0^2}{l_0}$,
- pressure: $F_p \approx \frac{p_0}{l_0\rho_0}$,
- viscosity: $F_t \approx \frac{\nu_0 w_0}{l_0^2}$,
- gravity: $F_g \approx g_0$,
- surface tension: $F_\sigma \approx \frac{\sigma_0}{l_0^2\rho_0}$.

By dividing the balance of forces acting in a phenomenon by one of the forces, we obtain dimensionless force ratios that can be reduced to the following relations:

$$\frac{F_p}{F_b} \approx \frac{p_0}{\rho_0 w_0^2} = \mathrm{Eu}, \qquad \frac{F_b}{F_t} \approx \frac{w_0 l_0}{\nu_0} = \mathrm{Re},$$
$$\frac{F_b}{F_g} \approx \frac{w_0^2}{g_0 l_0} = \mathrm{Fr}, \qquad \frac{F_b}{F_\sigma} \approx \frac{\rho_0 w_0^2 l_0}{\sigma_0} = \mathrm{We}. \tag{23}$$

The balance of forces does not always take into account all dimensionless numbers of energy relationships. Energy balance provides additional criteria numbers. Energy balances are treated in a similar way to force balances. They are divided by one of the terms, obtaining energy ratios that lead to criteria numbers.

The following types of energy are distinguished in relation to the volume of the system:

- conduction energy: $e_p \approx \frac{\lambda_0\,\Delta T_0}{\rho_0 l_0^2}$,
- convection energy: $e_k \approx \frac{w_0\, c_{p0}\Delta T_0}{l_0}$,

– friction energy: $e_t \approx \frac{\nu_0 w_0^2}{\rho_0 l_0^2}$,

– heat source energy: $e_v \approx q_{v0}$,

– energy accumulated in a non-stationary state:

$$e_n \approx \frac{c_{p0}\,\Delta T_0}{\tau_0}.$$

The ratios of these energies lead to the following criterion numbers:

$$\frac{e_t}{e_k} \approx \frac{w_0 \nu_0}{c_{p0}\Delta T_0 l_0} = \frac{\mathrm{Ec}}{\mathrm{Re}}, \tag{24a}$$

$$\frac{e_n}{e_p} \approx \frac{\rho_0 c_{p0} l_0^2}{t_0 \lambda_0} = \frac{l_0^2}{a_0 t_0} = \mathrm{Fo}, \tag{24b}$$

$$\frac{e_k}{e_p} \approx \frac{w_0 l_0 \rho_0 c_{p0}}{\lambda_0}, \tag{24c}$$

where $\mathrm{Ec} = \frac{w_0^2}{c_{p0}\Delta T_0}$ is the Eckert number.

Having the correct balance of forces and energy, one can find an appropriate set of criteria numbers describing the studied phenomenon.

2.3. Dimensional analysis

Dimensional analysis requires the least information about the phenomenon being studied, but is also the most unreliable. It is used only when the mathematical model of the phenomenon is not known or when we are unable to correctly formulate the balance of forces and energy [14,15].

With the help of dimensional analysis, a smaller number of dimensionless parameters m ($m < n$) is obtained from n physical parameters describing the phenomenon. This leads to the synthesis of information about the phenomenon, and thus to a reduction in the workload of research and then its description.

The basis of dimensional analysis is the so-called Buckingham-Driest theorem. It is based on the so-called Bridgman equation, stating that every physical quantity x can be represented as the product of a dimensionless number x^+ and the nomenclature:

$$x = x^+ [M]^a [L]^b [T]^c [\theta]^d, \tag{25}$$

where x^+ – number, M, L, T – basic dimensions, whose powers a, b, c, d are numbers. In the SI system of units, four basic units are sufficient to express the title of derived mechanical-thermal units (M – mass, L – linear dimension, T – time, θ – temperature).

Using the Bridgman equation, the Buckingham–Driest theorem can be formulated. If there is a functional relationship between n physical quantities:

$$f(x_1, x_2, x_3, \ldots, x_n) = 0, \tag{26}$$

then it can be presented in the form of a relationship of m dimensionless numbers π composed of physical quantities:

$$G(\pi_1, \pi_2, \pi_3, \ldots, \pi_m) = 0, \tag{27}$$

where $m = n - r$, r denotes the rank of a rectangular matrix created from exponents of powers of basic units representing the denomination of physical quantities describing the phenomenon. The rank of a matrix created from exponents of powers of denominations of physical quantities is understood as the rank of the highest non-zero determinant of a rectangular matrix. Obtaining the correct set of dimensional numbers using dimensional analysis requires knowledge of all physical parameters important for the phenomenon. Adding an insignificant parameter or omitting a significant one leads to an erroneous result.

The dimensional analysis method will be illustrated with a simple example of cooling steel spheres at a constant ambient temperature [9].

The excess temperature of the ball over the ambient temperature is $T - T_0$ and depends on:

– time elapsed from the moment the ball was inserted into the coolant (environment), τ [T],
– initial temperature difference, ($T_p - T_0$) [θ],
– heat capacity of the ball, $C = \rho c V$ [$ML^2 / T^2\,\theta$],
– thermal resistance of the ball surface, $R = 1/(\alpha A)$ or (αA) [$ML^2/T^3\,\theta$].

Physical quantities are therefore related to the relationship:

$$f\left[\tau, (T_p - T_0), C, \alpha A, (T - T_0)\right] = 0, \tag{28}$$

and the names of these quantities can be represented by independent basic quantities: M, L, T, θ. T_p stands for the initial temperature of the sphere, whereas the temperature T models the current temperature, which varies with time.

It is therefore possible to create a matrix of exponents of the powers of the basic units in which they appear in the names of quantities describing the phenomenon under consideration. This matrix is presented in the form of Table 1 as follows:

Table 1. Matrix of exponents of the powers of the basic units.

	τ	$T_p - T_0$	C	αA	$T - T_0$
[M]	0	0	1	1	0
[L]	0	0	2	2	0
[T]	1	0	−2	−3	0
[θ]	0	1	−1	−1	1

Looking at the rows of the matrix, we find that the second row of the matrix can be obtained by multiplying the first row by two. So the two rows of the matrix are linearly dependent, which means that the matrix is of order three, not four. Hence, $r = 3$, and there are $m = n - r = 5 - 3 = 2$ dimensionless numbers. As a result, we should obtain a relationship of the type:

$$G(\pi_1, \pi_2) = 0. \tag{29}$$

The numbers π_1 and π_2 can be constructed in various ways. Most often, three of the five quantities are selected, the name of which has all the basic dimensions, e.g. t, $T_p - T_0$, C; then, adding one of the remaining physical quantities, we obtain the required two dimensionless numbers in the form:

$$\pi_1 = \tau^{a1}\left(T_p - T_0\right)^{b1} C^{c1} (T - T_0), \tag{30a}$$

$$\pi_2 = \tau^{a2}\left(T_p - T_0\right)^{b2} C^{c2} (\alpha A). \tag{30b}$$

The unknown exponents of the powers $a1$, bl, cl and $a2$, $b2$ and $c2$ in each of the numbers are determined by equating the

exponents at each of the dimensions of the basic names of physical quantities (M, L, T, θ) to zero, which means that the resulting parameter from the physical quantities is dimensionless. In the example, the following two non-dimensional numbers were obtained:

$$\pi_1 = \frac{T-T_0}{T_p-T_0}, \qquad \pi_2 = \frac{\alpha A \tau}{C}. \tag{31}$$

So, the dimensional functional relationship f from Eq. (28) transforms into a dimensionless relationship G:

$$G\left(\frac{T-T_0}{T_p-T_0}, \frac{\alpha A \tau}{C}\right) = 0. \tag{32}$$

It is known from theory that the problem under consideration has an exact solution in the form:

$$\frac{T-T_0}{T_p-T_0} = exp\left(-\frac{\alpha A \tau}{C}\right). \tag{33}$$

Based on the relationship found in the dimensional analysis, one can look for an experimental correlation of the type:

$$\frac{T-T_0}{T_p-T_0} = f\left(\frac{\alpha A \tau}{C}\right), \tag{34}$$

and then compare it with the theoretical relationship and experimental data. A similar result is obtained from the analytical model applied to that issue based on the lumped capacitance method.

2.4. Principles of physical modelling

As previously mentioned, a model is a representation of one phenomenon by another, or of the same phenomenon under laboratory conditions. In many cases, testing a device or process under real-world conditions is not feasible due to high research costs, large dimensions of the system, or safety concerns. In such situations, experiments are conducted in laboratory settings using model devices.

For the model to be valid, both the model and the original system should be governed by the same set of differential-integral equations and boundary conditions expressed in dimensionless form. Experiments performed on the model allow researchers to identify relationships between similarity numbers. If the model enables experimentation under conditions where all independent dimensionless numbers (i.e. similarity criteria) are equal both in the model and in the original system, the modelling is considered *complete*.

Achieving complete similarity often requires the use of materials with physical properties different from those in the original system. This is necessary to satisfy the relationships implied by the equality of dimensionless numbers. However, if the number of required similarity conditions exceeds the number of available free variables, complete modelling becomes impossible. In such cases, *approximate* or *partial* modelling is employed.

One of the modelling approaches extensively practised by Authors are considerations of dissipation energy in application to complex convective flows. The energy has an additive property, and it is this property that has been used in the considered cases. Attention was focused on modelling flows with boiling or condensation under saturated conditions [16–18]. The proposed approach was also applied to the analysis of subcooled flow [19], mist flow [20], as well as supercritical heat transfer [21]. In these cases too, consistent results were obtained, which confirm the ability of the presented modelling to predict complex flows with heat transfer and non-linear effects. Recently, it proved to return satisfactory results in calculations of pressure drop at pressures close to the thermodynamic critical point [22] as well as during heat transfer under these conditions [23].

It should also be noted that the approach to obtaining a solution in a complex flow based on the summation of dissipation energies has also worked well in other cases. An approach using the concept of a dissipation energy summation model has previously been applied to the analysis of two-phase bubbly flow in a near-wall layer [24]. As a result of modelling, a non-dimensional velocity distribution in the boundary layer was obtained, inclusive of an effect of void fraction. Energy-based methods are an alternative to traditional modelling approaches, providing reliable results. Energy-based methods are appreciated in many engineering applications, see, for example, the Galerkin method or Huber stress folding in solids in mechanics.

Approximate modelling is used when less critical similarity criteria are satisfied to a sufficient degree, or when the research is conducted within a parameter range where one of the criteria has negligible influence on the phenomenon. This range is referred to as the *self-modelling area*. Approximate models are particularly useful in early-stage research or feasibility studies, where full similarity is not essential for drawing meaningful conclusions.

If no self-modelling region exists, **partial modelling** is applied. In this approach, the focus is placed on isolating the unknown effect of a phenomenon, assuming that all other effects are well understood and can be reliably predicted in both the original system and the model. Only the unknown aspect is subject to modelling. For example, when studying the resistance of a ship moving through water, it is known that the total resistance consists of frictional resistance and wave resistance. If the frictional resistance is well characterised, it can be subtracted from the total measured resistance, allowing the wave resistance to be isolated and modelled independently.

In practice, the choice between complete, approximate, and partial modelling depends on the research objectives, available resources, and the complexity of the phenomenon under investigation. It is also influenced by the desired accuracy of the results and the feasibility of reproducing the necessary similarity conditions.

Moreover, the design of a physical model must consider not only the similarity criteria but also practical aspects such as manufacturability, measurement accessibility, and the influence of scaling on material behaviour. For instance, certain materials may exhibit scale-dependent properties (e.g. surface roughness effects or thermal conductivity), which must be accounted for during model construction and interpretation of results.

Ultimately, physical modelling serves as a bridge between theoretical analysis and real-world application. When properly designed and interpreted, it provides valuable insights into complex systems that are otherwise difficult or impossible to study directly.

3. Conclusions

As has been shown, the modelling principles discussed are general in nature and can be applied to a wide variety of physical systems. Regardless of the specific substance or device under consideration, the method of analysis follows a common structure. First, the reference state of the system must be defined, which requires specifying the appropriate constitutive relations, such as for example governing equations, or alternatively other well established relations. Once the state description is established, the appropriate modelling approach can be applied.

In practice, determining the parameters that describe a system often relies on simplified analytical relations that capture the essential behaviour of the material or device. These developed models are not exact descriptions of real cases but idealised constructs that preserve the dominant physical mechanisms while neglecting secondary effects. For example, a real gas may be approximated by the ideal (perfect) gas model when intermolecular interactions are negligible; a simple magnetic material may be represented by the Curie law, which relates magnetisation to temperature and magnetic field; and an elastic solid may be described by Hooke's law, which assumes linear proportionality between stress and strain.

These models are examples of similitude in a broad sense: they allow different physical systems to be analysed using the same mathematical structure by identifying the relevant variables, reducing them through dimensional analysis, and expressing the governing relations in non-dimensional form. This approach underlies the Buckingham π theorem, which states that any physically meaningful relation between variables can be rewritten in terms of dimensionless groups. Such groups – like the Reynolds number in fluid mechanics or the Prandtl number in heat transfer – capture the essential similarity between systems of different scales or compositions. Thus, the use of idealised thermodynamic models is consistent with the general philosophy of similitude: replacing complex reality with a simpler, dimensionally consistent representation that preserves the key physical behaviour. For more information, the interested reader is referred to recent publications [25,26].

References

[1] Rayleigh, L. (1915). The principle of similitude. *Nature*, 95, 66−68.

[2] Fourier, J.B.J. (2009). *Théorie analytique de la chaleur* (1 st ed.). Cambridge University Press (in French).

[3] Carnot, S. (1824). *Réflexions sur la puissance motrice du feu et sur les machines propres à développer cette puissance*. Paris, Bachelier (in French)

[4] Goodier, J.N., & Thomson, W.T. (1944). *Applicability of similarity principles to structural models*. National Advisory Committee for Aeronautics; Technical Report NACA TN-933.

[5] Kline, S.J. (1965). *Similitude and approximation theory*. New York, Springer-Verlag.

[6] De Rosa, S., Franco, F., Li, X., & Polito, T. (2012). A similitude for structural acoustic enclosures. *Mechanical Systems and Signal Processing*, 30, 330–342. doi: 10.1016/j.ymssp.2012.01.018

[7] Macagno, E.O. (1971). Historico-critical review of dimensional analysis, *Journal of the Franklin Institute*, 292(6), 391−402.

[8] Mikielewicz, J. (1995). *Modeling thermal-hydraulic processes*. Ossolineum. IMP PAN Publishers (in Polish).

[9] Zierep, J. (1978). *Similarity criteria and modeling principles in fluid mechanics*. PWN, Warszawa (in Polish).

[10] Siedow, L.S. (1968). *Dimensional analysis and theory of similtude in mechanics*. WNT, Warszawa (in Polish).

[11] Krużylin, G.N. (1949). *Theory of similitude and modeling of heat transport*. NAUKA, Moskwa (in Russian).

[12] Muller, L. (1961). *Theory of mechanical similitude*. WNT, Warszawa (in Polish).

[13] Madejski, J. (1998). *Theory of heat transfer*. Politechnika Szczecińska, Szczecin (in Polish).

[14] Kasprzak, W., & Lysik, B. (1988). *Dimensional analysis. Algorithmic procedures for experimental planning*. WNT, Warszawa (in Polish).

[15] Száva, I., Gălățanu, T.-F., & Száva, I-R. (2025). Modern Dimensional Analysis Involved in Heat Transfer Problems. In *Heat and Mass Transfer – From Fundamentals to Advanced Applications*, InTechOpen (ed. D. Enescu). doi: 10.5772/intechopen.1009918

[16] Mikielewicz, J. (1974). Semi-empirical method of determination of HTC in flow boiling. *International Journal of of Heat and Mass Transfer*, 17, 1129-1134.

[17] Mikielewicz, D., Mikielewicz, J., & Tesmar, J. (2007). Improved Semi-Empirical Method for Determination of Heat Transfer Coefficient in Flow Boiling in Conventional and Small Diameter Tubes. *International Journal of of Heat and Mass Transfer*, 50(19–20), 3949–3956. doi: 10.1016/j.ijheatmasstransfer.2007.01.024

[18] Mikielewicz, D., & Mikielewicz, J. (2011). A Common Method for Calculation of Flow Boiling and Flow Condensation Heat Transfer Coefficients in Minichannels With Account of Nonadiabatic Effects. *Heat Transfer Engineering*, 32(13–14), 1173–1181. doi: 10.1080/01457632.2011.562728

[19] Mikielewicz, J., & Mikielewicz, D. (2017). A simplified energy dissipation based model of heat transfer for subcooled flow boiling. *International Journal of of Heat and Mass Transfer*, 106, 280–288. doi: 10.1016/j.ijheatmasstransfer.2016.10.077

[20] Mikielewicz, J., & Mikielewicz, D. (2018). A simplified energy dissipation based model of heat transfer for post–dryout flow boiling. *International Journal of Heat and Mass Transfer*, 124, 260–268. doi: 10.1016/j.ijheatmasstransfer.2018.03.063

[21] Mikielewicz, D., & Mikielewicz, J. (2020). Modelling of heat transfer in supercritical pressure recuperators. *Energy*, 207, 118251. doi: 10.1016/j.energy.2020.118251

[22] Mikielewicz, D., & Mikielewicz, J. (2022). An improved Müller-Steinhagen and Heck model for two phase pressure drop modelling at high reduced pressures. *Journal of Power Technologies*, 101(3), 81−87.

[23] Pysz, M., & Mikielewicz, D. (2023). Flow boiling of R1233zd(E) in a 3 mm vertical tube at moderate and high reduced pressures. *Experimental Thermal and Fluid Science*, 147, 110964. doi: 10.1016/j.expthermflusci.2023.110964

[24] Mikielewicz, D. (2003). Hydrodynamics and heat transfer in bubbly flow in the turbulent boundary layer. *International Journal of Heat and Mass Transfer*, 46(2), 207−220. doi: 10.1016/S0017-9310(02)00287-9

[25] Cristiano, P., Coutinho, C.P., Baptista, A.J., & Rodrigues, J.D. (2016). Reduced scale models based on similitude theory: A review up to 2015. *Engineering Structures*, 119, 81–94. doi: 10.1016/j.engstruct.2016.04.016

[26] Cheng, Y.-T., & Cheng, C.-M. (2004). Scaling, dimensional analysis, and indentation measurements. *Materials Science and Engineering: R: Reports*, 44(4−5), 91–149. doi: 10.1016/j.mser.2004.05.001

Co-published by
Institute of Fluid-Flow Machinery
Polish Academy of Sciences
Committee on Thermodynamics and Combustion
Polish Academy of Sciences

Copyright©2026 by the Authors under licence CC BY-NC-ND 4.0

http://www.imp.gda.pl/archives-of-thermodynamics/

An Innovative Device for Measuring Thermal Conductivity of Solids Utilising Transient Measurement Methods

M. S. Karthik[a], Mangalpady Aruna[b], P. Siva Kota Reddy[c,d]*

[a]Department of Mechanical Engineering, JSS Science and Technology University, Mysuru 570 006, Karnataka, India.
[b]Department of Mining Engineering, National Institute of Technology, Karnataka, Surathkal, Mangalore 575 025, Karnataka, India.
[c]Department of Mathematics, JSS Science and Technology University, Mysuru 570 006, Karnataka, India.
[d]Universidad Bernardo O'Higgins, Facultad de Ingeniería, Ciencia y Tecnología, Departamento de Formación y Desarrollo Científico en Ingeniería, Av. Viel 1497, Santiago, Chile.
*Corresponding author email: pskreddy@jssstuniv.in

Received: 06.21.2025; revised: 21.02.2026; accepted: 25.02.2026

Abstract

This paper presents the development of a novel experimental device for measuring the thermal conductivities of both non-conductive and conductive solids under transient conditions. The device comprises a sensor assembly coupled with an electronic bridge circuit and a direct current power source. The developed device was successfully used to measure the thermal conductivity of non-conducting and conducting solids, specifically granite and stainless steel 304, at room temperature. The device was also extended to two additional non-conducting solids, namely, limestone and basalt, to validate the testing. The thermal conductivities of granite, stainless steel-304, limestone and basalt were 2.14 W/(m·K), 14.93 W/(m·K), 2.91 W/(m·K), and 2.72 W/(m·K), respectively. These findings demonstrate excellent concordance with the existing literature for both non-conducting and conducting solid materials. The standard uncertainty of the developed device was ± 4.2%. The entire measurement process takes less than 5 s.

Keywords: Thermal conductivity; Sensor assembly; Electronic bridge circuit; Transient technique; Solids.

Vol. 47(2026), No. 1, 213–226; doi: 10.24425/ather.2026.158671

Cite this manuscript as: Karthik, M.S., Aruna, M., & Reddy, P.S.K. (2026). An Innovative Device for Measuring Thermal Conductivity of Solids Utilising Transient Measurement Methods. *Archives of Thermodynamics*, 47(1), 213−226.

1. Introduction

The ability to measure thermal conductivity is critical in determining the transfer of heat in numerous fields, including automotive, building insulation, mining, power generation, aerospace and engineering. The measurement of thermal conductivity can be accomplished through many methods, and for the majority of the methods, each method will be limited to a specific type of speed and solid and liquid materials. The thermal conductivity can be measured using experimental methods; these methods can be divided into two groups: steady-state methods (also known as continuous methods) and transient methods [1]. The principle behind steady-state devices that measure thermal conductivity is that one end of a sample is heated. At the same time, the other is cooled until equilibrium is reached, and data are collected to determine the sample's thermal conductivity (its thermal properties). However, measuring thermal conductivity with steady-state methods has drawbacks, as they require significant time for a sample to stabilise before it can be used for thermal conductivity measurements. In most laboratories where traditional devices are used to measure the thermal conductivity of solids, heat transfer must reach a steady state before experimenting, typically requiring 60 minutes. Different measuring devices are used to measure the thermal conductivities of different materials. Alterations in the sample's physical structure due to heating are an additional limitation of the steady-state approach for

Nomenclature

k – thermal conductivity, W/(m·K)
P – power input per unit length of heating wire, W/m
$T_{(t)}$ – temperature at time t, K
ΔT – temperature rise ($T_{(t2)} - T_{(t1)}$), K
t – time, s
u_k – standard uncertainty of thermal conductivity
u_m – standard uncertainty of temperature vs. ln time slope
u_p – standard uncertainty of power input

Subscripts

t_1 – initial time for measurement, s
t_2 – final time for measurement, s

Abbreviations and Acronyms

ADC – analogue-to-digital converter
ASTM – American Society for Testing and Materials
DC – direct current
GPIO – general purpose input/output
HDMI – high-definition multimedia interface
ISO – International Organization for Standardization
MOSFET– metal-oxide-semiconductor field-effect transistor
SBC – single-board computer
USB – universal serial bus

determination of the thermal conductivity. This phenomenon may influence or distort thermal conductivity measurements. Ailawalia and Priyanka [2] examined the influence of variable thermal conductivity within a semiconducting medium situated beneath an infinite elastic half-space. Leśniewski et al. [3] proposed a novel method for determining the thermal conductivity of porous ceramic materials based on the Stefan Boltzmann law of thermal radiation. Hemalatha et al. [4] used a two-slab guarded hot-plate apparatus to measure the thermal conductivities of natural fibre reinforced composites. The results from this study provided information for the future development of more sustainable materials for electrical component applications, including socket pins and switchboards. Using heat fluxes as the basis for balancing, Pistun et al. [5] developed a measurement apparatus to determine the thermal conductivity of solid materials; this apparatus uses both the steady-state technique and the bridge measurements method to determine thermal conductivity of solids. Huang and Wang [6] characterised the thermal conductance of their samples for the hotplate method by calculating the total error associated with their measurements to be ±5.2% due to uncertainty from standard techniques and also by using standard error propagation. Each test required approximately 40 minutes to reach steady-state heat transfer conditions.

1.1. Transient technique

Transient heat transfer is a critical area for many industries, including energy systems, electronics and material processing. A proper understanding of the dynamic behaviour of temperature fields within these industries contributes directly to the quality of many chemical products as well as to the reliability and safety of final manufactured goods, thus enabling more reliable estimates of future product quality. Accurate prediction of dynamic temperature processes within these types of industries also enables users to optimise their operations; therefore, prediction of temperature behaviour reduces costs associated with the production of goods. At the heart of the transient heat-transfer process is the unsteady heat conduction equation (this is a partial differential equation) derived from Fourier's law, which relates the rate of change in temperature over time (temporal) and the thermal conductivity (conductive heat) of the material being tested, as well as the temperature gradient within the material (spatial) and the time at which the temperature is measured. In contrast to steady-state collection methods, transient techniques enable rapid economical evaluation of a sample's thermal conductivity. Devices that use transient-state techniques produce a response upon introducing heat into the material over a defined time, allowing the time-dependent thermal response of the sample to be evaluated. When evaluating a sample using the transient technique, the sample does not have to reach equilibrium before a measurement can be taken. Another major reason why transient techniques are commonly used is that they offer several benefits over steady-state methods, including ease of setup, short testing times and, most importantly, low measurement uncertainty [7,8].

The transient measurement technique is ideal for measuring materials that consist of several layers or are heterogeneous materials (having multiple types of material in a single object). There are several different types of transient measurement techniques based on the mode of heat generation, temporal-based configurations of instruments and geometrical shapes (sources) of the heat source that are used. Some transient measurement techniques do not require any kind of physical interaction between the test specimen and the heating source, while other techniques require physical contact between the two. Yoon et al. [9] conducted research on the thermal conductivity of bentonite buffer materials using the hot-wire technique, and Wu et al. [10] studied the effect of natural convection on the thermal conductivity of liquids using the transitory plane source method, coupled with computational simulations to reflect the transitory heat transfer processes taking place in the liquid state.

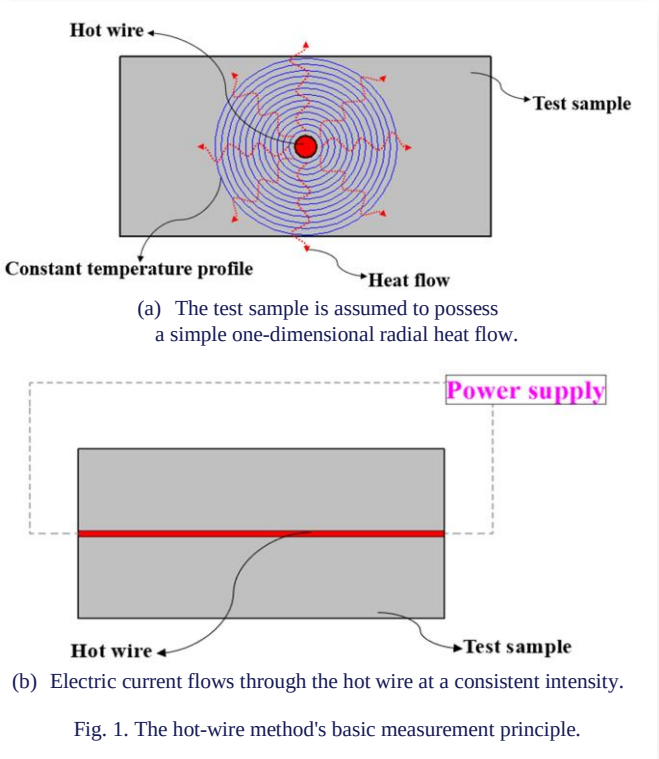
Kosowska-Golachowska et al. [11] employed a laser flash apparatus to quantify the thermal conductivity of an array of solid fuels, i.e. brown coal, hard coal and anthracite. Mo and Ban [12] studied the thermal conductivity of particulate beds at varying levels of compressive pressure, both under air and vacuum, via a hot-disk TPS 500 instrument. Memon [13] examined the thermal conductivity of cerasolzer CS186 and J-B epoxy-steel welded resins that were used for hermetic edge sealing, through the transient method. Zheng et al. [14] evaluated 17 models used to determine the thermal conductivity of frozen soil, focusing on silty clay, sand and sandy loam, via the transient method. Asadi et al. [15] investigated the thermal conductivities of cement mortars with a transient-plane-source (TPS) device. AlQdah [16] analysed the thermal conductivities of building materials in Medina, Saudi Arabia, under natural and local environmental conditions using a specialised equipment. Liu et al. [17] developed novel instruments for pre-drilling thermal-probe testing for evaluating thermo-physical properties of soil and rock.

1.2. Transient hot-wire method

The transient hot-wire technique is among the most important techniques to measure thermal conductivity [18]. The transient hot-wire method has become one of the most common, extensively used methods to determine thermal conductivities of liquids and solids, because of its superior accuracy (low level of uncertainty), and because of its capability for absolute measurement. Furthermore, there is an extensive body of literature that documents the establishment and theoretical framework behind the use of the transient hot-wire method [19,20]. The hot-wire method consists of heating a thin metallic wire by providing an electric current to it and inserting it in a sample. The wire temperature was determined as the heat dissipated from it into the sample. The sample material's ability to conduct heat can be determined by utilising the wire temperature and the logarithm of time. One variant of the hot-wire method is known as the "probe" technique. This arrangement measures the response of a "needle" that is inserted into the material to determine the sample's thermal conductivity [21]. The test methodology and data evaluation approach of the needle probe technique were established according to the American Society for Testing and Materials (ASTM) D5930 [22] and ASTM D5334 [23]. The probe incorporated both a thermocouple and a hot-wire heater. Other techniques include the dynamic hot-wire method, which employs an embedded wire in the sample to simultaneously function as a temperature sensor and heating element [24]. Constant electric power was utilised to heat the wire during the measurement. The wire's electrical resistance as a function of temperature was used to estimate the mean temperature of the heated wire over time. The way in which a specimen responds to a temperature change is primarily unaffected by its thermal conductivity, which is why so many researchers have turned to utilising the transient hot-wire method, due to the relative simplicity of its operation, for rapid determination of a material's thermal conductivity [7,8].

Transient hot-wire techniques have also been extensively developed into a widely accepted standard for accurately determining the thermal conductivity of various types of materials: solids [24], polymeric materials [25,26], liquids [25]. In addition, it has been established that transient hot-wire measurement techniques use a Fourier-type transient conduction method to transfer heat by conduction. The first use of the transient hot-wire technique for determining the thermal conductivity of rocks began in the 1960s [26]. Over the years, investigators have developed and refined various types of instruments for the transient hot-wire method to improve the precision of transient hot-wire measurement techniques [27–33]. In the recent past, the transient hot-wire technique has been used to determine the thermal conductivity of various kinds of materials that possess low thermal conductivities [34], for example, soil [35], ice cores [36,37], biological materials [38], ceramics, and refractory materials [39]. Transient hot-wire techniques, which have been utilised to characterise other materials including glass, porous elements and powdered chemicals, have also been applied within numerous different scientific disciplines to investigate the thermal characteristics of many different kinds of materials, including biological tissues, nano-scale liquids, and composite materials comprised of both nanometre and micrometre sized features. Many different research studies have focused on determining the thermal properties of a variety of these different materials using the transient hot-wire technique [40–44]. This is possible because the transient hot-wire technique enables investigators to measure both thermal diffusivity and thermal conductivity simultaneously. Comprehensive guidelines on the hot-wire measurement technique will be provided to those interested in performing thermal conductivity determination tests on refractory materials using the hot-wire technique in accordance with ASTM C1113 and ISO 8894 [39,45].

The hot-wire technique is established under the theoretical concept of "uniaxial radial heat flow," which occurs within a uniform and consistent test material, as shown in Fig. 1.



(a) The test sample is assumed to possess a simple one-dimensional radial heat flow.

(b) Electric current flows through the hot wire at a consistent intensity.

Fig. 1. The hot-wire method's basic measurement principle.

Variant (a) of Fig. 1 illustrates the test sample with an assumed simple one-dimensional radial heat flow originating from the centre of the hot-wire (sensor), creating a constant temperature profile that radiates outward radially. Variant (b) shows the electric current flowing through the hot wire embedded in the test sample at a consistent intensity (cross-sectional view). These illustrations together represent the basic measurement principle of the hot-wire method. These theoretical assumptions rely on the notion that the linear heat source is infinitely long and has a negligible diameter.

A variety of approaches to eliminating systematic errors in measurements taken under non-ideal conditions for accurately measuring the thermal conductivity of solid samples have been proposed by many researchers. Some solutions require the measurement of temperature at the end of the wire to be corrected [46,47], but these corrections tend to be smaller than those found under ideal conditions. The majority of corrections used to correct for systematic errors in hot-wire measurements relate to the effect of the heat lost from the wire due to convec-

tion and radiation. Some corrections are able to estimate the amount of heat lost through radiation by using mathematical models to determine the radiative losses, which are then applied as corrections to the temperature difference measured in the hot-wire system [48].

The objectives of the present work are as follows:

- to develop a novel device capable of measuring the thermal conductivity of both non-conductive and conductive solid samples,
- to establish a method to determine the thermal conductivity of both non-conductive and conductive solid test samples using the aforementioned device,
- to present a novel device and technique that functions under transient conditions and enables quicker measurements of thermal conductivity,
- to present a novel device and method that is accurate, cost-effective, straightforward and easily implementable.

The new thermal conductivity measurement device incorporates a unique combination of features that enable thermal conductivity measurements of both non-conductive and conductive solids. A U-shaped hot-wire configuration was incorporated into the design to increase sensitivity, flexibility and spatial resolution. To protect the hot-wire and minimise contact resistance with the sample, polyimide films were used for lamination. Additionally, a microprocessor-based electronic bridge circuit was used for improved data acquisition and processing. One of the most significant advantages of the new measurement device compared to conventional methods is that it measures the thermal conductivity of both non-conductive and conductive solids in less than 5 seconds, representing a substantial savings in measurement time. The proposed design is more efficient, more cost-effective and simpler than current technologies. However, the accuracy and precision of the new measurement device have been maintained through the use of modern electronic instrumentation. Because the exposure time of each sample is minimal, samples will not be altered due to changes in the physical structure of the sample. The device's portable design enables on-site measurement and makes it useful for a wide variety of applications. To evaluate the functionality of the new measurement device, a comparison of the thermal conductivity measurements made with the new device to literature values was performed. The results were found to be in good agreement and will be discussed in subsequent sections.

2. Experimental section

2.1. Origin of the test samples

The granite samples used in the present study were obtained from Ilakal, located in the Bagalkote district of Karnataka, India, an area renowned for its high-quality granite quarries. Limestone specimens were sourced from the Gulbarga district of Karnataka, India, which is recognised for its extensive limestone deposits. Basalt samples were collected from the Deccan Plateau region in Raichur (specifically from the Hutti gold mines area), Karnataka, India, which is characterised by widespread basaltic lava flows. Stainless steel – grade 304 (UNS S30400) was procured from AZO Materials.

2.2. Description of the experimental device

This investigation aims to use the transient dynamic hot-wire method to determine the thermal conductivity of both non-conductive and conductive solid materials. Figure 2 outlines the overall experimental workflow adopted in the present study. The procedure begins with the collection and preparation of reference samples, including non-conductive solids (granite, limestone, basalt) and a conductive solid (stainless steel 304). Concurrently, the design and development of the novel experimental setup are carried out, which involves reviewing the theoretical framework, designing the hot-wire sensor, developing the resistance sensing and heating circuit, and setting up the data acquisition system. The calibration procedure is then performed by testing the reference samples with known thermal conductivity. During the experiment, temperature changes are recorded over a defined time interval to determine thermal conductivity. If errors occur, adjustments are made by revisiting the experimental setup. Finally, the results are analysed, followed by interpretation and conclusions. The apparatus and methodology described herein adhered to the standards outlined in ISO-8894 [45] and ASTM C1113M – 09 [39].

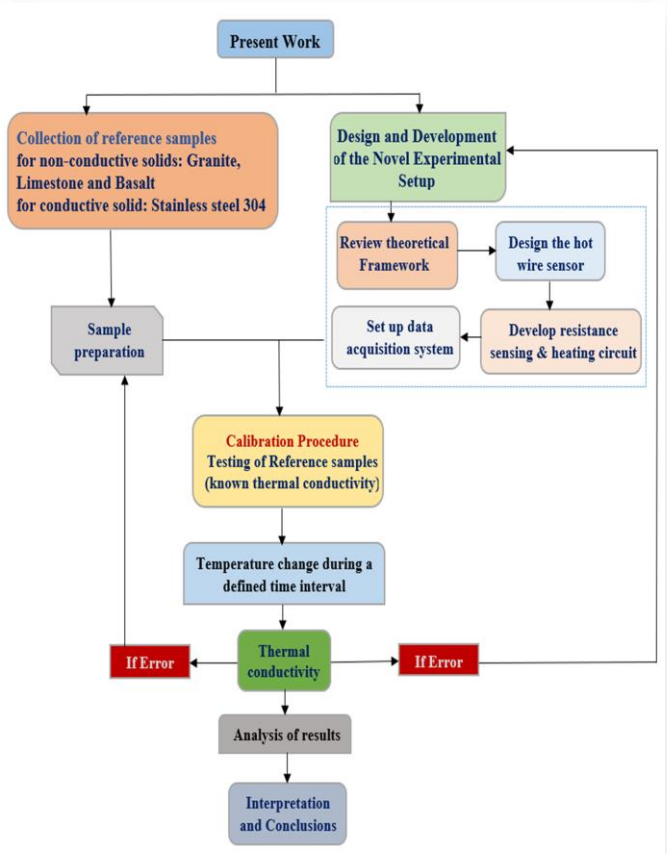


Fig. 2. Flow chart of the experimental procedure.

2.2.1. Sensor assembly

A newly developed device for measuring thermal conductivity consists of a sensor assembly, an electronic bridge circuit in electrical communication with the sensor assembly, and a direct current (DC) power source in electrical communication with the electronic bridge circuit. As shown in Fig. 3, the sensor assembly consists of a U-shaped hot-wire, a leading wire with one end spot-welded to the end of the U-shaped hot-wire, a barrel jack connection plug connected to the other end of the leading wire, and two polyimide films (Kapton) laminating the U-shaped hot-wire.

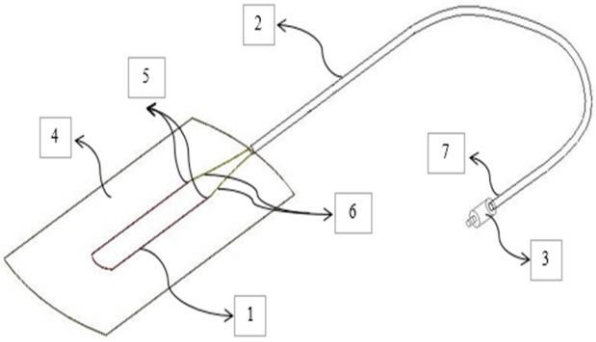


Fig. 3. Sensor assembly: 1. a U-shaped hot-wire, 2. a leading wire, 3. a barrel jack connection plug, 4. a polyimide film (Kapton), 5. an end of the U-shaped hot-wire (1), 6. an end of a leading wire connected to U-shaped hot-wire, 7. an end of a leading wire connected to barrel jack connection plug.

Figure 4 shows the geometry of the U-shaped hot-wire laminated using two polyimide films (Kapton). The U-shaped hot-wire is made up of an electrically resistive material wire of 150 µm diameter and 100 mm length. The electrically resistive material wire is platinum-rhodium wire with 90% platinum and 10% rhodium.

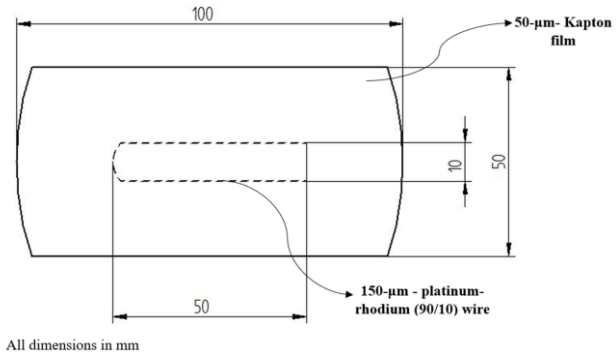


Fig. 4. Geometry of a U-shaped hot-wire laminated using two polyimide films.

The U-shaped configuration of a hot-wire must have its parallel legs separated by enough distance to decrease the heat transfer, which will increase the transfer capacity of the device while maintaining the uniformity of the radial heat flow between its legs. According to Lyu et al. [49], the spacing should be at least 6.8 times greater than the diameter of the pile, thereby ensuring that the pile-to-pile thermal interactions do not affect the radial heat flow patterns between piles. We therefore designed our U-shaped sensors with a spacing of approximately 10 mm between the parallel legs of the sensor, which is greater than the minimum needed to maintain isolated radial heat flow. In addition, Zhang and Fujii [50] found that by using insulating materials or coatings that are matched to or insulated from the heat properties of the materials they support, the radial distributions of heat flow from hot-wires can be improved. U-shaped hot-wire configurations can be effectively applied to a wide range of industrial, scientific and monitoring applications. U-shaped configurations of hot-wire sensors increase the sensors' sensitivity, flexibility and spatial resolution. Along with serving as a temperature sensor to record the increased temperature due to fluctuations in resistance, the U-shaped hot-wire also functions as a heating element when in contact with the solid test samples, establishing a temperature field that changes with time inside the solid test samples. The leading wire is a double-core and low-noise-shielded wire of 0.5 mm diameter. The leading wire serves as a support to the U-shaped hot-wire that is used as a sensor. With this arrangement, the U-shaped hot-wire that is used as a sensor is free from any kind of stress, when it is plugged or unplugged from the electrical connection. Further, laminating the U-shaped hot-wire by utilising two 25 µm thick heat-resistant sheets to protect the U-shaped hot-wire and minimise the contact resistance between the U-shaped hot-wire and the solid test sample.

2.2.2. Electronic bridge circuit

The electronic bridge circuit shown in Fig. 5 of this present work has consisted of a resistor divider circuit powered by a DC source, an analogue-to-digital converter (ADC) circuit connected to the resistor divider circuit, a metal-oxide-semiconductor field-effect transistor (MOSFET) used as a switch to control the voltage measurements across the resistor divider circuit, a transistor used to control the MOSFET switch, and a microprocessor connected to the ADC and transistor.

The resistor divider circuit, also known as a voltage divider circuit, is created by connecting the sensor assembly in series with a 0.5-ohm fixed resistor. This resistor divider circuit divides the input voltage from a continuous direct current (DC) power source into smaller voltages. The power source of direct current is used to supply power to the sensor assembly by maintaining a constant electrical current in the resistor divider circuit throughout the measurement procedure. The direct current is a regulated power source with the highest voltage and current setting a value of 30V and 2A, respectively. On drawing of current greater than the predetermined set limit by the electronic bridge circuit, the power supply of direct-current instantly transitions to the mode of constant current by lowering the voltage in a time period of the order of milliseconds after starting the process, as the load is minimal, considering 0.5-ohm resistances of the fixed resistor and resistance of the U-shaped hot-wire. Voltage data corresponding to different times at the junction point between the sensor assembly and the 0.5-ohm fixed resistor is measured using the ADC module and converted from an-

alogue to digital form. The MOSFET switch works with 5V logic, and the Raspberry Pi's general-purpose input/output (GPIO) pins can only provide 3.3V. A transistor is used to drive the MOSFET switch. The microprocessor (Raspberry Pi) via GPIO 4 drives the transistor. To turn on the transistor, a small current from the base to the emitter of the transistor is required. To limit this current, a 1-kiloohm resistor is used. The MOSFET switch is active low, which means that the MOSFET switch turns ON when the GPIO 4 is made low and turns OFF when the GPIO 4 is high. Low and high indicate the digital signals (0 and 1 in binary) whose voltage levels depend on the board used. On the Raspberry Pi microprocessor, low is 0V and high is 3.3V. The MOSFET switch requires 5V at the gate to turn it ON and 0V at the gate to turn it OFF. When GPIO 4 is high, the transistor is ON and pulls the MOSFET switch's gate terminal to 0V, turning it OFF. When GPIO 4 is low, the transistor is in OFF state, and the voltage at the gate becomes 5V because of the 10-kiloohm pull-up resistor, thus turning ON the MOSFET switch.

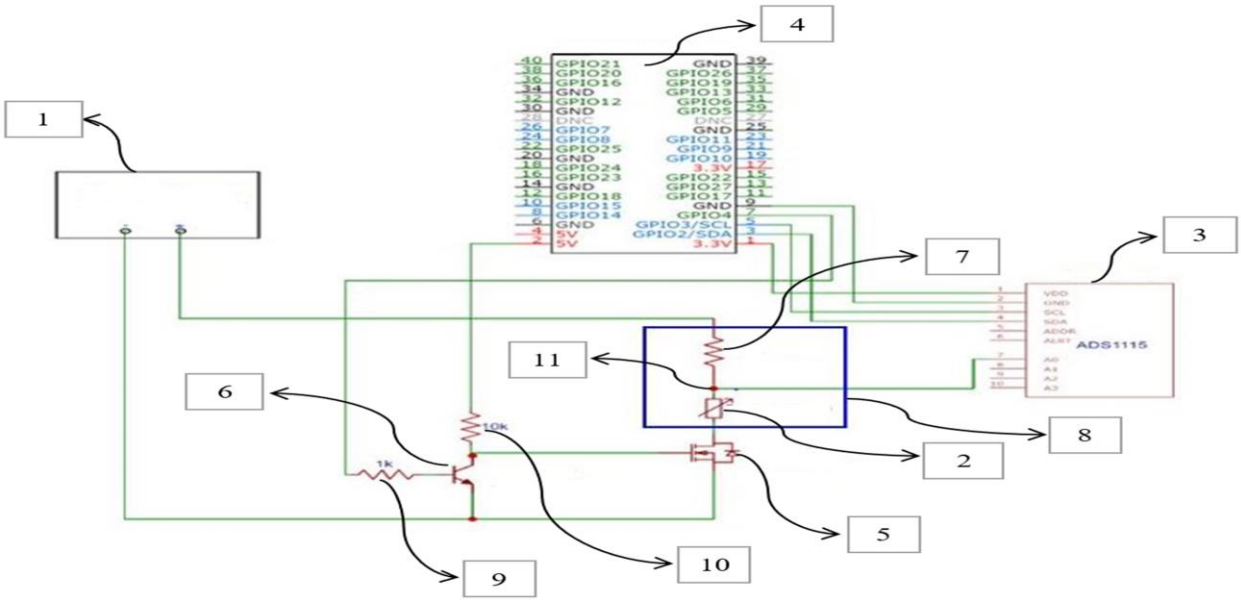


Fig. 5. Electronic bridge circuit: 1. a direct current (DC) power source, 2. a sensor assembly, 3. an analogue-to-digital converter (ADC) module, 4. a microprocessor, 5. a metal-oxide-semiconductor field-effect transistor (MOSFET) switch, 6. a transistor, 7. a 0.5-ohm fixed resistor, 8. a resistor divider circuit, 9. a 1 kiloohm resistor, 10. a pull-up resistor of 10 kiloohms, 11. a junction point of the sensor assembly (2) and the 0.5-ohm fixed resistor (7).

To keep the MOSFET switch OFF by default, a high signal is sent from GPIO 4. GPIO 4 is set to low only when the measurement is started. The microprocessor is used to convert the voltage measured with respect to time by the analogue-to-digital converter module to resistance and temperature for the calculation of thermal conductivity of solid test samples. The device operates in a transient condition, resulting in thermal conductivity measurement in a time period in a range of 1–5 seconds.

The Raspberry Pi functions as a single-board computer (SBC) equipped with a 64-bit Broadcom BCM2837 CPU featuring four cores operating at 1.2GHz and 1GB of RAM. This microprocessor utilises the Raspbian Operating System, which is stored on a 16GB SD card. The device is equipped with Universal Serial Bus (USB) and High-Definition Multimedia Interface (HDMI) ports, as well as 40 general-purpose input/output (GPIO) pins that facilitate connectivity with various hardware components. It is powered using a 5.1V 3A power adaptor. By connecting a mouse, a keyboard to the USB ports, and a monitor to the HDMI port, it can work as a small personal computer. A Python program is written on the Raspberry Pi. Figure 6 shows the flowchart for a Python program used to measure the thermal conductivity of a solid sample using an instrument as per the present work. When this program is executed, it turns on the resistor divider circuit by driving the MOSFET switch and collects the analogue data through an analogue-to-digital converter module. The final output of the code is a CSV file containing temperature-versus-time data.

By plotting temperature versus time and measuring the slope of the linear portion of the curve, the thermal conductivity of the test sample is calculated.

The thermal conductivity of the material under investigation was calculated by determining the slope of the line relating the temperature difference (ΔT) to the natural logarithm of time ($\ln t$). The temperature (T) of the U-shaped hot-wire was measured as a function of time (t), which was subsequently used to calculate the sample's thermal conductivity (k) using Eq. (1):

$$k = \frac{P}{4\pi\left(T_{(t2)} - T_{(t1)}\right)} \ln\left(\frac{t_2}{t_1}\right), \quad (1)$$

where k – thermal conductivity in W/(m·K), P – power input per unit distance along the linear heating source in W/m, $\Delta T = (T_{(t2)} - T_{(t1)})$ – temperature rise in K, and $\ln(t_2/t_1)$ – logarithm of time in seconds.

Table 1 provides a detailed description of the various components and specifications of the newly developed device for measuring the thermal conductivity of solids.

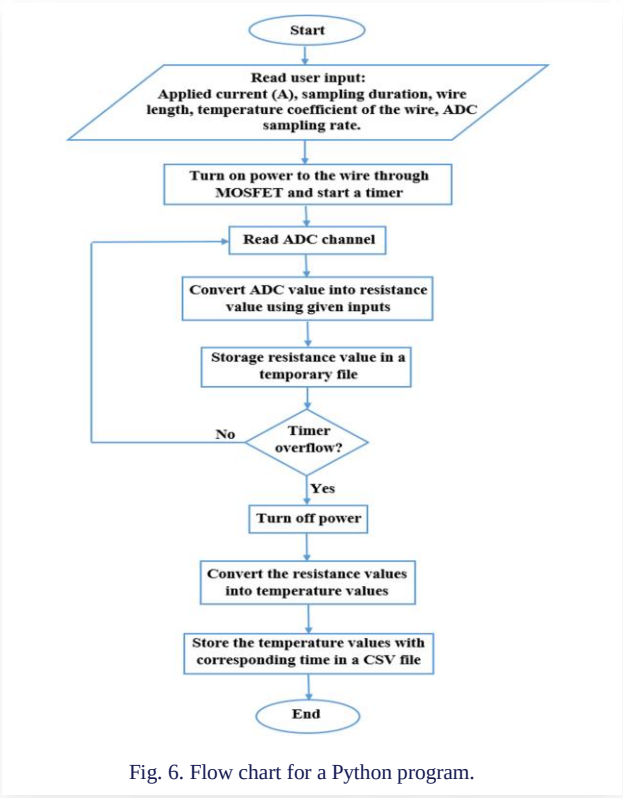


Fig. 6. Flow chart for a Python program.

3. Results and method for measuring thermal conductivity of solid samples

The device and method described in the present study are used to measure the thermal conductivity of solid test samples, including granite, stainless steel-304, limestone and basalt. The hot-wire sensor size cannot exceed the accessible sample size, as required by transient methods. Notably, each solid test sample should have a minimum thickness of 5 mm, a length of 100 mm, and a breadth of 50 mm, according to the U-shaped sensor's design requirements.

Several strategies can be employed to minimise the thermal contact resistance at the U-shaped sensor-solid sample interface. Optimising surface preparation is essential to ensure that sample surfaces are smooth, flat and thoroughly cleaned, thereby eliminating contaminants. Furthermore, in applications requiring a reduction in the contact resistance of electronic devices, the structural integrity and thermal stability of Kapton render it a preferred choice [51]. For instance, Romero et al. [52] focused on the laser ablation of Kapton polyimide, which demonstrated promising electrical and thermal characteristics, indicating its potential as a flexible, conductive substrate. The use of polyimide films (Kapton) is based on creating a uniform and conformal interface between the sensor and sample, which reduces the

Table 1. Components and specifications of the instrument as per the present work.

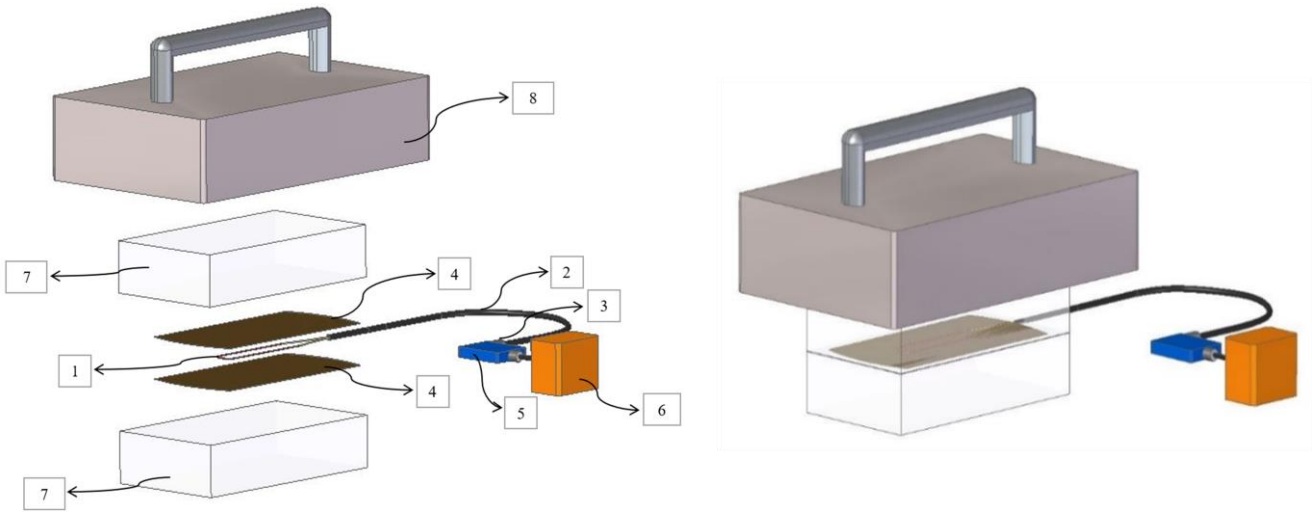
No.	Components	Specifications
1	U-shaped hot-wire	Platinum-rhodium with 90% platinum and 10% rhodium, diameter =150 µm , length = 100 mm
2	Leading wire	Double-core, low-noise-shielded wire, diameter = 0.5 mm
3	Connection plug	DC barrel jack plug
4	Polyimide film	Kapton, thickness = 25 µm + 25 µm = 50 µm
5	Power source	Maximum – 30 V and 2 A, DC power supply
6	analogue-to-digital converter (ADC) module	ADC - ADS1115, 16-bit conversion, maximum data rate of 860 samples per second
7	Microprocessor	The Raspberry Pi incorporates a 64-bit CPU, specifically, a Broadcom BCM2837 Quad Core processor operating at 1.2GHz. It is equipped with 1GB of RAM and includes a 16GB SD card for data storage purposes.
8	MOSFET switch	IRFZ44N – drain current DC = 49 A (maximum), drain source voltage = 55 V (maximum), drain-source on-resistance = 22 mΩ (maximum), fast switching
9	Transistor	2N3904, emitter - 40V(maximum), base – 60 V (maximum), collector current - 200 mA
10	Fixed resistor	0.5 Ω, 3 W
11	Resistor	1 kΩ
12	Pull-up resistor	10 kΩ

gaps and imperfections that typically contribute to increased contact resistance. In the present work, the U-shaped hot-wire laminated with two polyimide films (Kapton) is squeezed between two solid test samples to measure its material's thermal conductivity.

Empirical models and experimental observations indicate that the contact resistance decreases nonlinearly with increasing compression pressure. When pressure is applied, it deforms the asperities at the contacting interface, effectively increasing the real contact area, which in turn reduces the resistance to heat flow [53,54]. This effect is crucial in applications where minimising the thermal contact resistance is necessary for efficient thermal management [55]. In our studies, to apply a minimal force on the surfaces, a metallic mass of 2 kg was mounted on top of the sample. As a result, heat is transferred to the solid test samples from the U-shaped hot-wire via the polyimide films. This methodology effectively mitigated the thermal contact resistance, enabling the apparatus to function with minimal uncertainty. This technique has proven successful in reducing contact resistance in studies involving materials such as granite, stainless steel-304, limestone, and basalt.

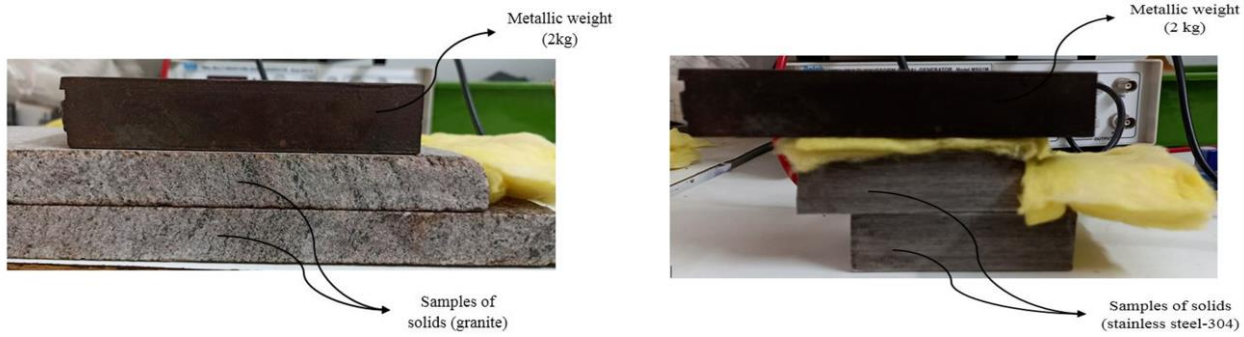
An arrangement of the device, as per the present work for measuring the thermal conductivity of a solid test sample, including a U-shaped hot-wire, two polyimide films, two solid test samples, and a metallic weight used to test the thermal conductivity at the surrounding temperature, is illustrated in Fig. 7.

Figure 8 is a photograph showing the arrangement of a device as used in the present work, positioned between solid test samples, with a weight applied for the measurement of thermal conductivity.



a) Exploded view b) Isometric view

Fig. 7. Arrangement of a device for measuring thermal conductivity of a solid test sample: 1. a U-shaped hot-wire, 2. a leading wire, 3. a barrel jack connection plug, 4. a heat-resistant Kapton sheet, 5. an electronic bridge circuit, 6. a direct current (DC) power source, 7. a solid test sample, 8. a metallic weight.



a) Granite b) Stainless steel-304

Fig. 8. Photograph showing an arrangement of the instrument with application of weight for measurement of thermal conductivity.

According to experimental findings by the instrument as per present work, a heat pulse of about 5 seconds that the U-shaped hot-wire transfers through the polyimide film (Kapton) to the solid test samples appears to be adequate to produce a temperature increase between the time t_1 and t_2 at a power (P) input of about 3 W. Total 1500 measurements are used for this run, ranging from 0 to 5 seconds.

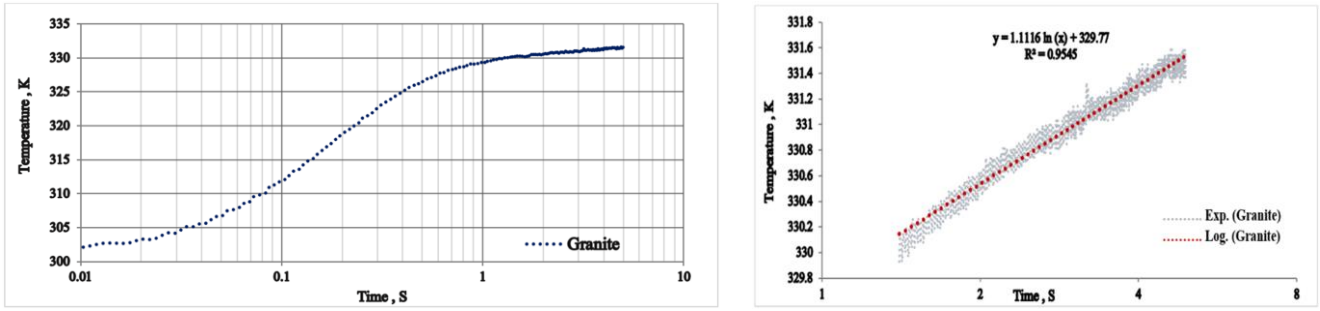
The transient hot-wire measurement method comprises three steps. Initially, experimental resistance measurements are obtained from a U-shaped hot-wire over a specified time period. Subsequently, the temperature was derived from these data. Over time, the temperature of the U-shaped hot-wire exhibited a logarithmic pattern. Therefore, when plotting the temperature against time on a semi-logarithmic graph to measure the thermal conductivity via the transient hot-wire method, it is standard practice to exclude the initial segment of the temperature versus time data points [44]. Hence, we focus our analysis on the upper linear portion of the plot. This methodology is essential for achieving precise thermal conductivity measurements and involves several critical factors. The initial segment of the temperature-time plot frequently exhibits transient effects that are inconsistent with the steady-state heat conduction model. During this phase, the temperature increase may be influenced by thermal inertia and other transient phenomena, potentially distorting the measurements [44]. The upper linear portion of the plot indicates the establishment of a quasi-steady state condition or thermal equilibrium, where the temperature increase follows a predictable and consistent pattern. This linear behaviour signifies that the system has reached a state in which the assumptions of the transient hot-wire model are applicable. At this point, the thermal conductivity can be accurately determined from the slope of the line [44]. By concentrating on the linear portion, the effects of noise and irregularities present in the initial transient phase can be avoided, thereby enhancing the precision of the measurement, as data points from the steady linear portion are less susceptible to such disturbances. The semi-logarithmic scale facilitates the clear identification of the linear region, simplifying the extraction of thermal properties by converting the exponential temperature increase into a linear relationship. This transformation is crucial for correlating the measured temperature increase with the theoretical model, enabling the calculation of the thermal conductivity and diffusivity [44]. These practices collectively ensure that the data used for calculating the thermal conductivity are derived from a range in which the heat transfer

mechanisms are well understood and accurately represented by the theoretical models employed in the analysis. Discarding the initial portion and focusing on the linear part mitigated errors and enhanced the reliability of the thermal conductivity measurements.

The upper linear segment is selected based on the premise that, during this phase, the temperature increase of the wire demonstrates a direct linear correlation with the natural logarithm of the time. This correlation is attributed to the predominance of heat conduction during this phase, with negligible influence from other effects, such as natural convection. The linear region was identified by ensuring that the plotted points formed a straight line with minimal deviation, thereby confirming that the conditions were primarily due to pure conduction [56]. It is advantageous if the R-squared value of the linear fit approaches 1, indicating a robust linear relationship, and if the selected region produces consistent results across multiple measurements of the same sample.

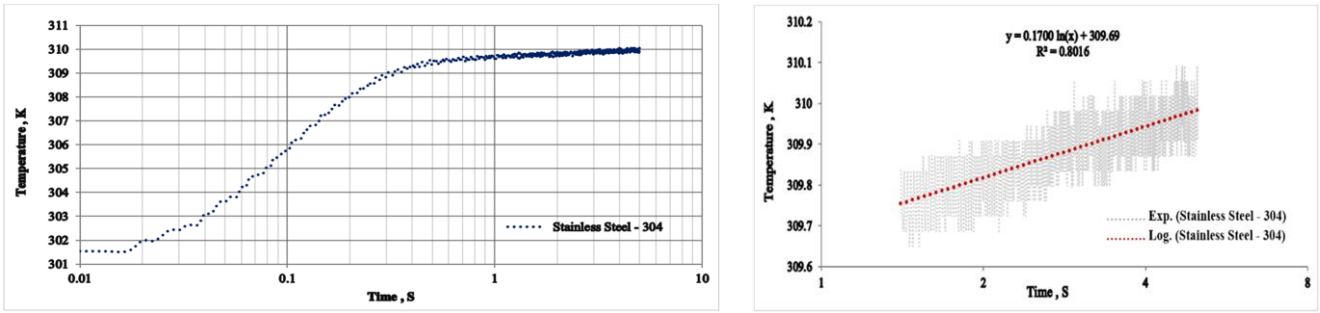
A typical experimental semi-logarithmic temperature vs. time response and its logarithmic fit for the linear portion of the experimental data for the solid test samples of granite and stainless steel 304 at the surrounding temperature are illustrated in Figs. 9 and 10, respectively. The thermal conductivity of granite and stainless steel 304 is near the upper end of the linear curve. For granite and stainless steel-304, the thermal conductivity values computed from the temperature against the time curve in a semi-logarithmic plot are 2.14 W/(m·K) and 14.93 W/(m·K), respectively. These values differ by –0.04 for granite and +0.01 to +0.59 for stainless steel 304 from the values suggested by the literature [57–60].

Tables 2 and 3 present an assessment of the measured thermal conductivity values for the granite and stainless steel-304 test samples, including their deviations, relative to the values recommended in the existing literature [57–60].



a) b)

Fig. 9. (a) Experimental temperature variation of granite with time, and (b) its logarithmic fit for the linear portion of the experimental data.



a) b)

Fig. 10. (a) Experimental temperature variation of stainless steel-304 with time, and (b) its logarithmic fit for the linear portion of the experimental data.

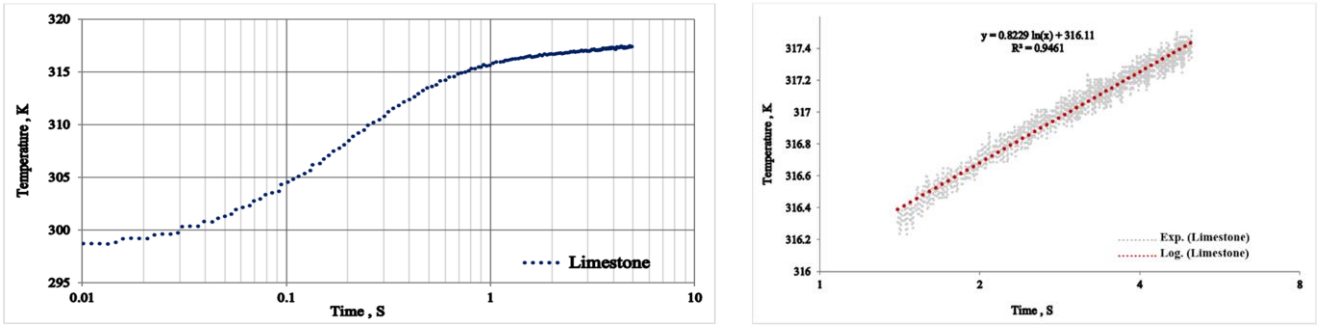
Table 2. Assessment of the granite samples measured thermal conductivity values, including their deviations, in relation to the value proposed in [57].

Non-conductive solid sample – granite			
Trial no.	Measured thermal conductivity at 300 K (W/(m·K))	Thermal conductivity at 300 K (W/(m·K)) [57]	Deviation
1	2.14	2.18	–0.04
2	2.16		
3	2.13		
Mean	2.14		
Standard deviation	0.016	–	
Random error in measurements (from repeated measurements) (%)	0.75%		

Table 3. Assessment of the stainless steel-304 samples measured thermal conductivity values, including their deviations, in relation to the values proposed in the literature ([58−60]).

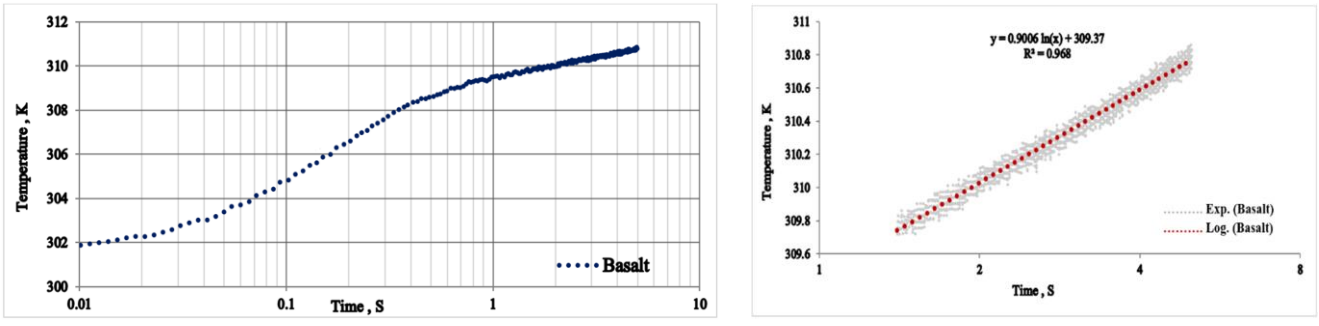
Conductive solid sample – stainless steel-304					
Trial no.	Measured thermal conductivity at 300 K (W/(m·K))	Thermal conductivity at 300 K (W/(m·K)) [58]	Thermal conductivity at 300 K (W/(m·K)) [59]	Thermal conductivity at 300 K (W/(m·K)) [60]	Deviations
1	14.94	14.92	14.84	14.34	+0.01 [58] +0.09 [59] +0.59 [60]
2	14.93				
3	14.91				
Mean	14.93				
Standard deviation	0.016	–			
Random error in measurements (from repeated measurements) (%)	0.11%				

To assess the broad applicability of the developed device, it is essential to incorporate various solid samples. By evaluating the device across different solid samples, we can determine its performance in various contexts and identify any limitations or areas for enhancement. The thermal conductivities of solid samples, such as limestone and basalt, were examined in this study. Figures 11 and 12 present semi-logarithmic graphs illustrating the correlations between the temperature and time for limestone and basalt. These findings were obtained at ambient temperature using the apparatus developed in this study. The thermal conductivities of limestone and basalt, as determined from the semi-logarithmic temperature-time graphs, were 2.91 W/(m·K) and 2.72 W/(m·K), respectively. These results showed deviations from the literature values, with −0.06 for limestone and +0.04 for basalt, respectively [61,62].



b) b)

Fig. 11(a) Experimental temperature variation of limestone with time, and (b) its logarithmic fit for the linear portion of the experimental data.



c) b)

Fig. 12. (a) Experimental temperature variation of basalt with time, and (b) its logarithmic fit for the linear portion of the experimental data.

Tables 4 and 5 provide an evaluation of the measured thermal conductivities and their deviations for the test samples using the developed apparatus, in comparison with the literature values [61,62].

This novel apparatus and methodology are appropriate for determining the thermal conductivities of both non-conductive and conductive solid materials under transient conditions. The measurement process required only 5s, facilitating a more rapid assessment than existing technologies. Moreover, this innovative approach provides a straightforward, efficient and cost-effective alternative to current methods.

Table 4. Assessment of the limestone samples measured thermal conductivity values, including their deviations, in relation to the value proposed in [61].

Non-conductive solid sample – limestone			
Trial no.	Measured thermal conductivity at 300 K (W/(m·K))	Thermal conductivity at 300 K (W/(m·K)) [61]	Deviations
1	2.89	2.97	–0.06
2	2.92		
3	2.93		
Mean	2.91		
Standard deviation	0.021	–	
Random error in measurements (from repeated measurements) (%)	0.72%		

Table 5. Assessment of the basalt samples measured thermal conductivity values, including their deviations, in relation to the value proposed in [62].

Non-conductive solid sample – basalt			
Trial no.	Measured thermal conductivity at 300 K (W/(m·K))	Thermal conductivity at 300 K (W/(m·K)) [62]	Deviations
1	2.69	2.68	+ 0.04
2	2.73		
3	2.74		
Mean	2.72		
Standard deviation	0.03	–	
Random error in measurements (from repeated measurements) (%)	1.10%		

3.1. Uncertainty analysis

The guide to the expression of uncertainty in measurement, a standard for estimating uncertainty published by the International Organisation for Standardisation (ISO) was used [63]. The contributions of the components to the standard uncertainty can be represented by the following Eq. (2):

$$u_k = \sqrt{\left(\frac{\partial k}{\partial P}\, u_P\right)^2 + \left(\frac{\partial k}{\partial m}\, u_m\right)^2}. \quad (2)$$

The standard uncertainty of the thermal conductivity is represented by u_k, where u_p and u_m denote the standard uncertainties of the power input per unit distance along the linear heating source and the slope of temperature rise versus logarithmic time, respectively.

In the present work, the uncertainty associated with the measurement of the thermal conductivity was evaluated as follows: the voltage applied to the voltage divider circuit, along with its variation during a transient experimental run, was monitored using a digital high-resolution multimeter with an uncertainty of ±1 μV. The uncertainty related to the power input per unit length of the platinum-rhodium wire (composed of 90% platinum and 10% rhodium) was assessed as ±0.2%. The temperature coefficient of the thin platinum-rhodium wire resistance was determined through calibration conducted during the measurement process, with an estimated uncertainty of ±0.2%. The experimental time was measured and recorded using an ADC (ADS1115) with a 16-bit conversion, a maximum data rate of 860 samples per second, and an uncertainty of ±1 μs. The slope of the temperature increase to the natural logarithmic time ratio was measured with an uncertainty of ±3.8%, as estimated by deviations from linearity. The experimental sensor was designed such that the thickness of the Kapton heat-resistant sheets was precisely defined and equal to 50μm, ensuring that it did not affect the uncertainty of the technique. The standard uncertainty of the developed device was assessed at ±4.2% for the measurement of the thermal conductivity of solids.

4. Conclusions

The development of novel devices based on the transient technique has been necessitated by the demand for information regarding the ability to conduct heat in both non-conductive and conductive solid test samples, and to analyse heat transfer in engineering applications without resorting to time-consuming laboratory tests. The developed apparatus exhibits multiple advantages over existing instruments, including operational simplicity and cost effectiveness alternative to current methods. The capability to evaluate thermal conductivity in both non-conductive and conductive solid specimens, with exceptional precision and accuracy facilitated by contemporary electronic instrumentation, and minimal sample exposure time is demonstrated.

The present study uses a newly developed portable instrument to analyse the thermal conductivity of both non-conductive and conductive solid test samples, such as granite, stainless steel-304, limestone and basalt, at room temperature. The transient technique applied to solid test samples yielded results that closely matched previously published data. The measured thermal conductivities were 2.14 W/(m·K), 14.93 W/(m·K), 2.91 W/(m·K) and 2.72 W/(m·K) for granite, stainless steel 304, limestone and basalt, respectively. The standard uncertainty of the developed instrument was ±4.2%. The results strongly align with existing literature. Notably, the measurement process takes around 5 seconds for solid test samples. It is realisable to employ the developed device to determine the thermal conductivity of non-conductive and conductive solid test samples, as evidenced

by the excellent agreement between experimental results and suggested data.

The future scope of this study includes several potential research directions. These studies involve exploring various wire materials and geometries to optimise the sensor performance and expand the range of measurable solids. Extending the measurement capabilities to encompass a broader range of temperatures and pressures could enhance the applicability of the device across diverse industrial settings.

Acknowledgements

The authors extend their sincere appreciation to JSS Science and Technology University in Mysore, Karnataka, India, and the National Institute of Technology in Surathkal, Karnataka, India, for providing the essential facilities required to conduct this research.

References

[1] Paul, G., Chopkar, M., Manna, I., & Das, P.K. (2010). Techniques for measuring the thermal conductivity of nanofluids: A review. *Renewable and Sustainable Energy Reviews*, 14(7), 1913–1924. doi 10.1016/j.rser.2010.03.017

[2] Ailawalia, P., & Priyanka, P. (2024). Effect of variable thermal conductivity in semiconducting medium underlying an elastic half-space. *Archives of Thermodynamics*, 45(3), 159–166. doi: 10.24425/ather.2024.151226

[3] Leśniewski, W., Czekaj, E., Wieliczko, P., & Wawrylak, M. (2019). Novel method of thermal conductivity measurement using Stefan-Boltzmann law. *Archives of Metallurgy and Materials*, 64(1), 311–315. doi: 10.24425/amm.2019.126253

[4] Hemalatha, C.K., Venkatachalam, G., & Bhuvaneshwari, M. (2025). Investigation of thermal conductivity of Prosopis juliflora/Acacia leucophloea/Acacia nilotica fibers/ceramic fillers/epoxy composites. *Results in Engineering*, 25, 104225. doi: 10.1016/j.rineng.2025.104225

[5] Pistun, Y., Matiko, H., Vasylkivskyi, I., Fedynets, V., & Krykh, H. (2024). Automated system for measuring thermal conductivity of solid materials. *Metrology and Measurement Systems*, 31(1), 179−193. doi: 10.24425/mms.2024.148538

[6] Huang, J.S., & Wang, C.Y. (2025). Numerical simulation and measurement of effective thermal conductivity of an additively manufactured lattice microstructure with gradient porosity. *Results in Engineering*, 25, 104177. doi: 10.1016/j.rineng.2025.104177

[7] Komini Babu, S., Praveen, K.S., Raja, B., & Damodharan, P. (2013). Measurement of thermal conductivity of fluid using single and dual wire transient techniques. *Measurement*, 46(8), 2746–2752. doi: 10.1016/j.measurement.2013.05.017

[8] Hong, S. W., Kang, Y.T., Kleinstreuer, C., & Koo, J. (2011). Impact analysis of natural convection on thermal conductivity measurements of nanofluids using the transient hot-wire method. *International Journal of Heat and Mass Transfer*, 54(15–16), 3448–3456. doi: 10.1016/j.ijheatmasstransfer.2011.03.041

[9] Yoon, S., Lee, G.J., Park, T.J., Lee, C., & Cho, D.K. (2022). Thermal conductivity evaluation for bentonite buffer materials under elevated temperature conditions. *Case Studies in Thermal Engineering*, 30, 101792. doi: 10.1016/j.csite.2022.101792

[10] Wu, K.F., Cao, T.F., Li, W.B., Zhang, H., & Tang, G.H. (2023). Quantitative evaluation of the natural convection effect on thermal conductivity measurement with transient plane source method. *Case Studies in Thermal Engineering*, 45, 102933. doi: 10.1016/j.csite.2023.102933

[11] Kosowska-Golachowska, M., Musiał, T., & Gajewski, W. (2014). Determination of the effective thermal conductivity of solid fuels by the laser flash method. *Archives of Thermodynamics*, 35(3), 3–16. doi: 10.2478/aoter-2014-0018

[12] Mo, J., & Ban, H. (2017). Measurements and theoretical modeling of effective thermal conductivity of particle beds under compression in air and vacuum. *Case Studies in Thermal Engineering*, 10, 423–433. doi: 10.1016/j.csite.2017.10.001

[13] Memon, S. (2017). Experimental measurement of hermetic edge seal's thermal conductivity for the thermal transmittance prediction of triple vacuum glazing. *Case Studies in Thermal Engineering*, 10, 169–178. doi: 10.1016/j.csite.2017.06.002

[14] Zheng, S.F., Wang, M., Li, X., Tai, B.W., Li, G.Y., & Mao, Z.Y. (2024). Evaluation of 17 thermal conductivity models for frozen soil. *Case Studies in Thermal Engineering*, 61, 104949. doi: 10.1016/j.csite.2024.104949

[15] Asadi, I., Ji, G., & Baghban, M.H. (2023). Evaluating the effective thermal conductivity of cement mortar through x-ray scanning. *Case Studies in Thermal Engineering*, 41, 102686. doi: 10.1016/j.csite.2022.102686

[16] AlQdah, K.S. (2021). Effect of using natural and local environment contents on the thermal conductivity of building materials: Case in Medina, Saudi Arabia. *Case Studies in Thermal Engineering*, 28, 101597. doi: 10.1016/j.csite.2021.101597

[17] Liu, Y., Mei, X., Wang, W., Zhang, G., & Cheng, W. (2023). Development and application of a novel pre-drilling thermal probe in-situ testing equipment. *Case Studies in Thermal Engineering*, 42, 102743. doi: 10.1016/j.csite.2023.102743

[18] Carslaw, H.S., & Jaeger, J.C. (1959). *Conduction of heat in solids* (2nd ed.). Oxford University Press, USA.

[19] Assael, M.J., Nieto de Castro, C.A., Roder, H.M., & Wakeham, W.A. (1991). Transient methods for thermal conductivity (Chapter 7). In *Experimental Thermodynamics. Vol. III: Measurement of the Transport Properties of Fluids* (Eds. Nagashima A., Sengers G.V., Wakeham W.A.), pp. 161 – 195. Blackwell Scientific Publications.

[20] Assael, M.J., Antoniadis, K.D., & Wakeham, W.A. (2010). Historical evolution of the transient hot-wire technique. *International Journal of Thermophysics*, 31(6), 1051–1072. doi: 10.1007/s10765-010-0814-9

[21] Tong, X. C. (2011). *Advanced materials for thermal management of electronic packaging*. Springer Series in Advanced Microelectronics, 30. Springer, New York. doi: 10.1007/978-1-4419-7759-5

[22] American Society for Testing and Materials. (1997). *Standard test method for determination of thermal conductivity plastics by means of a transient line-source technique (ASTM D5930−97)*. doi: 10.1520/D5930-97

[23] American Society for Testing and Materials. (2014). *Standard test method for determination of thermal conductivity of soil and soft rock by thermal needle probe procedure (ASTM D5334−14)*. doi: 10.1520/D5334-14

[24] Assael, M.J., Antoniadis, K.D., Metaxa, I., Mylona, S.K., Assael, Y., Wu, J., & Hu, M. (2015). A novel portable absolute transient hot-wire instrument for the measurement of the thermal conductivity of solids. *International Journal of Thermophysics*, 36(10−11), 3083–3105. doi: 10.1007/s10765-015-1964-6

[25] Nakamura, S., Hibiya, T., & Yamamoto, F. (1988). Measurement of the thermal conductivity of molten semiconductors. *International Journal of Thermophysics*, 9(6), 933–940. doi: 10.1007/BF01133261

[26] Jaeger, J.C., & Sass, J.H. (1964). A line source method for measuring the thermal conductivity and diffusivity of cylindrical specimens of rock and other poor conductors. *British Journal of Applied Physics*, 15(10), 1187–1194. doi: 10.1088/0508-3443/15/10/307

[27] Richard, R.G., & Shankland, I.R. (1989). A transient hot-wire method for measuring the thermal conductivity of gases and liquids. *International Journal of Thermophysics*, 10(3), 673–686. doi: 10.1007/BF00507988

[28] Nagasaka, Y., & Nagashima, A. (1981). Absolute measurement of the thermal conductivity of electrically conducting liquids by the transient hot-wire method. *Journal of Physics E: Scientific Instruments*, 14(12), 1435. doi: 10.1088/0022-3735/14/12/020

[29] Bleazard, J.G., & Teja, A.S. (1995). Thermal conductivity of electrically conducting liquids by the transient hot-wire method. *Journal of Chemical Engineering Data*, 40(4), 732–737. doi: 10.1021/je00020a003

[30] Roder, H.M. (1981). Transient hot wire thermal conductivity apparatus for fluids. *Journal of Research of the National Bureau of Standards*, 86, 457–493. doi: 10.6028/jres.086.020

[31] Perkins, R.A., Roder, H.M., & Nieto de Castro, C.A. (1991). High-temperature transient hot-wire thermal conductivity apparatus for fluids. *Journal of Research of the National Institute of Standards and Technology*, 96(3), 247–269. doi: 10.6028/jres.096.014

[32] Roder, H.M., Perkins, R.A., Laesecke, A., & Nieto De Castro, C.A. (2000). Absolute steady-state thermal conductivity measurements by use of a transient hot-wire system. *Journal of Research of the National Institute of Standards and Technology*, 105(2), 221–253. doi: org/10.6028/jres.105.028

[33] Johns, A.I., Scott, A.C., Watson, J.T.R., Ferguson, D., & Clifford, A.A. (1988). Measurement of the thermal conductivity of gases by the transient hot-wire method. *Philosophical Transactions of the Royal Society of London. Series A, Mathematical and Physical Sciences*, 325(1585), 295–356. doi: 10.1098/rsta.1988.0054

[34] Vozár, L. (1996). A computer-controlled apparatus for thermal conductivity measurement by the transient hot wire method. *Journal of Thermal Analysis*, 46(2), 495–505. doi: 10.1007/BF02135027

[35] Abu-Hamdeh, N.H., Khdair, A.I., & Reeder, R.C. (2000). A comparison of two methods used to evaluate thermal conductivity for some soils. *International Journal of Heat and Mass Transfer*, 44(5), 1073–1078. doi: 10.1016/s0017-9310(00)00144-7

[36] Festa, C., & Rossi, A. (1999). Apparatus for routine measurements of the thermal conductivity of ice cores. *Annals of Glaciology*, 29, 151–154. doi: 10.3189/172756499781821210

[37] Festa, C., & Rossi, A. (1997). Thermal conductivity measurement (TCM) of ice cores: Devices and procedures. *Geografia Fisica e Dinamica Quaternaria*, 20(2), 263–267.

[38] Liang, X.G., Zhang, Y., & Ge, X. (1999). The measurement of thermal conductivities of solid fruits and vegetables. *Measurement Science and Technology*, 10(7). doi: 10.1088/0957-0233/10/7/402

[39] ASTM International. (2009). *Standard test method for determination of thermal conductivity of refractories by hot wire (platinum resistance thermometer technique) (ASTM C1113/C1113M−09)*. doi: 10.1520/C1113_C1113M-09

[40] Murshed, S.M.S., Leong, K.C., & Yang, C. (2005). Enhanced thermal conductivity of TiO2-water based nanofluids. *International Journal of Thermal Sciences*, 44(4), 367–373. doi: 10.1016/j.ijthermalsci.2004.12.005

[41] Hu, Y.S., Xu, Y.S., Sun, D.A., Chen, B., & Zeng, Z.T. (2021). Temperature dependence of thermal conductivity of granular bentonites. *Yantu Lixue/Rock and Soil Mechanics*, 42(7), 1774–1782. doi: 10.16285/j.rsm.2020.1899

[42] Dos Santos, W.N., & Gregorio, R. (2002). Hot-wire parallel technique: A new method for simultaneous determination of thermal properties of polymers. *Journal of Applied Polymer Science*, 85(8), 1779–1786. doi: 10.1002/app.10681

[43] Murshed, S.M.S., Leong, K.C., & Yang, C. (2006). Determination of the effective thermal diffusivity of nanofluids by the double hot-wire technique. *Journal of Physics D: Applied Physics*, 39(24), 5316–5322. doi: 10.1088/0022-3727/39/24/033

[44] Xie, H., Gu, H., Fujii, M., & Zhang, X. (2006). Short hot wire technique for measuring thermal conductivity and thermal diffusivity of various materials. *Measurement Science and Technology*, 17(1), 208–214. doi: 10.1088/0957-0233/17/1/032

[45] International Organization for Standardization. (2010). *Refractory materials – Determination of thermal conductivity Part 1: Hot-wire (cross-array) and resistance thermometer methods*. ISO/DIS 8894-1 (pp. 1–17).

[46] Healy, J.J., & De Groot, J.J. (1976). The theory of the transient hot-wire method for measuring thermal conductivity. *Physica B+C*, 82(2), 392–408. doi: 10.1016/0378-4363(76)90203-5

[47] De Groot, J.J., Kestin, J., & Sookiazian, H. (1974). Instrument to measure the thermal conductivity of gases. *Physica*, 75(3), 454–482. doi: 10.1016/0031-8914(74)90341-3

[48] Daouas, N., Fguiri, A., & Radhouani, M.S. (2008). Solution of a coupled inverse heat conduction-radiation problem for the study of radiation effects on the transient hot wire measurements. *Experimental Thermal and Fluid Science*, 32(8), 1766–1778. doi: 10.1016/j.expthermflusci.2008.04.003

[49] Lyu, W., Pu, H., & Chen, J.N. (2020). Thermal performance of an energy pile group with a deeply penetrating u-shaped heat exchanger. *Energies*, 13(21), 5822. doi: 10.3390/en13215822

[50] Zhang, X., & Fujii, M. (2000). Simultaneous measurements of the thermal conductivity and thermal diffusivity of molten salts with a transient short-hot-wire method. *International Journal of Thermophysics*, 21(1), 71–84. doi: 10.1023/A:1006604820755

[51] Xie, Z., Dou, Z., Wu, D., Zeng, X., Feng, Y., Tian, Y., Fu, Q., & Wu, K. (2023). Joint-inspired liquid and thermal conductive interface for designing thermal interface materials with high solid filling yet excellent thixotropy. *Advanced Functional Materials*, 33(14), 2214071. doi: 10.1002/adfm.202214071

[52] Romero, F.J., Castillo, A.S., Rivadeneyra, A., Albrecht, A., Godoy, A., Morales, D.P., & Rodriguez, N. (2018). In-depth study of laser diode ablation of Kapton polyimide for flexible conductive substrates. *Nanomaterials*, 8(7), 517. doi: 10.3390/nano8070517

[53] Nitta, I., Himanen, O., & Mikkola, M. (2008). Thermal conductivity and contact resistance of compressed gas diffusion layer of PEM fuel cell. *Fuel Cells*, 8(2), 111–119. doi: 10.1002/fuce.200700054

[54] Babu, S.S., Santella, M.L., Feng, Z., Riemer, B.W., & Cohron, J.W. (2001). Empirical model of effects of pressure and temperature on electrical contact resistance of metals. *Science and Technology of Welding and Joining*, 6(3), 126–132. doi: 10.1179/136217101101538631

[55] Pan, X., Cui, X., Liu, S., Jiang, Z., Wu, Y., & Chen, Z. (2020). Research progress of thermal contact resistance. *Journal of Low Temperature Physics*, 201, 213–253. doi: 10.1007/s10909-020-02497-0

[56] Glatzmaier, G.C., & Ramirez, W.F. (1985). Simultaneous measurement of the thermal conductivity and thermal diffusivity of unconsolidated materials by the transient hot wire method. *Review of Scientific Instruments*, 56(7), 1394–1398. doi: 10.1063/1.1138491

[57] Chen, C., Zhu, C., Zhang, B., Tang, B., Li, K., Li, W., & Fu, X. (2021). Effect of Temperature on the Thermal Conductivity of Rocks and its Implication for In Situ Correction. *Geofluids*, 6630236. doi: 10.1155/2021/6630236

[58] Bogaard, R.H. (1985). Thermal Conductivity of Selected Stainless Steels . In: *Thermal Conductivity 18* (Eds. Ashworth, T., Smith, D.R.), pp. 175–185, Springer, Boston, MA. doi: 10.1007/978-1-4684-4916-7_20

[59] Bentz, D.P., & Prasad, K.R. (2007). *Thermal performance of fire restrictive materials I. characterization with respect to thermal performance models*. National Institute of Standards Technology IR 7401. doi: 10.6028/nist.ir.7401

[60] Assael, M.J., Gialou, K., Kakosimos, K., & Metaxa, I. (2004). Thermal Conductivity of Reference Solid Materials. *International Journal of Thermophysics*, 25(2), 397–408. doi: 10.1023/b:ijot.0000028477.74595.d5

[61] Tang, B., Zhu, C., Xu, M., Chen, T., & Hu, S. (2019). Thermal conductivity of sedimentary rocks in the Sichuan Basin, Southwest China. *Energy Exploration & Exploitation*, 37(2), 691–720. doi: 10.1177/0144598718804902

[62] Halbert, D., & Parnell, J. (2022). Thermal conductivity of basalt between 225 and 290 K. *Meteoritics & Planetary Science*, 57(8), 1617–1626. doi: 10.1111/maps.13829

[63] Joint Committee for Guides in Metrology. (2008). *Evaluation of measurement data — Guide to the expression of uncertainty in measurement*, JCGM 100:2008.

Co-published by
Institute of Fluid-Flow Machinery
Polish Academy of Sciences
Committee on Thermodynamics and Combustion
Polish Academy of Sciences

Copyright©2026 by the Authors under licence CC BY-NC-ND 4.0

http://www.imp.gda.pl/archives-of-thermodynamics/

Smart thermal management of bio-based aerogels: A paradigm shift from energy localisation to zero-energy anti-icing

Jincheng Su[a,b,c*], Jiliang Wang[b], Wei Zhou[c], Xiaozhuang Yang[a], Qinghua Miao[a], Bing Wang[a]

[a]Harbin University of Commerce, School of Energy and Civil Engineering, Xuehai 1, Songbei District, Harbin Heilongjiang 150028, China
[b]Heilongjiang Province Academy of Cold Area Building Research, Qingbin Road 60, Nangang District, Harbin Heilongjiang 150080, China
[c]Harbin Institute of Technology, School of Civil Engineering, Xidazhi 92, Nangang District, Harbin Heilongjiang 150001, China,
*Corresponding author email: suhuidong012@yeah.net

Received: 25.11.2025; revised: 06.01.2026; accepted: 23.01.2026

Abstract

Given the global energy crises and severe climate challenges, it is urgent to develop zero-energy anti-icing technologies to ensure infrastructure security. Bio-based aerogels, due to their environmental friendliness and renewable characteristics, excellent thermal insulation properties and structural design flexibility, provide an innovative opportunity for solar-powered intelligent thermal management. Therefore, we systematically review recent developments in bio-based aerogels for intelligent thermal management. The concept of 'localisation of solar thermal energy' is proposed to highlight a paradigm shift from passive insulation to active thermal management platforms. Through a critical analysis of green interface coupling, biomimetic anisotropic structures and photothermal-phase transition sequences, the importance of rational cross-scale design in overcoming performance barriers (such as high porosity, high strength, low thermal conductivity and high photothermal efficiency) is emphasised. In addition, research gaps in dynamic energy matching, environmental durability and system integration are identified, providing a theoretical framework and development path for designing future intelligent anti-icing materials. This review demonstrates that through integrated multi-scale design, bio-based aerogels can achieve a surface temperature increase of over 60°C under 1 solar irradiance, and maintain the bulk thermal conductivity below 0.025 W/(m K). This finding indicates a promising approach to achieving zero-energy anti-icing solutions.

Keywords: Bio-based aerogel; Intelligent thermal management; Energy localisation; Zero-energy anti-icing; Paradigm shift

Vol. 47(2026), No. 1, 227–235; doi: 10.24425/ather.2026.158672

Cite this manuscript as: Su, J., Wang, J., Zhou, W., Yang, X., Miao, Q., & Wang, B. (2026). Smart thermal management of bio-based aerogels: A paradigm shift from energy localisation to zero-energy anti-icing. *Archives of Thermodynamics*, 47(1), 227–235.

1. Introduction

The global energy transition and increasing frequency of extreme weather events pose significant challenges to the sustainability and safe operation of modern infrastructure [1,2]. In cold regions, the accumulation of ice and snow on building and infrastructure surfaces will threaten the structural integrity, resulting in significant energy consumption and environmental impact [3]. Current electric heating de-icing technologies have a high energy demand, often ranging from 200 W/m to 500 W/m. Annual consumption of chemical de-icing agents exceeds 20 million tons. This practice has led to heavy metal salinisation

Nomenclature

c_p – specific heat capacity, J/(kg K)
E_b – bonding energy, eV
H – enthalpy, J
k – thermal conductivity, W/(m K)
k_i – thermal conductivity, N/m
L – latent heat of phase transition, J/kg
m – mass, kg
N – number of atomic pairs in the interfacial bond
$Q_{photothermal}$ – solar heat gain, W/m^3
Q_{loss} – heat loss, W/m^3
r_i – actual bond length, pm
$r_{0,i}$ – equilibrium bond length, pm
T – temperature, K
t – time, s

Greek symbols

β – extinction coefficient, 1/m
ρ – density, kg/m^3
σ – Stefan-Boltzmann constant, 5.67×10^{-8} W/(m^2 K^4)
ϕ – porosity

Subscripts and Superscripts

eff – effective
g – gas phase
s – solid phase

Abbreviations and Acronyms

PCM – phase change material
PLA – polylactic acid

and alkalisation of soil and water [4]. Due to increased energy usage, substantial pollution and passive response, traditional methods cannot meet the requirements of dual carbon goals for green and low-carbon development [5,6]. Therefore, the development and utilisation of sustainable materials and active anti-icing technologies with near-zero external energy consumption have become a focus in the intersection of civil engineering materials, energy science and chemistry [7,8].

Due to nanoporous structures and excellent thermal insulation properties, aerogels have low thermal conductivity (< 0.025 W/(m K)) and high porosity (> 90%), making them an ideal platform for efficient thermal insulation [9]. However, traditional silica-based aerogels are hindered by their limited functions, high brittleness, and dependence on non-renewable raw materials. The development of bio-based aerogels, such as those derived from cellulose, chitosan, and polylactic acid, has initiated a green transformation in this field. These materials from renewable biomass have the advantage of biodegradability, excellent biocompatibility and mechanical flexibility, laying a foundation for creating environmentally friendly functional materials. In addition, early bio-based aerogels were mainly used as passive thermal insulators, lacking the ability to respond to or resist external icing [10]. Photothermal materials, such as MXene and black phosphorus [11,12], combined with bio-based aerogels, have the ability of active photothermal conversion. However, these composites show a fundamental scientific paradox: how to effectively generate, direct and spatially locate photothermal energy in an adiabatic system designed to suppress heat conduction [13]. This conflict between 'thermal insulation' and 'heating' poses a challenge to the development of intelligent thermal management systems [14]. To address this, it is essential to move away from the traditional functional layering approach and initiate a paradigm shift from passive materials to intelligent thermal management platforms. The core of this concept is to achieve surface-controlled thermal energy generation and accumulation while maintaining the overall thermal insulation performance of the system. The theoretical basis of heat conduction is expressed as follows:

$$\rho c_p \frac{\partial T}{\partial t} = \nabla(k\nabla T) + Q_{photothermal} - Q_{loss}, \quad (1)$$

where ρ represents the density of the material, c_p is the specific heat capacity at constant pressure, T is the absolute temperature and t is the time, term $\partial T/\partial t$ indicates the rate of change of temperature over time, k is the thermal conductivity of the material, $\nabla(k\nabla T)$ represents the thermal diffusion term, $Q_{photothermal}$ denotes the solar heat gain term and Q_{loss} represents the heat loss term. The key to achieving energy localisation is to maximise $Q_{photothermal}$ and minimise Q_{loss}.

To address this issue, the intelligent thermal management of bio-based aerogels is reviewed and evaluated from three fundamental mechanisms to achieve localisation of photothermal energy [15,16]:

1) Green interface energy coupling mechanism: This section investigates the effects of molecular-level interactions (such as hydrogen bonding) between bio-based frameworks and photothermal nano-units on energy injection efficiency and interface stability;
2) Biomimetic anisotropic thermal management: This analysis examines the strategy of guiding heat flow paths through microstructural design (such as unidirectional cryogenic casting) to achieve spatial localisation of surface thermal energy, while maintaining overall thermal insulation;
3) Photothermal-phase-change sequential coordination mechanism: This section elaborates on the role of phase-change materials as "thermal capacitors" in balancing energy supply and demand to promote all-weather anti-icing, especially under nighttime and low-light conditions.

We first define the main material systems and characteristics of bio-based aerogels, and explore the current state of the involved mechanisms and their relationships. Then the performance of various technical approaches is compared to identify the points of consensus, areas of disagreement, and critical gaps. Finally, a technological evolution from the principle of energy localisation to zero-energy anti-icing applications is proposed. Future challenges and research directions required for a true paradigm shift are anticipated, aiming to provide a guidance for theoretical innovation and engineering practice. The overall logical structure is shown in Fig. 1.

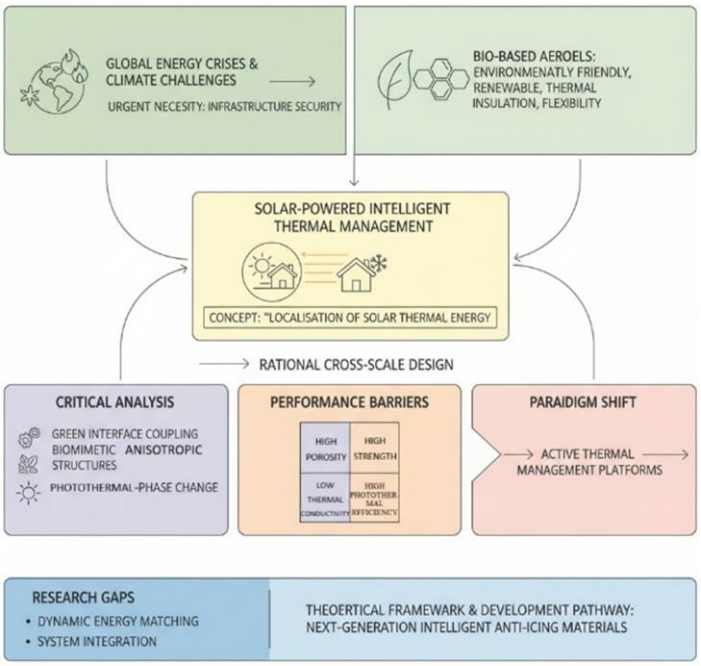


Fig. 1. Diagram of logical structure.

This review suggests that addressing the fundamental paradox of insulation and heat generation requires a comprehensive and multi-scale design strategy. Three main mechanisms: green interface energy coupling, biomimetic anisotropic thermal management and photothermal-phase-change sequential coordination are concentrated, not because they are the only relevant mechanisms, but because they collectively address the challenge at three essential design scales. First, at the molecular scale, interface coupling (such as through hydrogen bonds) helps to inject efficient photothermal energy into the insulating matrix. Second, at the microstructural scale, anisotropic pore architecture directs the injected heat flow to the material surface to achieve spatial localisation. Third, at the system level, phase-change coordination serves as a temporal buffer to balance energy supply and demand for all-weather operation. Therefore, these mechanisms are interrelated. They establish a hierarchical strategy, where interface coupling provides the foundation, anisotropic structures create the pathway and phase-change coordination provides assurance. Overall, they can accurately locate solar thermal energy within an adiabatic system, which is the foundation to achieve zero-energy anti-icing.

2. Material systems

The emergence of bio-based aerogels represents a significant paradigm shift in aerogels, from focusing on individual properties to emphasising balanced sustainability and multi-functionality. The continuous enrichment and evolution of these material systems provide multiple platforms for advanced thermal management technologies [17]. The preliminary research mainly aimed to replace traditional silica-based aerogels. Recent advancements have focused on the functional design based on the properties of biopolymers. Three predominant material systems are classified according to their chemical nature and functional characteristics: cellulose-based aerogels, chitosan-based aerogels and polylactic acid (PLA)-based aerogels [18] (Table 1).

Table 1. Comparative performance of key bio-based aerogel material systems.

Material systems	Precursor characteristics	Typical thermal conductivity (W/(m K))	Key advantages	Functional priorities and challenges	Applicable scenarios
Cellulose-based aerogels	Rich in hydroxyl groups, highly derivatisable	0.025–0.035	High mechanical strength, facilitating the construction of anisotropic structures	Light-heat interface coupling/prone to moisture absorption	Building envelopes
Chitosan-based aerogels	Amino groups confer pH responsiveness and antimicrobial properties	0.030–0.040	Excellent adsorption properties and biocompatibility	Bioactive function integration/ acid instability	Special environmental applications
Polylactic acid-based aerogels	Intrinsically hydrophobic, thermoplastic	0.035–0.045	Hydrophobic, easy to process and form	Superhydrophobic anti-icing coating/ relatively brittle	Surface coating

2.1. Cellulose-based aerogels

Cellulose, as the most abundant biopolymer in nature, has become the most extensively studied aerogel system due to its excellent mechanical properties and adjustable pore structure. The three-dimensional network formed by cellulose nanofibers (CNF) achieves high mechanical strength (tensile strength up to MPa level) and ultra-low thermal conductivity (ranging from 0.025 W/(m K) to 0.035 W/(m K)) [19]. In addition, the abundant hydroxyl groups on its surface are ideal reaction sites for subsequent functionalisation modifications.

The radial thermal conductivity of cellulose nanofiber aerogels produced by unidirectional freeze-casting technology is as low as 0.030 W/(m K), and the axial thermal conductivity reaches 0.060 W/(m K). This indicates significant anisotropy in thermal management, laying a structural foundation for directional thermal control. However, the hydrophilicity of cellulose aerogels limits their long-term application in humid environments, and usually requires post-treatment methods such as silane modification to improve environmental stability. The hydrophilicity of cellulose aerogels significantly reduces their thermal insulation stability in high-humidity environments. It is necessary to make modifications, such as achieving superhydrophilicity [20].

2.2. Chitosan-based aerogels

Chitosan is derived from chitin, which is the second most abundant biopolymer in nature. The amino groups in its molecular chains endow the material with unique biological activity and adsorption properties. This indicates significant antibacterial potential and makes it suitable for specialised applications that require antimicrobial suppression. Incorporating hollow glass microspheres into the chitosan matrix helps to develop low-density, high-performance thermal insulation materials. This enhancement is due to the synergistic interaction between the three-dimensional network structure of chitosan and the arrangement of microsphere frameworks. However, the instability of chitosan in acidic environments and its relatively high raw material cost have limited its large-scale engineering applications to some extent [21]. The size and surface charge of chitosan-based nanogels show pH responsiveness, and their properties will change significantly as pH decreases (under acidic conditions) [22].

2.3. Polylactic acid-based aerogels

Polylactic acid (PLA) is a biodegradable synthetic polymer with significant hydrophobicity and thermoplastic processing ability. It can develop integrated materials that combine super-hydrophobicity with photothermal properties. For example, the CFex-PLA composite aerogel has excellent hydrophobicity (with a contact angle ranging from 146.94° to 152.25°) and significant photothermal effect, effectively integrating anti-icing and de-icing functions [23]. In addition, PLA aerogels are still brittle and have limited thermal stability, highlighting the need to further improve their mechanical properties while maintaining their functions. The study on the structure-property relationship of PLA aerogels indicates they have high stiffness and elastic modulus up to 12.82 MPa [24]. This mechanical property is usually associated with low fracture strain and brittleness. Another study prepared PLA aerogel with excellent cyclic compression performance through special design, indicating that structural design can reduce its brittleness [25].

2.4. Positioning shift from 'green substrate' to 'functional platform'

Early studies usually characterised bio-based aerogels as 'green' passive thermal insulation materials. The introduction of functional fillers often damages their porous structure and mechanical properties. For example, although the physical mixing of MXene can improve photothermal performance, the stacking of nanosheets often leads to pore blockage, resulting in a significant increase in thermal conductivity. The limitation in this stage is due to a lack of understanding of the synergistic relationship between structure and function. Recent research has repositioned aerogels as a 'functional platform' that can be rationally designed. According to the strategies, such as in-situ growth and directed assembly, functional units are accurately fixed on the aerogel framework, thereby maximising functionality, while minimising performance loss. This paradigm shift lays a necessary foundation for achieving intelligent thermal management.

3. Core mechanisms and implementation pathways for energy localisation

The concept of 'energy localisation' addresses the contradiction between 'adiabatic behaviour' and 'heat generation' in aerogel systems. This concept combines multi-level synergistic mechanisms from molecular to system scales. It includes three main pathways: green interfacial energy coupling, biomimetic anisotropic structure guidance and photothermal-phase transition temporal coordination.

3.1. Green interfacial energy coupling mechanism

At the molecular scale, the design of interfaces is crucial for facilitating efficient energy transfer. The properties of the interface between bio-based aerogels and photothermal materials significantly affect the conversion and injection efficiency of light energy into thermal energy. MXene and black phosphorus, as narrow-bandgap semiconductors, can be used as excellent photothermal agents due to their ability to absorb a wide spectrum of light. However, the key determinant of their effectiveness is the nature of their interfacial interactions with the bio-based framework.

The interfacial structure formed by strong hydrogen bonds between cellulose and MXene can promote efficient phonon transport and improve photothermal conversion efficiency, as well as has a significantly higher interfacial bonding energy compared to physical adsorption. These hydrogen-bond-based 'green interfaces' pass complex chemical coupling steps, while providing stable and highly efficient energy transfer paths [26]. The hydroxyl groups in the cellulose framework form a molecular-level interfaces with terminal groups, such as –O and –F, on the MXene surface. The strength of these interactions can be quantified as follows:

$$E_b = \frac{1}{2N}\sum_{i=1}^{N} k_i\left(r_i - r_{0,i}\right)^2, \quad (2)$$

where E_b denotes the bonding energy, N represents the total number of atomic pairs involved in forming the interfacial bond, k_i is the force constant, r_i and $r_{0,i}$ denote the actual and equilibrium bond lengths, respectively.

Different bio-based backbones will significantly influence the interfacial properties. Cellulose is characterised by its linear molecular chains and densely distributed hydroxyl groups. Compared with branched-chain chitosan (–1.7 eV), it has a higher bonding energy with MXene (–2.1 eV). This difference results in a higher photothermal conversion efficiency of cellulose (88.5%) compared to chitosan (76%). This difference highlights the profound impact of molecular architecture on interfacial energy transfer behaviours, thereby providing a theoretical foundation for the accurate design of interfacial engineering.

3.2. Biomimetic anisotropic structures for thermal management

At the micro- and nanoscale, structural design plays a crucial role in directed thermal flow. Anisotropic structures can promote heat accumulation at material surfaces rather than internal diffusion, resulting in local 'external heat and internal cooling' effects. The unidirectional cryo-casting technology produces aerogels with highly oriented pore structures, forming a 'directional channel' of heat flow. The thermal conductivity along the axis of the hole (in-plane) significantly exceeds that perpendicular to it (out-of-plane), allowing for selective surface heat enrichment [27]. Thermal conductivity anisotropy can be significantly achieved by controlling the direction of ice crystal growth:

$$k_{eff} = \phi k_s + (1-\phi)k_g + \frac{16\sigma T^3}{3\beta\rho}, \quad (3)$$

where k_{eff} denotes the effective thermal conductivity, ϕ represents the porosity, k_s and k_g denote the thermal conductivities of the solid and gas phases, respectively, σ is the Stefan-Boltzmann constant, T is the absolute temperature, ρ is the material density, and β is the extinction coefficient.

This method achieves an in-plane to out-of-plane thermal conductivity ratio of 2:1, making the surface temperature rapidly increase to 85.2°C under illumination, and the substrate temperature increases slightly. Further structural comparisons reveal that the radial honeycomb structure exhibits an in-plane/out-of-plane thermal conductivity ratio of 2.5:1, which is significantly higher than the 1.8:1 ratio of the layered structure. This indicates that under the same solar thermal conditions, the surface thermal localisation is optimal. It is noteworthy that structural selection should be consistent with practical applications: planar anti-icing systems should prioritise the in-plane thermal conductivity through radial structures to promote rapid de-icing. Vertically channels are more effective in ensuring uniform thermal distribution on curved surfaces.

3.3. Photothermal-phase transition temporal coordination

At the system level, achieving all-weather anti-icing requires the adoption of a time-sequenced energy management mechanism. The integration of phase change materials (PCM) into aerogels provides the ability of 'thermal energy storage'. This allows aerogels to absorb excess heat during sunny periods and release latent heat under low-light or sub-zero conditions. This process reduces surface temperature fluctuations and solves the intermittent nature of solar thermal energy supply [28]. The introduction of phase change materials (PCMs) allows for the redistribution of energy over time. The thermal behaviour of composite PCMs can be calculated as follows:

$$\frac{dH}{dt} = mc_p\frac{dT}{dt} + mL\frac{df}{dt}, \quad (4)$$

where H denotes the enthalpy, m represents the mass, L denotes the latent heat of phase transition, and f is the liquid fraction.

Paraffin@silica microcapsules (latent heat > 180 J/g) can extend the anti-icing time of the system by 40−200%. However, the selection of phase change temperatures for phase change materials remains a controversial topic. On the one hand, some studies advocate for PCMs with a phase change temperature between 5°C and 10°C to achieve rapid de-icing. On the other hand, others propose that PCMs with a phase transition temperature between –3°C and 0°C can provide prolonged anti-icing protection by releasing latent heat during crystallisation. This disagreement fundamentally reflects the different energy management requirements in different applications. In addition, the hysteresis of phase transition may last for up to 30 min, thereby limiting the performance of PCMs under dynamic climatic conditions. As a result, developing systems with graded phase-change temperatures or moulded composite PCMs to optimise thermal release kinetics has become an important research area.

Achieving energy localisation is a systemic challenge that spans multiple scales. It requires an integrated design with three dimensions: interface coupling, structure-guided orientation and temporal coordination. This combination aims to reconcile the conflict between thermal insulation and heat generation. This method will advance bio-based aerogels to be intelligent thermal management platforms.

3.4. Synergistic integration of multi-scale mechanisms

Three core mechanisms are introduced independently. To achieve true 'energy localisation' and overcome the contradiction between 'insulation and heating', they should be integrated into a unified and multi-scale design paradigm. These mechanisms are not just cumulative; on the contrary, they form a hierarchical and functionally complementary system, each addressing a specific scale of challenge.

First, the coupling of the green interface lays a molecular foundation. By generating strong and stable interactions (such as hydrogen bonds) between the bio-based matrix and photothermal units, efficient phonon transfer is ensured. The incident light is maximally converted into thermal energy in the material. This step solves the main problem of 'how to efficiently generate heat in an insulator'. Without such efficient injection, any subsequent thermal management would prove ineffective.

Second, biomimetic anisotropic structures provide essential microstructural features. The directional pore channels and layered structure designed by techniques, such as unidirectional freeze-casting, create a preferential pathway for heat flow. This design strategically directs the heat generated internally to the material surface, while suppressing backward diffusion into the bulk. Consequently, it converts molecular-scale energy input into a spatial local thermal distribution characterised by 'hot surface, cool interior', thereby achieving surface-specific anti-icing and de-icing functions.

Third, the coordination of photothermal-phase change is a system-level guarantee for temporal stability. It solves the intermittency of solar energy by combining thermal energy storage. Phase change materials absorb excess heat during peak irradiation and release it at night or low-light conditions. This mechanism can buffer fluctuations in energy supply and ensure sustained thermal output from the surface. It maintains the functionality of the entire system over time, making all-weather, zero-energy anti-icing operation possible.

This integration follows a logical sequence: interface coupling injects energy; anisotropic structures direct it to the surface; and phase-change coordination stabilises it over time. This collaborative multi-scale approach transforms the bio-based aerogel from a simple insulating material to an intelligent thermal management platform that can achieve active, local and lasting anti-icing performance.

4. Challenges of performance synergy and cross-scale design

Integrating mechanisms, such as green interface coupling, anisotropic structures, and photothermal-phase transition synergies into a single material system requires a thorough examination of their synergistic effects and inherent conflicts. This analysis elucidates the fundamental challenges associated with achieving high-performance bio-based aerogels.

4.1. Paths to overcoming the impossible triangle

In the design of bio-based aerogels, the goal of achieving high porosity to obtain excellent thermal insulation, high strength, and high light heat conversion efficiency often leads to an impossible triangle of conflicting objectives. Most studies that focus on enhancing one property often sacrifice others. For example, increasing the loading of photothermal agents often leads to a decrease in porosity and an increase in thermal conductivity. Conversely, excessive emphasis on achieving high porosity often damages the mechanical strength of the material.

A feasible approach to achieve breakthroughs is to achieve collaborative optimisation of multiple attributes through reasonable cross-scale design [29,30]. For example, a synergistic approach of combining cryogenic casting with in-situ cross-linking can develop cellulose/MXene composite aerogels with radial pore structures. At the molecular level, hydrogen-bonded interfaces make MXene disperse stably, resulting in a porosity of over 90%, a thermal conductivity of 0.023 W/(m K), a tensile strength of 1.3 MPa and a photothermal efficiency of 88%. Success depends on achieving multi-scale collaborative regulation from molecular interfaces to macroscopic structures. This emphasises that future material design should move away from simplistic 'stir-fry-style' composite strategies and adopt a rational design paradigm that unifies structure and function [31], as shown in Fig. 2 and Table 2.

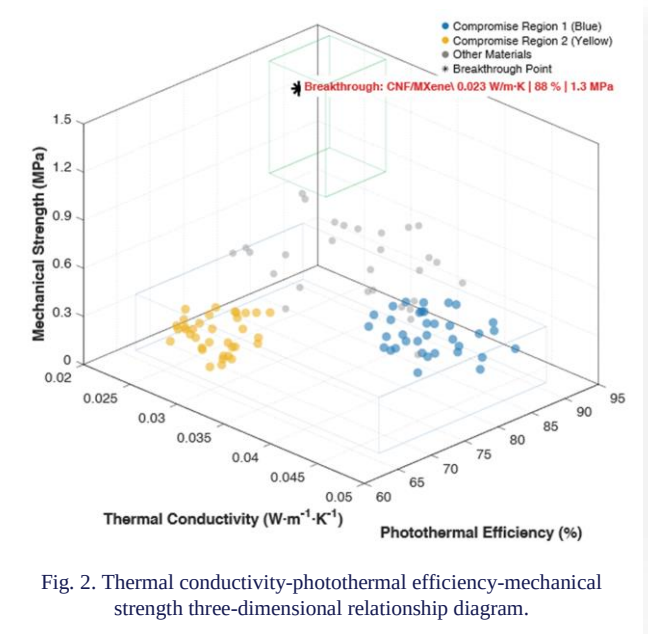


Fig. 2. Thermal conductivity-photothermal efficiency-mechanical strength three-dimensional relationship diagram.

Table 2. Performance synergy analysis of representative studies.

Research framework systems	Preparation strategies	Thermal conductivity (W/(m K))	Photothermal temperature rise (°C)	Mechanical strength	Synergy assessment
CNF/MXene physical mixture	Simple blend	0.038 (up by approximately 35%)	~60	Decline	Performance-sacrificing type: Deterioration in thermal insulation properties
CS/PCM composite foam	In-situ encapsulation	0.033	PCM-controlled temperature only	Good	Single-function type: Lacking active solar thermal capabilities
CNF/MXene anisotropy	Chilled casting + interface engineering	0.023 (radial)	~65	Enhance	Synergistic breakthrough approach: Achieving all three objectives simultaneously

4.2. Performance gap between laboratory and engineering

A significant issue is the disconnect between the standards for evaluating material performance and actual applications. Performance is often assessed under constant solar irradiance and dry, idealised conditions. In contrast, high-altitude cold environments in the real world often have complex factors, including low light levels (solar irradiance < 300 W/m², i.e. < 0.3 sun), high humidity and frequent freeze-thaw cycles.

Key engineering parameters, including structural integrity under repeated freeze-thaw cycles, thermal insulation retention in high-humidity environments, and activation efficiency under low-light conditions, are often overlooked in current research. This 'performance gap' significantly hinders the practical application of materials with excellent performance in laboratory settings. Therefore, future performance evaluations should establish testing standards that more accurately reflect real-world conditions. Such standards should systematically assess engineering indicators, including long-term durability, cycling stability and substrate compatibility. This approach will promote the transformation of bio-based aerogels from 'high-performance materials' to becoming truly 'available technologies'.

5. Pathways and future prospects of paradigm shift

The analysis indicates that bio-based aerogels are experiencing a significant paradigm shift in intelligent thermal management. This shift includes a transition from passive insulation to active thermal management, an evolution from single-function applications to system integration, and a shift in focus from performance demonstration to application-driven development.

5.1. Evolutionary trajectory of research paradigms

The development of this field follows a unique three-stage evolutionary path:

1) Early stage (prior to 2015): The research mainly focused on environmentally friendly preparation processes and fundamental thermal insulation properties of bio-based aerogels.
2) Mid-term phase (2016−2020): This stage marks the beginning of functional exploration, introducing single functional units, such as photothermal agents or phase change materials. These simple physical mixing methods bring challenges for performance trade-offs.
3) Recent phase (2021 to present): At this stage, multi-mechanism synergy has emerged, such as Janus structures and anisotropic design.

This evolutionary trajectory marks a fundamental shift from material innovation to system integration. Research focus shifts from pursuing individual performance metrics to emphasising overall system efficacy.

5.2. Key directions for future development

There are still several important gaps and challenges:

1) Insufficient understanding of potential mechanisms: Existing research has not yet elucidated the quantitative contribution of hydrogen bonding to energy transfer. There is still a substantial disconnect between the simulation of thermal-mechanical coupling in anisotropic structures and the study on the dynamics of ice layer separation.
2) Lack of performance data: There is almost no available data on the sustained anti-icing performance at temperatures close to 0°C. Environmental durability testing, such as ultraviolet (UV) aging for 3000 h, is cited in less than 5% of the literature.
3) System integration challenges are significant: There is no research on optimising green interface, anisotropic structure, and phase transition timing at the same time. The key characteristics of architectural applications, such as adhesion to substrates, have not received enough attention.

The following three issues require urgent attention:

1) Dynamic matching mechanism of energy chain: There is a lack of understanding of the dynamic coupling mechanism in the 'solar thermal-energy storage-thermal insulation' energy chain. There are also no performance prediction and optimisation models that take into account the fluctuations of real-world weather.
2) Systemic gaps in multiscale theory: From nanoscale interface behaviour to microscale pore structure and macroscopic device performance, there is a lack of 'structure-property' transfer theories and design principles.
3) Integration of durability and sustainability: Long-term service of materials under extreme conditions, including resistance to aging and fatigue, as well as their environmental footprint throughout the entire lifecycle (such as biodegradability and recyclability) are key factors affecting their final application. These factors are under-researched in current studies.

5.3. Proposed ways to drive paradigm shift

To address the earlier limitations and promote a true paradigm shift, three essential developmental directions are proposed: First, it is crucial to develop application-oriented in-situ characterisation techniques tailored to operating conditions. This method aims to establish a performance evaluation system for materials in real-world environments, thereby bridging the gap between laboratory performance and engineering. Second, a closed-loop system that integrates 'intelligent design' with advanced manufacturing should be established. This system combines artificial intelligence with multi-scale simulations for reverse material design. This will guide advanced manufacturing processes, such as cryogenic 3D printing and atomic layer deposition. Finally, a comprehensive lifecycle assessment system should be established. This system should incorporate life cycle assessment and life cycle cost analysis in the early stages of material development to ensure the true sustainability of technologies. These developments can signify technological advancements and indicate a fundamental paradigm shift from performance-driven to application-driven approaches. This transition will elevate bio-based aerogels from 'laboratory

curiosities' to 'engineering realities' that support future green and resilient infrastructure.

6. Conclusions

The intelligent thermal management of bio-based aerogels is experiencing a significant paradigm shift from passive materials to active functional systems. We systematically present the mechanism of achieving 'localised photothermal energy' through green interface coupling, bio-inspired structural orientation, and photothermal-phase change synergy. This approach provides a promising technical way for zero-energy anti-icing. However, transitioning from laboratory research to engineering applications will overcome critical challenges, including dynamic energy matching, environmental durability and system integration. Future advancements will establish a new paradigm of multiscale rational design that combines artificial intelligence, advanced manufacturing and life-cycle assessment systems. These developments will make smart materials a key technology to support green infrastructure. Bio-based aerogels provide a highly promising green way for zero-energy anti-icing. The paradigm shift framework in this review includes energy localisation and system integration. It provides a clear perspective for understanding existing technologies, highlights the limitations of current research and identifies future directions through critical analysis. This method provides an accurate roadmap for future investigation. Developing this trajectory has the potential to transform these smart materials from outstanding laboratory performance into engineering reality, thereby supporting future green and resilient infrastructure.

Acknowledgements

We gratefully acknowledge the support from Heilongjiang Province Philosophy and Social Sciences Research Planning Project (Research on the Evolutionary Game of Multi-Agent Collaborative Innovation in Intelligent Construction under the 'Dual Carbon' Goal, 23GLD043; A Study on the Relationship Between Innovation Capability and Performance in Heilongjiang's Construction Industry Under the Digital Construction Model, 21GLB063), Research Business Expenses for Provincial Research Institutes in 2024 (Research on the Calculation of Standard Frozen Depth of Seasonal Frozen Soil in Heilongjiang Province, CZKYF2024-1-B004) and Heilongjiang Province Postdoctoral General Grant Project 2023 (Research on the Mechanism and Prevention Technology of Pile Foundation Ice Damage in High Latitude Areas, LBH-Z23260).

References

[1] Kang, J., Nguyen, V.P., Lee, S.M., & Kim, D. (2025). Ultralight Pt-ALD-modified graphene aerogel achieving aluminum-class thermal resistance at 12% mass. *Materials & Design*, 259, 114742. doi: 10.1016/j.matdes.2025.114742

[2] Taner, T. (2021). The novel and innovative design with using H_2 fuel of PEM fuel cell: Efficiency of thermodynamic analyze. *Fuel*, 302, 121109. doi: 10.1016/j.fuel.2021.121109

[3] Niu, M., Zhao, J., Liu, Z., Li, H., Li, M., & Rao, Z. (2025). Review on methods to enhance the thermal insulation and flame-retardant properties of polyimide aerogels. *Applied Thermal Engineering*, 284(2), 129063. doi: 10.1016/j.applthermaleng.2025.129063

[4] Guo, Z.-G., Xiong, P.-Q., Nan, H.-F., Yan, D.-X., Zhong, G.-J., Lei, J., & Li, Z.-M. (2025). Biomimetic, hierarchical-programmed gel coating for adaptive and sustainable thermal modulation. *Matter*, 8(6), 102057. doi: 10.1016/j.matt.2025.102057

[5] Huang, M.-C., Xue, C.-H., Bai, Z., Cheng, J., Wu, Y.-G., Ma, C.-Q., Wan, L., Xie, L., Wang H.-D., Liu, B.-Y., Guo, X.-J. (2025). Bioinspired smart dual-layer hydrogels system with synchronous solar and thermal radiation modulation for energy-saving all-season temperature regulation. *Journal of Energy Chemistry*, 101, 175−190. doi: 10.1016/j.jechem.2024.09.051

[6] Taner, T. (2019). A flow channel with nafion membrane material design of PEM fuel cell. *Journal of Thermal Engineering*, 5(5), 456−468. doi: 10.18186/thermal.624085

[7] Carolan, J., Jakubec, M., Xavier Jr., N.F., Motala, A.P., Bifulco, E., Aars, J., Andersen, M., Schmidt, A.L., Cabré, M.B., Singh, V., Colavita, P.E., Selfors, E.W., Sacchi, M., O'Reilly, S., Halskau, Ø., Tiwari, M.K., Hobbs, R.G., & Holst, B. (2025). Anti-icing properties of polar bear fur. *Science Advances*, 11(5), eads7321. doi: 10.1126/sciadv.ads7321

[8] Liu, W., Dong, Y., Li, M., Liu, H., & Wang, X. (2025). Weather-adaptive Janus aerogel integrated with phase change materials enables dual-mode thermal regulation via radiative cooling and solar heating. *Advanced Functional Materials*, 36(7), e13665. doi: 10.1002/adfm.202513665

[9] Lin, P., Qing, X., Liu, Q., & Yang, Y. (2025). Flexible aerogels for thermal insulation: fabrication and application. *ACS Applied Materials & Interfaces*, 17(40), 55706–55719. doi: 10.1021/acsami.5c12107

[10] Hu, Z., Wang, S., Wu, J., Li, Z., Liu, S., Yao, Y., Duan, S., Mei, G., & Gong, X. (2025). Robust multi-scale bionic ANF/PMSQ aerogel featuring impact protection, thermal insulation and anti-icing functions. *Composites Part B: Engineering*, 297, 112304. doi: 10.1016/j.compositesb.2025.112304

[11] Li, J., Liang, C., Lin, C., Wang, Y., Liang, Y., & Dong, D. (2025). Lightweight, superhydrophobic, and superelastic MXene/carboxymethylcellulose sodium composite aerogels for efficient and multifunctional electromagnetic interference shielding. *Chemical Engineering Journal*, 506, 160274. doi: 10.1016/j.cej.2025.160274

[12] VahidMohammadi, A., Rosen, J., & Gogotsi, Y. (2021). The world of two-dimensional carbides and nitrides (Mxenes). *Science*, 372(6547), eabf1581. doi:10.1126/science.abf1581

[13] Ghasemi, H., Ni, G., Marconnet, A.M., Loomis, J., Yerci, S., Miljkovic, N., & Chen, G. (2014). Solar steam generation by heat localization. *Nature Communications*, 5, 4449. doi: 10.1038/ncomms5449

[14] Ma, J.-W., Zeng, F.-R., Lin, X.-C., Wang, Y.-Q., Ma, Y.-H., Jia, X.-X., Zhang, J.-C., Liu, B.-W., Wang, Y.-Z., & Zhao, H.B. (2024). A photoluminescent hydrogen-bonded biomass aerogel for sustainable radiative cooling. *Science*, 385(6704), 68−74. doi: 10.1126/science.adn5694

[15] Taner, T. (2017). The micro-scale modeling by experimental study in PEM fuel cell. *Journal of Thermal Engineering*, 3(6, Spec. Iss. 6), 1515−1526. doi: 10.18186/journal-of-thermal-engineering.331755

[16] Taner, T. (2018). Energy and exergy analyze of PEM fuel cell: A case study of modeling and simulations. *Energy*, 143, 284−294. doi: 10.1016/j.energy.2017.10.102

[17] Berger, M. (2024). Nanoscale fuller-dome aerogels enable new class of thermal insulating materials. *Nanowerk*. https://www.nanowerk.com/spotlight/spotid=65991.php [accessed 10 Nov. 2025].

[18] Huang, S., Wang, H., Yang, Z., Qiao, L., Li, C., Wang, C., & Huan, S. (2025). All-green foam for thermal management via

pickering templating. *Bioresource Technology*, 441, 133638. doi: 10.1016/j.biortech.2025.133638

[19] Li, L., Yin, R., Sheng, Z., & Zhang, X. (2025). Electro-manipulating of negative-charged aramid nanofibers towards micro-to-macro scale colloidal aerogel films. *Nature Communications*, 16, 8663. doi: 10.1038/s41467-025-63827-y

[20] Chen, S., Li, X., Zhang, C., Long, L., Zhao, X., Zhu, C., & Yi, X. (2024). Superhydrophobic nanocellulose aerogel for thermal insulation and thermal resistance up to 1300°C. *Chemical Engineering Journal*, 499, 156043. doi: 10.1016/j.cej.2024.156043

[21] Wang, T., Zhan, Y.-J., Chen, M.-J., He, L., An, W.-L., Xu, S., Wang, W., Shi, J.-J., Zhao, H.-B., & Wang, Y.Z. (2024). Reversible-gel-assisted, ambient-pressure-dried, multifunctional, flame-retardant biomass aerogels with smart high-strength-elasticity transformation. *National Science Review*, 11(11), nwae360. doi: 10.1093/nsr/nwae360

[22] Fernández-Solís, K.G., Domínguez-Fonseca, E., Martínez, B.M. G., Becerra, A.G., Ochoa, E.F., Mendizábal, E., Toriz, G., Loyer, P., Rosselgong, J., & Bravo-Anaya, L.M. (2024). Synthesis, characterization and stability of crosslinked chitosan-maltodextrin pH-sensitive nanogels. *International Journal of Biological Macromolecules*, 274(1), 133277. doi: 10.1016/j.ijbiomac.2024.133277

[23] Zhang, S., Zhang, Q., Huang, X., & Ming, J. (2025). Superhydrophobic and photothermal polylactic acid composite aerogels with anti-icing and deicing properties. *International Journal of Biological Macromolecules*, 332(1), 146680. doi: 10.1016/j.ijbiomac.2025.146680

[24] Lledó, J., Martín-de León, J., Gomez Álvarez-Arenas, T.G., Rodríguez-Pérez, M.A., & Merillas, B. (2025). Unraveling the structure-properties correlation in thermal insulating and mechanically stiff PLA aerogels. *Journal of Materials Research and Technology*, 36, 641−652. doi: 10.1016/j.jmrt.2025.03.135

[25] Tan, W., Zhang, S., Wang, J., Yan, D., Huang, X., Wang, X., Ning, X., & Ming, J. (2024). Flexible and superhydrophobicity polylactic acid hollow fiber aerogels for thermal insulation. *Applied Materials Today*, 37, 102118. doi: 10.1016/j.apmt.2024.102 118

[26] Wang, S., Jin, X., Yue, Y., Mei, C., Xu, X., Wu, Q., Xiao, H., & Han, J. (2023). Biomimetic patternable polyhydroxyl nanocellulose/MXene films sequentially bridged through a synergistic hydrogen and ionic interaction with tunable multi-photoresponsive performances. *Chemical Engineering Journal*, 470, 144225. doi: 10.1016/j.cej.2023.144225

[27] Xiao, W., Wang, P., Song, X., Liao, B., Yan, K., & Zhang, J.-J. (2021). Facile fabrication of anisotropic chitosan aerogel with hydrophobicity and thermal superinsulation for advanced thermal management. *ACS Sustainable Chemistry & Engineering*, 9(28), 9348−9357. doi: 10.1021/acssuschemeng.1c02217

[28] Yu, Z., Wang, F., He, W., Wang, Y., Dai, B., & Zhang, X. (2025). Phase-change material-integrated dual-mode thermal management Janus films with enhanced radiative cooling and solar heating. *ACS Applied Polymer Materials*, 7(6), 3555−3563. doi: 10.1021/acsapm.4c03524

[29] Xu, T., Song, Q., Liu, K., Liu, H., Pan, J., Liu, W., Dai, L., Zhang, M., Wang, Y., Si, C., Du, H., & Zhang, K. (2023). Nanocellulose-assisted construction of multifunctional MXene-based aerogels with engineering biomimetic texture for pressure sensor and compressible electrode. *Nano-Micro Letters*, 15, 98. doi: 10.1007/s40820-023-01073-x

[30] Wegst, U.G.K., Kamm, P.H., Yin, K., & García-Moreno, F. (2024). Freeze casting. *Nature Reviews Methods Primers*, 4, 28. doi: 10.1038/s43586-024-00307-5

[31] Shao, G., Hanaor, D.A.H., Shen, X., & Gurlo, A. (2020). Freeze casting: From low-dimensional building blocks to aligned porous structures − A review of novel materials, methods, and applications. *Advanced Materials*, 32(17), 1907176. doi: 10.1002/adma.201907176

Co-published by
Institute of Fluid-Flow Machinery
Polish Academy of Sciences
Committee on Thermodynamics and Combustion
Polish Academy of Sciences

Copyright©2026 by the Authors under licence CC BY-NC-ND 4.0

http://www.imp.gda.pl/archives-of-thermodynamics/

Novel design and energy analysis of hybrid system activated by low-grade thermal energy conversion

Youcef Maalem[a], Hakim Madani[b*]

[a]Ecole Nationale Polytechnique de Constantine, BP 75, A, Nouvelle ville RP, 25000 Constantine, Algeria
[b]University of Batna 2, Faculty of Technology, Department of Mechanical Engineering, Rue Chahid Boukhlouf M. El Hadi, 05000 Batna, Algeria
*Corresponding author email: h.madani@univ-batna2.dz

Received: 04.08.2025; revised: 08.12.2025; accepted: 23.01.2026

Abstract

A novel power-cooling system triggered by low-grade thermal energy is proposed and studied in this paper. The power-cooling unit combined the engine (organic Rankine cycle) and cooler (ejector-expansion refrigeration cycle employing a booster). Both cycles employ isobutene (R600a) as a working fluid and share a single condenser unit. The performance characteristics (overall coefficient of performance and working fluid mass flow rate per kW of cooling capacity) of the novel unit was investigated using thermodynamic analysis in comparison to the traditional unit that is commonly used. The latter combines the engine (organic Rankine cycle) with the cooler (vapour compression refrigeration cycle) in various operational conditions, including exit temperatures of a boiler unit (60−90°C), a condenser unit (30−55°C) and an evaporator unit (−15−15°C). It was discovered that in comparison to the traditional unit, the novel unit exhibited lower working fluid mass flow rate per kW of cooling capacity and higher overall coefficient of performance. The overall coefficients of performance for both systems increase by 0.5385 and 0.4476, respectively, when the boiler unit's temperature reaches 90°C and the other input specifications are set to typical values. On the other hand, the working fluid mass flow rate per kW cooling capacity of both systems drops by 0.0096 and 0.0064, respectively. Overall, the study demonstrates that the novel system triggered by low-grade thermal energy can be an alternative to the traditional system.

Keywords: Combined system; Working fluid; Expansion ratio; Compression ratio; Performance indicators

Vol. 47(2026), No. 1, 237–253; doi: 10.24425/ather.2026.158673

Cite this manuscript as: Maalem, Y, & Madani, H. (2026). Novel design and energy analysis of hybrid system activated by low-grade thermal energy conversion. *Archives of Thermodynamics*, 47(1), 237–253.

1. Introduction

With rising worldwide energy demands and developments in energy technologies, experts are concentrating on resource optimisation. As a result, there is growing interest in research on the generation and effective use of energy from natural sources like waste heat [1] or biomass [2], geothermal [3], thermal solar [4], etc. In this regard, one of the most promising pieces of equipment in energy engineering is thermodynamic machinery, which uses thermal energy from the aforementioned low-temperature heat source applications to activate cycle performances [5].

The search for environmentally friendly working fluids with high-energy efficiency [6], as well as the design of thermodynamic machinery combination cycles to improve cycle performance through efficient modification [7], are two increasingly popular topics in energy engineering [8].

The hybrid power-cooling system, which combines the organic Rankine cycle (ORC) with the most common cooling cycle, the vapour compression refrigeration cycle (VCRC), is one of the most promising combination cycles. It employs a low-boiling-point working fluid to convert heat input from a variety of low-grade energy sources into usable cooling or power energy [9–12]. Recently, several researchers have used an ORC to produce cooling as a power source for VCRC.

Nomenclature

c – velocity, m/s
CMR – compression ratio in the compressor
COP – coefficient of performance
dp – pressure drop, kPa
EPR – expansion ratio in expander
GWP – global warming potential
h – specific enthalpy, kJ/kg
m – mass flow rate, kg/s
MkW – working fluid mass flow rate per kW of cooling capacity, kg/(s kW)
P – pressure, kPa
Q_{boil} – boiler heat input, kW
Q_{evap} – evaporator cooling capacity, kW
s – specific entropy, kJ/(kg K)
T – temperature, °C
v – specific volume, m^3/kg
W_{comp} – compressor work input, kW
W_{exp} – expander work output, kW
W_{net} – net work output, kW
W_{pump} – pump power consumption, kW
$W_{booster}$ – booster compressor work input, kW
x – vapour quality

Greek symbols

β_{pr} – booster pressure ratio
η – isentropic efficiency
η_{ORC} – power cycle thermal efficiency
μ – entrainment ratio of ejector
ρ – density, kg/m^3

Subscripts

1,...,14 – numbering of states in thermodynamic cycles (ORC, VCRC and EERCIWB)
b – boiler process
boil – boiler
c – condensing process
comp – compressor
cond – condensation
d – diffusor
e – evaporation process
evap – evaporation
exp – expander
is – isentropic process
mn – motive nozzle
ms – mixing section
oval – overall
pf – primary flow
sf – secondary flow
sn – suction nozzle

Abbreviations and Acronyms

EERCIWB – ejector-expansion refrigeration cycle improved by a booster
ORC – organic Rankine cycle
VCRC – vapour compression refrigeration cycle

In the study of Aphornratanaa and Sriveerakul [13], the authors disclosed a simulation examination on a combined engine (ORC) – cooler (VCRC) using two substances, R22 and R164a, as a working fluid. They discovered the computed coefficient of performance values between 1.1 and 1.3 for these fluids, respectively.

The ORC-VCRC system combines steam compression refrigeration with an organic Rankine cycle. Mole et al. [14] studied a combination ORC-VCRC system under various operating conditions that was activated by low-temperature heat sources and used eco-friendly working fluids with R134a for the power and cooling cycles. Their analysis, evaluating working fluids like R1234yf, R1234ze(E) and R1336mzz(Z), was driven by the need for low global warming potential (GWP) alternatives. Quantitatively, they reported that the system could achieve a net power output of up to 45 kW and a cooling capacity of up to 52.5 kW under specific conditions. They concluded that R1336mzz(Z) and R1234ze(E) are the best candidates for the ORC-VCRC system, with R1336mzz(Z) providing the highest exergetic efficiency of approximately 34.3%.

After testing and assessing the ORC-VCRC system for four hydrocarbons (HCs) (propylene (R1270), butane (R600), propane (R290) and isobutane (R600a), Li et al. [15] determined that butane was the optimum working fluid for the ORC-VCRC system, with an overall coefficient of performance (COP) of 0.470. This evaluation was based on a boiler temperature of 90°C, a condensation temperature of 35°C, and an evaporation temperature of 5°C.

Asim et al. [16] looked at the working fluid selection and performance of a VCRC-ORC system, which recovers the waste heat rejected by the air conditioning system's condenser. The R600a-R123 was selected as the fluid pair for the integrated system based on thermodynamics (energy and exergy) and thermo-economic analysis, where the authors found that the system's combined COP could be raised from 3.10 to 3.54. This performance improvement of 14.2% was achieved by utilising a heat source temperature of 85°C.

Saleh [17] proposed using novel hydrofluoroolefins and common hydrofluorocarbons as working fluids in an ORC-VCRC system driven by low-grade thermal energy. The parametric study, evaluating fluids like R1234ze(E), R1234yf, R600 and R600a, identified R600 as optimal due to its superior thermodynamic properties. With a maximum overall performance of 0.718 at a condenser temperature of 30°C and basic values for the remaining parameters, the results demonstrated that working fluid R600 was the best choice compared to the other substances suggested for the hybrid (ORC-VCRC) system. Nonetheless, its flammability should demand enough attention.

The performance of a stand-alone cooling system made up of a cascade refrigeration system and a combined organic Rankine cycle (ORC-CRS), using NH_6/CO_2 for the cascade refrigeration system and toluene for the organic Rankine cycle, was examined by Lizarte et al. [18]. The system was designed for simultaneous refrigeration at two temperature levels: –30°C and 5°C, utilising a low-grade heat source. The highest overall COP value they calculated was 1.70, which significantly outperforms

conventional systems and demonstrates the efficacy of this advanced cascade configuration.

A combined ORC-VCRC system using R600, R600a, R245fa, and pentane as working fluids was theoretically analysed by Cihan [19]. According to the results, the combined system is best suited for R601 fluid.

Bu et al. [20] investigated six working fluids (R134a, R123, R245fa, R290, R600a and R600) to determine the optimal working fluids for an ORC-VCRC system powered by geothermal energy. Their analysis for air-conditioning applications, using a geothermal source at 100°C, showed that R600a provided the best overall performance. Quantitatively, it achieved a maximum overall COP of 0.41 and produced a net power output of 12.5 kW alongside a cooling capacity of 26.7 kW. They decided that R600a was the best option. Nonetheless, the flammability of R600a should be carefully considered.

Wang et al. [21] studied an ORC-VCRC system using two different working fluids for the organic Rankine cycle and conventional vapour compression cycle, namely R245fa and R134a, respectively. The investigation utilised a 6 kW boiler as the heat source. Under a heat source temperature of 120°C, the system achieved a cooling capacity of 5.27 kW, with the ORC subsystem attaining a thermal efficiency of 8.5%. The overall system coefficient of performance reached nearly 0.50, thereby validating the technical feasibility of the dual-fluid, combined cycle for converting low-grade heat into useful cooling.

In Yue et al.'s study [22], an ORC in conjunction with a car air conditioning system using cyclopentane, pentane, R134a and R245fa as working fluids was tested. The system was designed to recover waste heat from a truck engine's exhaust (around 200°C). Their thermo-economic analysis showed that R134a provided the lowest electricity production cost of 0.195 $/kWh and achieved a net power output of 7.8 kW under these conditions. They concluded that, given the operating conditions included in this study, R134a had the best thermal and economic performance when compared to the other working fluids.

The combined ORC-VCRC thermodynamic model was developed by Hu et al. [23] for ship air conditioning in order to effectively use cooling water and transfer waste heat from flue gases. Using five widely used working fluids (R22, R141b, R236ea, R218 and R601), the system performance was examined. Their analysis, based on a flue gas temperature of 350°C, demonstrated that R601 (pentane) achieved the highest exergy efficiency of 35.18% and the largest net power output of 122.9 kW.

Khatoon et al. [24] investigated the thermal performance of an ORC-VCRC system with a common shaft. The organic Rankine cycle used two refrigerants, R245fa and propane, whereas the vapour compression cycle used three: R245fa, R123 and R134a. The system was analysed for a heat source temperature of 120°C, targeting a cooling capacity of 5 kW. Under these conditions, the optimal fluid pair (propane-R123) also produced a net power output of 1.23 kW. At 40°C, propane was used as a working fluid in the organic Rankine cycle and R123 as a working fluid in the vapour compression cycle, yielding the greatest efficiency of 16.48% and a coefficient of performance of 2.85.

Eight working fluids (propane, ammonia, butane, isobutene, propane and R142a) were used in an ORC-VCRC system that was activated by low-grade sensible energy, according to Kim and Perez-Blanco's analysis [25]. The fluids were arranged in order of critical temperature. The study focused on a heat source temperature of 150°C. The results quantified that isobutene (R600a) achieved the highest overall system efficiency of 28.5% and a net power output of 18.3 kW.

Three distinct refrigerants (R123, R134a and R245ca) were assessed by Jeong and Kang [26] in order to determine which was the best fit for the ORC-VCR system. Their analysis for a system utilising a 90°C heat source and a 30°C condenser temperature showed that R123 achieved a thermal efficiency of 9.8% for the ORC and a COP of 4.2 for the VCRC.

Based on thermodynamics (energy and exergy), Egrican and Karakas [27] investigated an ORC-VCRC system with refrigerants R114 for the Rankine cycle and R22 for the vapour compression cycle. Their analysis of the system revealed a significant total exergy destruction of 68%, with the boiler identified as the primary contributor, responsible for over 40% of these losses. The system's overall energy efficiency was reported at approximately 20%. They concluded that it is vital to have as little irreversibility as feasible in the system in order to execute the task more cheaply and efficiently with natural resources.

González et al. [28] developed a rigorous model using the Helmholtz energy function to optimise VCRC-ORC systems, identifying pentane and R1233zd(E) as the best-performing fluids. Their analysis for a heat source temperature of 150°C demonstrated that R1233zd(E) achieved a superior overall system efficiency of 34.5% and an optimal COP of 0.48, outperforming pentane, which reached an efficiency of 32.1%. The study quantified that a 5°C increase in condenser temperature could lead to a system efficiency drop of up to 8%.

Bin Hu and Wang [29] studied methods to reduce greenhouse gas emissions, highlighting vapour compression heat pumps for waste heat recovery. Their comprehensive review of 17 low-GWP working fluids identified isobutene and propane as top performers for standard heat pump applications, achieving high heating capacities and COP comparable to traditional high-GWP fluids like R134a. For high-temperature industrial heat pumps, refrigerants like R1336mzz(Z) and R718 (water) were found to be suitable, capable of achieving temperatures up to 150°C. Quantitatively, systems using R600a demonstrated heating COP ranging from 2.5 to 5.5, depending on operating conditions, while natural working fluids like CO_2 were highlighted for their efficiency in applications requiring a large temperature glide. This review provides crucial application guidelines to facilitate the transition towards environmentally friendly refrigerants in heat pump technology.

Maalem and Madani [30] screened fourteen low-GWP working fluids for a solar-powered ORC-VCRC air conditioning system. Their thermodynamic analysis, based on a heat source temperature of 120°C, demonstrated that the natural working fluid RE170 (dimethyl ether) provided the best overall performance. Quantitatively, RE170 achieved the highest combined system COP of 0.198 and a superior solar system total efficiency of 16.4%, outperforming other candidates like R600a and R290.

A thorough review of the literature on using an organic Rankine cycle to generate cooling as a power source for a vapour

compression refrigeration cycle revealed that, in recent years, a large number of research studies have been conducted to evaluate their performance, with the majority of studies focusing on how well they perform in comparison to various working fluids and/or working conditions.

On the other hand, due to the lower COP of VCRCs, research and development into increasing the cooling performance of the VCRC system through various cycle adjustments has recently received considerable attention in the field of refrigeration engineering [31]. This is because, from a thermodynamics standpoint, employing standard expansion devices (such as capillary tubes, throttle valves, etc.) that use the isenthalpic process reduces the COP of the VCRC due to the high irreversibility in the throttling process. In order to recover this thermodynamic loss, academic experts have conducted numerous studies to identify new ways to increase the cycle performance of the VCRC and recover its energy losses. Ejectors have attracted significant attention as a method for reducing these expansion losses. A two-phase ejector cycle is considered one of the most effective expansion methods for improving the energy efficiency of the refrigeration cycle through a reduction in the expansion loss [32,33]. In this context, our research group has published multiple studies on this topic, including works [34–40].

In the present work, a novel configuration of a power-cooling system ORC-EERCIWB is proposed, in which an ejector-expansion refrigeration cycle with booster compressor (EERCIWB) is employed to enhance the performance of the standard power-cooling system (ORC-VCRC). To the best of our research group's knowledge and by surveying the mentioned literature reviews, such a modification for performance improvement of a standard power-cooling system has not been investigated to date. Therefore, the present study proposes an energy analysis of the proposed power-cooling system.

The energy analysis of the proposed system is carried out and compared with that of the standard power-cooling system (ORC-VCRC) using the same working fluid R600a and various operating conditions. The energy analysis has been performed to investigate the system thermodynamic performances, in particular the performance indicators: overall coefficient of performance (COP_{oval}) and working fluid mass flow rate per kW cooling capacity (MkW), by comparing it with the conventional ORC-VCRC system under boiler exit temperatures (T_{boil}) of 60°C to 90°C, condenser temperatures (T_{cond}) of 30°C to 55°C and evaporator temperatures (T_{evap}) of −15°C to 15°C.

The basic physical and environmental properties of the working fluid used in the investigation are shown in Table 1 [30,35].

Table 1. Basic physical and environmental properties of the working fluid (R600a) used in the investigation.

Specifications	Isobutene
Chemical formula	Iso-C_4H_{10}
Type of working fluid	Hydrocarbon
Standardized international designation	R600a
Molecular structure	
CAS Registry Number	75-28-5
Chemical structure	
Molar mass (kg/kmol)	58.122
Critical temperature (K)	407.85
Critical pressure (MPa)	3.6400
Normal boiling point (K)	261.4
Ozone depletion potential	0
Global warming potential	3

2. Description of power-cooling systems

2.1. ORC-VCRC system

The configuration of the hybrid ORC-VCRC system, which consists of two main thermodynamic cycles, is schematically illustrated in Fig. 1a. The first cycle is the organic Rankine cycle (ORC), designated as (1-2-3-4), and the second cycle is the vapour compression refrigeration cycle (VCRC), designated as (5-6-3-7). The ORC includes a feed pump, boiler unit, expander unit and condenser unit, while the VCRC includes a compressor unit, condenser unit, throttle valve and evaporator unit. This kind of configuration uses a low-temperature heat source as a heat input to power the hybrid system, which has a shaft connecting the compressor of the vapour compression refrigeration cycle and the expander of the organic Rankine cycle.

These four fundamental transformations of the hybrid system occur during each thermodynamic cycle, and the condensation processes of both the organic Rankine cycle (ORC) and the vapour compression refrigeration cycle (VCRC) take place in a shared condenser at the same pressure.

The different processes of the combined systems (ORC and VCRC) are presented as follows:

In the ORC:

- process (1→2s) − is an isentropic expansion process across the expander;
- process (1→2) − is the actual expansion process;
- process (2→3) − is a heat rejection (condensation) process across the condenser;
- process (3→4s) − is an isentropic pumping process;
- process (3→4) − is the actual pumping work;
- process (4→1) − is a heat addition process in the boiler.

In the VCRC:

- process (5→6s) − is an isentropic compression in the compressor;
- process (5→6) − is the actual compression process in the compressor;
- process (6→3) − is a heat rejection (condensation) process across the condenser;
- process (3→7) − is an isenthalpic expansion across the throttle valve;
- process (7→5) − is a heat absorption (evaporation) in the evaporator.

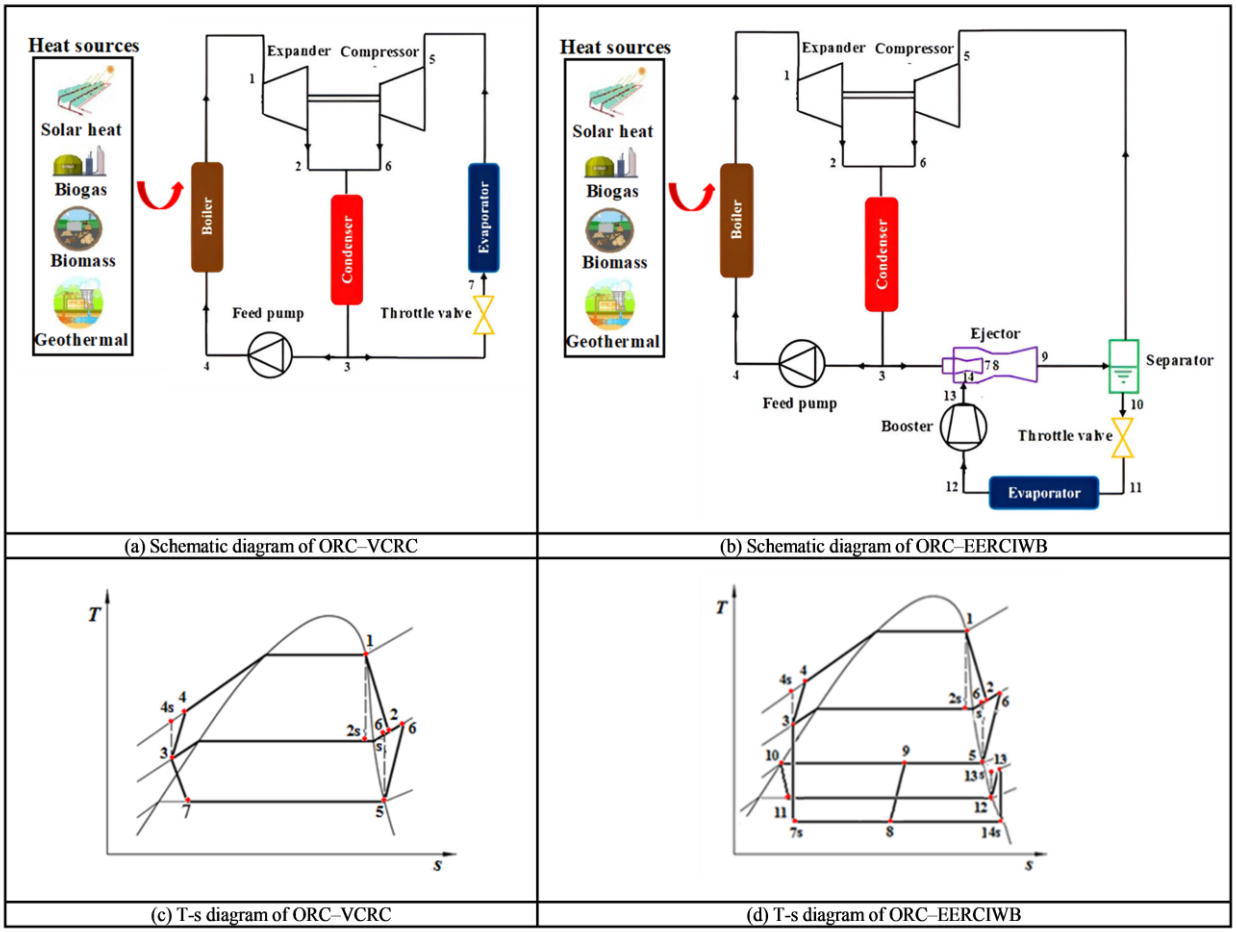


Fig. 1. Schematic illustrations (a, b) and *T*–*s* diagrams (c, d) of power-cooling systems.

The same refrigerant is used in the hybrid ORC-VCRC system's two thermodynamic cycles (ORC and VCRC), which operate in the following ways, respectively:

In the ORC: The heat absorbed from the low-temperature heat source causes the working fluid in the boiler to heat and evaporate at state 4. Next, the expander receives the high-pressure working fluid steam (state 1), whose enthalpy is transformed into power. After that, the working fluid enters the condenser (state 2), where the heat rejection from the external medium causes the condenser to condense at the condensation temperature. To complete the thermodynamic cycle, the working fluid then enters the feed pump (state 3), which transports it to the boiler. Lastly, the thermodynamic cycle's compressor (VCRC) is powered by the thermodynamic cycle's net mechanical power (ORC).

In the VCRC: In the compressor at state 5, the working fluid is compressed to high pressure (state 6). Then, the working fluid enters the condenser, where it condenses at the condensation temperature due to the heat rejection (condensation process) to the condensing medium. Next, the working fluid enters the throttle valve, where it expands at state 7. Finally, in the evaporator, the working fluid absorbs the cooling load from the cooling space at the VCRC evaporation temperature.

2.2. Proposed ORC-EERCIWB system

Figure 1b provides a schematic illustration of the cycle configuration for the suggested hybrid ORC-EERCIWB system. In contrast to the traditional hybrid ORC-VCRC system, the ORC (1-2-3-4) features an ejector-expansion refrigeration cycle improved by a booster circuit connected to its main circuit, which is designated as (5-6-3-7-8-9-10-11-12-13-14). The EERCIWB is made up of different components than the VCRC; it consists of a compressor, condenser, throttle valve, two-phase ejector, gas–liquid separator, booster and an evaporator. The ORC contains the same components as the ORC of the conventional hybrid system ORC-VCRC.

Such as a conventional hybrid ORC-VCRC system, a heat input from a low-temperature heat source drives the proposed hybrid system, where the compressor of the EERCIWB and the expander of the ORC are directly attached through a shaft.

Figure 1d shows the proposed system's temperature-entropy (*T*–*s*) diagram. The subsystems (ORC and EERCIWB) in this proposed system both use the same working fluid, and subsystem condensation occurs in a common condenser at the same pressure.

The following are the different processes that characterise the EERCIWB of the suggested combined ORC-EERCIWB system:

- process (9→5) − send the vapour of the mixture to the compressor;
- process (9→10) − send the liquid portion to the throttle valve;
- process (5→6s) − is an isentropic compression across the compressor;
- process (5→6) − is the actual compression process in the compressor;
- process (6→3) − is a heat rejection (condensation) process across the condenser;
- process (3→7s) − is an ideal expansion process throughout the motive nozzle;
- process (13→14s) − is an ideal process in the suction nozzle;
- process (7→8) − is a mixing process in the mixing section at constant pressure;
- process (8→9) − is a compression process of mixing in a diffuser section;
- process (10→11) − is an isenthalpic expansion across the throttle valve;
- process (11→12) − is a heat absorption (evaporation) in the evaporator;
- process (12→13) − is the actual compression process in the booster;
- process (12→13s) − is an isentropic compression across the booster.

The thermodynamic cycle EERCIWB of the proposed combined system works as follows:

The saturated liquid leaving the condenser (state 3) expands in the ejector's motive nozzle, causing its pressure to drop dramatically at state point 7. As a result, the suction nozzle directs the secondary flow (state 13) into the ejector device, where the pressure at the exit (state 14) equals that of state point 7. In the ejector's mixing section, the two streams are continuously mixed to create stream 8, which is released at the end of the section. When this stream reaches the diffuser, its pressure rises and its velocity falls, creating a two-phase flow (state 9). The vapour portion of the two-phase flow enters the compressor unit, where it is forced to rise in pressure (state 6) and travels to the condenser unit after being separated in a vapour-liquid separator. When the saturated liquid exits the separator at state point 10, the throttling valve reduces it until it reaches the evaporator's pressure and temperature (state 11). Cooling occurs when heat from a cooled medium is absorbed and evaporated by the stream passing through the evaporator. As the saturated vapour exits the evaporator (state 12), it enters the booster compressor and accumulates pressure until it reaches the ejector's secondary flow (state 13).

3. Mathematical models and computational procedures

3.1. Thermodynamic assumptions

Based on previously published literature [15,41,42], the following thermodynamic assumptions form the foundation for the modelling and analysis of both systems in this study:

- The systems are working under steady state conditions.
- Pressure losses in the pipelines and through the heat exchangers are disregarded.
- The system's constituent parts are adiabatic.
- The kinetic energy and potential energies of operating modes are neglected in all sub-systems.
- The working fluid at the exit of the boiler is assumed to be saturated.
- At the evaporators' exit of the subsystems (VCRC and EERCIWB), the working fluid is in the saturated vapour state.
- To prevent cavitation in the boiler feed pump, the working fluid is subcooled to 3°C at the condenser exit of the subsystems (ORC, VCRC and EERCIWB).
- The throttling process in the throttle valve is isenthalpic.
- The vapour stream from the separator is a saturated vapour, and the liquid stream from the separator is a saturated liquid.
- The transformations in all heat exchangers are isobaric processes.
- The compressors are working with an appropriate value of isentropic efficiency.
- The ejector's flow dynamics were modelled as a 1D homogeneous equilibrium.
- The kinetic energy of the flow streams at the ejector inlet and outlet is negligible.
- The mixing pressure in the mixing chamber of the ejector is constant.
- In ejector modelling, the friction losses inside the ejector are taken into account using appropriate values for nozzle, diffuser and mixing section efficiencies.
- The efficiencies of the ejector remain constant.
- The net power produced by the ORC is the power consumed by the compressor of the VCRC and EERCIWB.

3.2. Theoretical models

To simulate the thermodynamic performance of the combined refrigeration and power systems (ORC-VCRC and ORC-EERCIWB), the first stage in the modelling method is to compute the required thermodynamic parameters (such as pressure, enthalpy, entropy, etc.) of R600a at the outlets of each component of the thermodynamic cycles, as defined in Fig 1. This is done prior to modelling the considered thermodynamic cycles.

The Coolprop library, implemented in Matlab, was employed to determine the thermodynamic properties of the working fluid in the present study. The following thermodynamic models are used to calculate the thermodynamic properties (such as pressure, enthalpy, entropy, etc.) of the subcycles ORC, VCRC and EERCIWB, based on the operating conditions (such as boiler temperature, condenser temperature, evaporator temperature, etc.) using Matlab.

The thermodynamic parameters of the state of saturated vapour at the boiler unit outlet of the subcycle ORC are obtained as:

$$P_1 = P(T_{boil}, x = 1), \quad (1)$$

$$h_1 = h(T_{boil}, x = 1), \quad (2)$$

$$s_1 = s(T_{boil}, x = 1), \quad (3)$$

$$\rho_1 = \rho(T_{boil}, x = 1). \quad (4)$$

The specific volume of saturated vapour is determined by

$$v_1 = \frac{1}{\rho_1}. \quad (5)$$

The thermodynamic parameters of the state of saturated vapour at the evaporator unit outlet of the subcycle VCRC are obtained as:

$$P_5 = P(T_{evap}, x = 1), \quad (6)$$

$$h_5 = h(T_{evap}, x = 1), \quad (7)$$

$$s_5 = s(T_{evap}, x = 1). \quad (8)$$

The thermodynamic parameters of the state of subcooled liquid leaving the shared condenser of subcycles (ORC, VCRC and EERCIWB) are obtained as:

$$P_3 = P(T_{cond}, x = 0), \quad (9)$$

$$T_3 = T_{cond} - 3, \quad (10)$$

$$h_3 = h(T_3, P_3), \quad (11)$$

$$s_3 = s(T_3, P_3). \quad (12)$$

At the throttle valve, the throttling process is an isenthalpic process. Therefore, the enthalpy at the outlet of the throttle valve of the subcycle VCRC is calculated as

$$h_7 = h_3. \quad (13)$$

The thermodynamic parameters of the working fluid at the feed pump outlet of the subcycle ORC are obtained as:

$$P_4 = P_1, \quad (14)$$

$$s_4 = s_3, \quad (15)$$

$$h_{4s} = h(P_4, s_4). \quad (16)$$

The actual outlet enthalpy is determined by

$$h_4 = h_3 + \frac{h_{4s} - h_3}{\eta_{pump}}, \quad (17)$$

where η_{pump} refers to the isentropic efficiency of the feed pump. The thermodynamic parameters of the working fluid at the compressor unit outlet of the subcycle VCRC are obtained as:

$$P_6 = P_3, \quad (18)$$

$$s_6 = s_5, \quad (19)$$

$$h_{6s} = h(P_6, s_6). \quad (20)$$

The actual outlet enthalpy is determined by

$$h_6 = h_5 + \frac{h_{6s} - h_5}{\eta_{comp}}, \quad (21)$$

where η_{comp} refers to the isentropic efficiency of the compression process.

The thermodynamic parameters of the working fluid at the expander unit outlet of the subcycle ORC are obtained as:

$$P_2 = P_3, \quad (22)$$

$$s_2 = s_1, \quad (23)$$

$$h_{2s} = h(P_2, s_2). \quad (24)$$

The actual outlet enthalpy is determined by

$$h_2 = h_1 + \frac{h_{2s} - h_1}{\eta_{exp}}, \quad (25)$$

where η_{exp} refers to the isentropic efficiency of the expansion process.

The specific volume of the working fluid at the expander unit outlet of the subcycle ORC is determined by

$$v_2 = \frac{1}{\rho_2}, \quad (26)$$

where

$$\rho_2 = \rho\,(h_2, P_2). \quad (27)$$

The thermodynamic parameters of the state of saturated vapour at the evaporator unit outlet of the subcycle EERCIWB are obtained as:

$$P_{12} = P(T_{evap}, x = 1), \quad (28)$$

$$h_{12} = h(T_{evap}, x = 1), \quad (29)$$

$$s_{12} = s(T_{evap}, x = 1). \quad (30)$$

The thermodynamic parameters of the working fluid at the booster unit outlet of the subcycle EERCIWB are obtained as [41]:

$$P_{13} = P_{12}\beta_{pr}, \quad (31)$$

$$s_{13} = s_{12}, \quad (32)$$

$$h_{13s} = h(P_{13}, s_{13}), \quad (33)$$

where β_{pr} is the booster pressure ratio. The isentropic efficiency of the booster unit is calculated as

$$\eta_{booster} = 0.874 - 0.0135\beta_{pr}. \quad (34)$$

The actual outlet enthalpy is determined by

$$h_{13} = h_{12} + \frac{h_{13s} - h_{12}}{\eta_{booster}}. \quad (35)$$

For the gas-liquid separator outlet of the subcycle EERCIWB, the enthalpy of saturated vapour and the saturated liquid are calculated respectively as:

$$h_5 = h(P_9, x = 1), \quad (36)$$

$$h_{10} = h(P_9, x = 0). \quad (37)$$

At the throttle valve, the throttling process is isenthalpic. Therefore, the enthalpy at the outlet of the throttle valve of the subcycle EERCIWB is calculated as

$$h_{11} = h_{10}. \quad (38)$$

3.2.1. Ejector modelling

The ejector is a critical component in the ORC-EERCIWB system. The effectiveness of the system is determined by the entrainment ratio (μ), which is the mass flow rate ratio between the secondary and primary flows:

$$\mu = \frac{m_{sf}}{m_{pf}}. \quad (39)$$

When modelling an ejector device, two models are typically used to simulate the ejector's performance. These models divide the ejector into two categories, based on where the motive nozzle exit plane is located:

- constant-pressure ejector,
- constant-area ejector.

Both models have been extensively investigated in the past [43], with a number of scholars demonstrating that the constant-pressure ejector outperforms the constant-area ejector and hence is more commonly utilised. Thus, in the current investigation, a constant-pressure ejector is adopted. This paper uses the constant-pressure ejector mathematical model that was used by Maalem et al. [34,36,39]. The motivation nozzle, suction nozzle, mixing section, and diffusion section ejector modelling equations in this model are developed as follows:

At the suction nozzle outlet, the thermodynamic parameters of the primary flow can be calculated as:

$$P_{14} = P_{13} - dp, \quad (40)$$

$$s_{14} = s_{13}, \quad (41)$$

$$h_{14s} = h(P_{14}, s_{14}). \quad (42)$$

The suction nozzle enthalpy is determined from its isentropic relationship and given as

$$h_{14} = h_{13} - \eta_{sn}(h_{13} - h_{14s}). \quad (43)$$

The velocity of the secondary flow at the suction nozzle outlet is determined as

$$c_{14} = \sqrt{2(h_{13} - h_{14})}. \quad (44)$$

At the motive nozzle outlet, the thermodynamic parameters of the secondary flow can be calculated as:

$$P_7 = P_{14}, \quad (45)$$

$$h_{7s} = h(P_7, s_3). \quad (46)$$

The motive nozzle exit enthalpy is determined from its isentropic relationship and given as

$$h_7 = h_3 - \eta_{mn}(h_3 - h_{7s}). \quad (47)$$

The velocity of the motive fluid at the motive nozzle exit is calculated as

$$c_7 = \sqrt{2(h_3 - h_7)}. \quad (48)$$

The two streams coming out of the motive and suction nozzles are mixed at a constant pressure. So, for the mixing section:

$$P_8 = P_7. \quad (49)$$

Applying the momentum and energy conservation on the mixing section would result in relations for its exit velocity and enthalpy:

$$c_8 = \sqrt{\eta_{ms}}[c_7/(1+\mu) + c_{14}\mu/(1+\mu)], \quad (50)$$

$$h_8 = \frac{1}{1+\mu}(h_7 + c_7^2/2) + \frac{\mu}{1+\mu}(h_{14} + c_{14}^2/2) - c_8^2/2, \quad (51)$$

$$s_8 = s(P_8, h_8). \quad (52)$$

The mixed flow is decelerated in the diffuser part, converting kinetic energy back into pressure rise.

Similarly, applying the conservation of energy and the isentropic relation gives the following equations for the diffuser:

$$h_9 = h_8 + \frac{c_8^2}{2}, \quad (53)$$

$$h_{9s} = h_8 + \eta_d(h_9 - h_8). \quad (54)$$

The pressure of the mixture at the ejector exit is determined by the following formula:

$$P_9 = P(h_{9s}, s_8). \quad (55)$$

In the ejector calculations, state 9 is the most important. Previous calculations cannot calculate the vapour quality at the ejector output due to the unknown entrainment ratio. To address this issue, the initial guess value of μ is assumed during the iterative computation procedure. Furthermore, the isentropic efficiencies for the ejector component and operating temperatures are given. To verify the preliminary input value for the entrainment ratio, the results of the two formulas are compared:

$$x_9 = x(h_9, P_9), \quad (56)$$

$$x_9' = \frac{1}{1+\mu}. \quad (57)$$

If the two values match each other, then the assumed μ is maintained; otherwise, another value of μ is chosen, and the loop is started again, as shown in the flowchart displayed in Fig. 2. With all state points defined above, the following key performance indicators are calculated in the next sections to evaluate and compare the systems.

3.2.2. ORC modelling

The governing equations of the organic Rankine cycle are developed as follows [15]:

The expander's output power is calculated using

$$W_{exp} = m_{ORC}(h_1 - h_{2s})\,\eta_{exp}. \quad (58)$$

The required power to the pump can be written as

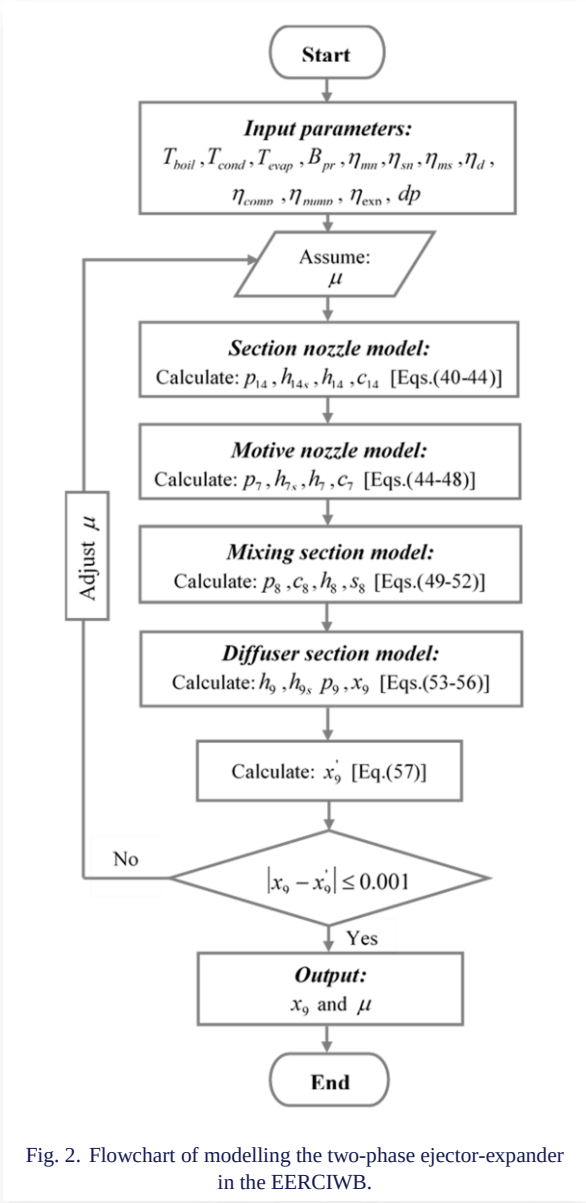


Fig. 2. Flowchart of modelling the two-phase ejector-expander in the EERCIWB.

$$W_{pump} = m_{ORC}\,\frac{h_{4s}-h_3}{\eta_{pump}}. \quad (59)$$

The net output power from the ORC is defined as

$$W_{net} = W_{exp} - W_{pump}. \quad (60)$$

The rate of heat transfer in the boiler can be expressed as

$$Q_{boil} = m_{\mathrm{ORC}}(h_1 - h_4). \quad (61)$$

The expansion ratio across the expander is given by

$$\mathrm{EPR} = \frac{v_2}{v_1}. \quad (62)$$

The thermal efficiency of the ORC is defined as

$$\eta_{\mathrm{ORC}} = \frac{W_{net}}{Q_{boil}}. \quad (63)$$

3.2.3. VCRC modelling

The governing equations of the VCRC are developed as follows:

For the compressor, the input power in the VCRC can be written as [44]:

$$W_{comp,VCRC} = W_{net}. \quad (64)$$

The compression ratio across the compressor is given by

$$\mathrm{CMR} = \frac{P_6}{P_5}. \quad (65)$$

The cooling capacity of VCRC is calculated by

$$Q_{evap,VCRC} = m_{VCRC}(h_5 - h_7), \quad (66)$$

with

$$m_{VCRC} = \frac{W_{comp,VCRC}(h_5 - h_{6s})}{\eta_{comp}}. \quad (67)$$

The COP of the VCRC is given by

$$\mathrm{COP}_{VCRC} = \frac{Q_{evap,VCRC}}{W_{comp,VCRC}}. \quad (68)$$

To characterise the ORC-VCRC system performance, the overall COP and the working fluid mass flow rate per kW cooling capacity are computed using the following two formulas, respectively:

$$\mathrm{COP}_{oval,ORC-VCRC} = \eta_{ORC}\mathrm{COP}_{VCRC}, \quad (69)$$

$$\mathrm{MkW}_{ORC-VCRC} = \frac{m_{ORC}+m_{VCRC}}{Q_{evap,VCRC}}. \quad (70)$$

3.2.4. EERCIWB modelling

The governing equations of the EERCIWB are developed as follows:

For the compressor unit, the input power in the EERCIWB can be written as

$$W_{comp,EERCIWB} = W_{net}. \quad (71)$$

The compression ratio across the compressor is given by

$$\mathrm{CMR} = \frac{P_6}{P_5}. \quad (72)$$

The cooling capacity of EERCIWB can be expressed as

$$Q_{evap,EERCIWB} = m_{sf}(h_{12} - h_{11}), \quad (73)$$

with

$$m_{sf} = m_{pf}\mu, \quad (74)$$

$$m_{pf} = \frac{W_{comp,EERCIWB}}{h_6 - h_5}. \quad (75)$$

For the booster, the input power in the EERCIWB can be written as

$$W_{booster,EERCIWB} = m_{sf}(h_{13} - h_{12}). \quad (76)$$

The COP of the EERCIWB is given by

$$\mathrm{COP}_{EERCIWB} = \frac{Q_{evap,EERCIWB}}{W_{comp,EERCIWB} + W_{booster,EERCIWB}}. \quad (77)$$

Table 2. Relative errors of performance indicators according to [15].

Refrigerant	Indicators	Average relative error (%)	Maximum relative error (%)
R290	COP_{oval}	0.05	0.10
	MkW	0.53	0.83
R600	COP_{oval}	0.04	0.07
	MkW	0.71	1.20
R600a	COP_{oval}	0.04	0.07
	MkW	0.74	1.05
R1270	COP_{oval}	0.10	0.30
	MkW	0.68	0.68

To characterise the ORC-EERCIWB system performance, the overall COP and the working fluid mass flow rate per kW of cooling capacity are computed using the following two formulas, respectively:

$$\mathrm{COP}_{oval,ORC-EERCIWB} = \eta_{ORC}\mathrm{COP}_{EERCIWB}, \quad (78)$$

$$\mathrm{MkW}_{ORC-EERCIWB} = \frac{m_{ORC}+m_{sf}}{Q_{evap,EERCIWB}}. \quad (79)$$

3.3. Conditions of operation for the ORC-VCRC and ORC-EERCIWB computation

The cycles are simulated under a variety of operating conditions in order to compare the thermodynamic performances of the systems ORC-VCRC and ORC-EERCIWB. The following are the given operating conditions [15,34]:

- The working fluid is R600a.
- The temperature of the heat source is 100°C.
- The boiler temperature ranges from 60°C to 90°C.
- The condensation temperature ranges from 30°C to 55°C.
- The evaporation temperature ranges from −15°C to 15°C.
- The working fluid mass flow rate in ORC is 1.0 kg/s.
- The booster pressure ratio is 1.5.
- The isentropic efficiency of the compressor, feed pump and expander is 75%, 75% and 80%, respectively.
- The isentropic efficiency of the motive nozzle, suction nozzle, mixing section and diffusion section is 85%, 85%, 95% and 85%, respectively.

3.4. Model validation

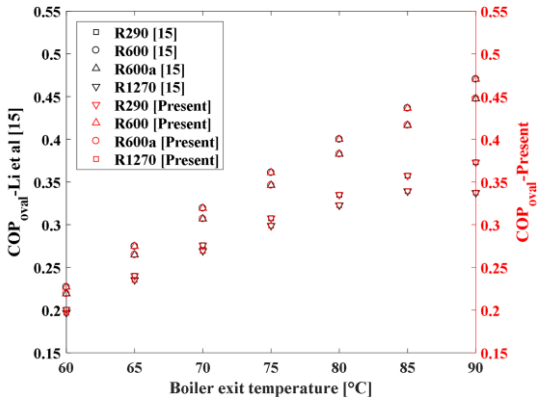
Before presenting the simulation findings, it is appropriate to have a quick discussion about the validation of the system's simulation models.

The proposed hybrid (ORC-EERCIWB) system is a novel power-cooling system design that has not been investigated in any previous studies. As a result, to validate the numerical solution, the established simulation model is solved under the identical operating conditions as those described in [15] for the basic hybrid (ORC-VCRC) system and the same working fluids (R290, R600, R600a and R1270). The effect of boiler temperature is displayed against performance indicators (overall coefficient of performance (COP_{oval}) and working fluid mass flow rate per kW of cooling capacity (MkW), according to [15]. The comparison results are displayed in Fig. 3. The relative error between the present model and the Ref. [15] data was calculated for each data point. The maximum relative errors for each fluid and performance indicators are summarised in Table 2.

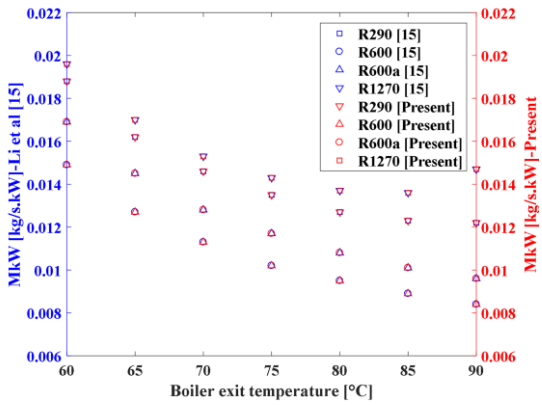
The comparison for different boiler temperatures demonstrates an excellent agreement between the results. It is found that the average error for the COP_{oval} is less than 0.11%, peaking at 0.30% for an individual fluid. Similarly, the MkW shows an average error under 0.75% and a maximum of 1.20%. These minimal deviations confirm the validity of our simulation model.

4. Simulation results and discussion

The results are presented with four significant figures to accurately reflect the comparative trends generated by the simulation. The calculations were performed using the Matlab software with built-in high-accuracy refrigerant property databases (Coolprop library). The solver convergence criterion was set to 10^{-6}, ensuring negligible numerical error. The precision of the reported values is therefore representative of the model's internal consistency and is sufficient for the comparative analysis presented.



(a)



(b)

Fig. 3. Verification of the simulation results of the present work compared with those from [15].

4.1. Effect of boiler temperature on performance indicators

The following Figs. 4−6 show the impact of boiler temperature on ORC-VCRC and ORC-EERCIWB performances using R600a as a working fluid, while maintaining the other parameters constant (T_{cond} = 40°C and T_{evap} = 5°C).

Figure 4 exhibits the evolution of both $COP_{oval\text{-}(ORC–VCRC)}$ and $COP_{oval\text{-}(ORC–EERCIWB)}$ with the boiler exit temperature of the combined refrigeration and power systems (ORC-VCRC and ORC–EERCIWB), respectively. As can be seen from the obtained simulation results, the $COP_{oval\text{-}(ORC–VCRC)}$ and $COP_{oval\text{-}(ORC–EERCIWB)}$ of the two combined systems improve with boiler temperature. Lower boiler exit temperatures (60°C) resulted in lower values of $COP_{oval\ (ORC–VCRC)}$ and $COP_{oval\text{-}(ORC–EERCIWB)}$, but both systems' COP_{oval} increased as the boiler exit temperature rose. This can be explained by the fact that as boiler temperature rises, the amount of heat added to the boiler increases as well, leading to an increase in COP_{oval} values.

It was discovered that the COP_{oval} obtained with the R600a in the ORC-VCRC and ORC-EERCIWB systems was 0.4476 and 0.5385, respectively, with the high boiler exit temperature (90°C). It should be mentioned that when the boiler exit temperature rises from 60°C to 90°C, the COP_{oval} values for the two systems increase from 0.2192 to 0.4476 and from 0.2637 to 0.5385, respectively.

The proposed hybrid ORC-EERCIWB system outperforms the hybrid ORC-VCRC system in terms of COP_{oval}, and the differences between the $COP_{oval\text{-}(ORC–VCRC)}$ and $COP_{oval\text{-}(ORC–EERCIWB)}$ are greater at high boiler exit temperatures than they are at low ones, according to a comparison of the results obtained for the two hybrid systems.

The findings show that, within the boiler temperature range taken into consideration, the COP_{oval} values increase by 20.30% when compared to those of the hybrid (ORC-VCRC) system. It is clear that the ORC-EERCIWB configuration offers a viable way to enhance the efficiency of the traditional ORC-VCRC system for recovering low-grade thermal energy.

Figure 5 illustrates the effects of the boiler exit temperature on the MkW of the combined refrigeration and power systems

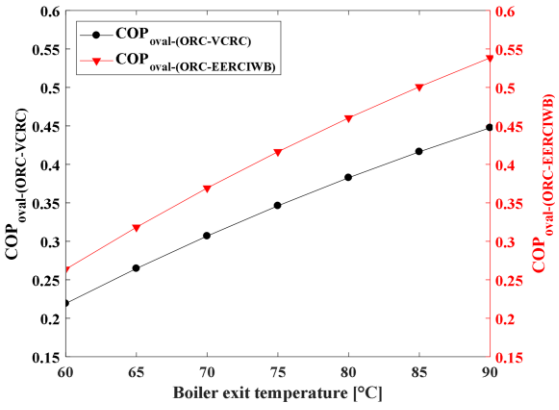


Fig. 4. Effect of boiler temperature on COP_{oval} of the ORC-VCRC and ORC-EERCIWB.

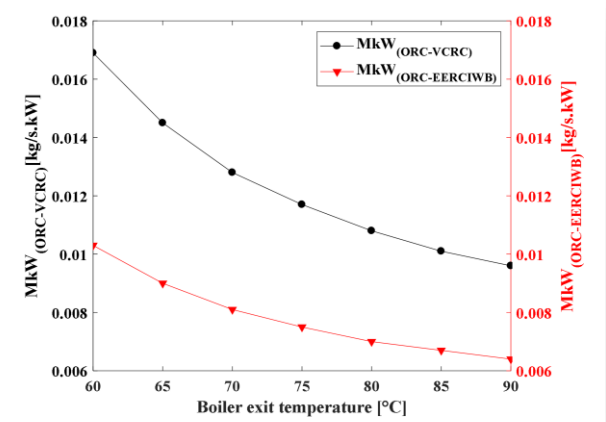


Fig. 5. Effect of boiler temperature on MkW in the ORC-VCRC and ORC-EERCIWB.

using R600a as a working fluid, $MkW_{(ORC–VCRC)}$ and $MkW_{(ORC–EERCIWB)}$, respectively.

The results presented in Fig. 5 demonstrate that the $MkW_{(ORC–VCRC)}$ and $MkW_{(ORC–EERCIWB)}$ generally decrease with boiler exit temperature. Specifically, higher values of $MkW_{(ORC–VCRC)}$ and $MkW_{(ORC–EERCIWB)}$ were observed at lower boiler exit temperatures (60°C); conversely, as boiler exit temperature increased, the MkW of both systems also decreased, which signifies that both investigated systems become more efficient in their use of the R600a to produce cooling. The comparison of simulation results for the two hybrid systems reveals that, within the boiler temperature range considered, the proposed hybrid system ORC-EERCIWB produced the lowest MkW compared to the hybrid system ORC-VCRC. This can be explained by the fact that the ORC-EERCIWB system needs less working fluid mass to deliver the same amount of cooling power as the ORC-VCRC system. Figure 5 shows that when the boiler exit temperature rises from 60°C to 90°C, the MkW values obtained for the two systems using the R600a decrease from 0.0169 to 0.0096 and from 0.0103 to 0.0064, respectively. According to the data, the MkW in the ORC-EERCIWB system is lower than in the ORC-VCRC system by 39.05 % to 33.33 %, leading to a higher COP_{oval}. Furthermore, it is worth noting that the ORC-EERCIWB configuration presents a viable option for lowering the MkW of the traditional ORC-VCRC system in order to recover low-grade thermal energy.

Figure 6 illustrates the effects of the boiler exit temperature on the EPR of both considered combined refrigeration and power systems using the hydrocarbon R600a as a working fluid. The figure indicates that when the boiler exit temperature rises, the EPR rises as well, where it is evident that the minimum EPR is reached at 60°C, while the maximum EPR is reached at 90°C. This rise can be explained by the fact that the saturation pressure of a fluid increases exponentially with its temperature, and the increase in the boiler exit temperature forces both systems to achieve a much higher pressure at the expander inlet. As a result, the EPR rises as well. As the boiler exit temperature rises from 60°C to 90°C, the EPR values obtained for the two systems using the hydrocarbon R600a increase from 1.6850 to 3.4951.

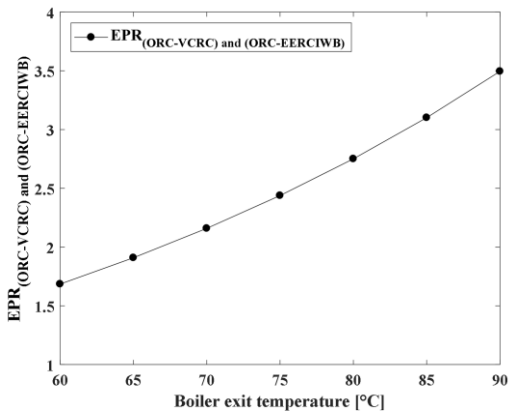


Fig. 6. Effect of boiler temperature on EPR in the ORC-VCRC and ORC-EERCIWB.

4.2. Effect of condensation temperature on the performance indicators

The following Figs. 7–10 show the effect of condensation temperature on the ORC-VCRC and ORC-EERCIWB systems' performances using the hydrocarbon R600a as a working fluid, while maintaining the other parameters constant (T_{boil} = 80°C, T_{evap} = 5°C).

Figure 7 shows the evolution of the $COP_{oval\text{-}(ORC–VCRC)}$ and $COP_{oval\text{-}(ORC–EERCIWB)}$ with the condensation temperature of the combined refrigeration and power systems, respectively. It is evident from looking at the profiles in the figure that the condensation temperature has a significant impact on the COP_{oval} of the two systems, with an increase in condensation temperature leading to a decrease in both $COP_{oval\text{-}(ORC–VCRC)}$ and $COP_{oval\text{-}(ORC–EERCIWB)}$. This is because, while the compressor's inlet temperature and pressure remain constant, the condenser temperature rises at the compressor's outlet, increasing pressure, enthalpy, and resulting in a decrease in COP_{oval} The maximum $COP_{oval\text{-}(ORC–VCRC)}$ and $COP_{oval\text{-}(ORC–EERCIWB)}$ values are reached at low condensation temperatures (30°C), whereas the minimum values are reached at higher condensation temperatures (55°C). It should be noted that when the condensation temperature increases from 30°C to 55°C, the COP_{oval} values for the two systems obtained with the R600a fall from 0.6952 to 0.1562 and from 0.8206 to 0.1966, respectively.

It is clear from a comparison of the suggested hybrid ORC-EERCIWB system's results with those of the hybrid ORC-VCRC system that the proposed hybrid system achieves a higher COP_{oval}. The findings show that when compared to hybrid ORC-VCRC values, the COP_{oval} values increase by 18.03% to 25.86%.

Figure 8 illustrates the effects of the condensation temperature on the MkW values of both systems, ORC-VCRC and ORC-EERCIWB, $MkW_{(ORC–VCRC)}$ and $MkW_{(ORC–EERCIWB)}$, respectively, using the hydrocarbon R600a as a working fluid.

It is evident that as the condensation temperature rises, the MkW of both systems increase. Figure 8 makes it clear that for the ORC-VCR and ORC-EERCIWB systems, a lower condensation temperature (30°C) resulted in a lower value for the $MkW_{(ORC–VCRC)}$ and $MkW_{(ORC–EERCIWB)}$; on the other hand, a higher condensation temperature (55°C) resulted in a higher value for the $MkW_{(ORC–VCRC)}$ and $MkW_{(ORC–EERCIWB)}$. When the condensation temperature rises from 30°C to 55°C, the MkW values of the two systems using the hydrocarbon R600a increase from 0.0070 to 0.0238 and from 0.0047 to 0.0150, respectively, which signifies that the efficiency of both investigated systems is decreasing. The following provides an explanation of the situation's cause. The rise of the condensation temperature forces the compressor units of the investigated systems to consume more power while simultaneously reducing the cooling capacity each kilogram of a refrigerant can provide. Consequently, the MkW increases substantially.

By comparing the results obtained for the hybrid ORC-VCRC system, it is observed that the MkW values of the proposed hybrid ORC-EERCIWB system are lower than those of the ORC-VCRC system across the entire condensation temperature range, and the variations between the values of $MkW_{(ORC–VCRC)}$ and $MkW_{(ORC–EERCIWB)}$ are greater at high condenser temperatures than at low ones. The following provides an explanation of the situation's cause. When the condenser temperature rises, the compressor in the traditional (ORC-VCRC) system is penalised more severely as it must overcome a much larger pressure gap. Consequently, the performance advantage of the novel system is most pronounced under these demanding conditions,

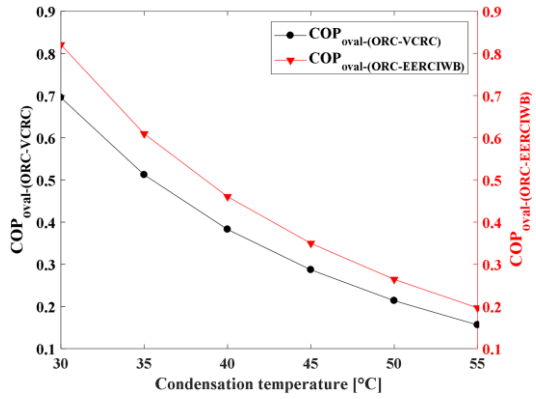


Fig. 7. Effect of condensation temperature on COP_{oval} of the ORC-VCRC and ORC-EERCIWB.

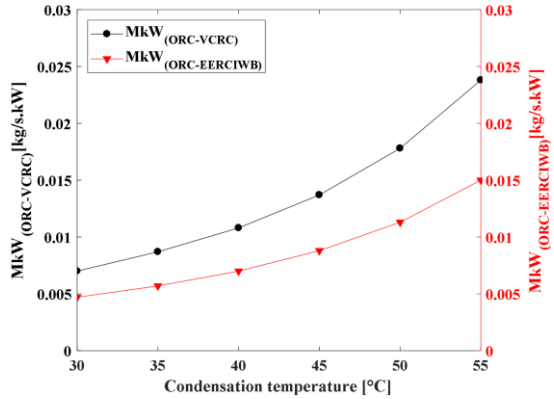


Fig. 8. Effect of condensation temperature on MkW of the ORC-VCRC and ORC-EERCIWB.

where its compressor unit starts at a higher inlet pressure compared to the traditional system, which leads to a sharp decrease in the working fluid mass flow required for each unit of cooling (MkW).

According to the obtained data, the MkW in the ORC-EERCIWB system is lower than in the ORC-VCRC system by 32.85% to 36.97%, leading to a higher COP_{oval}.

Figure 9 depicts the evolution of EPR as a function of condensation temperature for both systems (ORC-VCRC and ORC-EERCIWB) using the hydrocarbon R600a as a working fluid. It is clear that when the condensation temperature rises, the EPR decreases. The reason for this behaviour is that a higher condenser temperature forces a higher condensation pressure. Consequently, the expander unit faces a higher outlet pressure while its inlet pressure, which is set by the boiler temperature, is unchanged. This reduced pressure difference across the expander unit results in a smaller expansion in the volume of the working fluid, which directly leads to a lower EPR for the investigated systems. The EPR values for both systems increase from 3.6239 to 1.8586 as the condensation temperature rises from 30 to 55°C.

Figure 10 shows the impact of changes in condensation temperatures on the CMR values of the ORC-VCRC and ORC-EERCIWB combined refrigeration and power systems, $CMR_{(ORC–VCRC)}$ and $CMR_{(ORC–EERCIWB)}$, respectively. The figure indicates that both $CMR_{(ORC–VCRC)}$ and $CMR_{(ORC–EERCIWB)}$ increase as the condenser temperature rises. This is because the compressor's discharge pressure in the investigated systems is determined by the condensing temperature. As the condensation temperature rises, the pressure the compressor must push against significantly increases. On the other hand, the pressure at the inlet of the compressor remains constant. Because of these two effects, the compressors of the investigated systems have to raise the gas from a fixed suction pressure to a much higher discharge pressure. As a result, the CMR increases substantially. This places a greater thermodynamic load on the compressors of the investigated systems, reducing their efficiency. The CMR values obtained for both systems using the R600a increase from 2.1675 to 4.1398 and from 1.3785 to 2.4205, respectively, as the condensation temperature increases from 30°C to 55°C. It is also noticeable

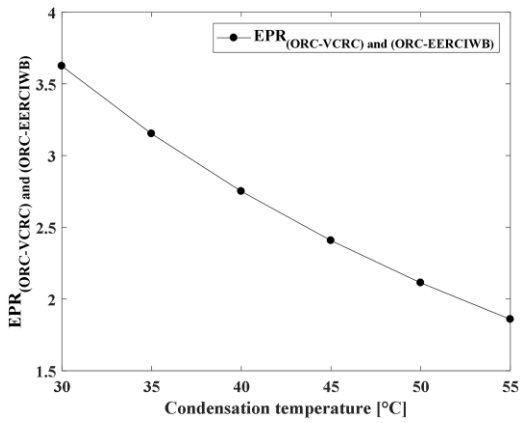


Fig. 9. Effect of condensation temperature on EPR in the ORC-VCRC and ORC-EERCIWB.

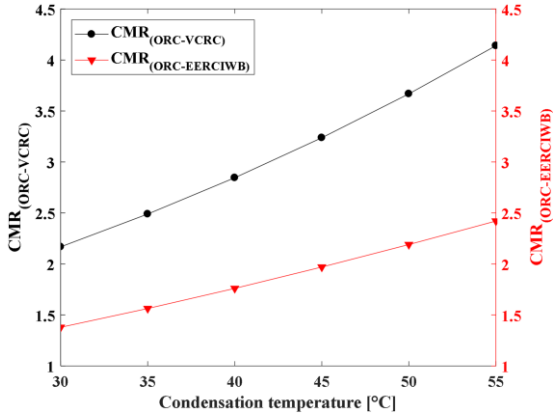


Fig. 10. Effect of condensation temperature on CMR in the ORC-VCRC and ORC-EERCIWB.

that the minimum $CMR_{(ORC–VCRC)}$ and $CMR_{(ORC–EERCIWB)}$ are attained at 30°C, but the maximum $CMR_{(ORC–VCRC)}$ are at 55°C.

Upon comparing the results obtained for the two systems, it can be observed that the ORC-VCRC system achieves the maximum CMR, while the proposed ORC-EERCIWB system achieves the minimum CMR. The new system has a lower MkW because its compressor unit starts at a higher inlet pressure, precompressed by the booster unit and ejector device. This proposed architecture results in a much lower compression ratio. Specifically, the CMR in the ORC-EERCIWB system is reduced by 36.40% to 41.53% compared to the ORC-VCRC system.

4.3. Effect of evaporation temperature on performance indicators

The following Figs. 11–14 show the impact of evaporation temperature on the ORC-VCRC and ORC-EERCIWB performances using the hydrocarbon R600a as a working fluid, while maintaining the other parameters constant (T_{boil} = 80°C, T_{cond} = 40°C).

The effects of the evaporation temperature on the COP_{oval} of the two systems, ORC-VCRC and ORC-EERCIWB, respectively, are displayed in Fig.11. According to the figure, the simulation results demonstrate that the evaporation temperature has

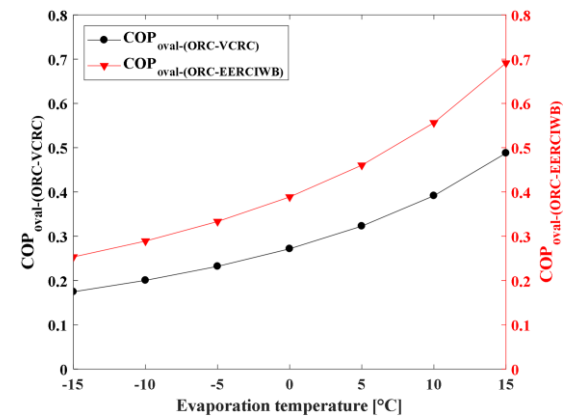


Fig. 11. Effect of evaporation temperature on COP_{oval} of the ORC-VCRC and ORC-EERCIWB.

a significant impact on the overall COP of both systems. Specifically, increasing the evaporation temperature significantly increases the COP_{ovals} of both systems. This, in turn, improves the overall COP of the combined refrigeration and power systems. An increase in temperature within the system's evaporator leads to an improvement in cooling capacity due to the resulting increase in the refrigeration effect. Both effects boost the overall COP of the systems, ORC-VCRC and ORC-EERCIWB. As the evaporation temperature reaches 15°C, the COP of the two systems, i.e. $COP_{oval\text{-}(ORC–VCRC)}$ and $COP_{oval\text{-}(ORC–EERCIWB)}$, increases, as shown in Fig.11. The COP_{oval} obtained with the hydrocarbon R600a in the ORC-VCRC system and ORC-EERCIWB system is 0.4877 and 0.6912, respectively. It should be noted that as the evaporation temperature rises from –15°C to 15°C, the determined COP_{oval} values of the two systems rise from 0.1745 to 0.4877 and 0.2532 to 0.6912, respectively.

When the overall COP of the two systems are compared, it is observed that the ORC-EERCIWB system is the most efficient, where the ORC-EERCIWB system reveals the highest COP_{oval} values by 45.10% to 41.72% than that in the ORC-VCRC system. This improvement is due to a gain in refrigeration in the ORC-EERCIWB system compared to the ORC–VCRC system.

Figure 12 shows how the evaporation temperature affects the MkW for R600a in the ORC-VCRC and ORC-EERCIWB systems. It is evident from the graphs that the MkW of both systems decreases, which signifies that the refrigeration of both investigated systems becomes fundamentally more efficient with the rise of the evaporation temperature. This variation can be explained by the fact that, as the evaporator temperature rises, a higher evaporator pressure reduces the compressor's workload in the investigated systems, allowing it to circulate more mass flow of a working fluid using the same power input for both systems. Simultaneously, the amount of cooling each kilogram of the working fluid can provide increases. This results in the cooling capacity growing much faster than the working fluid mass flow rate, causing the mass flow per unit of cooling to fall. When the evaporation temperature rises from –15°C to 15°C, the MkW values of the two systems, ORC-VCRC and ORC-EERCIWB, decrease from 0.0227 to 0.0102 and from 0.0119 to 0.0051, respectively.

Comparing the MkW simulation results for the two systems, it is found that the ORC-VCRC system achieves the maximum MkW, while the proposed ORC-EERCIWB system achieves the minimum MkW. This can be explained by the fact that for the same cooling power output, the proposed (ORC-EERCIWB) system requires a lower mass flow rate of refrigerant than the traditional (ORC-VCRC) system. The MkW in the ORC-EERCIWB system is lower than that of the ORC-VCRC system by 47.6% (at lower evaporation temperature) to 50% (at higher evaporation temperature), and the differences between the values of $MkW_{(ORC–VCRC)}$ and $MkW_{(ORC–EERCIWB)}$ are greater at low evaporation temperatures than they are at high evaporation temperatures.

Figure 13 represents the effect of the evaporation temperature on the CMR of the combined refrigeration and power systems, ORC-VCR and ORC-EERCIWB, respectively, using R600a as a working fluid. It is observed from the figure that the two curves of $CMR_{(ORC–VCRC)}$ and $CMR_{(ORC–EERCIWB)}$ decrease with an increase in evaporation temperature. This is justified as the temperature and pressure are kept constant at the outlet of the compressors of both systems, and an increase in the evaporation temperature causes the rise of pressure and enthalpy at the inlet of the compressor, which leads to the decrease in CMR of both systems as the evaporation temperature rises. The figure also shows that when the evaporation temperature rises from –15°C to 15°C, the CMR values for the two investigated systems using the R600a increase from 5.9651 to 2.0511 and from 3.3708 to 1.3056, respectively.

When the results for the two systems are compared, it can be seen that the ORC-VCRC system achieves the maximum CMR, while the proposed ORC–EERCIWB system achieves the minimum CMR. This difference can be explained as follows: The compressor unit of the traditional system (ORC-VCRC) must raise pressure from the very low evaporator pressure all the way up to the condenser pressure. In contrast, the investigated new (ORC-EERCIWB) system uses a booster unit and an ejector device to compress the working fluid before it reaches the main compressor unit of the proposed system. The booster unit elevates the pressure from the evaporator unit to a higher intermediate pressure, and the ejector device further increases it. Therefore, the main compressor unit in the proposed system starts

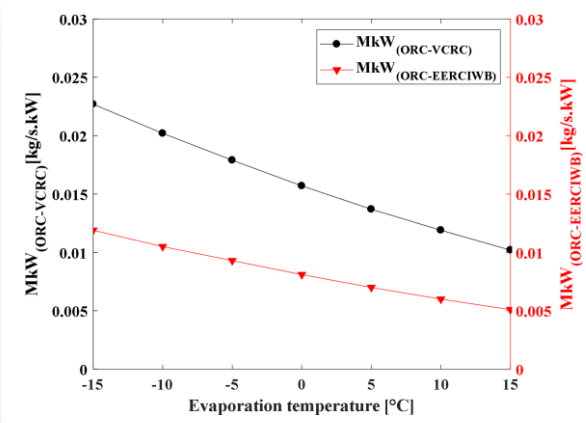


Fig. 12. Effect of evaporation temperature on MkW in the ORC-VCR and ORC-EERCIWB.

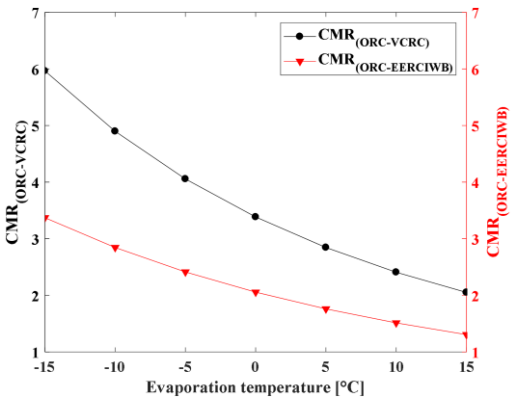


Fig. 13. Effect of evaporation temperature on CMR in the ORC–VCRC and ORC–EERCIWB.

from a significantly higher inlet pressure, resulting in a much lower and more efficient CMR. The CMR in the ORC-EERCIWB system is lower than that of the ORC-VCRC system by 43.49% to 36.34%, and the differences in values between $CMR_{(ORC–VCRC)}$ and $CMR_{(ORC–EERCIWB)}$ are greater at low evaporation temperatures than they are at high evaporation temperatures.

5. Conclusions

In the present work, a unique setup for a combined power-cooling (ORC–EERCIWB) system that is activated by low-grade thermal energy is proposed and investigated.

The preferred architecture for the power-cooling system is a combined organic Rankine cycle (ORC) and an ejector-expansion refrigeration cycle that improves with a booster (EERCIWB) unit.

The suggested system employs the R600a as a working fluid. The energy analysis is performed to analyse the suggested system's performance indicators by comparing it to the classic power-cooling (ORC-VCRC) system, which is widely utilised, under the same operating conditions. Furthermore, an analysis and discussion are undertaken on the impact of operational factors, notably the boiler, condensation and evaporation temperatures, on the performance indicators of the ORC-EERCIWB and ORC-VCRC power-cooling systems.

The energy analysis and comparison of the ORC-EERCIWB and ORC-VCRC systems were carried out at temperatures ranging from 60°C to 90°C for the boiler, 30°C to 55°C for condensation and −15°C to 15°C for evaporation.

The simulation results include the following performance indicators: cooling capacity, expansion ratio, compression ratio and overall coefficient of performance.

Overall, the numerical findings show that the ORC-EERCIWB system outperformed the ORC-VCRC system in terms of performance. Furthermore, the three thermodynamic parameters, the boiler, condensation and evaporation temperatures, have a considerable impact on both systems' expansion ratio, compression ratio and performance indicators.

Based on the obtained results for the examined configurations (ORC-VCRC and ORC-EERCIWB), the following concluding remarks have been set:

- The thermodynamic performances of both systems are significantly influenced by the temperatures of the boiler, condenser and evaporator.
- For the two systems under investigation, when both the boiler temperature and the evaporation temperature rise, the overall coefficient of performance rises, and the working fluid mass flow rate per kW of cooling capacity falls.
- As the condensation temperature rises, the overall coefficient of performance for the two systems examined decreases, and the working fluid mass flow rate per kW of cooling capacity rises.
- The expansion ratio in the expander for the two systems under study rises as the boiler temperature rises and falls as the condensation temperature rises.
- The compression ratio in the compressor for the two systems under investigation increases as the condensation temperature rises and falls as the evaporation temperature rises.
- Boiler temperature was the most crucial variable for both systems, followed by evaporator and condenser temperatures.
- When the same operating conditions are taken into account, the ORC-EERCIWB system performs better overall than the ORC-VCRC system and has a lower working fluid mass flow rate per kW of cooling capacity, as well as a compression ratio in the compressor.
- At a boiler exit temperature of 90°C, the maximum coefficient of performance values for both systems were found to be 0.5385 and 0.4476, respectively; the value of the ORC-EERCIWB system increased by 20.30% compared to that of the ORC-VCRC system.
- At a boiler exit temperature of 90°C, the minimum working fluid mass flow rates per kW of cooling capacity were found to be 0.0064 and 0.0096, respectively, where the value of ORC-EERCIWB dropped by 33.33% compared to ORC-VCRC.
- At an evaporation temperature of 15°C, the maximum coefficient of performance values for both systems were found to be 0.6912 and 0.4877, respectively; the value of the ORC-EERCIWB system increased by 41.72% compared to the ORC-VCRC system.
- For an evaporation temperature of 15°C, the minimum working fluid mass flow rates per kW of cooling capacity of the two systems were found to be 0.0051 and 0.0102, respectively, with the value of the ORC-EERCIWB system decreased by 50% compared to that of the ORC-VCRC system.

The study's findings promote future research on unique configurations of combined power-cooling utilisation that incorporate the two-phase ejector-expander in cooling cycles. Based on the findings, it can be concluded that the usage of the EERCIWB, which is meant to be utilised for combined power-cooling systems and is commonly used to replace VCRC in standard combined power-cooling systems, is effective.

References

[1] Hung, T.C., Wang, S.K., Kuo, C.H., Pei, B.S., & Tsai, K.F. (2010). A study of organic working fluids on system efficiency of an ORC using low-grade energy sources. *Energy*, 35(3), 1403–1411. doi: 10.1016/j.energy.2009.11.025

[2] Drescher, U., & Brüggemann, D. (2007). Fluid selection for the Organic Rankine Cycle (ORC) in biomass power and heat plants. *Applied Thermal Engineering*, 27(1), 223–228. doi: 10.1016/j.applthermaleng.2006.04.024

[3] Guo, C., Du, X., Yang, L., & Yang, Y. (2014). Performance analysis of organic Rankine cycle based on location of heat transfer pinch point in evaporator. *Applied Thermal Engineering*, 62(1), 176–186. doi: 10.1016/j.applthermaleng.2013.09.036

[4] Rafique, M.M. (2020). Evaluation of metal–organic frameworks as potential adsorbents for solar cooling applications. *Applied System Innovation*, 3(2), 26. doi: 10.3390/asi3020026

[5] Bellos, E., & Tzivanidis, C. (2020). Financial optimization of a solar-driven organic Rankine cycle. *Applied System Innovation*, 3(2), 23. doi: 10.3390/asi3020023

[6] Deng, J., Wang, R.Z., & Han, G.Y. (2011). A review of thermally activated cooling technologies for combined cooling, heating and power systems. *Progress in Energy and Combustion Science*, 37(2), 172–203. doi: 10.1016/j.pecs.2010.05.003

[7] Wang, H., Peterson, R., & Herron, T. (2011). Design study of configurations on system COP for a combined ORC (organic Rankine cycle) and VCC (vapor compression cycle). *Energy*, 36(8), 4809–4820. doi: 10.1016/j.energy.2011.05.015

[8] Pektezel, O., & Acar, H.I. (2019). Energy and exergy analysis of combined organic Rankine cycle-single and dual evaporator vapor compression refrigeration cycle. *Applied Sciences*, 9(23), 5028. doi: 10.3390/app9235028

[9] Sun, W., Yue, X., & Wang, Y. (2017). Exergy efficiency analysis of ORC (Organic Rankine Cycle) and ORC-based combined cycles driven by low-temperature waste heat. *Energy Conversion and Management*, 135, 63–73. doi: 10.1016/j.enconman.2016.12.042

[10] Xu, F., Goswami, D.Y., & Bhagwat, S.S. (2000). A combined power/cooling cycle. *Energy*, 25(3), 233–246. doi: 10.1016/S0360-5442(99)00071-7

[11] Zhang, N., & Lior, N. (2007). Methodology for thermal design of novel combined refrigeration/power binary fluid systems. *International Journal of Refrigeration*, 30(6), 1072–1085. doi: 10.1016/j.ijrefrig.2006.12.005

[12] Vijayaraghavan, S., Goswami, D.Y. (2003). On evaluating efficiency of a combined power and cooling cycle. *Journal of Energy Resources Technology*, 125(3), 221–227. doi:10.1115/1.1595110.

[13] Aphornratanaa, S., & Sriveerakul, T. (2011). Analysis of a combined Rankine–vapour–compression refrigeration cycle. *Energy Conversion and Management*, 51(12), 2557–2564. doi: 10.1016/j.enconman.2010.04.016

[14] Molés, F., Navarro-Esbrí, J., Peris, B., Mota-Babiloni, A., & Kontomaris, K. (2015). Thermodynamic analysis of a combined organic Rankine cycle and vapor compression cycle system activated with low temperature heat sources using low GWP fluids. *Applied Thermal Engineering*. 87, 444–453. doi: 10.1016/j.applthermaleng.2015.04.083

[15] Li, H., Bu, X., Wang, L., Long, Z., & Lian, Y. (2013). Hydrocarbon working fluids for a Rankine cycle powered vapor compression refrigeration system using low-grade thermal energy. *Energy and Buildings*, 65, 167–172. doi: 10.1016/j.enbuild.2013.06.012

[16] Asim, M., Leung, M.K.H., Shan, Z., Li, Y., Leung, D.Y.C., & Ni, M. (2017). Thermodynamic and Thermo-economic Analysis of Integrated Organic Rankine Cycle for Waste Heat Recovery from Vapor Compression Refrigeration Cycle. *Energy Procedia*, 143, 192–198. doi: 10.1016/j.egypro.2017.12.670

[17] Saleh, B. (2016). Parametric and working fluid analysis of a combined organic Rankine-vapor compression refrigeration system activated by low-grade thermal energy. *Journal of Advanced Research*, 7(5), 651–660. doi: 10.1016/j.jare.2016.06.006

[18] Lizarte, R., Palacios-Lorenzo, M.E., & Marcos, J.D. (2017). Parametric study of a novel organic Rankine cycle combined with a cascade refrigeration cycle (ORC-CRS) using natural refrigerants. *Applied Thermal Engineering*, 127, 378–389. doi: 10.1016/j.applthermaleng.2017.08.063

[19] Cihan, E. (2014). Cooling Performance Investigation of a System with an Organic Rankine Cycle Using Waste Heat Sources. *Journal of Thermal Science and Technology*, 34(1), 101–109. https://dergipark.org.tr/en/pub/isibted/issue/33968/375961 (in Turkish)

[20] Bu, X., Wang, L., & Li, H. (2013). Performance analysis and working fluid selection for geothermal energy-powered organic Rankine-vapor compression air conditioning. *Geothermal Energy*, 1, 2. doi: 10.1186/2195-9706-1-2

[21] Wang, H., Peterson, R., Harada, K., Miller, E., Ingram-Goble, R., Fisher, L., Yih, J., & Ward, C. (2011). Performance of a combined organic Rankine cycle and vapor compression cycle for heat activated cooling. *Energy*, 36(1), 447–458. doi: 10.1016/j.energy.2010.10.020

[22] Yue, C., You, F., & Huang, Y. (2016). Thermal and economic analysis of an energy system of an ORC coupled with vehicle air conditioning. *International Journal of Refrigeration*, 64, 152–167. doi: 10.1016/j.ijrefrig.2016.01.005

[23] Hu, B., Guo, J., Yang, Y., & Shao, Y. (2022). Performance analysis and working fluid selection of organic Rankine steam compression air conditioning driven by ship waste heat. *Energy Reports*, 8(S3), 194–202. doi: 10.1016/j.egyr.2022.01.094.

[24] Khatoon, S., Almefreji, N.M.A., & Kim, M.H. (2021). Thermodynamic study of a combined power and refrigeration system for low-grade heat energy source. *Energies*, 14(2), 410. doi: 10.3390/en14020410

[25] Kim, K.H., & Perez-Blanco, H. (2015). Performance analysis of a combined organic Rankine cycle and vapor compression cycle for power and refrigeration cogeneration. *Applied Thermal Engineering*, 91, 964–974. doi: 10.1016/j.applthermaleng.2015.04.062

[26] Jeong, J., & Kang, Y.T. (2004). Cycle of a refrigeration cycle driven by refrigerant steam turbine. *International Journal of Refrigeration*, 27(1), 33–41. doi:10.1016/S0140-7007(03)00101-4.

[27] Egrican, A.N., & Karakas, A. (1986). Second law analysis of a solar powered Rankine cycle/vapor compression cycle. *Journal of Heat Recovery Systems*, 6(2), 135–141. doi: 10.1016/0198-7593(86)90073-1

[28] González, J., Llovell, F., Matías Garrido, J., & Quinteros-Lama, H. (2023). A study of the optimal conditions for organic Rankine cycles coupled with vapour compression refrigeration using a rigorous approach based on the Helmholtz energy function. *Energy*, 285, 129554. doi: 10.1016/j.energy.2023.129554

[29] Wu, D., Hu, B., & Wang, R.Z. (2021). Vapor compression heat pumps with pure Low-GWP refrigerants. *Renewable and Sustainable Energy Reviews*, 138, 110571. doi: 10.1016/j.rser.2020.110571

[30] Maalem, Y., & Madani, H. (2025). Performance Characteristics Investigation of a Solar Rankine Cycle Powered Air Conditioning System for Residential Buildings using Low GWP Working Fluids. *Archives of Thermodynamics*, 46(1), 97–107. doi: 10.24425/ather.2025.154184

[31] Elbel, S., & Lawrence, N. (2016). Review of recent developments in advanced ejector technology. *International Journal of Refrigeration*, 62, 1–18. doi: 10.1016/j.ijrefrig.2015.10.031

[32] Chen, X., Omer, S., Worall, M., & Riffat, S. (2013). Recent developments in ejector refrigeration technologies. *Renewable and Sustainable Energy Reviews*, 19, 629–651. doi: 10.1016/j.rser.2012.11.028

[33] Hacipaşaoğlu, S.G., & Öztürk, I. (2023). Energy and exergy analysis in the ejector expansion refrigeration cycle under optimum conditions. *International Advanced Researches and Engineering Journal*, 7(1), 23–34. doi: 10.35860/iarej.1171637

[34] Maalem, Y., Fedali, S., Madani, H., & Tamene, Y. (2020). Performance analysis of ternary azeotropic mixtures in different vapor compression refrigeration cycles. *International Journal of Refrigeration*, 119, 139–151. doi: 10.1016/j.ijrefrig.2020.07.021

[35] Leila, B., Fedali, S., Bougriou, C., & Madani, H. (2022). Influence of azeotropic binary mixtures on single-stage refrigeration system performance. *High Temperatures–High Pressures*, 51(4), 319–339. doi: 10.32908/hthp.v51.1185

[36] Maalem, Y., Tamene, Y., & Madani, H. (2023). Performances Investigation of the Eco-friendly Refrigerant R13I1 used as Working Fluid in the Ejector-Expansion Refrigeration Cycle. *International Journal of Thermodynamics*, 26(3), 25–35. doi: 10.5541/ijot.1263939

[37] Mehemmai, M., Grine, H., Madani, H., & Bougriou, C. (2023). Performance analysis of ejector refrigeration cycle with zeotropic mixtures. *International Journal of Thermofluid Science and Technology*, 10(4), 100404. doi: 10.36963/IJTST.2023100404

[38] Abdou, C., Madani, H., & Hasseine, A. (2023). Study of the performances of an ejector refrigeration cycle using CO2-based mixtures in subcritical and transcritical mode. *International Journal of Thermofluid Science and Technology*, 10(3), 100304. doi: 10.36963/IJTST.2023100304

[39] Maalem, Y., & Madani, H. (2024). Energetic performance investigation of ejector air conditioning cycles using the environment friendly gas R161 (Fluoroethane) as substitute to the phase-out R22 (Chlorodifluoromethane). *International Journal of Thermofluid Science and Technology*, 11(2), 110201. doi: 10.36963/IJTST.2024110201

[40] Maalem, Y., Boulebbina. C, & Madani, H. (2025). Enhancement of the capabilities of energy and exergy efficiencies of low cascade cooling process. *International Journal of Ambient Energy*, 46(1), 2574415. doi: 10.1080/01430750.2025.2574415

[41] Rostamnejad Takleh, H., & Zare, V. (2019). Performance improvement of ejector expansion refrigeration cycles employing a booster compressor using different refrigerants: Thermodynamic analysis and optimization. *International Journal of Refrigeration*, 101, 56–70. doi: 10.1016/j.ijrefrig.2019.02.031

[42] Liang, Y., Yu, Z., & Li, W. (2019). A waste heat-driven cooling system based on combined organic Rankine and vapour compression refrigeration cycles. *Applied Sciences*, 9(20), 4242. doi: 10.3390/app9204242

[43] Sumeru, K., Nasution, H., & Ani, F.N. (2012). A review on two-phase ejector as an expansion device in vapor compression refrigeration cycle. *Renewable and Sustainable Energy Reviews*, 16(7), 4927–4937. doi: 10.1016/j.rser.2012.04.058

[44] Maalem, Y., & Madani, H. (2025). Performance investigation of an automotive hybrid air-conditioning system without and with an internal heat exchanger (IHX) using R1234ze (E) as substitute for R134a. *International Journal of Automotive Science and Technology*, 9(2), 194–207. doi: 10.30939/ijastech.1594100